Hydrogen Assisted Catalytic Biomass Pyrolysis for Green Fuels

Stummann, Magnus Zingler

Publication date:
2018

Document Version
Publisher's PDF, also known as Version of record

DTU Chemical Engineering
Department of Chemical and Biochemical Engineering

Hydrogen Assisted Catalytic Biomass Pyrolysis for Green Fuels

Magnus Zingler Stummann

Hydrogen Assisted Catalytic Biomass Pyrolysis for Green Fuels

PhD Thesis

Author:
Magnus Zingler Stummann

Technical University of Denmark
Department of Chemical and Biochemical Engineering
Research Center: CHEC
30th November 2018

Preface

This thesis has been written as part of the Ph.D. project by Magnus Zingler Stummann carried out in the period from October 2015 to December 2018 at the Technical University of Denmark (DTU) at the Department of Chemical and Biochemical Engineering (KT) in the research group Combustion and Harmful Emission Control (CHEC). Professor Anker Degn Jensen from KT has been the main supervisor on the project, with senior scientist Peter Arendt Jensen (KT), assistant professor Martin Høj (KT), and Senior R&D Manager Dr. Jostein Gabrielsen (Haldor Topsøe A/S) as co-supervisors.
I greatly acknowledge funding from DTU and the Danish Council for Strategic Research (now Innovation Fund Denmark).

I would like to thank all the people whom have been involved in this project and helped shaping it. First I would like to thank Anker Degn Jensen for being my mentor within the field of catalysis for the last 5 years. You have always being willing to discuss all kinds of problems and you never got tired of hearing me complain about the setup when it did not work. I would also like to thank Martin Høj who designed the catalytic hydropyrolysis setup and with whom I worked closely with during the commissioning of the setup. Peter Arendt Jensen has also been very helpful and we have had many interesting discussion on how to optimize the setup. Jostein Gabrielsen was also my supervisor during my bachelor and master thesis and his deep insight into refinery has been of great value.

I would also like to thank the KT workshop, without their support and great expertise we would never have been able to make the setup work. I will particularly thank Søren Vestergaard Madsen and Jens Henry Poulsen who constructed most of the catalytic hydropyrolysis setup and with whom I have had many fruitful technical discussions.

This Ph.D. has been in close collaboration with several researchers at Haldor Topsøe A/S. I will therefore like to thank Asger Baltzer Hansen and Peter Wiwel for conducting several advanced oil analysis on my samples. You have done an amazing work and always been very helpful. I will also like to thank Bente Davidsen who analyzed my samples with SEM-EDS, I think that these results are some of the most important results in my Ph.D. and I am very thank full for your great contribution. Lars Pilsgaard Hansen analyzed my samples with HAADF-STEM, which besides producing fascinating images also gave us a unique insight into the transfer of alkali metal from the biomass to the catalyst. I have always enjoyed our discussions from which I have learnt a lot about catalyst characterization and I greatly appreciate all your good and constructive comments, which has been very helpful during writing of the articles. I will also like to thank Søren Birk Rasmussen and Pablo Beato who has assisted me with Raman spectroscopy. I also thank Nadia Luciw Ammitzbøll for fruitful discussions, Caroline Piper Hem for assistant with X-ray diffraction measurements, Aino Nielsen for technical assistant with Raman spectroscopy, Heidie Christina Baes Husby for assistants with sending samples to DB lab, and Vivian Grindsted for analyzing my samples with oxygen and sulfur specific GC-AED. Furthermore, I will also like to acknowledge the Inorganic Analysis Department at Haldor Topsøe A/S for elemental analysis of the fresh and spent catalysts, and the Organic Analysis Department for analysis of the organic phases.

I also had the pleasure to supervise Christian Bækhøj Schandel and Elaine Elevera, which helped me to develop as a researcher and I am very pleased that much of your great work has found its way to this thesis and several articles.

I would also like to thank all my colleagues at CHEC, for many good conversations and fruitful discussions. A special thanks goes to Trine Dabros Arndal who also has been working within the field of deoxygenation of bio-oil and with whom I wrote a review article. I am grateful for your help with catalyst preparation and GC-MS/FID. I will also thank my friends Anna Leth-Espensen, Line Riis Christensen and Steen Riis Christensen whom I have had the privilege of calling my friends since we started at DTU 8 years ago. Line Riis Christensen, whom I also have known since continuation school, convinced me that I should study at DTU, which I am very thankful for. A special thanks also goes to my friend and officemate Kasper Hartvig Lejre, I can not image a better officemate than you.

Last but not least heartfelt thanks are directed to my dear wife Kjestine, who have endured listening to many monologues about catalytic hydropyrolysis and experimental problems.

Sincerely,
Magnus Zingler Stummann

Abstract

This thesis is dedicated to the investigation and optimization of catalytic hydropyrolysis of biomass for the production of renewable hydrocarbon fuels. This has been achieved through studying the effect of process conditions and the type of catalyst in the fluid bed hydropyrolysis reactor.

The experiments were conducted in a bench scale setup up, where up to 1 kg of biomass, mainly beech wood, was continuously fed into a fluid bed reactor in a high pressure hydrogen atmosphere containing a catalytic material, which produces char, light gasses (CO_x, C_1-C_3), water, and oil. The char was removed with a filter and the vapors were sent to a deep hydrodeoxygenation (HDO) reactor, which could be by-passed, followed by a 3 step condensation system. Support materials, commercial catalysts, and catalysts prepared in-house were tested in the experimental setup and the produced organic phases were extensively analyzed e.g. gas chromatography (GC) with atomic emission detector (AED) and GC×GC-mass spectrometry (MS)/flame ionization detector (FID). The prepared fresh and spent catalysts were characterized with NH_3 temperature programmed desorption (TPD), X-ray diffraction (XRD), Raman spectroscopy, electron microscopy (SEM and HAADF-STEM) and the surface area and elemental composition were determined.

An oxygen free (<0.01 wt.%) oil with a condensable organic (condensed organics and C_{4+} in gas) yield of 16.6-22.5 wt.% dry ash free (daf) was obtained using a commercial $CoMoS/MgAl_2O_4$ catalyst supplied by Haldor Topsøe A/S in the fluid bed reactor (365-511°C) and a $NiMoS/Al_2O_3$ catalyst in the HDO reactor (350-400°C) and operating at a hydrogen pressure of 15.9 bar or higher. GC×GC-MS/FID of the condensed organic phase showed that it consisted of 42-75 % FID-area aromatics. and that the concentration was kinetically controlled at fluid bed temperatures below 430°C and controlled by the thermodynamics at higher temperatures. Decreasing the hydrogen partial pressure to 8.0 and 3.0 bar increased the oxygen content in the organic phase to 3.3 and 7.8 wt.% dry basis (db), respectively, where the remaining oxygen was mainly in the form of phenols. The maximum concentration of monoaromatics (57 % FID-area) was detected at 15.9 bar and further increasing the hydrogen pressure decreased the monoaromatics concentration forming naphthenes. This indicated that the concentration of monoaromatics is controlled by the thermodynamics at hydrogen partial pressures of 15.9 bar and higher, while the concentration is controlled by the kinetics for conversion of phenols at lower hydrogen partial pressures.

Using pure support materials ($MgAl_2O_4$ and H-ZSM-5-Al_2O_3) in the fluid bed reactor increased the char and coke yield up to 21.1 wt.% daf, while it was between 11.4 and 13.1 wt.% daf when using different commercial catalysts. Having a catalyst in the fluid bed reactor decreases the degree of coking due to stabilization of the reactive oxygenates by hydrogenation. Furthermore, an energy recovery of up to 58 % in the condensable organics was obtained when using bog iron, a cheap and non-toxic natural mineral, in the fluid bed reactor, while the highest energy recovery obtained with a commercial catalyst was 54 % ($NiMoS/H\text{-}ZSM\text{-}5\text{-}Al_2O_3$). This indicates that bog iron can replace the more expensive and toxic Co(/Ni)Mo catalysts in catalytic hydropyrolysis.

To investigate the difference in deoxygenation activity, selectivity and product composition for sulfided CoMo, NiMo, and MoS, these catalysts were prepared, using $MgAl_2O_4$ as support, and tested in the fluid bed reactor without the HDO reactor. This showed that the NiMo catalyst had the highest hydrogenation, cracking, decarboxylation and/or decarbonylation activity, while the Mo catalyst had the lowest. The carbon recovery in the condensable organics for the NiMo catalyst was 37 %, while it was 39 % for both the CoMo

and Mo catalyst. The CoMo catalyst had the highest hydrodeoxygenation activity and the Mo the lowest, thus the CoMo catalyst is considered to be the most suitable catalyst for the fluid bed reactor.

Varying the CoMo loading between 4.0 and 12.0 wt.% and using $MgAl_2O_4$ as support showed that increasing the CoMo loading increased the yield of light gasses (C_1-C_3), decreased the oxygen content from 9.0 to 4.7 wt.% db, but decreased the carbon recovery of the condensable organics from 39 to 37 %. The effect of varying the catalyst acidity was also investigated by using a mixture of zeolite and alumina (H-ZSM-5-Al_2O_3) instead of $MgAl_2O_4$, while maintaining a CoMo concentration at approximately 4.0-4.3 wt.%. This showed that using a more acidic support increases the hydrocracking activity and decreases the oxygen content in the condensed organic phase from 9.0 wt.% db to between 5.2 and 6.1 wt.% db, depending on the zeolite to alumina ratio. However, the carbon recovery was not affected by the acidity, most likely because the zeolite increases the alkylation activity, which increases the aromatic yield through incorporation of light oxygenates and olefins into the condensable organics.

In order to test the process stability a 5 day semi-continuous experiment was conducted with a commercial CoMoS/$MgAl_2O_4$ catalyst in the fluid bed reactor and a NiMoS/Al_2O_3 catalyst in the HDO reactor. The total time on stream was 16.2 h and approximately 5 kg of biomass was used with 50 g of catalyst. The condensable organic yield was fairly stable during the experiment and varied between 21.2 and 23.2 wt.% daf, but the oxygen content in the organic phase increased during the experiment from 40 to 2832 wt-ppm, indicating that some deactivation of the catalyst in fluid bed and the HDO reactor may have occurred. It should also be noted that 40 wt.% of the catalyst in fluid bed reactor was lost during the experiment due entrainment, which most likely also decreased the conversion of reactive oxygenates in the fluid bed reactor and thereby accelerated the deactivation of the HDO reactor. Furthermore, analysis of the spent catalyst from the fluid bed reactor showed that the carbon content increased with time on stream. It was 3.7 wt.% after 3.5 h, but 7.2 wt.% after 16.2 h, indicating that the carbon deposition rate decreased with time on stream. Interestingly the potassium and calcium content on the spent catalysts increased proportionally to the time on stream, hence proportionally to the amount of biomass used, thus it was 0.14 and 0.075 wt.% after 3.5 hours, respectively, but 0.67 and 0.28 wt.% after 16.2 hours, respectively. Calcium was found as single particles (40-200 nm) and therefore only expected to have a minor effect on the catalytic activity, while potassium was well-distributed on the catalyst and could therefore have a larger impact on the activity. To investigate this a CoMo catalyst was prepared and doped with 1.9 wt.% potassium prior to the sulfidation, tested in the fluid bed reactor and compared to a similar un-doped CoMoS catalyst. This showed that potassium decreases the cracking and hydrogenation while increasing the decarboxylation activity and only led to a small decrease in the total deoxygenation activity. However, it should be noted that potassium also altered the catalyst morphology by increasing the MoS_2 slab length and increasing the degree of stacking. This most likely led to the formation of the more active type II sites, which may have enhanced the deoxygenation activity. Interestingly doping the catalyst with potassium led to encapsulation of the catalyst particles with coke, indicating that potassium can act as a catalyst for polymerization reactions. Furthermore, using wheat straw instead of beech wood as feedstock, which contains 10 times more potassium, led to fast defluidization due to agglomeration and SEM images of the agglomerates showed that that potassium had acted as a catalyst for polymerization reactions.

Based on the experimental results the important chemical reactions in catalytic hydropyrolysis have been identified and a mechanistic model for catalytic hydropyrolysis is proposed. Catalytic hydropyrolysis has also been compared to other pyrolysis technologies, which indicated that it is promising process for the production of renewable liquid hydrocarbon fuels.

Resumé

Denne afhandling er dedikeret til at undersøge og optimere katalytisk hydropyrolyse af biomasse til produktion af vedvarede brændstof. Dette er blevet opnået ved at undersøge effekten af at variere proces betingelserne og katalysatoren i fluid bed reaktoren.

Forsøgene er blevet udført i et pilot anlæg, hvor op til 1 kg biomasse, hovedsageligt bøgetræ, blev fødet ind i en fluid bed reaktor i en brint atmosfære med et katalytisk materiale, hvilket producerer koks, lette gasser (CO_x, C_1-C_3), vand og olie. Koksen blev fjernet med et filter og gasserne blev sendt til en hydrodeoxygneringsreaktor (HDO reaktor), som kunne bypasses, efterfulgt af et 3 trins kondensations system. Bærer materialer, kommercielle katalysatorer og katalysatorer produceret på Danmarks tekniske universitet (DTU) er blevet testet i anlægget og den produceret olie blev grundigt analyseret med f.eks. gas kromatografi (GC) med atom emission detektor (AED) og GC×GC- masse spektroskopi detektor (MS)/ flamme ionisation detektor (FID). De produceret friske og brugte katalysatorer blev karakteriseret med NH_3 temperatur programmeret desorption (TPD), X-ray diffraktion (XRD), Raman spektroskopi, elektron mikroskopi (SEM og HAADF-STEM) og overfalde areal og elementær sammensætning blev bestemt.

En ilt fri (<0.01 vægt (wt.) %) olie med et kondensérbart organisk (kondenseret olie og C_{4+} i gassen) udbytte på 16.6-22.5 wt.% tør aske fri basis (daf) blev opnået ved brug af en kommerciel CoMoS/$MgAl_2O_4$ katalysator i fluid bed reaktoren (365-511°C) og en NiMoS/Al_2O_3 katalysator i HDO reaktoren (350-400°C) og ved brug af et brint tryk på 15.9 bar eller højere. Begge katalysatorer var leveret af Haldor Topsøe A/S. GC×GC-MS/FID på den organisk fase viste at den bestod af 42-75 % areal-FID aromater og at koncentrationen var kinetisk styret ved fluid bed temperaturer under 430°C og termodynamisk styret ved højre temperature. Mindske brint trykket til 8.0 og 3.0 bar øgede ilt indholdet i den organiske fase til 3.3 og 7.8 wt.% tør basis (db), respektivt, hvor det tilbageværende ilt hovedsageligt var phenoler. Den maksimale koncentration af monoaromater (57 % areal-FID) var detekteret ved 15.9 bar og yderligere øgning af brint trykket mindskede koncentrationen. Dette viser at koncentrationen af monoaromater er kontrolleret af termodynamikken ved brint tryk på 15.9 bar og højere, mens koncentration er kinetisk styret ved lavere brint tryk.

Brug af rene bærer materialer ($MgAl_2O_4$ og H-ZSM-5-Al_2O_3) i fluid bed reaktoren øgede koks og kul udbyttet op til 21.1 wt.% daf, mens det var mellem 11.4 og 13.1 wt.% daf ved brug af kommercielle katalysatorer. Hvilket indikere at katalysatoren i fluid bed reaktoren mindsker graden af kulaflejring grundet stabilisering af de reaktive ilt indeholdende forbindelser. Yderligere, en energi genindvinding på op til 58 % i den kondensérbar olie var opnået ved brug af myremalm, et billigt og ikke giftig naturligt mineral, i fluid bed reaktoren, mens den højeste energi genindvinding med en kommerciel katalysator var 54 % (NiMo/H-ZSM-5-Al_2O_3). Dette indikerer at myremalm kan erstatte de dyre og giftige Co(/Ni)Mo katalysatorer i katalytisk hydropyrolyse.

For at undersøge forskellen i HDO aktivitet, selektivitet og produkt sammensætning for sulfideret CoMo, NiMo, og Mo, blev disse katalysatorer produceret, ved brug af $MgAl_2O_4$ som bærer materiale, og testet i fluid bed reaktoren uden brug af HDO reaktoren. Dette viste at NiMo katalysatoren har den højeste brintnings, kraknings, og decarboxylering/decarbonylering aktivitet, mens Mo katalysatoren havde den laveste. Kulstof genindvindingen i den kondensérbar organiske fase for NiMo katalysatoren var 37 %, mens den var 39 % for både CoMo og Mo katalysatorerne. CoMo katalysatoren havde den højeste iltfjernelses aktivitet og Mo katalysatoren den laveste, derfor kan CoMo katalysatoren anses for at være den bedst egnet i fluid bed reaktoren.

Effekten af at varier CoMo indholdet mellem 4.0 og 12.0 wt.% og bruge $MgAl_2O_4$ som bærer materiale viste at udbyttet af lette gasser (C_1-C_3) steg når CoMo indholdet blev øget, dette førte også til fald i ilt indholdet i den organiske fase fra 9.0 til 4.7 wt.% db, men mindskede kulstof genindvindingen fra 39 til 37 %. Effekten af at varier katalysator surheden blev også undersøgt ved at bruge en blanding af zeolit og alumina (H-ZSM-5-Al_2O_3) i stedet for $MgAl_2O_4$, mens indholdet af CoMo blev holdt konstant (4.0-4.3 wt.%). Dette viste at brugen af et mere surt bærer materiale øger brintkraknings aktiviteten og mindsker ilt indholdet i den kondenseret organiske fase fra 9.0 wt.% db til mellem 5.2 og 6.1 wt.% db, afhængig af zeolit til alumina forholdet. Men kulstof genindvindingen var ikke påvirket af surheden, hvilket øgede alkylerings aktiviteten og derved øgede aromat udbyttet ved indbinding af korte ilt forbindelser.

For at teste hvor stabil processen er, blev et fem dages delvist kontinueret forsøg udført med en CoMoS/$MgAl_2O_4$ katalysator i fluid bed reaktoren og en NiMoS/Al_2O_3 katalysator i HDO reaktoren. Den totale forsøgs tid var 16.2 timer og cirka 5 kg biomasse blev brugt. Det kondensérbar olie udbyttet var forholdsvist konstant og varieret mellem 21.2 og 23.2 wt.% daf, mens det totale ilt indhold i den organiske fase steg underforsøget fra 40 til 2832 wt-ppm, hvilket indikere at deaktivering af katalysatoren i fluid bed og HDO reaktoren kan have fundet sted. 40 wt.% af katalysatoren i fluid bed reaktoren blev også overført til filteret under forsøget, hvilket sandsynligvis har mindsket omdannelsen af de reaktive oxygenater. Yderligere analyse af den brugte katalysator fra fluid bed reaktoren viste at kulstofindholdet blev øget med tiden, derved mængden af brugt biomasse. Kulstof koncentration på katalysatoren var derfor 3.7 wt.% efter 3.5 timer, men 7.2 wt.% efter 16.2 timer. Kalium og calcium indholdet på den brugte katalysator steg proportionalt med tiden, deraf mængden af biomasse brugt. Mængden af kalium var 0.14 wt.% efter 3.5 timer og 0.67 wt.% efter 16.2 timer og mængden af calcium var 0.075 wt.% efter 3.5 timer og 0.14 wt.% efter 16.2 timer. Calcium blev fundet som isoleret partikler (40-200 nm) og har derfor højst sandsynlig kun en mindre effekt på katalysator aktiviteten, mens kalium var velfordelt over hele katalysatoren og kan derfor have en større indflydelse på dens aktivitet. En CoMo katalysator blev derfor dopet med 1.9 wt.% kalium inden sulfidering, testet i fluid bed reaktoren og sammenlignet med en lignede katalysator uden kalium. Dette viste at kalium mindsker krakning og brintnings aktiviteten, mens det øger decarboxylering aktiviteten, som dog faldt med tiden. Tilsætning af kalium ændrede også katalysatorens morfologi ved at øge længden og graden af stabling af de aktive sites, hvilket indikerer dannelsen af den mere aktive type II site, som kan have øget iltfjernelses aktiviteten. Bemærkelsesværdigt, dope katalysatoren med kalium førte til indkapsling af katalysator partiklerne med kul, derved indikere at kalium kan ager som en katalysator og for polymeriseringsreaktioner. Ved brug af halm i stedet for bøgetræ, som indeholder 10 gange så meget kalium, førte til defludisering grundet dannelse af agglomerater og SEM billeder af disse indikerede også at kalium fungerede som en katalysator for polymeriseringsreaktioner og var derfor højst sandsynligvis årsagen til agglomerationen.

På basis af disse resultater er de vigtigste kemiske reaktioner i katalytisk hydropyrolyse identificeret og en mekanistisk model for katalytisk hydropyrolyse er udarbejdet. Katalytisk hydropyrolyse er også blevet sammenlignet med andre pyrolyse teknologier, hvilket indiker at katalytisk hydropyrolyse er en lovede proces for produktion af bæredygtige flydende brændstof.

Publications and conference contributions

Articles published in peer-reviewed journals

Trine M. H. Dabros, Magnus Z. Stummann, Martin Høj, Peter A. Jensen, Jan-Dierk Grundwaldt, Jstein Gabrielsen, Peter M. Mortensen, Anker D. Jensen, "*Transportation fuels from biomass fast pyrolysis, catalytic hydrodeoxygenation, and catalytic fast hydropyrolysis*", Prog. Energy Combust. Sci. 68 (2018) 268-309.

Magnus Z. Stummann, Martin Høj, Christian B. Schandel, Asger B. Hansen, Peter Wiwel, Jostein Gabrielsen, Peter A. Jensen, Anker D. Jensen, "*Hydrogen assisted catalytic biomass pyrolysis. Effect of temperature and pressure*", Biomass and Bioenergy. 115 (2018) 97–107.

Magnus. Z. Stummann, Martin Høj, Bente Davidsen, Asger B. Hansen, Lars P. Hansen, Peter Wiwel, Christian B. Schandel, Jostein Gabrielsen, Peter A. Jensen, Anker D. Jensen, "*Effect of the catalyst in fluid bed catalytic hydropyrolysis*", Catal. Today. (2019) doi:10.10.16/j.cattod.2019.01.047.

Magnus Z. Stummann, Asger B. Hansen, Lars P. Hansen, Bente Davidsen, Søren B. Rasmussen, Peter Wiwel, Jostein Gabrielsen, Peter A. Jensen, Anker D. Jensen, Martin Høj, "*Catalytic hydropyrolysis of biomass using molybdenum sulfide based catalysts. Effect of the promoters"*, Energy & Fuels. 33 (2019) 1302-1313.

Articles submitted to peer-reviewed journals

Magnus Z. Stummann, Martin Høj, Asger B. Hansen, Bente Davidsen, Peter Wiwel, Jostein Gabrielsen, Peter A. Jensen, Anker D. Jensen, "*New insights into the effect of pressure on catalytic hydropyrolysis of biomass*", To be submitted 2018.

Magnus Z. Stummann, Elaine Elevera, Asger B. Hansen, Lars P. Hansen, Pablo Beato, Bente Davidsen, Peter Wiwel, Jostein Gabrielsen, Peter A. Jensen, Anker D. Jensen, Martin Høj, "*Catalytic hydropyrolysis of biomass using supported CoMo catalysts – Effect of metal loading and support acidity*", To be submitted 2019.

Articles in Preparation

Magnus Z. Stummann, Martin Høj, Asger B. Hansen, Pablo Beato, Peter Wiwel, Jostein Gabrielsen, Peter A. Jensen, Anker D. Jensen, "*Deactivation of CoMoS catalysts during catalytic hydropyrolysis. Part I: Product distribution and composition*", To be submitted 2019.

Magnus Z. Stummann, Martin Høj, Bente Davidsen, Lars P. Hansen, Pablo Beato, Jostein Gabrielsen, Peter A. Jensen, Anker D. Jensen, "*Deactivation of CoMoS catalysts during catalytic hydropyrolysis. Part II: characterization of the spent catalysts and char*", To be submitted 2019

Magnus Z. Stummann, Martin Høj, Jostein Gabrielsen, Peter A. Jensen, Anker D. Jensen, "*Trends in catalytin hydropyrolysis of biomass*", To be submitted 2019

Oral conference contributions

Magnus Z. Stummann, Martin Høj, Bente Davidsen, Asger B. Hansen, Peter Wiwel, Peter A. Jensen, Jostein Gabrielsen, Anker D. Jensen, "*Hydrogen assisted catalytic biomass pyrolysis for green fuels. Effect of catalyst in the fluid bed*". Presented at Thermal & Catalytic Sciences Symposium, 2018, Auburn, United States.

Magnus Z. Stummann, Martin Høj, Bente Davidsen, Asger B. Hansen, Peter Wiwel, Peter A. Jensen, Jostein Gabrielsen, Anker D. Jensen, "*Hydrogen assisted catalytic biomass pyrolysis for green fuels. Effect of catalyst in the fluid bed*". Presented at The 10th International Conference on Environmental Catalysis. The 3rd International Symposium on Catalytic Science and Technology in Sustainable Energy and Environment, 2018, Tianjin, China.

Magnus Z. Stummann, Martin Høj, Bente Davidsen, Asger B. Hansen, Peter Wiwel, Peter A. Jensen, Jostein Gabrielsen, Anker D. Jensen, "*Hydrogen assisted catalytic biomass pyrolysis for green fuels. Effect of catalyst in the fluid bed*". Presented at the 18th Nordic Symposium on Catalysis, 2018, Copenhagen, Denmark.

Magnus Z. Stummann, Martin Høj, Bente Davidsen, Asger B. Hansen, Peter Wiwel, Peter A. Jensen, Jostein Gabrielsen, Anker D. Jensen, "*Hydrogen assisted catalytic biomass pyrolysis for green fuels*". Presented at the 26th European Biomass Conference and Exhibition, 2018, Copenhagen, Denmark.

Magnus Z. Stummann, Martin Høj, Jostein Gabrielsen, Peter A. Jensen, Anker D. Jensen, "*Hydrogen Assisted Catalytic Biomass Pyrolysis for Green Fuels*". Presented at Sustain DTU, 2017, Kgs. Lyngby, Denmark.

Magnus Z. Stummann, Martin Høj, Jostein Gabrielsen, Peter A. Jensen, Anker D. Jensen, "*H2CAP - Hydrogen assisted catalytic biomass pyrolysis for green fuels*". Presented at the 13th European Congress on Catalysis, 2017, Florence, Italy.

Magnus Z. Stummann, Martin Høj, Jostein Gabrielsen, Peter A. Jensen, Anker D. Jensen, "*H2CAP - Hydrogen assisted catalytic biomass pyrolysis for green fuels*". Presented at the 25th European Biomass Conference and Exhibition, 2017, Stockholm, Sweden.

Poster conference contributions

Magnus Z. Stummann, Martin Høj, Jostein Gabrielsen, Peter A. Jensen, Anker D. Jensen, "*H2CAP - Hydrogen Assisted Catalytic Biomass Pyrolysis for Green Fuels*". Presented at North American Catalysis Society Meeting, 2017, Denver, United States.

Magnus Z. Stummann, Martin Høj, Christian B. Schandel, Asger B. Hansen, Peter Wiwel, Peter A. Jensen, Jostein Gabrielsen, Anker D. Jensen, "*Hydrogen Assisted Catalytic Biomass Pyrolysis for Green Fuels*". Presented at TCSbiomass, 2017, Chicago, United States.

Magnus Z. Stummann, Martin Høj, Jostein Gabrielsen, Peter A. Jensen, Anker D. Jensen, "*H2CAP - Hydrogen Assisted Catalytic Biomass Pyrolysis for Green Fuels*". Presented at Sustain DTU, 2016, Kgs. Lyngby, Denmark. This presentation was awarded with a poster award at Sustain DTU.

Trine M. H. Arndal, Magnus Z. Stummann, Martin Høj, Peter A. Jensen, Anker D. Jensen, Lasse R. Clausen, Jan-Dierk Grunwaldt, Jostein Gabrielsen, Delfina Pitos, Felix Studt, "*H2CAP - Hydrogen Assisted Catalytic Biomass Pyrolysis for Green Fuels*". Presented at Sustain DTU, 2015, Kgs. Lyngby, Denmark.

Abstracts submitted to conferences

Magnus Z. Stummann, Asger B. Hansen, Bente Davidsen, Søren B. Rasmussen, Peter Wiwel, Jostein Gabrielsen, Peter A. Jensen, Martin Høj, Anker D. Jensen, "*Catalytic hydropyrolysis using sulfided Mo, CoMo and NiMo catalysts in a fluid bed reactor*". Submitted to the North American Catalysis Society Meeting, 2019, Chicago, United States.

Magnus Z. Stummann, Asger B. Hansen, Jostein Gabrielsen, Peter A. Jensen, Martin Høj, Anker D. Jensen, "*Catalytic hydropyrolysis – Effect of CoMo loading and support acidity*". Submitted to the 14th European Congress on Catalysis, 2019, Aachen, Germany.

Other publications

Magnus Z. Stummann, Martin Høj, Peter A. Jensen, Jostein Gabrielsen, Lasse Røngaard, Anker D. Jensen, "*Fremstilling af CO_2-neutral benzin og diesel:- ved katalytisk hydropyrolyse af biomasse - en spændende teknologi med mulighed for energilagring*", Dansk kemi 99 (2018) 18-20.

Table of Contents

Chapter 1 Introduction

The global energy production increases and will most likely continue this trend in the future due to the increasing energy consumption in non-OECD countries and the increasing world population [1,2]. Today's energy demand is mainly covered by the combustion of fossil fuels [1], which leads to greenhouse gas (GHG) emission and thereby global warming. Even a temperature increase of 2°C can lead to a significant increase in the sea level [3,4] and it is therefore evident that the emission of GHG must be drastically decreased in the near future by reducing the use of fossil fuels. In this transition, biomass may play an important role. Compared to other renewable energy resources biomass has the advantages that it consist of hydrocarbons and can therefore be transformed into liquid fuels, which can easily be used in the transport sector. The amount of biomass available for energy consumption is much debated. Some studies indicate that improved agriculture and technology developments would make it possible to cover the worlds transportation fuel demand [5], other studies indicates that the production of bioethanol only can cover 32 % of the global gasoline consumption [6]. However, some studies indicate that there is only enough biomass to cover 5-8 % of the worlds primary energy consumption and using biomass for energy production could threaten the food security, accelerating climate changes, due to emission of carbon stored in the biomass [7,8]. Biomass must therefore been considered as a precious energy resource and should be harvested and used with circumspection, thus it is therefore important that the available biomass is used as efficiently as possible.

There are many ways to generate liquid fuels from biomass, some of the most well-known are the production of bioethanol through enzymatic hydrolysis and fermentation [9,10], gasification followed by Fischer-Tropsch synthesis [11], and fast pyrolysis [12–14]. In fast pyrolysis the biomass is rapidly heated to 500 °C in an inert atmosphere, which converts the biomass into char, light gasses, and bio-oil also called pyrolysis oil [12], which can contain up to 75 % of the energy from the biomass [15]. The produced bio-oil has a heating value, which is approximately half the heating value of conventional liquid fuels, which is due to its high oxygen content (up to 50 wt.%) [12–17]. Furthermore the high oxygen content makes it immiscible with conventional liquid fossil fuels, acid, unstable, and problematic to distill [12,13,18], thus further upgrading of the bio-oil is needed before it can be used as a transportation fuel. It is possible to upgrade the bio-oil through hydrodeoxygenation (HDO), which takes place at high hydrogen pressure (100-300 bar) and temperature (250-400°C), and using a conventional hydrotreating catalyst [14]. However, due to the reactive nature of the oxygenates in the bio-oil, polymerization on the catalyst, which leads to deactivation, is a common problem in HDO [14].

Despite the unfavorable properties of pyrolysis oil the number of publications on this topic has continued to increase during the last two decades and 2260 articles related to a combination of the key words "fast", "pyrolysis" and "biomass" was published in 2017, see Figure 1.1(A). Catalytic pyrolysis, where the pyrolysis takes place in the present of a zeolite based catalyst in an inert atmosphere, is considered to be an alternative process for the production of a more stable bio-oil. The hydrogen availability limits the reaction, and the oxygen is mainly removed as CO_x and the maximum oxygen free liquid yield is 42 wt.% [19], assuming that carbon is not lost as coke. However, catalytic pyrolysis generally gives a high coke yield between 13 and 34 wt.%, while the oxygen content in the produced liquid remains considerable (16-42 wt.%) [20–22]. Therefore, as pointed out by Venderbosch [23], the used catalysts in catalytic pyrolysis are not selective enough to produce bio-oil with a low oxygen content and catalytic hydropyrolysis followed by further hydrogenation could therefore be a better alternative. Interestingly, the interest for catalytic pyrolysis continuous to in-

crease, thus 570 articles related to a combination of the key words “pyrolysis”, “catalytic”, and “biomass” were published in 2017, while only 11 articles related to the key words “hydropyrolysis”, “catalytic”, and “biomass” were published that year, as shown in Figure 1.1 (B) & (C). Therefore despite that the interest for hydropyrolysis and especially catalytic hydropyrolysis has increased the recent years Figure 1.1(C) clearly indicates that this is still a fairly unexplored process.

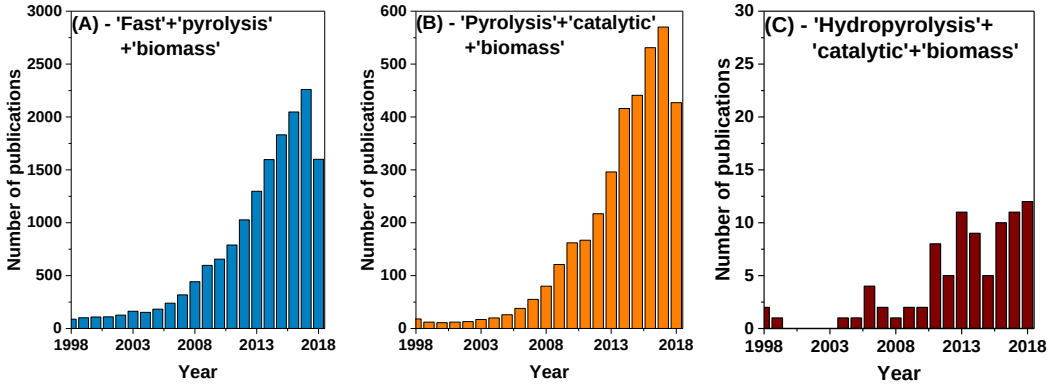

Figure 1.1 Number of publications in the last 20 years with the key words ‘fast’ + ‘pyrolysis’ + ‘biomass’ (A), ‘pyrolysis’ + ‘catalytic’ + ‘biomass’ (B), and ‘hydropyrolysis’ + ‘catalytic’ + ‘biomass’ (C). (Search conducted with web of science September 2018)

1.1 Reactor configuration in hydropyrolysis

There are several different reactor configurations, which can be used for hydropyrolysis as shown in Figure 1.2. In reactor configuration a the hydropyrolysis takes place in a fluid bed reactor with an inert bed material, which serves as a heat carrier, and the vapors are condensed after the fluid bed reactor. In configuration b an active catalyst is used as bed material in the fluid bed reactor. In configuration c an inert bed material is used in the fluid bed, similar to configuration a, but a secondary fixed bed hydrotreating reactor is located after the fluid bed reactor. In reactor configuration d an active catalyst is used in the fluid bed reactor and the vapors are upgraded in a second fixed bed hydrotreating reactor prior condensation.

Dayton et al. [24], using configuration a in Figure 1.2, observed that conducting the pyrolysis at 20.7 bar with 3 bar hydrogen instead of pure nitrogen decreased the oxygen content in the produced bio-oil from 39.2 to 34.6 wt.%, thus showing that hydropyrolysis can be used to decrease the oxygen content the bio-oil. Likewise Tarves et al. [25] using active char coal observed a 25 % decrease in the oxygen content when conducting the pyrolysis in hydrogen instead of nitrogen. These results show that only conducting a fast hydropyrolysis does decrease the oxygen content in the produced bio-oil, but the oxygen content is still significantly higher than in conventional fossil liquid fuels, and thus the reactor configuration in Figure 1.2 a is less promising.

Recent research has shown that catalytic hydropyrolysis (case b in Figure 1.2) is more promising and this approach has therefore gained increasing attention during the last decade. Dayton et al. [24,26,27] conducted catalytic hydropyrolysis in a fluid bed reactor using mixed wood as feedstock and tested the effect of process conditions and catalyst. Using a reduced NiMo catalyst (further details were not given) and varying the fluid bed temperature (375-475 °C) and the hydrogen pressure showed that the solid yield (char and coke) increased with decreasing hydrogen pressure [26]. Furthermore, increasing the temperature increased the for-

mation of aliphatics and aromatics and decreased the formation of oxygenates [26]. A 10 day experiment was also conducted, where the setup was run for 4 hours each day and the catalyst was regenerated by oxidizing the catalyst in order to remove any char and coke and then reducing the catalyst each day before the biomass feeding was started. This showed that the process was stable and the liquid organic yield was 22.5±1.35 wt.% with an oxygen content of 2.8±1 wt.% [26]. Several different reduced catalysts were also tested at atmospheric pressure and a carbon recovery of 43.0 % with 6.2 wt.% oxygen in the organic phase was obtained with a molybdenum oxide catalyst [27]. Marker et al. [28] also conducted catalytic hydropyrolysis of mixed wood in a fluid bed reactor at 22.4 bar and 392-453 °C they obtained an organic and C_{4+} yield between 24.1 and 25.1 wt.% daf with an oxygen content between 0.48 and 7.74 wt.%, however the type of catalyst was not provided.

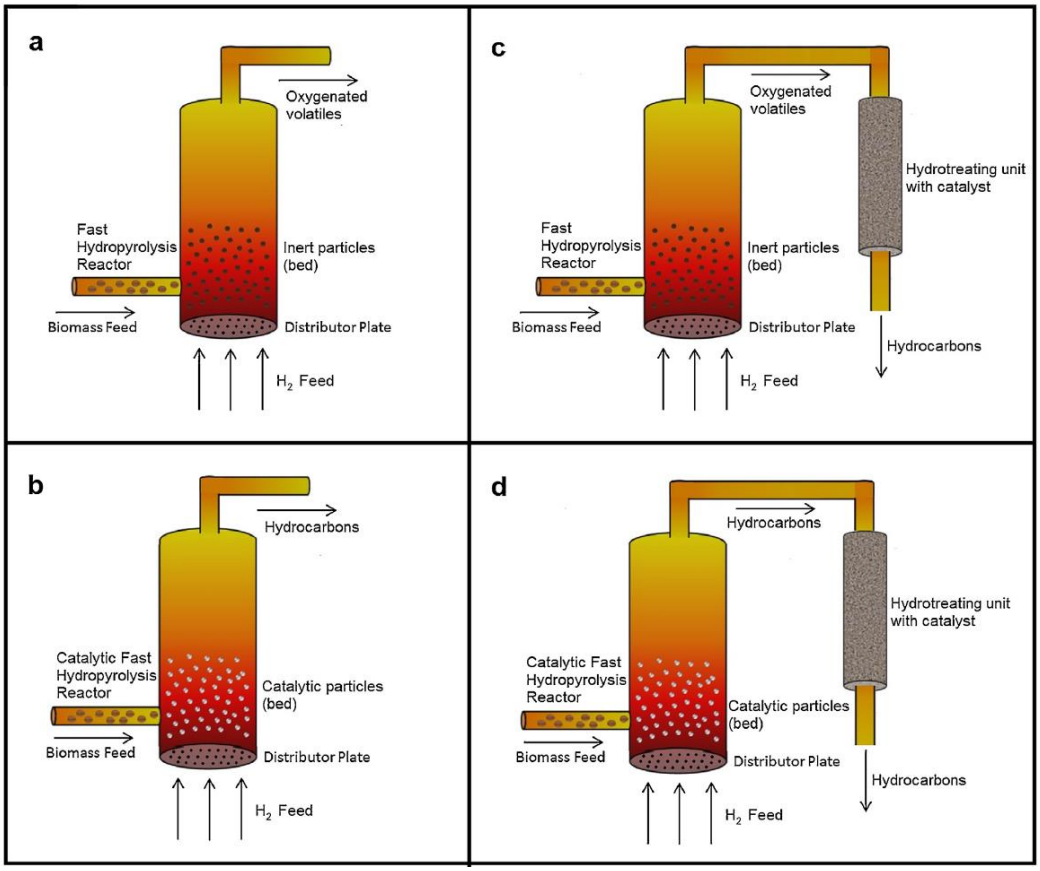

Figure 1.2 Overview of the different reactor configurations for hydropyrolysis of biomass for fuels in a fluid bed reactor: (a) fast hydropyrolysis, (b) catalytic fast hydropyrolysis, (c) fast hydropyrolysis followed by a hydrotreating unit, (d) catalytic fast hydropyrolysis followed by a hydrotreating unit. Reprint with permission from ref. [29]**.**

Several other groups have studied catalytic hydropyrolysis in pyroprobes using H-ZSM-5 as a catalyst [30–37] or as a support [31–33,36–39]. Impregnating H-ZSM-5 with different metals (Ni, Co, Mo, Pt, Ru and Pd) and testing them at reducing conditions increases the yield of aromatics [31,32,37]. Gamliel et al. [37] also investigated the effect of different supports (H-ZSM-5, SiO_2, Al_2O_3) and found that the acidity of the support

was important and high acidity could increase the amount of oxygen removed and thereby minimizing secondary polycondensation reactions, thus decreasing the solid yield.

Conducting the hydropyrolysis without a catalyst in the fluid bed followed by a HDO reactor (configuration c in Figure 1.2) could make it possible to optimize the hydropyrolysis and HDO reactions separately [40], particularly since the pyrolysis reaction requires temperatures up to 500 °C – higher than for normal hydrotreating processes. Philips 66 has therefore investigated non-catalytic hydropyrolysis in a fluid bed reactor followed by HDO in a fluid bed reactor [40,41]. They were able to obtain a carbon recovery of the C_{5+} organic fraction between 35.2 and 46.7 % with an oxygen content in the organic phase between 2 and 17 wt.% depending on the process conditions [40]. Furthermore, the produced organics were stable when stored for two months at 40 °C [40]. Characterization of the condensed organics with nuclear magnetic resonance (NMR) showed that the oxygenates mainly were monofunctional phenols and ketones, thus multifunctional oxygenates, which are normally found in bio-oil, were removed in the process [41]. It also showed that at high temperatures in the HDO reactor more alkyl branches were observed on the aromatics, thus indicating that alkylation or transalkylation reactions takes place [41]. Venkatakrishnan [42,43] studied non-catalytic fast hydropyrolysis (temperature: 480-580°C) in a cyclone reactor followed by a fixed bed HDO reactor, operated at 375 °C with a 2% Ru and Pt on Al_2O_3 catalyst, (configuration c in Figure 1.2) and found that by conducting the hydropyrolysis at high temperature (580 °C) suppressed the formation of light reactive oxygenates. A C_{4+} carbon recovery of 32 and 45 % was obtained when using cellulose and poplar as feedstock, respectively. These results therefore indicate that non-catalytic hydropyrolysis followed by HDO in a second reactor could also be a promising method for production of fuels. This reactor configuration has the advantages that the catalyst does not have any direct contact with solids, thus significantly decreasing the risk of catalyst deactivation by e.g. alkali metals transferred from the biomass to the catalyst [44].

GTI has invented a process called IH^2® in which the catalytic hydropyrolysis reactor is followed by a fixed bed HDO reactor [28,45]. With this process it is possible to produce an oxygen free oil (oxygen <1 wt.%) with a condensed organic and C_{4+} yield between 25.8 and 29.5 wt.% daf when using wood as feedstock and using microalgae can increase the yield to 46.3 wt.% daf [28]. Furthermore a 50 kg biomass/day IH^2® pilot plant has been operated successfully for 750 hours with no sign of catalyst deactivation [45]. However, 2% of the catalyst had to be added each day to the fluid bed, because of catalyst loss due to entrainment [45]. Thermodynamic analysis of polygeneration of systems based on the IH^2® process indicates that it is possible to achieve an energy efficiency for the overall process of 89 % (LHV) [46]. Life cycle assessments of the IH^2® process have also shown that producing liquid fuels from this process can decrease the GHG emission with 30-96 %, depending of the type of feedstock, where bagasse gives the largest reduction in the GHG emission [47–49].

1.2 Sulfided catalysts

At the moment only reduced (metallic) or oxide catalysts have been reported to be used for catalytic hydropyrolysis of biomass, however, most of these catalysts are not sulfur tolerant, and since most biomass sources contain sulfur [50] it is likely that these catalyst over time will deactivate. Sulfided CoMo, NiMo, and Mo catalysts have the advantage that they are sulfur tolerant and they are widely used as hydrotreating catalysts in oil refineries and are known to be fairly stable in hydrodeoxygenation reactions of both bio-oil and model components [51–59]. Addition of a promoter (Co or Ni) to MoS_2 increases the formation of the coordinated unsaturated sites (CUS) [60–62], hence increases the catalysts activity [56,63], and makes it less vulnerable to deactivation [56,64]. One of the differences between using Co and Ni as a promoter is that Ni promotes the hydrogenation (HYD) pathway of phenols, where the aromatic ring is hydrogenated prior to the

removal of the oxygen, while Co promotes the direct deoxygenation (DDO) pathway, thus removing the oxygen without hydrogenating the aromatic ring [57,63,65–67]. Another difference between the two promoters is that CoMoS is inhibited by CO, which is not the case for NiMoS [63]. Figure 1.3 shows a STEM image and a ball model of the CoMoS catalysts and as shown on the figure Co is located at the edge of the nanocluster, where it provides active sites in the form of sulfur vacancies [68]. The bright brim site is located along the edge of the cluster and as indicated by Figure 1.3 a it is stronger at the promoted edges [69,70]. Recent research has shown that the Brim sites facilitate hydrogenation reactions, while the sulfur vacancies facilitate the desulfurization reactions [69]. Furthermore, the structure is also often divided into Type I and Type II, where Type II is substantially more active than type I [71]. The reason for the lower activity for the Type I is that it contains Mo-O-Al linkages (Al being the support), which makes it very difficult for it to form the sulfur vacancies [72]. The Type I sites can be transformed into Type II sites by conducting the sulfidation at high the temperatures, however this leads to sintering, thus loss of edge sites and alternative procedures such as the introduction of additives or chelating agents are preferred [71]. Multi-stack MoS_2 structures are often observed in catalysts with Type II structure, but is most likely just a product of a weaker interaction with the support [71]. It should be noted that in case of stacking the Brim sites will only be available at the top layer [71]. More information regarding pyrolysis, catalytic hydropyrolysis, and the catalysts used in hydrodeoxygenation can be found in a recent review by Dabros et al. [14].

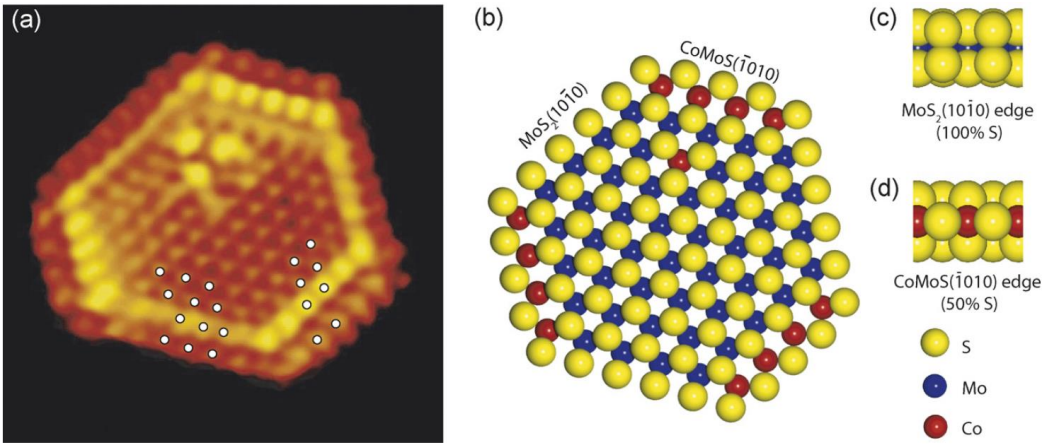

Figure 1.3 Atom-resolved STEM image of Co-Mo-S (a), ball model of the Co-Mo-S (b), side view of the MoS_2 edge (c), and side view of Co-substituted CoMoS edge (d). Reprint with permission from ref. [68].

1.3 Perspectives for catalytic hydropyrolysis

The above discussion shows that catalytic hydropyrolysis is a promising emerging process for the production of renewable liquid fuels. The byproducts CO_x, C_1-C_3, and char can also be used to generate energy. The char can either be burned or gasified and used for the production of electricity or district heating. The light hydrocarbons can be used as natural gas and the CO_x can be hydrogenated to methane together with the CO_x formed during the gasification of char. The process can also be combined with other renewable energy technologies, such as wind and solar energy as shown in Figure 1.4. These technologies can generate energy for the production of hydrogen, by electrolysis of water, which is incorporated into the oil and light gasses, thus increasing their heating value. Alternatively, can the hydrogen needed for the process be generated from reforming of the light gasses. This could make catalytic hydropyrolysis a flexible technology, where the hy-

drogen needed for the process can be generated from other renewable energy technologies when they are producing a surplus of energy or alternatively be self-sufficient and produce the hydrogen required from recycling of the light gasses, therefore this technology could be used to store surplus of renewable energy. However, despite that catalytic hydropyrolysis is a promising technology, there is little information available regarding the composition of the used catalyst in the process or to what extent the catalyst over time deactivates due to coking or transfer of alkali metals from the biomass. Furthermore, prior to this project sulfided catalysts have to the knowledge of the author not been tested in this process in the open literature.

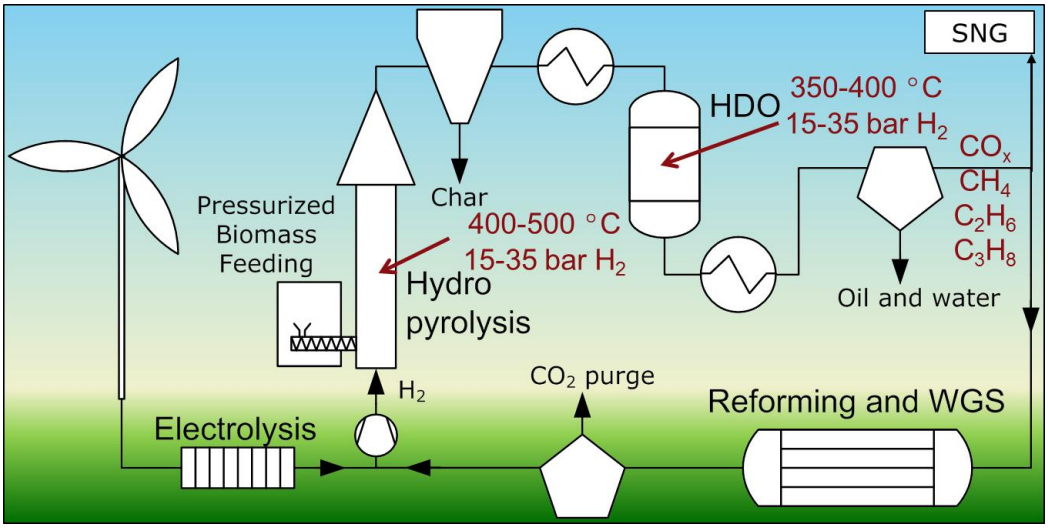

Figure 1.4 Proposed hydropyrolysis process

1.4 Outline

This thesis is to a large extent a compilation of the articles written during the PhD project. Each of the chapters (2-9) consists of manuscripts that are either submitted or prepared for submission to a journal and they therefore contain both an introduction and method section, and so some repetition occurs. In order to help the reader an overview of the content is given below:

- Chapter 2 is a reprint of our first article with the title "*Hydrogen assisted catalytic biomass pyrolysis. Effect of temperature and pressure*". This chapter contains the first results obtained at the experimental catalytic hydropyrolysis setup, where the effect of the temperature in the two reactors and the operating pressure was studied. The operating conditions applied in the following chapters were decided on the basis of results presented in this chapter.
- Chapter 3 is a reprint of an article in preparation for submission with the title "*New insights into the effect of pressure on catalytic hydropyrolysis*". Here we further investigated the effect of the hydrogen pressure on catalytic hydropyrolysis and the spent catalysts were characterized with SEM-EDS.
- Chapter 4 is a reprint of the article published in Catalysis Today with the title "*Effect of the catalyst in fluid bed catalytic hydropyrolysis*". This an explorative study where several very different bed materials were tested as catalysts in the fluid bed reactor.
- Chapter 5 is a reprint of an article published in Energy & Fuels with the title "*Catalytic hydropyrolysis of biomass using molybdenum sulfide based catalysts. Effect of the promoters*". For this work we

prepared a Mo, CoMo, and NiMo catalyst, where the difference between them was the promoter and the effect of the promoter on the product distribution and composition was investigated.

- Chapter 6 is a reprint of an article prepared for submission with the title "*Catalytic hydropyrolysis – Effect of CoMo loading and support acidity"*. In this work the effect of the metal loading was investigated and the three different supports, with different acidity ($MgAl_2O_4$ and two different mixtures of H-ZSM-5-Al_2O_3), were tested.
- Chapter 7 is a reprint of an article prepared for submission with the title "*Deactivation of a CoMo catalyst during catalytic hydropyrolysis of biomass. Part I: Product distribution and composition*
- *".* In this study we investigated the deactivation of a sulfided CoMo catalyst both by conducting a stability experiment and by predeactivating the catalyst by impregnating it with K_2CO_3 prior to the sulfidation.
- Chapter 8 is a reprint of an article prepared for submission with the title "*Deactivation of a CoMo catalyst during catalytic hydropyrolysis of biomass. Part II: Characterization of the spent catalysts and char".* Here the spent catalysts used in chapter 7 a characterized. In addition the effect of using straw instead of beech wood is also investigated.
- Chapter 9 is general discussion of the results obtained within the field of catalytic hydropyrolysis. This chapter is also in the moment being prepared for submission as a review or perspective article with the title "*Trends in catalytic hydropyrolysis of biomass*".
- Chapter 10 is an overall conclusion on the results obtained in this project.
- Appendix A-H contains supplementary information for the different chapters presented in this thesis.
- Appendix I contains a more detailed description of the catalytic hydropyrolysis setup and a description of some of the operational problems.
- Appendix J is a short study of the effect of the H_2O partial pressure in catalytic hydropyrolysis on the product distribution.
- Appendix K contains a report, where the effect of the char particle size on the char removal in the fluid bed is investigated. The experiments were conducted in a cold glass fluid bed reactor during the construction of the catalytic hydropyrolysis setup.

References

[1] Independent Statistics & Analysis - U.S. Energy Information Administration, International energy outlook 2016 - DOE/EIA-0484, 2016. https://www.eia.gov/outlooks/ieo/pdf/0484(2016).pdf (accessed July 7, 2017).

[2] United Nations, World Population Prospects The 2017 Revision Key Findings and Advance Tables, World Popul. Prospect. 2017. (2017) 1–46. doi:10.1017/CBO9781107415324.004.

[3] J. Hansen, M. Sato, P. Hearty, R. Ruedy, M. Kelley, V. Masson-Delmotte, G. Russell, G. Tselioudis, J. Cao, E. Rignot, I. Velicogna, B. Tormey, B. Donovan, E. Kandiano, K. Von Schuckmann, P. Kharecha, A.N. Legrande, M. Bauer, Ice melt, sea level rise and superstorms: Evidence from paleoclimate data, climate modeling, and modern observations that 2 °C global warming could be dangerous, Atmos. Chem. Phys. 16 (2016) 3761–3812. doi:10.5194/acp-16-3761-2016.

[4] B.P. Horton, S. Rahmstorf, S.E. Engelhart, A.C. Kemp, Expert assessment of sea-level rise by AD 2100 and AD 2300, Quat. Sci. Rev. 84 (2014) 1–6. doi:10.1016/j.quascirev.2013.11.002.

[5] B.J.M. de Vries, D.P. van Vuuren, M.M. Hoogwijk, Renewable energy sources: Their global potential for the first-half of the 21st century at a global level: An integrated approach, Energy Policy. 35 (2007) 2590–2610. doi:10.1016/j.enpol.2006.09.002.

[6] S. Kim, B.E. Dale, Global potential bioethanol production from wasted crops and crop residues, Biomass and Bioenergy. 26 (2004) 361–375. doi:10.1016/j.biombioe.2003.08.002.

[7] J. Elliott Campbell, D.B. Lobell, R.C. Genova, C.B. Field, The global potential of bioenergy on

abandonded agricultural lands, Environ. Sci. Technol. 42 (2008) 5791–5794. doi:10.1021/es800052w.
[8] C.B. Field, J.E. Campbell, D.B. Lobell, Biomass energy: the scale of the potential resource, Trends Ecol. Evol. 23 (2008) 65–72. doi:10.1016/j.tree.2007.12.001.
[9] M.J. Taherzadeh, K. Karimi, Enzyme based hydrolysis processes for ethanol from lignocellulosic materials : a review . BioResources, 2007. doi:10.15376/biores.2.4.707-738.
[10] P. Binod, R. Sindhu, R.R. Singhania, S. Vikram, L. Devi, S. Nagalakshmi, N. Kurien, R.K. Sukumaran, A. Pandey, Bioethanol production from rice straw: An overview, Bioresour. Technol. 101 (2010) 4767–4774. doi:10.1016/j.biortech.2009.10.079.
[11] M. Balat, M. Balat, E. Kirtay, H. Balat, Main routes for the thermo-conversion of biomass into fuels and chemicals. Part 2: Gasification systems, Energy Convers. Manag. 50 (2009) 3158–3168. doi:10.1016/j.enconman.2009.08.013.
[12] A.V. Bridgwater, Review of fast pyrolysis of biomass and product upgrading, Biomass and Bioenergy. 38 (2012) 68–94. doi:10.1016/j.biombioe.2011.01.048.
[13] R.H. Venderbosch, W. Prins, Fast pyrolysis technology development, Biofuels, Bioprod. Biorefining. 4 (2010) 178–208. doi:10.1002/bbb.205.
[14] T.M.H. Dabros, M.Z. Stummann, M. Høj, P.A. Jensen, J.-D. Grunwaldt, J. Gabrielsen, P.M. Mortensen, A.D. Jensen, Transportation fuels from biomass fast pyrolysis, catalytic hydrodeoxygenation, and catalytic fast hydropyrolysis, Prog. Energy Combust. Sci. 68 (2018) 268–309. doi:10.1016/j.pecs.2018.05.002.
[15] T.N. Trinh, P.A. Jensen, K. Dam-Johansen, N.O. Knudsen, H.R. Sørensen, S. Hvilsted, Comparison of lignin, macroalgae, wood, and straw fast pyrolysis, Energy & Fuels. 27 (2013) 1399–1409. doi:10.1021/ef301927y.
[16] S. Czernik, A.V. Bridgwater, Overview of applications of biomass fast pyrolysis oil, Energy & Fuels. 18 (2004) 590–598. doi:10.1021/Ef034067u.
[17] A. Oasmaa, S. Czernik, Fuel oil quality of biomass pyrolysis oils-State of the art for the end users, Energy & Fuels. 13 (1999) 914–921. doi:10.1021/ef980272b.
[18] D. Mohan, C.U. Pittman, P.H. Steele, Pyrolysis of wood/biomass for bio-oil: A critical review, Energy & Fuels. 20 (2006) 848–889. doi:10.1021/ef0502397.
[19] A. V. Bridgwater, Catalysis in thermal biomass conversion, Appl. Catal. A, Gen. 116 (1994) 5–47. doi:10.1016/0926-860X(94)80278-5.
[20] S.D. Stefanidis, K.G. Kalogiannis, E.F. Iliopoulou, A.A. Lappas, P.A. Pilavachi, In-situ upgrading of biomass pyrolysis vapors: Catalyst screening on a fixed bed reactor, Bioresour. Technol. 102 (2011) 8261–8267. doi:10.1016/j.biortech.2011.06.032.
[21] C.A. Mullen, A.A. Boateng, D.J. Mihalcik, N.M. Goldberg, Catalytic fast pyrolysis of white oak wood in a bubbling fluidized bed, Energy and Fuels. 25 (2011) 5444–5451. doi:10.1021/ef201286z.
[22] E.F. Iliopoulou, S. Stefanidis, K. Kalogiannis, A.C. Psarras, A. Delimitis, K.S. Triantafyllidis, A.A. Lappas, Pilot-scale validation of Co-ZSM-5 catalyst performance in the catalytic upgrading of biomass pyrolysis vapours, Green Chem. 16 (2014) 662–674. doi:10.1039/c3gc41575a.
[23] R.H. Venderbosch, A Critical View on Catalytic Pyrolysis of Biomass, ChemSusChem. 8 (2015) 1306–1316. doi:10.1002/cssc.201500115.
[24] D.C. Dayton, J. Carpenter, J. Farmer, B. Turk, R. Gupta, Biomass hydropyrolysis in a pressurized fluidized bed reactor, Energy & Fuels. 27 (2013) 3778–3785. doi:10.1021/ef400355t.
[25] P.C. Tarves, C.A. Mullen, A.A. Boateng, Effects of Various Reactive Gas Atmospheres on the Properties of Bio-Oils Produced Using Microwave Pyrolysis, ACS Sustain. Chem. Eng. 4 (2016) 930–936. doi:10.1021/acssuschemeng.5b01016.
[26] D.C. Dayton, J. Hlebak, J.R. Carpenter, K. Wang, O.D. Mante, J.E. Peters, Biomass hydropyrolysis in a fluidized bed reactor, Energy & Fuels. 30 (2016) 4879–4887. doi:10.1021/acs.energyfuels.6b00373.
[27] K. Wang, D.C. Dayton, J.E. Peters, O.D. Mante, Reactive catalytic fast pyrolysis of biomass to produce high-quality bio-crude, Green Chem. 19 (2017) 3243–3251. doi:10.1039/C7GC01088E.
[28] T.L. Marker, L.G. Felix, M.B. Linck, M.J. Roberts, Integrated hydropyrolysis and hydroconversion (IH^2) for the direct production of gasoline and diesel fuels or blending components from biomass, Part 1: Proof of principle testing, Environ. Prog. Sustain. Energy. 31 (2012) 191–199. doi:10.1002/ep.10629.

[29] F.L.P. Resende, Recent advances on fast hydropyrolysis of biomass, Catal. Today. 269 (2016) 148–155. doi:10.1016/j.cattod.2016.01.004.

[30] S. Thangalazhy-Gopakumar, S. Adhikari, R.B. Gupta, M. Tu, S. Taylor, Production of hydrocarbon fuels from biomass using catalytic pyrolysis under helium and hydrogen environments., Bioresour. Technol. 102 (2011) 6742–9. doi:10.1016/j.biortech.2011.03.104.

[31] S. Thangalazhy-Gopakumar, S. Adhikari, R.B. Gupta, Catalytic pyrolysis of biomass over H^+ZSM-5 under hydrogen pressure, Energy & Fuels. 26 (2012) 5300–5306. doi:10.1021/ef3008213.

[32] O. Jan, R. Marchand, L.C.A. Anjos, G.V.S. Seufitelli, E. Nikolla, F.L.P. Resende, Hydropyrolysis of lignin using Pd/HZSM-5, Energy & Fuels. 29 (2015) 1793–1800. doi:10.1021/ef502779s.

[33] F. Melligan, M.H.B. Hayes, W. Kwapinski, J.J. Leahy, Hydro-pyrolysis of biomass and online catalytic vapor upgrading with Ni-ZSM-5 and Ni-MCM-41, Energy & Fuels. 26 (2012) 6080–6090. doi:10.1021/ef301244h.

[34] P. Choudhary, A. Malik, K.K. Pant, Mass-Scale Algal Biomass Production Using Algal Biofilm Reactor and Conversion to Energy and Chemical Precursors by Hydropyrolysis, ACS Sustain. Chem. Eng. 5 (2017) 4234–4242. doi:10.1021/acssuschemeng.7b00233.

[35] R.. Pindoria, a Megaritis, a. . Herod, R. Kandiyoti, A two-stage fixed-bed reactor for direct hydrotreatment of volatiles from the hydropyrolysis of biomass: effect of catalyst temperature, pressure and catalyst ageing time on product characteristics, Fuel. 77 (1998) 1715–1726. doi:10.1016/S0016-2361(98)00079-9.

[36] D.P. Gamliel, G.M. Bollas, J.A. Valla, Two-stage catalytic fast hydropyrolysis of biomass for the production of drop-in biofuel, Fuel. 216 (2018) 160–170. doi:10.1016/j.fuel.2017.12.017.

[37] D.P. Gamliel, L. Wilcox, J.A. Valla, The effects of catalyst properties on the conversion of biomass via catalytic fast hydropyrolysis, Energy & Fuels. 31 (2017) 679–687. doi:10.1021/acs.energyfuels.6b02781.

[38] F. Melligan, M.H.B. Hayes, W. Kwapinski, J.J. Leahy, A study of hydrogen pressure during hydropyrolysis of Miscanthus x giganteus and online catalytic vapour upgrading with Ni on ZSM-5, J. Anal. Appl. Pyrolysis. 103 (2013) 369–377. doi:10.1016/j.jaap.2013.01.005.

[39] D.P. Gamliel, G.M. Bollas, J.A. Valla, Bifunctional Ni-ZSM-5 catalysts for the pyrolysis and hydropyrolysis of biomass, Energy Technol. 5 (2017) 172–182. doi:10.1002/ente.201600136.

[40] L. Zhang, K. Gong, J. Lai, P. Alvey, Chemical composition and stability of renewable hydrocarbon products generated from a hydropyrolysis vapor upgrading process, Green Chem. 19 (2017) 3628–3641. doi:10.1039/c7gc01075c.

[41] J. Lai, L. Zhang, K. Gong, Nuclear magnetic resonance characterization of renewable products from a two-step ex-situ hydropyrolysis vapor upgrading process, ChemistrySelect. 3 (2018) 297–307. doi:10.1002/slct.201702431.

[42] V.K. Venkatakrishnan, J.C. Degenstein, A.D. Smeltz, W.N. Delgass, R. Agrawal, F.H. Ribeiro, High-pressure fast-pyrolysis, fast-hydropyrolysis and catalytic hydrodeoxygenation of cellulose: Production of liquid fuel from biomass, Green Chem. 16 (2014) 792–802. doi:10.1039/c3gc41558a.

[43] V.K. Venkatakrishnan, W.N. Delgass, F.H. Ribeiro, R. Agrawal, Oxygen removal from intact biomass to produce liquid fuel range hydrocarbons via fast-hydropyrolysis and vapor-phase catalytic hydrodeoxygenation, Green Chem. 17 (2015) 178–183. doi:10.1039/c4gc01746c.

[44] G. Yildiz, F. Ronsse, R. Van Duren, W. Prins, Challenges in the design and operation of processes for catalytic fast pyrolysis of woody biomass, Renew. Sustain. Energy Rev. 57 (2016) 1596–1610. doi:10.1016/j.rser.2015.12.202.

[45] T.L. Marker, L.G. Felix, M.B. Linck, M.J. Roberts, P. Ortiz-Toral, J. Wangerow, Integrated hydropyrolysis and hydroconversion ($IH^{2®}$) for the direct production of gasoline and diesel fuels or blending components from biomass, Part 2: Continuous testing, Environ. Prog. Sustain. Energy. 33 (2014) 762–768. doi:10.1002/ep.11906.

[46] T. Van Nguyen, L.R. Clausen, Thermodynamic analysis of polygeneration systems based on catalytic hydropyrolysis for the production of bio-oil and fuels, Energy Convers. Manag. 171 (2018) 1617–1638. doi:10.1016/j.enconman.2018.06.024.

[47] E. Maleche, R. Glaser, T. Marker, D. Shonnard, A preliminary life cycle assessment of biofuels produced by the $IH^{2\ TM}$ process, Environ. Prog. Sustain. Energy. 33 (2014) 322–329.

doi:10.1002/ep.11773.

[48] J. Fan, J. Gephart, T. Marker, D. Stover, B. Updike, D.R. Shonnard, Carbon Footprint Analysis of Gasoline and Diesel from Forest Residues and Corn Stover using Integrated Hydropyrolysis and Hydroconversion, ACS Sustain. Chem. Eng. 4 (2016) 284–290. doi:10.1021/acssuschemeng.5b01173.

[49] O. Winjobi, H. Tavakoli, B. Klemetsrud, R. Handler, T. Marker, M. Roberts, D. Shonnard, Carbon Footprint Analysis of Gasoline and Diesel from Forest Residues and Algae using Integrated Hydropyrolysis and Hydroconversion Plus Fischer–Tropsch (IH 2 Plus cool GTL), ACS Sustain. Chem. Eng. 6 (2018) 10766–10777. doi:10.1021/acssuschemeng.8b02091.

[50] T.N. Trinh, P.A. Jensen, D.J. Kim, N.O. Knudsen, H.R. Sørensen, S. Hvilsted, Comparison of lignin, macroalgae, wood, and straw fast pyrolysis, Energy and Fuels. 27 (2013) 1399–1409. doi:10.1021/ef301927y.

[51] O.İ. Şenol, E.-M. Ryymin, T.-R. Viljava, A.O.I. Krause, Reactions of methyl heptanoate hydrodeoxygenation on sulphided catalysts, J. Mol. Catal. A Chem. 268 (2007) 1–8. doi:10.1016/j.molcata.2006.12.006.

[52] O.İ. Şenol, T.-R. Viljava, A.O.I. Krause, Hydrodeoxygenation of aliphatic esters on sulphided NiMo/γ-Al_2O_3 and CoMo/γ-Al2O3 catalyst: The effect of water, Catal. Today. 106 (2005) 186–189. doi:10.1016/j.cattod.2005.07.129.

[53] O.İ. Şenol, T.-R. Viljava, A.O.I. Krause, Effect of sulphiding agents on the hydrodeoxygenation of aliphatic esters on sulphided catalysts, Appl. Catal. A Gen. 326 (2007) 236–244. doi:10.1016/j.apcata.2007.04.022.

[54] E.-M. Ryymin, M.L. Honkela, T.-R. Viljava, A.O.I. Krause, Competitive reactions and mechanisms in the simultaneous HDO of phenol and methyl heptanoate over sulphided NiMo/γ-Al_2O_3, Appl. Catal. A Gen. 389 (2010) 114–121. doi:10.1016/j.apcata.2010.09.010.

[55] A. Gutierrez, E.-M. Turpeinen, T.-R. Viljava, O. Krause, Hydrodeoxygenation of model compounds on sulfided CoMo/γ-Al2O3 and NiMo/γ-Al2O3 catalysts; Role of sulfur-containing groups in reaction networks, Catal. Today. 285 (2017) 125–134. doi:10.1016/j.cattod.2017.02.003.

[56] T.M.H. Dabros, A. Gaur, D.G. Pintos, P. Sprenger, M. Høj, T.W. Hansen, F. Studt, J. Gabrielsen, J.-D. Grunwaldt, A.D. Jensen, Influence of H2O and H2S on the composition, activity, and stability of sulfided Mo, CoMo, and NiMo supported on MgAl2O4 for hydrodeoxygenation of ethylene glycol, Appl. Catal. A Gen. 551 (2018) 106–121. doi:10.1016/j.apcata.2017.12.008.

[57] V.N. Bui, D. Laurenti, P. Afanasiev, C. Geantet, Hydrodeoxygenation of guaiacol with CoMo catalysts. Part I: Promoting effect of cobalt on HDO selectivity and activity, Appl. Catal. B Environ. 101 (2011) 239–245. doi:10.1016/j.apcatb.2010.10.025.

[58] A. Centeno, E. Laurent, B. Delmon, Influence of the support of CoMo sulfide catalysts and of the addition of potassium and platinum on the catalytic performances for the hydrodeoxygenation of carbonyl, carboxyl, and guaiacol-type molecules, J. Catal. 154 (1995) 288–298. doi:10.1006/jcat.1995.1170.

[59] M. Badawi, J.-F. Paul, S. Cristol, E. Payen, Guaiacol derivatives and inhibiting species adsorption over MoS_2 and CoMoS catalysts under HDO conditions: A DFT study, Catal. Commun. 12 (2011) 901–905. doi:10.1016/j.catcom.2011.02.010.

[60] P. Raybaud, J. Hafner, G. Kresse, S. Kasztelan, H. Toulhoat, Structure, energetics, and electronic properties of the surface of a promoted MoS2 catalyst: An ab initio local density functional study, J. Catal. 190 (2000) 128–143. doi:10.1006/jcat.1999.2743.

[61] B.R.G. Leliveld, J.A.J. van Dillen, J.W. Geus, D.C. Koningsberger, M. de Boer, Structure and Nature of the Active Sites in CoMo Hydrotreating Catalysts. An EXAFS Study of the Reaction with Selenophene, J. Phys. Chem. B. 101 (1997) 11160–11171. doi:10.1021/jp9723933.

[62] H. Topsøe, B.S. Clausen, F.E. Massoth, Cataltsis - Science and Technology. Hydrotreating catalysis, Volume 11, Springer-Verlag, Berlin Heidelberg, Germany, 1996.

[63] C. Bouvier, Y. Romero, F. Richard, S. Brunet, Effect of H_2S and CO on the transformation of 2-ethylphenol as a model compound of bio-crude over sulfided Mo-based catalysts: propositions of promoted active sites for deoxygenation pathways based on an experimental study, Green Chem. 13 (2011) 2441–2451. doi:10.1039/c1gc15181a.

[64] M. Badawi, J.-F. Paul, S. Cristol, E. Payen, Y. Romero, F. Richard, S. Brunet, D. Lambert, X. Portier, A. Popov, E. Kondratieva, J.M. Goupil, J. El Fallah, J.P. Gilson, L. Mariey, A. Travert, F. Maugé, Effect of water on the stability of Mo and CoMo hydrodeoxygenation catalysts: A combined experimental and DFT study, J. Catal. 282 (2011) 155–164. doi:10.1016/j.jcat.2011.06.006.

[65] V.N. Bui, D. Laurenti, P. Delichère, C. Geantet, Hydrodeoxygenation of guaiacol. Part II: Support effect for CoMoS catalysts on HDO activity and selectivity, Appl. Catal. B Environ. 101 (2011) 246–255. doi:10.1016/j.apcatb.2010.10.031.

[66] V.O.O. Gonçalves, S. Brunet, F. Richard, Hydrodeoxygenation of cresols over Mo/Al_2O_3 and $CoMo/Al_2O_3$ sulfided catalysts, Catal. Letters. 146 (2016) 1562–1573. doi:10.1007/s10562-016-1787-5.

[67] E. Schachtl, J.S. Yoo, O.Y. Gutiérrez, F. Studt, J.A. Lercher, Impact of Ni promotion on the hydrogenation pathways of phenanthrene on MoS_2/γ-Al_2O_3, J. Catal. 352 (2017) 171–181. doi:10.1016/j.jcat.2017.05.003.

[68] J.V. Lauritsen, J. Kibsgaard, G.H. Olesen, P.G. Moses, B. Hinnemann, S. Helveg, J.K. Nørskov, B.S. Clausen, H. Topsøe, E. Lægsgaard, F. Besenbacher, Location and coordination of promoter atoms in Co-and Ni-promoted MoS_2-based hydrotreating catalysts, J. Catal. 249 (2007) 220–233. doi:10.1016/j.jcat.2007.04.013.

[69] A.K. Tuxen, H.G. Füchtbauer, B. Temel, B. Hinnemann, H. Topsøe, K.G. Knudsen, F. Besenbacher, J. V. Lauritsen, Atomic-scale insight into adsorption of sterically hindered dibenzothiophenes on MoS_2 and Co-Mo-S hydrotreating catalysts, J. Catal. 295 (2012) 146–154. doi:10.1016/j.jcat.2012.08.004.

[70] F. Besenbacher, M. Brorson, B.S. Clausen, S. Helveg, B. Hinnemann, J. Kibsgaard, J.V. Lauritsen, P.G. Moses, J.K. Nørskov, H. Topsøe, Recent STM, DFT and HAADF-STEM studies of sulfide-based hydrotreating catalysts: Insight into mechanistic, structural and particle size effects, Catal. Today. 130 (2008) 86–96. doi:10.1016/j.cattod.2007.08.009.

[71] H. Topsøe, The role of Co-Mo-S type structures in hydrotreating catalysts, Appl. Catal. A Gen. 322 (2007) 3–8. doi:10.1016/j.apcata.2007.01.002.

[72] B. Hinnemann, J.K. Nørskov, H. Topsøe, A Density Functional Study of the Chemical Differences between Type I and Type II MoS_2 -Based Structures in Hydrotreating Catalysts †, J. Phys. Chem. B. 109 (2005) 2245–2253. doi:10.1021/jp048842y.

Chapter 2 Hydrogen assisted catalytic biomass pyrolysis. Effect of temperature and pressure

The following chapter has been published in Biomass & Bioenergy 115 (2018) 97-107. This article was based our initial results obtained with the catalytic hydropyrolysis setup and in this work we investigated the effect of varying the temperature and pressure on the product distribution and composition. The supplementary information for this chapter can be found in Appendix A.

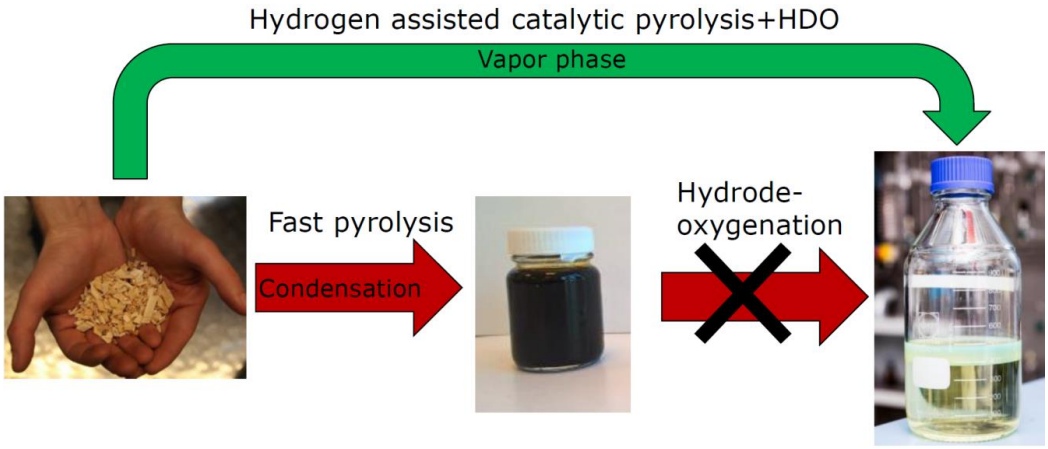

Abstract

Beech wood has been converted into a mixture of oxygen-free naphtha and diesel boiling point range hydrocarbons by using catalytic hydropyrolysis in a fluid bed reactor with a $CoMoS/MgAl_2O_4$ catalyst, followed by deep hydrodeoxygenation (HDO) in a fixed bed reactor loaded with a $NiMoS/Al_2O_3$ catalyst. The effect of varying the temperature (365-511 ^oC) and hydrogen pressure (1.6-3.6 MPa) on the product yield and organic composition was studied. The mass balance closed by a mass fraction between 90 and 101 % dry ash free basis (daf). The yield of the combined condensed organics and C_{4+} varied between a mass fraction of 17 and 22 % daf, corresponding to an energy recovery of between 40 and 53 % in the organic product. The yield of the non-condensable gases varied between a mass fraction of 24 and 32 % daf and the char yield varied between 9.6 and 18 % daf. The condensed organics contained a mass fraction of 42 to 75 % aromatics, based on GC×GC-FID chromatographic peak area, and the remainder was primarily naphthenes with minor amounts of paraffins. The condensed organics were essentially oxygen free (mass fraction below 0.001 %) when both reactors were used. Bypassing the HDO reactor increased the oxygen concentration in the condensed liquid to a mass fraction of 1.8 %. The results show that catalytic hydropyrolysis may be a viable way to process solid biomass into liquid and gaseous fuels.

Abbreviations

AED	Atomic emission detector
conc	Concentration
daf	Dry ash free basis
diAro	Diaromatics
DMDS	Dimethyl disulfide
FID	Flame ionization detector
GC	Gas chromatograph
HDO	Hydrodexoygenation
HHV	Higher heating value
mAro	Monoaromatics
MS	Mass spectrometry
Naph	Naphthenes
O-Ali	Oxygenated aliphatics
Par	Paraffins
PhO-	Oxygenated aromatics
SIMDIS	Simulated distillation by GC
Temp.	Temperature
tetAro+	Tetraaromatics
triAro	Triaromatics

2.1 Introduction

Recent research has shown that catalytic hydropyrolysis is an efficient process for producing diesel and gasoline hydrocarbons from biomass [1,2]. The reactive molecules formed by fast pyrolysis are immediately hydrogenated, thus inhibiting polymerization and other undesired properties of conventional fast pyrolysis bio-oil. In this process, the pyrolysis takes place at an elevated hydrogen pressure and in the presence of a HDO catalyst. The basic concept of hydropyrolysis share similarities with the Bergius process (high temperature and high hydrogen pressure) [3–5], however in the Bergius process coal and heavy oil is mixed into a slurry, while hydropyrolysis is a gas phase process. Steinberg et al. [6] showed in 1985 that using fast hydropyrolysis of wood at high temperatures (600-1000 °C) over 90 % of the carbon can be converted into hydrocarbons, mainly methane and other gases. It has also been shown that catalytic hydropyrolysis of lignin can give oil mass yields up to 80 % [7]. Despite that hydropyrolysis is not a new concept it has first in the recent years become a popular method for producing liquid fuels from biomass. Using a pyroprobe reactor, Melligan et al.[8] showed that conducting the pyrolysis of Miscanthus in an atmosphere of H_2 instead of He decreased the concentration of ethanoic acids in bio-oil. It has also been shown that zeolites impregnated with reduced transition metals increase the hydrocarbon yield and decrease the molecular size of the phenols [8–10]. Other groups have been pursuing the high pressure, non-catalytic hydropyrolysis of biomass in an inverted cyclone or fluid bed reactors followed by downstream catalytic HDO of the product vapors prior to oil and water condensation [11–13]. Marker et al.[1,2] have proposed a process called Integrated Hydropyrolysis and Hydroconversion (IH^2®). Their process consists of a fluid bed reactor, where the catalytic hydropyrolysis takes place, and a fixed bed hydroconversion reactor, where the deep HDO takes place. Different types of biomass were tested, and the yield of condensed organic liquid and C_{4+} hydrocarbons in the product gas phase varied between a mass fraction of 20.6 and 46.3 %. The IH^2® process has been able to run continuously for 750 h in a pilot plant with a biomass feeding rate of 50 kg per day. The composition of the catalyst used in the IH^2® process has not been reported. Carbon footprint analysis of the IH^2® process showed that producing liquid fuels from this process, when compared to conventional production from fossil fuels, decreases the emission of greenhouse gases with 67-86 % [14]. Dayton et al. [15–17] also conducted several studies on catalytic hydropyrolysis using loblolly pine with a setup that did not include an additional HDO reactor after the fluid bed catalytic hydropyrolysis reactor. Using a commercially available hydrotreating catalyst gave an initial low oil yield (mass fraction below 5 %), but the oil yield increased over time to a mass fraction of 12.5 % as the catalyst deactivated [15]. Several experiments at different temperatures and hydrogen pressures with a commercially available NiMo hydrotreating catalyst have also been conducted with the same setup [16]. The catalyst was reduced in hydrogen and not sulfided prior to the experiments. Liquid organic yields between a mass fraction of 12.6 and 25.6 % with an oxygen mass fraction between 2.4 and 11.9 % and a char yield between 7.4 and 26 % were obtained depending on temperature, total pressure and hydrogen partial pressure. The carbon recovery in the organic liquid and C_{4+} gases varied between 34.8 and 42.0 %, thus being significantly higher than for zeolite based catalytic pyrolysis [16]. These results indicate that catalytic hydropyrolysis is a potential technology for converting solid biomass to liquid transportation fuels. The knowledge base on this type of process in the open literature is however still scarce. Often the catalyst composition is not reported and the liquid oil produced is not characterized in depth. Furthermore the combination of catalytic hydropyrolysis followed by HDO is not fully understood.

In this study, catalytic hydropyrolysis of beech wood has been performed in a fluid bed reactor with a sulfided commercial $CoMo/MgAl_2O_4$ catalyst followed by a HDO reactor loaded with a sulfided commercial $NiMo/Al_2O_3$ catalyst. The concept is thus similar to the IH^2® process [1]. With this reactor combination it is expected that the biomass can be converted into a mixture of naphtha and diesel. It is well-known that the

temperature is an important parameter in pyrolysis [18], thus the effect of the temperature is investigated in the range relevant for catalytic hydropyrolysis (365 to 511 °C). There is also a lack of knowledge of the effect of hydrogen pressure on catalytic hydropyrolysis of wood, and the effect of pressure is therefore investigated in the range 1.6 to 3.6 MPa. Furthermore equilibrium calculations indicate that the liquid product composition changes in the tested temperature and pressure range. This is to our knowledge the first study in the open literature of hydropyrolysis of wood using a sulfided hydrotreating catalyst. In order to get a comprehensive understanding of the effect of the temperature and pressure the produced oil is extensively characterized.

2.2 Material and methods

2.2.1 Biomass feedstock

Bark free beech wood supplied by Dansk Træmel (Product number: 10000251250390) was used as biomass. The particle size was approximately 200-700 µm. The moisture mass fraction was 6.72 % (dried at 105 °C) and the ash mass fraction was 0.59 % dry basis. The composition and the higher heating value (HHV) of the beech wood are shown in Table 2.1.

Table 2.1. Composition of bark free beech wood

C	499	g kg^{-1} dry
H	60	g kg^{-1} dry
N	1.3	g kg^{-1} dry
O	430	g kg^{-1} dry
K	1.2	g kg^{-1} dry
Ca	1.3	g kg^{-1} dry
S	48	mg kg^{-1} dry
Na	9.9	mg kg^{-1} dry
Mg	350	mg kg^{-1} dry
Si	140	mg kg^{-1} dry
P	75	mg kg^{-1} dry
Cl	2.0	mg kg^{-1} dry
Mn	170	mg kg^{-1} dry
Fe	24	mg kg^{-1} dry
Cu	2.1	mg kg^{-1} dry
Zn	4.9	mg kg^{-1} dry
Sr	4.6	mg kg^{-1} dry
HHV*	19.7	MJ kg^{-1}

**Calculated from Milne formula: $0.341\times C+1.322\times H-0.12*O-0.12\times N+0.0686*S-0.0153\times ash$*[19]

2.2.2 Catalysts

The catalyst used in the fluid bed reactor was a $CoMo/MgAl_2O_4$ catalyst supplied by Haldor Topsøe A/S. The active CoMo phase was chosen because it is an efficient hydrodeoxygenation catalyst [20–27], and $MgAl_2O_4$ was chosen as support due to its mechanical strength and moderate acidity, anticipating it would lead to less attrition and char formation in the fluidized bed. The catalyst was received as extrudates and was crushed and sieved to obtain a particle size between 180-355 µm. This particle size distribution was chosen to obtain a good fluidization of the bed. A fresh load of 50 g catalyst was used in each experiment. The fixed

bed reactor was loaded with 173 g NiMo/Al_2O_3 catalyst supplied by Haldor Topsøe A/S. The catalyst was shaped as extrudates and was used as received. To ensure a high degree of deoxygenation in all experiments the catalyst in the fixed bed reactor was replaced between experiment 5 and 6. The catalysts in both reactors were sulfided prior to each experiment to obtain the most active phase.

2.2.3 Experimental setup

A bench scale setup was constructed and a simplified piping and instruction (PI) diagram is shown in Figure 2.1. The feeding system consists of a gas mixing system (H_2, H_2S, N_2), where the gas flows are controlled by Brooks mass flow controllers (Model: SLA5850). A liquid feeding system supplying dimethyl disulfide (DMDS; Sigma-Aldrich ≥99 %) with a pump and evaporator (operating temperature: 200 °C) was used for sulfidation of the catalysts. Because of the relatively high cost of bottled H_2S, DMDS was used during the sulfidation. A pressurized vessel with a volume of 4 L was used for biomass feeding. A screw placed at the bottom of the vessel was used to push the biomass to the feeding tube, where it was rapidly transported by a flow of hydrogen to the reactor. The biomass was preheated before entering the fluid bed reactor by heating the feeding tube to approximately 200 °C. To ensure a steady biomass feeding rate the biomass in the vessel was continually stirred by an impeller.

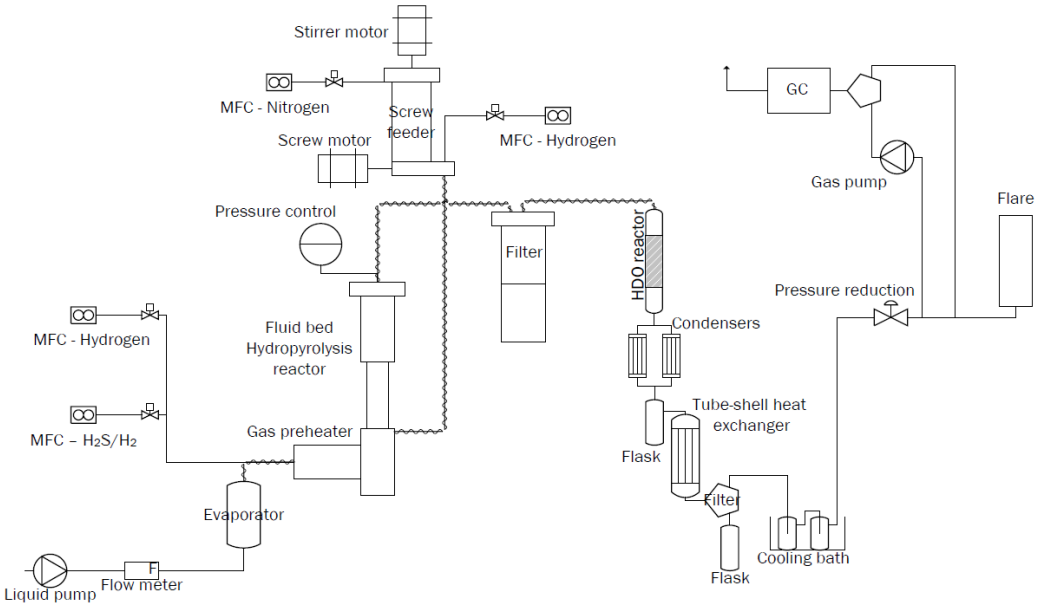

Figure 2.1. Simplified piping and instrumentation diagram of the used setup

The reactor system consisted of a fluid bed hydropyrolysis reactor, a filter, and a fixed bed hydrodeoxygenation (HDO) reactor. The basic principle of the used setup is similar to the IH^2® process [1]. The fluid bed reactor was made of Incoloy 800 HT and the HDO reactor and filter were made of 316L stainless steel. The fluid bed consisted of an electrical gas preheater, a gas distribution tube, a reaction zone, and a disengagement zone. In order to ensure that the gas was well distributed a sintered metal plate (GKN Sinter Metals SIKA-IL 10 IS, 5 mm height) was placed between the gas distribution tube and the reaction zone. The reaction zone consisted of a 200 mm long tube with an inner diameter of 29.46 mm. The disengagement zone was a 200 mm long tube with an inner diameter of 49.25 mm. The products exited through a tube (inner di-

ameter: 3.87 mm) located 3.6 cm from the start of the disengagement zone, however this distance was increased to 8.6 cm after experiment 1. The reactor is designed in such a way that the char will be entrained out of the disengagement zone while the catalyst primarily will stay in the reaction zone. A multipoint thermocouple measured the temperature every 80 mm in the reaction zone. The entrained solids (char and catalyst fines) were captured with a heated (350 °C) filter. The vapors and gas were further upgraded in a fixed bed HDO reactor. This reactor consisted of a tube and a flange with a total length of 642 mm and an inner diameter of 32.46 mm. The top part (200 mm) of the reactor was filled with glass beads and the next 360 mm of the reactor was loaded with the $NiMo/Al_2O_3$ catalyst. In order to keep the catalyst in position, 20 mm of quartz wool and a 60 mm holder were placed below the catalyst bed. A multipoint thermocouple (4 points) measured the temperature through the catalyst bed. In order to avoid condensation of the vapors the tubing between the fluid bed, filter, and HDO reactor were heat traced to approximately 350 °C.

The liquid product was collected in a cooling section with 3 stage cooling (20 °C, 2 °C, and −40 °C). The pressure was controlled with a backpressure regulator, and the remaining gas was sent to a flare. A small fraction of the gas was pumped through a filter to an online gas chromatograph (GC) with a flame ionization detector (FID) and two thermal conductivity detectors (TCD), which measured the gas composition (H_2, H_2S, N_2, CO, CO_2, C_1 to C_5, and C_{6+} hydrocarbons) every 10 minutes. The total mass of the collected liquid products was determined. The amount of aqueous phase was determined by measuring the volume in a 500 cm^3 graduated cylinder and assuming the density was 996.5 kg m^{-3}, corresponding to the density of water at 25 °C and atmospheric pressure. GC-MS of the aqueous phase showed that it was essentially pure water. The amount of organic phase was then determined by subtracting the mass of the aqueous phase from the mass of the condensed liquids. The aqueous phase was separated from the organic phase using a separation funnel. The H_2S dissolved in the organic phase was removed by bubbling with N_2 for approximately one hour, which lead to a mass loss between 2 and 7 %, mostly due to vaporization of light hydrocarbons.

After each experiment, the catalyst and remaining char was removed from the fluid bed, and replaced by a fresh batch of catalyst to be used in the subsequent experiment. The catalyst was initially sulfided at 2.6 MPa, 350 °C with 2-7.5 mole % H_2S, 5 mole % N_2 in 87.5-93 mole % H_2 by feeding DMDS (flow: 0.710-2.770 cm^3 min^{-1}) to the system. After sulfidation, the system was depressurized and the unconverted DMDS was collected. Then the reaction conditions listed in Table 2.2 were established. When the temperature in the reactors reached steady state, the experiment was started by turning on the screw feeder. The total gas inlet flow at the reaction temperature and pressure corresponded to approximately three times the minimum fluidization velocity for the used catalyst particles.

2.2.4 Analysis methods

2.2.4.1 Liquid products

Several different methods were used to analyze the condensed organic phase. The hydrogen content was measured with H-NMR on a Bruker minispec mq20. The samples were preheated to 50 ^oC for 25 minutes and then moved to the measuring cell, also heated to 50 ^oC. The procedure followed the ASTM method D7171. The sulfur content was measured by energy dispersive X-ray fluorescence using an X-Supreme8000 instrument from Oxford Instruments, according to ASTM D4294. The simulated distillation (SIMDIS) curves were measured on two different GC's: Agilent 7890 A and Agilent 6890N. The ASTM D86 distillation curve was then calculated according to ASTM D 7213 C.

The condensed organic liquid samples were characterized by GC×GC-ToF/MS or -FID using a LECO® Pegasus 4D^{TM} instrument. The instrument included an Agilent 7890A GC equipped with a Gerstel® CIS 4

PTV inlet, a secondary oven, a quad-jet, dual-stage cryogenic-based (liquid N_2) modulator, a time-of-flight (ToF) mass spectrometer (MS) and a flame ionization detector (FID). The primary (1D) and secondary (2D) columns were Restek® Rxi-5Sil MS and Restek® Rxi-17Sil MS, respectively.

0.3 mm^3 sample was injected in pulsed split mode (split ratio 1:50) into the PVT inlet at 40°C, and then raised to 300°C (10K s^{-1}), with a total hold up time of 1.5 min. The main oven with the 1D column was held at 40°C for 1.5 min and then ramped to 290°C at 2.5 K min^{-1}; the secondary oven and modulator were run with offsets to the main oven of +5°C and +20°C, respectively; total run time was 101.5 min. Helium (He) was used as carrier gas at constant flow rate of 1.5 cm^3 min^{-1}, and the modulation period was 9 sec. For selected samples, compounds in the condensed organic phase were identified using the ToF/MS detector. The transfer line and ion source were operated at constant temperatures of 250°C and 225°C, respectively. The ToF/MS was run in EI mode at 70 eV and an acquisition rate of 100 spectra sec^{-1} for m z^{-1} = 41 to 441. The NIST2008 mass spectral database was used as reference. For group quantification, the FID was used. The detector was operated at 300°C and with a sampling rate of 100 Hz. Based on the GC×GC-ToF/MS analysis the compounds were classified into six groups: paraffins, naphthenes, mono-, di- and tri- and higher aromatics, phenolics, and in some samples oxygenated aliphatics. The relative amount (FID area-%) of each compound class was estimated as the sum of areas of all detected peaks in that class divided by the total peak area of all compound classes. All data was processed using the ChromaTof® 4.50 software.

Selective analysis of oxygenates was conducted using a GC with an atomic emission detector (AED). An Agilent 7890A GC was coupled to a JAS 2370 AED in oxygen selective mode. The oxygen emission line at 171nm was used in combination with reaction gases of 10% methane in nitrogen and pure hydrogen and with a makeup helium gas flow of 80 ml min^{-1}. Cavity and transfer line were heated to 320°C. The GC column was a Phenomenex ZB-50 (60m X 0.25mm X 0.25µm) in connection with a JAS PTV inlet in split mode (1:5) and 0.5 mm^3 injection. The oven was held at 40°C for 1 min and then ramped to 340°C @ 7 K min^{-1}.

Quantification was done by adding known amounts of 4-fluorophenol (CAS number: 371-41-5) to known amounts of the sample. The signal for the internal standard was used for calibration of the other oxygenates in the sample. To increase the sensitivity of the method and to remove potential interferences from the sample matrix the polar compounds were extracted from the sample by use of Solid Phase Extraction on silica based cartridges. The weighted sample including the internal standard was transferred to the Si-SPE cartridge with n-heptane and the non-polar fraction eluted from the cartridge with 10 absorbent volumes of n-heptane. The polar compounds were subsequently eluted with 3 absorbent volumes of acetone. The acetone fraction containing the polar compounds were reduced over nitrogen to about 300 mm^3 and injected in the GC for oxygen selective detection. Identification of individual compounds was done after analysis of pure compounds.

Selective analysis of sulfur containing compounds was also conducted using GC-AED using the sulfur emission line at 181nm. The GC column was a Phenomenex ZB-1 (30m X 0.25mm X 1.0µm) in connection with a JAS split/splitless inlet in split mode (1:10) and 0.5 mm^3 injection. The oven was held at 40°C for 5 min and then ramped to 340°C @ 10 K min^{-1} and a final time of 10 min.

Quantification was done using an external standard sample containing known amounts of benzothiophene, dibenzothiophene and 4-methyl-dibenzothiophene. Identification of individual compounds was done after analysis of pure compounds. The samples were diluted if necessary in a suitable solvent prior to GC analysis.

The aqueous phase was analyzed on a Shimadzu GC-MS/FID with a Supelco Equity-5 column. The compounds were identified on the MS and quantified using the parallel FID. The concentration of phenol was

determined by use of external standards. The concentration of the remaining hydrocarbons was determined from the FID signal using the effective carbon number method [28].

2.2.5 Solid sample analysis

The elemental composition (CHNS) of the biomass was analyzed on a Eurovector EA-3000 elemental analyzer and the oxygen content was determined by difference. The elemental composition (CHNSO) of the produced char was analyzed at DB Lab A/S using a Flash 2000 elemental analyzer from Thermo Fisher. The relative uncertainty for the C, H, N, O, and S on the char was 1.0, 2.0, 2.0, 3.0, 2.0 %, respectively. In order to obtain a more homogeneous sample the char was crushed prior to this analysis. Other elements were determined by wavelength dispersive X-ray fluorescence using a Supermini 200 XRF instrument from Rigaku. Samples were ashed and the ash fused to a bead with lithium metaborate (BO_2Li) prior to analysis. The ash and catalyst content in the produced char was measured by combusting the samples at 600 ^oC in air. The ash content in char was calculated by assuming that all the ash in the biomass ends in the char and the catalyst content was calculated by difference.

2.3 Results and Discussion

2.3.1 Effect of temperature and pressure on the product distribution

The effect of operating conditions on catalytic hydropyrolysis of beech wood was studied by varying the total pressure and the temperature in the fluid bed and the HDO reactor as shown in Table 2.2. The temperature in the fluid bed was between 365 and 511 °C and the temperature in the HDO reactor was between 345 and 400 °C. The total pressure was varied between 1.6 and 3.6 MPa. In experiments 1 to 8 the H_2S concentration was 460×10^{-6} mole fraction, while it was approximately 50×10^{-6} mole fraction in experiments 9 to 11. Due to the short experimental time (1.2-4 hours) the catalysts have most likely remained sulfided during the experiments with low H_2S concentration. The obtained mass balances varied between 90 and 101 % daf on the basis of the used biomass. In experiment 6 the entrance to the fluid bed plugged, thus stopping the experiment after only 1.2 hours, which is the reason for the poor mass balance of 90 daf. The short operation time of experiment 6 is part of the reason for the low obtained yields, with exception of the char yield. The organic yield (mass fraction daf basis) including condensed organics and C_{4+} gases varied between 16.6 to 22.5 % daf, the C_1-C_3 gas yield varied between 10.6 to 15.5 %, the CO+CO_2 yield varied between 13.2 to 17.5 %, the char yield varied between 9.56 to 18.5 %, and the aqueous yield varied between 31.2 to 37.8 %. The carbon recovery for the condensed organics and C_{4+} gases varied between 28.0 and 38.4 %, and for the C_1-C_3 gases the carbon recovery was 19.0-24.3 %. An overview of hydrogen and oxygen recovery compared to the biomass input is shown in Table A.1. The yields of condensed organics and C_{4+} are lower than what has been reported for the IH^2® process, where the yield was between a mass fraction of 26 and 30 % daf, when using wood [1,2]. The reason for this difference may be due to a different biomass or the use of a different catalyst. The repeatability was tested in experiment 4 and 5, where the process conditions were similar. The product distribution in experiment 5 was quite similar to experiment 4 with yields deviating less than a mass fraction of 1 % points, indicating that experiments were reproducible. Depending on the applied test conditions between 2.6 and 33 % of the catalyst loaded in the fluid bed was transported to the filter during the experiments. The biomass feeding rate was difficult to control and varied between 161 and 300 g h^{-1}. However, due to the large excess of hydrogen it is expected that the feeding rate and weight hourly space velocity (g biomass (g catalyst hr)$^{-1}$) did not have an impact on the results, and this is also supported by the experimental results.

Table 2.2. Summary of reaction conditions and mass balances for catalytic hydropyrolysis of beech wood

Test:	**1**	**2**	**3**	**4**	**5**	**6**	**7**	**8**	**9**	**10**	**11**
Test conditions											
Hydropyrolysis T. (°C)	430	400	400	470	468	365	451	511	453	449	450
HDO T. (°C)	370	345	400	390	394	395	371	363	370	364	-
Pressure (MPa)	2.6	2.6	2.6	2.6	2.6	2.6	2.6	2.6	1.6	3.6	2.6
Feed time (h)	3.5	2.6	4.0	4	3.6	1.2	4.0	3.0	4.0	4.0	3.9
Feeding rate (g h^{-1})	282	194	212	233	300	239	250	171	161	159	174
H_2S (mole frac. $\times 10^6$)	460	460	460	460	460	460	460	460	47	50	48
H_2 flow (mole min^{-1})	3.35	3.27	3.27	3.35	3.35	3.35	3.35	3.35	2.14	5.08	3.57
N_2 flow (mole min^{-1})	0.20	0.20	0.20	0.20	0.20	0.20	0.20	0.20	0.02	0.03	0.03
$\frac{H_2 \text{ consumed (g)}}{\text{Biomass used (kg)}}$	44	42	39	47	47	33	46	45	35	46	35
Yields (mass fraction % daf)											
Gas	30.0	25.8	28.8	32.3	31.3	23.9	31.5	32.2	30.3	26.3	27.4
Char	14.2	14.6	15.0	11.4	11.9	18.5	11.4	9.56	11.0	12.7	12.2
Aqueous phase	35.7	37.8	35.9	36.1	36.0	31.2	35.2	35.6	33.2	37.7	37.0
Organics	11.6	8.8	9.9	11.4	12.7	7.9	12.4	11.1	11.0	10.6	12.0
C_{4+} in the gas	8.6	10.1	11.5	10.3	8.7	8.8	9.1	11.3	8.7	10.3	8.4
Organics + C_{4+}	20.2	18.9	21.4	21.7	21.4	16.7	21.5	22.4	19.7	20.9	20.4
Mass balance	100.1	97.1	101.1	101.5	100.6	90.3	99.6	99.8	94.2	97.6	97.0
Carbon recovery (%)											
C_1-C_3	21.5	19.7	23.1	22.9	21.6	19.4	22.5	24.3	18.9	20.7	19.0
C_{4+}	14.2	16.8	18.9	16.9	14.5	14.4	15.1	18.8	14.4	17.1	13.9
$CO+CO_2$	11.4	9.3	10.1	12.7	12.5	8.2	12.1	12.7	13.3	10.3	12.6
Char	20.9	21.0	22.0	17.3	18.2	26.4	17.2	15.5	15.5	18.9	18.4
Organics	19.9	15.1	17.2	20.3	22.6	13.6	21.4	19.6	19.4	18.6	20.9
Aqueous phase	0.0	0.0	0.0	0.0	0.0	0.0	0.0	0.0	0.0	0.0	0.6
Sum	87.9	82.0	91.3	90.1	89.5	82.0	88.4	90.9	81.4	85.5	85.4
Organic composition (mass fraction %)											
C*	87.5	87.7	88.3	88.8	88.2	88.2	88.0	88.32	88.4	88.1	89.5
H	12.5	12.3	11.7	11.2	11.7	11.8	11.9	10.89	11.2	11.6	10.2
O	<0.001	<0.001	<0.001	<0.001	<0.001	<0.001	<0.001	<0.001	<0.001	<0.001	1.8
S	0.0699	0.34	ND	0.113	0.0909	ND	0.117	0.794	0.417	0.246	0.302
Aqueous phase composition (mass fraction %)											
Organics	0	0	0	0	0	0	0	0	0	0	1.15
Gas composition (mass fraction % daf)											
CO	8.01	6.76	8.31	10.4	9.64	6.48	9.74	11.7	10.8	9.92	11.1
CO_2	8.27	6.51	5.60	6.90	7.88	4.83	7.96	5.05	7.55	3.26	5.71
C_1-C_3	13.7	12.5	14.8	14.7	13.8	12.4	12.9	15.5	12.0	13.2	12.1
C_{4+}	8.58	10.1	11.5	10.3	8.74	8,78	8.83	11.3	8.67	10.3	8.35
Char composition (mass fraction %)											
C	71	69	73	72	68	67	72	76	67	70	72
H	3.7	3.8	3.9	3.4	3.4	4.0	3.7	3.4	3.5	3.5	3.4
N	0.54	0.54	0.56	0.45	0.37	0.45	0.41	0.39	0.40	0.40	0.41
S	0.50	0.55	0.48	0.66	0.63	0.49	0.53	0.77	1.13	0.62	0.61
O	20	21	21	18	16	22	18	13	23	19	19
Ash	4.0	5.0	4.4	5.6	5.3	6.5	5.0	6.5	4.6	5.5	4.8

*By difference

The temperature in the two reactors was varied simultaneously in experiments 1 to 8. The results from experiment 2 and 3 show that increasing the temperature in the HDO reactor increased the yield of C_1-C_3 slightly, but in general only had a minor effect on the product distribution. Varying the temperature in the fluid bed

reactor changed the product distribution as shown in Figure 2.2. Increasing the temperature in the fluid bed reactor mainly decreased the char yield, while increasing the gas yield, in agreement with the general observations in the pyrolysis literature [29–32] and with the results obtained with IH^2® process [1]. The organic yield including condensed organics and C_{4+} gases increased when the fluid bed temperature increased from 365 to 400 °C above which it remained constant within the experimental uncertainty. The aqueous mass yield increased from 31 to 36 % daf when the fluid bed temperature increased from 365 to 400 °C, while further increasing the fluid bed temperature had a negligible impact on the aqueous yield. Hydrocarbons were not observed in the aqueous phase for experiments 1 to 10 where the HDO reactor was used. Interestingly, Dayton et al.[16] using a reduced NiMo catalyst observed an increase in char yield from 10.8 to 26.0 % daf and a decreased yield of condensed organics from 25.6 to 16.8 % daf when the temperature increased from 375 to 475 °C. Their results indicate accelerated cracking over the applied catalyst at elevated temperatures, which was not observed in our study.

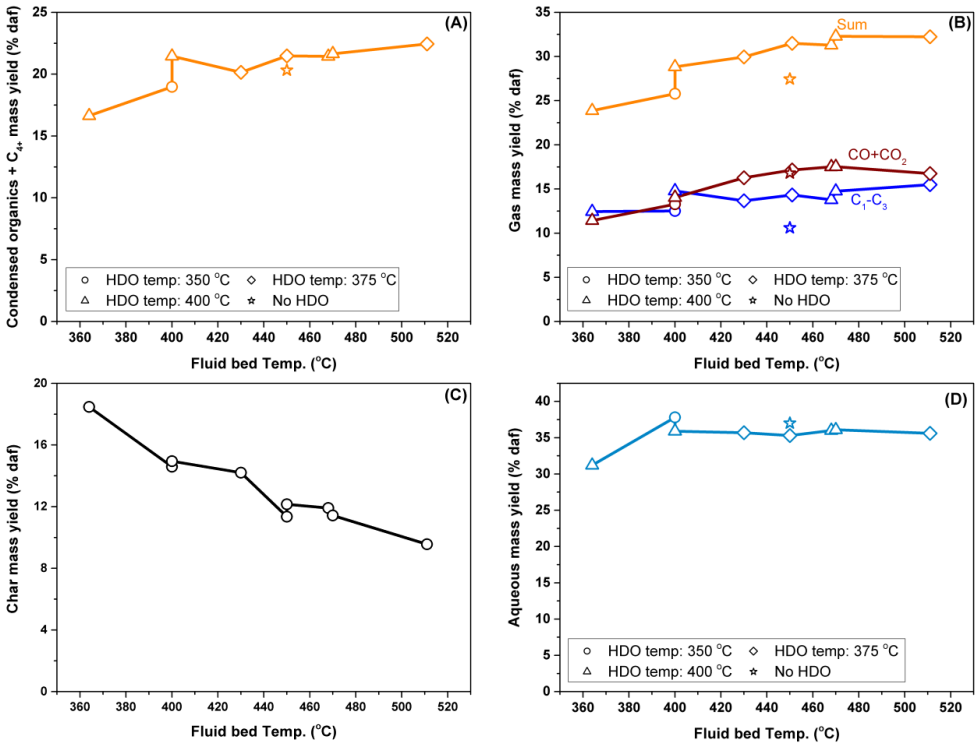

Figure 2.2. Effect of temperature on the yield of condensed organic liquid and C_{4+} gases (A), yield of light gases (B), char yield (C), and aqueous yield (D). Conditions: pressure: 2.6 MPa, H_2 flow: 3.27-3.35 mole min^{-1}, N_2 flow: 0.20 mole min^{-1}, biomass feeding rate: 212-300 g h^{-1}, H_2S concentration: 460 × 10^{-6} mole fraction.

A small decrease in the yield of condensed organic liquid and C_{4+} gases and an increase in the aqueous yield was observed when the HDO reactor was bypassed as seen by comparison of experiments 7 and 11 in Table 2.2. GC-FID/MS of the aqueous phase from experiment 11 showed that it contained small amounts of oxygenated aliphatics and phenols, with a total organic mass fraction of 1.15 % corresponding to an organic yield of a mass fraction of 0.51 % daf. The dissolved oxygenates in the aqueous phase can partly explain the observed decrease in yield of condensed organics and C_{4+} when comparing experiment 11 with experiment 7.

The total CO and CO_2 yield did not decrease when the HDO reactor was bypassed, but a decrease in the C_1-C_3 yield was observed. This indicates that the remaining oxygen is mainly removed by hydrogenation in the HDO reactor, but hydrocracking also takes place in the HDO reactor. However, the CO_2 mass yield decreased from 7.96 % daf in the experiment with the HDO reactor (experiment 7) to 5.71 % daf when the HDO reactor was bypassed (experiment 11), while the CO yield increased from 9.71 to 11.1 % daf. Considering that the aqueous phase yield also increased when the HDO reactor was bypassed, this indicates that the water gas shift reaction takes place in the HDO reactor. In the experiments where the HDO reactor was used no olefins were detected in the gaseous products. However, when the HDO reactor was bypassed, olefins accounted for 26 % of the C_2-C_5 hydrocarbons in the gas phase. The hydrogen to biomass consumption also decreased from 46 g kg^{-1} to 35 g kg^{-1} when the HDO reactor was bypassed.

The influence of pressure on the product distribution is shown in Figure 2.3, by comparison of experiment 7, 9, and 10 in Table 2.2. Increasing the total pressure did not affect the liquid organic yield, but it increased the aqueous yield, while decreasing the CO and CO_2 yield. This was most likely due to the increase in hydrogen partial pressure, which makes oxygen removal by hydrodeoxygenation more favorable compared to cracking. The hydrogen to biomass consumption also increased from 35 g kg^{-1} at 1.6 MPa to 46 g kg^{-1} at 3.6 MPa, but did not increase further when the pressure increased to 3.6 MPa. The char yield also increased slightly with increasing pressure; however this is within the experimental uncertainty. Dayton et al.[16] observed an increase in the hydrogen to biomass consumption from between 20 to 25 g kg^{-1} at a H_2 volume fraction of 20 %, to between 35 to 38 g kg^{-1} at 40 % at 2.168 MPa. However, they did not observe a related increase in the aqueous yield, thus indicating that hydrogenation of the olefins increased with increasing hydrogen partial pressure [16].

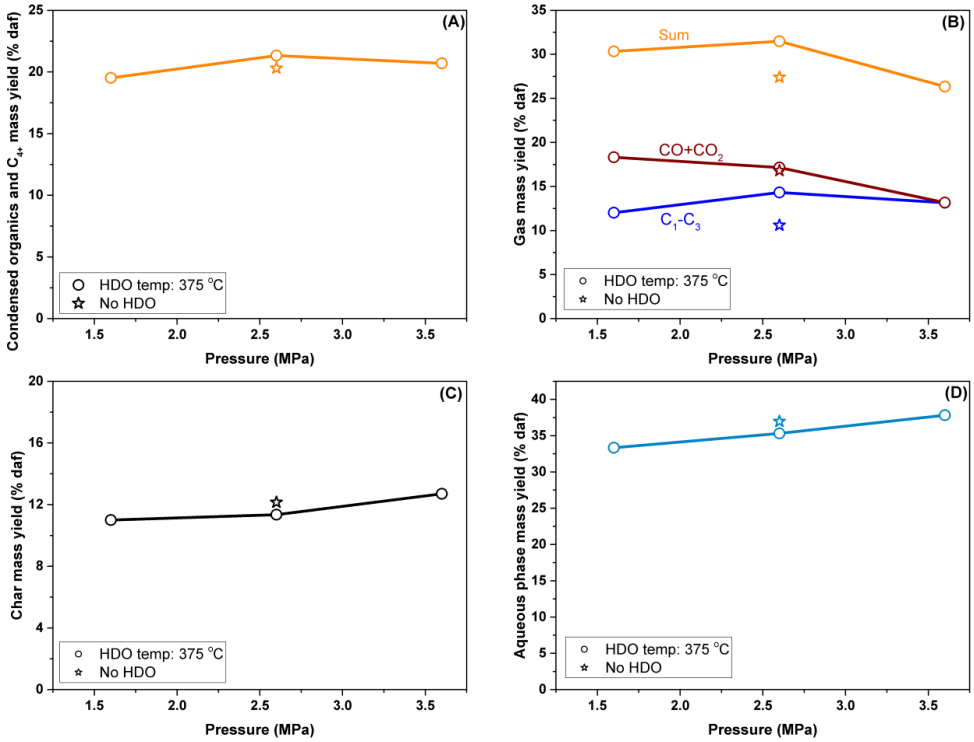

Figure 2.3. Effect of pressure on the organic liquid and C_{4+} gases yield (A), gas yield (B), char yield (C), and aqueous liquid yield (D). Conditions: Fluid bed temperature: 453-449 °C, HDO temperature: 364-371 °C, H_2 flow: 2.14-5.08 mole min^{-1}, N_2 flow: 0.02-0.03 mole min^{-1}, biomass feeding rate: 159-250 g h^{-1}, H_2S concentration: 47-460 $\times$ 10^{-6} mole fraction.

2.3.2 Chemical composition of the condensed organics

In the experiments where the HDO reactor was used the hydrogen mass fraction of the condensed organics was between 10.9 % and 12.5 %. When the HDO reactor was bypassed the hydrogen mass fraction decreased to 10.2 %, indicating that olefins and aromatics are saturated in the HDO reactor. The simulated distillation curves for the condensed organics are shown in Figure 2.4. As can be seen, a volume fraction of 20 to 40 % was naphtha, while the rest were in the diesel boiling point range. However, the uncondensed C_{4+} organics, that were detected in the gas phase, are most likely mainly naphtha, making a total naphtha mass fraction of 50-70 % of the condensed organics and C_{4+} in the gas. Comparing the simulated distillation curves for experiment 7 and 11 shows that the boiling point for the condensed organics increased when the HDO reactor was bypassed (see supplementary information Figure A.1), this was due to the increased oxygen concentration in the product. For the condensed organics from experiment 8, a volume fraction of 99.5 % of the organics had a boiling point below 308 °C, thus indicating that increasing the fluid bed temperature to 511 °C decreased the boiling point, possibly due to increased cracking of the vapors. Varying the pressure only had a small effect on the distillation curves (experiment: 7,9 and 10) that was within the experimental uncertainty.

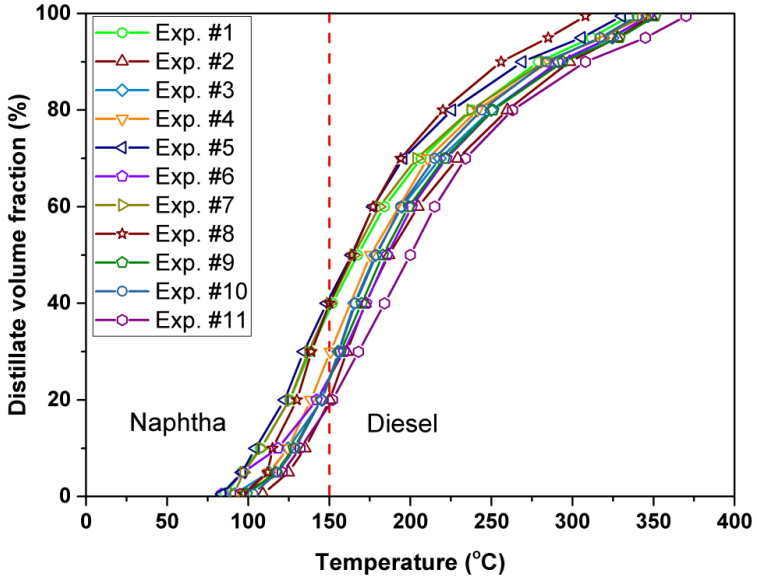

Figure 2.4. GC simulated distillation curves for the condensed organics. The curves are calculated using D86 according to ASTM D 7213 C.

GC×GC-FID and GC-AED was used to gain a deeper insight into composition of the condensed organics. GC-AED was used to selectively identify the sulfur and oxygen containing compound classes in the condensed organics. GC×GC-FID was used to measure the concentration of the different types of hydrocarbons and an example of a chromatogram is shown in Figure 2.5.

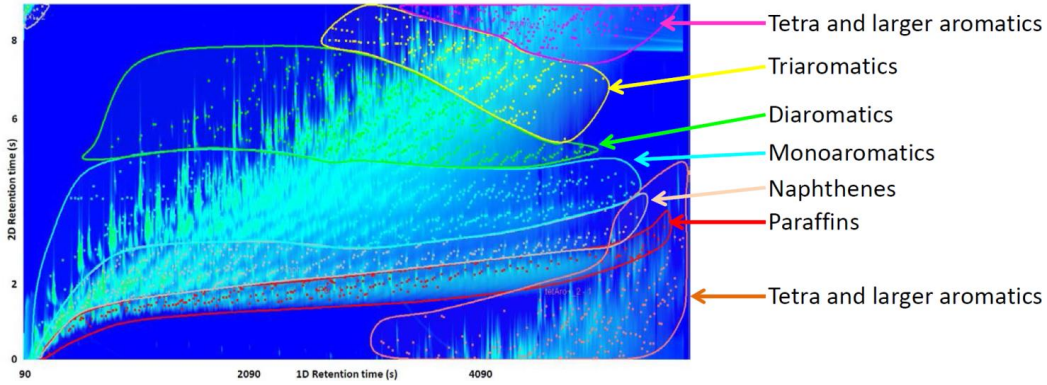

Figure 2.5. GC×GC-FID contour plot of the condensed organics from experiment 4. Conditions: Fluid bed temperature: 470 °C, HDO temperature: 390 °C, pressure: 2.6 MPa, H_2 flow: 3.35 mole min^{-1}, N_2 flow: 0.20 mole min^{-1}, biomass feeding rate: 233 g h^{-1}, H_2S concentration: 4.6×10^{-6} mole fraction.

The concentration of paraffins was between 2.5 and 5.1 % peak area. The concentration of aromatics and naphthenes are shown as a function of the fluid bed temperature and the total pressure in Figure 2.6. Between 35 % (experiment 1) and 60 % area-FID (experiment 4) of the aromatics were monoaromatics, but considerable amounts of diaromatics were also present (up to 13 %), while only low concentrations (below

4.5 %) of tri- and larger aromatics were observed. The concentration of aromatics decreased when the temperature in the fluid bed was increased from 365 to 430 °C, but increased when the temperature was further increased. Equilibrium calculations for monoaromatics show that they are favored over the corresponding naphthenes when the temperature is above 405 °C (see supplementary information Figure A.2 and Figure A.3). This indicates that the hydrogenation of aromatics to naphthenes was kinetically controlled below 430 °C and equilibrium controlled at higher temperatures. The HDO reactor has only a minor influence on the aromatic concentration. In experiments 2 and 3 the fluid bed temperature was 400 °C, and the temperature in the HDO reactor was 345 and 400 °C respectively, but the concentration of aromatics did not change. As shown in Figure 6B, increasing the total pressure at 450 °C in the fluid bed decreased the aromatic concentration and increased the naphthenes concentration, which is most likely due to the increased hydrogen pressure shifting the equilibrium towards the saturated products and increasing the rate of hydrogenation (see supplementary information Figure A.4).

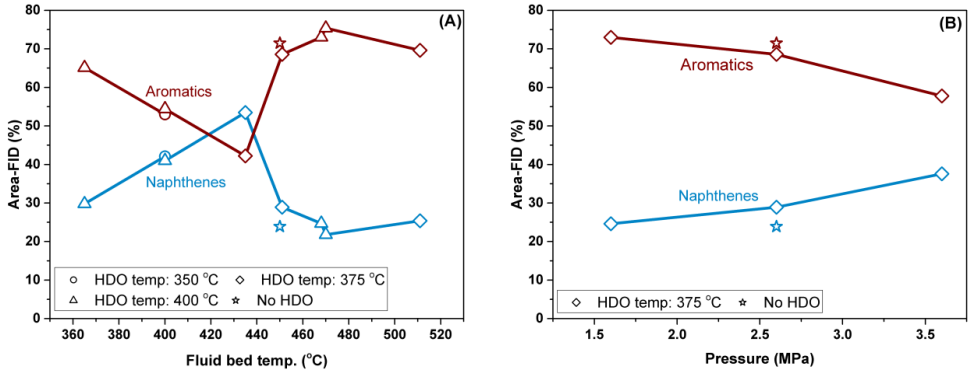

Figure 2.6. The effect of temperature at 2.6 MPa (A) and pressure at 450 °C (B) on the aromatic (including phenols) and naphthene content in the condensed organic liquid. Conditions: H_2 flow: 2.14-5.08 mole min^{-1}, N_2 flow: 0.02-0.20 mole min^{-1}, biomass feeding rate: 159-300 g h^{-1}, H_2S concentration: 47-460 × 10^{-6} mole fraction.

The result of the GC×GC-FID/MS analysis of the condensed organics in experiment 7 and 11 is shown in Figure 2.7. The reaction conditions in these two experiments were the same except that the HDO reactor was bypassed in experiment 11. When the HDO reactor was bypassed (experiment 11) the relative area of hydrocarbons with less than 10 carbon atoms was 41 % and hydrocarbons between 10 and 15 carbon atoms was 43 %. When the HDO reactor was used (experiment 7) the relative area for hydrocarbons with less than 10 carbon atoms increased to 53 %, while it decreased to 33 % for hydrocarbons with between 10 and 15 carbon atoms. This decrease in carbon number mainly decreased the concentration of diaromatics. For both experiment 7 and 11 alkyl benzenes with between 15 and 20 carbon atoms were detected. In the experiment without the HDO reactor, oxygenated aliphatics and phenols were detected in the product, but they were hydrodeoxygenated in the experiment with the HDO reactor. Oxygen specific GC-AED showed that when the HDO reactor was bypassed the total oxygen mass fraction in the condensed organics was 1.8 % and that the main oxygenates were different phenols (see supplementary information Figure A.5). When the HDO reactor was used the oxygen mass fraction was below 0.001 % and only traces of phenols, naphthol, and dibenzofurans were detected in the condensed organics.

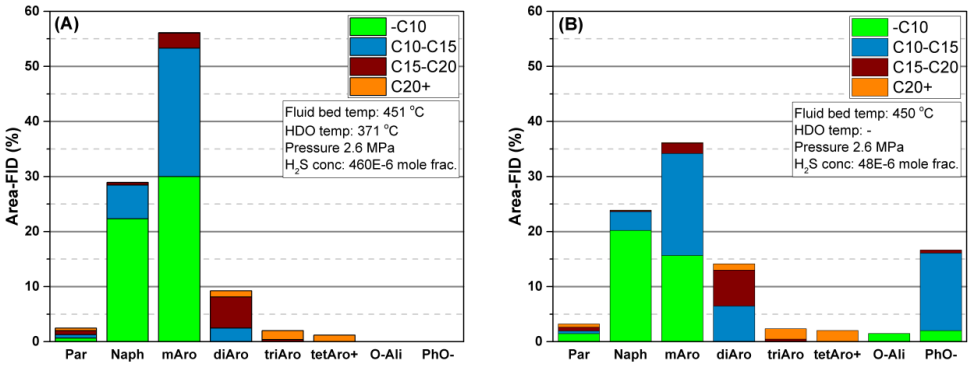

Figure 2.7. The composition of the condensed organic phase from experiment 7 (with HDO reactor) (A) and experiment 11 (without HDO reactor) (B). Conditions: H_2 flow: 3.35-3.57 mole min^{-1}, N_2 flow: 0.20-0.02 mole min^{-1}, biomass feeding rate: 174-250 g h^{-1}, H_2S concentration: 48-460 $\times 10^{-6}$ mole fraction. The components in the condensed organics is divided into paraffins (Par), naphthenes (Naph), monoaromatics (mAro), diaromatics (diAro), triaromatics (triAro), tetraaromatics and larger aromatics (tetAro+), oxygenated aliphatics (O-Ali) and oxygenated aromatics (PhO-). The components are also divided into the following groups based on the number of carbon atoms in the components: less than 10 carbons atoms (-C10) between 10 and 15 carbons atoms (C10-C15), between 15 and 20 carbon atoms (C15-C20), more than 20 carbon atoms (C20+).

The sulfur mass fraction in the condensed organics phase varied between 0.06 and 0.8 %, which is very high for oil produced from biomass. Therefore, the condensed organics from experiment 7 was analyzed with sulfur specific GC-AED. This showed that a large part of the sulfur was H_2S, which was not properly stripped from the condensed organic phase. DMDS was also detected, thus indicating that part of the DMDS used in the sulfidation of the catalyst ended up in the condensed organics. Trimethylthiophen (S mass fraction: 0.036 %), benzothiophene (S mass fraction: 0.003 %), and a S mass fraction of 0.45 % from larger unknown sulfur containing components were also detected. It is possible that part of the sulfur from the H_2S added to the gas phase is incorporated into the organics. The detected sulfur compounds are commonly encountered in petrochemical refining and can be removed by further hydrotreating – either in the online HDO reactor by increasing the residence time, or in a separate reactor. This would slightly increase the hydrogen consumption.

2.3.3 Chemical composition of the char

The carbon mass fraction in the produced char varied between 71 and 81 % and increased with increasing temperature in the fluid bed reactor as shown in Figure 2.8. The oxygen mass fraction varied between 14 and 24 % and decreased with increasing temperature in the fluid bed reactor. The carbon mass fraction increased and the oxygen mass fraction decreased when the pressure increased from 1.6 to 2.6 MPa, but further increasing the pressure to 3.6 MPa did not have a substantial impact on the carbon and oxygen concentration. The hydrogen mass fraction decreased from 4.3 % at 365 °C to 3.7 at 511 °C. The sulfur mass fraction varied between 0.39 and 1.13 % and the nitrogen mass fraction varied between 0.39 and 0.56 %.

Comparing the char composition in Figure 2.8 with the biomass composition in Table 2.1 shows an enrichment of carbon and nitrogen in the char, which is an well-known phenomenon for pyrolysis [33]. The significant sulfur enrichment in the char, indicates that part of the sulfur in the char comes from H_2S that is incorporated into the char. The retention of nitrogen, carbon, oxygen and hydrogen in the char decreased when the fluid bed temperature increased (see supplementary information Figure A.6). The variations in the carbon content with pressure is within the experimental uncertainty.

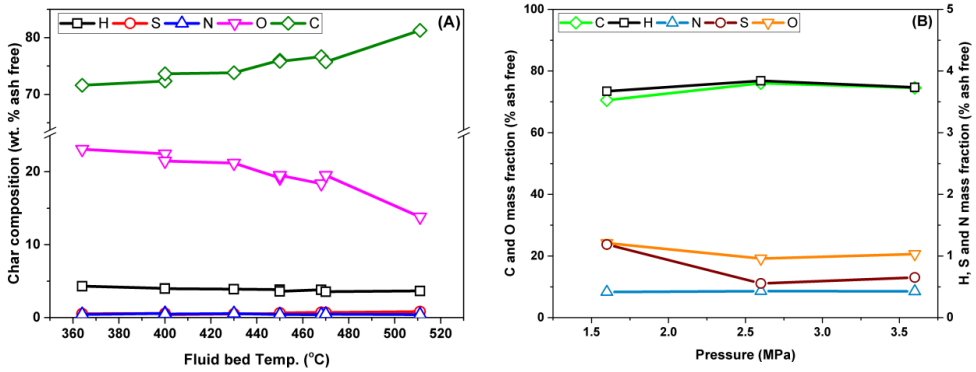

Figure 2.8. The effect of temperature at 2.6 MPa (A) and pressure at 450 °C (B) on the CHNSO composition of the char in the filter. Conditions: H_2 flow: 2.14-5.08 mole min^{-1}, N_2 flow: 0.02-0.2 mole min^{-1}, biomass feeding rate: 159-300 g h^{-1}, H_2S concentration: 47-460 $\times$ 10^{-6} mole fraction.

2.3.4 Energy recovery

The energy recovery was calculated on the basis of the higher heating value (HHV) of the biomass fed to the setup and the HHV of the different phases. The heating value of the char was calculated from the Milne formula (see section 3.2.1), the heating value for the gas was calculated on the basis of the heating value of the different compounds detected in the gas, and the heating value of the condensed organics was calculated from their elemental (CHNSO) composition according to ref. [34]. The resulting energy recoveries for each product are shown in Figure 2.9. The energy recovery for the condensed organics and C_{4+} was between 40 and 53 %, the energy recovery for the gas was between 36 and 45 %, and the energy recovery for the char was between 14 and 19 %. The total energy recovery for all of the experiments was more than 100 %, which is due to incorporation of hydrogen that increases the heating value of the products. The energy added to the products by hydrogen corresponded to between 0.26 and 0.34 MJ MJ^{-1} biomass used. The exothermic hydrogenation reactions decrease the energy recovery in the products compared to the energy in the consumed biomass and hydrogen. The energy recovery for the condensed organics and C_{4+} was directly proportional to the yield indicating that the oil quality was rather constant. At 1.6 MPa the energy recovery was 46 %, while it was 51 and 50 % at 2.6 and 3.6 MPa, respectively. This is because the condensed organics and C_{4+} yield and hydrogen content were slightly lower at 1.6 MPa compared to 2.6 and 3.6 MPa. Thus the differences in the energy recovery at the different pressures are not statistically significant.

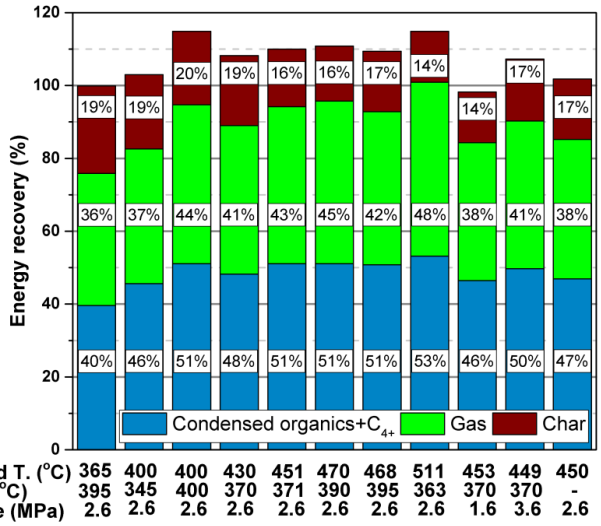

Figure 2.9. The effect of the process conditions on the energy recovery. Conditions: H_2 flow: 2.14-5.08 mole min^{-1}, N_2 flow: 0.02-0.2 mole min^{-1}, biomass feeding rate: 159-250 g h^{-1}, H_2S concentration: 47-460 $\times 10^{-6}$ mole fraction.

Trinh et al. [35] achieved a bio-oil mass yield from fast pyrolysis of wood of 68 % daf, corresponding to an energy recovery of 74 %, which is significantly higher than the energy recovery achieved in this study. However, the bio-oil had an oxygen mass fraction of 35.3 % dry basis. Baldauf et al. [36] tested the ability of a commercial CoMoS catalyst to upgrade pyrolysis oil in a fixed bed reactor and showed that it is possible to achieve a degree of deoxygenation of 99.9 % with an oil mass yield of 33 %. This shows that a total oil mass yield of 22 % daf and energy recovery of 53 % is possible with fast pyrolysis followed by HDO, which is comparable with the results from experiment 8. This indicates that catalytic hydropyrolysis is competitive with fast pyrolysis followed by HDO. Furthermore, Baldauf et al. [36] experienced problems with rapid catalyst deactivation and operational problems due to the instability and coking potential of the used bio-oil, which are problems that were not encountered in this study.

The produced gas could through steam reforming be used to generate the hydrogen needed in the hydropyrolysis and HDO reactor, as proposed by Marker et al. [2]. The process could also be combined with other renewable energy technologies. For instance, electricity produced from wind turbines could be used to generate the hydrogen needed in the process by electrolysis, and the produced gas could instead be converted fully to substitute natural gas by methanation of CO and CO_2. Since the amount of hydrogen added to the products depend on the applied process conditions the process could be adjusted to correspond to the energy available from excess renewable electricity, resulting in energy storage in the form of liquid and gaseous fuels. Our experimental results confirm and expand on the positive results obtained by Marker et al. [1,2] by a similar combined catalytic hydropyrolysis and downstream hydrotreating process.

2.4 Conclusion

In this work, beech wood was converted into liquid fuels by catalytic hydropyrolysis in a fluid bed reactor with a sulfided $CoMo/MgAl_2O_4$ catalyst followed by a deep hydrodeoxygenation in a fixed bed reactor with a sulfided $NiMo/Al_2O_3$ catalyst. The char yield decreased and the gas yield increased with increasing fluid bed temperature, while the condensable organic yield was less affected by the temperature. Increasing the

total pressure mainly increased the aqueous phase yield and decreased the CO and CO_2 yield, while only negligible changes in the yields of condensable organics and char yield were observed. Detailed analysis of the condensed organics showed that it consisted of species in the diesel and naphtha boiling point range. The condensed organics had a high concentration of aromatics and the concentration was mainly controlled by the fluid bed temperature and the total pressure. Comparing the experimental results with equilibrium calculations indicated that the aromatic to naphthene ratio was controlled by the thermodynamic equilibrium at high temperatures, but was kinetically controlled at low temperatures. When using both reactors the condensed organics were essentially oxygen free. Bypassing the HDO reactor increased the oxygen content in the organics, however, the oxygen content was still significantly lower than the oxygen content in normal pyrolysis oil and the oxygen was mainly different phenols, but minor amounts of oxygenated aliphatics were also observed. Overall, the present experimental results indicate that catalytic hydropyrolysis of biomass may be a viable path to green transportation fuels.

Acknowledgments

This work is part of the H2CAP project (Hydrogen assisted catalytic pyrolysis for green fuels) conducted at the CHEC research center at The Department of Chemical and Biochemical Engineering at DTU, Denmark. The work was supported by The Danish Council for Strategic Research (now Innovation Fund Denmark, project 1377-00025A), The Programme Commission on Sustainable Energy and Environment. Funding from DTU is also gratefully acknowledged. The authors would also like to thank Research Engineer Nadia Luciw Ammitzbøll (Haldor Topsøe A/S) for fruitful discussions.

References

[1] T.L. Marker, L.G. Felix, M.B. Linck, M.J. Roberts, Integrated hydropyrolysis and hydroconversion ($IH^{2®}$) for the direct production of gasoline and diesel fuels or blending components from biomass, part 1: Proof of principle testing, Environ. Prog. Sustain. Energy. 31 (2012) 191–199. doi:10.1002/ep.10629.

[2] T.L. Marker, L.G. Felix, M.B. Linck, M.J. Roberts, P. Ortiz-Toral, J. Wangerow, Integrated hydropyrolysis and hydroconversion ($IH^{2®}$) for the direct production of gasoline and diesel fuels or blending components from biomass, Part 2: Continuous testing, Environ. Prog. Sustain. Energy. 33 (2014) 762–768. doi:10.1002/ep.11906.

[3] F. Bergius, Process for distilling and liquefying coal, US Patent 1,669,439, 1928.

[4] F. Bergius, J. Billwiller, Process for producing liquid or soluble organic combinations from hard coal and the like., US Patent 1,251,954, 1918.

[5] Friedrich Bergius, Chemical reactions under high pressure, Nobel Lect. (1932) 33.

[6] M. Steinberg, P.T. Fallon, M.S. Sundaram, Flash pyrolysis of biomass with reactive and non-reactive gas, Biomass. 9 (1986) 293–315. doi:10.1016/0144-4565(86)90080-6.

[7] D. Meier, R. Ante, O. Faix, Catalytic hydropyrolysis of lignin: Influence of reaction conditions on the formation and composition of liquid products, Bioresour. Technol. 40 (1992) 171–177. doi:10.1016/0960-8524(92)90205-C.

[8] F. Melligan, M.H.B. Hayes, W. Kwapinski, J.J. Leahy, Hydro-pyrolysis of biomass and online catalytic vapor upgrading with Ni-ZSM-5 and Ni-MCM-41, Energy & Fuels. 26 (2012) 6080–6090. doi:10.1021/ef301244h.

[9] D.P. Gamliel, L. Wilcox, J.A. Valla, The effects of catalyst properties on the conversion of biomass via catalytic fast hydropyrolysis, Energy & Fuels. 31 (2017) 679–687. doi:10.1021/acs.energyfuels.6b02781.

[10] S. Thangalazhy-Gopakumar, S. Adhikari, R.B. Gupta, Catalytic pyrolysis of biomass over H^+ZSM-5 under hydrogen pressure, Energy & Fuels. 26 (2012) 5300–5306. doi:10.1021/ef3008213.

[11] V.K. Venkatakrishnan, W.N. Delgass, F.H. Ribeiro, R. Agrawal, Oxygen removal from intact biomass to produce liquid fuel range hydrocarbons via fast-hydropyrolysis and vapor-phase catalytic hydrodeoxygenation, Green Chem. 17 (2015) 178–183. doi:10.1039/c4gc01746c.

[12] V.K. Venkatakrishnan, J.C. Degenstein, A.D. Smeltz, W.N. Delgass, R. Agrawal, F.H. Ribeiro, High-pressure fast-pyrolysis, fast-hydropyrolysis and catalytic hydrodeoxygenation of cellulose: Production of liquid fuel from biomass, Green Chem. 16 (2014) 792–802. doi:10.1039/c3gc41558a.

[13] L. Zhang, K. Gong, J. Lai, P. Alvey, Chemical composition and stability of renewable hydrocarbon products generated from a hydropyrolysis vapor upgrading process, Green Chem. 19 (2017) 3628–3641. doi:10.1039/C7GC01075C.

[14] J. Fan, J. Gephart, T. Marker, D. Stover, B. Updike, D.R. Shonnard, Carbon Footprint Analysis of Gasoline and Diesel from Forest Residues and Corn Stover using Integrated Hydropyrolysis and Hydroconversion, ACS Sustain. Chem. Eng. (2015). doi:10.1021/acssuschemeng.5b01173.

[15] D.C. Dayton, J. Carpenter, J. Farmer, B. Turk, R. Gupta, Biomass hydropyrolysis in a pressurized fluidized bed reactor, Energy & Fuels. 27 (2013) 3778–3785. doi:10.1021/ef400355t.

[16] D.C. Dayton, J. Hlebak, J.R. Carpenter, K. Wang, O.D. Mante, J.E. Peters, Biomass hydropyrolysis in a fluidized bed reactor, Energy & Fuels. 30 (2016) 4879–4887. doi:10.1021/acs.energyfuels.6b00373.

[17] K. Wang, D.C. Dayton, J.E. Peters, O.D. Mante, Reactive catalytic fast pyrolysis of biomass to produce high-quality bio-crude, Green Chem. 19 (2017) 3243–3251. doi:10.1039/C7GC01088E.

[18] A.V. Bridgwater, Review of fast pyrolysis of biomass and product upgrading, Biomass and Bioenergy. 38 (2012) 68–94. doi:10.1016/j.biombioe.2011.01.048.

[19] T.A. Milne, A.H. Brenan, B.H. Glenn, Sourcebook of Methods of Analysis for Biomass and Biomass Conversion Processes, Elsevier Applied Science, New York, 1990.

[20] T.M.H. Dabros, A. Gaur, D.G. Pintos, P. Sprenger, M. Høj, T.W. Hansen, F. Studt, J. Gabrielsen, J.-D. Grunwaldt, A.D. Jensen, Influence of H 2 O and H 2 S on the composition, activity, and stability of sulfided Mo, CoMo, and NiMo supported on MgAl 2 O 4 for hydrodeoxygenation of ethylene glycol, Appl. Catal. A Gen. 551 (2018) 106–121. doi:10.1016/j.apcata.2017.12.008.

[21] P.M. Mortensen, D. Gardini, H.W.P. de Carvalho, C.D. Damsgaard, J.-D. Grunwaldt, P.A. Jensen, J.B. Wagner, A.D. Jensen, Stability and resistance of nickel catalysts for hydrodeoxygenation: Carbon deposition and effects of sulfur, potassium, and chlorine in the feed, Catal. Sci. Technol. 4 (2014) 3672–3686. doi:10.1039/c4cy00522h.

[22] V.N. Bui, D. Laurenti, P. Afanasiev, C. Geantet, Hydrodeoxygenation of guaiacol with CoMo catalysts. Part I: Promoting effect of cobalt on HDO selectivity and activity, Appl. Catal. B Environ. 101 (2011) 239–245. doi:10.1016/j.apcatb.2010.10.025.

[23] P. Grange, E. Laurent, R. Maggi, A. Centeno, B. Delmon, Hydrotreatment of pyrolysis oils from biomass: Reactivity of the various categories of oxygenated compounds and preliminary techno-economical study, Catal. Today. 29 (1996) 297–301. http://www.sciencedirect.com/science/article/pii/0920586195002952.

[24] O.İ. Şenol, E.-M. Ryymin, T.-R. Viljava, A.O.I. Krause, Effect of hydrogen sulphide on the hydrodeoxygenation of aromatic and aliphatic oxygenates on sulphided catalysts, J. Mol. Catal. A Chem. 277 (2007) 107–112. doi:10.1016/j.molcata.2007.07.033.

[25] O.İ. Şenol, T.-R. Viljava, A.O.I. Krause, Effect of sulphiding agents on the hydrodeoxygenation of aliphatic esters on sulphided catalysts, Appl. Catal. A Gen. 326 (2007) 236–244. doi:10.1016/j.apcata.2007.04.022.

[26] O.İ. Şenol, E.-M. Ryymin, T.-R. Viljava, A.O.I. Krause, Reactions of methyl heptanoate

hydrodeoxygenation on sulphided catalysts, J. Mol. Catal. A Chem. 268 (2007) 1–8. doi:10.1016/j.molcata.2006.12.006.

[27] C. Bouvier, Y. Romero, F. Richard, S. Brunet, Effect of H_2S and CO on the transformation of 2-ethylphenol as a model compound of bio-crude over sulfided Mo-based catalysts: propositions of promoted active sites for deoxygenation pathways based on an experimental study, Green Chem. 13 (2011) 2441–2451. doi:10.1039/c1gc15181a.

[28] K. Schofield, The enigmatic mechanism of the flame ionization detector: Its overlooked implications for fossil fuel combustion modeling, Prog. Energy Combust. Sci. 34 (2008) 330–350. doi:10.1016/j.pecs.2007.08.001.

[29] M. Garcia-Perez, X.S. Wang, J. Shen, M.J. Rhodes, F. Tian, W.-J. Lee, H. Wu, C.-Z. Li, Fast pyrolysis of oil mallee woody biomass: Effect of temperature on the yield and quality of pyrolysis products, Ind. Eng. Chem. Res. 47 (2008) 1846–1854. doi:10.1021/ie071497p.

[30] T.N. Trinh, P.A. Jensen, Z. Sárossy, K. Dam-Johansen, N.O. Knudsen, H.R. Sørensen, H. Egsgaard, Fast pyrolysis of lignin using a pyrolysis centrifuge reactor, Energy and Fuels. 27 (2013) 3802–3810. doi:10.1021/ef400527k.

[31] N. Bech, M.B. Larsen, P.A. Jensen, K. Dam-Johansen, Modelling solid-convective flash pyrolysis of straw and wood in the pyrolysis centrifuge reactor, Biomass and Bioenergy. 33 (2009) 999–1011. doi:10.1016/j.biombioe.2009.03.009.

[32] T.N. Trinh, P.A. Jensen, K. Dam-Johansen, N.O. Knudsen, H.R. Sørensen, Influence of the pyrolysis temperature on sewage sludge product distribution, bio-oil, and char properties, Energy & Fuels. 27 (2013) 1419–1427. doi:10.1021/ef301944r.

[33] T. Lang, A.D. Jensen, P.A. Jensen, Retention of organic elements during solid fuel pyrolysis with emphasis on the peculiar behavior of nitrogen, Energy and Fuels. 19 (2005) 1631–1643. doi:10.1021/ef049739a.

[34] W.G. Lloyd, D.A. Davenport, Applying thermodynamics to fossil fuels: Heats of combustion from elemental compositions, J. Chem. Educ. 57 (1980) 56. doi:10.1021/ed057p56.

[35] T.N. Trinh, P.A. Jensen, K. Dam-Johansen, N.O. Knudsen, H.R. Sørensen, S. Hvilsted, Comparison of lignin, macroalgae, wood, and straw fast pyrolysis, Energy & Fuels. 27 (2013) 1399–1409. doi:10.1021/ef301927y.

[36] W. Baldauf, U. Balfanz, M. Rupp, Upgrading of flash pyrolysis oil and utilization in refineries, Biomass and Bioenergy. 7 (1994) 237–244. http://linkinghub.elsevier.com/retrieve/pii/0961953494000652 (accessed January 18, 2016).

Chapter 3 New insights into the effect of pressure on catalytic hydropyrolysis of biomass

In the previous chapter the spent catalysts were not analyzed and lowest tested hydrogen partial pressure was 15.9 bar. This chapter is based on a new series of experiments at hydrogen partial pressures between 3.0 and 8.0 bar and this chapter should therefore be considered as a continuation of the previous chapter. Furthermore, in this work we measured the carbon content on all the spent catalysts from both the fluid bed and HDO reactor, which made it possible to correlate the carbon content on the spent catalyst with the hydrogen partial pressure. The supplementary information can be found in Appendix B.

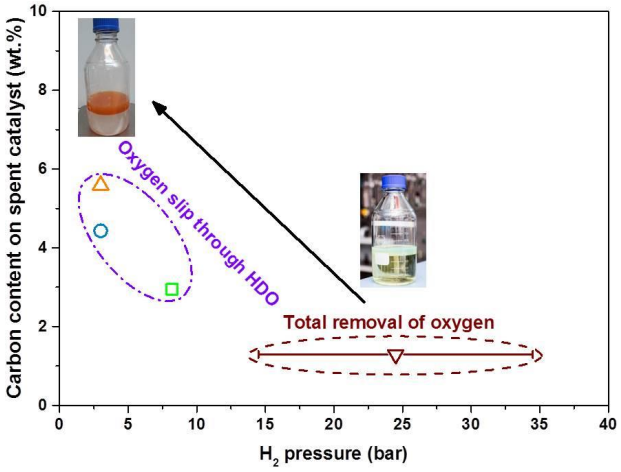

Abstract

Catalytic hydropyrolysis of beech wood has been conducted in a fluid bed reactor at 450 °C with a sulfided CoMo catalyst followed by a fixed bed hydrodeoxygenation (HDO) reactor with a sulfided NiMo catalyst at hydrogen pressures between 3.0 and 35.8 bar. Using both reactors the condensable organic yield (condensed organic and C_{4+} in gas) varied between 18.7 and 21.5 wt.% dry ash free basis (daf) and was independent of the hydrogen pressure. At 15.9 bar hydrogen or higher the condensed organic phase was essentially oxygen free (<0.01 wt.% dry basis (db)), but decreasing the hydrogen pressure to 3.0 bar increased the oxygen content to 7.8 wt.% db. The CO_2 yield decreased with increasing hydrogen pressure and was 12.9 wt.% daf at 3.0 bar hydrogen and 3.3 wt.% daf at 35.8 bar hydrogen. The char and coke yield was close to constant (11.0-12.7 wt.% daf) at hydrogen pressures between 15.9 and 35.8 bar, but increased to 15.7 wt.% at 3.0 bar hydrogen due to an increase in the polymerization of pyrolysis vapors. The condensed organic phase was analyzed with GC×GC-MS/FID, which showed that the concentration of monoaromatics was kinetically controlled at hydrogen pressures between 3.0 and 15.9 bar, but controlled by the thermodynamics at higher hydrogen pressures. The measured carbon content on the spent catalysts from both the fluid bed and HDO reactor showed that coking of the catalysts increased when the hydrogen pressure was decreased below 15.9 bar. Bypassing the HDO reactor at 3.0 and 25.8 bar hydrogen showed that the oxygenates was mainly monofunctional phenols at 25.8 bar, while acid, furans, ketones, and multifunctional phenols were also detected at 3.0 bar hydrogen. Therefore, the increased coking of the catalysts at low hydrogen pressure (<15.9 bar) was ascribed to the polymerization of the more reactive oxygenates produced in the fluid bed reactor.

Abbreviations

AED	Atomic emission detector	mAro	Monoaromatics
conc	Concentration	MS	Mass spectrometry
daf	Dry, ash free basis	Naph	Naphthenes
db	Dry basis	O-Ali	Oxygenated aliphatics
diAro	Diaromatics	O-Aro	Larger oxygenated aromatics
DMDS	Dimethyl disulfide	Par	Paraffins
EDS	Energy dispersive X-ray spectroscopy	PhOH	Phenols
FB	Fluid bed	Ph(OH)2	Dihydroxybenzene
FID	Flame ionization detector	Temp.	Temperature
ToF	Time of flight	tetAro+	Tetra- and higher aromatics
GC	Gas chromatograph	triAro	Triaromatics
HDO	Hydrodeoxygenation		

3.1 Introduction

Recent research have shown that catalytic hydropyrolysis of biomass is an efficient method for production of renewable liquid fuels with a low carbon footprint [1–4]. In this process pyrolysis takes place in a hydrogen atmosphere and a catalyst is used as heat carrier. This enables the hydrogenation of the oxygenates as soon as they are formed by the pyrolysis process, thus decreasing the extent of polymerization reactions [5]. Since catalytic hydropyrolysis is exothermic, as opposed to inert pyrolysis, additional heat to the fluid bed reactor is not required.

In GTI's process called IH$^{2®}$ catalytic hydropyrolysis takes place in a fluid bed reactor at temperatures between 336-469°C and the produced vapors are sent to a fixed bed hydrodeoxygenation (HDO) reactor operated at 343-399°C and the total pressure is between 19.5 and 24.1 bar [1,2]. Using maple and pine the IH$^{2®}$ process has been running continuously for 750 hours with a feeding rate of 50 kg/h at a hydrogen pressure of 24 bar with a condensable organic (condensed organics + C_{4+} in gas) of 26 wt.% dry as free (daf)[2].

Dayton et al. [6–8] also investigated catalytic hydropyrolysis of wood in a fluid bed reactor. Using a reduced NiMo hydrotreating catalyst they investigated the effect of the pressure by varying the total pressure between 10.3 and 20.7 bar and varying the hydrogen concentration between 20 and 60 % [9]. They found that the char yield increased at low hydrogen partial pressure and that higher partial pressure of hydrogen decreased the oxygen content and increased the carbon content in the organic phase favoring the formation of hydrocarbons [9]. Furthermore, conducting catalytic hydropyrolysis at 450°C and using hydrogen at atmospheric pressure with a molybdenum based reduced metal oxide catalyst resulted in a carbon recovery in the organic phases and C_{4+} of 43 % and an oxygen content of 6.2 wt.% [8]. The results show that catalytic hydropyrolysis can be conducted at low pressure with a high yield and reasonable degree of deoxygenation.

Several groups have investigated catalytic hydropyrolysis using Pyroprobe reactors and H-ZSM-5, often impregnated with Ni [10–16]. Melligan et al.[16] investigated the effect of hydrogen pressure at 600 °C using a Ni/H-ZSM-5 catalyst and found that increasing the hydrogen pressure increased the higher heating value (HHV) of the products, due to an increased degree of deoxygenation. Other groups have investigated hydropyrolysis either in a cyclone reactor or fluid bed reactor followed by a fixed bed HDO reactor [17–19].

In our previous study [20] we investigated the effect of pressure and temperature on catalytic hydropyrolysis of beech wood using a two reactor system, where the catalytic hydropyrolysis took place in a fluid bed reactor with a sulfided CoMo/$MgAl_2O_4$ catalyst followed by a fixed bed reactor with a sulfided NiMo/Al_2O_3 catalyst. Operating the fluid bed reactor at 450 °C and varying the total pressure between 16 and 36 bar did not have an impact on the condensed organics and C_{4+} gas yield [20]. The spent catalysts were not investigated. In this study we have conducted a more thorough investigation of the effect of the total pressure and the hydrogen partial pressure. The total pressure has been varied between 5.0 and 36 bar and the hydrogen partial pressure has been varied between 3.0 and 35.8 bar. The liquid products have been extensively characterized and the carbon content on the spent catalysts from both the HDO reactor and fluid bed reactor has been measured.

3.2 Material and methods

3.2.1 Biomass feedstock

Bark free beech wood was used as biomass feedstock and was supplied by Dansk Træmel (Product number: 10000251250390). The moisture and ash contents were 6.72 wt.% (dried at 105 °C) and 0.59 wt.% on dry

basis (db), respectively. The particle sizes were between 200-700 µm. The beech wood was analyzed by Celignis Analytical (analysis P10) and consisted of 24 wt.% db lignin, 40 wt.% db cellulose, 18 wt.% db hemicellulose, 3 wt.% db other polysaccharides, 3 wt.% db extractives and 12 wt.% db unknown. A detailed elemental composition of the biomass, including the ash composition, can be found elsewhere [20].

3.2.2 Catalysts

A $CoMo/MgAl_2O_4$ catalyst was used in the fluid bed reactor. The catalyst was received as extrudates and was crushed and sieved to a particle size between 180 and 355 µm. A $NiMo/Al_2O_3$ catalyst was used in the HDO reactor, was received as extrudates and used as received. Both catalysts were supplied by Haldor Topsøe A/S and were also used in our previous work [20].

3.2.3 Experimental setup

The catalytic hydropyrolysis experiments were conducted in a bench scale setup shown in Figure 3.1. The setup is described in detail elsewhere [20]. The setup consisted of a feeding system, which included a gas mixing system and a screw feeder for biomass feeding, a fluid bed hydropyrolysis reactor, a filter for char removal, a fixed bed hydrotreating reactor, which can be bypassed, and a three stage condensation system (20°C, 2°C, and -40°C). The temperature in the last step in the condensation system was in some experiments increased to -20°C, to avoid plugging of the heat exchanger due to formation of wax. The uncondensed gases were sent to a flare. A small fraction of the gas was sent to an online gas chromatograph (GC), which measured the gas composition (H_2, N_2, H_2S, CO, CO_2, C_1 to C_5 and C_{6+} hydrocarbons) every 10 min. The tubes between the fluid bed, filter and condensation section were heated to 350°C in order to avoid condensation. The biomass feeding tube was preheated to approximately 200°C to preheat the biomass and carrier gas while avoiding premature pyrolysis.

The total mass of the condensed liquid was determined by weighing and the organic phase and the aqueous phase were separated with a separation funnel. In experiment 1-4 the mass of the condensed organics and aqueous were determined as described in [20], while in experiment 5-8 the mass of the aqueous phase was measured and the mass of the organic phase was determined by subtracting the mass of the aqueous phase from the total mass of condensed liquid. The differences between these two methods are below the experimental uncertainty. The H_2S dissolved in the liquid phases was for safety reasons removed by bubbling with N_2 until hydrogen sulfide test strips (Sigma Aldrich) showed no sign of H_2S. This lead to a mass loss between 1.2 and 7.9 wt.% for the organic phase and between 0.43 and 5.1 wt.% of the aqueous phase. The mass loss in the organic phase was mainly due to vaporization of light hydrocarbons while the mass loss in the aqueous phase was mainly due to vaporization of water.

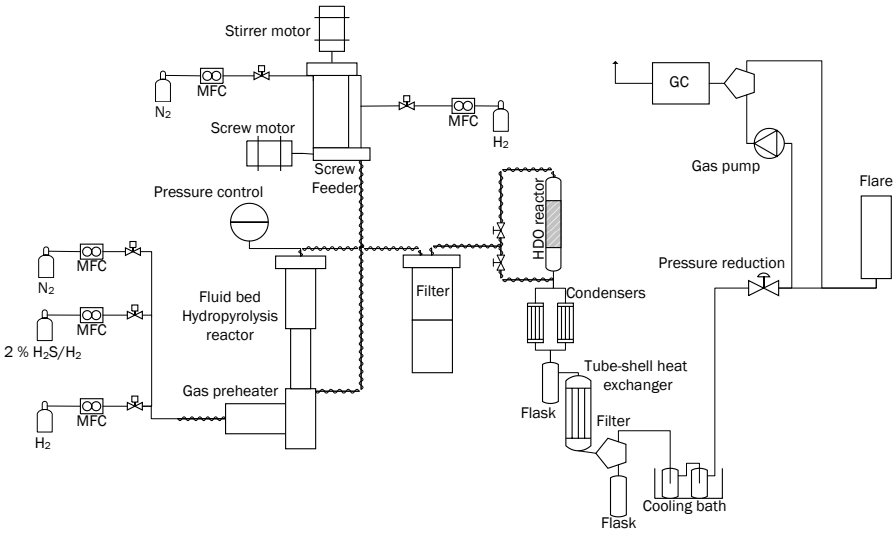

Figure 3.1. Simplified piping and instrumentation diagram of the catalytic hydropyrolysis setup

After each experiment the catalyst and the remaining char was removed from the fluid bed, and replaced with the fresh catalyst for the subsequent experiment. The same catalyst was used in the HDO reactor in experiments 1 to 4, but the catalyst in the HDO reactor was replaced before experiments 5, 6, and 7. The solid yield was defined as the char (un-vaporized biomass particles) and coke (carbon on the catalyst) yield, and was calculated by subtracting the mass of loaded catalyst from the total mass of solids collected from the filter and fluid bed.

In experiments 1 to 4 a liquid feeding system consisting of a pump and evaporator was used to supply the setup with dimethyl disulfide (DMDS) during the sulfidation of the catalysts, more information can be found in ref. [20]. However, DMDS lead to coking of the gas preheater and bottled H_2S was therefore used in experiments 5 to 8. The catalysts were sulfided at 26 bar by heating the reactors from 180 to 350 °C with 1.8 mol % H_2S, 11 mol % N_2 in 87 % H_2 by feeding 2 % H_2S in H_2 (flow: 4 NL/min) and N_2 (flow: 0.5 NL/min). The temperature ramp was 10 °C/min and the holding time was 3 hours, when both reactors were used and 2 hours when only the fluid bed reactor was used.

3.2.4 Analysis methods

3.2.4.1 Organic phase

The produced organic phases were analyzed with several different methods and a detailed description of the methods can be found elsewhere [20]. The hydrogen and sulfur content was measured with ASTM method D7171 and ASTM method D4294, respectively. The viscosity at 40 °C was measured with ASTM method D7042, the density at 40 °C was measured with ASTM method D4052. The water content was measured with Karl Fisher titration.

For the organic phases with less than 2 wt.% oxygen, the oxygen content was measured using a GC with an atomic emission detector (AED). The GC was an Agilent 7890 coupled to a JAS 2370 AED in oxygen selective mode. The total amount of oxygen in the samples was quantified by adding a known amount of 4-fluorophenol to the sample. For organic phases with more than 2 wt.% oxygen, the oxygen content was ana-

lyzed at DB Lab A/S using a Flash 2000 elemental analyzer (Thermo Scientific). The uncertainty of this measurement was 3.0 %, defined as two standard deviations for the measurement uncertainty, corresponding to a confidence interval of 95 %.

Selective analysis of the sulfur containing compounds in the condensed oil was conducted using the above described GC with the AED detector in sulfur specific mode. Quantification was done by adding known amounts of benzothiophene, dibenzothiophene and 4-methyl-dibenzothiophene to the sample.

The condensed organic liquid samples were characterized by GC×GC-time of flight (ToF)/ mass spectrometry (MS) or –flame ionization detector (FID) using a LECO® Pegasus 4D^{TM} instrument. The instrument included an Agilent 7890A GC equipped with a Gerstel® CIS 4 PTV inlet, a secondary oven, a quad-jet, dual-stage cryogenic (liquid N_2) modulator, a Tof/MS, and a FID detector. The primary (1D) and secondary (2D) columns were Restek® Rxi-5Sil MS and Restek® Rxi-17Sil MS, respectively. Based on the GC×GC-ToF/MS analysis the compounds were classified into eleven classes: naphthenes, monoaromatics, diaromatics, triaromatics, larger aromatics, phenols, dihydroxybenzenes, larger oxygenated aromatics, oxygenated aliphatics, paraffins, and sterols. Based on the paraffins retention time on the 1D column the component classes where divided into subgroups on the basis on the number of carbon atoms in the molecules : -C10, C11-C15, C16-C20, and C20+. However, it should be noted that other component classes do not necessarily have the same carbon number distribution as the paraffins, thus caution is needed when correlating the relative amount of each subgroup with its carbon number distribution. The relative amount (FID area-%) of each compound class was estimated as the sum of areas of all detected peaks in that class divided by the total peak area of all compound classes. All data was processed using the ChromaTof® 4.50 software.

3.2.4.2 Aqueous phase

The carbon content in the aqueous phase was determined with GC-AED. The quantification was done by external standards using benzyl alcohol dissolved in water. Calibration concentrations ranged from 10 ppm to 1100 ppm carbon. No identification of individual compounds was done and the total detected carbon was taken as a figure of the total carbon content in the aqueous sample. No sample pretreatment was done prior to analysis. A more thorough description of the method can be found elsewhere (see section 4.2.1.2).

The aqueous phase was also analyzed on a Shimadzu GC-MS/FID with a Supelco Equity-5 column. The compounds were identified on the MS and quantified using the parallel FID. Based on the GC-FID/MS analysis the components were classified into 8 groups: unidentified, ethers, ketones, alcohols, sugars, phenols, acids and furans. The relative amount (FID area-%) of each component class was estimated as the sum of all the detected peaks in that class divided by the total peak area.

3.2.4.3 Catalyst characterization

The carbon content on the spent $NiMo/Al_2O_3$ catalyst from the HDO reactor was measured with a LECO CS-200. The sample was combusted in an O_2 atmosphere and the formed CO_2 was measured with IR-absorption.

The catalyst in the fluid bed reactor was during the experiment mixed with char particles, which makes it difficult to measure that carbon content on the spent catalyst from the fluid bed by combustion. The carbon content on the spent catalysts from the fluid bed reactor was therefore measured with scanning electron microscopy (SEM) combined with an energy-dispersive detector (EDS), and a detailed description of the method can be found elsewhere (see section 4.2.4.2). A FEI QUANTA600 scanning electron microscope with tungsten filament and equipped with a liquid nitrogen cooled EDAX EDS detector was used for these measurements. EDS element quantification was conducted at four different acceleration voltages: 3 kV, 5 kV, 10 kV, and 15 kV to probe different interaction volumes between the incident electron beam and the sample.

The maximum penetration depth for $MgAl_2O_4$ was estimated with CASINO Monte Carlo Software to be approximately 0.170 µm for 3 kV and 1.60 µm for 15 kV (see section 4.2.4.2)., thus mainly probing the composition close to the catalyst surface. The standard deviation for the measurement was 1.5 wt.% at 3 kV, 0.8 wt.% at 5 kV, 1.0 wt.% at 10 kV and 1.5 wt.% at 15 kV.

3.3 Results and Discussion

The tested process conditions and their effect on the product distribution are shown in Table 3.1. It should be noted that experiment 1-4 has previously been published [20]. However, in this work the produced liquid phases and the spent catalysts have been more extensively characterized and combining the previous obtained results with the new results gives a more in-depth understanding of the effect of pressure. The feed time varied between 1.4 and 4.0 hours and the mass balance closed between 99.5 and 92.1 wt.% daf. The reason for the short feeding time of 1.4 hours in experiment 6 is that the tube between fluid bed reactor and filter plugged. This was probably due to condensation and polymerization of heavy oxygenates in the tube. The mass balance in experiment 8 only closed with 92.1 wt.% daf. In this experiment the HDO reactor was bypassed, the total pressure was 10 bar and the hydrogen partial pressure only 3.0 bar. The produced organic phase was thus heavier than the aqueous phase and part of the reason for the poor mass balance in experiment 8, is therefore most likely due to accumulation of organics in the setup. The biomass feeding rate was difficult to control and varied between 161 and 389 g/h, but only had a limited influence on the results [20].

Table 3.1 Summary of the reactions conditions and mass balances for catalytic hydropyrolysis of beech wood at different total and hydrogen partial pressures.

Test	1	2	3	4	5	6	7	8
Test conditions								
FB temperature (°C)	451	450	447	449	452	450	450	454
FB catalyst amount	50.1	49.6	49.7	50.2	50.0	50.0	50.1	50.0
HDO temperature (°C)	371	-	370	364	386	383	376	-
HDO catalyst amount	173	-	173	173	175	175	171	-
Total pressure (bar)	26	26	16	36	10	5	10	10
H_2 pressure (bar)	24.5	25.8	15.9	35.8	8.2	3.0	3.0	3.0
Feed time (h)	4.0	3.9	4.0	4.0	2.6	1.4	2.8	2.8
Feeding rate (g/h)	250	174	161	159	354	389	350	350
H_2S conc.(ppm)	460	48	47	50	475	460	464	464
H_2 flow (NL/min)	82	87	52.4	124.2	30.9	10.4	11.4	11.4
N_2 flow (NL/min)	5.0	0.62	0.37	0.62	7.0	7.0	26.5	26.5
$\frac{H_2 \text{ consumed (g)}}{\text{Biomass used (kg)}}$	46	35	35	46	34	20	19	9.4
Yields (wt. daf %)								
Gas	31.5	27.4	30.3	26.3	32.1	33.2	33.5	24.0
Solid	11.4	12.3	11.0	12.7	13.2	13.6	15.7	15.3
Aqueous phase	35.2	37.0	33.2	37.7	32.3	29.0	28.8	27.5
Organic phase	12.3	12.0	11.0	10.6	13.0	10.1	12.6	23.0
C_{4+} in the gas	9.1	8.3	8.7	10.3	7.9	8.5	7.6	2.3
Organics + C_{4+}	21.5	20.3	19.7	20.9	20.9	18.7	20.2	25.3
Mass balance	99.5	96.9	94.2	97.6	97.5	94.5	98.2	92.1
Carbon recovery (%)								
C_1-C_3	23	19	19	21	22	21	21	8
C_{4+}	15	14	14	17	13	15	13	4
CO+CO_2	12	13	13	10	13	15	16	13
Organic phase	21	21	19	19	23	16	19	30
Aqueous phase	0.014	1.1	<0.008	<0.009	0.51	0.59	0.47	8.5
Organic phase + C_{4+}	37	35	34	36	36	31	32	34
Organic phase composition								
Water (wt.%)	ND	0.35	ND	ND	0.36	3.32	1.6	11.3
C* (wt.% db)	88	88	88	88	87	84	83	74
H (wt.% db)	11.93	10.22	11.19	11.63	9.58	9.55	9.56	7.60
O (wt.% db)	0.003	1.8	0.0009	0.0001	3.3	6.0	7.8	18.3
S (wt.% db)	0.117	0.303	0.417	0.246	0.036	0.045	0.033	0.093
Organic phase physical properties								
Density at 40°C (g/ml)	0.8273	0.8890	0.8518	0.8428	0.8632	.09360	0.9443	1.0589
Viscosity at 40°C (cSt)	1.052	1.607	1.225	1.204	1.136	2.879	3.590	8.774
Aqueous phase composition (wt.%)								
C	0.017	1.3	<0.01	<0.01	0.66	0.81	0.7	12.3
Gas composition (wt.% daf)								
CO	9.0	11.1	10.8	9.9	8.8	10.0	10.0	8.7
CO_2	8.1	5.7	7.6	3.3	10.3	12.4	12.9	10.8
C_1-C_3	14.3	12.1	12.0	13.2	13.0	10.9	10.6	4.5
C_{4+}	9.1	8.3	8.7	10.3	7.9	8.5	7.6	2.3

*By difference

3.3.1 Product distribution

In the experiments where both reactors were used the condensable organic yield (condensed organics + C_{4+} in the gas) varied between 18.7 and 21.5 wt.% daf, as shown in Figure 3.2(A), with no apparent correlation between the hydrogen pressure and condensable organic yield. However, when the HDO reactor was by-passed the condensable organic yield was 20.3 wt.% daf at 25.8 bar hydrogen and increased to 25.3 wt.% daf at 3.0 bar hydrogen. The reason for the increased condensable organic yield is due to increased oxygen content in the organic phase. Using the HDO reactor, the total gas yield (Figure 3.2(B)) decreased from 33.5 to 26.3 wt.% daf when partial pressure of hydrogen was increased from 3.0 to 35.8 bar. This was due to a decrease in the CO and CO_2 yield, which decreased from 22.9 wt.% daf at 3.0 bar to 13.2 wt.% daf at 35.8 bar,

while the C_1-C_3 yield varied between 10.6 and 14.3 wt.% daf. The CO and CO_2 yield most likely decreased due to a higher hydrodeoxygenation activity at higher hydrogen partial pressure, which is a competing reaction with decarbonylation and decarboxylation. The lower C_1-C_3 yield when the HDO reactor is bypassed, 4.5 wt.% daf at 3.0 bar hydrogen and 10.6 wt.% at 25.8 bar hydrogen, could be due to cracking of the vapors in the HDO reactor, but it is probably also due to deoxygenation of C_1-C_3 oxygenates, which are recovered in the aqueous and organic phases when the HDO reactor is bypassed. Interestingly, the CO and CO_2 yield is unchanged when the HDO reactor is bypassed at 25.8 bar hydrogen, but decreased from 22.9 to 19.6 wt.% daf at 3.0 bar hydrogen.

As shown in Figure 3.2(C) the solid yield decreased from 15.7 wt.% daf at 3.0 bar hydrogen to 11 wt.% at 15.9 bar hydrogen. Furthermore, at 3.0 bar hydrogen it was observed that coke builds up on the filter and the filter cake was approximately 0.5 cm thick (see supplementary information Figure B.1), indicating that the catalyst in the fluid bed reactor is not able sufficiently remove the reactive oxygenates, leading to increased polymerization reactions. Furthermore, the solid yield increased to 12.7 wt.% daf when the hydrogen pressure was increased to 35.8 bar, which could indicate that too high pressure also increases the solid yield. However, the increase is close to the experimental uncertainty. The aqueous phase yield increased with increasing hydrogen pressure from 28.8 wt.% daf at 3.0 bar hydrogen to 37.7 wt.% daf at 35.8 bar hydrogen, see Figure 3.2(D). This increase is both due to an increased degree of hydrogenation and hydrodeoxygenaton of the organics, and decreased carboxylation/carbonylation reactions. The change in aqueous phase yield, when the HDO reactor is bypassed is within the experimental uncertainty, however, bypassing the HDO reactor increased the carbon content in the aqueous phase, which is discussed in section 3.3.2.

In both experiments 6 and 7 the hydrogen partial pressure was 3.0 bar, but in experiment 6 the total pressure was 5 bar, while it was 10 bar in experiment 7. The difference in the condensable organic, CO+CO_2, C_1-C_3, and aqueous phase yields in these two experiments where 0.6 wt.% daf or lower. The largest difference was in the solid yield, which was 13.6 wt.% daf in experiment 6 (5 bar) and 15.7 wt.% daf in experiment 7 (10 bar). However, the reason for the lower solid yield in experiment 6 compared to 7 is that the tube between the fluid bed and filter blocked in experiment 6, thus leading to a solid build up in the tube, which was not accounted for in the mass balance. Therefore, considering the relatively large difference in the product distribution (>2 wt.% for CO+CO_2, C_1-C_3, solid and aqueous phase yield) between experiment 5 (10 bar pressure, 8.2 bar hydrogen) and 7 (10 bar pressure, 3 bar hydrogen), the experiments show that the product distribution is mainly dependent on the hydrogen partial pressure, and not on the total pressure.

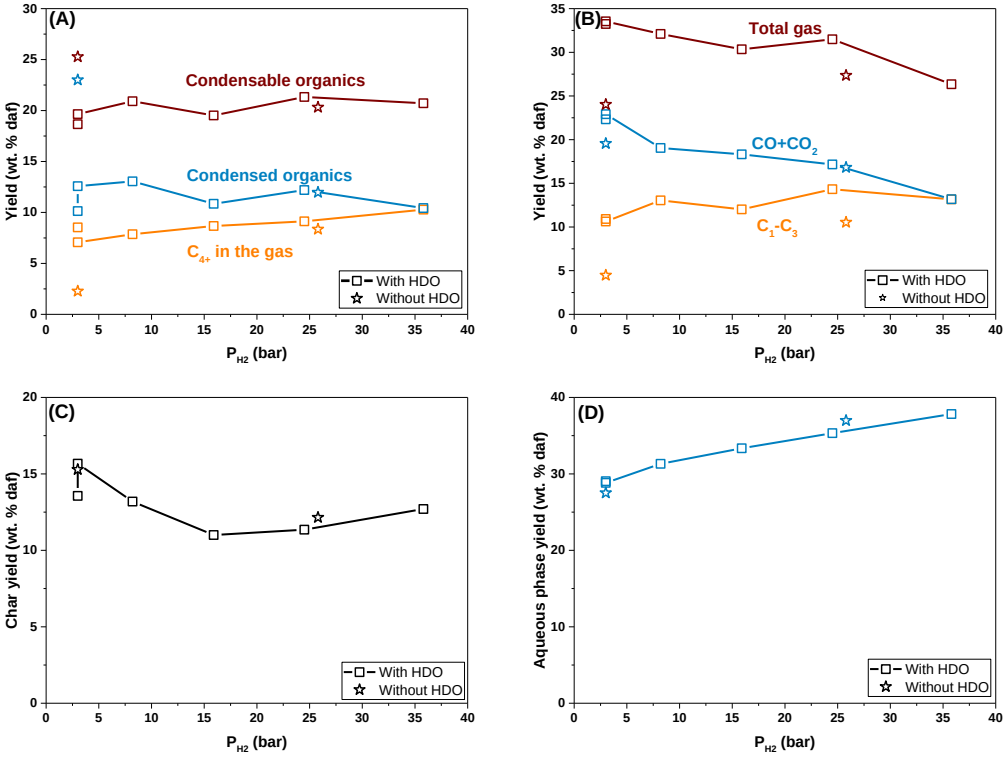

Figure 3.2 Effect of hydrogen partial pressure on the condensable organic yield (A), gas yield (B), char yield (C), and aqueous phase yield (D). Conditions: fluid bed temperature 447-454 °C, HDO temperature: 364-386 °C, biomass feeding rate: 159-389 g/min, H_2S concentration: 47-475 ppm, H_2 flow: 11.4-124.4 NL/min, N_2 flow: 0.37-26.5 NL/min.

The CO and CO_2 yield is shown in Figure 3.3(A). The CO yield varied between 8.8 and 11.1 wt.% daf, and no correlation between the CO yield and the hydrogen pressure was observed. While the CO_2 yield decreased from 12.9 wt.% daf at 3.0 bar hydrogen to 3.3 wt.% daf at 35.8 bar hydrogen. The reason for the decreasing CO_2 yield might be that when the hydrogen pressure is increased, the CO_2 is converted through the reverse water gas shift reaction (3.1).

$$CO_2 + H_2 \rightleftharpoons CO + H_2O \quad (3.1)$$

The C_2-C_3 paraffin and olefin yields in Figure 3.3(B) show that when the HDO is used at hydrogen pressures between 15.9 and 35.8 bar all the olefins were converted into paraffins. However, at lower hydrogen pressures the olefin conversion decreased, thus at 8.2 bar hydrogen the C_2-C_3 olefin yield was 0.8 wt.% daf and at 3.0 bar hydrogen the olefin yield was 3.1-3.3 wt.% daf. Bypassing the HDO reactor increased the olefin yield to 1.5 wt.% at 25.8 bar hydrogen, thus showing that the olefins are removed in the HDO reactor at this pressure. However, bypassing the HDO reactor at 3.0 bar H_2 decreased the olefin yield to 1.7 wt.% daf, which is probably due to a higher yield of light oxygenates, which are not deoxygenated.

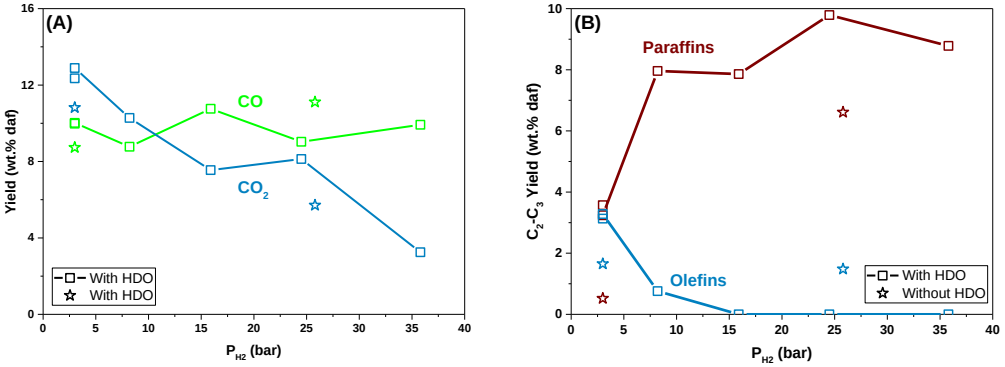

Figure 3.3 Effect of hydrogen partial pressure on the CO and CO_2 yield (A) and the C_2-C_3 paraffin and olefin yield (B). Conditions: fluid bed temperature 447-454 °C, HDO temperature: 364-386 °C, biomass feeding rate: 159-389 g/min, H_2S concentration: 47-475 ppm, H_2 flow: 11.4-124.4 NL/min, N_2 flow: 0.37-26.5 NL/min.

3.3.2 Chemical composition of the condensed liquids

The oxygen and hydrogen content in the condensed organic phase are shown in Figure 3.4. When the HDO reactor was used the oxygen content was close to 0 wt.% db at hydrogen pressures between 15.9 and 25.8 bar; however, decreasing the hydrogen pressure to 8.2 increased the oxygen content to 3.3 wt.% db and further decreasing the hydrogen pressure to 3.0 bar increased to oxygen content to between 6.0 and 7.8 wt.% db. This shows that in order to produce oxygen free oil the hydrogen pressure should be above 8.2 bar. Bypassing the HDO reactor when the hydrogen pressure was 25.8 bar increased the oxygen content in the organic phase to 1.8 wt.% db, showing that at this hydrogen pressure most of the deoxygenation takes place in the fluid bed reactor. However, bypassing the HDO reactor at 3.0 bar hydrogen pressure increased the oxygen content to 18.3 wt.% db, thus under these conditions most of the oxygen must be removed in the HDO reactor.

Using the HDO reactor and increasing the hydrogen pressure from 3.0 to 24.5 bar increased the hydrogen content in the organic phase from 9.55 to 11.93 wt.% db, while further increasing the hydrogen pressure to 35.8 bar decreased the hydrogen content to 11.63 wt.% db. However, this decrease is most likely due to the experimental uncertainty. Bypassing the HDO reactor also decreased the hydrogen content in the condensed organic phase to 10.22 wt.% db at 25.8 bar hydrogen and 7.60 wt.% db at 3.0 bar hydrogen. The lower hydrogenation activity could also be seen on the lower hydrogen consumption at low hydrogen pressures, thus the hydrogen consumption was between 19 and 20 g H_2/kg biomass at 3.0 bar hydrogen which increased to 34 g H_2/kg biomass at 15.9 bar hydrogen and further increased to 46 g H_2/kg biomass at 24.5 and 35.8 bar hydrogen. The hydrogen consumption also decreased with approximately 10 g H_2/kg biomass when the HDO reactor was bypassed at both 3.0 and 25.8 bar hydrogen, indicating that the hydrogen consumed in the HDO reactor is independent of the pressure in the tested range.

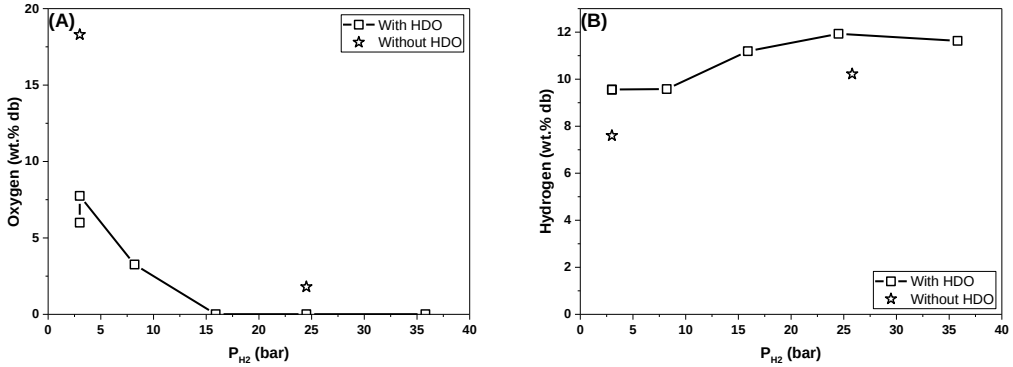

Figure 3.4 Effect of the hydrogen partial pressure on the oxygen (A) and hydrogen (B) content of the condensed organic phase. Conditions: fluid bed temperature 447-454 °C, HDO temperature: 364-386 °C, biomass feeding rate: 159-389 g/min, H_2S concentration: 47-475 ppm, H_2 flow: 11.4-124.4 NL/min, N_2 flow: 0.37-26.5 NL/min.

The density and the viscosity of the condensed organic phase were measured at 40 °C and are shown in Figure 3.5(A) and (B), respectively. Using the HDO reactor the density was between 0.9360 and 0.9443 g/ml at 3.0 bar hydrogen, and increasing the hydrogen pressure to 24.5 bar decreased the density to 0.8273 g/ml, but further increasing the hydrogen pressure to 35.8 bar increased the density to 0.8428 g/ml. This increase could be due to the slightly lower hydrogen content at 35.8 bar hydrogen compared to at 24.5 bar hydrogen. Bypassing the HDO reactor increased the density to 1.0589 g/ml at 3.0 bar hydrogen and 0.8890 g/ml at 25.8 bar hydrogen. The viscosity varied between 1.052 and 1.225 cSt when the hydrogen pressure was between 8.2 and 35.8 bar and the HDO reactor was used. Decreasing the hydrogen pressure to 3.0 increased the viscosity to between 2.879 and 3.590 cSt, and bypassing the HDO reactor increased the viscosity to 1.607 cSt at 25.8 bar hydrogen and 8.774 cSt at 3.0 bar. The density of fast pyrolysis oil is typically between 1.1 and 1.3 g/ml and the viscosity is between 13 and 100 cSt [5]. Therefore, and despite that both the density and viscosity increased significantly when the HDO reactor was bypassed at 3.0 bar they were still significantly lower than typical values for untreated fast pyrolysis oil. Furthermore, the density and viscosity of diesel are 0.82-0.85 g/ml and 1.9-4.5 cSt, respectively [5]. This shows that the organic phases from the experiments with the HDO were more similar to light gas oil than pyrolysis oil and due to the fairly low oxygen content in the organic phase it is most likely possible to co-feed into a refinery diesel hydrotreater.

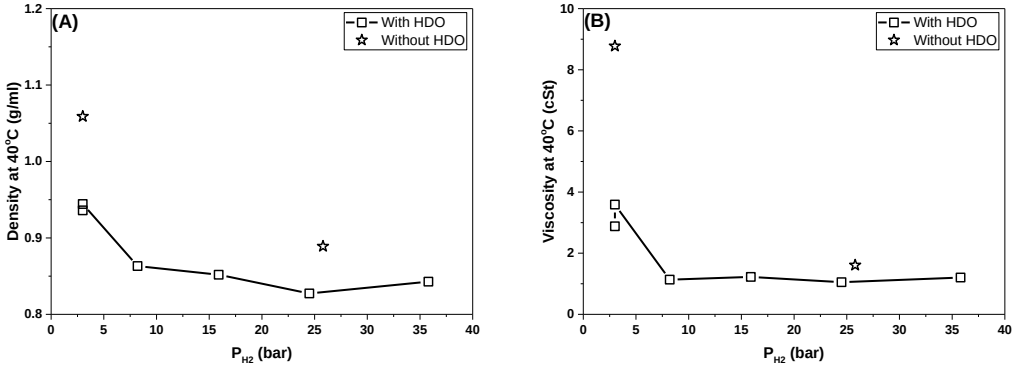

Figure 3.5 Effect of the hydrogen partial pressure on the density (A) and viscosity (B) of the condensed organic phase. Conditions: fluid bed temperature 447-454 °C, HDO temperature: 364-386 °C, biomass feeding rate: 159-389 g/min, H_2S concentration: 47-475 ppm, H_2 flow: 11.4-124.4 NL/min, N_2 flow: 0.37-26.5 NL/min.

In order to gain a deeper insight into the condensed organic phases they were analyzed with GC×GC-MS/FID and the detected components were divided into eleven groups naphthenes, monoaromatics, diaromatics, triaromatics, larger aromatics, phenols, dihydroxybenzenes, larger oxygenated aromatics, oxygenated aliphatics, paraffins, and sterols. Using the HDO reactor the concentration of paraffins was between 1.2 and 4.6 % area-FID, and the concentration of oxygenated alpihatics was between 1.5 and 2.6 % area-FID when the hydrogen pressure was below 15.9 bar, but 0 % area-FID at higher hydrogen pressures (see supplementary information Figure B.2). This indicates that even at low hydrogen pressures most of the reactive oxygenates are removed. The concentration of phenols and larger oxygenated aromatics are shown in Figure 3.6(A). The concentration of phenols was between 44 and 45 % area-FID at 3.0 bar hydrogen, but decreased to 12 % area-FID at 8.2 bar hydrogen and further increasing the hydrogen pressure lead to an almost complete removal (non detected) of the phenols. Similarly, the concentration of larger oxygenated aromatics decreased from between 4.5 and 5.4 % area-FID at 3.0 bar hydrogen to 1.5 % area-FID at 8.2 bar hydrogen; none were detected at higher hydrogen pressures. The concentration of naphthenes increased from 17 % area-FID at 3.0 bar hydrogen to 38 % area-FID at 35.8 bar hydrogen, while the concentration of diaromatics decreased from between 15 and 17 % area-FID at 3.0 bar hydrogen to 7.8 % area-FID at 35.8 bar hydrogen, see Figure 3.6(A).

Interestingly, the concentration of monoaromatics increased from between 12 and 14 % area-FID at 3.0 bar hydrogen to 57 % area-FID at 15.9 bar hydrogen, but further increasing the hydrogen pressure to 35.8 bar decreased the concentration to 48 % area-FID. This indicates an optimum hydrogen pressure for the production of monoaromatics. At hydrogen pressures below the 15.9 bar the reaction rate of HDO is too low to efficiently deoxygenate the phenols and larger oxygenated aromatics despite that benzene is favored by the equilibrium [5]. At hydrogen pressures above the 15.9 bar the oxygenates are converted, and the naphthenes are favored by the thermodynamics [20], hence the aromatics are also hydrogenated which decreases the concentration of mono- and di-aromatics. This indicates that the concentration of monoaromatics is kinetically controlled at low hydrogen pressures (<15.9 bar), but controlled by the equilibrium at high hydrogen pressure (>15.9 bar).

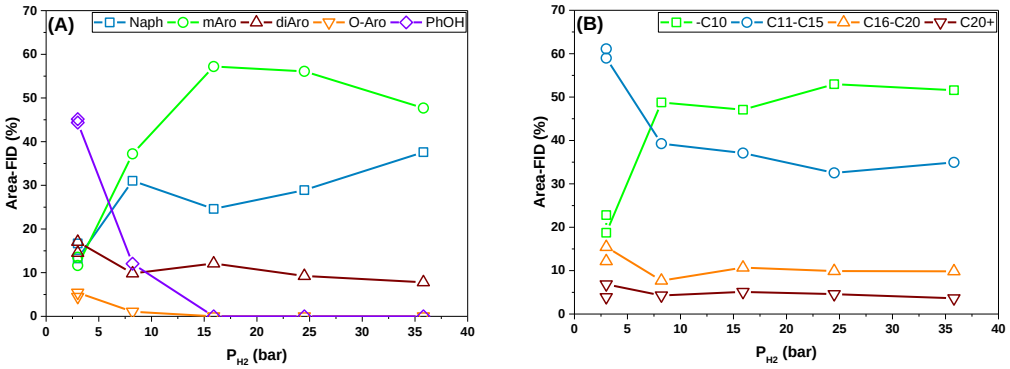

Figure 3.6 Effect of the hydrogen partial pressure on the concentration of naphthenes (Naph), monoaromatics (mAro), diaromatics (diAro), phenols (PhOH), and larger oxygenated aromatics (O-Aro) (A), and on the concentration of hydrocarbons with 10 or fewer carbon atoms (-C10), between 11 and 15 carbon atoms (C11-C15), between 16 and 20 carbon atoms (C16-C20), and more than 20 carbon atoms (C20+) (B). Conditions: fluid bed temperature 447-454 °C, HDO temperature: 364-386 °C, biomass feeding rate: 159-389 g/min, H_2S concentration: 47-475 ppm, H_2 flow: 11.4-124.4 NL/min, N_2 flow: 0.37-26.5 NL/min.

Based on the paraffins retention time on the 1D column it was possible to estimate the number of carbon atoms in the products. However, it should be noted that other component classes do not necessarily have the same carbon number distribution as the paraffins and caution is needed when correlating the results. As shown in Figure 3.6(B) the molecules were divided into 4 groups: less than 10 carbon atoms (-C10), between 11 and 15 carbon atoms (C11-C15), between 16 and 20 carbon atoms (C16-C20), and more than 20 carbon atoms (C20+). The concentration of molecules with less than 10 carbon atoms increased from between 19 and 23 % area-FID at 3.0 bar hydrogen to 49 % area-FID at 8.2 bar, further increasing the hydrogen pressure to 35.8 bar increased the concentration to 52 % area-FID. The reverse trend was observed for molecules with between 11 and 15 carbon atoms for which the concentration decreased from between 60 and 61 % area-FID at 3.0 bar to 39 % area-FID at 8.2 bar, and to 35 % area-FID at 35.8 bar. This indicates that increasing the hydrogen pressure from 3.0 to 8.2 bar significantly increases the hydrocracking activity, while further increasing the hydrogen pressure has less effect on the hydrocracking activity. It should be noted that the concentration of molecules with between 16 and 20 carbon atoms was between 12 and 15 % area-FID at 3.0 bar hydrogen and decreased to 9.9 % area-FID at 35.8 bar hydrogen. This indicates that hydrogen pressure only has a limited effect on the concentration of larger molecules and the concentration of molecules with more 20 carbon atoms was 3.9 % area-FID at 3.0 bar hydrogen and 3.6 % area-FID at 35.8 bar hydrogen.

The chromatograms and composition of the organic phases from the experiments where the HDO reactor was bypassed (#2 and #8) are shown in Figure 3.7. The organic phases from the two experiments are very different. At 3.0 bar hydrogen 77 % area-FID of the organics are oxygenates, while only 26 % area-FID is oxygenates at 25.8 bar hydrogen. At 3.0 bar hydrogen the concentration of oxygenated aliphatics was 33 % area-FID, while it was 4.0 % area-FID at 25.8 bar hydrogen, which shows that at the low hydrogen pressure (3.0 bar) the rate of HDO it too low to convert even simple and reactive oxygenates. Likewise, the concentration of larger oxygenated aromatics and dihydroxybenzenes was 18 and 5.2 % area-FID, respectively, at 3.0 bar hydrogen. Increasing the hydrogen pressure to 25.8 bar decreased the concentration of larger oxygenated aromatics to 0.1 % area-FID and dihydroxybenzenes were not detected at this hydrogen pressure. Traces of sterols (0.1 % area-FID) were also detected at 3.0 bar hydrogen, but not at 25.8 bar hydrogen. These results indicate that the organic phase produced at 25.8 bar hydrogen is more stable and less reactive than the organ-

ic phase produced at 3.0 bar hydrogen. It is therefore likely that the organic phase produced at 25.8 bar hydrogen can easily be co-feed into an existing refinery unit, while co-feeding the organic phase produced at 3.0 bar will most likely lead to catalyst deactivation due to the furans and multifunctional phenols present in the organic phase. However, it should also be noted that dihydroxybenzenes were not detected in any of the experiments with the HDO reactor, thus multifunctional phenols were only detected at 3.0 bar hydrogen when the HDO reactor was bypassed. Furthermore, the molecular size distribution was also very different for produced organics when the HDO reactor was bypassed. 32 % area-FID of the molecules contains less than 10 carbon atoms at 3.0 bar hydrogen, while 41 % contains less than 10 carbon atoms at 25.8 bar hydrogen, showing that decreasing the hydrogen pressure leads to a heavier organic phase.

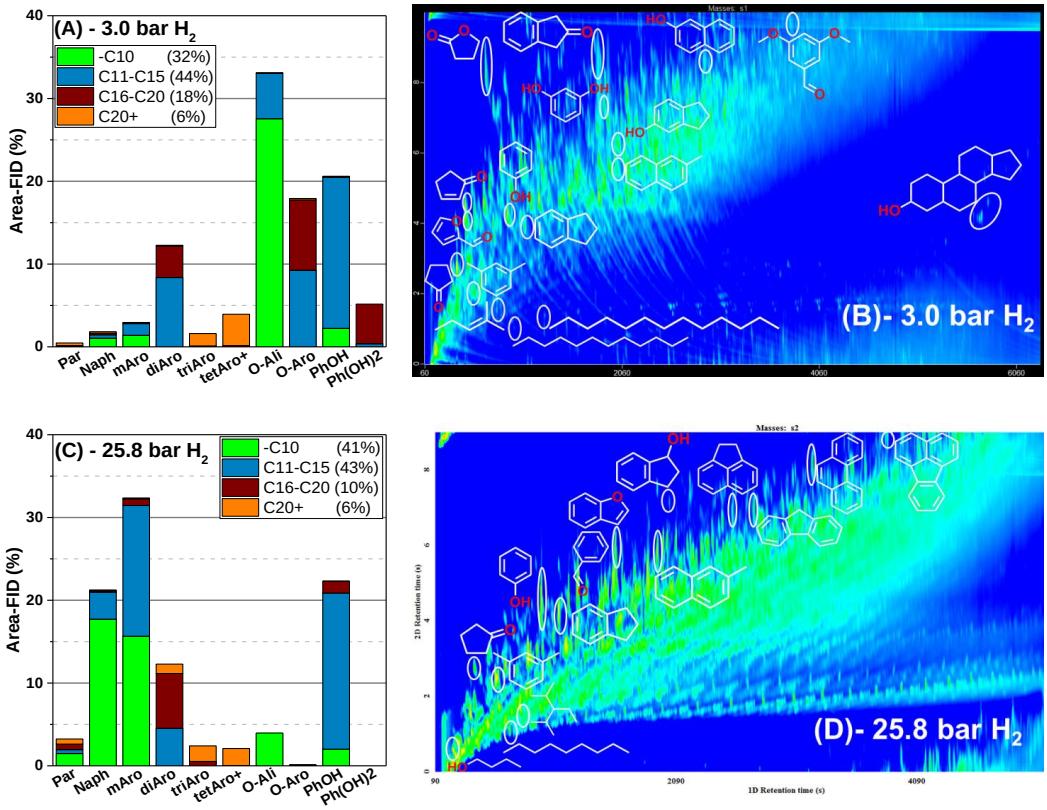

Figure 3.7 Composition of the organic phase when the HDO reactor is bypassed at 3.0 bar hydrogen (A,B) and at 25.8 bar hydrogen (C,D). The components in the condensed organics are divided into paraffins (Par), naphthenes (Naph), monoaromatics (mAro), diaromatics (diAro), triaromatics (triAro), tetraaromatics and larger aromatics (tetAro+), oxygenated aliphatics (O-ali), phenols (PhOH), dihydroxybenzenes (Ph(OH)2), and larger oxygenated aromatics (O-aro). Conditions: fluid bed temperature 450-454 °C, biomass feeding rate: 174-350 g/min, H_2S concentration: 48-475 ppm, H_2 flow: 87-11.4 NL/min, N_2 flow: 0.62-26.5 NL/min.

The sulfur content in the condensed organic phases was measured to be between 0.033 and 0.417 wt.% db with energy dispersive X-ray fluorescence, which indicates an incorporation of sulfur into the produced organics. Therefore, 5 of the condensed organic phases were analyzed with sulfur specific GC-AED and the detected compounds were divided into thiols, thiophenes, benzothiophenes, other sulfur containing hydro-

carbons such as DMDS and carbonylsulfide, and unidentified. Detailed lists of the detected compounds are shown in supplementary information Table B.1 - B.5. This showed that the samples contained between 17 and 232 wt-ppm S as H_2S, which was not properly removed during the stripping. When the HDO reactor was bypassed at 3.0 bar hydrogen the concentration of thiols was 23 wt-ppm S, but between 0 and 3 wt-ppm S when the HDO reactor was used, see Figure 3.8, showing that even at low hydrogen pressures the thiols were removed in the HDO reactor. The concentration of thiophenes was 220 wt-ppm S at 3.0 bar hydrogen without the HDO reactor, but 298 wt-ppm S at 3.0 bar hydrogen (10 bar total pressure) with HDO reactor, indicating that thiophenes are formed in the HDO reactor. However, it should be noted that the concentration of unidentified compounds was 96 wt-ppm S when the HDO reactor was bypassed and 34 wt-ppm S when the HDO reactor was used, thus it is likely that the organic phase from experiments without the HDO reactor contains some unidentified thiophenes or benzothiophenes.

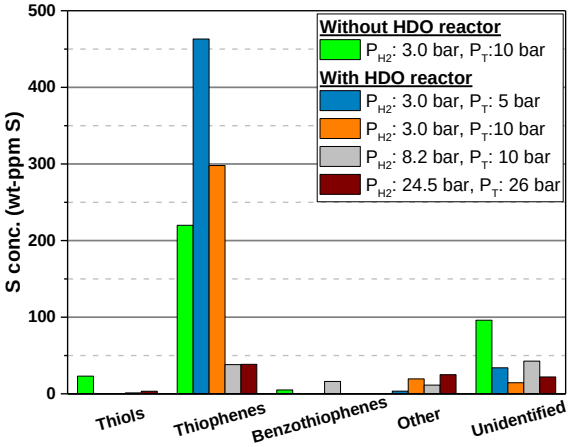

Figure 3.8 Effect of the hydrogen partial pressure and the total pressure on the concentration of organic sulfur species in the condensed organic phase. Conditions: fluid bed temperature 447-454 °C, HDO temperature: 364-386 °C, biomass feeding rate: 159-389 g/min, H_2S concentration: 47-475 ppm, H_2 flow: 11.4-124.4 NL/min, N_2 flow: 0.37-26.5 NL/min.

Interestingly, the concentration of thiophenes was 463 wt-ppm S when the total pressure was 5 bar (3.0 bar hydrogen), but 298 wt-ppm S when the total pressure was 10 bar (3.0 bar hydrogen), both with the HDO reactor, indicating that the total pressure influences the thiophene concentration. The thiophene concentration was 38 wt-ppm S both at 8.2 and 24.5 bar hydrogen, indicating that varying the hydrogen pressure in this interval only has a limited effect on the thiophene concentration. However, the concentration of benzothiophenes was 16 wt-ppm S at 8.2 bar hydrogen, but was not detected at 24.5 bar hydrogen. Furthermore, the total concentration of sulfur containing compounds was 109 wt-ppm S at 8.2 bar hydrogen and 84 wt-ppm S at 24.5 bar hydrogen.

The carbon content in the aqueous phases was below 0.02 wt.% in the experiments where the HDO reactor was used and the hydrogen pressure was 15.9 bar or higher, see Table 3.1. Decreasing the hydrogen pressure to 8.2 bar increased the carbon content in the aqueous phase to 0.66 wt.% and further decreasing the hydrogen pressure to 3.0 bar increased the carbon content to between 0.70 and 0.81 wt.%, depending on the total pressure. Furthermore, bypassing the HDO reactor at 3.0 bar hydrogen the carbon content in the aqueous phase was 12.3 wt.%, while it was 1.3 wt.% at 25.8 bar hydrogen. This shows that conducting catalytic hy-

dropyrolysis at low hydrogen pressures (<15.8 bar) even with a HDO reactor lead to higher carbon content in the aqueous phase, which could increase the operating expenses for waste water treatment.

In order to obtain a more thorough understanding of the oxygenates the aqueous phase, the aqueous phases with more than 0.02 wt.% carbon were analyzed with GC-MS/FID. The detected oxygenates were divided into 8 groups: alcohols, furans, acids, ketones, phenols, sugars, esters, aldehydes and unidentified. Lists of the detected compounds can be found in supplementary information Tables B.6-B.10. To compare the concentrations in the different aqueous phases the relative FID area (the FID area of one group divided with total area) was multiplied with the concentration of carbon in the aqueous phase, as shown in Figure 3.9. When the HDO reactor was used most of the aqueous phase oxygenates were phenols and the phenol concentration increased from 0.11 to 0.31 wt.% when the hydrogen pressure was decreased from 8.2 to 3.0 bar (10 bar total pressure). At 8.2 bar hydrogen no acids were detected, but at 3.0 bar hydrogen (10 bar total pressure) acetic acid, propanoic acid, and butanoic acid were detected, corresponding to a total concentration of 0.009 wt.%. Ketones were also observed at 3.0 bar hydrogen at both 5 and 10 bar total pressure, showing that at 3.0 bar hydrogen the rate of HDO too low to convert even the more reactive oxygenates. However, the concentration of alcohols was below 0.1 wt.% in all the experiments with the HDO reactor.

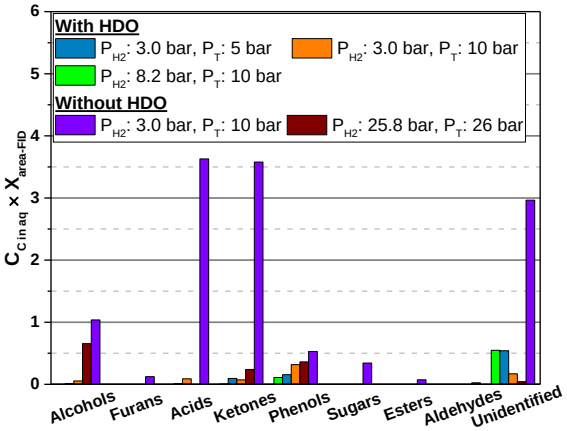

Figure 3.9 Effect of the hydrogen partial pressure and total pressure on composition of the aqueous phase. The concentration is calculated by multiplying the total concentration of the carbon in the aqueous phase with the fraction (area-FID) of the different compounds.

Bypassing the HDO reactor increased the concentration of alcohols to 1.0 wt.% at 3.0 bar hydrogen and 0.66 wt.% at 25.8 bar hydrogen. Likewise, the phenols concentration increased to 0.53 wt.% at 3.0 bar hydrogen and 0.36 wt.% at 25.8 bar hydrogen and the concentration of ketones increased to 3.6 wt.% at 3.0 bar hydrogen and 0.24 wt.% at 25.8 bar hydrogen. At 3.0 bar hydrogen furans (0.12 wt.%), sugars (0.34 wt.%), esters (0.073 wt.%), aldehydes (0.024 wt.%) were also observed, none of these compounds were detected at 25.8 bar hydrogen, showing that the aqueous phase formed at 3.0 bar hydrogen contains much more reactive oxygenates than the aqueous phase formed at 25.8 bar.

3.3.3 Characterization of the spent catalysts

The carbon content on the spent catalysts from the fluid bed reactor was investigated with SEM-EDS and the acceleration voltage was varied between 3 and 15 kV. At 3 kV the carbon concentration at the surface was

measured and at 15 kV a concentration closer to the bulk (penetration depth: 1.6 µm) was measured, as described in detail in Chapter 4. In order to account for the background carbon measurement, the carbon content on the catalysts was calculated by subtracting the measured carbon content on the fresh catalyst from the carbon on the spent catalysts (see supplementary information equation B.1). The measured carbon content on the catalysts is shown at different acceleration voltages in supplementary information Table B.11. Figure 3.10 shows the measured concentration of carbon at 15 kV as a function of the hydrogen pressure. It can be seen that at hydrogen pressures between 15.9 and 35.8 bar the carbon concentration varied between 4.8 and 6.2 wt.%, differences within the measurement uncertainty, and hence the coke formation was unaffected by the hydrogen pressure in this range. However, decreasing the hydrogen pressure to 8.2 bar increased the carbon concentration to 8.8 wt.% and further decreasing the hydrogen pressure to 3.0 increased the carbon content to between 12.2 and 20.7 wt.%. Part of the reason for the large variation in the carbon content at 3.0 bar hydrogen is that different amounts of biomass were used. When 513 g daf biomass was used the carbon content was 12.2 wt.%, while it was 16.0 wt.% when 972 g daf was used and 20.7 wt.% when 899 g daf was used. As shown in supplementary information Figure B.3 the carbon content on the catalysts, which had a bulk carbon content of 16.0 and 20.7 wt.% (measured at 15 kV), had a higher carbon concentration at surface (between 20.8 and 25.6 wt.%). This indicates that carbon was building up on the surface of the catalyst, which over time could lead to blocking of the pores. The carbon content on the spent catalysts from the fluid bed reactor therefore indicates that at hydrogen pressures of 15.9 bar and above there is sufficient hydrogen for the catalyst to stabilize the reactive molecules before they can participate in polymerization reactions on the surface.

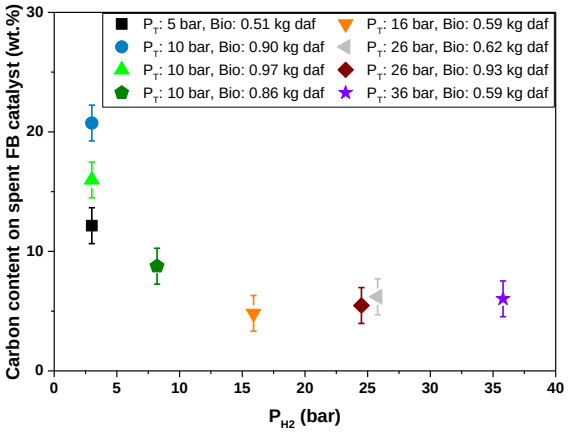

Figure 3.10 Carbon content on the spent catalysts from the fluid bed (FB) reactor, measured with SEM-EDS at 15 kV. Conditions: fluid bed temperature 447-454 °C, HDO temperature: 364-386 °C, biomass feeding rate: 159-389 g/min, H_2S concentration: 47-475 ppm, H_2 flow: 11.4-124.4 NL/min, N_2 flow: 0.37-26.5 NL/min.

The carbon content on the spent catalysts from the HDO reactor was also measured as shown in Figure 3.11. The catalyst in the HDO reactor was not exchanged between experiments 1 to 4, and had prior to experiment 1 also been used in another experiment at 24.5 bar hydrogen. Despite that this catalyst had been used for several experiments (at high hydrogen partial pressure), the carbon content was only 1.29 wt.%, while it was 2.94 wt.% on the catalyst that was tested at 8.2 bar hydrogen, 4.43 wt.% on the catalyst tested at 3.0 bar hydrogen (0.51 kg daf biomass used), and 5.59 wt.% on the catalyst that was tested at 3.0 bar hydrogen (0.90 kg daf biomass used). This shows that the degree of coking of the catalyst in the HDO reactor increased with

decreasing hydrogen partial pressure. The reason for this observation is most likely a combination of the low hydrogen pressure, the higher oxygen content in the hydrocarbons produced in the fluid bed reactor and the more reactive and multifunctional oxygenates, as discussed in the Section 3.2. These experiments therefore indicate that in order to minimize coking of the HDO reactor the hydrogen pressure should be above 8.2 bar, when the herein applied catalyst combination is used.

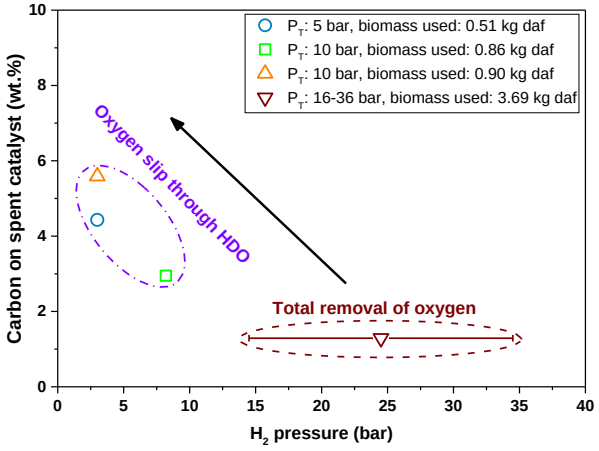

Figure 3.11 Carbon content on the spent catalyst from the HDO reactor. Conditions: fluid bed temperature 447-454 °C, HDO temperature: 364-386 °C, biomass feeding rate: 159-389 g/min, H_2S concentration: 47-475 ppm, H_2 flow: 11.4-124.4 NL/min, N_2 flow: 0.37-26.5 NL/min.

3.4 Conclusion

Catalytic hydropyrolysis of beech wood was conducted in a fluid bed reactor followed by a fixed bed HDO reactor, at a total pressure between 5 and 36 bar and a hydrogen pressure between 3.0 and 35.8 bar. At hydrogen pressures below 15.9 bar the solid yield increased from 11.0 wt.% daf at 15.9 bar hydrogen up to 15.7 wt.% daf at 3.0 bar hydrogen, showing that at low hydrogen pressures the pyrolysis vapors are not sufficiently stabilized, leading to polymerization. The organic phase produced at between 15.9 and 35.8 bar hydrogen pressure was essentially oxygen free (<0.01 wt.% oxygen), but the oxygen content increased with decreasing pressure and an oxygen content up to 7.8 wt.% db was measured at 3.0 bar hydrogen, where the oxygenates were mainly phenols.

Detailed analysis of the condensed organic phases showed that the maximum monoaromatic yield was obtained at 15.9 bar hydrogen pressure. At lower hydrogen pressures not all of the phenols were deoxygenated, despite that aromatic hydrocarbons are favored by equilibrium, indicating that the aromatic formation was kinetically controlled. However, increasing the hydrogen pressure to above 15.9 bar led to an increase in the naphthenes and a comparison with thermodynamic calculations indicated that the concentration of monoaromatics is controlled by the thermodynamics at high hydrogen pressures (15.9-35.8 bar).

The carbon content on the spent catalysts from both the fluid bed and HDO reactor was measured. Varying the hydrogen partial pressure between 15.9 and 35.8 bar did not have an impact on the carbon content on the spent catalyst from the fluid bed, however further decreasing the hydrogen pressure increased the carbon content, indicating an increased deactivation of the catalyst. Although the same catalyst was used in the

HDO reactor for the experiments conducted at hydrogen pressures between 15.9 and 35.8 bar the carbon content was only 1.3 wt.%. Decreasing the hydrogen pressure increased the carbon content on the spent HDO reactor catalyst, hence the carbon content was 5.6 wt.% on the HDO catalyst after one experiment at 3.0 bar hydrogen.

Conducting experiments at 3.0 and 25.8 bar hydrogen pressure without the HDO reactor, showed that the oxygenates in condensed organic phase at 25.8 bar hydrogen mainly consisted of phenols, while the oxygenates from the experiment conducted at 3.0 bar consisted of, besides phenols, dihydroxybenzenes, larger aromatics, and a high concentration of oxygenated aliphatics. Furthermore, GC-MS/FID analysis of the aqueous phases showed that it contained acids, ketones, furans, and sugars. This shows that the oxygenates produced at 3.0 bar hydrogen pressure are more reactive, which is most likely the reason for the higher carbon content on the catalysts from the experiments at low pressures. The results show, that despite being easier to feed biomass at low pressure, it may lead to a more reactive product, which can decrease the catalyst life time and may limit further processing in a refinery.

Acknowledgments

This work is part of the project “Hydrogen assisted catalytic pyrolysis for green fuels” conducted at The Department of Chemical and Biochemical Engineering at the Technical University of Denmark (DTU). The work was supported by The Danish Council for Strategic Research (now Innovation Fund Denmark, project 1305-00015B), The Programme Commission on Sustainable Energy and Environment. Funding from DTU is also gratefully acknowledged. The authors acknowledge the Organic Analysis Department at Haldor Topsøe A/S for analysis of the organic phase.

References

[1] T.L. Marker, L.G. Felix, M.B. Linck, M.J. Roberts, Integrated hydropyrolysis and hydroconversion (IH^2) for the direct production of gasoline and diesel fuels or blending components from biomass, Part 1: Proof of principle testing, Environ. Prog. Sustain. Energy. 31 (2012) 191–199. doi:10.1002/ep.10629.

[2] T.L. Marker, L.G. Felix, M.B. Linck, M.J. Roberts, P. Ortiz-Toral, J. Wangerow, Integrated hydropyrolysis and hydroconversion ($IH^{2®}$) for the direct production of gasoline and diesel fuels or blending components from biomass, Part 2: Continuous testing, Environ. Prog. Sustain. Energy. 33 (2014) 762–768. doi:10.1002/ep.11906.

[3] E. Maleche, R. Glaser, T. Marker, D. Shonnard, A preliminary life cycle assessment of biofuels produced by the $IH^{2\ TM}$ process, Environ. Prog. Sustain. Energy. 33 (2014) 322–329. doi:10.1002/ep.11773.

[4] J. Fan, J. Gephart, T. Marker, D. Stover, B. Updike, D.R. Shonnard, Carbon Footprint Analysis of Gasoline and Diesel from Forest Residues and Corn Stover using Integrated Hydropyrolysis and Hydroconversion, ACS Sustain. Chem. Eng. 4 (2016) 284–290. doi:10.1021/acssuschemeng.5b01173.

[5] T.M.H. Dabros, M.Z. Stummann, M. Høj, P.A. Jensen, J.-D. Grunwaldt, J. Gabrielsen, P.M. Mortensen, A.D. Jensen, Transportation fuels from biomass fast pyrolysis, catalytic hydrodeoxygenation, and catalytic fast hydropyrolysis, Prog. Energy Combust. Sci. 68 (2018) 268–309. doi:10.1016/j.pecs.2018.05.002.

[6] O.D. Mante, D.C. Dayton, J. Gabrielsen, N.L. Ammitzboll, D. Barbee, S. Verdier, K. Wang, Integration of catalytic fast pyrolysis and hydroprocessing: a pathway to refinery intermediates and

"drop-in" fuels from biomass, Green Chem. 18 (2016) 6123–6135. doi:10.1039/c6gc01938b.

[7] D.C. Dayton, J. Carpenter, J. Farmer, B. Turk, R. Gupta, Biomass hydropyrolysis in a pressurized fluidized bed reactor, Energy & Fuels. 27 (2013) 3778–3785. doi:10.1021/ef400355t.

[8] K. Wang, D.C. Dayton, J.E. Peters, O.D. Mante, Reactive catalytic fast pyrolysis of biomass to produce high-quality bio-crude, Green Chem. 19 (2017) 3243–3251. doi:10.1039/C7GC01088E.

[9] D.C. Dayton, J. Hlebak, J.R. Carpenter, K. Wang, O.D. Mante, J.E. Peters, Biomass hydropyrolysis in a fluidized bed reactor, Energy & Fuels. 30 (2016) 4879–4887. doi:10.1021/acs.energyfuels.6b00373.

[10] S. Thangalazhy-Gopakumar, S. Adhikari, R.B. Gupta, M. Tu, S. Taylor, Production of hydrocarbon fuels from biomass using catalytic pyrolysis under helium and hydrogen environments., Bioresour. Technol. 102 (2011) 6742–9. doi:10.1016/j.biortech.2011.03.104.

[11] S. Thangalazhy-Gopakumar, S. Adhikari, R.B. Gupta, Catalytic pyrolysis of biomass over H^+ZSM-5 under hydrogen pressure, Energy & Fuels. 26 (2012) 5300–5306. doi:10.1021/ef3008213.

[12] O. Jan, R. Marchand, L.C.A. Anjos, G.V.S. Seufitelli, E. Nikolla, F.L.P. Resende, Hydropyrolysis of lignin using Pd/HZSM-5, Energy & Fuels. 29 (2015) 1793–1800. doi:10.1021/ef502779s.

[13] F. Melligan, M.H.B. Hayes, W. Kwapinski, J.J. Leahy, Hydro-pyrolysis of biomass and online catalytic vapor upgrading with Ni-ZSM-5 and Ni-MCM-41, Energy & Fuels. 26 (2012) 6080–6090. doi:10.1021/ef301244h.

[14] P. Choudhary, A. Malik, K.K. Pant, Mass-Scale Algal Biomass Production Using Algal Biofilm Reactor and Conversion to Energy and Chemical Precursors by Hydropyrolysis, ACS Sustain. Chem. Eng. 5 (2017) 4234–4242. doi:10.1021/acssuschemeng.7b00233.

[15] R.. Pindoria, a Megaritis, a. . Herod, R. Kandiyoti, A two-stage fixed-bed reactor for direct hydrotreatment of volatiles from the hydropyrolysis of biomass: effect of catalyst temperature, pressure and catalyst ageing time on product characteristics, Fuel. 77 (1998) 1715–1726. doi:10.1016/S0016-2361(98)00079-9.

[16] F. Melligan, M.H.B. Hayes, W. Kwapinski, J.J. Leahy, A study of hydrogen pressure during hydropyrolysis of Miscanthus x giganteus and online catalytic vapour upgrading with Ni on ZSM-5, J. Anal. Appl. Pyrolysis. 103 (2013) 369–377. doi:10.1016/j.jaap.2013.01.005.

[17] V.K. Venkatakrishnan, J.C. Degenstein, A.D. Smeltz, W.N. Delgass, R. Agrawal, F.H. Ribeiro, High-pressure fast-pyrolysis, fast-hydropyrolysis and catalytic hydrodeoxygenation of cellulose: Production of liquid fuel from biomass, Green Chem. 16 (2014) 792–802. doi:10.1039/c3gc41558a.

[18] V.K. Venkatakrishnan, W.N. Delgass, F.H. Ribeiro, R. Agrawal, Oxygen removal from intact biomass to produce liquid fuel range hydrocarbons via fast-hydropyrolysis and vapor-phase catalytic hydrodeoxygenation, Green Chem. 17 (2015) 178–183. doi:10.1039/c4gc01746c.

[19] L. Zhang, K. Gong, J. Lai, P. Alvey, Chemical composition and stability of renewable hydrocarbon products generated from a hydropyrolysis vapor upgrading process, Green Chem. 19 (2017) 3628–3641. doi:10.1039/c7gc01075c.

[20] M.Z. Stummann, M. Høj, C.B. Schandel, A.B. Hansen, P. Wiwel, J. Gabrielsen, P.A. Jensen, A.D. Jensen, Hydrogen assisted catalytic biomass pyrolysis. Effect of temperature and pressure, Biomass and Bioenergy. 115 (2018) 97–107. doi:10.1016/j.biombioe.2018.04.012.

Chapter 4 Effect of the catalyst in fluid bed catalytic hydropyrolysis

The following chapter has been submitted to Catalysis Today with the title "*Effect of the catalyst in fluid bed catalytic hydropyrolysis*" and is currently under review. The supplementary information can be found in Appendix C.

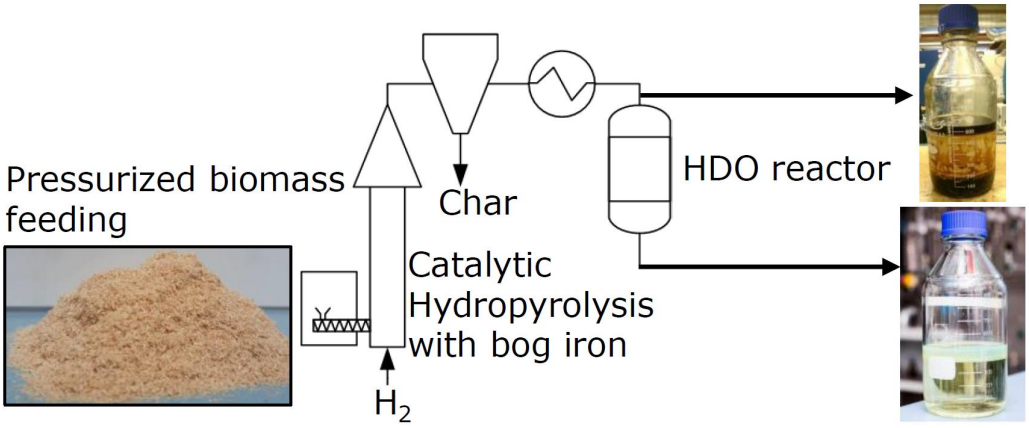

Abstract

Catalytic hydropyrolysis of beech wood was conducted in a fluid bed reactor followed by a hydrodeoxygenation reactor with a sulfided NiMo/Al_2O_3 catalyst. In order to evaluate the effect of the catalyst in the fluid bed reactor five different bed materials were tested. Conducting the hydropyrolysis using only the catalyst support materials $MgAl_2O_4$ or zeolite mixed with Al_2O_3 (H-ZSM-5-Al_2O_3) gave a high char and coke yield (18.7-21.1 wt.% dry ash free (daf), CO and CO_2 (18.9 and 20.0 wt.% daf), and low yield of condensed organics and C_{4+} gasses (17.8-20.4 wt.% daf). Using the supported catalysts CoMo/$MgAl_2O_4$ or NiMo/ZSM-5-Al_2O_3 significantly decreased the char yield to between 11.4 and 13.1 wt.% daf, while the condensed organics and C_{4+} yield increased to 21.5 wt.% daf for the CoMo/$MgAl_2O_4$ and 24.0 wt.% daf for the NiMo/ZSM-5-Al_2O_3. Furthermore, scanning electron microscopy (SEM) combined with energy dispersive X-ray spectroscopy (EDS) showed that using a supported catalyst instead of just the support significantly decreased the amount of carbon deposited on the spent catalyst. As an alternative to the (commercial) supported catalysts, a cheap natural mineral bog iron was tested as catalyst and gave a condensed organics and C_{4+} yield of 22.8 wt.% daf when pre-sulfiding the bog iron, while the yield was 24.7 wt.% daf when the bog iron was used unsulfided, but reduced prior to the experiment. This indicates that bog iron is the most suitable catalyst in the fluid bed reactor. The reason for the high yields obtained with bog iron was attributed to its low cracking activity. X-ray diffraction (XRD) and scanning transmission electron microscopy (STEM) equipped with EDS indicated that the active phase for sulfided and reduced bog iron was pyrrhotite and magnetite, respectively. The carbon level on the spent bog iron catalyst was at the same level as for the spent CoMo/$MgAl_2O_4$ and NiMo/ ZSM-5-Al_2O_3 catalysts. This indicates that bog iron is able to stabilize the reactive oxygenates before they can participate in char and coke forming polymerization reactions. Hence, the natural mineral bog iron may replace the more expensive and toxic CoMo and NiMo catalysts in the fluid bed.

Abbreviations

AED	Atomic emission detector	MgAl	$MgAl_2O_4$
BET	Brunauer–Emmett–Teller	MS	Mass spectrometry
BI	Bog iron	Naph	Naphthenes
CoMo	CoMo/$MgAl_2O_4$	NiMoZA	NiMo/H-ZSM-5 mixed with Al_2O_3
conc	Concentration	O-Ali	Oxygenated aliphatics
daf	Dry, ash free basis	O-Aro	Larger oxygenated aromatics
db	Dry basis	OS	Olivine sand
diAro	Diaromatics	Par	Paraffins
DMDS	Dimethyl disulfide	PhOH	Oxygenated aromatics (phenols)
EDS	Energy dispersive X-ray emission spectroscopy	Ph(OH)2	Dihydroxybenzene
FB	Fluid bed	SEM	Scanning electron microscopy
FID	Flame ionization detector	SIMDIS	Simulated distillation by GC
GC	Gas chromatograph	STEM	Scanning transmission electron microscopy
HAADF	High-angle annular dark-field	Temp.	Temperature
HDO	Hydrodeoxygenation	tetAro+	Tetra- and higher aromatics
ICP-OES	Inductive coupled plasma optical emission spectroscopy	triAro	Triaromatics
mAro	Monoaromatics	ZA	H-ZSM-5 mixed with Al_2O_3

4.1 Introduction

The worlds energy consumption continues to increase, with transport being one of the major energy consumers [1,2]. The transportation sector is responsible for more than one fourth of the energy consumption in the United States [1], where liquid transportation fuels are mainly produced from crude oil. However, the reserves of fossil oil are depleting [3] and their use contributes to global warming through emission of carbon dioxide [4]. Therefore, it is necessary to find carbon neutral alternative fuels. Lignocellulosic biomass can be converted into a liquid bio-oil by fast pyrolysis, where the biomass is rapidly heated to approximately 500 °C in an inert atmosphere [5]. The produced bio-oil has a high oxygen and water content [5–8], thus its heating value is less than half that of conventional liquid fuel [8,9]. Due to the high oxygen content the bio-oil is immiscible with conventional petroleum oils, it is acidic and has a tendency to polymerize during storage [5,10,11]. Before bio-oil can replace the fossil fuels used in the transportation sector upgrading is necessary [12]. This could be achieved by catalytic hydrodeoxygenation (HDO) where bio-oil oxygenates are hydrogenated to hydrocarbons with water as byproduct. Unfortunately, however, the reactive nature of the bio-oil leads to rapid deactivation of the HDO catalyst by coking [13]. Furthermore, studies have shown that some of the larger, and more problematic molecules, such as anhydro-oligosaccharides, in the bio-oil are formed by polymerization of the pyrolysis vapors in the short time between pyrolysis and condensation of the bio-oil [14]. Catalytic pyrolysis, where the pyrolysis takes place in the presence of a zeolite catalyst in an inert atmosphere, has been used to produce a bio-oil with lower oxygen content. However, the carbon recovery for this process is only between 10 and 20 wt.% and the oxygen content is still significant [15].

Catalytic hydropyrolysis has gained an increasing interest since Marker et al. [16,17] showed that it is possible to obtain an oxygen free oil with a condensed oil and C_{4+} yield of up to 28 wt.% daf from maple wood in their process called Integrated Hydropyrolysis and Hydroconversion ($IH^{2®}$). In this process biomass is fed under pressure into a fluid bed reactor, where the catalytic hydropyrolysis takes place, followed by a fixed bed reactor with a hydrotreating catalyst [16,17]. The composition of the catalyst in the fluid bed and HDO reactor used in the studies by Marker et al. [16, 17] has not been reported. Dayton et al. [18] tested catalytic hydropyrolysis of woody residue with a commercially available hydrotreating catalyst. This gave an initial low oil yield (<5 wt.%), which increased over time to 12.5 wt.%, as the catalyst deactivated. Replacing the catalyst with SiC increased the bio-oil yield to 26.6-42.5 wt. % with an oxygen content of 34.6-38.8 wt.% db depending on the operating conditions and thus not much oxygen was removed from the oil [18]. Dayton et al. [19] also investigated the effect of temperature and pressure with a commercially available NiMo hydrotreating catalyst. The used catalyst was prior to the experiment reduced in hydrogen rather than the normal activation by sulfidation to the NiMoS form. Liquid organic yields between 12.6 and 25.6 wt.% was obtained with an oxygen content between 2.4 and 11.9 wt.%. The carbon recovery was between 34.8 and 42.0 %, which is significantly higher than for catalytic pyrolysis with zeolites. Wang et al. [20] tested 5 different catalysts in a fluid bed reactor at atmospheric hydrogen pressure and was able to obtain an oil and C_{4+} yield corresponding to a carbon recovery of 43.2 %, with an oxygen content in the oil of 6.2 wt.%. Other groups have been pursuing high pressure non-catalytic hydropyrolysis in an inverted cyclone or fluid bed reactor followed by a second hydrotreating reactor prior to the oil and water condensation [21–23]. Catalytic hydropyrolysis has also been studied by several groups using Pyroprobe instruments. Melligan et al. [24,25] have shown that pyrolysis in a H_2 atmosphere at elevated pressure with a Ni-ZSM-5 catalyst significantly decreases the concentration of ethanoic acids in the bio-oil compared to performing the pyrolysis in He. Gamliel et al. [26–28] investigated the difference between Ni supported on SiO_2, Al_2O_3 and ZSM-5 and found that ZSM-5 gave the lowest solid yield, thus the lowest solid yield was obtained with the catalyst with the highest acidity. They ascribed this to an increase in the acid-catalyzed decarbonylation and aromatization

of anhydrosugars and furans to stable products prior to secondary polycondensation reactions [26]. Catalytic hydropyrolysis is to some extent similar to the Bergius process, where coal and heavy oil are mixed into a slurry [29–31] with the purpose of transforming coal to a liquid fuel. However, the Bergius process is a liquid phase reaction, while catalytic hydropyrolysis is a gas phase reaction. Iron sulfide is, due to its moderate price and activity, the most conventional catalyst used in the Bergius process [32] and pyrrhotite ($Fe_{1-x}S$) is assumed to be active phase [33,34]. The size of the catalyst particles has a significant influence on the catalyst activity and smaller particles are preferred [32,33]. Furthermore, it has been observed that the oil yield increases with decreasing crystallite size of pyrrhotite [35]. Rocha et al. [36] showed using a pyroprobe that conducting hydropyrolysis of cellulose at 10 MPa with a colloid FeS catalyst decreased the oxygen content in the produced bio-oil from 19.9 % to 11.5 %.

Despite the recent progress, the knowledge base on catalytic hydropyrolysis is still scarce. Often the catalyst composition is not reported and in most cases when it is reported the experiments are conducted in Pyroprobe instruments and not in continuous fluid bed reactors closer to industrial application. Furthermore, the catalysts are often fairly expensive and toxic, containing elements such as Ni, Mo and Co. The latter could be a problem because the catalyst is crushed over time and is mixed with the produced char, which might increase the cost for handling this.

In our previous study [37], catalytic hydropyrolysis of beech wood was conducted in a fluid bed reactor with a sulfided commercial $CoMo/MgAl_2O_4$ catalyst followed by a HDO reactor loaded with a sulfided commercial $NiMo/MgAl_2O_4$ catalyst. The produced organic phase was essentially oxygen free and consisted of naphtha and diesel range hydrocarbons. The fluid bed temperature and pressure were varied, which showed that the interconversion of aromatics into naphthenes was kinetically controlled at temperatures below 430 °C and equilibrium controlled (limited) at higher temperatures [37]. In this study the effect of the highly important catalyst in the fluid bed reactor is investigated in order to optimize the oil yield, to study the influence on the products and to better understand the interplay between the two catalytic reactors. Commercial catalysts, support materials, and natural minerals were tested in the fluid bed reactor, with aim of exploring the possibility to replace the fairly expensive and toxic CoMo and NiMo catalysts with a cheap and non-toxic alternative. The produced liquid products were analyzed and the spent catalysts were characterized with scanning transmission electron microscopy (STEM), scanning electron microscopy (SEM) combined with energy-dispersive X-ray spectroscopy (EDS), and X-ray diffraction (XRD).

4.2 Material and methods

4.2.1 Biomass feedstock

Bark free beech wood supplied by Dansk Træmel (Product number: 10000251250390) was used as biomass. The wood particles size was approximately 200-700 µm. The ash content was 0.59 wt. % on dry basis (db) and the moisture content was 6.72 wt. % (weight loss by drying at 105 ^{o}C). The biomass elemental composition can be found elsewhere [37]. The biomass was analyzed by Celignis Analytical (analysis P10) and consisted of 24 wt.% db lignin, 40 wt.% db cellulose, 18 wt.% db hemicellulose, 3 wt.% db extractives and 12 wt.% db unknown.

4.2.2 Catalysts

Six different catalysts were tested in the fluid bed: A $CoMo/MgAl_2O_4$ (CoMo), a spinel carrier $MgAl_2O_4$ (MgAl), Olivine sand (OS), bog iron (BI), zeolite (H-ZSM-5) mixed with alumina (ZA), and NiMo on zeolite mixed with alumina (NiMoZA). Bog iron was tested both as a sulfide catalyst (BI-S) and as a reduced

catalyst (BI-R). The CoMo, MgAl, NiMoZA and ZA were tested as sulfide catalysts. MgAl was prior to the experiments calcined in air at 960°C for 4 hours. The OS (F grade) was supplied by LKAB minerals and more information can be found in the supplementary information Table C.1 and Table C.2. The other catalysts (CoMo, NiMo, MgAl, ZA, NiMo, and BI) were supplied by Haldor Topsøe A/S. The composition of bog iron is shown in supplementary information Table C.3. In order to obtain a good fluidization of the bed, the particles were crushed to different particle sizes due to the difference in particle density (see supplementary information Table C.4). BI-R and OS were reduced by heating them in situ in 95 % H_2 and 5 % N_2 to 400-440 °C with a heating rate of 10 °C/min for 1 h prior to the experiment. The HDO reactor was loaded with approximately 180 g $NiMo/Al_2O_3$ catalyst supplied by Haldor Topsøe A/S. The catalysts were sulfided by heating from ~180°C to 350°C in 1.8-5 mole % H_2S with a ramp of 10 °C/min and hold time of 2 hours at 350 °C. It was assumed that the sulfidation does not affect H-ZSM-5 and therefore this catalyst was not sulfided prior to the experiment, but heated from 300 to 450 °C in 471 ppm H_2S.

4.2.3 Experimental setup

The catalytic hydropyrolysis experiments were conducted in a bench scale setup as shown in Figure 4.1. The unit was previously used to conduct a parametric study with a $CoMo/MgAl_2O_4$ catalyst in the fluid bed and a $NiMo/Al_2O_3$ in the HDO reactor [37]. The feeding system consisted of a gas mixing system where the gas flows were controlled by Brooks mass flow controllers. A liquid feeding system was used to supply the setup with dimethyl disulfide (DMDS) with a pump and an evaporator (operating at 200 °C) for the sulfidation of the catalysts in experiment 1, 2, 3 and 4. DMDS was used instead of H_2S during the sulfidation because of the high price of bottled H_2S. However, using DMDS lead to coking of the gas preheater, and thus bottled H_2S was used during the sulfidation in the remaining experiments. The biomass was loaded into a pressurized vessel (volume: 4 L) with a feed screw placed at the bottom, which was used to transport the biomass to the feeding tube, where it was rapidly transported by a flow of hydrogen to the reactor. Before entering the fluid bed reactor, the biomass was preheated by heating the feeding tube to approximately 200 °C. The reactor system consisted of a fluid bed hydropyrolysis reactor, a filter and a fixed bed hydrodeoxygenation (HDO) reactor. In order to avoid condensation between the reactors and filter the tubes were heated to approximately 350 °C. The liquid product was collected in a cooling section with three stages (20 °C, 2 °C, and -40 °C). The pressure was controlled with a backpressure regulator and the gas was sent to a flare. A small fraction of the gas was sent to an online gas chromatograph (GC) with a flame ionization detector (FID) and two thermal conductivity detectors (TCD), which measured the gas composition (H_2, H_2S, N_2, CO, CO_2, C_1 to C_5, and C_{6+} hydrocarbons) every 10 min. The total mass of the condensed liquid was determined and the organic phase and the aqueous phase were separated with a separation funnel. The mass of the aqueous phase was measured and the mass of the organic phase was determined by subtracting the mass of the aqueous phase from the total mass of condensed liquid. The H_2S dissolved in the liquid phases was for safety reasons removed by bubbling with N_2 for approximately 0.5-1 h for the organic phase and 1-2 hours for the aqueous phase. This lead to a mass loss between 2.5 and 6.5 wt.% for the organic phase and between 0.4 and 3.8 wt.% in the aqueous phase. The mass loss in the organic phase was mainly due to vaporization of light hydrocarbons while the mass loss in the aqueous phase was mainly due to vaporization of water.

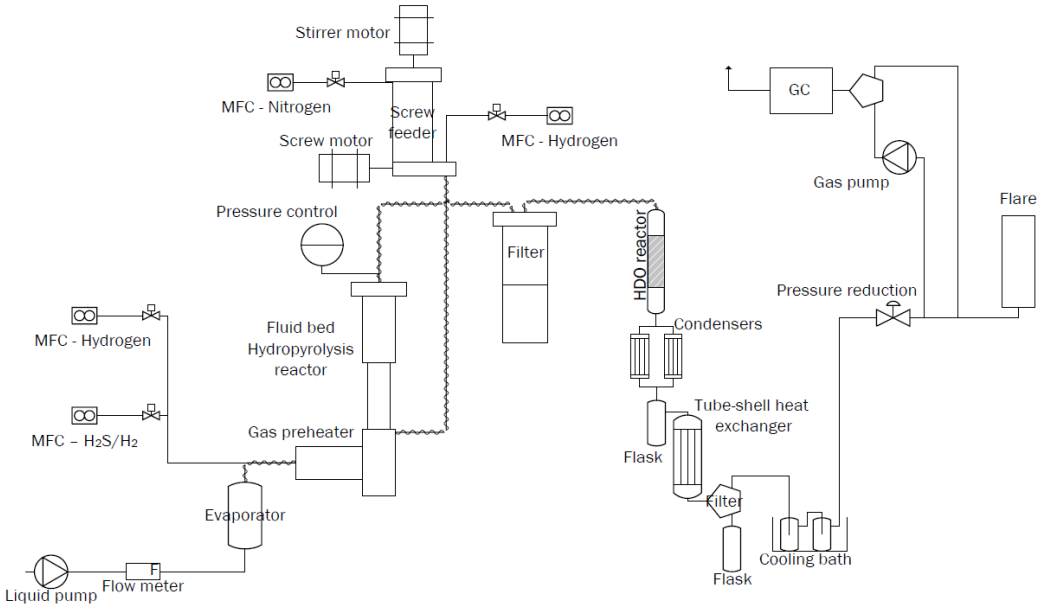

Figure 4.1. Simplified piping and instrumentation diagram of the fluid bed hydropyrolysis setup

After each experiment the catalyst and remaining char was removed from the fluid bed and filter, and replaced with a fresh batch in the subsequent experiment. The total char and coke yield was calculated by subtracting the amount of loaded catalyst from the total mass of solids collected from the filter and fluid bed.

The catalyst in the HDO reactor was changed after experiment 1, 3, 4 and 5. The same batch of catalyst was used in the HDO reactor in experiment 4, 7, 9, 10 and 11 and several unpublished experiments have also been conducted with this batch of catalyst in the HDO reactor. After experiment 11 approximately 9750 g of biomass had been used in experiments with the same catalyst batch in the HDO reactor.

4.2.4 Analysis methods

4.2.4.1 Liquid products

4.2.4.1.1 Organic phase

Several different methods were used to analyze the condensed organic phase and a more detailed description can be found elsewhere [37]. The hydrogen content was measured with ASTM method D7171. The sulfur content was measured according to ASTM D4294. The simulated distillation (SIMDIS) curves were measured with ASTM method D 7213 C. The density at 40 ˚C was measured with ASTM method D 4052, the viscosity at 40 ˚C was measured with ASTM method D 7042 and the water content was measured with Karl Fisher titration.

The condensed organic liquid samples were characterized by GC×GC-ToF/MS or -FID using a LECO® Pegasus 4D^{TM} instrument. The instrument included an Agilent 7890A GC equipped with a Gerstel® CIS 4 PTV inlet, a secondary oven, a quad-jet, dual-stage cryogenic-based (liquid N_2) modulator, a time-of-flight (ToF) mass spectrometer (MS) and a flame ionization detector (FID). The primary (1D) and secondary (2D)

columns were Restek® Rxi-5Sil MS and Restek® Rxi-17Sil MS, respectively. Based on the GC×GC-ToF/MS analysis the compounds were classified into eleven groups: paraffins, naphthenes, mono-, di- and tri- and higher aromatics, oxygenated aliphatics, phenolics, dihydroxybenzenes, larger oxygenated aromatics, and sterols. Based on the retention times of the n-paraffins on the 1D column the component classes were split into subgroups on the basis of the number of carbon atoms in the components, i.e. –C10, C11-C15, C16-C20, C20+. However it should be noted that other components classes do not necessarily have the same carbon number distribution as the paraffins, and caution is needed when correlating the relative amount of each subgroup with its carbon number distribution. The relative amount (FID area-%) of each compound class was estimated as the sum of areas of all detected peaks in that class divided by the total peak area of all compound classes. All data were processed using the ChromaTof® 4.50 software.

Selective analysis of oxygenates was conducted using a GC with an atomic emission detector (AED). An Agilent 7890A GC was coupled to a JAS 2370 AED in oxygen selective mode. Quantification was done by adding known amounts of 4-fluorophenol to known amounts of the sample.

For condensed organics phases with a high oxygen content (>2 wt.%) the carbon or oxygen content was measured by DB Lab A/S using a Flash 2000 elemental analyzer. The uncertainty for this measurement was 3.0 % and 1.0 % for the oxygen and carbon analysis, respectively, defined as two standard deviations for the measurement uncertainty, corresponding to a confidence interval of 95 %. The carbon and oxygen content in each sample was measured twice and the reported oxygen content is the average of the two measurements.

4.2.4.1.2 Aqueous phase

The carbon content in the aqueous phase was determined with GC-AED. The samples were analyzed using an Agilent 7890A GC coupled to a JAS 2370 Atomic Emission Detector (AED) in carbon selective mode. The carbon emission line at 193 nm was used combined with a makeup helium gas flow of 80 ml/min. The cavity was set at 320°C and transfer line temperature was set at 380°C. The GC column used was a Phenomenex ZB-5 Inferno (30m X 0.25mm X 0.25µm) in connection with a JAS PTV inlet in split mode (1:100) held at 325°C and 0.5µl injection. The oven was held at 40°C for 1 min and then ramped to 380°C @ 10°C/min. The quantification was done by external calibration using benzyl alcohol dissolved in water as standard. Calibration concentrations ranged from 10 ppm to 1100 ppm carbon. The external standard was used for calibration of unknown carbon containing compounds in the sample as the AED has equimolar and linear response for carbon. No identification of individual compounds was done and the total added amount of detected carbon was taken as a figure of the total carbon content in the water sample. The samples were analyzed as received and no sample pretreatment was done prior to analysis.

The aqueous phase was also analyzed on a Shimadzu GC-MS/FID with a Supelco Equity-5 column. The compounds were identified on the MS and quantified using the parallel FID. Based on the GC-MS/FID analysis the components were classified into 8 groups: unidentified, ethers, ketones, alcohols, sugars, phenols, acids and furans. The relative amount (FID area-%) of each component class was estimated as the sum of all the detected peaks in that class divided by the total peak area.

4.2.4.2 Catalyst characterization

The composition (Al, Ca, Cr, Fe, Mg, Mn, Ni, Si, As, P) of the fresh OS and BI was determined with inductive coupled plasma optical emission spectroscopy (ICP-OES) and the surface area was measured with N_2-physisorption (BET). Fresh BI and spent BI-S and BI-R were also analyzed by XRD using a Panalytical XPert Pro instrument system in Bragg-Brentano geometry working in reflectance mode using Cu K_α radiation (λ = 1.541 Å). Rietveld analysis was performed using the Topas Software and reference structures for

$FeCO_3$ (ICSD 100678), α-FeO(OH) (ICSD 77327), SiO_2 (ICSD 16331), FeS (ICSD 156618), $Fe_{0.88}S$ (ICSD 151767), FeS_2 (ICSD 316), Fe (ICSD (180969), $CaCO_3$ (ICSD 18166), Fe_3O_4 (ICSD 26410), Fe_2O_3 (ICSD 15840), and $MgCO_3$ (ICSD 10264). The symmetry and atomic position were fixed and the lattice parameters and average crystal size were refined.

The scanning electron microscopy (SEM) was performed on a FEI QUANTA600 scanning electron microscope with tungsten filament and equipped with a liquid nitrogen cooled EDAX EDS detector. All samples were sprinkled on carbon tabs on Al-stubs and conducted without any coating to prevent charging in the sample chamber. EDS element quantifications were acquired on 0.11 mm x 0.11 mm areas on the surface of the catalyst grains at 3 kV, 5 kV, 10 kV and 15 kV to probe different interaction volumes between the incident electron beam and the sample. The composition of the sample was determined in EDAX software (version 5.2.42) using a normalized, standardless, ZAF-corrected and SEC-factor corrected quantification of the acquired EDS spectra. The uncertainty of the quantification was estimated by measuring the carbon concentration at different acceleration voltages from the same areas of 3 spent catalyst particles from each experiment 10 and 11 (see Table 4.1 and supplementary information Figure C.1 and Table C.5). This showed that the standard deviation for the carbon measurement was 1.5 wt.% at 3 kV, 0.8 wt.% at 5 kV, 1.0 wt.% at 10 kV, and 1.5 wt.% at 15 kV. The measured carbon content on the fresh and spent catalysts are shown in Table C.6.

The transmission electron microscopy was performed on a FEI Talos™ F200X transmission electron microscope equipped with high-brightness field emission gun (X-FEG) and Super-X G2 EDS detector. The sample was crushed in a mortar and dispersed dry on a Cu-TEM grid covered with a continuous carbon film (SPI supplies). Images and elemental EDS maps were acquired in scanning transmission mode (STEM) with a camera length of 125 cm. Elemental EDS maps of 2.1 μm x 2.1 μm (512 pixels x 512 pixels) were acquired for 5 min in Brüker software (Esprit 1.9) using a probe current of 0.7 nA. The elemental EDS maps were processed in Esprit with a smoothing filter (3x3) and selected elements (Fe, O, S, Al, Si) were displayed as total counts of the K_α-lines, respectively. The full spectra are shown in Supplementary Information Figures C.2 and C.3. The relative composition at selected areas were determined in the Brüker software using peak fit by series deconvolution and Cliff-Lorimer quantification.

4.3 Results and Discussion

4.3.1 Effect of catalyst in fluid bed on the product distribution

The process conditions and the mass balances for all the conducted experiments are shown in Table 4.1. The data from experiments 1 and 2 have previously been published [37], and are used as benchmarks in this work. In experiments 7 and 8 the catalyst in the fluid bed was not sulfided. In experiment 7 the catalyst in the HDO reactor was maintained in the sulfided state by adding the H_2S to the gas after the fluid bed reactor. The OS and ZA bed materials were not sulfided prior to the experiments. When MgAl and OS were used as catalysts the temperature in the fluid bed reactor decreased when the biomass feeding started, see supplementary information Figure C.4, indicating that the exothermic hydrodeoxygenation reactions only occurred to a limited degree and that the hydropyrolysis overall was endothermic. The opposite was observed with the rest of the catalysts where the hydropyrolysis overall was exothermic.

Table 4.1 Summary of reaction conditions and mass balances for catalytic hydropyrolysis of beech wood using different catalysts. The data from experiment 1 and 2 has previously been published [37], but are listed here as benchmark experiments.

Test:	1	2	3	4	5	6	7	8	9	10	11
Test conditions											
Catalyst in FB	CoMo	CoMo	MgAl	OS	BI-S	BI-S	BI-R	BI-R	ZA	NiMoZA	NiMoZA
Catalyst mass (g)	50.0	49.6	50.1	140.1	94.2	94.0	94.8	94.2	50.1	49.9	50.0
Sulfided	Yes	Yes	Yes	Yes	Yes	Yes	No	No	Yes	Yes	Yes
Hydropyrolysis Temp. (°C)	451	450	451	450	454	453	450	453	443	453	453
HDO Temp. (°C)	371	-	394	391	389	-	394	-	370	370	370
Pressure (bar)	26	26	26	26	26	26	26	26	26	26	26
Feed time (h)	4.0	3.9	4.0	0.75	3.2	3.8	3.2	3.7	1.4	3.0	3.0
Biomass feeding rate (g/h)	250	174	258	194	302	271	312	272	293	277	277
H_2S conc.(ppm)	460	48	460	460	470	470	470	-	471	462	462
H_2 flow (NL/min)	82	87.4	82	68.7	89.2	89.2	89.2	87	54.4	60	60
N_2 flow (NL/min)	5	0.62	5	5	5	5	5	5	5	5	5
Yields (wt.% daf)											
Gas	31.5	27.4	27.9	27.7	25.2	19.3	24.6	17.3	28.6	29.7	30.2
Char and coke	11.4	12.2	18.7	Na	13.5	13.1	10.5	12.7	21.1	13.1	13.0
Aqueous phase	35.2	37.0	31.8	27.8	36.3	35.4	44.6	30.8	21.2	32.8	34.0
Organics	12.4	12.0	11.5	7.7	14.8	24.0	14.8	31.3	14.4	15.6	15.0
C_{4+} in the gas	9.1	8.4	6.4	8.2	7.9	3.0	9.9	3.01	5.9	8.2	9.1
Organics + C_{4+}	21.5	20.4	17.8	15.8	22.8	27.0	24.7	34.4	20.4	23.9	24.0
Mass balance	99.6	96.9	96.4	72.3	97.8	94.8	101.2	95.1	91.3	99.5	101.2
Organic phase composition											
Water (wt.%)	ND	0.35	ND	ND	ND	17	ND	5.5	ND	ND	ND
C (wt.% db)	88.0*	87.7*	87.1*	ND	88.0*	69.4	88.6*	77.1*	88.1*	88.8*	88.8*
H (wt.% db)	11.9	10.2	12.1	ND	11.65	8.06	11.32	8.83	11.9	11.2	11.2
O (wt.% db)	0.0030	1.8	0.0085	0.0018	0.0205	22.1*	0.0050	14.1	0.037	0.11	0.14
S (wt.% db)	0.117	0.303	0.763	ND	0.397	0.45	0.060	0.017	Na	0.018	0.013
Organic phase physical properties											
Density at 40°C (g/ml)	0.8273	0.8890	0.8253	ND	0.8378	1.0123	0.8583	0.9822	Na	0.8544	0.8574
Viscosity at 40°C (cSt)	1.041	1.607	1.062	ND	1.088	Na	1.27	4.668	1.08	1.104	1.153
Energy recovery in organic phase and C_{4+} (%)	51	47	42	34	54	44	58	61	45	53	54
Aqueous phase composition (wt.%)											
Organics	0.017	1.3	0.005	0.005	0.006	9.7	0.012	8.5	0.31	0.055	0.07
Gas composition (wt.% daf)											
CO	9.7	11.1	9.4	8.8	7.5	5.1	6.4	4.3	9.3	7.5	7.8
CO_2	8.0	5.7	9.5	9.9	6.5	9.9	6.7	9.9	10.8	9.0	9.1
C_1-C_3	12.9	12.1	9.0	8.9	11.2	4.3	11.6	3.2	8.6	13.2	13.2
C_{4+}	8.8	8.4	6.4	8.2	7.9	3.0	9.9	3.1	5.9	8.2	9.1

*By difference

The total mass balance varied between 71.3 and 101 wt.% daf (see Table 4.1), where particularly experiment 4 using OS as bed material resulted in low recovery. In experiment 4, when the OS was tested, the tube between the fluid bed and filter was blocked after 45 minutes of operation. This was most likely due to bio-oil condensation in the pipe, which lead to char build up which consequently lead to blocking of the pipe. Thus, it was not possible to estimate the char yield for this experiment resulting in the very low mass recovery. The technical difficulties using OS as bed material, combined with the observation that using OS leads to an overall endothermic reaction in the fluid bed, indicates that OS is not a suitable catalyst for catalytic hydropyrolysis. Consequently, the experiment was not repeated. Using ZA lead to defluidization of the bed after 85 min, which is the reason for the poor mass balance of 91.3 wt.% daf for experiment 9. The mass balances in the remaining experiments varied between 94.8 and 101 wt.% daf.

The C_1-C_3 gas yields were between 3.2 and 14.3 wt.% daf, the CO and CO_2 yields were between 13.1 and 20.0 wt.% daf, the condensed organics and C_{4+} yields were between 15.8 and 34.1 wt.% daf, and the char and coke yields were between 10.5 and 21.1 wt.% daf. The carbon balance is shown in supplementary infor-

mation Table C.7 and a detailed gas composition is shown in supplementary information Table C.8. In order to evaluate the repeatability, experiments 10 and 11 were performed at similar conditions. The largest difference in the yields was for the aqueous phase, where the difference was 1.2 wt.% daf, however, the difference in the C_1-C_3 yield was <0.1 wt.% daf, CO and CO_2 yield was 0.4 wt.% daf, char and coke yield was 0.1 wt.% daf, and the condensed organics and C_{4+} in the gas yield was 0.1 wt.% daf. Furthermore, only a small deviation in the char and coke yield (0.4 wt.% daf) was observed between experiment 5 and 6 where the same catalyst was used in the HDO reactor. It is therefore assumed that the experimental error is less than 0.5 wt.% daf for the char and coke yield, 0.2 wt.% daf for the C_1-C_3 yield, 0.5 wt.% daf for the total CO and CO_2 yield, 1.5 wt.% for the aqueous phase yield, and less than 0.5 wt.% daf for the condensed organics and C_{4+} in the gas yield. However, the uncertainly also depends on the mass balance, thus the uncertainty is most likely higher for the experiment with OS (experiment 4) and ZA (experiment 9). A larger difference in the char and coke yield (2.1 wt.% daf) was also observed between experiment 7 and 8. This was because the spent catalyst in experiment 7 was not oxygen passivated prior to unloading the fluid bed reactor, thus it self-ignited when exposed to air during the unloading, which combusted some of the char, decreasing the char yield.

The energy recovery was calculated on the basis of the higher heating value (HHV) of the biomass fed to the setup and the HHV of the different phases. The heating value of the gas was calculated on the basis of the heating value of the different compounds detected in the gas, and the heating value of the condensed organics was calculated on the basis of its elemental (CHNSO) composition according to ref. [38]. The energy recovery in the condensed organics and C_{4+} was between 34 and 61 %. Using OS in the fluid bed (experiment 4) gave the lowest energy recovery (34 %), while the highest values were obtained when BI-R was used in the fluid bed: 58 % when the HDO reactor was used (experiment 7) and 61 % when the HDO reactor was not used (experiment 8). Using the pure support materials MgAl (experiment 3) and ZA (experiment 9) gave a lower energy recovery, between 42 and 45 %, compared to when the supported catalysts CoMo (experiment 1) and NiMoZA (experiment 10 and 11) were used, between 51 and 54 %.

The char and coke, gas, aqueous phase, and condensable organics yields for the experiments, where both the fluid bed and the HDO reactor are used, are shown in Figure 4.2. Using the pure support materials MgAl and ZA lead to a high char and coke yield of 18.9 and 21.2 wt.% daf, respectively. Using the supported catalysts significantly decreased the char and coke yield to 11.4 wt.% daf for the CoMo and between 13.1 and 13.0 wt.% daf for the NiMoZA, indicating that the active catalysts stabilized the pyrolysis vapors before secondary coke forming reactions took place. Using BI-S and BI-R gave a char yield of 13.5 and 12.7 wt.% daf, respectively. Remarkably the C_1-C_3 gas yield was almost the same when using OS (8.9 wt.% daf), MgAl (9.0 wt.% daf), and ZA (8.6 wt.% daf). The CO and CO_2 yield for these three catalysts were also almost the same: 18.7 wt.% daf when using OS, 18.9 wt.% daf when using MgAl, and 20.0 wt.% daf when using ZA. However, the aqueous phase and condensable organics yields seemingly varied for these materials. This could be due to the large differences in how well the mass balance closed. Using the supported active catalysts (experiment 1, 10 and 11) increased the C_1-C_3 yield, but decreased the total CO and CO_2 yield due to less cracking and more hydrogenation activity.

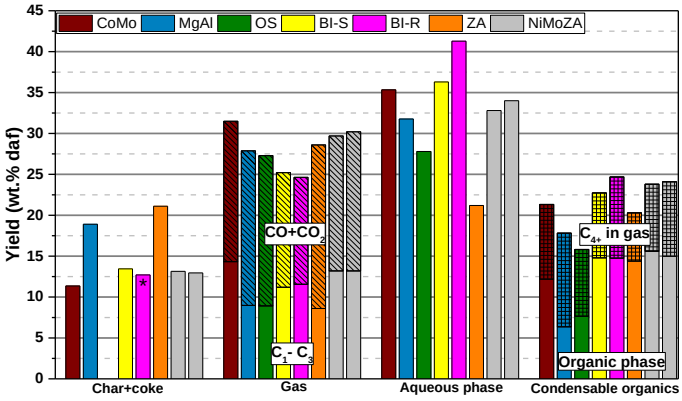

Figure 4.2 Effect of the catalyst on the product distribution when the HDO reactor is used. *The char yield from the experiment with BI-R is shown from the experiment (#8) without the HDO reactor. (Fluid bed temperature: 443-454 °C, HDO temperature: 370-394 °C, pressure: 26 bar, biomass feeding rate: 174-302 g/h, H_2S concentration: 0-471 ppm, H_2 flow: 54.4-89.2NL/min, N_2 flow: 0.62-5 NL/min)

Using BI-S and BI-R lead to a low C_1-C_3 yield; 11.2 wt.% daf when using BI-S and 11.6 wt.% daf when using BI-R. Furthermore, both catalysts also have a low total CO and CO_2 yield; 14.0 wt.% daf when using the BI-S and 13.1 wt.% daf when using BI-R. BI-R also has the highest aqueous phase yield (41.3 wt.%), while it was lower when using the BI-S (36.3 wt. %). Comparing the char and coke yield for BI-R in experiment 8 (12.7 wt.%) with the char yield for BI-S in experiment 5 (13.5 wt.%) and 6 (13.1 wt.%) indicates that the catalysts produces the same amount of char and coke. Comparing the aqueous phase yields with the total CO and CO_2 yields in the experiments where the HDO reactor is used (experiment 1, 2, 3, 4, 5, 7, 9, 10, 11) indicates that using an active catalyst in the fluid bed reactor gives a low total CO and CO_2 yield and a high aqueous phase yield. Considering that the condensable organics is essentially oxygen free when the HDO reactor is used this correlation is expected. For both MgAl and ZA an increase in the condensable organics yield was observed using the supported catalysts (experiment 1, 10 and 11) compared with the pure support materials (experiment 3 and 9). Using MgAl gave a condensed organics and C_{4+} yield of 17.8 wt.% daf, which increased to 21.5 wt.% daf when the CoMo was used, and using ZA gave a condensed organics and C_{4+} yield of 20.3 wt.% daf, which increased to 23.9-24.0 wt.% daf when using NiMoZA. Interestingly, the condensed organics and C_{4+} yield was 24.7 wt.% daf for BI-R (experiment 7) and 22.8 wt.% daf for BI-S (experiment 5) when the HDO reactor was used, showing that it is favorable to run the BI as a reduced catalyst instead of as a sulfided catalyst.

The effect of bypassing the HDO reactor is shown in Figure 4.3, where the product distribution is shown for experiments with and without the HDO reactor when CoMo, BI-S and BI-R is used in the fluid bed reactor. For all the catalysts a decrease in the total C_1-C_3 and total CO and CO_2 yields were observed when the HDO reactor was bypassed, showing that cracking reactions take place in the HDO reactor. This trend was pronounced when BI-R and BI-S were tested without the HDO reactor. For BI-R and BI-S the C_1-C_3 yields were only 3.2 wt.% daf and 4.3 wt.% daf, respectively, and the total CO and CO_2 yield was 14.1 wt.% daf for BI-R and 15.0 wt.% daf for BI-S. This shows that BI-S and -R have a low cracking activity, which may be the reason for the high condensable organic yield observed when using these catalysts. The amount of C_{4+} also decreased and the amount of condensed organics increased when the HDO reactor was bypassed in the experiments with BI-S (experiment 6) and BI-R (experiment 8), in part due to a significant oxygen content.

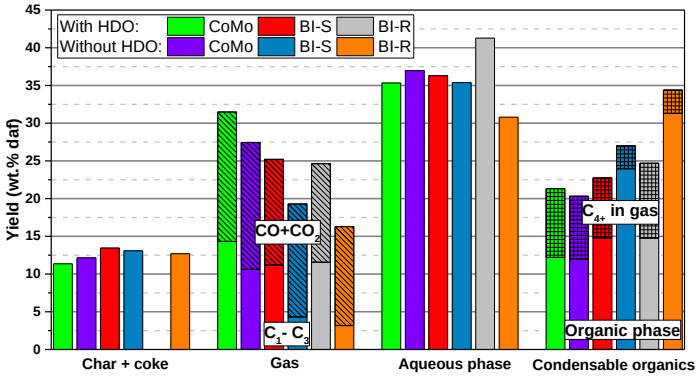

Figure 4.3. Product distribution with and without HDO reactor. (Fluid bed temperature: 450-454 °C, HDO temperature: 371-394 °C, pressure: 26 bar, biomass feeding rate: 174-302 g/h, H_2S concentration: 0-470 ppm, H_2 flow: 87.4-89.2NL/min, N_2 flow: 0.62-5 NL/min).

The CO and CO_2 yield and the CO/CO_2 ratio on molar basis is shown in Figure 4.4. The molar ratio between CO and CO_2 is almost the same (between 1.5 and 1.8) when the HDO reactor is used. Bypassing the HDO reactor shows a significant difference between the CoMo and BI-S/R. The molar ratio between CO and CO_2 was 3.1 for the CoMo, but 0.8 and 0.7 for BI-S and BI-R, respectively. This indicates that when the CoMo is used in the fluid bed reactor water gas shift (see reaction 4.1) takes place in the HDO reactor, but when BI-S/R is used in the fluid bed reactor, reverse water gas shift takes place in the HDO reactor instead. Since the CO and CO_2 molar ratio is almost the same when the HDO reactor is used, this indicates that the water gas shift equilibrium is approached in the HDO reactor. A low CO/CO_2 ratio is preferable because this increases the relative oxygen removal compared to the amount of carbon lost to the gas phase, thus BI-S/R has a desirable CO/CO_2 selectivity compared to the CoMo catalyst.

$$CO+H_2O \rightleftharpoons CO_2+H_2 \tag{4.1}$$

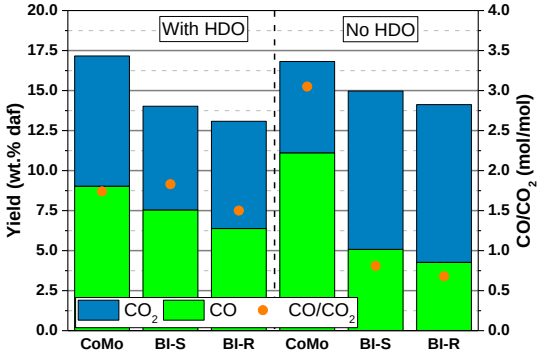

Figure 4.4. Effect of bypassing the HDO reactor on the CO and CO_2 yield and the CO and CO_2 ratio. (Fluid bed temperature: 450-454 °C, HDO temperature: 371-394 °C, pressure: 26 bar, biomass feeding rate: 174-302 g/h, H_2S concentration: 0-470 ppm, H_2 flow: 87.4-89.2NL/min, N_2 flow: 0.62-5 NL/min).

4.3.2 Chemical composition of the condensed liquids

4.3.2.1 Organic phase

In the experiments were the HDO reactor was used the hydrogen content in the condensed organics was between 11.16 and 12.14 wt.% db. Bypassing the HDO reactor decreased the hydrogen content from 11.93 to 10.22 wt.% db when the CoMo was used in the fluid bed reactor. The hydrogen content when the HDO reactor was used was 11.65 wt.% db for BI-S and 11.32 wt.% db for BI-R, which decreased to 8.06 wt. % db for BI-S and 8.83 wt.% db for BI-R when the HDO reactor was bypassed. The reason for the lower hydrogen content when the HDO reactor was bypassed is the much lower extent of HDO as evidenced by the higher oxygen content. For CoMo the oxygen content was 1.8 wt.% db when the HDO reactor was bypassed, while it was 22.1 and 14.1 wt.% db for BI-S and BI-R, respectively.

The density at 40°C of the condensed organic phase was between 0.8253 and 0.8583 g/ml when the HDO reactor was used, see Table 4.1. Bypassing the HDO reactor increased the density when using the CoMo catalyst from 0.8273 g/ml to 0.8890 g/ml, from 0.8378 g/ml to 1.0123 g/ml when using BI-S and from 0.8583 to 0.9822 g/ml when using BI-R. Thus using the HDO reactor decreases the density of the organic phase. The high density of the organic phase when using BI-S and bypassing the HDO reactor (experiment 6) is partly because of the high water content in the organic phase of 17 wt. %. Trinh et al [6] measured the density at 40 °C of conventional pyrolysis oil from wood to be 1.12 g/mL, which is significantly higher than the density of the organic phase in the experiments without the HDO reactor.

The kinematic viscosity of the produced organic phase was between 1.041 and 1.153 cSt when the HDO reactor was used. Bypassing the HDO reactor increased the kinematic viscosity to 1.607 cSt when the CoMo catalyst was used and 4.668 cSt when BI-R was used. Thus the kinematic viscosity increased with increasing oxygen content of the oil, as expected.

The simulated distillation curve for the condensed organics from the experiments where the HDO reactor was used is shown in Figure 4.5. Between 20 to 40 vol. % of the condensed organics was naphtha, while the remaining was in the diesel boiling point range. The highest fraction of naphtha was obtained with the CoMo (40 %), while the lowest was obtained with the BI-R (20 %). However, it should be noted that the C_{4+} detected in the gas should be considered as naphtha, increasing its fraction to 60-70 wt.%. The NiMoZA catalyst produced the organics with the highest boiling point, while the MgAl produced organics with the lowest boiling point. The reason for the high boiling point when using NiMoZA could be that more alkylation took place when zeolite was mixed into the carrier, which is probably due to the acidity of the zeolite. Lai et al. [39] also observed that alkylation reactions occurred when upgrading the hydropyrolysis vapors at high temperature in a separate fluid bed reactor with a HDO catalyst.

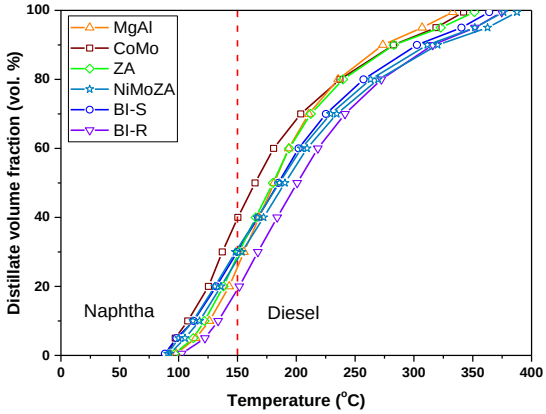

Figure 4.5 Simulated distillation of the condensed organics from experiments 1, 3, 4, 5, 7, 9, 10 and 11. (Fluid bed temperature: 443-454 °C, HDO temperature: 370-394 °C, pressure: 26 bar, biomass feeding rate: 174-302 g/h, H_2S concentration: 0-471 ppm, H_2 flow: 54.4-89.2NL/min, N_2 flow: 0.62-5 NL/min)

The composition of the condensed organics was further investigated by GC×GC-MS/FID. On this basis the condensed organics can be divided into the following groups: paraffins (Par), naphthenes (Naph), monoaromatics (mAro), diaromatics (diAro), triaromatics (triAro), larger aromatics (tetAro+), oxygenated aliphatics (o-Ali), and phenols (PhOH). Furthermore the components are also divided into the following groups based on the number of carbon atoms in the components: less than 10 carbons atoms (-C10), between 11 and 15 carbons atoms (C11-C15), between 16 and 20 carbon atoms (C16-C20), and more than 20 carbon atoms (C20+). The composition of the organics for the experiments where the HDO reactor was used is shown in Figure 4.6. In some of the condensed organics phenol was observed. For MgAl (Figure 4.6 (B)) and BI-S (Figure 4.6 (D)) this is most likely due to small impurities from previous experiments, while it could also be due to deactivation of the HDO reactor for ZA (Figure 4.6 (F)) and NiMoZA (Figure 4.6 (G) and (H)). The condensed organics from the experiment with the CoMo catalyst in the fluid bed (Figure 4.6 (A)) had the highest concentration of monoaromatics. The organics from the experiments with NiMoZA (Figure 4.6 (G) and (H)) had almost the same total concentration of aromatics as for the CoMo, however, a larger fraction of them were diaromatics, triaromatics or larger aromatics, which also indicates that alkylation and condensation reactions took place over NiMoZA. The concentration of tri- and larger aromatics were low for MgAl (Figure 4.6 (B) – 0.9 %) and ZA (Figure 4.6 (F) – 1.9 %) compared to the supported active catalyst (CoMo: 3.2 %, NiMoZA: 4.9-6.4 %). Furthermore the concentration of naphthenes was higher for MgAl (Figure 4.6 (B) - 49 %) compared to CoMo (Figure 4.6 (A) – 29 %) and for ZA (Figure 4.6 (F) – 41 %) compared to NiMoZA (Figure 4.6 (G) and (H) - 34-30 %). The reason for this observation could be that the molecules that would have turned into aromatics in the experiments with CoMo and NiMoZA instead polymerized and turned into coke and char when MgAl and ZA were used. Using OS gave a high concentration of di-, tri- and larger aromatics compared to MgAl and ZA. For MgAl and ZA the concentration of components with less than 10 carbon atoms were 50 and 52 %, respectively, however interestingly for OS it was only 34 % that contained less than 10 carbon atoms.

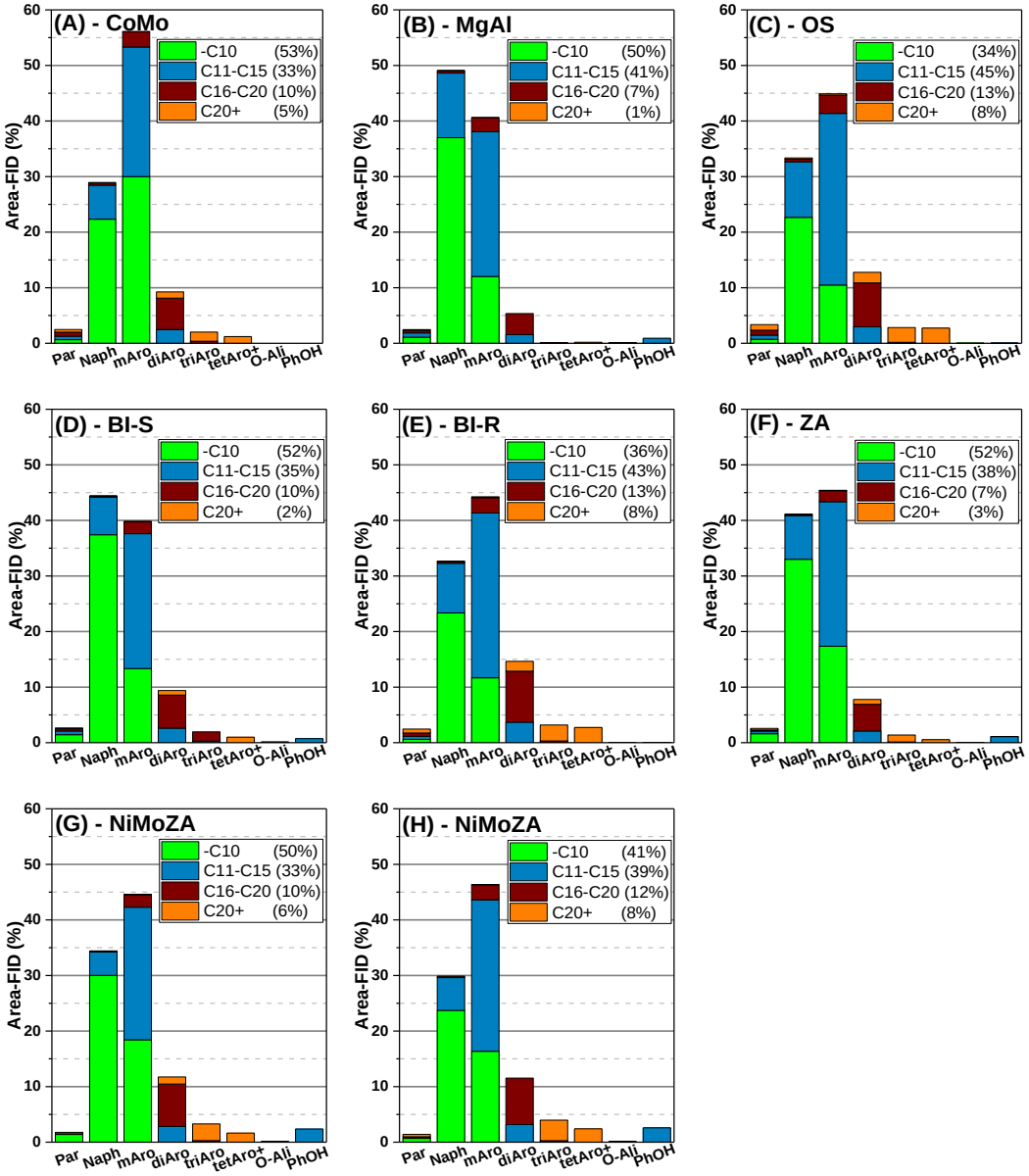

Figure 4.6 The composition of the condensed organic phase from experiment 1 (A), experiment 3 (B), experiment 4 (C), experiment 5 (D), experiment 7 (E), experiment 9 (F), experiment 10 (G) and experiment 11 (H). The components in the condensed organics are divided into paraffins (Par), naphthenes (Naph), monoaromatics (mAro), diaromatics (diAro), triaromatics (triAro), tetraaromatics and larger aromatics (tetAro+), oxygenated aliphatics (O-Ali) and phenols (PhOH). The components are also divided into the following groups based on the number of carbon atoms in the components: less than 10 carbons atoms (-C10) between 10 and 15 carbons atoms (C11-C15), between 15 and 20 carbon atoms (C16-C20), more than 20 carbon atoms (C20+). (Fluid bed temperature: 443-454 °C, HDO temperature: 370-394 °C, pressure: 26 bar, biomass feeding rate: 174-302 g/h, H_2S concentration: 0-471 ppm, H_2 flow: 54.4-89.2NL/min, N_2 flow: 0.62-5 NL/min)

There was a significant difference between the composition of the condensed organics for BI-S (Figure 4.6 (D)) and BI-R (Figure 4.6 (E)). The condensed organics from BI-S consisted of 44 % naphthenes, while only 33 % of the condensed organics from BI-R was naphthenes. The size of the components also varied, for BI-S 52 % of the components contained less than 10 carbon atoms, compared to 36 % of the components for BI-R. 2.0 % of the components in the condensed organics for the experiment with BI-R had more than 20 carbon atoms, but for BI-R 8.4 % of the components had more than 20 carbon atoms. This indicates that BI-S had a higher cracking activity than BI-R, which is also supported by the observed higher C_1-C_3 and CO and CO_2 yield for BI-S than BI-R. The effect of the catalyst in the fluid bed reactor is compared on the basis of the type of compounds and the molecular size distribution in the condensed organic phase in supplementary information Figure C.5 and Figure C.6, respectively.

The composition of condensed organics from the experiments without the HDO reactor is shown in Figure 4.7. Comparing the CoMo with HDO (Figure 4.6 A) to the CoMo without the HDO reactor (Figure 4.7 (A)) shows that the number of carbon atoms in the size range C11-C15 increased and –C10 decreased when the HDO reactor was bypassed. In the experiment without the HDO reactor most of the oxygenates were phenols (area-FID: 22 %) but small amounts of oxygenated aliphatics (area-FID: 4 %) were also observed, showing that the CoMo was able to remove most of the oxygenated aliphatics. Small amounts of larger oxygenated aromatics (0.11 % FID-area), and traces of indoles (<1 ppm-wt) and Pyrroles (~1 ppm-wt) were also detected. Comparing the concentrations for the experiments where the HDO reactor was bypassed for BI-S (Figure 4.7 (B)) and BI-R (Figure 4.7 (C)) to the experiments with the HDO reactor (Figure 4.6 (D) and (E)), shows that bypassing the HDO reactor decreased the concentration of naphthenes, mono and diaromatics, while increasing the concentration of larger aromatics and oxygenated hydrocarbons. The concentration of oxygenated aliphatics were significantly higher for BI-S (51 % area-FID) and BI-R (39 % area-FID) than the CoMo catalyst (4 % area-FID). Furthermore the condensed organics from the experiment with BI-S and BI-R contained between 8 and 10 % area-FID dihydroxybenzenes, which was not detected in the condensed organics from the experiment with the CoMo. Sterols were also detected in small amounts (<0.2 % area-FID) when the BI-S and BI-R catalysts were used. This shows that the BI-S and BI-R have a significantly lower deoxygenantion and hydrogenation activity compared to CoMo. The effect of the catalyst in the fluid bed reactor without the HDO reactor is compared on the basis on the type of compounds and the molecular size distribution in the condensed organic phase in supplementary information Figure C.7 and Figure C.8, respectively.

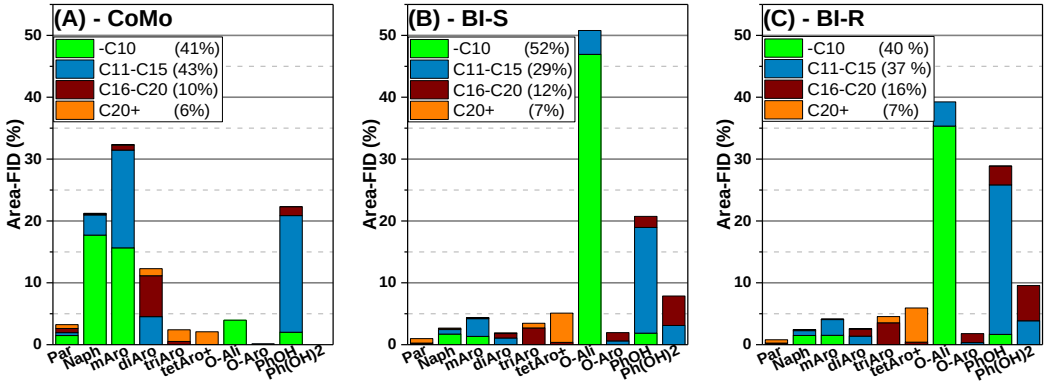

Figure 4.7 The composition of the condensed organic phase from experiment 2 (A), experiment 6 (B) and experiment 8 (C). The components in the condensed organics are divided into paraffins (Par), naphthenes (Naph), monoaromatics (mAro), diaromatics (diAro), triaromatics (triAro), tetraaromatics and larger aromatics (tetAro+), oxygenated aliphatics (O-Ali), phenols (PhOH), dihydroxybenzenes (Ph(OH)2), and oxygenated aromatics (O-Aro). The components are also divided into the following groups based on the number of carbon atoms in the components: less than 10 carbons atoms (-C10) between 10 and 15 carbons atoms (C11-C15), between 15 and 20 carbon atoms (C16-C20), more than 20 carbon atoms (C20+). (Fluid bed temperature: 450-454 °C, HDO temperature: 371-394 °C, pressure: 26 bar, biomass feeding rate: 174-302 g/h, H_2S concentration: 0-470 ppm, H_2 flow: 87.4-89.2NL/min, N_2 flow: 0.62-5 NL/min)

4.3.2.2 Aqueous phase

The carbon yield and the hydrocarbon distribution in the aqueous phases from experiment 2 (CoMo), 6 (BI-S) and 8 (BI-R) are shown in Figure 4.8. The carbon yield in the aqueous phase from the experiment with the CoMo catalyst was 0.96 wt.% daf, while the carbon yield in the aqueous phase when using BI-S and BI-R was 6.8 and 4.8 wt.% daf, respectively. The higher carbon yield in the aqueous phase from the experiments with BI-S and BI-R compared to the experiment with CoMo is because of the higher oxygen concentration in the produced oil makes it more soluble in the aqueous phase. GC-MS/FID showed that the hydrocarbons in the aqueous phase from the experiment with the CoMo catalyst consisted of phenols, ketones and alcohols. For BI-S and BI-R ketones, ethers, phenols, alcohols, and acids were detected. Sugars were only detected when using BI-S and furans were only detected when using BI-R. The relative concentration (Area-FID (%)) of phenols and alcohols were lower in the experiment with BI-S and BI-R compared to the experiment with CoMo. This is not because BI-S and BI-R were better at deoxygenating these molecules, but because the phenols are dissolved in the (more oxygen rich) organic phase. The organic phase also contained larger amounts of water when using the BI-S/R catalysts compared to the CoMo catalyst resulting in a larger partition coefficient for phenols in the organic phase. The detection of acids in the aqueous phase when using BI-R/S as catalysts indicates that conducting the catalytic hydropyrolysis without a second hydrotreating reactor could lead to storage problems for the liquid product.

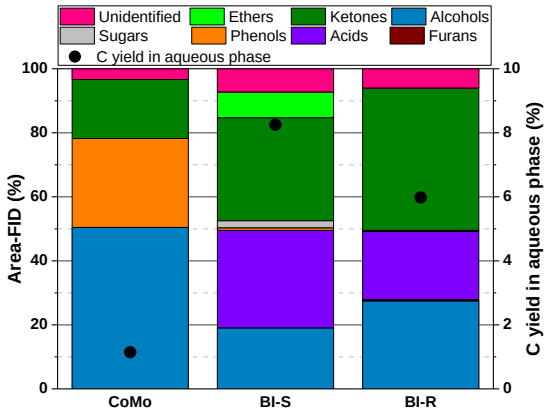

Figure 4.8 The total amount of carbon and composition of the hydrocarbons in the aqueous phase when the HDO reactor is bypassed (experiment 2, 6 and 8). (Fluid bed temperature: 450-454 °C, HDO temperature: 371-394 °C, pressure: 26 bar, biomass feeding rate: 174-302 g/h, H_2S concentration: 0-470 ppm, H_2 flow: 87.4-89.2NL/min, N_2 flow: 0.62-5 NL/min)

4.3.3 Characterization of the spent catalysts

4.3.3.1 SEM

The spent catalysts from the fluid bed reactor were studied with SEM combined with EDS. Figure 4.9 shows the measured carbon content as a function of the electron acceleration voltage for the spent catalysts. The signal measured at 3 kV corresponds to the surface of the sample (low penetration), while at 15 kV the signal integrates the signal from surface towards the bulk of the sample. Comparing the carbon contents on the spent MgAl and CoMo (Figure 4.9 (A)), shows that there was significantly less carbon on the spent CoMo (5.5-7.9 wt.% at 15 keV) than MgAl (49 wt.% at 15 keV) and that the carbon concentration was relatively higher at the surface for MgAl (67 wt.% at 3 keV) than for CoMo (7.2-7.9 at 3 keV), suggesting a more even distribution of carbon on the CoMo. A similar trend was also observed when comparing ZA from experiment 9 with NiMoZA from experiment 10 and 11 (Figure 4.9 (B)), however, the trend was less pronounced in this case, as only half the amount of biomass was used in the experiment with ZA compared to the experiments with NiMoZA. An experiment with ZA was also conducted where 625 g of biomass (experiment #12, which is not reported in Table 4.1) was used compared to 413 g in experiment 9, however, the experiment was conducted at similar conditions to experiment 9, but the catalyst was not sulfided. Comparing these two spent ZA catalysts, and assuming that the sulfur did not had an impact on the catalyst, shows a significant increase in the amount of carbon on the spent catalyst when 625 g of biomass was used compared to 413 g. This indicates that over time the pores in the ZA may be filled with carbon due to coking. A similar time effect are observed when comparing the spent CoMo from experiment 1 and 2, see Figure 4.9 (A), thus indicating that coking might also be an issue for supported catalysts, but much longer operating time is required to show this with certainty.

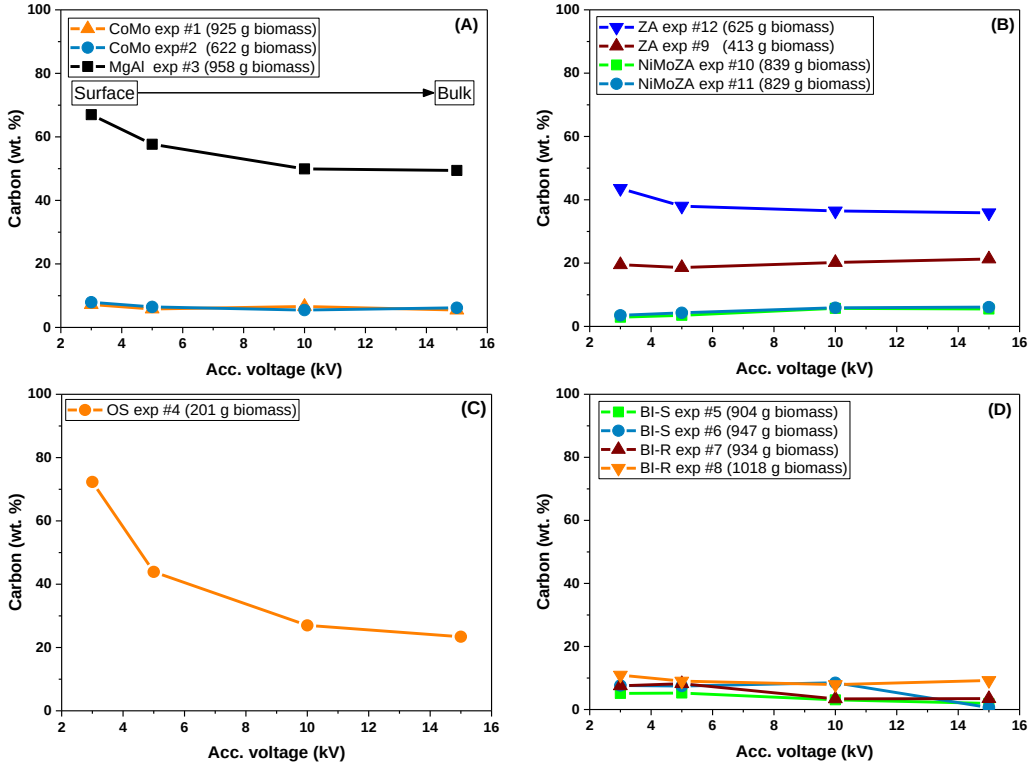

Figure 4.9. Carbon contents as a function of acceleration voltage on the spent CoMo and MgAl (A), ZA and NiMoZA (B), OS (C), and BI-S and BI-R (D). (Fluid bed temperature: 443-454 °C, HDO temperature: 370-394 °C, pressure: 26 bar, biomass feeding rate: 174-302 g/h, H_2S concentration: 0-471 ppm, H_2 flow: 54.4-89.2NL/min, N_2 flow: 0.62-5 NL/min)

The spent OS (Figure 4.9 (C)) was the catalyst with most carbon on the surface (72 wt. %). However, the average carbon content decreased to 23 wt.% as the acceleration voltage was increased to 15 kV, which is significantly less than the corresponding concentration of carbon for MgAl (49 wt. %). This is possibly because MgAl has a significantly higher surface area (see supplementary information Table C.4), thus probably also a larger pore volume than OS, so more carbon can be accumulated in the bulk. The lower carbon concentration in the bulk than on the surface, which is observed for both OS and MgAl, indicates that the catalyst over time can become covered by coke. The carbon content on the two BI-S catalysts varied between 0.6 and 7.6 wt.% and the carbon content on the two BI-R catalysts varied between 3.4 and 11 wt.%, hence there was slightly more carbon on the reduced than the sulfided catalysts.

These results show that having a supported catalyst in the fluid bed compared to the pure support or OS gave a lower degree of coking of the catalysts. This supports the hypothesis that that the catalyst can stabilize the reactive products from the fast pyrolysis, which otherwise would polymerize and deactivate the catalyst by coking. Furthermore, the low carbon content on the surface of BI-R and BI-S shows that despite that BI has a lower activity than the CoMo they are able to stabilize the vapors before they can polymerize on the surface of the catalyst.

4.3.3.2 X-ray diffraction

In order to investigate the active phase for bog iron, the fresh bog iron (i.e. in its oxide form), BI-S (from exp. 6) and BI-R (from exp. 8) were analyzed with X-ray diffraction. The X-ray diffraction patterns are shown in Figure 4.10 and the Rietveld fitted concentration and size of the crystals are shown in Table 4.2. XRD on the fresh bog iron showed strong reflections of goethite (α-FeOOH) corresponding to a concentration of 96.3 wt.% and reflections for siderite (FeCO3) (3.2 wt.%) and SiO_2 (1.3 wt.%). BI-S consisted mainly of pyrrhotite ($Fe_{1-x}S$) (74.5 wt.%) and troilite (FeS) (11.0 wt.%), and smaller reflection from Pyrite (FeS_2) (1.5 wt.%) was also observed. It is well-known that pyrrhotite ($Fe_{1-x}S$) can be formed from γ-FeOOH [35], thus pyrrhotite and troilite are probably formed from Goethite (α-FeOOH). Furthermore, pyrrhotite is well-known for its activity in coal liquefaction [32,33,35,40] and is most likely also the active phase in the BI-S catalyst. The average crystallite size of the formed pyrrhotite was 20 nm, and thus a fairly small crystallite size was obtained, which was desirable since smaller crystallites are expected to increase the activity [32]. Interestingly, Mochida et al. [32] studied the effect of sulfiding temperature on the pyrrhotite crystallite size and found that when sulfiding γ-FeOOH at 400-450°C the crystallite size was approximately 20 nm, in good agreement with our results.

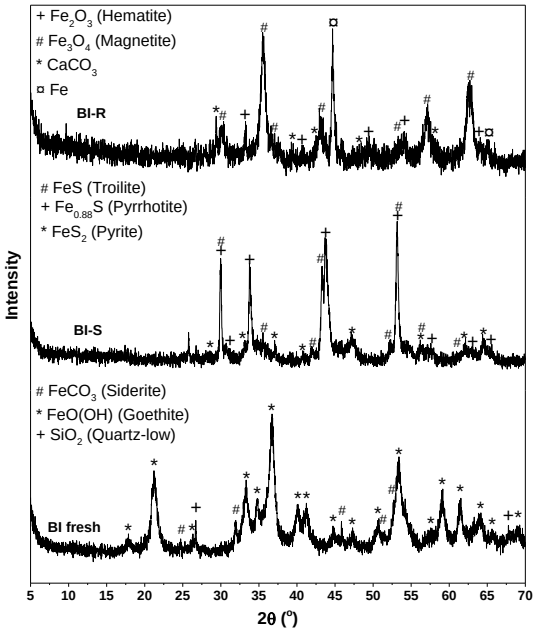

Figure 4.10 X-ray diffraction patterns for fresh BI, BI-S (experiment 6), and BI-R (experiment 8).

The X-ray diffraction pattern for BI-R showed strong reflections for hematite (Fe_2O_3) and magnetite (Fe_3O_4) and minor reflections for $CaCO_3$ and Fe. Hematite was most likely formed from magnetite during the passivation of the catalyst prior to the unloading. The small crystallite size (12 nm) of magnetite could be the reason for the high activity for BI-R. Magnetite has also been used for treatment of pyrolysis gas and was found to reduce the amount of acetic acid, phenols, catechol and non-aromatic ketones [41]. One of the advantages of magnetite is that it is magnetic [42,43], thus it might be possible to recover entrained catalyst by a magnet.

Table 4.2 Rietveld fitted concentrations and crystallite sizes for fresh BI, BI-S (experiment 6), and BI-R (experiment 8). (X-ray diffraction patterns shown in Figure 4.10)

	Conc. (wt.%)	D (Å)
BI fresh		
$FeCO_3$ (Siderite)	3.2	469
α-FeO(OH) (Goethite)	96.3	114
SiO_2 (Quartz-low)	0.5	4509
BI-S		
FeS (Troilite)	11	632
$Fe_{0.88}S$ (Pyrrhotite)	74.5	202
FeS_2 (Pyrite)	1.5	680
BI-R		
Fe	11.1	336
$CaCO_3$	-	-
Fe_3O_4 (Magnetite)	71.9	123
Fe_2O_3 (Hematite)	9.4	405

4.3.3.3 STEM

The spent BI-S (experiment 6) and BI-R (experiment 8) were studied with STEM (see Figure 4.11). The EDS element distribution of BI-S reveals iron well distributed on the particles together with a coincident signal of sulfur (supplementary information Figure C.2), consistent with iron sulfides. The primary particle sizes for BI-S (Figure 4.11 (A)) was between 10 and 30 nm, thus the STEM images supports the crystallite size estimated by XRD (Table 4.2). The presence of an oxygen signal in the element map, most pronounced at the surfaces of iron sulfide particles, indicates that some oxidation of the catalyst has taken place after it was unloaded.

The iron and oxygen was well distributed on the spent BI-R catalyst (Figure 4.11 (D) and (F)). Only negligible amounts of sulfur (<0.5wt.%) was observed. The particle sizes were between 10-20 nm (Figure 4.11 E). However, some of the particles were encapsulated with a 2-3 nm surface layer. EDS analyses of the core and the surface layer indicated a higher oxygen-to-iron ratio at the surface of these particles compared to the core (Figure 4.11 G). Thus the STEM-HAADF images support the hypothesis that the hematite was formed from magnetite at the particle surfaces during the passivation of the catalyst.

Aluminum and silicon were detected in both BI-R and BI-S (Figure 4.11) and the EDS element distribution indicates that the concentration of these compounds was not uniform. Phosphorus, potassium, and calcium were also detected in the spent bog iron and the EDS elemental distribution (Figure C.2 and Figure C.3) indicated that these compounds were uniformly distributed in the particles. As aluminum, silicon, phosphorus, potassium, and calcium were also detected in the fresh bog iron with ICP-OES (Table C.3), it is not possible to determine if these compounds were also transferred from the biomass to the catalyst.

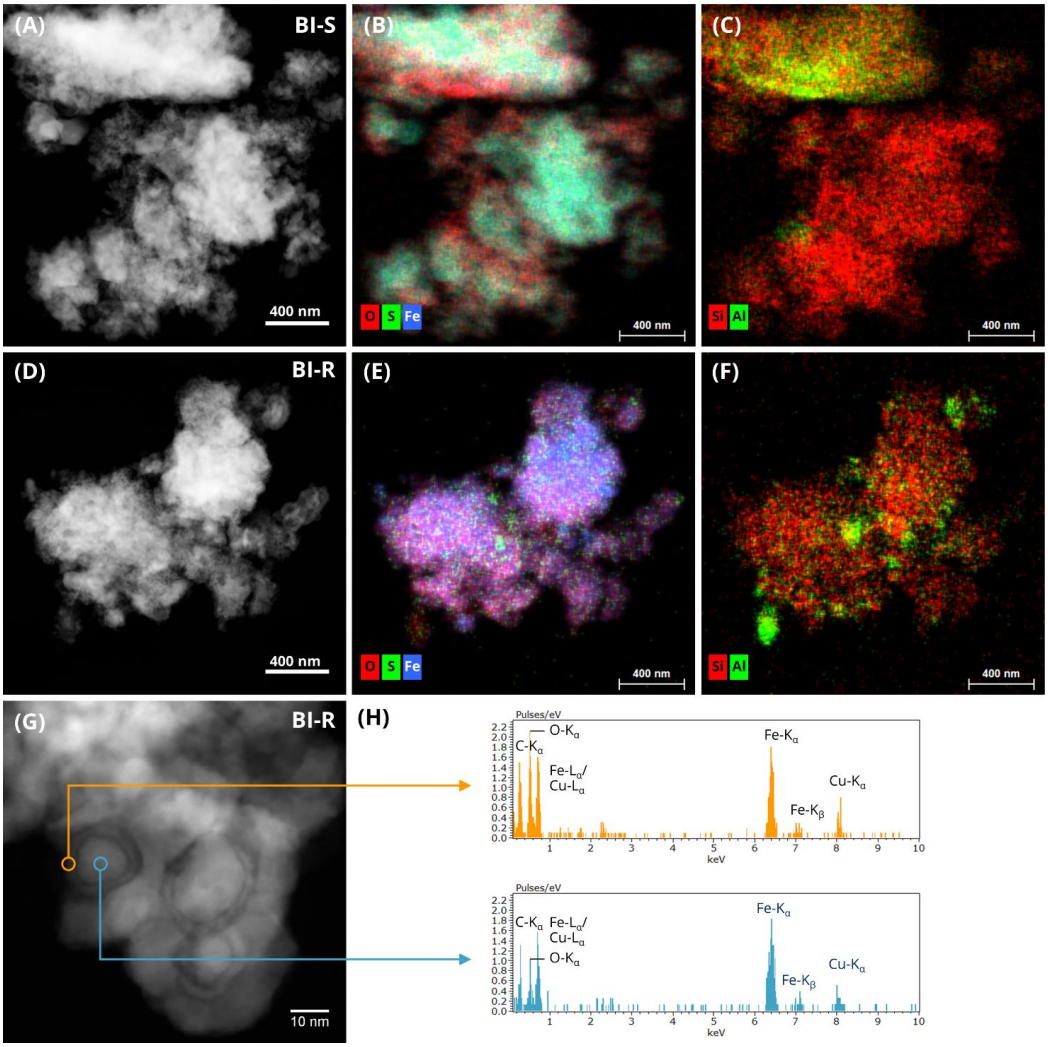

Figure 4.11 a) HAADF-STEM image of BI-S (from experiment 6) and EDS element distribution of B) oxygen, sulfur and iron, and C) silicium and aluminium. D) HAADF-STEM image of BI-R (from experiment 8) and EDS element distribution of E) oxygen, sulfur and iron, and F) silicium and aluminium. G) High-resolution STEM image of BI-R and H) selected area EDS spectra from regions as indicated in G).

4.4 Conclusion

The effect of the catalyst in catalytic hydropyrolysis of beech wood was studied by testing six different bed materials in the fluid bed reactor showing the importance of an active catalyst. The fluid bed reactor was followed by a fixed bed reactor with a sulfided $NiMo/Al_2O_3$ catalyst, which ensured that the condensed organics was almost oxygen free (<0.2 wt.%) independent on the catalyst in the fluid bed. The product distributions varied significantly for the different bed materials. Using $MgAl_2O_4$ and zeolite (H-ZSM-5) mixed with Al_2O_3 as bed materials produced large amounts of char (18.7-21.1 wt.% daf), CO and CO_2 (18.9 and

20.0 wt.% daf), and low amounts of condensed organics and C_{4+} (17.8-20.4 wt.% daf). Using the supported catalysts $CoMo/MgAl_2O_4$ and NiMo/zeolite mixed with Al_2O_3 significantly decreased the char yield to between 11.4 and 13.1 wt.% daf, while the condensed organics and C_{4+} yield increased to 21.5 wt.% daf for the $CoMo/MgAl_2O_4$ and 24.0 wt.% daf for the NiMo/zeolite mixed with Al_2O_3. The higher yield with the NiMo/zeolite mixed with Al_2O_3 compared to $CoMo/MgAl_2O_4$ could be due to a higher alkylation activity. Interestingly, the most promising catalyst was the natural mineral bog iron, which had a condensed organics and C_{4+} yield of 24.7 wt.% daf when it was used in reduced form and 22.8 wt.% daf when it was used in sulfided form. Thus bog iron can be used in the fluid bed reactor without the need to continuously add H_2S and it is at the same time fairly sulfur resistant since it is also active in its sulfide form. Furthermore, entrainment of bog iron from the fluid bed, mixing into the char, is less problematic than for CoMo or NiMo catalysts because it has a low toxicity, and thus handling of the char-catalyst mixture becomes less problematic.

Testing the effect of bypassing the HDO reactor with the sulfided $CoMo/MgAl_2O_4$ catalyst and the sulfided and reduced bog iron catalysts showed that bog iron has a significantly lower cracking, hydrodeoxygenation, decarbonylation and decarboxylation activity than the $CoMo/MgAl_2O_4$ catalyst. The oxygen content in the condensed organics for $CoMo/MgAl_2O_4$ was 1.5 wt.% db while it was 22 and 14 wt.% db for sulfided and reduced bog iron, respectively.

The carbon content on the spent catalysts from the fluid bed reactor was characterized by SEM-EDS. The pure supports had a significantly higher carbon content than the supported catalysts, thus indicating that the supported catalysts are able to stabilize the reactive oxygenates before they can participate in polymerization reactions. The carbon content on the spent bog iron catalysts was at the same level as on the spent $CoMo/MgAl_2O_3$ and NiMo/zeolite mixed with Al_2O_3, thus showing that despite that they have a significantly lower activity than the $CoMo/MgAl_2O_4$ they are active enough to suppress coking reactions. X-ray diffraction patterns and STEM imaging and EDS analysis of the spent bog iron catalysts indicated that the active phase for the sulfided bog iron was pyrrhotite and the active phase for the reduced bog iron was magnetite.

The present results show that the catalyst in the fluid bed reactor in catalytic hydropyrolysis is important and can be optimized in order to increase the condensable organic yield and lowering the degree of coking and the char yield. Furthermore, it is possible to replace the well-known hydrotreating CoMo or NiMo catalysts in the fluid bed reactor with a cheaper and non-toxic catalyst such as bog iron and at the same time increase the yield of condensable organics.

Acknowledgments

This work is part of the project “Hydrogen assisted catalytic pyrolysis for green fuels” conducted at The Department of Chemical and Biochemical Engineering at the Technical University of Denmark (DTU). The work was supported by The Danish Council for Strategic Research (now Innovation Fund Denmark, project 1305-00015B), The Programme Commission on Sustainable Energy and Environment. Funding from DTU is also gratefully acknowledged. The authors would also like to thank Nadia Luciw Ammitzbøll (Haldor Topsøe A/S) for fruitful discussions, Caroline Piper Hem (Haldor Topsøe A/S) for assistant with X-ray diffraction measurements, the Inorganic Analysis Department at Haldor Topsøe A/S for the elemental analysis of the bog iron and olivine sand by inductive coupled plasma optical emission spectroscopy (IPC-OES), and the Organic Analysis Department at Haldor Topsøe A/S for analysis of the organic phase

References

[1] U.S.E.I. Administration, Annual Energy Outlook 2017, (2017). http://www.eia.gov/outlooks/aeo/pdf/0383(2017).pdf.

[2] ESA, World Population Prospects The 2015 Revision, (2015). http://esa.un.org/unpd/wpp/Publications/Files/Key_Findings_WPP_2015.pdf.

[3] S. Sorrell, J. Speirs, R. Bentley, A. Brandt, R. Miller, Global oil depletion: A review of the evidence, Energy Policy. 38 (2010) 5290–5295. doi:10.1016/j.enpol.2010.04.046.

[4] Core Writing Team, R.K. Pachauri, L.A. Meyers, Climate change 2014: Synthesis report, IPCC, Geneva, 2014. http://www.ipcc.ch/pdf/assessment-report/ar5/syr/SYR_AR5_FINAL_full.pdf.

[5] A.V. Bridgwater, Review of fast pyrolysis of biomass and product upgrading, Biomass and Bioenergy. 38 (2012) 68–94. doi:10.1016/j.biombioe.2011.01.048.

[6] T.N. Trinh, P.A. Jensen, K. Dam-Johansen, N.O. Knudsen, H.R. Sørensen, S. Hvilsted, Comparison of lignin, macroalgae, wood, and straw fast pyrolysis, Energy & Fuels. 27 (2013) 1399–1409. doi:10.1021/ef301927y.

[7] S. Czernik, A.V. Bridgwater, Overview of applications of biomass fast pyrolysis oil, Energy & Fuels. 18 (2004) 590–598. doi:10.1021/Ef034067u.

[8] A. Oasmaa, S. Czernik, Fuel oil quality of biomass pyrolysis oils-State of the art for the end users, Energy & Fuels. 13 (1999) 914–921. doi:10.1021/ef980272b.

[9] D. Chiaramonti, A. Oasmaa, Y. Solantausta, Power generation using fast pyrolysis liquids from biomass, Renew. Sustain. Energy Rev. 11 (2007) 1056–1086. doi:10.1016/j.rser.2005.07.008.

[10] D. Mohan, C.U. Pittman, P.H. Steele, Pyrolysis of wood/biomass for bio-oil: A critical review, Energy & Fuels. 20 (2006) 848–889. doi:10.1021/ef0502397.

[11] R.H. Venderbosch, W. Prins, Fast pyrolysis technology development, Biofuels, Bioprod. Biorefining. 4 (2010) 178–208. doi:10.1002/bbb.205.

[12] P.M. Mortensen, J.-D. Grunwaldt, P.A. Jensen, K.G. Knudsen, A.D. Jensen, A review of catalytic upgrading of bio-oil to engine fuels, Appl. Catal. A Gen. 407 (2011) 1–19. doi:10.1016/j.apcata.2011.08.046.

[13] P.M. Mortensen, PhD Thesis: Catalytic Conversion of Bio-oil to Fuel for Transportation, Technical University of Denmark, Dept. of Chemical and Biochemical Engineering, 2013.

[14] M.R. Hurt, J.C. Degenstein, P. Gawecki, D.J. Borton II, N.R. Vinueza, L. Yang, R. Agrawal, W.N. Delgass, F.H. Ribeiro, H.I. Kenttämaa, On-line mass spectrometric methods for the determination of the primary products of fast pyrolysis of carbohydrates and for their gas-phase manipulation, Anal. Chem. 85 (2013) 10927–10934. doi:10.1021/ac402380h.

[15] R.H. Venderbosch, A critical view on catalytic pyrolysis of biomass, ChemSusChem. 8 (2015) 1306–1316. doi:10.1002/cssc.201500115.

[16] T.L. Marker, L.G. Felix, M.B. Linck, M.J. Roberts, Integrated hydropyrolysis and hydroconversion (IH^2) for the direct production of gasoline and diesel fuels or blending components from biomass, Part 1: Proof of principle testing, Environ. Prog. Sustain. Energy. 31 (2012) 191–199. doi:10.1002/ep.10629.

[17] T.L. Marker, L.G. Felix, M.B. Linck, M.J. Roberts, P. Ortiz-Toral, J. Wangerow, Integrated hydropyrolysis and hydroconversion ($IH^{2®}$) for the direct production of gasoline and diesel fuels or blending components from biomass, Part 2: Continuous testing, Environ. Prog. Sustain. Energy. 33 (2014) 762–768. doi:10.1002/ep.11906.

[18] D.C. Dayton, J. Carpenter, J. Farmer, B. Turk, R. Gupta, Biomass hydropyrolysis in a pressurized fluidized bed reactor, Energy & Fuels. 27 (2013) 3778–3785. doi:10.1021/ef400355t.

[19] D.C. Dayton, J. Hlebak, J.R. Carpenter, K. Wang, O.D. Mante, J.E. Peters, Biomass hydropyrolysis in a fluidized bed reactor, Energy & Fuels. 30 (2016) 4879–4887. doi:10.1021/acs.energyfuels.6b00373.

[20] K. Wang, D.C. Dayton, J.E. Peters, O.D. Mante, Reactive catalytic fast pyrolysis of biomass to produce high-quality bio-crude, Green Chem. 19 (2017) 3243–3251. doi:10.1039/C7GC01088E.

[21] V.K. Venkatakrishnan, W.N. Delgass, F.H. Ribeiro, R. Agrawal, Oxygen removal from intact biomass to produce liquid fuel range hydrocarbons via fast-hydropyrolysis and vapor-phase catalytic hydrodeoxygenation, Green Chem. 17 (2015) 178–183. doi:10.1039/c4gc01746c.

[22] V.K. Venkatakrishnan, J.C. Degenstein, A.D. Smeltz, W.N. Delgass, R. Agrawal, F.H. Ribeiro, High-pressure fast-pyrolysis, fast-hydropyrolysis and catalytic hydrodeoxygenation of cellulose: Production of liquid fuel from biomass, Green Chem. 16 (2014) 792–802. doi:10.1039/c3gc41558a.

[23] L. Zhang, K. Gong, J. Lai, P. Alvey, Chemical composition and stability of renewable hydrocarbon products generated from a hydropyrolysis vapor upgrading process, Green Chem. 19 (2017) 3628–3641. doi:10.1039/C7GC01075C.

[24] F. Melligan, M.H.B. Hayes, W. Kwapinski, J.J. Leahy, Hydro-pyrolysis of biomass and online catalytic vapor upgrading with Ni-ZSM-5 and Ni-MCM-41, Energy & Fuels. 26 (2012) 6080–6090. doi:10.1021/ef301244h.

[25] F. Melligan, M.H.B. Hayes, W. Kwapinski, J.J. Leahy, A study of hydrogen pressure during hydropyrolysis of Miscanthus x giganteus and online catalytic vapour upgrading with Ni on ZSM-5, J. Anal. Appl. Pyrolysis. 103 (2013) 369–377. doi:10.1016/j.jaap.2013.01.005.

[26] D.P. Gamliel, L. Wilcox, J.A. Valla, The effects of catalyst properties on the conversion of biomass via catalytic fast hydropyrolysis, Energy & Fuels. 31 (2017) 679–687. doi:10.1021/acs.energyfuels.6b02781.

[27] D.P. Gamliel, G.M. Bollas, J.A. Valla, Bifunctional Ni-ZSM-5 catalysts for the pyrolysis and hydropyrolysis of biomass, Energy Technol. 5 (2017) 172–182. doi:10.1002/ente.201600136.

[28] D.P. Gamliel, G.M. Bollas, J.A. Valla, Two-stage catalytic fast hydropyrolysis of biomass for the production of drop-in biofuel, Fuel. 216 (2018) 160–170. doi:10.1016/j.fuel.2017.12.017.

[29] F. Bergius, J. Billwiller, Process for producing liquid or soluble organic combinations from hard coal and the like., US Patent 1,251,954, 1918.

[30] F. Bergius, Process for distilling and liquefying coal, US Patent 1,669,439, 1928.

[31] Friedrich Bergius, Chemical reactions under high pressure, Nobel Lect. (1932) 33.

[32] I. Mochida, K. Sakanishi, N. Suzuki, M. Sakurai, Y. Tsukui, T. Kaneko, Progresses of coal liquefaction catalysts in Japan, 2 (1998) 17–30.

[33] Y. Nakao, S. Yokoyama, Y. Maekawa, K. Kaeriyama, Coal liquefaction by colloidal iron sulphide catalyst, Fuel. 63 (1984) 721–722. doi:10.1016/0016-2361(84)90176-5.

[34] S. Yokoyama, R. Yoshida, H. Narita, K. Kodaira, Y. Maekawa, Catalytic activity of various iron sulphides in coal liquefaction, Fuel. 65 (1986) 164–170. doi:10.1016/0016-2361(86)90002-5.

[35] T. Kaneko, K. Tazawa, N. Okuyama, M. Tamura, Effect of highly dispersed iron catalyst on direct liquefaction of coal, 79 (2000) 263–271.

[36] J. Dilcio Rocha, C. a. Luengo, C.E. Snape, The scope for generating bio-oils with relatively low oxygen contents via hydropyrolysis, Org. Geochem. 30 (1999) 1527–1534. doi:10.1016/S0146-6380(99)00124-2.

[37] M.Z. Stummann, M. Høj, C.B. Schandel, A.B. Hansen, P. Wiwel, J. Gabrielsen, P.A. Jensen, A.D. Jensen, Hydrogen assisted catalytic biomass pyrolysis. Effect of temperature and pressure, Biomass and Bioenergy. 115 (2018) 97–107. doi:10.1016/j.biombioe.2018.04.012.

[38] W.G. Lloyd, D.A. Davenport, Applying thermodynamics to fossil fuels: Heats of combustion from elemental compositions, J. Chem. Educ. 57 (1980) 56–60. doi:10.1021/ed057p56.

[39] J. Lai, L. Zhang, K. Gong, Nuclear magnetic resonance characterization of renewable products from a two-step ex-situ hydropyrolysis vapor upgrading process, ChemistrySelect. 3 (2018) 297–307. doi:10.1002/slct.201702431.

[40] H.F. Ades, A.L. Companion, K.R. Subbaswamy, Molecular orbital calculations for iron catalysts, Energy & Fuels. 8 (1994) 71–76. doi:10.1021/ef00043a012.

[41] P.H. Moud, E. Kantarelis, K.J. Andersson, K. Engvall, Biomass pyrolysis gas conditioning over an iron-based catalyst for mild deoxygenation and hydrogen production, Fuel. 211 (2018) 149–158. doi:10.1016/j.fuel.2017.09.062.

[42] S. Bae, S. Gim, H. Kim, V. Dorcet, M. Pasturel, J.M. Grenèche, G.K. Darbha, K. Hanna, New Features and Uncovered Benefits of Polycrystalline Magnetite as Reusable Catalyst in Reductive Chemical Conversion, J. Phys. Chem. C. 121 (2017) 25195–25205. doi:10.1021/acs.jpcc.7b08178.

[43] V.N. Nikiforov, Y.A. Koksharov, S.N. Polyakov, A.P. Malakho, A. V. Volkov, M.A. Moskvina, G.B. Khomutov, V.Y. Irkhin, Magnetism and Verwey transition in magnetite nanoparticles in thin polymer film, J. Alloys Compd. 569 (2013) 58–61. doi:10.1016/j.jallcom.2013.02.059.

Chapter 5 Catalytic hydropyrolysis of biomass using molybdenum sulfide based catalyst. Effect of promoters

In this chapter we used molybdenum sulfide based catalysts and investigate the effect of the promoter on the product distribution and selectivity. The condensed organic phases were thoroughly analyzed and both the fresh and spent catalysts were characterized. The supplementary information can be found in Appendix D.

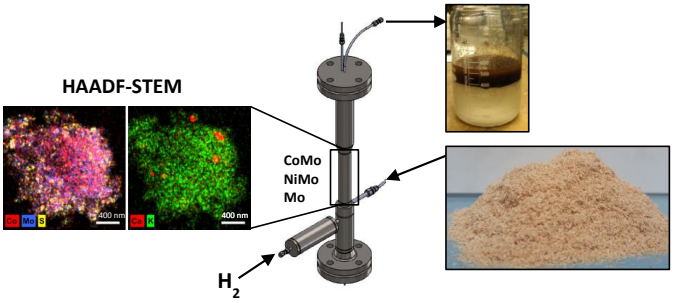

Abstract

Catalytic hydropyrolysis of beech wood has been conducted in a fluid bed reactor at 450°C and a total pressure of 26 bar. The differences in hydrodeoxygenation activity, selectivity and the resulting product composition between sulfided $Mo/MgAl_2O_4$, $CoMo/MgAl_2O_4$ or $NiMo/MgAl_2O_4$ catalysts have been investigated. The acidity and molybdate species in the oxide catalyst precursors were characterized with ammonia temperature programmed desorption (NH_3-TPD) and Raman spectroscopy. The spent sulfided catalysts were also extensively characterized by scanning electron microscopy (SEM) and by scanning transmission electron microscopy (STEM) coupled with energy dispersive X-ray spectroscopy (EDS). The catalytic hydropyrolysis of beech wood produced four main products: Liquid organic and aqueous phases, solid char and gasses. The solid char and aqueous phase yields were not affected by the type of catalyst. The sum of condensed organics and C_{4+} gas yield varied between 24.3 and 26.4 wt.% on dry, ash free basis (daf) and was highest for the Mo catalyst and lowest for the NiMo catalyst. The NiMo catalyst had the highest hydrogenation, cracking, and de-carbonylation activity. The oxygen content in the condensed organic phase was between 9.0 and 12 wt.% on dry basis (db) and was lowest for the CoMo catalyst and highest for the Mo catalyst. The carbon recovery in the condensable organics was 39 % for both the CoMo and the Mo, and 37 % for the NiMo catalyst. These results indicate that the CoMo, due to its high deoxygenation activity and high carbon recovery, is the most suitable catalyst for catalytic hydropyrolysis. The carbon content on the spent CoMo was between 1.5 and 3.3 wt.% and between 0.9 and 3.1 on the spent NiMo catalyst, but between 5.0 and 5.5 wt.% on the spent Mo catalyst. The higher carbon content on the spent Mo catalyst was probably due to its lower deoxygenation and hydrogenation activity. Calcium particles and small amounts of potassium (≤1.5 wt.%) were detected on all spent catalysts using STEM-EDS, showing that alkali metals are transferred from the biomass to the catalyst, which potentially could lead to catalyst deactivation.

Abbreviations

AED	Atomic emission detector	ICP-OES	Inductive coupled plasma optical emission spectroscopy
BET	Brunauer–Emmett–Teller	mAro	Monoaromatics
conc	Concentration	MS	Mass spectrometry
CUS	Coordinatively unsaturated sites	Naph	Naphthenes
daf	Dry, ash free basis	O-Ali	Oxygenated aliphatics
db	Dry basis	O-Aro	Larger oxygenated aromatics
DDO	direct deoxygenation	Par	Paraffins
diAro	Diaromatics	PhOH	Phenolics
DMDS	Dimethyl disulfide	Ph(OH)2	Dihydroxybenzene
EDS	Energy dispersive X-ray spectroscopy	SA	Surface area
FB	Fluid bed	SEM	Scanning electron microscopy
FCC	Fluid catalytic cracking	STEM	Scanning transmission electron microscopy
FID	Flame ionization detector	Temp.	Temperature
GC	Gas chromatograph	TPD	Temperature programmed desorption
HAADF	High-angle annular dark-field	tetAro+	Tetra- and higher aromatics
HDO	Hydrodeoxygenation	triAro	Triaromatics
HYD	Hydrogenation		

5.1 Introduction

Catalytic hydropyrolysis, the concerted combination of fast pyrolysis and catalytic hydrodeoxygenation (HDO), has been shown to be an efficient method for production of renewable diesel and gasoline range hydrocarbons from biomass [1,2]. In this process the reactive oxygenates formed during pyrolysis, which otherwise may undergo polymerization reactions [3], are immediately hydrogenated producing a stable product with a significantly lower oxygen content than conventional fast pyrolysis oil. Marker et al. [1,2] were able to produce an oxygen free oil with a condensed organic and C_{4+} gas yield of 21 to 46 wt.% dry ash free (daf) basis by conducting catalytic hydropyrolysis of different types of biomass (the high yield of 46 wt.% daf was obtained with microalgae) in a fluid bed reactor followed by deep HDO in a fixed bed reactor, in a process called IH^2®. Furthermore, life cycle assessments of the IH^2® process have shown that its fuel products have 30-96 % lower greenhouse gas emissions compared to fossil fuels, mainly depending on the biomass feedstock where bagasse shows the highest reduction [4,5].

Using a fluid bed reactor, Dayton et al. [6–8] have tested several pre-reduced catalysts, including a commercial NiMo hydrotreating catalyst and a Mo based catalyst, for catalytic hydropyrolysis of woody biomass at temperatures between 375 and 500 °C and pressures of hydrogen between 1 and 31 bar. They were able to obtain a condensed organic and C_{4+} carbon yield of 43 %, with an oxygen content in the condensed liquid of 6.2 wt.% [8]. However, the composition of the catalysts was not reported and the spent catalysts were not characterized. Gamliel et al. [9–11] also studied the effect of reduced metal catalysts in catalytic hydropyrolysis using a Pyroprobe analyzer focusing mainly on Ni metal on a zeolite (ZSM-5) support. The fresh catalysts were characterized, but the spent catalysts were not studied. Therefore, despite that catalytic hydropyrolysis is a promising technology, there is very little information available about the composition of catalysts and to what degree the catalysts may be deactivated e.g. by carbon deposition or transfer of alkali metals, inherently present in biomass.

Sulfided CoMo, NiMo, and Mo, which are widely used as hydrotreating catalysts in oil refineries, are also known to be active and stable in hydrodeoxygenation reactions of bio-oil and model components [12–20]. Since most biomass sources contain sulfur [21], a major advantage of the sulfided catalysts is that they are sulfur tolerant, as opposed to many reduced metal catalysts. It is well-known that the addition of a promoter (Co or Ni) to MoS_2 increases the formation of the coordinated unsaturated sites (CUS) [22–24], thus enhancing the catalytic activity [17,25]. One of the differences between Co and Ni as promoter is that Co promotes the direct deoxygenation (DDO) pathway, while Ni promotes the hydrogenation (HYD) pathway, where aromatic rings are saturated prior to deoxygenation [18,25–28].

In our previous work we conducted catalytic hydropyrolysis of beech wood in a fluid bed reactor with a commercial, sulfided CoMo/$MgAl_2O_4$ catalyst (supplied by Haldor Topsøe A/S), followed by a fixed bed reactor with a commercial, sulfided NiMo/Al_2O_3 hydrotreating catalyst [29]. The effect of temperature and pressure in the fluid bed hydropyrolysis reactor was evaluated. An essentially oxygen free organic phase (oxygen<0.01 wt.%) was obtained with a yield between 17 and 22 wt.% daf, corresponding to an energy recovery between 40 and 53 % [29]. The concentration of aromatics could be controlled between 42 and 75 % by varying the operating conditions [29]. Furthermore we previously studied the differences between sulfided Mo, CoMo, and NiMo, catalysts supported on $MgAl_2O_4$ in the hydrodeoxygenation of ethylene glycol in a fixed bed reactor [17], and found that the Mo catalyst had the lowest conversion and the lowest stability, but the highest selectivity to C_2 and C_3 hydrocarbons and C-C coupling products, rather than C_1 cracking products. This therefore indicates that it could be an advantage to use a catalyst with a moderate activity in catalytic hydropyrolysis.

In this work the differences between using a sulfided Mo, CoMo, and NiMo supported on $MgAl_2O_4$ in catalytic hydropyrolysis of beech wood in a fluid bed reactor was studied. The oxide catalyst precursors were characterized by Raman spectroscopy and NH_3-TPD to obtain specific information about the surface molybdate species and acid properties. The spent catalysts were investigated with electron microscopy (SEM and STEM) coupled with energy dispersive X-ray spectroscopy (EDS) to reveal composition and elemental distribution of the catalysts as well as the structure and particle sizes of the catalytically active molybdenum sulfide. Furthermore, the organic phase products were characterized in depth with sulfur specific gas chromatography (GC) using an atomic emission detector (AED) and GC×GC-mass spectrometry (MS)/flame ionization detector (FID). To our knowledge this is the first study published in the open literature where the composition of the catalyst used in a continuous, bench scale catalytic hydropyrolysis setup is reported, where the catalysts are characterized in depth and where the influence of the catalyst type on the product properties is provided.

5.2 Experimental

5.2.1 Biomass feedstock

Bark free beech wood was used as biomass feedstock and was supplied by Dansk Træmel (Product number: 10000251250390). The moisture and ash contents were 6.72 wt.% and 0.59 wt.% on dry basis (db), respectively [29]. The particle sizes were between 200-700 µm. The beech wood was analyzed by Celignis Analytical (analysis P10) and consisted of 24 wt.% db lignin, 40 wt.% db cellulose, 18 wt.% db hemicellulose, 3 wt.% db other polysaccharides, 3 wt.% db extractives and 12 wt.% db unknown. The potassium was 0.12 wt.% db and calcium content was 0.13 wt.% db. A detailed elemental composition of the biomass, including the ash composition, can be found elsewhere [29].

5.2.2 Catalyst preparation

The CoMo, NiMo, and Mo catalysts were prepared by sequential incipient wetness impregnation of the $MgAl_2O_4$ spinel support, which was supplied by Haldor Topsøe A/S. The support was crushed to a particle size of 180-355 µm, to ensure a good fluidization of the fluid bed. Prior to impregnation, the support was calcined at 995°C for 10 hours. The calcined support had a pore volume of 0.58-0.62 g_{water}/g and 110 % of this volume was used for the impregnation. The specific surface area (SSA) was between 54-58 m^2/g.

The support was impregnated with an aqueous solution of $(NH_4)_6Mo_7O_{24}\cdot 4H_2O$ (Fluka≥99.0%), then aged with stirring for approximately 3 hours and dried over night at approximately 110°C in air. For the promoted catalysts, a second impregnation with $Co(NO_3)_2\cdot 6H_2O$ (Fluka ≥ 98%) or $Ni(NO_3)_2\cdot 6H_2O$ (Sigma-Aldrich ≥97%) was conducted with ageing for approximately 3 hours followed by drying over night at approximately 110°C in air. The calcination was conducted under a flow of technical air by heating to 500°C with a ramp of 5°C/min and holding for 3 hours. After calcination the catalyst was sieved to 180-355 µm again in order to remove any dust or agglomerates formed during the preparation. The composition of the catalysts is shown in Table 5.1. A Mo loading between 3.5 and 3.7 atoms/nm^2 was obtained. Mo loadings lower than 4 atoms/nm^2 should give a sub monolayer of MoO_x on $MgAl_2O_4$, assumed similar to γ-Al_2O_3 [30], which should lead to a high dispersion of small MoS_2 particles (when sulfided) with a moderate activity, hence minimizing the formation of the very active type II sites [31]. The (Co/Ni) to Mo atomic ratio was aimed at 0.3, because this should ensure that the less active Co_9S_8 phase is not formed [32]. The acidity of the as calcined catalysts in the oxide form was measured using NH_3 adsorption and subsequent TPD. No significant difference in the acidity of the three catalysts was observed (see supplementary information Figure D.1 and Table D.1), indicating that the main difference between these catalysts are the promoter.

The catalysts were sulfided in-situ in the catalytic hydropyrolysis setup at 26 bar, 350°C with 1.8 mol % H_2S, 11 mol % N_2 in 87 mol % H_2 by feeding 2% H_2S in H_2 (flow: 4 NL/min) and N_2 (flow: 0.5 NL/min). The temperature ramp was 10 °C/min and the holding time was 2 hours. After the sulfidation, the test conditions shown in Table 5.2 were established.

Table 5.1 Composition of the fresh catalysts

Catalyst	Mo (wt.%)	Ni (wt.%)	Co (wt.%)	(Co/Ni)/Mo (molar)	Mo load (Atoms/nm^2)	BET SSA (m^2/g)
CoMo	3.41	-	0.637	0.30	3.6	60
NiMo	3.27	0.585	-	0.29	3.5	58
Mo	3.50	-	-	-	3.7	60

5.2.3 Experimental setup

The catalytic hydropyrolysis experiments were conducted in a bench scale setup shown schematically in Figure 5.1 and described in detail elsewhere [29]. In brief, the setup consisted of a feeding system, which included a gas mixing system and a screw feeder for biomass feeding, a fluid bed hydropyrolysis reactor, a filter for char removal and a three stage condensation system (20°C, 2°C, and -40°C). The uncondensed gases were sent to a flare. A small fraction of the gas was set to an online gas GC, which measured the gas composition (H_2, N_2, H_2S, CO, CO_2, C_1 to C_5 and C_{6+} hydrocarbons) every 10 min. The piping between the fluid bed, filter and condensation section was heated to 350°C in order to avoid condensation. During the experiments 52 NL/min hydrogen passed through a sinter plate in the bottom of the fluid bed reactor and 30 NL/min hydrogen and 5 NL/min nitrogen passed through the biomass feeding tube, thus ensuring a rapid transfer of the biomass from the screw feeder to fluid bed reactor.

The total mass of the condensed liquid was determined by weighing and the organic phase and the aqueous phase were separated with a separation funnel. The mass of the aqueous phase was measured and the mass of the organic phase was determined by subtracting the mass of the aqueous phase from the total mass of condensed liquid. The H_2S dissolved in the liquid phases was for safety reasons removed by bubbling with N_2 until hydrogen sulfide test strips (Sigma Aldrich) showed no sign of H_2S. This lead to a mass loss between 0 and 4.8 wt.% for the organic phase and between 1.0 and 1.5 wt.% of the aqueous phase. The mass loss in the organic phase was mainly due to vaporization of light hydrocarbons while the mass loss in the aqueous phase was mainly due to vaporization of water.

Regarding the experimental uncertainty, a previously reported repeated experiment (see Chapter 4) has shown that the largest uncertainty is the aqueous phase yield, where the difference between two experiments was 1.2 wt.% daf. The difference in the C_1-C_3 yield was <0.1 wt.% daf, CO and CO_2 yield was 0.4 wt.% daf, char and coke yield was 0.1 wt.% daf, and condensed organics and C_{4+} in the gas yield was 0.1 wt.% daf. It is therefore assumed that the experimental error is less than 0.5 wt.% daf for the char and coke yield, 0.2 wt.% daf for the C_1-C_3 yield, 0.5 wt.% daf for the total CO and CO_2 yield, 1.5 wt.% for the aqueous phase yield, and less than 0.5 wt.% daf for the condensed organics and C_{4+} in the gas yield.

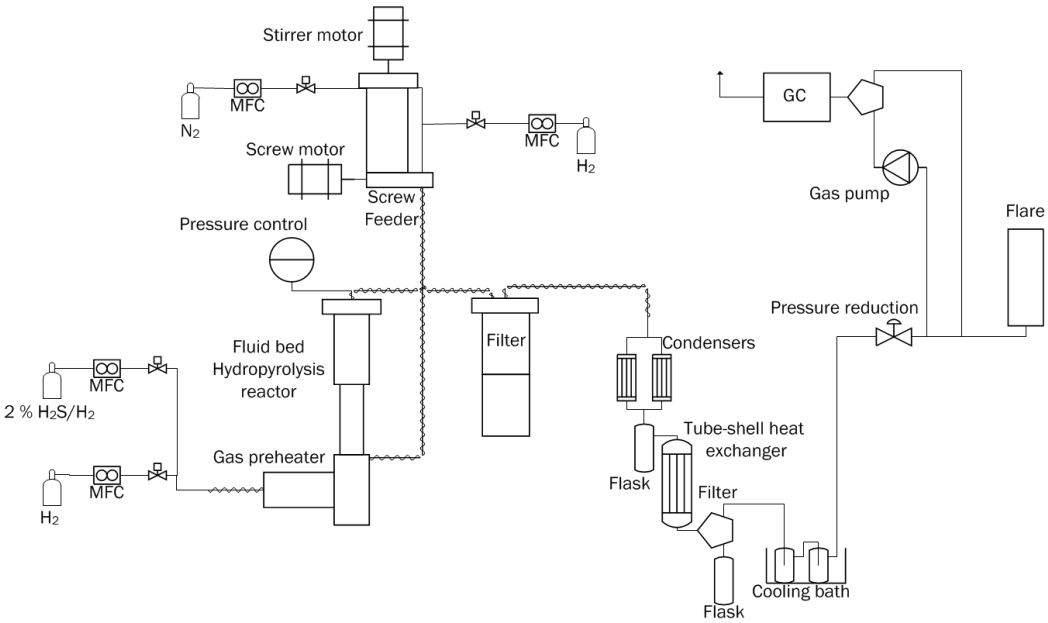

Figure 5.1. Simplified piping and instrumentation diagram of the catalytic hydropyrolysis setup

After each experiment the catalyst and the remaining char was removed from the fluid bed, and replaced with the fresh catalyst for the subsequent experiment. The sum of char (un-vaporized biomass residue) and coke (carbon on the catalysts) yield was calculated by subtracting the mass of loaded catalyst from the total mass of solids collected from the filter and fluid bed.

5.2.4 Analysis methods

5.2.4.1 Organic phase

Several methods were used to analyze the condensed organic phase and a more detailed description can be found elsewhere [29]. The hydrogen content was measured with the ASTM method D7171. The sulfur content was measured according to ASTM D4294. The density at 40 ˚C was measured with ASTM method D 4052 and the water content was measured with Karl Fisher titration.

The oxygen content in the condensed organic phase was analyzed at DB Lab A/S using a Flash 2000 elemental analyzer (Thermo Scientific). The uncertainty of this measurement was 3.0 %, defined as two standard deviations for the measurement uncertainty, corresponding to a confidence interval of 95 %.

The condensed organic liquid samples were characterized by GC×GC-ToF/MS or –FID and a detailed description can be found elsewhere [29]. Based on the GC×GC-ToF/MS analysis the compounds were classified into seven groups: paraffins, naphthenes, mono-, di- and tri- and higher aromatics, oxygenated aliphatics, phenolics, dihydroxybenzenes, larger oxygenated aromatics, and sterols. The relative uncertainty for this analysis is estimated to be below 5 %.

Selective analysis of sulfur containing compounds was conducted using a GC with an atomic emission detector (AED) [29].

5.2.4.2 Aqueous phase

The carbon content in the aqueous phase samples was determined with GC-AED using an Agilent 7890A GC coupled to a JAS 2370 AED in carbon selective mode. The carbon emission line at 193 nm was used in combination with a helium makeup gas flow of 80 ml/min. The cavity temperature was 320°C and the transfer line temperature was 380°C. The GC column was a Phenomenex ZB-5 Inferno (30m X 0.25mm X 0.25µm) in connection with a JAS PTV inlet in split mode (1:100) held at 325°C and 0.5 µl injection. The oven was held at 40°C for 1 min and then ramped to 380°C @ 10°C/min. The quantification was done by external standards using benzyl alcohol dissolved in water. Calibration concentrations ranged from 10 ppm to 1100 ppm carbon. No identification of individual compounds was done and the total detected carbon was taken as a figure of the total carbon content in the aqueous sample. No sample pretreatment was done prior to analysis.

The aqueous phase was also analyzed on a Shimadzu GC-MS/FID as previously described [29]. Based on the GC-FID/MS analysis the components were classified into 8 groups: unidentified, ethers, ketones, alcohols, sugars, phenols, acids and furans. The relative amount (FID area-%) of each component class was estimated as the sum of all the detected peaks in that class divided by the total peak area.

5.2.4.3 Catalyst characterization

The composition (Co, Ni, Mo) of the fresh catalysts was determined with inductive coupled plasma optical emission spectroscopy (ICP-OES) and the surface area was measured with N_2-physisorption (BET). Temperature programmed ammonia desorption (NH_3-TPD) of the fresh catalysts were conducted on a Mettler Toledo TGA/DSC 1. A complete blank measurement was first conducted with an empty crucible. The sample was subjected to the same procedure, which was heating at 20°C/min to 500 °C, where the sample was held for 60 min in 75 ml/min 31 % He and 69 % Ar. Thereafter the sample was cooled to 150°C (-20°C/min), and left to settle at 150°C for 20 minutes. The gas was then changed to 75 ml/min 2 % NH_3 in 29% He and 69% Ar for 30 min and the sample was flushed in the Ar/He mixture for 233 min. Afterwards the sample was cooled to 140°C and the NH_3 desorption ramp (10 C°/min) up to 600°C was initiated. To assess the desorbed NH_3 the weight loss in the temperature interval 150-500°C was used.

Raman spectroscopy on the calcined oxidic samples was performed at ambient conditions with a Labram 800 HR from Jobin Yvon using a Koheras solid state 488 nm laser.

The scanning electron microscopy (SEM) was performed on a FEI QUANTA600 scanning electron microscope with tungsten filament and equipped with a liquid nitrogen cooled EDAX ultra-thin window (UTW) EDS detector. All samples were sprinkled on carbon tabs on Al-stubs and conducted without any coating to prevent charging in the sample chamber.

EDS element quantifications were acquired on 0.11 mm x 0.11 mm areas on the surface of the catalyst grains at acceleration voltages of 3 kV, 5 kV, 10 kV and 15 kV to probe different interaction volumes between the incident electron beam and the sample. The composition of the sample was determined in EDAX software (version 5.2.42) using a normalized, standardless, ZAF-corrected and SEC-factor corrected quantification of the acquired EDS-spectra. The maximum penetration depth of the incident electron beam in $MgAl_2O_4$ was estimated with the CASINO Monte Carlo Software v.3.3.04 (see Table D.2, Figure D.2 and Figure D.3) to be approximately 0.170 µm for 3 kV and 1.60 µm for 15 kV, and serves as a rough indication of the maximum depth from where the detected X-rays may have been generated. The standard deviation for the carbon measurement was 1.5 wt.% at 3 kV, 0.8 wt.% at 5 kV, 1.0 wt.% at 10 kV and 1.5 wt.% at 15 kV, and the

standard deviation for the potassium measurements was 0.6 wt.% at 5 kV, 0.3 wt.% at 10 kV, and 0.2 wt.% at 15 kV.

The transmission electron microscopy was performed on a FEI Talos™ F200X transmission electron microscope equipped with high-brightness field emission gun (X-FEG) and Super-X G2 EDS detector. The catalyst powders were crushed in a mortar and dispersed dry on a Cu TEM grid covered by a continuous carbon film (SPI Supplies). Images and elemental EDS maps were acquired in scanning transmission mode (STEM) with a camera length of 125 cm. Elemental EDS maps of 512 pixels x 512 pixels (2.1 μm x 2.1 μm) were acquired for 22 min in Brüker software (Esprit 1.9) using a probe current of 0.7 nA. It is noted that the EDS sulfur K-line (S-K_α 2.309 keV) may overlap with the molybdenum L-line (Mo-L_α 2.292keV) as the separation in energy is less than the EDS resolution of about 0.13 keV (full-width-half-maximum of Mn-K_α peak). Therefore, the elemental maps were processed in Esprit by a Bremsstrahlung background subtraction and series deconvolution of the EDS pixel spectra (using a 4x-binning) to display the net counts of Mo-K_α (17.480 keV), S-K_α (2.309 keV), Co-K_α (6.931 keV), Ni-K_α (7.480 keV), K-K_α (3.314 keV), and Ca-K_α (3.692 keV) respectively. The EDS analyses were complimented by high-resolution STEM imaging (probe size about 0.16nm) using the high-angle annular dark field detector (HAADF). For particle size measurements, HAADF-STEM images of 1024 pixels x 1024 pixels were recorded with a pixel size of 0.061 nm thus enabling the lattice spacing of 2H-MoS_2 (001) of 0.615 nm to be resolved. The sizes of the identified particles were measured manually from the images using ImageJ software.

5.3 Results and Discussion

The reaction conditions, mass balance and properties of the condensed liquid phases are shown in Table 5.2. The mass balance for the experiments closed between 96.7 and 99.1 wt.% daf. A more detailed gas composition is shown in supplementary information Table D.3.

Table 5.2 Summary of reaction conditions and mass balance for catalytic hydropyrolysis of beech wood in fluid bed reactor with sulfided CoMo, NiMo and Mo as catalysts. (Catalyst used: 50.0 g catalyst, feed time: 3.5 hours, Pressure 26 bar, H_2 flow: 82 NL/min, N_2 flow: 5 NL/min, and H_2S conc: 460 ppm)

Test:	CoMo	NiMo	Mo
Test conditions			
Hydropyrolysis Temp. (°C)	451	451	452
Feeding rate (g/h)	275	271	275
Yields (wt. daf %)			
Gas	26.1	28.2	23.3
Char and coke	13.3	13.2	13.5
Aqueous phase	33.3	33.4	33.6
Organic phase	17.7	16.5	20.0
C_{4+} in the gas	7.5	7.8	6.4
Organics + C_{4+}	25.2	24.3	26.4
Mass balance	97.8	99.1	96.7
Carbon recovery (%)			
C_1-C_3	19	20	17
C_{4+}	13	13	11
CO+CO_2	11	12	9.3
Char	Na	Na	Na
Organic phase	26	24	28
Aqueous phase	3.2	2.8	4.2
C_{4+} + organic phase	39	37	39
Organic phase composition			
Water (wt.%)	3.3	2.6	4.1
C (wt.% db) [a]	81	80	79
H (wt.% db)	9.39	9.44	9.26
O (wt.% db)	9.0	10.2	11.7
S (wt.% db)	0.22	0.26	0.38
Organic phase density			
Density at 40°C (g/ml)	0.9428	0.9396	0.9560
Aqueous phase carbon content			
C (wt.%)	4.3	3.7	5.6
Gas composition (wt.% daf)			
CO	3.5	7.6	4.8
CO_2	9.2	9.4	9.5
C_1-C_3	10.3	11.2	8.9
C_{4+}	7.5	7.8	6.4

[a]Calculated by difference

5.3.1 Product distribution

The product distribution for three experiments using the CoMo, NiMo and Mo as catalysts at similar reaction conditions is shown in Figure 5.2. The combined char and coke yield varied between 13.2 and 13.5 wt.% daf, thus the difference in char and coke yield was not significant, which indicates that the char yield is not influenced by the promoter. However, a significant difference in the total gas yield (between 23.3 and 28.2 wt.% daf) was observed. The C_1-C_3 yield varied between 8.9 and 11.2 wt.% daf and was highest for the NiMo catalyst and lowest for the Mo catalyst. A similar trend was observed for the total CO and CO_2 yield, which was 17.0 wt.% daf for the NiMo, 15.8 wt.% for the CoMo, and 14.4 wt.% daf for the Mo. Interestingly, the CO_2 yield was almost the same for all catalysts (9.2-9.5 wt.% daf), thus the differences was due to changes in

the CO yield (4.8-7.6 wt.% daf), indicating differences in the catalyst's decarbonylation activity. However, the CO could also be formed through decarboxylation followed by reverse water gas shift. It can therefore be assumed that the NiMo catalyst has the highest decarbonylation/decarboxylation activity.

The C_2-C_3 paraffins yield for the NiMo catalyst (4.6 wt.% daf) was significantly higher than for the CoMo (3.1 wt.% daf), and Mo (2.8 wt.% daf), while the olefins yield was lower for the NiMo catalyst (2.6 wt.% daf) than for the CoMo (3.6 wt.% daf) and Mo catalyst (3.1 wt.% daf), see supplementary information Figure D.4. Thus the paraffins to olefins ratio was 1.83 for the NiMo, but 0.90 for both the CoMo and Mo catalysts, showing that the NiMo catalyst had the highest hydrogenation activity, which is in agreement with experiments using 2-ethylphenol as a model components at significantly lower temperatures (340°C) and higher pressures (70 bar) [25].

The aqueous phase yield varied between 33.3 and 33.6 wt.% daf, which is the same for all catalysts within the experimental uncertainty. The highest observed condensable organics yield was 26.4 wt.% daf for the Mo and the lowest was 24.3 wt.% daf for the NiMo. Thus, an inverse relationship between the gas yield and condensable organics yield was observed, as opposed to our previous study where the temperature in the fluid bed reactor was varied and an inverse relationship between the gas and char yield was observed [29]. This shows that the char yield is mainly influenced by the process conditions [29] and the condensable organic yield is mainly influenced by the catalyst properties, while the gas yield is very dependent on both the process conditions and the catalyst properties.

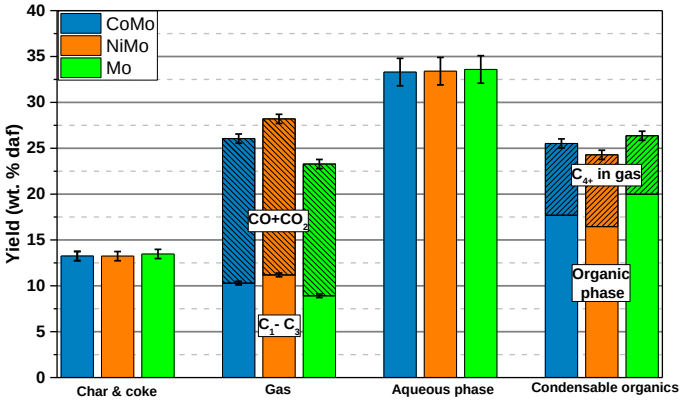

Figure 5.2 Product distribution for catalytic hydrolysis of beech wood using sulfided CoMo, NiMo and Mo as catalyst. Conditions: Fluid bed temperature: 451-452°C, total pressure: 26 bar, biomass feeding rate: 271-275 g/h, biomass used: 946-964 g, H_2 flow: 82 NL/min, N_2 flow: 5 NL/min, and H_2S conc: 460 ppm.

The difference between using sulfided CoMo, NiMo and Mo supported on $MgAl_2O_4$ has also been studied for HDO of ethylene glycol in a continuous flow setup by our group [17]. It was observed that Mo had the lowest cracking activity, but that the cracking activities of the CoMo and NiMo were similar. The difference in the relative cracking activity for the CoMo and NiMo catalysts in this study and the study conducted in the fixed bed setup [17] is probably because a simple molecule (ethylene glycol) was used in the flow setup, while the real biomass used here is significantly more complex. Laurent et al. [33] also studied the difference between sulfided CoMo and NiMo catalyst for HDO of pyrolysis model compounds in a batch reactor and found that the NiMo catalysts had the highest decarboxylation activity. Krause et al. [12–16] studied the hydrodeoxygenation of different model compounds with sulfided CoMo and NiMo catalysts. They also

found that the NiMo catalyst had the highest hydrogenation activity and carboxylation/carbonylation activity. Thus the results obtained in this study are in agreement with the HDO literature.

The CO to CO_2 molar ratio for the CoMo was 1.1, while in our previous hydropyrolysis study, where a commercial $CoMo/MgAl_2O_4$ was used in the fluid bed reactor, the CO to CO_2 molar ratio was 3.1 [29]. However, the commercial $CoMo/MgAl_2O_4$ had a higher activity, the oxygen content in the condensed organic phase was only 1.8 wt.%, compared to 9.0 wt.% for the CoMo catalyst tested in this study. Thus, the difference in CO to CO_2 ratio is most likely, because the more active commercial catalyst almost establishes the water gas shift equilibrium (see supplementary information Figure D.5).

5.3.2 Chemical composition of the condensed liquids

The chemical composition of the condensed organic phases is shown in Table 5.2. The oxygen content in the condensed organic phase for the CoMo catalyst was 9.0 wt.% db, 10 wt.% db for the NiMo, and 12 wt.% db for the Mo catalyst, thus indicating that the deoxygenation activity of the catalysts followed the trend: CoMo>NiMo>Mo. The carbon efficiency for the C_{4+} organics is 39 % for both the CoMo and the Mo, but only 37 % for the NiMo, thus the trend for the carbon efficiency is: CoMo≈Mo>NiMo. Furthermore, since the oxygen content in the produced organics is lower for the CoMo compared to the Mo, the CoMo catalyst is considered to be favorable.

The organic phase from the experiment with the NiMo catalyst had a slightly higher hydrogen concentration (9.44 wt.% db), than the CoMo (9.39 wt.% db) and Mo (9.26 wt.% db), however the difference is within the experimental uncertainty. The density of the organic phase was also lower using the NiMo (0.9396 g/ml), compared to when the CoMo (0.9428 g/ml) and the Mo (0.9560 g/ml) were used. The lower density is most likely due to the observed cracking activity for the NiMo.

The concentration of sulfur in the condensed organics, when the Mo catalyst was used, was 0.38 wt.% db, which is significantly higher than when the CoMo (0.22 wt.% db) and the NiMo (0.26 wt.% db) were used. Since the beech wood only contained 43 wt.-ppm S most of the sulfur in the organic phase must come from incorporation of S from the H_2S in the gas phase, through the activity of the sulfided catalysts. In order to obtain a better understanding of the sulfur containing species in the condensed organics, the samples were analyzed with sulfur specific GC-AED, see Figure 5.3 (a detailed list of the detected compounds is shown in supplementary information tables D.4-D.6). This showed that there was between 382 and 572 ppm H_2S dissolved in the samples, despite the N_2 stripping procedure employed. The main sulfur containing molecules identified in the organic phase were thiols, thiophenes, and benzothiophenes, including dibenzothiophenes. Methyl-ethylsulfide and dimethyl disulfide (DMDS) were also detected in the organic phase, but a large fraction of the sulfur compounds was not identified. Since the applied temperature in the fluid bed reactor is close to the temperature used in fluid catalytic cracking (FCC) [34,35], it is possible that the sulfur from the H_2S is incorporated into the organics by similar reactions routes as in FCC. The concentration of thiophenes was significantly higher from the experiment with the Mo catalyst, Figure 5.3, than from the experiments with the CoMo, and NiMo indicating that hydrodesulfurization also takes place in the fluid bed reactor. The concentration of thiols was 23 wt-ppm S when the NiMo catalyst was used and 55 and 88 wt-ppm S when the CoMo and Mo was used, respectively. This is probably because of the higher hydrogenation activity of the NiMo catalyst, which decreased the concentration of olefins, thus minimizing the incorporation of H_2S through recombination between olefins and H_2S [36–39]. Alternatively the thiols could have been formed from the alcohols through a nucleophilic substitution [12,16]. It should be noted that in order to minimize the cracking activity the activity for these catalysts were purposely fairly low, which is part of the reason for the high sulfur content in the condensed organics. In our previous work we showed that it is possible to reduce

the sulfur concentration in the organic phase to 0.06 wt.% by using a second HDO reactor [29]. Since sulfur compounds are commonly encountered in petrochemical refining and removed by hydrotreating the high sulfur concentration is of minor concern.

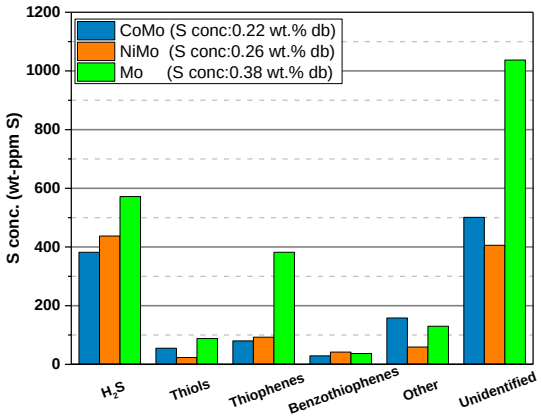

Figure 5.3 Concentration of sulfur species in the condensed organic phase from experiments with the CoMo, NiMo, and Mo catalyst analyzed with S specific GC-AED. Conditions: Fluid bed temperature: 451-452°C, pressure: 26 bar, biomass feeding rate: 271-275 g/h, biomass used: 946-964 g, H_2 flow: 82 NL/min, N_2 flow: 5 NL/min, and H_2S conc: 460 ppm.

The composition of the condensed organic phases was studied with GC×GC-ToF/MS or –FID and concentrations of paraffins (Par), naphthenes (Naph), monoaromatics (mAro), diaromatics (diAro), triaromatics (triAro), and larger aromatics (tetAro+), oxygenated aliphatics (O-Ali), phenols (PhOH), dihydroxybenzenes (Ph(OH)2) and oxygenated di- and larger aromatics (O-Aro) were measured, see Figure 5.4. Comparing the CoMo, Figure 5.4(A), with the NiMo, Figure 5.4(B), the concentration of paraffins, naphthenes, and oxygenated aliphatics are almost the same. However, the concentration of diaromatics and larger aromatics were 16 % for the CoMo and 13 % for the NiMo. This is most likely because the NiMo catalyst mainly removes oxygen (and sulfur) by first hydrogenating the aromatic ring and then removing the oxygen (HYD pathway) [25,28], while the CoMo catalyst removes the oxygen without first hydrogenating the ring (DDO pathway) [18,25–27]. At the applied reaction conditions the monoaromatics-naphthenes equilibrium is shifted towards aromatics [29], which makes it more difficult for the NiMo catalyst to remove the oxygen resulting in a slightly higher phenols yield. Thus, the lower concentration of di- and larger aromatics and higher concentration of monoaromatics and phenols for the NiMo catalyst is probably due to its higher hydrogenation activity, since hydrogenation of di- and higher aromatics is not equilibrium limited. Furthermore, the number of carbon atoms in the molecules is lower for the NiMo than the CoMo catalyst, due to its higher cracking activity.

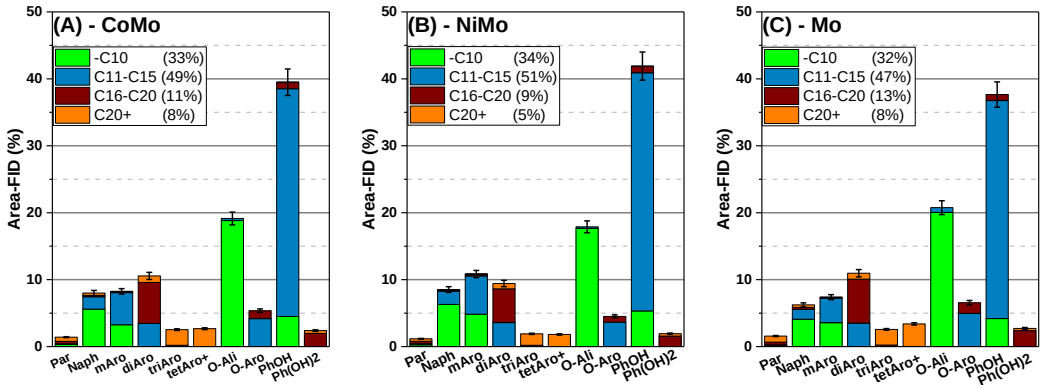

Figure 5.4 The composition of the condensed organic phases using the CoMo catalyst (A), the NiMo catalyst (B), and the Mo catalyst (C). Conditions: Fluid bed temperature: 451-452°C, pressure: 26 bar, biomass feeding rate: 271-275 g/h, biomass used: 946-964 g, H_2 flow: 82 NL/min, N_2 flow: 5 NL/min, and H_2S conc: 460 ppm.

The organic phase from the experiment with the Mo catalyst, Figure 5.4(C), contains more oxygenated aliphatics (21 %) than for the CoMo (19 %) and NiMo (18 %) catalysts. This indicates that Mo has a lower HDO activity than the CoMo and NiMo, as expected. The concentration of phenols is lowest for the Mo, however, this could be due to a higher concentration of other oxygenated hydrocarbons, which decreases the relative FID-area for the phenols. The lower concentration of naphthenes shows that the Mo has the lowest hydrogenation activity. Traces (<0.2 % area-FID) of sterols were detected in all the condensed organic phases.

The carbon recovery and the composition of the aqueous phases are shown in Table 5.2. The carbon recovery in the aqueous phase was 2.8 % for the NiMo catalyst and 3.2 % for the CoMo catalyst, which is not a significant difference. The higher carbon recovery for Mo (4.2 %) in the aqueous phase is probably due to the higher oxygen content in the organic phase which makes it more miscible with water.

The composition of the aqueous phases was similar for the three catalysts, see Figure 5.5. It mainly consisted of alcohols (66-69 %), which was mostly methanol and ethanol (see supplementary information tables D.7-D.9), and ketones (18-20 %) in the C_2-C_5 range. The amount of phenol was between 2.1 and 6.7 %, the amount of furans was 0.43 % independent of the type of catalyst, and the amount of acids was 6.9 % for the Mo, but only 3.3 and 3.8 % for the NiMo and the CoMo, respectively. Acetic acid was the only acid or ester detected in the aqueous phase in the experiment with the NiMo and CoMo, while butyl formate was also observed for the Mo. The observed acetic acid indicate, that if catalytic hydropyrolysis is conducted without the additional HDO reactor, the downstream equipment should be acid resistant. Dabros [40] tested hydrodeoxygenation of acetic acid over a NiMo catalyst and observed plugging above the catalyst bed after 2 h on stream due to coke formation. Therefore, it would be desirable to remove as much of the acetic acid as possible during the initial catalytic hydropyrolysis step.

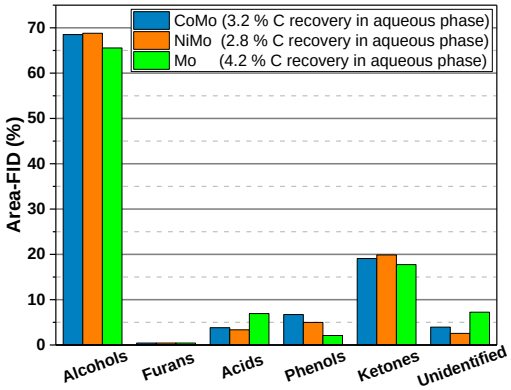

Figure 5.5 Composition of the aqueous phase when the CoMo (A), NiMo (C), and Mo(C) catalyst was used. Conditions: Fluid bed temperature: 451-452°C, pressure: 26 bar, biomass feeding rate: 271-275 g/h, biomass used: 946-964 g, H_2 flow: 82 NL/min, N_2 flow: 5 NL/min, and H_2S conc: 460 ppm.

5.3.3 Characterization of the catalysts

5.3.3.1 Raman spectroscopy of the oxide catalyst precursors

Raman spectroscopy was used in order to determine the phases and dispersion for the oxide precursors, see Figure 5.6. Three spectra were recorded for each sample at different spots. The slight variations between the spectra for the same catalyst sample indicate some degree of heterogeneity. For the CoMo catalyst the bands for the carrier $MgAl_2O_4$ are observed at 760, 673 and 405 cm^{-1}. The peak observed close to 872 cm^{-1} can be assigned to hydrated $CoMoO_4$ and would represent a Mo-O distance of 1.75 Å, according to the observed relationship for Mo-O stretching frequencies and bond distances proposed by Hardcastle and Wachs [41]. This could be a Mo-O-X (X = carrier or active metal) entity. The broad convoluted peak observed at 923-945 cm^{-1} in all the samples corresponds to a Mo-O distance of around 1.7 Å and could come from terminal Mo=O units. The presence of crystalline MoO_3, which exhibit a sharp Mo=O stretching mode at 992 cm^{-1}, can be ruled out and thus the peak assembly probably originated from hydrated, amorphous MoO_x phases [42]. Dabros et al. [17] observed peaks at 315 and 910 cm^{-1} and assigned them to tetrahedral monomolybdate, thus the observed peak at 320 and 923-945 cm^{-1} could be this species. The monolayer coverage of Mo on Al_2O_3 is around 4.5 Mo/nm^2 [42], which means that these samples exhibit around 80% of a monolayer coverage. Therefore, some interaction between molybdenum oxide species would be expected and the existence of truly isolated sites is not likely. Since the $MgAl_2O_4$ phase is quite porous, capillary condensation of water inside the pores is likely to occur, and the observed species are probably mixtures of e.g. MoO_4^{2-}(aq) (isolated, tetrahedral), $Mo_7O_{24}^{6-}$ and $Mo_8O_{26}^{4}$(aq) (the two latter both polymerized octahedral) dissolved in the ambient air exposed calcined samples. MoO_4^{2-} would contribute at 897, 837 and 317 cm^{-1}, $Mo_7O_{24}^{6-}$ at 943, 903,570,362 and 210 cm^{-1}, while $Mo_8O_{26}^{4-}$ at 965, 925, 590, 370 and 230 cm^{-1} [42,43]. Given the relatively high MoO_X surface density combined with the major contributions of the 940-960 cm^{-1} features it seems likely that the observed species are hydrated pre-cursors for polymeric molybdenum oxides. Co_3O_4 would have its major contribution at 692 cm^{-1}, which is not observed, which indicates that Co is mainly present as hydrated $CoMoO_4$.

For the NiMo catalyst the 954 cm^{-1} band coincides with α-NiMoO4 and the 878 cm^{-1} band with its hydrated form. No obvious peaks of crystalline MoO_3 (992, 820, 667 cm^{-1}) were observed. However, it is possible that

the peak at 326 and 954 cm^{-1} is due to a mixture of the previously mentioned hydrated molybdates. No pure Ni oxide phase was observed, indicating that the Ni was located as $NiMoO_4$.

The bands observed at 316 and 957 cm^{-1} for the Mo catalyst can be assigned to a hydrated MoO_x phase and again no peaks of crystalline MoO_3 (992, 820, 667 cm^{-1}) were observed.

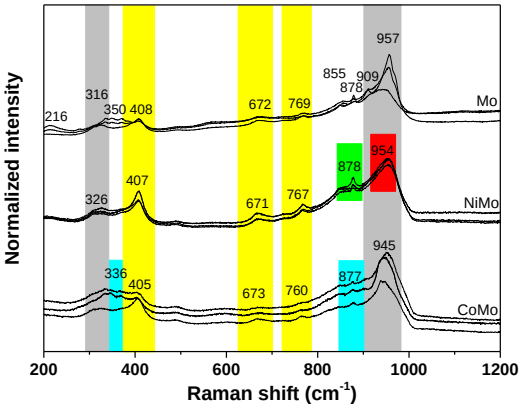

Figure 5.6 Baseline corrected Raman spectra of CoMo, NiMo, and Mo in the oxide phase (calcined, not dehydrated). The Raman bands were assigned to hydrated, MoO_x (gray), hydrated $CoMoO_4$ (cyan), alfa $NiMoO_4$ (red), hydrated $NiMoO_4$ (green), and $MgAl_2O_4$ (yellow).

5.3.3.2 Characterization of the spent catalysts

The carbon and potassium contents on the spent and fresh catalysts were measured with SEM combined with EDS. In order to account for the carbon signal from the carbon tabs the actual carbon content on the catalysts were calculated by subtracting the measured carbon content on the fresh catalysts from the measured carbon content on the spent catalysts, and the results is shown as a function of the acceleration voltage in Figure 5.7. With increased acceleration voltage the electron beam penetrates slightly deeper into the sample, therefore at low acceleration voltages (3 kV) the surface concentration on the catalyst particles is measured, while at high acceleration voltages (15 kV) the concentration slightly into the particle is measured. The estimated interaction depth ranges from 170 to 1600 nm with acceleration voltage between 3 and 15 kV, respectively, see Table D.2. Due to the relatively high molar mass of potassium it is not possible to excite its core electrons at 3 kV (K-K_α line at 3.31 keV). The carbon content on the spent Mo catalyst was between 5.0 and 5.5 wt.%, while it was between 0.9 and 3.3 wt.% for the spent CoMo and NiMo catalysts (Figure 5.7(A)), showing that the lower hydrodeoxygenation activity for the Mo catalyst lead to an increased degree of coking. The carbon content on the spent NiMo and CoMo decreased with increasing accelerating voltage, showing that more coke was located at the surface of the catalysts. The potassium content on the spent catalysts (Figure 5.7(B)), was between 0.3 (in the bulk) and 2.4 wt.% (at the surface) and no significant difference between the catalysts was observed. Potassium was not detected on the fresh catalysts (See supplementary information Table D.10), showing that the potassium has been transferred from the biomass to the surface of the catalysts. Potassium is a known poison for HDO catalysts [39,44], thus the transfer of potassium from the biomass to the catalyst could potentially deactivate it. This should be investigated further in the future by longer experiments and/or tests with catalysts pre-impregnated with potassium.

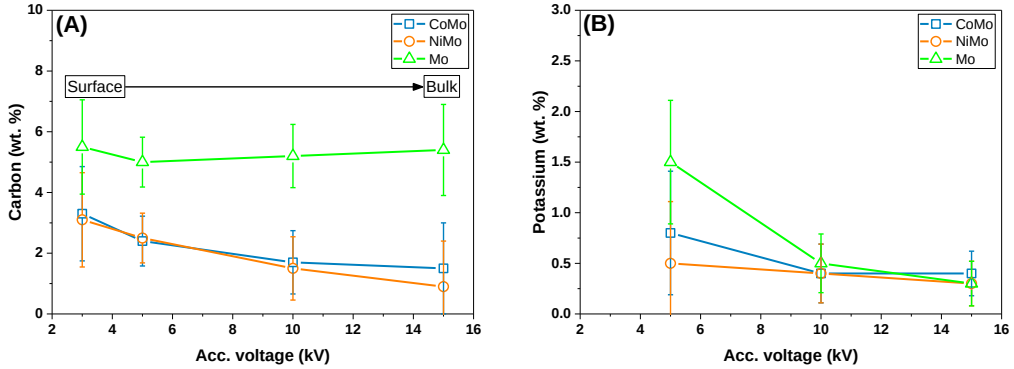

Figure 5.7 Carbon (A) and potassium (B) content on the spent measured with SEM combined with EDS. The carbon and potassium for the fresh and spent catalysts are shown in supplementary information Table D.10. Conditions: Fluid bed temperature: 451-452°C, pressure: 26 bar, biomass feeding rate: 271-275 g/h, biomass used: 946-964 g, H_2 flow: 82 NL/min, N_2 flow: 5 NL/min, and H_2S conc: 460 ppm.

Figure 5.8 shows HAADF-STEM images of the spent CoMo, NiMo, and Mo catalysts and reveal nanometer-sized slab structures of bright contrast distributed on the surface of larger support grains (about 10-30 nm in size) of less image contrast. Occasionally, the slab structures were found with 2 or more layers (up to 4) stacked with an interlayer-distance of 0.62 nm, consistent with a MoS_2 (001) spacing (Figure 5.8(A)). The bright-contrasted slab structures are therefore attributed to single, double- or multilayer layer MoS_2 nanocrystals viewed with the (001) basal plane along the electron beam direction, and situated with the basal plane along the surfaces of the larger $MgAl_2O_4$ grains, as previously reported [45]. Based on 10 images per catalyst, and measuring between 111 and 128 slabs per sample, the MoS_2 nanocrystals were predominantly found as single layer structures (>98%), and the slab lengths were measured (Figure 5.8(E)-(F)). The slab lengths were between 1 and 5.5 nm with an average between 2.8 and 2.9 nm for all the catalysts. Thus the slab size and distribution was similar for all the spent catalysts, which indicates that the MoS_2 edge dispersions of the tested catalysts were comparable. Furthermore, the single layer structure indicates that the catalysts were in the less active type I CoMoS phase [31], which is most likely the reason for their relatively low activity.

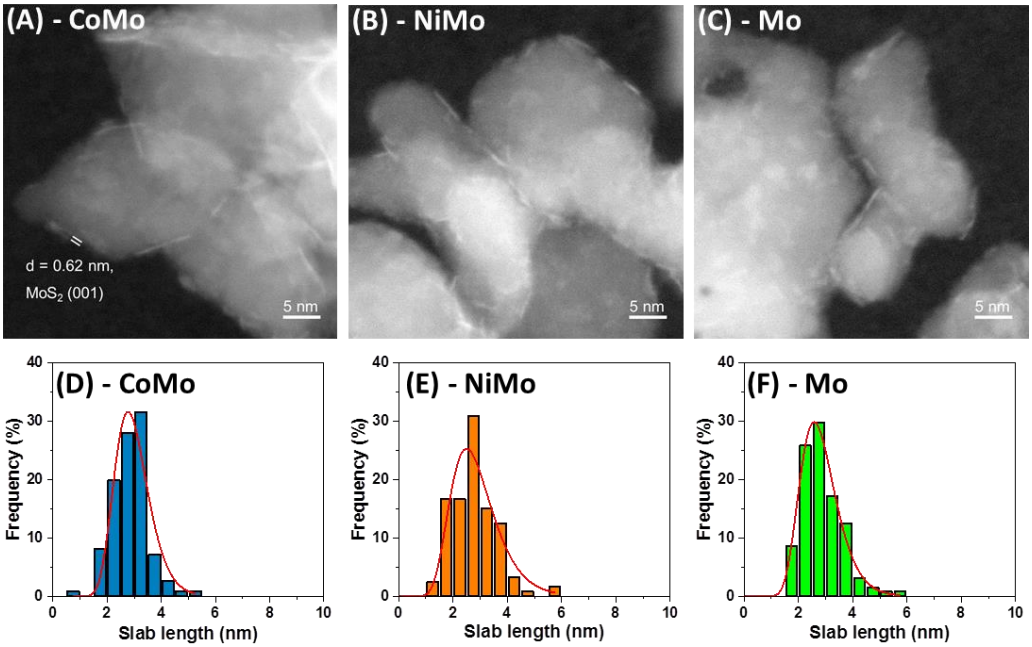

Figure 5.8 HAADF-STEM images of CoMo (A), NiMo (B), and Mo (C), and single layer slab size distribution of CoMo (D), NiMo (E), and Mo (F). The images in (A)-(C) were contrast adjusted (gamma) to improve visibility. Conditions: Fluid bed temperature: 451-452°C, pressure: 26 bar, biomass feeding rate: 271-275 g/h, biomass used: 946-964 g, H_2 flow: 82 NL/min, N_2 flow: 5 NL/min, and H_2S conc: 460 ppm.

The distribution of the promoter, molybdenum and sulfur on the spent catalysts is shown on the elemental maps in Figure 5.9 (For single element EDS maps see supplementary material Figures D.6-D.8). The molybdenum (and sulfur) is well distributed on the $MgAl_2O_4$ support for the three catalysts, consistent with a uniform and high degree of MoS_2 dispersion (Figure 8). Furthermore, the promoter (Co/Ni) is also highly dispersed and mainly located the same places as molybdenum, as shown in Figure 5.9(B) and Figure 5.9(E), suggesting successful incorporation of promoters into the MoS_2 structures in the so-called CoMoS or NiMoS phase [24]. Thereby, the similarity in MoS_2 slab sizes of the three catalysts and the highly distributed promoters represents a good data set for directly comparing the effect of the promoters. Besides the expected (promoted) MoS_2 structures, calcium particles were observed on all the spent catalysts. The calcium originates from the biomass ash. However, since calcium was only detected as larger particles (40-200 nm), it has only blocked a low fraction of the catalyst surface, thus it can be assumed that the calcium only has a small influence on the catalytic activity. Potassium was likewise also observed on all the spent catalysts and was well-distributed on the particles, which might have decreased the catalyst activity [39,44]. Thus the results from the STEM-EDS images supports the results obtained from SEM-EDS.

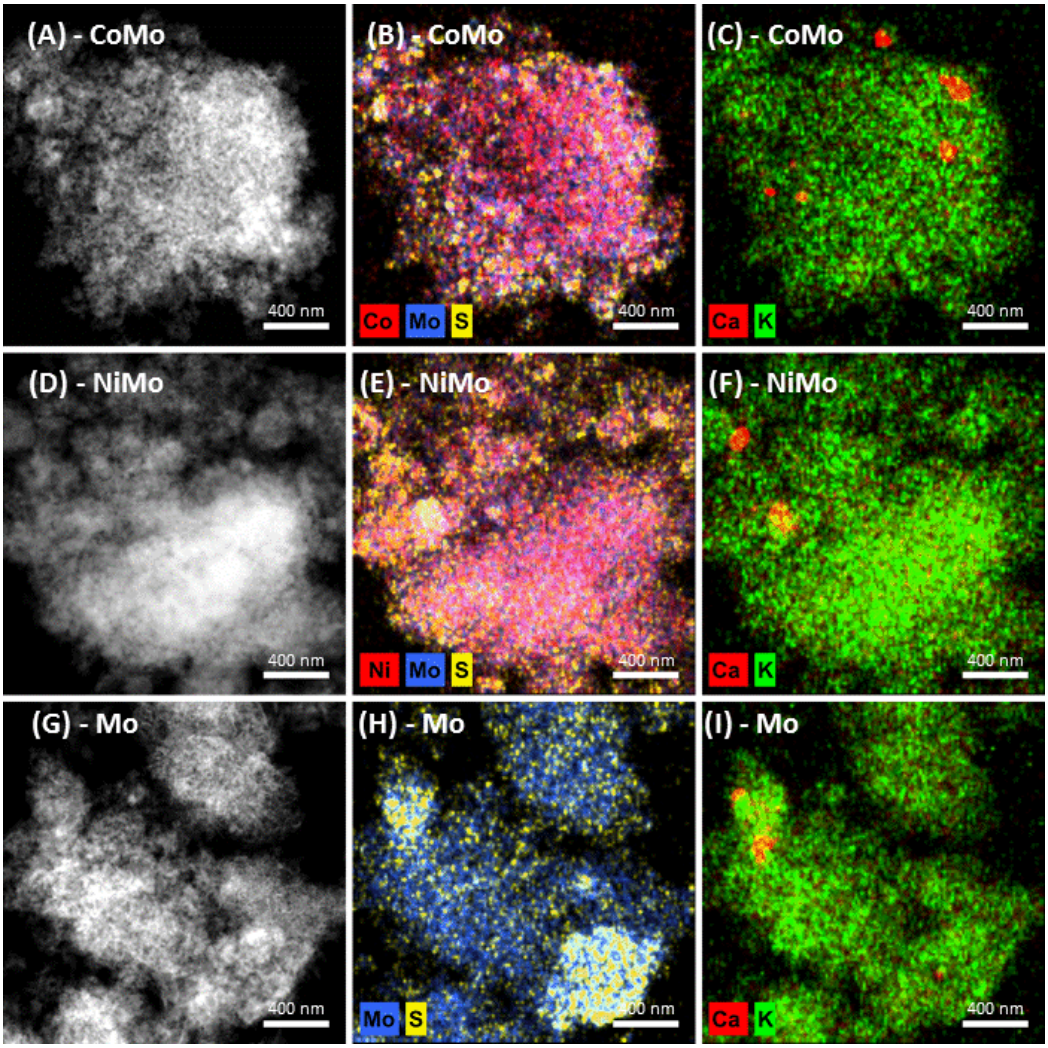

Figure 5.9 STEM-HAADF micrograph of molybdenum, cobalt, sulfur, potassium, and calcium EDS element distribution on CoMo (A-C), molybdenum, nickel, sulfur, potassium and calcium EDS element distribution on NiMo (D-F), and molybdenum, sulfur, potassium and calcium EDS element distribution on Mo (G-I). Conditions: Fluid bed temperature: 451-452°C, pressure: 26 bar, biomass feeding rate: 271-275 g/h, biomass used: 946-964 g, H_2 flow: 82 NL/min, N_2 flow: 5 NL/min, and H_2S conc: 460 ppm.

5.4 Conclusion

Catalytic hydropyrolysis of beech wood has been conducted in a fluid bed reactor at 450°C and 26 bar with three different sulfided catalysts: CoMo/$MgAl_2O_4$, NiMo/$MgAl_2O_4$, and Mo/$MgAl_2O_4$. BET surface area, elemental analysis, Raman spectroscopy and STEM images of the spent catalysts showed that the three catalysts had identical composition and morphology, therefore the influence of the promoters on catalytic activity

and selectivity could be investigated. The char and aqueous phase yields were not affected by the applied promoter type. The char and aqueous phase yields were not affected by the type of catalyst. The NiMo/$MgAl_2O_4$ catalyst had the highest cracking, decarbonylation/decarboxylation, and hydrogenation activity, while the Mo/$MgAl_2O_4$ catalyst had the lowest. The highest condensed organics and C_{4+} yield was obtained with the Mo/$MgAl_2O_4$ (26.4 wt.% daf) and the lowest with the NiMo/$MgAl_2O_4$ (24.3 wt.% daf). However, the organic phase from the experiment with the Mo/$MgAl_2O_4$ had an oxygen content of 12 wt.% db, while it was 10 wt.% db and 9.0 wt.% db when the NiMo/$MgAl_2O_4$ and CoMo/MgAl2O4 were used, respectively. This difference, was ascribed to the main reaction pathway, hydrogenation for the NiMo and direct deoxygenation for the CoMo, for the deoxygenation of phenols. The carbon recovery (C_{4+} and condensed organics) was 39 % for both the CoMo/$MgAl_2O_4$ and Mo/$MgAl_2O_4$, but 37 % for the NiMo/$MgAl_2O_4$. Therefore, this study indicates that CoMo/$MgAl_2O_4$ is favorable for use in catalytic hydropyrolysis compared to NiMo/$MgAl_2O_4$ and Mo/$MgAl_2O_4$.

The carbon content on the spent Mo/$MgAl_2O_4$ catalyst was higher than on the CoMo/$MgAl_2O_4$ and NiMo/$MgAl_2O_4$, which was probably because of its lower activity, which increased the degree of coking. Calcium and potassium were transferred from the biomass ash to the catalysts under reaction conditions. Calcium was observed as larger (40-200 nm) single particles, which only had a minor impact on the catalytic activity. Potassium was highly dispersed on the catalyst particles, which has potentially decreased the catalytic activity. The transfer of alkali metals from the biomass to the catalyst could be a serious problem in full scale applications, and should be further investigated in order to better understand how the alkali metals are transferred and their effect on the catalytic activity. Such investigations are on-going in our laboratories.

Acknowledgments

This work is part of the project “Hydrogen assisted catalytic pyrolysis for green fuels” conducted at The Department of Chemical and Biochemical Engineering at the Technical University of Denmark (DTU). The work was supported by The Danish Council for Strategic Research (now Innovation Fund Denmark, project 1305-00015B), The Programme Commission on Sustainable Energy and Environment. Funding from DTU is also gratefully acknowledged. The authors also acknowledge Aino Nielsen (Haldor Topsøe A/S) for technical assistant with the Raman spectroscopy, the Inorganic Analysis Department at Haldor Topsøe A/S for the elemental analysis of the fresh oxide precursors by inductive coupled plasma optical emission spectroscopy (IPC-OES), and the Organic Analysis Department at Haldor Topsøe A/S for analysis of the organic phase.

References

[1] T.L. Marker, L.G. Felix, M.B. Linck, M.J. Roberts, Integrated hydropyrolysis and hydroconversion (IH^2) for the direct production of gasoline and diesel fuels or blending components from biomass, Part 1: Proof of principle testing, Environ. Prog. Sustain. Energy. 31 (2012) 191–199. doi:10.1002/ep.10629.

[2] T.L. Marker, L.G. Felix, M.B. Linck, M.J. Roberts, P. Ortiz-Toral, J. Wangerow, Integrated hydropyrolysis and hydroconversion ($IH^{2®}$) for the direct production of gasoline and diesel fuels or blending components from biomass, Part 2: Continuous testing, Environ. Prog. Sustain. Energy. 33 (2014) 762–768. doi:10.1002/ep.11906.

[3] M.R. Hurt, J.C. Degenstein, P. Gawecki, D.J. Borton II, N.R. Vinueza, L. Yang, R. Agrawal, W.N. Delgass, F.H. Ribeiro, H.I. Kenttämaa, On-line mass spectrometric methods for the determination of the primary products of fast pyrolysis of carbohydrates and for their gas-phase manipulation, Anal.

Chem. 85 (2013) 10927–10934. doi:10.1021/ac402380h.

[4] E. Maleche, R. Glaser, T. Marker, D. Shonnard, A preliminary life cycle assessment of biofuels produced by the IH^{2} ™ process, Environ. Prog. Sustain. Energy. 33 (2014) 322–329. doi:10.1002/ep.11773.

[5] J. Fan, J. Gephart, T. Marker, D. Stover, B. Updike, D.R. Shonnard, Carbon Footprint Analysis of Gasoline and Diesel from Forest Residues and Corn Stover using Integrated Hydropyrolysis and Hydroconversion, ACS Sustain. Chem. Eng. 4 (2016) 284–290. doi:10.1021/acssuschemeng.5b01173.

[6] D.C. Dayton, J. Carpenter, J. Farmer, B. Turk, R. Gupta, Biomass hydropyrolysis in a pressurized fluidized bed reactor, Energy & Fuels. 27 (2013) 3778–3785. doi:10.1021/ef400355t.

[7] D.C. Dayton, J. Hlebak, J.R. Carpenter, K. Wang, O.D. Mante, J.E. Peters, Biomass hydropyrolysis in a fluidized bed reactor, Energy & Fuels. 30 (2016) 4879–4887. doi:10.1021/acs.energyfuels.6b00373.

[8] K. Wang, D.C. Dayton, J.E. Peters, O.D. Mante, Reactive catalytic fast pyrolysis of biomass to produce high-quality bio-crude, Green Chem. 19 (2017) 3243–3251. doi:10.1039/C7GC01088E.

[9] D.P. Gamliel, L. Wilcox, J.A. Valla, The effects of catalyst properties on the conversion of biomass via catalytic fast hydropyrolysis, Energy & Fuels. 31 (2017) 679–687. doi:10.1021/acs.energyfuels.6b02781.

[10] D.P. Gamliel, G.M. Bollas, J.A. Valla, Bifunctional Ni-ZSM-5 catalysts for the pyrolysis and hydropyrolysis of biomass, Energy Technol. 5 (2017) 172–182. doi:10.1002/ente.201600136.

[11] D.P. Gamliel, G.M. Bollas, J.A. Valla, Two-stage catalytic fast hydropyrolysis of biomass for the production of drop-in biofuel, Fuel. 216 (2018) 160–170. doi:10.1016/j.fuel.2017.12.017.

[12] O.İ. Şenol, E.-M. Ryymin, T.-R. Viljava, A.O.I. Krause, Reactions of methyl heptanoate hydrodeoxygenation on sulphided catalysts, J. Mol. Catal. A Chem. 268 (2007) 1–8. doi:10.1016/j.molcata.2006.12.006.

[13] O.İ. Şenol, T.-R. Viljava, A.O.I. Krause, Hydrodeoxygenation of aliphatic esters on sulphided NiMo/γ-Al_2O_3 and CoMo/γ-Al2O3 catalyst: The effect of water, Catal. Today. 106 (2005) 186–189. doi:10.1016/j.cattod.2005.07.129.

[14] O.İ. Şenol, T.-R. Viljava, A.O.I. Krause, Effect of sulphiding agents on the hydrodeoxygenation of aliphatic esters on sulphided catalysts, Appl. Catal. A Gen. 326 (2007) 236–244. doi:10.1016/j.apcata.2007.04.022.

[15] E.-M. Ryymin, M.L. Honkela, T.-R. Viljava, A.O.I. Krause, Competitive reactions and mechanisms in the simultaneous HDO of phenol and methyl heptanoate over sulphided NiMo/γ-Al_2O_3, Appl. Catal. A Gen. 389 (2010) 114–121. doi:10.1016/j.apcata.2010.09.010.

[16] A. Gutierrez, E.-M. Turpeinen, T.-R. Viljava, O. Krause, Hydrodeoxygenation of model compounds on sulfided CoMo/γ-Al2O3 and NiMo/γ-Al2O3 catalysts; Role of sulfur-containing groups in reaction networks, Catal. Today. 285 (2017) 125–134. doi:10.1016/j.cattod.2017.02.003.

[17] T.M.H. Dabros, A. Gaur, D.G. Pintos, P. Sprenger, M. Høj, T.W. Hansen, F. Studt, J. Gabrielsen, J.-D. Grunwaldt, A.D. Jensen, Influence of H2O and H2S on the composition, activity, and stability of sulfided Mo, CoMo, and NiMo supported on MgAl2O4 for hydrodeoxygenation of ethylene glycol, Appl. Catal. A Gen. 551 (2018) 106–121. doi:10.1016/j.apcata.2017.12.008.

[18] V.N. Bui, D. Laurenti, P. Afanasiev, C. Geantet, Hydrodeoxygenation of guaiacol with CoMo catalysts. Part I: Promoting effect of cobalt on HDO selectivity and activity, Appl. Catal. B Environ. 101 (2011) 239–245. doi:10.1016/j.apcatb.2010.10.025.

[19] A. Centeno, E. Laurent, B. Delmon, Influence of the support of CoMo sulfide catalysts and of the addition of potassium and platinum on the catalytic performances for the hydrodeoxygenation of carbonyl, carboxyl, and guaiacol-type molecules, J. Catal. 154 (1995) 288–298.

doi:10.1006/jcat.1995.1170.

[20] M. Badawi, J.-F. Paul, S. Cristol, E. Payen, Guaiacol derivatives and inhibiting species adsorption over MoS_2 and CoMoS catalysts under HDO conditions: A DFT study, Catal. Commun. 12 (2011) 901–905. doi:10.1016/j.catcom.2011.02.010.

[21] T.N. Trinh, P.A. Jensen, K. Dam-Johansen, N.O. Knudsen, H.R. Sørensen, S. Hvilsted, Comparison of lignin, macroalgae, wood, and straw fast pyrolysis, Energy & Fuels. 27 (2013) 1399–1409. doi:10.1021/ef301927y.

[22] P. Raybaud, J. Hafner, G. Kresse, S. Kasztelan, H. Toulhoat, Structure, energetics, and electronic properties of the surface of a promoted MoS2 catalyst: An ab initio local density functional study, J. Catal. 190 (2000) 128–143. doi:10.1006/jcat.1999.2743.

[23] B.R.G. Leliveld, J.A.J. van Dillen, J.W. Geus, D.C. Koningsberger, M. de Boer, Structure and Nature of the Active Sites in CoMo Hydrotreating Catalysts. An EXAFS Study of the Reaction with Selenophene, J. Phys. Chem. B. 101 (1997) 11160–11171. doi:10.1021/jp9723933.

[24] H. Topsøe, B.S. Clausen, F.E. Massoth, Cataltsis - Science and Technology. Hydrotreating catalysis, Volume 11, Springer-Verlag, Berlin Heidelberg, Germany, 1996.

[25] C. Bouvier, Y. Romero, F. Richard, S. Brunet, Effect of H_2S and CO on the transformation of 2-ethylphenol as a model compound of bio-crude over sulfided Mo-based catalysts: propositions of promoted active sites for deoxygenation pathways based on an experimental study, Green Chem. 13 (2011) 2441–2451. doi:10.1039/c1gc15181a.

[26] V.N. Bui, D. Laurenti, P. Delichère, C. Geantet, Hydrodeoxygenation of guaiacol. Part II: Support effect for CoMoS catalysts on HDO activity and selectivity, Appl. Catal. B Environ. 101 (2011) 246–255. doi:10.1016/j.apcatb.2010.10.031.

[27] V.O.O. Gonçalves, S. Brunet, F. Richard, Hydrodeoxygenation of cresols over Mo/Al_2O_3 and $CoMo/Al_2O_3$ sulfided catalysts, Catal. Letters. 146 (2016) 1562–1573. doi:10.1007/s10562-016-1787-5.

[28] E. Schachtl, J.S. Yoo, O.Y. Gutiérrez, F. Studt, J.A. Lercher, Impact of Ni promotion on the hydrogenation pathways of phenanthrene on $MoS_2/\gamma\text{-}Al_2O_3$, J. Catal. 352 (2017) 171–181. doi:10.1016/j.jcat.2017.05.003.

[29] M.Z. Stummann, M. Høj, C.B. Schandel, A.B. Hansen, P. Wiwel, J. Gabrielsen, P.A. Jensen, A.D. Jensen, Hydrogen assisted catalytic biomass pyrolysis. Effect of temperature and pressure, Biomass and Bioenergy. 115 (2018) 97–107. doi:10.1016/j.biombioe.2018.04.012.

[30] S. Houssenbay, E. Payen, S. Kasztelan, J. Grimblot, Oxidic precursors of molybdena supported on nickel and magnesium aluminate hydrotreating catalysts, Catal. Today. 10 (1991) 541–560. doi:10.1016/0920-5861(91)80038-B.

[31] H. Topsøe, The role of Co-Mo-S type structures in hydrotreating catalysts, Appl. Catal. A Gen. 322 (2007) 3–8. doi:10.1016/j.apcata.2007.01.002.

[32] C. Wivel, R. Candia, B.S. Clausen, S. Mørup, H. Topsøe, On the catalytic significance of a CoMoS phase in CoMo Al2O3hydrodesulfurization catalysts: Combined in situ Mössbauer emission spectroscopy and activity studies, J. Catal. 68 (1981) 453–463. doi:10.1016/0021-9517(81)90115-9.

[33] E. Laurent, B. Delmon, Study of the hydrodeoxygenation of carbonyl, carboxylic and guaiacyl groups over sulfided $CoMo/\gamma\text{-}Al_2O_3$ and $NiMo/\gamma\text{-}Al_2O_3$ catalyst: II. Influence of water, ammonia and hydrogen sulfide, Appl. Catal. A Gen. 109 (1994) 97–115. http://www.sciencedirect.com/science/article/B6TF5-4489SG6-5/2/f4650b679b2d8629ce66e9a765da08b4.

[34] P. Leflaive, J.L. Lemberton, G. Pérot, C. Mirgain, J.Y. Carriat, J.M. Colin, On the origin of sulfur impurities in fluid catalytic cracking gasoline - Reactivity of thiophene derivatives and of their

possible precursors under FCC conditions, Appl. Catal. A Gen. 227 (2002) 201–215. doi:10.1016/S0926-860X(01)00936-X.

[35] A. Corma, C. Martínez, G. Ketley, G. Blair, On the mechanism of sulfur removal during catalytic cracking, Appl. Catal. A Gen. 208 (2001) 135–152. doi:10.1016/S0926-860X(00)00693-1.

[36] N. Dos Santos, H. Dulot, N. Marchal, M. Vrinat, New insight on competitive reactions during deep HDS of FCC gasoline, Appl. Catal. A Gen. 352 (2009) 114–123. doi:10.1016/j.apcata.2008.09.035.

[37] J.A. Anabtawi, S.A. Ali, M. Abdul Bari Siddiqui, S.M. Javaid Zaidi, Factors influencing the performance of naphtha hydro-desulfurization catalysts, in: 1996: pp. 225–234. doi:10.1016/S0167-2991(96)80023-1.

[38] X. Si, D. Xia, Y. Xiang, Y. Zhou, Effect of H2S on the transformation of 1-hexene over NiMoS/γ-Al2O3 with hydrogen, J. Nat. Gas Chem. 19 (2010) 185–188. doi:10.1016/S1003-9953(09)60054-2.

[39] P.M. Mortensen, D. Gardini, C.D. Damsgaard, J.-D. Grunwaldt, P.A. Jensen, J.B. Wagner, A.D. Jensen, Deactivation of Ni-MoS_2 by bio-oil impurities during hydrodeoxygenation of phenol and octanol, Appl. Catal. A Gen. 523 (2016) 159–170. doi:10.1016/j.apcata.2016.06.002.

[40] T.M.H. Dabros, A Step in Understanding and Optimizing Fuel Production from Solid Biomass PhD Thesis, Technical University of Denmark, Dept. of Chemical and Biochemical Engineering, 2017.

[41] F.D. Hardcastle, I.E. Wachs, Determination of molybdenum–oxygen bond distances and bond orders by Raman spectroscopy, J. Raman Spectrosc. 21 (1990) 683–691. doi:10.1002/jrs.1250211009.

[42] H. Hu, I.E. Wachs, Surface structures of supported molybdenum oxide catalysts. Characterization by raman and Mo L3-edge XANES, J. Phys. Chem. 99 (1995) 10897–10910. doi:10.1021/j100027a034.

[43] H. Jeziorowski, H. Knözinger, Raman and ultraviolet spectroscopic characterization of molybdena on alumina catalysts, J. Phys. Chem. 83 (1979) 1166–1173. doi:10.1021/j100472a012.

[44] P.M. Mortensen, D. Gardini, H.W.P. de Carvalho, C.D. Damsgaard, J.-D. Grunwaldt, P.A. Jensen, J.B. Wagner, A.D. Jensen, Stability and resistance of nickel catalysts for hydrodeoxygenation: Carbon deposition and effects of sulfur, potassium, and chlorine in the feed, Catal. Sci. Technol. 4 (2014) 3672–3686. doi:10.1039/c4cy00522h.

[45] L.P. Hansen, E. Johnson, M. Brorson, S. Helveg, Growth mechanism for single- and multi-layer MoS2 nanocrystals, J. Phys. Chem. C. 118 (2014) 22768–22773. doi:10.1021/jp5069279.

Chapter 6 Catalytic hydropyrolysis of biomass using supported CoMo catalysts – Effect of metal loading and support acidity

In this chapter the effect of the support acidity and the CoMo loading on the product distribution and composition are studied. The supplementary information can be found in Appendix E.

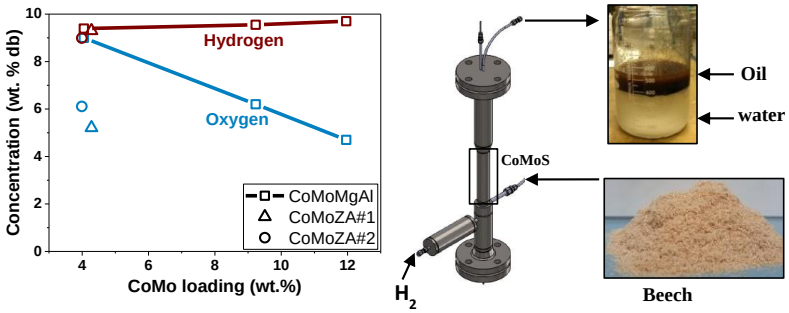

Abstract

The effect of varying the CoMo(S) loading and the support acidity on catalytic hydropyrolysis of beech wood in a fluid bed reactor at 450 °C and a total pressure of 26 bar has been investigated. Using $MgAl_2O_4$ as support material and varying the CoMo loading between 4.1 and 12.0 wt.% decreased the oxygen content in the condensed organic phase from 9.0 to 4.7 wt.% dry basis (db), while the condensed organic and C_{4+} yield decreased from 25.2 to 22.7 wt.% dry ash free (daf), thus leading to a decrease in the carbon recovery from 39 to 37 %. Using a zeolite (H-ZSM-5) mixed with alumina as support with a CoMo loading of 4.1 wt.% instead of $MgAl_2O_4$, resulted in an oxygen content in the condensed organics between 6.1 and 5.2 wt.% db, depending on the zeolite to alumina ratio. However, using the zeolite mixed with alumina as support only decreased the condensed organics and C_{4+} yield to between 23.9 and 24.4 wt.% db, hence the carbon recovery was between 39 and 40 %. This indicates that using a more acidic support can remove the oxygen without decreasing the carbon recovery. This observation was ascribed to a higher degree of alkylation of aromatics with oxygenated aliphatics when the zeolite based support was used. Increasing the CoMo loading increased the yield of light gasses (C_1-C_3), while increasing the zeolite content in the support only increased the formation of C_2-C_3 due to an increased cracking and/or hydrocracking activity.

Both the fresh and spent catalysts were characterized in-depth. STEM images of the spent catalysts showed that the CoMo phase was mainly located as a monolayer MoS_2 slab structure (>93 %) on the support and element mapping by STEM-EDS indicated a high dispersion of cobalt consistent with incorporation of Co into the MoS_2 structure in the so-called CoMoS phase. Potassium was detected on all the spent catalysts, indicating a transfer of alkali metal from the biomass to the catalyst. Potassium may decrease the acidity of the catalyst over time, thus reducing the positive effect of using a more acidic support.

Abbreviations

AED	Atomic emission detector	MgAl	$MgAl_2O_4$
BET	Brunauer–Emmett–Teller	MS	Mass spectrometry
CUS	Coordinatively unsaturated sites	Naph	Naphthenes
daf	Dry, ash free basis	O-Ali	Oxygenated aliphatics
db	Dry basis	O-Aro	Larger oxygenated aromatics
DDO	direct deoxygenation	Par	Paraffins
diAro	Diaromatics	PhOH	Phenolics
EDS	Energy dispersive X-ray spectroscopy	Ph(OH)2	Dihydroxybenzene
FB	Fluid bed	SSA	Specific surface area
FCC	Fluid catalytic cracking	SEM	Scanning electron microscopy
FID	Flame ionization detector	STEM	Scanning transmission electron microscopy
GC	Gas chromatograph	Temp.	Temperature
HAADF	High-angle annular dark-field	TPD	Temperature programmed desorption
HDO	Hydrodeoxygenation	tetAro+	Tetra- and higher aromatics
HYD	Hydrogenation	triAro	Triaromatics
ICP-OES	Inductive coupled plasma optical emission spectroscopy	ZA	H-ZSM-5 mixed with Al_2O_3
mAro	Monoaromatics		

6.1 Introduction

The current production and consumption of energy is responsible for 60 % of the global greenhouse gas (GHG) emissions [1], which is responsible for global warming [2], and the global energy consumption will most likely continue to increase in the near future [3]. The current greenhouse gas emission targets aim at a temperature rise of no more than 2°C, however, even a global average temperature increase of 2°C can lead to multi-meter sea level rise [2,4], and thus it is evident that the emissions of GHG must be drastically decreased immediately. One way of decreasing our GHG emission is to use thermochemical conversion of biomass for the production of liquid fuels. Marker et al. [5,6] have shown that catalytic hydropyrolysis is an efficient method for production of gasoline and diesel from biomass. With their process, called $IH^{2®}$, they are able to produce oxygen free oil (oxygen<1 wt.%) with a condensed organic and C_{4+} yield between 25.8 and 29.5 wt.% dry ash free (daf) for woody biomass [5,6]. In the $IH^{2®}$ process pyrolysis of the biomass and hydrodeoxygenation (HDO) of the oxygenates takes place simultaneously in a fluid bed reactor and the remaining oxygenates are removed in a fixed bed HDO reactor. Life cycle assessments of catalytic hydropyrolysis of biomass for the generation of renewable fuels have shown that this technology can decrease the GHG emissions of liquid transportation fuels with between 30-96 % compared to the fossil counterpart, depending on the type of biomass feedstock, with bagasse giving the largest reduction [7–9]. Furthermore thermodynamic analysis of polygeneration systems based on catalytic hydropyrolysis has shown that it should be possible obtain an energy efficiency for the overall process of 89 % (LHV) [10].

Other groups have also investigated catalytic hydropyrolysis. Dayton et al. [11–13] investigated catalytic hydropyrolysis of woody biomass in a fluid bed reactor at temperatures between 375 and 500 °C and with hydrogen pressures between 1 and 31 bar and tested several different pre-reduced catalysts. At 1 bar and 450 °C and using a molybdenum-based reduced metal catalyst they were able to achieve a carbon recovery for the condensed organics and C_{4+} of 43.0 % with an oxygen content in the organic phase of 6.2 wt.% dry basis (db) [13]. However, a detailed composition of the used catalysts was not reported. Gamliel et al. [14–16] investigated the effect of pressure and catalyst properties in catalytic hydropyrolysis using a Pyroprobe reactor. Testing different supports (H-ZSM-5, SiO_2, Al_2O_3) showed that the Brønsted acidity was important for the oxygen removal and could decrease the char formation by catalyzing decarbonylation and aromatization of the oxygenates, thus minimizing secondary condensation reactions [15]. However, too high acidity can also lead to polymerization and coke formation [15]. Several other research groups have also used H-ZSM-5 in catalytic hydropyrolysis both as a catalyst [17–22] and as support [18–20,23]. Using H-ZSM-5 as support and impregnating it with different metals (Ni, Co, Mo, Pt, Ru and Pd) generally increases the aromatic yield [15,18,19].

Unfortunately, limited research within catalytic hydropyrolysis is conducted with sulfided CoMo, NiMo and Mo catalysts. These catalysts are widely used in modern refineries for hydrogenation of crude oil, and have the advantages, compared to most reduced catalysts, that they are sulfur tolerant [24]. This is important because most biomass sources contains sulfur (0.03-3.4 wt.% db) [25]. Furthermore, it is well-known that these catalysts both are active and stable in hydrodeoxygenation of model compounds and real bio-oil [26–34]. Adding a promoter (Co or Ni) to MoS_2 lead to an increased formation of the coordinated unsaturated sites (CUS) [35–37], thereby enhancing the deoxygenation activity [31,38]. One of the important differences between the two promoters (Co and Ni) are that Ni promotes the hydrogenation (HYD) pathway, where the aromatic ring is saturated prior to the deoxygenation, while Co promotes the direct deoxygenation (DDO) pathway, where oxygen is removed without saturating the aromatic ring [32,38–41]. However, at the commonly applied temperatures (T≥400-500°C) in catalytic hydropyrolysis the (mono)aromatics are favored by equilibrium [42], thus making it more ideal to use the Co as promoter.

In our previous work, we investigated the effect of the catalyst in the fluid bed reactor (see Chapter 4) and obtained a condensable oil yield (condensed organics and C_{4+}) of 24.0 wt.% daf with a NiMo/H-ZSM-5 mixed with Al_2O_3, while using a $CoMo/MgAl_2O_4$ catalyst gave a condensable organic yield of 21.5 wt.%. A fixed bed HDO reactor with a $NiMo/Al_2O_3$ catalyst was used after the fluid bed reactor and the condensed organics contained less than 0.2 wt.% oxygen. However, the industrial catalysts used could not be characterized in detail and it was not possible to determine the reason for the high yield with NiMo/H-ZSM-5 mixed with Al_2O_3. Furthermore, we have previously shown (see Chapter 5) that it is more beneficial to use a sulfided CoMo than NiMo catalyst in the fluid bed reactor. Therefore in this study, we investigate the effect of the CoMo loading and the effect of the support acidity on the product distribution and deoxygenation activity. In order to obtain a thorough understanding of the effect of the catalyst properties on the products, the oxide precursors are characterized with Raman spectroscopy, NH_3-TPD and BET and the spent catalysts were characterized with electron microscopy (SEM and STEM) and energy dispersive X-ray spectroscopy (EDS). Furthermore, the condensed products were extensively analyzed with carbon specific gas chromatography (GC) using an atomic emission detector (AED) and GC×GC time of flight (ToF)/ mass spectrometry (MS) and flame ionization detector (FID).

6.2 Material and methods

6.2.1 Biomass feedstock

Bark free beech wood was used as biomass feedstock in the conducted experiments and has previously been used in catalytic hydropyrolysis experiments [42]. The moisture and ash content in the beech wood was 6.72 wt.% and 0.59 wt.% on dry basis (db), respectively. The potassium content was 0.12 wt.% db and a detailed elemental composition can be found elsewhere [42]. The beech wood was analyzed by Celignis Analytical (analysis P10) and consisted of 24 wt.% db lignin, 40 wt.% db cellulose, and 18 wt.% db hemicellulose, 3 wt.% other polysaccharides, 3 wt.% db extractives and 12 wt.% db unknown. The particle sizes were between 200-700 µm.

6.2.2 Catalyst preparation

The tested catalysts were prepared by sequential incipient wetness impregnation on three different support materials, supplied by Haldor Topsøe A/S. $MgAl_2O_4$ (MgAl) was used as support for testing the effect of the CoMo loading and two supports consisting of zeolite (H-ZSM-5) mixed with alumina, denoted as ZA#1 and ZA#2, were used for testing the effect of the support acidity. ZA#2 consisted of 44 % more H-ZSM-5 than ZA#1. The supports were crushed to obtain particle sizes of 180-355 µm, this particle size distribution was used to obtain a good fluidization of the bed. Prior to the impregnation, MgAl was calcined in air for 10 hours and in order to keep Mo/nm^2 surface loading constant, the calcination temperature was varied (see Table 6.1) and the calcined MgAl had a specific surface area (SSA) between 56 and 200 m^2/g. In order to maintain the properties of the zeolite based supports, ZA#1 and ZA#2, were not calcined prior to the impregnation. The supports had a pore volume between 0.60 and 0.95 g_{water}/g.

Table 6.1 Calcination temperature, specific surface area, and pore volume of the tested supports.

Support	Calcination temp. (°C)	BET SSA (m^2/g)	Pore volume (g_{water}/g)
MgAl#1	995	56	0.62
MgAl#2	905	96	0.82
MgAl#3	800	143	0.91
MgAl#4	600	200	0.95
ZA#1	-	ND	0.69
ZA#2	-	ND	0.60

The support was impregnated with an aqueous solution (corresponding to 110 % the pore volume) of $(NH_4)_6Mo_7O_{24}\cdot 4H_2O$ (Fluka≥99.0%), then aged with stirring for approximately 3 hours and dried overnight at approximately 110 °C in air. A second impregnation with $Co(NO_3)_2\cdot 6H_2O$ (Fluka ≥ 98%) was conducted using the same procedure. The calcination was conducted with an air flow of 1.24-1.30 NL/min technical air (20% O_2 in N_2) by heating to 500°C with a ramp of 5°C/min and holding for 3 hours. After calcination the catalysts were sieved to 180-355 µm again in order to remove any dust or agglomerates formed during the preparation. The composition of the tested catalysts is shown in Table 6.2. An estimated Mo loading between 3.3 and 3.4 atoms/nm^2 was obtained for CoMoMgAl#1 – #3, while it was 4.7 atoms/nm^2 for CoMoMgAl#4. The higher atoms/nm^2 loading for CoMoMgAl#4 was due to a significant decrease in the surface area from 200 to 148 m^2/g possibly due to pore blocking during the preparation. Loadings lower than 4 atoms/nm^2 corresponds to a sub monolayer dispersion of Mo-oxide on $MgAl_2O_4$, assumed similar to γ-Al_2O_3 [43], which should lead to a high dispersion of smaller MoS_2 particles (when sulfided) with a moderate activity, hence minimizing the formation of the very active type II sites [44]. The loading for CoMoZA#1 was 0.71 atoms/nm^2 and the loading for CoMoZA#2 was 0.60 atoms/nm^2. The Co to Mo ratio was aimed at 0.3, which should ensure that the less active Co_9S_8 phase is not formed [45].

The catalysts were sulfided in-situ in the catalytic hydropyrolysis setup at 26 bar, 350°C with 1.8 mol % H_2S, 11 mol % N_2 in 87 mol % H_2 by feeding 2% H_2S in H_2 (flow: 4 NL/min) and N_2 (flow: 0.5 NL/min). The temperature ramp was 10 °C/min and the holding time was 2 hours. After the sulfidation the test conditions were established.

Table 6.2 Composition of the fresh catalysts

Catalyst	Mo (wt.%)	Co (wt.%)	Co/Mo (molar)	Mo load (Atoms/nm^2)	BET SSA (m^2/g)
CoMoMgAl#1	3.41	0.64	0.30	3.6	60
CoMoMgAl#2	5.58	0.99	0.29	3.4	102
CoMoMgAl#3	7.74	1.49	0.31	3.3	136
CoMoMgAl#4	10.1	1.86	0.30	4.7	148
CoMoZA#1	3.61	0.67	0.29	0.71	319
CoMoZA#2	3.39	0.60	0.29	0.60	354

6.2.3 Experimental setup and procedure

The catalytic hydropyrolysis experiments were conducted in a bench scale setup shown in Figure 6.1. The setup is described in detail elsewhere [42], but is here described in brief. The setup consisted of a feeding system, which included a gas mixing system and a screw feeder, a fluid bed hydropyrolysis reactor, a filter for char removal and a three stage condensation system (20°C, 2°C, and -40°C). The uncondensed gasses were analyzed using an online GC, which measured the gas composition (H_2, N_2, H_2S, CO, CO_2, C_1 to C_5

and C_{6+} hydrocarbons) every 10 min. The piping between the fluid bed, filter, and condensation section was heated to 350°C in order to avoid premature condensation. During the experiments 52 NL/min hydrogen passed through a sinter plate in the bottom of the fluid bed reactor and 30 NL/min hydrogen and 5 NL/min nitrogen passed through the biomass feeding tube, thus ensuring a rapid transfer of the biomass from the screw feeder to fluid bed reactor.

The total mass of the condensed liquid was determined and the organic phase and the aqueous phase were separated with a separation funnel. The mass of the aqueous phase was measured and the mass of the organic phase was determined by subtracting the mass of the aqueous phase from the total mass of condensed liquid. The H_2S dissolved in the liquid phases was for safety reasons removed by bubbling with N_2 until hydrogen sulfide test strips (Sigma Aldrich) showed no sign of H_2S. This lead to a mass loss between 0 and 6.7 wt.% for the organic phase and between 1.0 and 2.0 wt.% in the aqueous phase. The mass loss in the organic phase was mainly due to vaporization of light hydrocarbons while the mass loss in the aqueous phase was mainly due to vaporization of water.

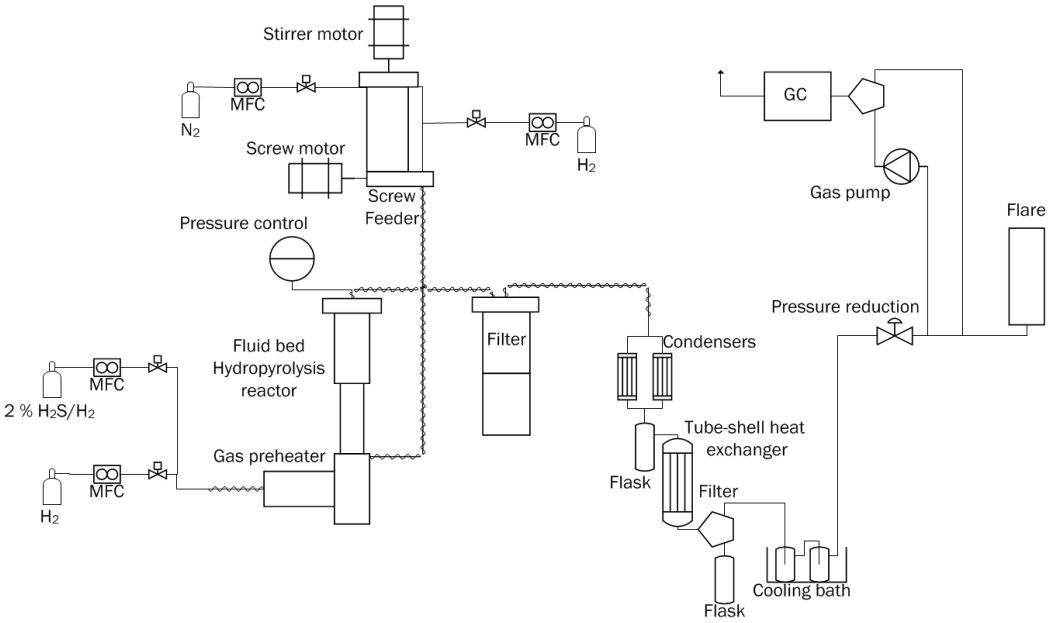

Figure 6.1. Simplified piping and instrumentation diagram of the catalytic hydropyrolysis setup

6.2.4 Liquid phase analysis methods

6.2.4.1 Organic phase

Several different methods were used to analyze the condensed organic phase and a more detailed description can be found elsewhere [42]. The hydrogen content was measured with ASTM method D7171. The sulfur content was measured according to ASTM D4294 and the density at 40 ˚C was measured with ASTM method D 4052. The oxygen content in the condensed organic phase was analyzed at DB Lab A/S using a Flash 2000 elemental analyzer (Thermo Scientific). The uncertainty of this measurement was 3.0 %, defined as

two standard deviations for the measurement deviation, corresponding to a confidence interval of 95 %. The water content was measured with Karl Fisher titration.

The condensed organic liquid samples were characterized by GC×GC-ToF/MS or -FID using a LECO® Pegasus 4D^{TM} instrument. Based on the GC×GC-ToF/MS analysis the compounds were classified into eleven groups: paraffins, naphthenes, mono-, di- and tri- and higher aromatics, oxygenated aliphatics, phenolics, dihydroxybenzenes, larger oxygenated aromatics, and sterols. The relative amount (FID area-%) of each compound class was estimated as the sum of areas of all detected peaks in that class divided by the total peak area of all compound classes. All data were processed using the ChromaTof® 4.50 software.

Selective analysis of the sulfur containing hydrocarbons was conducted using GC-AED using the sulfur emission line at 181 nm. Identification of individual compounds was done after analysis of pure compounds. The quantification was done using an external standard sample containing known amount of benzothiophene, dibenzothiophene and 4-methyl-dibenzothiophene.

6.2.5 Aqueous phase

The carbon content in the aqueous phase was determined with GC-AED. The samples were analyzed using an Agilent 7890A GC coupled to a JAS 2370 Atomic Emission Detector (AED) in carbon selective mode. The quantification was done by external calibration using benzyl alcohol dissolved in water as standard. Calibration concentrations raged from 10 ppm to 1100 ppm carbon. A more through description can be found elsewhere (see Chapter 5)

The aqueous phase was also analyzed on a Shimadzu GC-MS/FID with a Supelco Equity-5 column. The compounds were identified on the MS and quantified using the parallel FID. Based on the GC FID-MS analysis the components were classified into 6 groups: alcohols, furans, acids, phenols, ketones, and unidentified. The relative amount (FID area-%) of each component class was estimated as the sum of all the detected peaks in that class divided by the total peak area.

6.2.6 Catalyst characterization

Several methods were used to characterize the fresh and spent catalysts and a detailed description can be found elsewhere (see Chapter 5). The composition (Co, Mo) of the fresh catalysts was determined with inductive coupled plasma optical emission spectroscopy (ICP-OES) when MgAl was used as support material and wavelength dispersive X-ray fluorescence (WD-XRF) when ZSM-5 mixed with alumina was used as support material. The surface area was measured with N_2-physisorption (BET). Temperature programmed ammonia desorption (NH_3-TPD) of the fresh catalysts were conducted on a Mettler Toledo TGA/DSC 1. Raman spectroscopy on the samples was performed in ambient conditions with a Labram 800 HR from Jobin Yvon using a Koheras solid state 488 nm laser. The samples were both analyzed in a fluidized bed set-up as described by Beato et al. [46] and at different spatial spots.

The scanning electron microscopy (SEM) was performed on a FEI QUANTA600 scanning electron microscope with tungsten filament and equipped with a liquid nitrogen cooled EDAX ultra-thin window (UTW) EDS detector. All samples were sprinkled on carbon tapes on Al-stubs and conducted without any coating to prevent charging in the sample chamber. EDS element quantifications were acquired on 0.11 mm x 0.11 mm areas on the surface of the spent catalysts catalyst grains at 3 kV, 5 kV, 10 kV and 15 kV. Using CASINO Monte Carlo Software v.3.3.04 the penetration depth of the incident electron beam in $MgAl_2O_4$ was estimated to be 0.170 µm at 3 kV and 1.6 µm at 15 kV. The standard deviation for the carbon measurement was 1.5

wt.% at 3 kV, 0.8 wt.% at 5 kV, 1.0 wt.% at 10 kV and 1.5 wt.% at 15 kV, and the standard deviation for the potassium measurements was 0.6 wt.% at 5 kV, 0.3 wt.% at 10 kV, and 0.2 wt.% at 15 kV.

The transmission electron microscopy was performed on a FEI Talos™ F200X transmission electron microscope equipped with high-brightness field emission gun (X-FEG) and Super-X G2 EDS detector. Images and elemental EDS maps were acquired in scanning transmission mode (STEM) with a camera length of 125 cm. Elemental EDS maps of 512 pixels x 512 pixels (2.1 μm x 2.1 μm) were acquired for 20 min in Brüker software (Esprit 1.9) using a probe current of 0.7 nA.

6.3 Results and Discussion

The reaction conditions, mass balance, and properties of the condensed organic and aqueous phase are shown in Table 6.3. The mass balance closed between 97.8 and 100.4 wt.% daf, the feeding rate varied between 270 and 282 g/h, and the feeding time varied between 2.5 and 3.5 hours. The liquid phases from experiment 2 were contaminated and were therefore not analyzed. A more detailed gas composition can be found in supplementary information Table E.1. It should be noted that the results from experiment 1 has previously been published (see Chapter 5), but is here used as a reference.

Table 6.3 Summary of reaction conditions and mass balance for catalytic hydropyrolysis of beech wood in fluid bed reactor with sulfided CoMo catalysts with different loadings and on different supports. (50 g catalyst was used in each experiment)

Test	1	2	3	4	5	6
Test conditions						
FB temperature (°C)	451	450	454	450	454	454
FB catalyst	CoMoMgAl#1	CoMoMgAl#2	CoMoMgAl#3	CoMoMgAl#4	CoMoZA#1	CoMoZA#2
Pressure (bar)	26	26	26	26	26	26
Feed time (h)	3.5	3.5	3.4	3.4	3.5	2.5
Feeding rate (g/h)	275	275	280	276	270	282
H_2S conc.(ppm)	460	460	460	460	460	460
H_2 flow (NL/min)	82	82	82	82	82	82
N_2 flow (NL/min)	5	5	5	5	5	5
Yields (wt. daf %)						
Gas	26.1	28.8	30.8	29.7	29.7	30.0
Char + coke	13.3	13.0	13.1	13.2	13.0	13.3
Aqueous phase	33.3	33.2	32.6	33.1	33.1	33.2
Organic phase	17.7	13.4	12.1	11.9	14.3	14.0
C_{4+} in the gas	7.5	10.1	10.6	10.8	10.1	9.9
Organics + C_{4+}	25.2	23.5	22.7	22.7	24.4	24.1
Mass balance	97.8	98.5	99.2	98.8	98.8	100.4
Carbon recovery (%)						
C_1-C_3	19	23	25	24	25	27
C_{4+}	13	17	18	18	17	17
CO+CO_2	11	11	12	11	11	11
Organic phase	26	ND	18	18	22	22
Aqueous phase	3.2	ND	1.1	0.97	0.67	0.97
C_{4+} efficiency	39	ND	36	37	40	39
Organic phase composition						
Water (wt.%)	3.3	ND	1.6	1.2	1.3	1.3
C* (wt.% db)	81	ND	84	85	85	85
H (wt.% db)	9.39	ND	9.56	9.70	9.30	8.99
O (wt.% db)	9.0	ND	6.2	4.7	5.2	6.1
S (wt.% db)	0.22	ND	0.27	0.27	0.18	ND
Organic phase physical properties						
Density at 40°C (g/ml)	0.9428	ND	0.9308	0.9185	0.9511	0.9515
Aqueous phase composition (wt.%)						
C	4.3	ND	1.5	1.3	0.9	1.3
Gas composition (wt.% daf)						
CO	6.5	8.3	8.9	8.9	6.7	7.7
CO_2	9.2	7.7	7.8	8.9	8.3	8.4
C_1-C_3	10.3	12.7	14.1	14.0	13.0	13.9
C_{4+}	7.5	10.1	10.6	10.8	10.1	9.9

*By difference

6.3.1 Product distribution

The product distribution is shown in Figure 6.2. The condensable organic yield decreased from 25.2 to 22.7 wt.% daf when the CoMo loading was increased from 4.1 to 11.6 wt.%, see Figure 6.2(A). Likewise the condensable organic yield decreased from 25.2 to 24.4 and 23.9 wt.% daf when CoMoMgAl#1 was replaced with CoMoZA#1 and CoMoZA#2, respectively. Thus only a minor difference was observed between CoMoZA#1 and CoMoZA#2. The total gas yield, shown in Figure 6.2(B), increased with the CoMo loading from 26.1 wt.% daf when the CoMo loading was 4.1 wt.% to 30.8 wt.% daf when the CoMo loading was increased to 9.2 wt.%. Further increasing the CoMo loading to 12.0 wt.% decreased the total gas yield to 29.7 wt.% daf, where the decrease was due to a decrease in the CO and CO_2 yield. The total CO and CO_2

yield varied between 15.8 and 16.7 wt.% daf when the CoMo loading was varied, and thus was almost constant. The C_1-C_3 yield increased from 10.3 to 14.1 wt.% daf when the CoMo loading was increased from 4.1 to 9.2 wt.% and remained constant for higher CoMo loading (11.6 wt.%). The total gas yield also increased when CoMoZA#1 (27.9 wt.% daf) and CoMoZA#2 (30.0 wt.% daf) was used instead of CoMoMgAl#1 (26.1 wt.%). This was due to an increased yield of C_1-C_3, which was 10.3 wt.% daf for CoMoMgAl#1, 13.0 wt.% daf for CoMoZA#1 and 13.9 wt.% daf for CoMoZA#2. CoMoZA#2 produced more CO, CO_2 and C_1-C_3 than CoMoZA#1. The char and coke yield varied between 13.0 and 13.3 wt.%, thus the variations were within the experimental uncertainty, which indicates that the char and coke yield are independent of the CoMo loading and the support acidity, in the tested range. Likewise, the variations in the aqueous phase yield between 32.6 and 33.3 wt.% daf was within the experimental uncertainty.

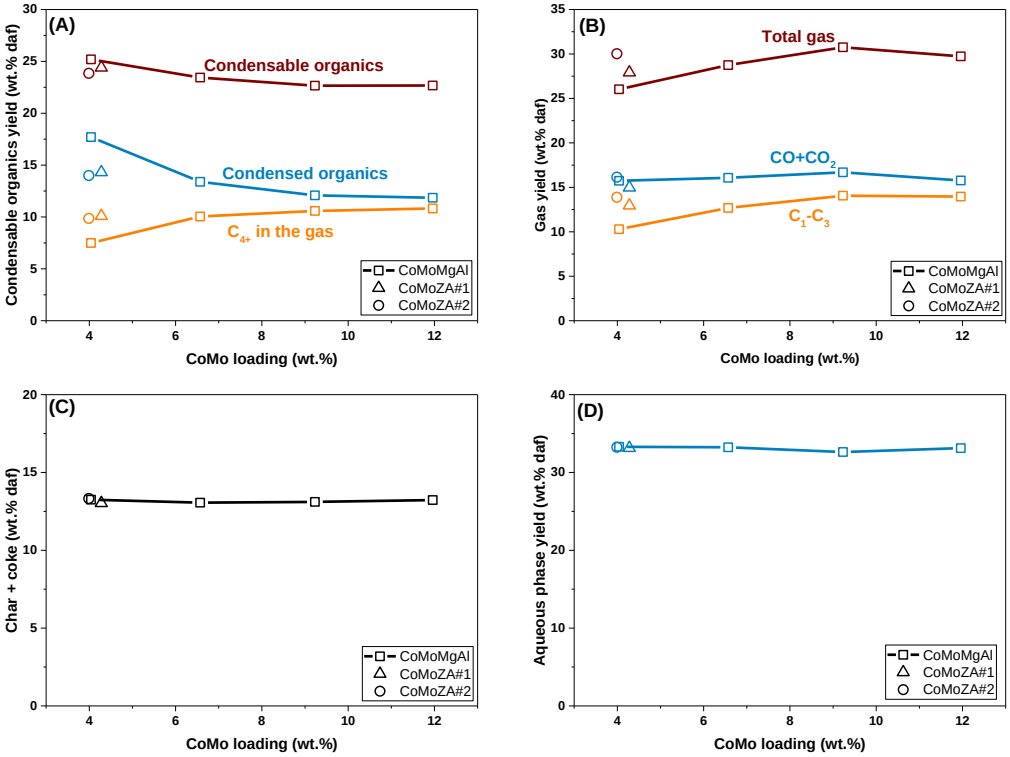

Figure 6.2 Effect of CoMo loading and support on the condensable organic yield (A), gas yield (B), solid yield (C), and aqueous phase yield (D). Conditions: Fluid bed temperature: 450-455°C, total pressure: 26 bar, biomass feeding rate: 270-282 g/h, feed time: 2.5-3.5 h, H_2 flow: 82 NL/min, N_2 flow: 5 NL/min, and H_2S conc: 460 ppm.

Figure 6.3(A) shows the CO and CO_2 yield and indicates that the CO_2 yield decreases with increasing CoMo loading. The CO_2 yield was 9.2 wt.% daf when the CoMo loading was 4.1 wt.%, which decreased to 7.7 wt.% daf when the CoMo loading was increased to 12.0 wt.%. Furthermore, increasing the CoMo loading from 4.05 to 9.22 wt.% increased the CO yield from 7.6 to 8.9 wt.% daf, but further increasing the CoMo loading did not increase the CO yield. These results indicate that the catalyst's reversed water-gas shift (see reaction (6.1)) activity increases with increasing CoMo loading, thus the CO/CO_2 ratio approaches equilibrium (see supplementary information Figure E.1). However, it could also be due changes in the catalysts de-

carbonylation and decarboxylation activity. Using CoMoZA#2 instead of CoMoMgAl#1 decreased the CO_2 yield from 9.2 to 8.4 wt.% daf and increased the CO yield from 6.5 to 7.7 wt.% daf. Interestingly the CO_2 yield also decreased, to 7.8 wt.% daf, when the CoMoZA#1 was used, but the CO yield only increased to from 6.5 to 6.7 wt.% daf. This indicates that the change in the support alters the catalyst's decarbonylation and/or decarboxylation activity and the CO/CO_2 ratio increases and approaches equilibrium.

$$CO_2 + H_2 \rightleftharpoons CO + H_2O \tag{6.1}$$

Increasing the CoMo loading from 4.1 wt.% to 12.0 wt.% daf decreased the olefin yield from 3.6 to 2.1 wt.% daf and the paraffin yield increased from 3.2 to 5.9 wt.% (see Figure 6.3 B), thus showing an increase in the catalyst's hydrogenation activity. Using CoMoZA#1 and CoMoZA#2 instead of CoMoMgAl#1 increased both the C_2-C_3 olefin and paraffin yield. The paraffin yield increased to 5.8 wt.% daf for CoMoZA#1 and 6.0 wt.% daf for CoMoZA#2 and the olefin yield increased to 4.2 wt.% daf for CoMoZA#1 and 4.6 wt.% daf for CoMoZA#2. Furthermore it should be noted that the observed increase in the total C_1-C_3 yield, shown in Figure 6.2(B), is due to the increase in the C_2-C_3 yield, while the methane yield decreased from 3.5 wt.% for CoMoMgAl#1 to 2.9 wt.% daf for CoMoZA#1 and 3.3 wt.% daf for CoMoZA#2. It is therefore likely that the increased C_2-C_3 paraffin and olefin yield is due to an increased cracking and hydrocracking activity for the CoMoZA#1 and CoMoZA#2 compared to CoMoMgAl#1, which can be ascribed to their higher acidity.

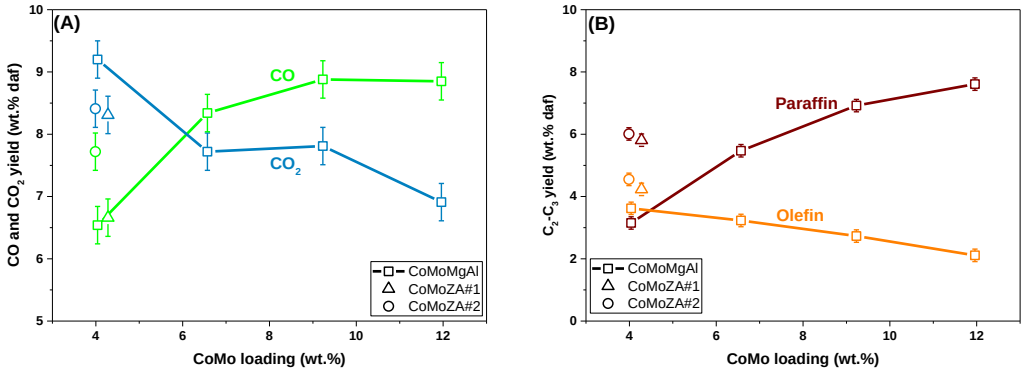

Figure 6.3 Effect of CoMo loading and support on the CO and CO_2 yield (A) and C_2-C_3 paraffin and olefin yield (B). Conditions: Fluid bed temperature: 450-455°C, total pressure: 26 bar, biomass feeding rate: 270-282 g/h, feed time: 2.5-3.5 h, H_2 flow: 82 NL/min, N_2 flow: 5 NL/min, and H_2S conc: 460 ppm.

6.3.2 Chemical composition of the condensed liquid

6.3.2.1 Organic phase

The oxygen and hydrogen content in the condensed organics are shown in Figure 6.4. As the CoMo loading is increased from 4.1 to 12.0 wt.% for the spinel carrier the oxygen concentration decreased from 9.0 to 4.7 wt.% db and the hydrogen concentration increased from 9.39 to 9.70 wt.% db, hence showing that the deoxygenation and hydrogenation activity increased with increasing CoMo loading. Using CoMoZA#1 and CoMoZA#2 also decreased the oxygen content in the condensed organics, thus the oxygen content was 5.2 wt.% db for CoMoZA#1 and 6.1 wt.% db for CoMoZA#2. The increased deoxygenation activity cannot be explained with an increased decarboxylation and/or decarbonylation activity, since the CO and CO_2 yield did not increase, thus indicating that the ZA#1 and ZA#2 supports have a promoting effect on the hydrodeoxygenation activity. Using CoMoZA#1 and CoMoZA#2 also decreased the hydrogen content from 9.39 wt.%

db when using CoMoMgAl#1 to 9.30 and 8.99 wt.% db, respectively, thus indicating a decrease in the hydrogenation activity. As shown in Table 6.3 increasing the CoMo loading from 4.05 wt.% to 11.6 wt.% also decreased the density of the condensed organics from 0.9428 to 0.9355 g/ml, which was probably due to the decreased oxygen content. However, the density increased from 0.9428 g/ml when using CoMoMgAl#1 to 0.9515 and 0.9678 g/ml when using CoMoZA#1 and CoMoZA#2, respectively.

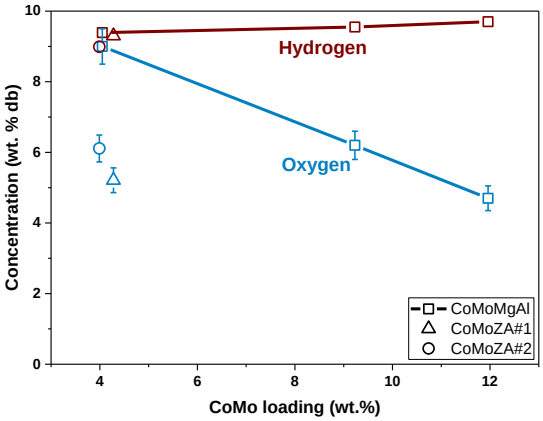

Figure 6.4 Effect of CoMo loading and support on the oxygen and hydrogen concentration in the condensed organics. Conditions: Fluid bed temperature: 450-455°C, total pressure: 26 bar, biomass feeding rate: 270-282 g/h, feed time: 2.5-3.5 h, H_2 flow: 82 NL/min, N_2 flow: 5 NL/min, and H_2S conc: 460 ppm.

To obtain a more thorough understanding of the composition of the condensed organic phases, they were analyzed with GC×GC-MS/FID and the components were divided into naphthenes, monoaromatics, diaromatics, triaromatics, larger aromatics, phenols, dihydroxybenzenes, larger oxygenated aromatics, oxygenated aliphatics, paraffins, and sterols. The concentration of paraffins was between 0.46 and 2.2 % area-FID, see supplementary information Figure E.2. The concentration of tri-and larger aromatics varied between 5.9 and 3.9 % area-FID and decreased with the increasing CoMo loading. Changing the support did not significantly change concentration of tri-and larger aromatics, thus the concentration was 5.2 % area-FID when CoMoMgAl#1 was used and 5.9 and 5.4 % area-FID when CoMoZA#1 and CoMoZA#2 were used, respectively. The concentration of dihydroxybenzenes was between 1.0 and 2.4 % area-FID and decreased with increasing CoMo loading. Traces of sterols (<0.2 % area-FID) were found in all the analyzed organic phases.

Figure 6.5(A) shows the concentration of the naphthenes, monoaromatics and diaromatics. As the CoMo loading is increased from 4.1 to 12.0 wt.% the concentration of monoaromatics increased from 8.3 to 27.1 % area-FID, the concentration of diaromatics was constant between 10.6 and 12.1 % area-FID, and the concentration of naphthenes increased from 8.0 to 15.3 % area-FID. The increase in the concentration of naphthenes was probably due to an increased hydrogenation activity, when the CoMo loading was increased. Using the zeolite based supports increased the monoaromatic concentration from 8.0 % area-FID with CoMoMgAl#1 to 19.0 and 27.7 % area-FID for CoMoZA#1 and CoMoZA#2, respectively. Only a small change in the concentration of naphthenes was observed, which was 8.0 % area-FID for CoMoMgAl#1, 8.2 % area-FID for CoMoZA#1 and 5.7 % area-FID for CoMoZA#2. The concentration of diaromatics also increased from 10.6 % area-FID for CoMoMgAl#1 to 22.1 and 17.4 area-FID for CoMoZA#1 and CoMoZA#2, respectively.

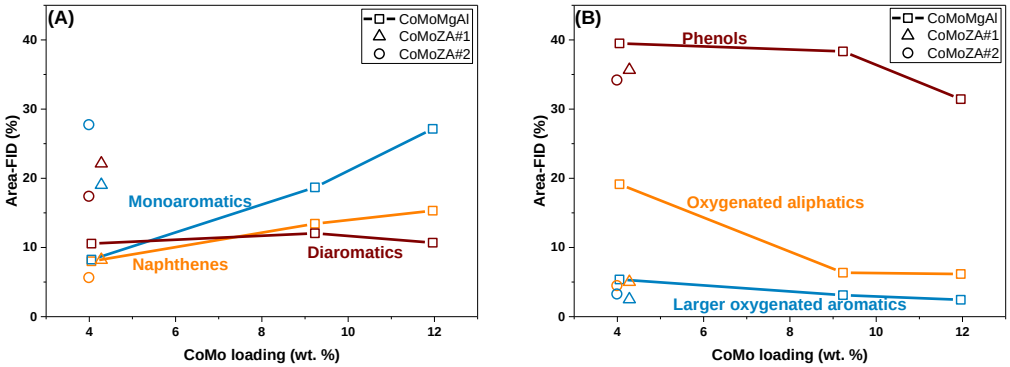

Figure 6.5 Effect of CoMo loading and support on the concentration of naphthenes, monoaromatics, and diaromatics (A) and the concentration of oxygenated aliphatics, phenols, and larger oxygenated aromatics (B). Conditions: Fluid bed temperature: 450-455°C, total pressure: 26 bar, biomass feeding rate: 270-282 g/h, feed time: 2.5-3.5 h, H_2 flow: 82 NL/min, N_2 flow: 5 NL/min, and H_2S conc: 460 ppm.

The concentration of phenols decreased from 39.5 to 38.3 % area-FID when the CoMo loading was increased from 4.05 to 9.23 wt.%, but decreased to 31.4 % area-FID when the loading was increased to 11.96 wt.% (see Figure 6.5(B). The concentration of oxygenated aliphatics decreased from 19.1 to 6.3 % area-FID when the CoMo loading was increased from 4.1 to 9.2 wt.%, but further increasing the loading to 12.0 wt.% only decreased the concentration to 6.2 % area-FID, thus the difference was within the uncertainty. The concentration of larger oxygenates decreased with the CoMo loading from 5.4 % area-FID at 4.05 wt.% to 2.4 area-FID at 11.96 wt.%. Overall, this indicates that the oxygenates are easily removed when the CoMo loading is increased, while more activity is needed to remove the phenols. The decrease in the concentration of phenols is not enough to explain the increased concentration of monoaromatics and naphthenes, thus it is very likely that some of the oxygenated aliphatics have participated in alkylation reactions with the aromatics, thus increasing the monoaromatic yield. Similarly Lai et al. [47] observed alkylation reactions when upgrading catalytic hydropyrolysis vapors in a fluid bed reactor.

The concentration of oxygenated aliphatics decreased from 19.1 % area-FID for the CoMoMgAl#1 to 5.0 and 4.5 % area-FID for CoMoZA#1 and CoMoZA#2, respectively. The phenol concentration decreased from 39.5 % area-FID to 35.7 % area-FID when the CoMoZA#1 was used instead of CoMoMgAl#1 and using CoMoZA#2 decreased the concentration to 34.2 % area-FID, thus indicating a similar deoxygenation activity for CoMoZA#1 and CoMoZA#2. The concentration of naphthenes varied between 5.7 and 8.2 when the support was varied, but was not correlated to the amount of zeolite in the support. Interestingly, the concentration of monoaromatics increased from 8.3 % area-FID when the CoMoMgAl#1 was used to 19.0 and 27.8 % area-FID when the CoMoZA#1 and CoMoZA#2 were used, respectively. The diaromatic concentration also increased from 10.6 % area-FID when the CoMoMgAl#1 was used to 22.1 and 17.4 % area-FID when the CoMoZA#1 and CoMoZA#2 were used, respectively. Showing that the zeolite supported catalysts increased the aromatic yield both by deoxygenation of the phenols, but also by enhancing alkylation reactions. Furthermore, the selectivity for monoaromatics increased with the zeolite loading likely due to enhanced alkylation.

The condensed organics from the experiment with the CoMoMgAl#1, CoMoMgAl#3, CoMoMgAl#4, and CoMoZA#2 where analyzed with sulfur specific GC-AED and a list of the detected S containing hydrocarbons are shown in supplementary information Table E.2-E.6. The samples contained between 185 and 970

wt-ppm organic S, which was divided into five groups: thiols, thiophenes, benzothiophenes, other (methylethylsulfide, dimethylsulfide, carbonylsulfide, dihexyldisulfide), and unidentified as shown in Figure 6.6. Increasing the CoMo loading from 4.1 to 9.2 wt.% decreased the thiol concentration from 55 to 11 wt-ppm S, which probably was due to a lower concentration of olefins, which otherwise can be converted into thiols through recombination reactions [48–51]. Interestingly, increasing the CoMo loading also increased the concentration of thiophenes from 80 to 250 wt-ppm S and the concentration of benzothiophenes from 29 to 71 wt-ppm S. However, the concentration of unidentified molecules decreased from 501 to 268 wt-ppm, thus the concentration of organic bound sulfur decreased from 823 to 766 wt-ppm S. Further increasing the CoMo loading to 12.0 wt.% decreased the organic sulfur concentration to 545 wt-ppm S, hence showing that increasing the CoMo loading decreases the sulfur concentration. The reason for the increase in the concentration of thiophenes and benzothiophenes, when the CoMo loading is increased, is because a larger fraction of the molecules is identified and the concentration of unidentified molecules therefore decreases (see Figure 6.6).

Increasing the fraction of H-ZSM-5 in the support increased the concentration of thiophenes, hence it was 80 wt-ppm S when CoMoMgAl#1 was used, 341 wt-ppm S when CoMoZA#1 was used, and 605 wt-ppm S when CoMoZA#2 was used. The total concentration of organic bound sulfur increased from 823 wt-ppm S for the CoMoMgAl#1, to 1121 wt-ppm S for CoMoZA#1, and to 1060 wt-ppm S for the CoMoZA#2, thus H-ZSM-5 increases the amount of sulfur incorporated into the organics. Since formation of thiophenes occurs in fluid catalytic cracking units where zeolite catalysts are used, it is assumed that the incorporation of sulfur in catalytic hydropyrolysis takes place through similar reaction mechanisms as in an FCC unit [52,53].

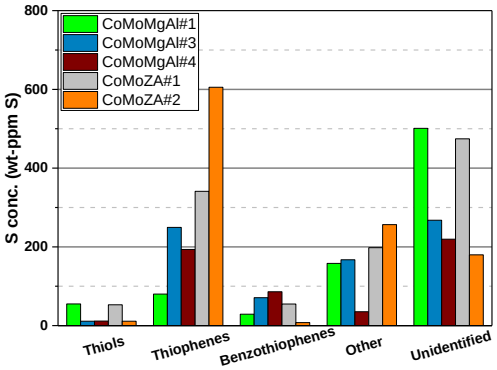

Figure 6.6 Concentration of sulfur species in the condensed organic phase from experiments with the CoMoMgAl#1, CoMoMgAl#3, CoMoMgAl#4, CoMoZA#1, and CoMoZA#2 catalyst analyzed with S specific GC-AED. Conditions: Fluid bed temperature: 450-455°C, total pressure: 26 bar, biomass feeding rate: 270-282 g/h, feed time: 2.5-3.5 h, H_2 flow: 82 NL/min, N_2 flow: 5 NL/min, and H_2S conc: 460 ppm.

6.3.2.2 Aqueous phase

The carbon recovery in the aqueous phase was determined by carbon specific GC-AED and is shown in Figure 6.7(A). Increasing the CoMo loading from 4.1 to 9.2 wt.% for the spinel carrier decreased the carbon recovery in the aqueous phase from 3.2 to 1.1 %, further increasing the CoMo loading to 11.6 wt.% decreased the carbon recovery to 0.97 %, thus as the CoMo loading is increased its impact on the carbon recovery in the aqueous phase decreased. Changing the support material decreased the carbon recovery in the aqueous phase from 3.2 % for CoMoMgAl#1 to 0.67 % for CoMoZA#1 and 0.97 % for CoMoZA#2.

The aqueous phase was also analyzed with GC-MS/FID and the detected molecules were divided into 6 groups: alcohols, furans, acids, phenols, ketones and unidentified as shown in Figure 6.7(B) and detailed lists of the detected species in the aqueous phases are shown in supplementary information Table E.7-E.11. Increasing the CoMo loading from 4.05 to 11.6 wt.% decreased the concentration of alcohols from 68.5 to 35.8 % area-FID and decreased the concentration of ketones from 19.1 to 7.6 % area-FID, while the phenol concentration increased from 6.7 to 47.1 % area-FID. The increased relative concentration of phenols when the CoMo loading was increased was due to the decreased concentration of alcohols and ketones and decreased carbon in the aqueous phase overall. The concentration of acids increased from 3.8 to 5.5 % area-FID when the CoMo loading was increased from 4.1 to 11.6 wt.%. However, because of the concurrent decrease in the carbon recovery in the aqueous phase the total amount of acids decreased. Varying the support material also lead to a decrease in the concentration of alcohols, thus the concentration was 68.5 % area-FID when the CoMoMgAl#1 was used, but 21.1 and 16.1 % area-FID when the CoMoZA#1 and CoMoZA#2 were used, respectively. This supports the observation for the organic phase that the zeolite supported catalysts removes the oxygenated aliphatics. The relative concentration of phenols increased from 6.7 % area-FID to 48.8 % area-FID for CoMoZA#1 and 59.1 % area-FID for CoMoZA#2. The relative concentration of acids increased from 3.8 % area-FID for CoMoMgAl#1 to 5.5 % area-FID for CoMoZA#1 and 5.6 % area-FID for CoMoZA#2. The relative concentration of ketones was close to constant at 19.1 % area-FID for CoMoMgAl#1, 20.0 % area-FID for CoMoZA#1, and 17.8 % area-FID for CoMoZA#2. Furans were only detected in the aqueous phase from the experiment with CoMoMgAl#1 (0.43 % area-FID) and CoMoZA#1 (0.54 % area-FID).

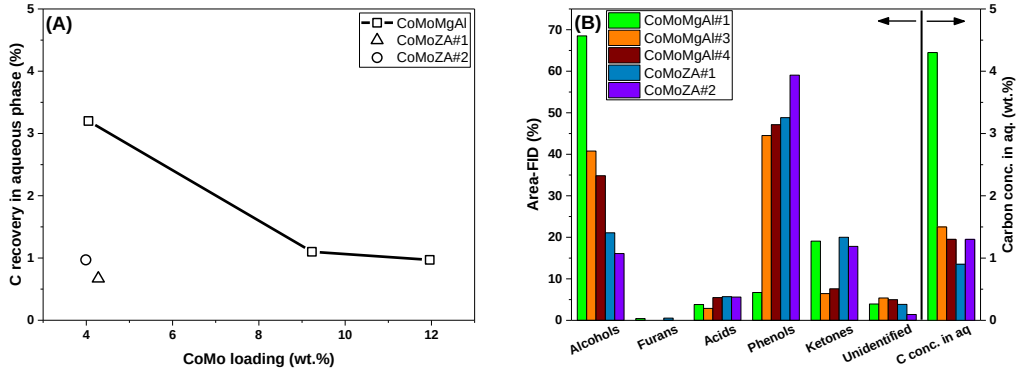

Figure 6.7 Effect of CoMo loading and support on carbon recovery in the aqueous phase (A) and the composition of the aqueous phase (B). Conditions: Fluid bed temperature: 450-455°C, total pressure: 26 bar, biomass feeding rate: 270-282 g/h, feed time: 2.5-3.5 h, H_2 flow: 82 NL/min, N_2 flow: 5 NL/min, and H_2S conc: 460 ppm.

6.3.3 Characterization of catalysts

6.3.3.1 Characterization of catalyst oxide precursors

6.3.3.1.1 NH_3-TPD

The acidity of the fresh oxide precursors were investigated with NH_3-TPD, as shown in Figure 6.8. For CoMoMgAl#1 – CoMoMgAl#4 the number of acidic sites increased with increasing surface area (see supplementary information Figure E.3), as expected. Furthermore, the desorption rate peaks at 255 °C for CoMoMgAl#1 and at 270 °C for CoMoMgAl#4, thus the desorption rate peaks at a higher temperature when the

surface area is increased, indicating that the acid strength increases when the calcination temperature is decreased and/or the CoMo loading is increased.

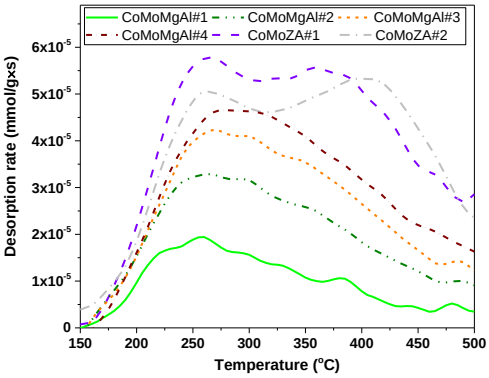

Figure 6.8 NH_3-TPD profiles for the oxide precursors

The two zeolite based catalyst precursors CoMoZA#1 and CoMoZA#2 both have a higher number of acidic sites than the spinel based catalysts, which both can be seen by the higher desorption rate in Figure 6.8 and the higher amount of NH_3 adsorbed and desorbed as shown in Table 6.4. A substantial difference between the desorption curve of the MgAl supported catalysts and ZA supported catalysts is that the MgAl supported catalysts only has one peak around 260°C, while ZA catalysts have two around 260 °C and 360-410 °C. For the ZA catalysts the first peak is probably mainly due to desorption of NH_3 from the alumina, while the second peak is mainly due to desorption from the zeolite. Interestingly, the amount of NH_3 adsorbed is 0.564 mmol/g for the CoMoZA#1 and 0.529 mmol/g for the CoMoZA#2, thus indicating that there are more acidic sites on CoMoZA#1 than CoMoZA#2, which shows that the alumina contains more acid sites than the zeolite. However, the second desorption peak on CoMoZA#1 is at 360 °C while it is at 410 °C for CoMoZA#2, showing that CoMoZA#2 has stronger acid sites than CoMoZA#1 and that the reason for a higher amount of NH_3 adsorbed on CoMoZA#1 than CoMoZA#2 is likely to due NH_3 adsorbed on the alumina, which contains more acid sites than the zeolite.

Table 6.4 Concentration of acid sites (NH_3-TPD) for the oxide precursors

	CoMoMgAl#1	CoMoMgAl#2	CoMoMgAl#3	CoMoMgAl#4	CoMoZA#1	CoMoZA#2
NH_3 adsorbed (mmol/g)	0.127	0.259	0.333	0.378	0.564	0.529
NH_3 desorbed (mmol/g)	0.124	0.251	0.323	0.374	0.516	0.494

6.3.3.1.2 Raman spectroscopy

Raman spectroscopy was used to determine the phases for the oxide precursors, as shown in Figure 6.9. Between three and four spectra were measured at different spatial spots for each sample, see supplementary information Figure E.4, which showed a slight variation between the spectra for the same catalyst, hence indicating some degree of phase heterogeneity. For CoMoMgAl#1 the bands observed at 407, 678, and 771 cm^{-1} was ascribed to the $MgAl_2O_4$ spinel carrier [54]. The intensity of these bands decreased with increasing CoMo loading. This was probably due to lower $MgAl_2O_4$ surface concentration, darkening of the sample, but also the calcination temperatures were decreasing with increasing CoMo loading. This was done to maintain available surface area for the carrier, and might have led to less complete formation of the spinel phase (see supplementary information Figure E.5). For CoMoZA#1 and CoMoZA#2 the bands at 301, 373, 470, and

828 cm^{-1} were ascribed to H-ZSM-5, while the bands at 565 and 670 cm^{-1} were ascribed to Al_2O_3. Crystalline MoO_3 has a sharp peak at 992 cm^{-1} due to terminal Mo=O stretching [55], which can therefore be ruled out. The broad band at 920-950 cm^{-1} observed for all the $MgAl_2O_4$ supported samples corresponds to a Mo-O distance of approximately 1.7 Å, which could come from terminal Mo=O units. Since the supports are fairly porous it is very likely that capillary condensation of water in the pores have occurred, thus the observed species are probably mixtures of MoO_4^{2-} (aq) (isolated, tetrahedral), $Mo_7O_{24}^{6-}$ and $Mo_8O_{26}^{4-}$ (aq) dissolved in the capillary water of the ambient air exposed calcined samples. Therefore the observed band at 320-340 cm^{-1} is most likely also due to distorted MoO_4^{2-} species [56], which also contributes at 837 and 897 cm^{-1}. Furthermore $Mo_7O_{24}^{6-}$ contributes at 210, 270, 362, 903, and 943 cm^{-1}, while $Mo_8O_{26}^{4-}$ at 230, 370, 590, 925, 965 cm^{-1} [55,56]. Therefore, the intensity of the band at 595 cm^{-1}, which increased with increasing CoMo loading, indicates that more $Mo_8O_{26}^{4-}$ are formed at high loadings. A monolayer coverage of Mo on Al_2O_3 corresponds to 4.5 Mo atoms/nm^2 [55], assuming an even distribution of CoMo on the support, the $MgAl_2O_4$ support samples exhibits a monolayer coverage of approximately 73-104 %, thus some interactions between the molybdenum species are expected and true isolated sites are unlikely. However, the coverage for CoMoZA#1 and CoMoZA#2 was 16 and 13 %, respectively, which makes isolated sites more likely and band at 301 cm^{-1} could be due to isolated molybdenum oxide [57]. The observed peak at 370 cm^{-1} (only observed for CoMoMgAl#1) and 879 cm^{-1} can be assigned to hydrated $CoMoO_4$ and would represent a Mo-O distance of 1.75 Å [58] and is most likely a Mo-O-X (X=carrier or active metal) entity. The presence of a sharp doublet at 940-950 cm^{-1} only observed for CoMoMgAl#1 is ascribed to β-CoMoO4 [59]. However, the hydrated $CoMoO_4 \cdot xH_2O$ phase typically has a small band at ~870 cm^{-1} together and a broad band at ~930 cm^{-1} [59], but the metal coordination for $CoMoO_4 \cdot xH_2O$ and β-CoMoO4 are very similar, both containing CoO_6 octahedra and MoO_4 tetrahedra [60]. It is noted that the small band at ~870 cm^{-1} decreases with increasing metal loading. Co_3O_4 would have its main contribution at 692 cm^{-1}, which is not observed, thus indicating that Co is mainly located as hydrated $CoMoO_4$. Furthermore, crystalline α-MoO_3, which has a characteristic sharp band at 992 cm^{-1} [55], can be excluded.

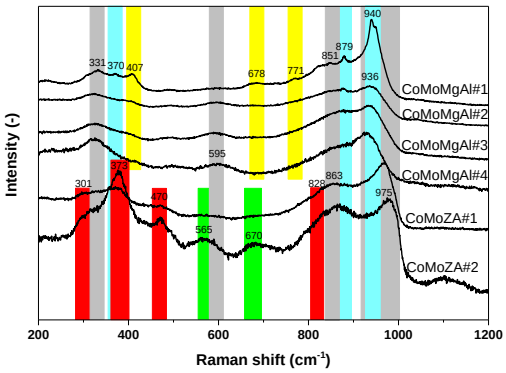

Figure 6.9 Raman spectra of oxide precursors (calcined, not dehydrated). The Raman bands were assigned to hydrated, MoO_x (gray), hydrated $CoMoO_4$ (blue), spinel $MgAl_2O_4$ (yellow), H-ZSM-5 (red), and Al_2O_3 (green)

6.3.3.2 Characterization of the spent catalysts

6.3.3.2.1 SEM-EDS

In order to study the carbon and potassium content on the spent catalysts, the spent catalysts were analyzed with SEM combined with EDS. The carbon and potassium content of both the fresh and spent catalysts were

measured at 3, 5, 10 and 15 kV. Where at 3 kV the concentration near the surface was measured, and at 15 kV a larger volume towards the bulk was measured integrating the signals from both the surface and bulk, although even at 15 kV the expected penetration depth is only 1.7 µm, as described in Chapter 5. The measured carbon and potassium concentration on the fresh and spent catalysts are shown in supplementary information Table E.12. Since the sample is placed on carbon tape it is assumed that this gives an offset for the carbon measurement, however this is accounted for by subtracting the carbon content measured on the fresh catalyst (placed on the same tape) from the content measured on the spent catalyst.

Figure 6.10(A) shows the carbon content (measured at 15 kV) per square meter surface area of the corresponding fresh catalyst and the relative carbon content on the spent catalyst increased from 0.25 mg_{carbon}/m^2 to 0.92 mg_{carbon}/m^2 when the surface area increased from 60 to 148 m^2/g. Part of the reason for the increasing carbon content is that the number of acidic sites and the acid strength of the fresh oxide precursor increased with increasing surface area (see Figure 6.8 and Table 6.4). de Jong et al. [61] investigated coking of MoS_2/Al_2O_3 catalysts during hydro processing of vacuum gas oil and observed an increase in the degree of coking when the Mo loading was increased. The increase was most likely because the Brønsted sites on MoS_2 promote the formation of coke through the formation of carbonium cations as intermediates [62]. Therefore, the increased loading, and thus increased Brønsted acidity, has most likely also increased the carbon content on the spent catalyst in this work. The carbon content on the spent CoMoZA#1 and CoMoZA#2 was 0.11 and 0.092 mg_{carbon}/m^2, hence significantly lower than for CoMoMgAl#1 (0.25 mg_{carbon}/m^2). This is probably because the micro pores in the zeolites, are too narrow for the larger aromatics to enter. It should therefore be noted that despite that the carbon content per square meter decreased, the total carbon content ($mg_{carbon}/g_{catalyst}$) on the spent CoMoZA#1 and CoMoZA#2 increased compared to CoMoMgAl#1 (see supplementary information Figure E.6).

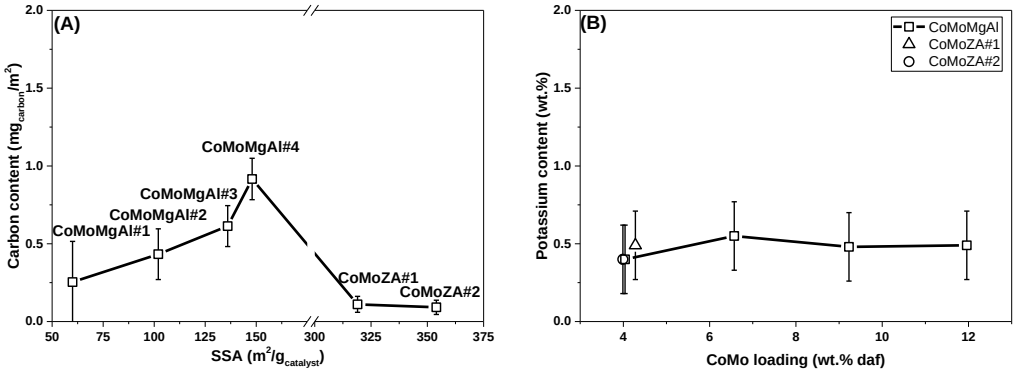

Figure 6.10 Effect of CoMo loading and support on carbon content (A) and potassium measured at 15 kV (B) content on the spent catalysts. Conditions: Fluid bed temperature: 450-455°C, total pressure: 26 bar, biomass feeding rate: 270-282 g/h, feed time: 2.5-3.5 h, H_2 flow: 82 NL/min, N_2 flow: 5 NL/min, and H_2S conc: 460 ppm.

The potassium content on the spent catalysts varied between 0.40 and 0.55 wt.% (see Figure 6.10 (B)), which was within the uncertainty of the measurement. It is well-known that that potassium can decrease the number of Brønsted acid sites [63–67] and decreases the HDO activity for sulfided NiMo catalysts [51], thus the transfer of potassium from the biomass to the catalysts could be a serious problem. Since the catalyst saturation level, at which potassium does no longer diffuse into the catalyst, is correlated with the number of Brønsted sites [63], significantly more potassium can potentially be transferred to the zeolite based catalysts, CoMoZA#1 and CoMoZA#2. However, since there is no significant difference in the potassium level of the

spent catalyst, this indicates that the catalysts are not saturated with potassium and content of potassium was limited by the transfer from the biomass to catalyst, but the total amount of biomass used per catalyst mass was also relatively low in these experiments. Thus, the advantage of using zeolite based supports might decrease when the process is up-scaled, because they will lose their acidity over time.

6.3.3.2.2 HAADF-STEM

The spent catalysts were also characterized with HAADF-STEM and an image of the spent CoMoMgAl#3 is shown in Figure 6.11(A). This shows nanometer sized slab structures of the bright contrast, which are well-distributed on the surface of larger support grains. An example of a two-layer slab structure is indicated in the figure, where the interlayer distance was 0.62 nm, consistent with the MoS_2 (001) spacing. Therefore the bright-contrasted slab structures are ascribed to MoS_2 nanocrystals observed with the (001) basal plane along the electron beam direction and located with the basal-plane on the surface of the $MgAl_2O_4$, which also previously has been reported [68]. The slab lengths for the spent catalysts were measured from the STEM images (173-199 slabs per sample) and fitted with a Log Normal distribution as Figure 6.11(B). The slab length distribution was more narrow for the zeolite mixed with alumina supported catalysts compared to the catalysts supported on $MgAl_2O_4$. The mean slab length was 1.96 nm for CoMoZA#1 and 2.25 nm for CoMoZA#2, while it was between 2.65 and 3.07 nm for the catalysts supported on $MgAl_2O_4$. The frequency of monolayer slabs was between 94 and 99 % for all the tested catalysts, as shown in Figure 6.11(C), indicating a fairly similar degree of stacking and indicating that most of the active sites were of the Type I structure [44]. The difference in slab length is most likely due to a lower Mo loading on the CoMoZA#1 (0.71 atoms/nm^2) and CoMoZA#2 (0.60 atoms/nm^2) compared to the catalysts on $MgAl_2O_4$ (3.3-4.7 atoms/nm^2).

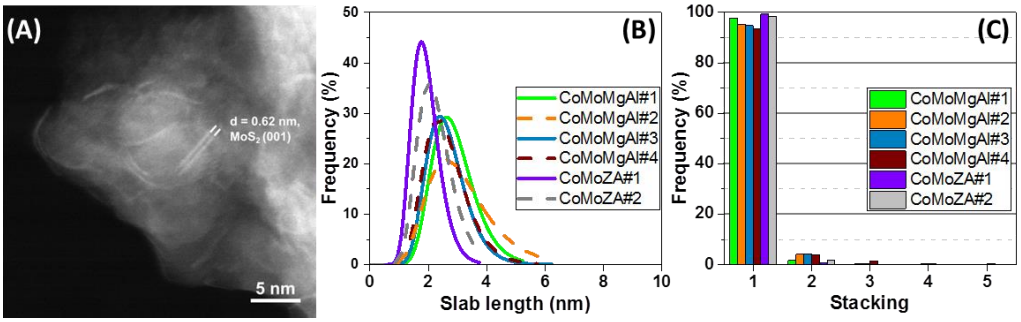

Figure 6.11 HAADF-STEM image of CoMoMgAl#3 (A), log-normal distribution of the slab length for the tested catalysts (B), and the stacking for the different catalysts (C).

An example of the distribution of cobalt, molybdenum, and sulfur is shown for CoMoZA#2 in Figure 6.12. The alumina and zeolite phases are clearly discriminated by having a high concentration in aluminum or silicium EDS signals, respectively, see Figure 6.12 (A). It is observed that a layer of about 50-100 nm alumina is surrounding the zeolite crystals and that the cobalt, molybdenum, and sulfur are well-distributed on the alumina parts of the catalyst, which is consistent with the observed uniformly and well-distributed MoS_2 structures in Figure 6.11(A), and indicates a successful incorporation of the cobalt into the MoS_2 structure, forming the so-called CoMoS phase [37]. Element maps of the other catalysts also showed the formation of the CoMoS phase (See supplementary information Figure E.7-E.12), indicating that the catalysts are representative for a comparison of the effect of the CoMo loading and the support acidity. Potassium was also observed on all the catalysts and it was well-distributed on the particles (See supplementary information Figure E.7-E.12), and in particular found with a high concentration on the zeolite parts, as indicated in Figure

6.12 (D), confirming the potassium transfer from the biomass to the catalysts observed with SEM-EDS. Furthermore, it also indicates that the potassium primary absorbs on the strong acid sites.

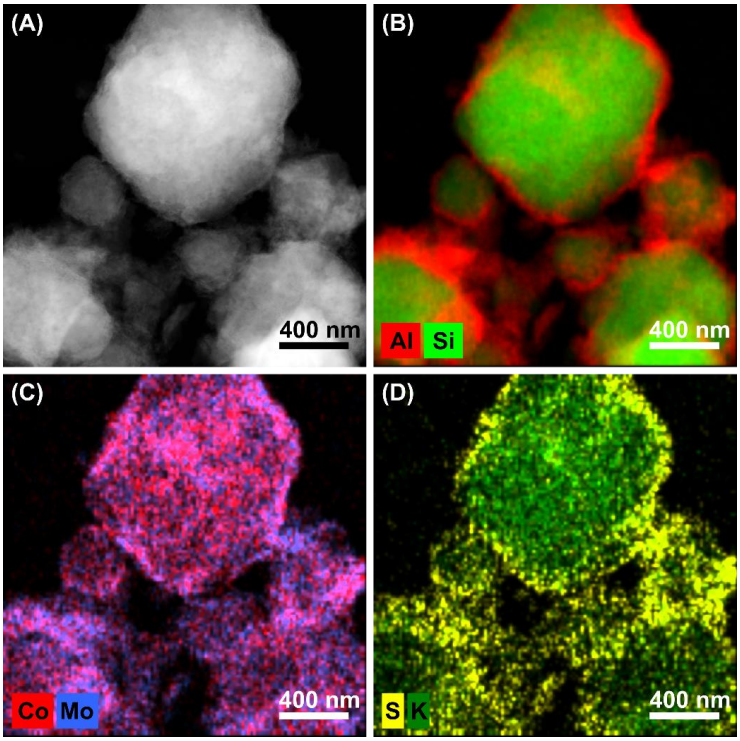

Figure 6.12 HAADF-STEM image of CoMoZAl#2 (A), EDS element distribution of alumina and silicum (B) cobalt and molybdenum, (C) and EDS element distribution of sulfur and potassium (D).

6.4 Conclusion

Catalytic hydropyrolysis of beech wood using sulfided CoMo catalysts in a fluid bed reactor at 450 °C and 26 bar pressure have been conducted. Using $MgAl_2O_4$ as support material the effect of varying the CoMo loading between 4.04 and 11.96 wt.% was investigated. In order to ensure the formation of a monolayer on the support, the surface area of the support was controlled by calcination between 600 and 1000 °C prior to the impregnation. However, NH_3-TPD showed that the total number of acidic sites increased with increasing metal loading and support surface area. Nevertheless, STEM-HAADF showed that the metal catalyst MoS_2 structure were comparable in slab length and the degree of stacking, thus making them fairly comparable, and both STEM-HAADF and Raman spectroscopy indicated a successful incorporation of Co into the CoMoS structure. Increasing the CoMo loading from 4.04 to 11.96 wt.% decreased the condensable organic yield from 25.2 to 22.7 wt.% and decreased the oxygen content from 9.0 to 4.7 wt.% db. The carbon recovery in the condensable organics (condensed organics and C_{4+} in the gas) decreased from 39 to 37 wt.%, where the decrease in carbon recovery was most likely due to an increased yield of C_1-C_3, which increased from 10.3 to 14.0 wt.% daf. GC×GC showed that remaining oxygenates in the organic phase was mainly phenols.

The effect of the support acidity was also investigated by testing a CoMo catalyst on $MgAl_2O_4$ and two CoMo catalysts supported on zeolite (H-ZSM-5) mixed with alumina at different ratios. This showed that using zeolite as support increased the hydrocracking and/or cracking activity. Furthermore, it also decreased the oxygen content in organic phase from 9.0 wt.% db to between 5.2 and 6.1 wt.% db, depending on the zeolite content. This decrease was mainly ascribed to a decrease in the concentration of the oxygenated aliphatics. The results further indicated an increased degree of alkylation reactions when the zeolite based supports were used and the yield of mono-and diaromatics increased when the zeolite based supports were used. Using zeolite based supports lead to a carbon recovery in the condensable organics between 39 and 40 %, thus showing that using a more acidic support can decrease the oxygen content in organic phase without decreasing the carbon recovery. Interestingly, the total char and coke yield was not affected by the CoMo loading or the support acidity.

SEM combined with EDS showed that increasing the surface area of the support and the CoMo loading increased the relative carbon content per surface area (mg_{carbon}/m^2) on the spent catalysts, which was most likely due to the increase in acidic sites. Using the zeolites mixed with alumina decreased the carbon content per surface area, but this was ascribed to a significantly larger surface area of these supports compared to $MgAl_2O_4$. Comparing the total amount of carbon on the spent catalyst showed that more carbon was deposited on the zeolite based supports compared to $MgAl_2O_4$. Potassium was observed on all the spent catalysts both with SEM-EDS and STEM, indicating that the catalyst in the fluid bed could be poisoned by potassium over time. Since it is well-known that the addition of potassium decreases the number of acidic sites, it is very likely that the positive effect of using zeolites will be lost over time. Therefore further investigations are needed in order to understand the transfer of potassium from the biomass to the catalyst and how it influences the catalyst activity.

Acknowledgments

This work is part of the project “Hydrogen assisted catalytic pyrolysis for green fuels” project conducted at The Department of Chemical and Biochemical Engineering at the Technical University of Denmark (DTU). The work was supported by The Danish Council for Strategic Research (now Innovation Fund Denmark, project 1305-00015B), The Programme Commission on Sustainable Energy and Environment. Funding from DTU is also gratefully acknowledged. The authors also acknowledge Aino Nielsen (Haldor Topsøe A/S) for technical assistance with the Raman spectroscopy, Søren Birk Rasmussen for assistance with NH_3-TPD, the Inorganic Analysis Department at Haldor Topsøe A/S for technical assistance with the elemental analysis of the fresh oxide precursors by inductive coupled plasma optical emission spectroscopy (IPC-OES) and wavelength dispersive X-ray fluorescence (WD-XRF), and the Organic Analysis Department at Haldor Topsøe A/S for analysis of the organic phase.

References

[1] United Nations, Sustainable development goals, (2016). http://www.un.org/sustainabledevelopment/energy/ (accessed April 21, 2016).

[2] IPCC - Intergovernmental Panel on Climate Change, Global Warming of 1.5°C an IPCC special report on the impacts of global warming of 1.5 °C above pre-industrial levels and related global greenhouse gas emission pathways, in the context of strengthening the global response to the threat of climate change, (2018). http://www.ipcc.ch/report/sr15/.

[3] Independent Statistics & Analysis - U.S. Energy Information Administration, International energy outlook 2016 - DOE/EIA-0484, 2016. https://www.eia.gov/outlooks/ieo/pdf/0484(2016).pdf

(accessed July 7, 2017).

[4] J. Hansen, M. Sato, P. Hearty, R. Ruedy, M. Kelley, V. Masson-Delmotte, G. Russell, G. Tselioudis, J. Cao, E. Rignot, I. Velicogna, B. Tormey, B. Donovan, E. Kandiano, K. Von Schuckmann, P. Kharecha, A.N. Legrande, M. Bauer, Ice melt, sea level rise and superstorms: Evidence from paleoclimate data, climate modeling, and modern observations that 2 °C global warming could be dangerous, Atmos. Chem. Phys. 16 (2016) 3761–3812. doi:10.5194/acp-16-3761-2016.

[5] T.L. Marker, L.G. Felix, M.B. Linck, M.J. Roberts, Integrated hydropyrolysis and hydroconversion (IH^2) for the direct production of gasoline and diesel fuels or blending components from biomass, Part 1: Proof of principle testing, Environ. Prog. Sustain. Energy. 31 (2012) 191–199. doi:10.1002/ep.10629.

[6] T.L. Marker, L.G. Felix, M.B. Linck, M.J. Roberts, P. Ortiz-Toral, J. Wangerow, Integrated hydropyrolysis and hydroconversion ($IH^{2®}$) for the direct production of gasoline and diesel fuels or blending components from biomass, Part 2: Continuous testing, Environ. Prog. Sustain. Energy. 33 (2014) 762–768. doi:10.1002/ep.11906.

[7] E. Maleche, R. Glaser, T. Marker, D. Shonnard, A preliminary life cycle assessment of biofuels produced by the $IH^{2\ TM}$ process, Environ. Prog. Sustain. Energy. 33 (2014) 322–329. doi:10.1002/ep.11773.

[8] J. Fan, J. Gephart, T. Marker, D. Stover, B. Updike, D.R. Shonnard, Carbon Footprint Analysis of Gasoline and Diesel from Forest Residues and Corn Stover using Integrated Hydropyrolysis and Hydroconversion, ACS Sustain. Chem. Eng. 4 (2016) 284–290. doi:10.1021/acssuschemeng.5b01173.

[9] O. Winjobi, H. Tavakoli, B. Klemetsrud, R. Handler, T. Marker, M. Roberts, D. Shonnard, Carbon Footprint Analysis of Gasoline and Diesel from Forest Residues and Algae using Integrated Hydropyrolysis and Hydroconversion Plus Fischer–Tropsch (IH 2 Plus cool GTL), ACS Sustain. Chem. Eng. 6 (2018) 10766–10777. doi:10.1021/acssuschemeng.8b02091.

[10] T. Van Nguyen, L.R. Clausen, Thermodynamic analysis of polygeneration systems based on catalytic hydropyrolysis for the production of bio-oil and fuels, Energy Convers. Manag. 171 (2018) 1617–1638. doi:10.1016/j.enconman.2018.06.024.

[11] D.C. Dayton, J. Carpenter, J. Farmer, B. Turk, R. Gupta, Biomass hydropyrolysis in a pressurized fluidized bed reactor, Energy & Fuels. 27 (2013) 3778–3785. doi:10.1021/ef400355t.

[12] D.C. Dayton, J. Hlebak, J.R. Carpenter, K. Wang, O.D. Mante, J.E. Peters, Biomass hydropyrolysis in a fluidized bed reactor, Energy & Fuels. 30 (2016) 4879–4887. doi:10.1021/acs.energyfuels.6b00373.

[13] K. Wang, D.C. Dayton, J.E. Peters, O.D. Mante, Reactive catalytic fast pyrolysis of biomass to produce high-quality bio-crude, Green Chem. 19 (2017) 3243–3251. doi:10.1039/C7GC01088E.

[14] D.P. Gamliel, G.M. Bollas, J.A. Valla, Two-stage catalytic fast hydropyrolysis of biomass for the production of drop-in biofuel, Fuel. 216 (2018) 160–170. doi:10.1016/j.fuel.2017.12.017.

[15] D.P. Gamliel, L. Wilcox, J.A. Valla, The effects of catalyst properties on the conversion of biomass via catalytic fast hydropyrolysis, Energy & Fuels. 31 (2017) 679–687. doi:10.1021/acs.energyfuels.6b02781.

[16] D.P. Gamliel, G.M. Bollas, J.A. Valla, Bifunctional Ni-ZSM-5 catalysts for the pyrolysis and hydropyrolysis of biomass, Energy Technol. 5 (2017) 172–182. doi:10.1002/ente.201600136.

[17] S. Thangalazhy-Gopakumar, S. Adhikari, R.B. Gupta, M. Tu, S. Taylor, Production of hydrocarbon fuels from biomass using catalytic pyrolysis under helium and hydrogen environments., Bioresour. Technol. 102 (2011) 6742–9. doi:10.1016/j.biortech.2011.03.104.

[18] S. Thangalazhy-Gopakumar, S. Adhikari, R.B. Gupta, Catalytic pyrolysis of biomass over H^+ZSM-5 under hydrogen pressure, Energy & Fuels. 26 (2012) 5300–5306. doi:10.1021/ef3008213.

[19] O. Jan, R. Marchand, L.C.A. Anjos, G.V.S. Seufitelli, E. Nikolla, F.L.P. Resende, Hydropyrolysis of lignin using Pd/HZSM-5, Energy & Fuels. 29 (2015) 1793–1800. doi:10.1021/ef502779s.

[20] F. Melligan, M.H.B. Hayes, W. Kwapinski, J.J. Leahy, Hydro-pyrolysis of biomass and online catalytic vapor upgrading with Ni-ZSM-5 and Ni-MCM-41, Energy & Fuels. 26 (2012) 6080–6090. doi:10.1021/ef301244h.

[21] P. Choudhary, A. Malik, K.K. Pant, Mass-Scale Algal Biomass Production Using Algal Biofilm Reactor and Conversion to Energy and Chemical Precursors by Hydropyrolysis, ACS Sustain. Chem. Eng. 5 (2017) 4234–4242. doi:10.1021/acssuschemeng.7b00233.

[22] R.. Pindoria, a Megaritis, a. . Herod, R. Kandiyoti, A two-stage fixed-bed reactor for direct hydrotreatment of volatiles from the hydropyrolysis of biomass: effect of catalyst temperature, pressure and catalyst ageing time on product characteristics, Fuel. 77 (1998) 1715–1726. doi:10.1016/S0016-2361(98)00079-9.

[23] F. Melligan, M.H.B. Hayes, W. Kwapinski, J.J. Leahy, A study of hydrogen pressure during hydropyrolysis of Miscanthus x giganteus and online catalytic vapour upgrading with Ni on ZSM-5, J. Anal. Appl. Pyrolysis. 103 (2013) 369–377. doi:10.1016/j.jaap.2013.01.005.

[24] T.M.H. Dabros, M.Z. Stummann, M. Høj, P.A. Jensen, J.-D. Grunwaldt, J. Gabrielsen, P.M. Mortensen, A.D. Jensen, Transportation fuels from biomass fast pyrolysis, catalytic hydrodeoxygenation, and catalytic fast hydropyrolysis, Prog. Energy Combust. Sci. 68 (2018) 268–309. doi:10.1016/j.pecs.2018.05.002.

[25] T.N. Trinh, P.A. Jensen, K. Dam-Johansen, N.O. Knudsen, H.R. Sørensen, S. Hvilsted, Comparison of lignin, macroalgae, wood, and straw fast pyrolysis, Energy & Fuels. 27 (2013) 1399–1409. doi:10.1021/ef301927y.

[26] O.İ. Şenol, T.-R. Viljava, A.O.I. Krause, Hydrodeoxygenation of aliphatic esters on sulphided NiMo/γ-Al_2O_3 and CoMo/γ-Al2O3 catalyst: The effect of water, Catal. Today. 106 (2005) 186–189. doi:10.1016/j.cattod.2005.07.129.

[27] O.I. Şenol, E.M. Ryymin, T.R. Viljava, A.O.I. Krause, Reactions of methyl heptanoate hydrodeoxygenation on sulphided catalysts, J. Mol. Catal. A Chem. 268 (2007) 1–8. doi:10.1016/j.molcata.2006.12.006.

[28] O.İ. Şenol, T.-R. Viljava, A.O.I. Krause, Effect of sulphiding agents on the hydrodeoxygenation of aliphatic esters on sulphided catalysts, Appl. Catal. A Gen. 326 (2007) 236–244. doi:10.1016/j.apcata.2007.04.022.

[29] E.-M. Ryymin, M.L. Honkela, T.-R. Viljava, A.O.I. Krause, Competitive reactions and mechanisms in the simultaneous HDO of phenol and methyl heptanoate over sulphided NiMo/γ-Al_2O_3, Appl. Catal. A Gen. 389 (2010) 114–121. doi:10.1016/j.apcata.2010.09.010.

[30] A. Gutierrez, E.-M. Turpeinen, T.-R. Viljava, O. Krause, Hydrodeoxygenation of model compounds on sulfided CoMo/γ-Al2O3 and NiMo/γ-Al2O3 catalysts; Role of sulfur-containing groups in reaction networks, Catal. Today. 285 (2017) 125–134. doi:10.1016/j.cattod.2017.02.003.

[31] T.M.H. Dabros, A. Gaur, D.G. Pintos, P. Sprenger, M. Høj, T.W. Hansen, F. Studt, J. Gabrielsen, J.-D. Grunwaldt, A.D. Jensen, Influence of H2O and H2S on the composition, activity, and stability of sulfided Mo, CoMo, and NiMo supported on MgAl2O4 for hydrodeoxygenation of ethylene glycol, Appl. Catal. A Gen. 551 (2018) 106–121. doi:10.1016/j.apcata.2017.12.008.

[32] V.N. Bui, D. Laurenti, P. Afanasiev, C. Geantet, Hydrodeoxygenation of guaiacol with CoMo catalysts. Part I: Promoting effect of cobalt on HDO selectivity and activity, Appl. Catal. B Environ. 101 (2011) 239–245. doi:10.1016/j.apcatb.2010.10.025.

[33] A. Centeno, E. Laurent, B. Delmon, Influence of the support of CoMo sulfide catalysts and of the addition of potassium and platinum on the catalytic performances for the hydrodeoxygenation of

carbonyl, carboxyl, and guaiacol-type molecules, J. Catal. 154 (1995) 288–298. doi:10.1006/jcat.1995.1170.

[34] M. Badawi, J.-F. Paul, S. Cristol, E. Payen, Guaiacol derivatives and inhibiting species adsorption over MoS_2 and CoMoS catalysts under HDO conditions: A DFT study, Catal. Commun. 12 (2011) 901–905. doi:10.1016/j.catcom.2011.02.010.

[35] P. Raybaud, J. Hafner, G. Kresse, S. Kasztelan, H. Toulhoat, Structure, energetics, and electronic properties of the surface of a promoted MoS2 catalyst: An ab initio local density functional study, J. Catal. 190 (2000) 128–143. doi:10.1006/jcat.1999.2743.

[36] B.R.G. Leliveld, J.A.J. van Dillen, J.W. Geus, D.C. Koningsberger, M. de Boer, Structure and Nature of the Active Sites in CoMo Hydrotreating Catalysts. An EXAFS Study of the Reaction with Selenophene, J. Phys. Chem. B. 101 (1997) 11160–11171. doi:10.1021/jp9723933.

[37] H. Topsøe, B.S. Clausen, F.E. Massoth, Cataltsis - Science and Technology. Hydrotreating catalysis, Volume 11, Springer-Verlag, Berlin Heidelberg, Germany, 1996.

[38] C. Bouvier, Y. Romero, F. Richard, S. Brunet, Effect of H_2S and CO on the transformation of 2-ethylphenol as a model compound of bio-crude over sulfided Mo-based catalysts: propositions of promoted active sites for deoxygenation pathways based on an experimental study, Green Chem. 13 (2011) 2441–2451. doi:10.1039/c1gc15181a.

[39] V.N. Bui, D. Laurenti, P. Delichère, C. Geantet, Hydrodeoxygenation of guaiacol. Part II: Support effect for CoMoS catalysts on HDO activity and selectivity, Appl. Catal. B Environ. 101 (2011) 246–255. doi:10.1016/j.apcatb.2010.10.031.

[40] V.O.O. Gonçalves, S. Brunet, F. Richard, Hydrodeoxygenation of cresols over Mo/Al_2O_3 and $CoMo/Al_2O_3$ sulfided catalysts, Catal. Letters. 146 (2016) 1562–1573. doi:10.1007/s10562-016-1787-5.

[41] E. Schachtl, J.S. Yoo, O.Y. Gutiérrez, F. Studt, J.A. Lercher, Impact of Ni promotion on the hydrogenation pathways of phenanthrene on MoS_2/γ-Al_2O_3, J. Catal. 352 (2017) 171–181. doi:10.1016/j.jcat.2017.05.003.

[42] M.Z. Stummann, M. Høj, C.B. Schandel, A.B. Hansen, P. Wiwel, J. Gabrielsen, P.A. Jensen, A.D. Jensen, Hydrogen assisted catalytic biomass pyrolysis. Effect of temperature and pressure, Biomass and Bioenergy. 115 (2018) 97–107. doi:10.1016/j.biombioe.2018.04.012.

[43] S. Houssenbay, E. Payen, S. Kasztelan, J. Grimblot, Oxidic precursors of molybdena supported on nickel and magnesium aluminate hydrotreating catalysts, Catal. Today. 10 (1991) 541–560. doi:10.1016/0920-5861(91)80038-B.

[44] H. Topsøe, The role of Co-Mo-S type structures in hydrotreating catalysts, Appl. Catal. A Gen. 322 (2007) 3–8. doi:10.1016/j.apcata.2007.01.002.

[45] C. Wivel, R. Candia, B.S. Clausen, S. Mørup, H. Topsøe, On the catalytic significance of a CoMoS phase in CoMo Al2O3hydrodesulfurization catalysts: Combined in situ Mössbauer emission spectroscopy and activity studies, J. Catal. 68 (1981) 453–463. doi:10.1016/0021-9517(81)90115-9.

[46] P. Beato, E. Schachtl, K. Barbera, F. Bonino, S. Bordiga, Operando Raman spectroscopy applying novel fluidized bed micro-reactor technology, Catal. Today. 205 (2013) 128–133. doi:10.1016/j.cattod.2012.09.030.

[47] J. Lai, L. Zhang, K. Gong, Nuclear magnetic resonance characterization of renewable products from a two-step ex-situ hydropyrolysis vapor upgrading process, ChemistrySelect. 3 (2018) 297–307. doi:10.1002/slct.201702431.

[48] N. Dos Santos, H. Dulot, N. Marchal, M. Vrinat, New insight on competitive reactions during deep HDS of FCC gasoline, Appl. Catal. A Gen. 352 (2009) 114–123. doi:10.1016/j.apcata.2008.09.035.

[49] J.A. Anabtawi, S.A. Ali, M. Abdul Bari Siddiqui, S.M. Javaid Zaidi, Factors influencing the

performance of naphtha hydro-desulfurization catalysts, in: 1996: pp. 225–234. doi:10.1016/S0167-2991(96)80023-1.

[50] X. Si, D. Xia, Y. Xiang, Y. Zhou, Effect of H2S on the transformation of 1-hexene over NiMoS/γ-Al2O3 with hydrogen, J. Nat. Gas Chem. 19 (2010) 185–188. doi:10.1016/S1003-9953(09)60054-2.

[51] P.M. Mortensen, D. Gardini, C.D. Damsgaard, J.-D. Grunwaldt, P.A. Jensen, J.B. Wagner, A.D. Jensen, Deactivation of Ni-MoS_2 by bio-oil impurities during hydrodeoxygenation of phenol and octanol, Appl. Catal. A Gen. 523 (2016) 159–170. doi:10.1016/j.apcata.2016.06.002.

[52] P. Leflaive, J.L. Lemberton, G. Pérot, C. Mirgain, J.Y. Carriat, J.M. Colin, On the origin of sulfur impurities in fluid catalytic cracking gasoline - Reactivity of thiophene derivatives and of their possible precursors under FCC conditions, Appl. Catal. A Gen. 227 (2002) 201–215. doi:10.1016/S0926-860X(01)00936-X.

[53] A. Corma, C. Martínez, G. Ketley, G. Blair, On the mechanism of sulfur removal during catalytic cracking, Appl. Catal. A Gen. 208 (2001) 135–152. doi:10.1016/S0926-860X(00)00693-1.

[54] V. D'Ippolito, G.B. Andreozzi, D. Bersani, P.P. Lottici, Raman fingerprint of chromate, aluminate and ferrite spinels, J. Raman Spectrosc. 46 (2015) 1255–1264. doi:10.1002/jrs.4764.

[55] H. Hu, I.E. Wachs, Surface structures of supported molybdenum oxide catalysts. Characterization by raman and Mo L3-edge XANES, J. Phys. Chem. 99 (1995) 10897–10910. doi:10.1021/j100027a034.

[56] H. Jeziorowski, H. Knözinger, Raman and ultraviolet spectroscopic characterization of molybdena on alumina catalysts, J. Phys. Chem. 83 (1979) 1166–1173. doi:10.1021/j100472a012.

[57] X. Gao, Q. Xin, Effect of cobalt oxide on surface structure of alumina supported molybdena catalysts studied by in situ Raman spectroscopy, Catal. Letters. 18 (1993) 409–418. doi:10.1007/BF00765287.

[58] F.D. Hardcastle, I.E. Wachs, Determination of molybdenum–oxygen bond distances and bond orders by Raman spectroscopy, J. Raman Spectrosc. 21 (1990) 683–691. doi:10.1002/jrs.1250211009.

[59] E. Payen, M.C. Dhamelincourt, P. Dhamelincourt, J. Grimblot, J.P. Bonnelle, Study of Co(or Ni)-Mo Oxide Phase Transformation and Hydrodesulfurization Catalysts by Raman Microprobe Equipped with New Cells, Appl. Spectrosc. 36 (1982) 30–37. doi:10.1366/0003702824638953.

[60] K. Eda, Y. Uno, N. Nagai, N. Sotani, M.S. Whittingham, Crystal structure of cobalt molybdate hydrate CoMoO4· nH2O, J. Solid State Chem. 178 (2005) 2791–2797. doi:10.1016/j.jssc.2005.06.014.

[61] K.P. de JongZ, D. Reinalda, C.A. Emeis, Coke deposition in trickle-bed reactors during heavy oil processing — Catalytic and physical effects, in: Stud. Surf. Sci. Catal., 1994: pp. 155–166. doi:10.1016/S0167-2991(08)62736-6.

[62] E. Furimsky, F.E. Massoth, Deactivation of hydroprocessing catalysts, Catal. Today. 52 (1999) 381–495. doi:10.1016/S0920-5861(99)00096-6.

[63] B.K. Olsen, F. Kügler, F. Castellino, A.D. Jensen, Poisoning of vanadia based SCR catalysts by potassium: Influence of catalyst composition and potassium mobility, Catal. Sci. Technol. 6 (2016) 2249–2260. doi:10.1039/c5cy01409c.

[64] Y. Zheng, A.D. Jensen, J.E. Johnsson, J.R. Thøgersen, Deactivation of V2O5-WO3-TiO2SCR catalyst at biomass fired power plants: Elucidation of mechanisms by lab- and pilot-scale experiments, Appl. Catal. B Environ. 83 (2008) 186–194. doi:10.1016/j.apcatb.2008.02.019.

[65] J.P. Chen, R.T. Yang, Mechanism of poisoning of the V2O5 / TiO2 catalyst for the reduction of NO by NH3, J. Catal. 125 (1990) 411–420. doi:10.1016/0021-9517(90)90314-A.

[66] D. Nicosia, M. Elsener, O. Kröcher, P. Jansohn, Basic investigation of the chemical deactivation of V2O5/WO3-TiO2 SCR catalysts by potassium, calcium, and phosphate, Top. Catal. 42–43 (2007) 333–336. doi:10.1007/s11244-007-0200-4.

[67] M. Klimczak, P. Kern, T. Heinzelmann, M. Lucas, P. Claus, High-throughput study of the effects of

inorganic additives and poisons on NH3-SCR catalysts-Part I: V2O5-WO3/TiO2 catalysts, Appl. Catal. B Environ. 95 (2010) 39–47. doi:10.1016/j.apcatb.2009.12.007.

[68] L.P. Hansen, E. Johnson, M. Brorson, S. Helveg, Growth mechanism for single- and multi-layer MoS_2 nanocrystals, J. Phys. Chem. C. 118 (2014) 22768–22773. doi:10.1021/jp5069279.

Chapter 7 Deactivation of a CoMo catalyst during catalytic hydropyrolysis of biomass. Part I: Product distribution and composition

In this chapter the process stability is evaluated by conducting a semi continuous 5 days experiment. Furthermore the potential deactivation of potassium, which is transferred from the biomass to the catalyst, is studied by predeactivating the catalyst in the fluid bed reactor by doping it with potassium prior to the sulfidation. The supplementary information can be found in Appendix F.

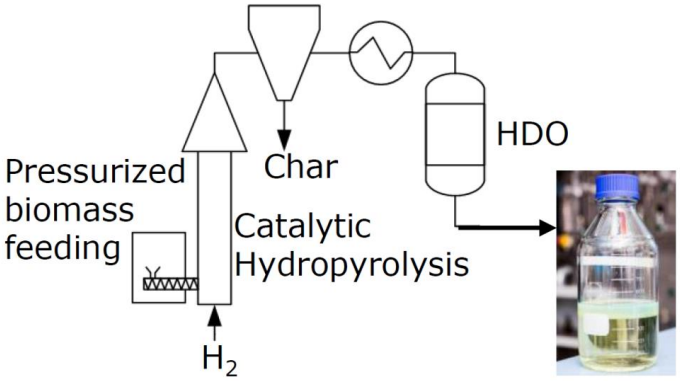

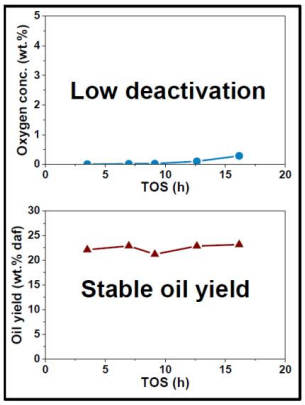

Abstract

Deactivation of a sulfided CoMo/$MgAl_2O_4$ catalyst during catalytic hydropyrolysis of beech wood has been studied in a fluid bed reactor. The stability of the process was tested by using approximately 5 kg of biomass and collecting the liquid and solid products for every 1 kg fed. The total time on stream was 16.2 h. A secondary fixed bed hydrotreating reactor with a sulfided NiMo/Al_2O_3 catalyst was used after the fluid bed reactor to ensure total deoxygenation of the vapors. The condensed organics and C_{4+} yield varied between 21.2 and 23.2 wt.% dry ash free (daf), the CO and CO_2 yield during the experiment increased from 14.9 to 18.2 wt.% daf, while the aqueous phase yield decreased from 38.0 to 35.1 wt.% daf. The change in CO, CO_2, and aqueous phase yields was ascribed to an increase in decarbonylation and/or decarboxylation activity and a decrease in hydrodeoxygenation activity. The oxygen content in the condensed organic phase increased during the experiment from 40 to 2832 ppm, indicating that deactivation of the HDO reactor may have occurred. Since the potassium, a known catalyst poison, is transferred from the biomass to the catalyst, the effect of doping the catalyst with potassium was also investigated. The results were compared to a similar experiment with a fresh catalyst, both experiments performed without the secondary HDO reactor. This showed that potassium decreases the catalyst's cracking, hydrogenation, and hydrodeoxygenation activity, while increasing the decarboxylation activity. Interestingly, doping the catalyst with potassium only increased the oxygen content in the condensed organics from 9.0 to 9.5 wt.% dry basis (db), indicating that potassium only has a small impact on the catalyst deoxygenation activity. Doping the catalyst with potassium also increased the char and coke yield from 13.3 to 14.6 wt.% daf, indicating that potassium can act as a catalyst for polymerization of the pyrolysis vapors.

Abbreviations

AED	Atomic emission detector	Naph	Naphthenes
BET	Brunauer–Emmett–Teller	O-Ali	Oxygenated aliphatics
daf	Dry, ash free basis	O-Aro	Larger oxygenated aromatics
db	Dry basis	Par	Paraffins
DDO	direct deoxygenation	PhOH	Phenolics
diAro	Diaromatics	Ph(OH)2	dihydroxybenzene
FB	Fluid bed	SSA	Specific surface area
FID	Flame ionization detector	SIMDIS	Simulated distillation by GC
GC	Gas chromatograph	STEM	Scanning transmission electron microscopy
HDO	Hydrodeoxygenation	Temp.	Temperature
ICP-OES	Inductive coupled plasma optical emission spectroscopy	TPD	Temperature programmed desorption
mAro	Monoaromatics	tetAro+	Tetra- and higher aromatics
MS	Mass spectrometry	triAro	Triaromatics

7.1 Introduction

Catalytic hydropyrolysis of biomass has been an emerging field since Marker et al. [1,2] showed that it is possible to obtain high yields, between 21 to 46 wt.% dry ash free (daf), of oxygen free oil (<1 wt.%) with the process IH$^{2®}$. In this process, catalytic hydropyrolysis takes place in a fluid bed reactor where char, light gasses, water and oil vapors with a low oxygen content are formed. The char is removed immediately after the fluid bed and the vapors are transferred to a fixed bed reactor where deep hydrodeoxygenation (HDO) of the vapors takes place [1,2]. The IH$^{2®}$ process has been running continuously for 750 hours with a biomass feeding rate of 50 kg/h without any observed deactivation. However, due to catalyst entrainment new catalyst was added to the fluid bed reactor during the experiment [2]. Life cycle assessments of the IH$^{2®}$ process have shown that fuel produced in this process have 30-96 % lower greenhouse gas (GHG) emissions compared to fossil fuels. The difference in the GHG emissions mainly depends on the type of biomass used, where bagasse gives the largest reduction [3,4].

Dayton et al. [5–7] also used a fluid bed reactor to study catalytic hydropyrolysis of woody biomass and have tested several different pre-reduced catalysts, including a commercial NiMo hydrotreating catalyst and a molybdenum oxide based catalyst. Their experiments were conducted at temperatures between 375 to 500 °C and between 1 and 31 bar total pressure. They were able to obtain a condensed organic and C_{4+} carbon yield of 43 %, with an oxygen content in the liquid of 6.2 wt.% dry basis (db) at atmospheric pressure [7]. However, the fresh catalysts were only to a limited extent characterized and the spent catalysts were not characterized. Using a pyroprobe analyzer Gamliel et al. [8–10] also studied the effect of the using reduced metal catalysts and focused on Ni on a zeolite (H-ZSM-5) support. Only the fresh, but not the spent, catalysts were characterized.

Sulfided CoMo, NiMo, and Mo catalysts are widely used as hydrotreating catalysts in oil refineries and are also active for hydrodeoxygenation of bio-oil and model components [11–19]. Since most types of biomass contains sulfur [20], one of the advantages of the sulfided CoMo, NiMo, and Mo catalysts is that they are sulfur tolerant as opposed to many reduced metal catalysts. We have therefore mainly used these catalysts for catalytic hydropyrolysis of beech wood in our previous work, where we have tested the effect of temperature and pressure [21], the effect of using catalytically inactive pure supports, different commercial hydrotreating catalysts, and the natural mineral bog iron (see Chapter 4). Additionally we tested the difference between using a CoMo, NiMo, and Mo catalyst in the fluid bed (see Chapter 5). Our work showed that the CoMo catalyst was more favorable to use in the fluid bed reactor compared to the NiMo and Mo catalyst. Furthermore, we observed that alkali metals are transferred from the biomass to the catalyst, and since potassium is a known poison for hydrodeoxygenation catalysts [22,23], this could lead to catalyst deactivation.

In the present work, the deactivation of a CoMoS/$MgAl_2O_4$ catalyst was investigated in a series of hydropyrolysis experiments using a fluid bed reactor. Firstly, the stability of the catalyst was investigated by a 16.2 h semi continuous experiment conducted over five days, where the product distribution and composition were followed by collecting products each day. Secondly, the effect of poisoning the catalyst by doping it with potassium, in the form of K_2CO_3, was studied. The produced organic phase was characterized in depth with sulfur and oxygen specific gas chromatography (GC) using an atomic emission detector (AED) and GC×GC time of flight (ToF)/ mass spectrometry (MS)/flame ionization detector (FID). This is to our knowledge the first study in the open literature where the effect of the time on stream on catalytic hydropyrolysis with a well-defined catalyst is tested and investigates the effect of potassium on the catalyst activity in catalytic hydropyrolysis.

7.2 Material and methods

7.2.1 Biomass feedstock

Bark free beech wood was used as biomass feedstock. The beech wood has previously been used in catalytic hydropyrolysis experiments [21]. The moisture and ash content in the beech wood was 6.72 wt.% and 0.59 wt.% on dry basis (db), respectively, the particle size was between 200-700 µm, and the potassium content was 0.12 wt.% db [21].

7.2.2 Catalyst preparation

The catalysts used in the fluid bed reactor were prepared by sequential incipient wetness impregnation of the $MgAl_2O_4$ spinel support, supplied by Haldor Topsøe A/S. The support was crushed to a particle size of 180-355 µm, this particle size distribution was chosen to ensure a good fluidization of the bed. Prior to the impregnation the support was calcined at 995 °C for 10 hours. The calcined support had a pore volume of 0.55-0.62 g_{water}/g (110 % of this volume was used for the impregnation) and the specific surface area (SSA) was between 54-58 m^2/g.

The support was impregnated with a aqueous solution of $(NH_4)_6Mo_7O_{24}\cdot 4H_2O$ (Fluka≥99.0%), then aged with stirring for approximately 3 hours and dried overnight at approximately 110 °C in air and followed by a second impregnation with $Co(NO_3)_2\cdot 6H_2O$ (Fluka ≥ 98%). The calcination was conducted with an air flow of 1.24-1.29 NL/min technical air (20% O_2 in N_2) by heating to 500°C with a ramp of 5°C/min and a holding for 3 hours. After calcination, the catalyst was sieved to 180-355 µm again in order remove any dust or agglomerates formed during the preparation. For the CoMo catalyst doped with potassium, a third impregnation was performed with K_2CO_3 (Sigma-Aldrich ≥99.0%) and the catalyst was re-calcined at 500°C and sieved. The composition of the catalysts is shown in Table 7.1. A Mo loading between 3.5 and 3.9 atoms/nm^2 was obtained. Loadings lower than 4 atoms/nm^2 should give a sub monolayer for $MgAl_2O_4$, assuming that it is similar to γ-Al_2O_3 [24]. This should lead to a high distribution of small MoS_2 particles with moderate activity and thereby minimizing the formation of the very active type II sites [25]. Furthermore the Co to Mo ratio was aimed at 0.3, since this should ensure that the less active Co_9S_8 phase is not formed [26].

The catalysts were sulfided in-situ in the catalytic hydropyrolysis setup at 26 bar, 350°C with 1.8 mol % H_2S, 11 mol % N_2 in 87 mol % H_2 by feeding 2% H_2S in H_2 (flow: 4 NL/min) and N_2 (flow: 0.5 NL/min). The temperature ramp was 10 °C/min and the holding time was 2 hours. After the sulfidation the test conditions were established.

Table 7.1 Composition of the fresh catalysts

Catalyst	Mo (wt.%)	Co (wt.%)	K (wt.%)	Co/Mo (molar)	Mo load (Atoms/nm^2)	BET SSA (m^2/g)
CoMo#1	3.41	0.637	-	0.30	3.6	60
CoMo#2	3.29	0.615	-	0.30	3.8	58
CoMoK#1	3.43	0.603	1.935	0.29	3.9	55

The HDO reactor was loaded with 173 g $NiMo/Al_2O_3$ catalyst supplied by Haldor Topsøe A/S. The catalyst was shaped as extrudates and used as received. In the experiment where the HDO reactor was used, the catalysts in the fluid bed and HDO reactor were sulfided simultaneously, using the same procedure as for the experiments with only the fluid bed reactor. However, the holding time was increased to 3 hours to ensure that the catalysts in both reactors were in the sulfided phase. After the sulfidation of the $NiMo/Al_2O_3$ catalyst

in the HDO reactor, it was by accident exposed to an air flow for ~5 seconds and the temperature in the bottom of the reactor increased to ~600 °C, indicating oxidation of the catalyst. Therefore the HDO reactor was resulfided for 1 hour at 350 °C. Dabros [27] investigated the reactivation of a coked sulfided NiMo catalyst by oxidation and subsequent resulfidation and found that it led to a decrease in the cracking and HDO activity. The change was ascribed to a change in the catalyst morphology and composition; it was observed that the Mo content had decreased. Furthermore, sintering had occurred, which had led to an increased degree of stacking, thus a loss in the number of brim sites [27]. The catalyst in the HDO reactor had therefore most likely lost some of its activity, prior to the experiment.

7.2.3 Catalyst characterization

The catalyst characterization methods have previously been described in detail (see Chapter 5), and are here described briefly. The composition (Co, Mo, K) of the fresh catalysts was determined with inductive coupled plasma optical emission spectroscopy (ICP-OES) and the surface area was measured with N_2-physisorption (BET). Temperature programmed ammonia desorption (NH_3-TPD) of the fresh catalysts was conducted on a Mettler Toledo TGA/DSC 1. Raman spectroscopy on the calcined oxidic samples was performed at ambient conditions with a Labram 800 HR microscope from Jobin Yvon using a Coherent Sapphire laser at 488 nm.

7.2.4 Experimental setup and procedure

The catalytic hydropyrolysis experiments were conducted in a bench scale setup shown in Figure 7.1. The setup is described in detail elsewhere [21]. The setup consisted of a feeding system, which included a gas mixing system and a screw feeder, a fluid bed hydropyrolysis reactor, a filter for char removal, a fixed bed hydrodeoxygenation (HDO) reactor, which could be bypassed, and a three stage condensation system (20°C, 2°C, and -40°C). The uncondensed gases were sent to a flare. A small fraction of the gas was sent to an online gas chromatograph (GC), which measured the gas composition (H_2, N_2, H_2S, CO, CO_2, C_1 to C_5 and C_{6+} hydrocarbons) every 10 min. The tubes between the fluid bed, filter, HDO reactor and condensation section was heated to 350°C in order to avoid premature condensation. During the experiments 52 NL/min hydrogen passed through a sinter plate at the bottom of the fluid bed reactor and 30 NL/min hydrogen and 5 NL/min nitrogen passed through the biomass feeding tube, thus ensuring a rapid transfer of the biomass from the screw feeder to fluid bed reactor.

The total mass of the condensed liquid was determined and the organic phase and the aqueous phase were separated with a separation funnel. The mass of the aqueous phase was measured and the mass of the organic phase was determined by subtracting the mass of the aqueous phase from the total mass of condensed liquid. The H_2S dissolved in the liquid phases was for safety reasons removed by bubbling with N_2 until hydrogen sulfide test strips (Sigma Aldrich) showed no sign of H_2S. This led to a mass loss between 0 and 4.3 wt.% for the organic phase and between 1.0 and 5.2 wt.% for the aqueous phase. The mass loss for the organic phase was mainly due to vaporization of light hydrocarbons while the mass loss for the aqueous phase was mainly due to vaporization of water.

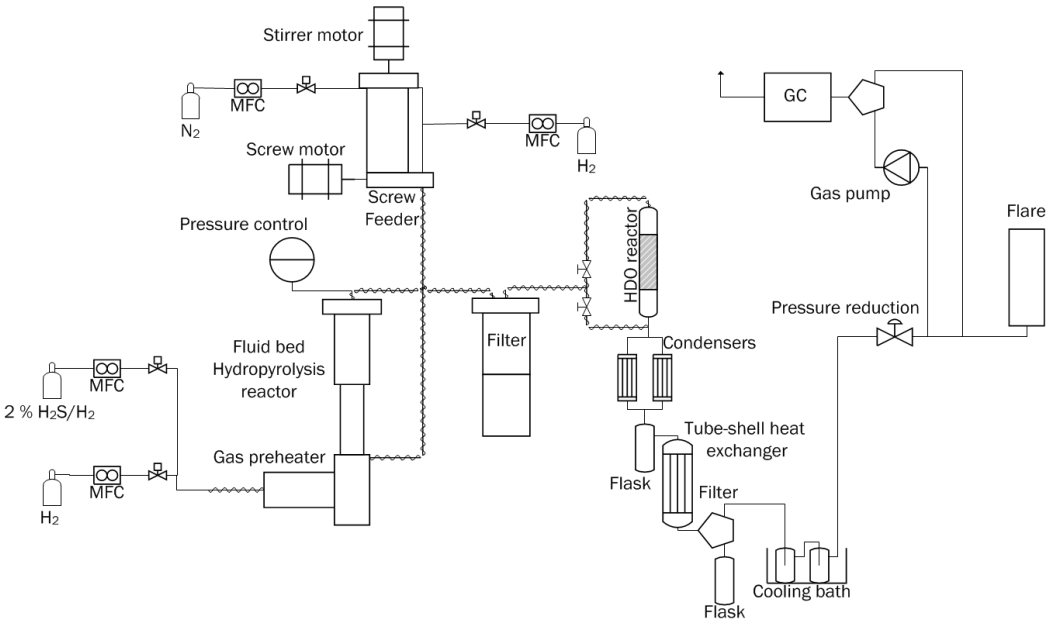

Figure 7.1. Simplified piping and instrumentation diagram of the used setup

For the 16.2 h experiment conducted over five days, the setup was depressurized, flushed with N_2 and the remaining biomass (beech wood) in the screw feeder was weighed and replaced with a new batch each day. The filter and tracing was cooled to room temperature, while the reactor temperatures were decreased to 150 °C. The solids in the filter was removed and considered as the solid yield and the condensed liquids were collected. The setup was leak tested and the reaction conditions listed in Table 7.2 were established. When the temperature in the reactor reached steady state the experiment was started by turning on the screw feeder.

After each complete experiment the catalyst and the remaining char was removed from the fluid bed, and replaced with the fresh catalyst for the subsequent experiment. The total solid yield for experiment 1 (obtained on day 5), experiment 2 and 3 was calculated by subtracting the mass of loaded catalyst from the total mass of solids collected from the filter and fluid bed.

7.2.5 Liquid phase analysis methods

7.2.5.1 Organic phase

The condensed organic phase was analyzed with several different methods and a more detailed description can be found elsewhere [21]. The hydrogen content was measured with ASTM method D7171. The sulfur content was measured according to ASTM D4294. The simulated distillation (SIMDIS) curve was measured with ASTM method D 7213 C. The density at 40 ˚C was measured with ASTM method D 4052, the viscosity at 40 ˚C was measured with ASTM method D 7042 and the water content was measured with Karl Fisher titration.

The condensed organic liquid samples were characterized by GC×GC-ToF/MS or -FID using a LECO® Pegasus 4D^{TM} instrument. The instrument included an Agilent 7890A GC equipped with a Gerstel® CIS 4 PTV inlet, a secondary oven, a quad-jet, dual-stage cryogenic-based (liquid N_2) modulator, a ToF/MS and

FID detector. The primary (1D) and secondary (2D) columns were Restek® Rxi-5Sil MS and Restek® Rxi-17Sil MS, respectively. Based on the GC×GC-ToF/MS analysis the compounds were classified into eleven groups: paraffins, naphthenes, mono-, di- and tri- and higher aromatics, sterols, oxygenated aliphatics, phenols, dihydroxybenzene, and larger oxygenated aromatics. Based on the retention time for the n-paraffins on the primary column the components classes were split into subgroups on the basis of the number of carbon atoms in the components, i.e. –C10, C11-C15, C16-C20, and C20+. It should be noted that other components classes do not necessarily have the same carbon number distribution as the paraffins, thus caution is needed when correlating the relative amount of each subgroup with its carbon number distribution. The relative amount (FID area-%) of each compound class was estimated as the sum of areas of all detected peaks in that class divided by the total peak area of all compound classes. All data was processed using the ChromaTof® 4.50 software.

For organic phases with an oxygen content above 1 wt.%, the oxygen content was analyzed at DB Lab A/S using a Flash 2000 elemental analyzer (Thermo Scientific). The uncertainty of this measurement was 3.0 %, defined as two standard deviations for the measurement uncertainty, corresponding to a confidence interval of 95 %. For organic phases with an oxygen content below 1 wt.%, the oxygen content was measured using a GC with an atomic emission detector (AED). An Agilent 7890A GC was coupled to a JAS 2370 AED in oxygen selective mode and quantification was done by adding known amounts of 4-fluorophenol to known amounts of the sample.

Selective analysis of sulfur containing compounds was conducted using GC-AED. The GC column was a Phenomenex ZB-1 (30m X 0.25mm X 1.0µm) in connection with a JAS split/splitless inlet in split mode (1:10) and 0.5 µl injection. Quantification was done using an external standard sample containing known amounts of benzothiophene, dibenzothiophene and 4-methyl-dibenzothiophene. Identification of individual compounds was done after analysis of pure compounds.

7.2.5.2 Aqueous phase

The carbon content in the aqueous phase was determined with GC-AED. The samples were analyzed using an Agilent 7890A GC coupled to a JAS 2370 AED in carbon selective mode. The quantification was done by external calibration using benzyl alcohol dissolved in water as standard. Calibration concentrations ranged from 10 ppm to 1100 ppm carbon. The external standard was used for calibration of unknown carbon containing compounds in the sample as the AED has equimolar and linear response for carbon. No identification of individual compounds was done and the total added amount of detected carbon was taken as a figure of the total carbon content in the water sample. A more detailed description of the method can be found in elsewhere (see Chapter 5).

The aqueous phase was also analyzed on a Shimadzu GC-MS/FID with a Supelco Equity-5 column. The compounds were identified on the MS and quantified using the parallel FID. Based on the GC FID-MS analysis the components were classified into 7 groups: unidentified, ketones, alcohols, sugars, phenols, acids and furans. The relative amount (FID area-%) of each component class was estimated as the sum of all the detected peaks in that class divided by the total peak area.

7.2.6 Char analysis

The elemental composition (CHNSO) of the produced char was analyzed at DB Lab A/S by use of a Flash 2000 elemental analyzer from Thermo Fisher. The total ash and catalyst content in the produced char were measured by combusting the char at 600°C in air. A more detailed description of the analysis can be found elsewhere [21].

7.3 Results and Discussion

7.3.1 Characterization of the oxide catalyst precursors

7.3.1.1 NH_3-TPD

The acidity of the fresh oxide precursors were investigated with NH_3-TPD, see Figure 7.2. This showed that the number of acidic sites and their acid strength on the fresh CoMo#1 and CoMo#2 was comparable, but that the number of acidic sites on the fresh CoMoK#1 catalyst was significantly lower than for the fresh CoMo#1 and CoMo#2 catalyst, as expected. It is well-known that the Brønsted acidity facilitates the transport of the potassium onto the catalyst and that potassium decreases the number of acidic sites [28–35]. The observed changes after the addition of K_2CO_3 is therefore in agreement with the literature and potassium is most likely located at the acidic sites.

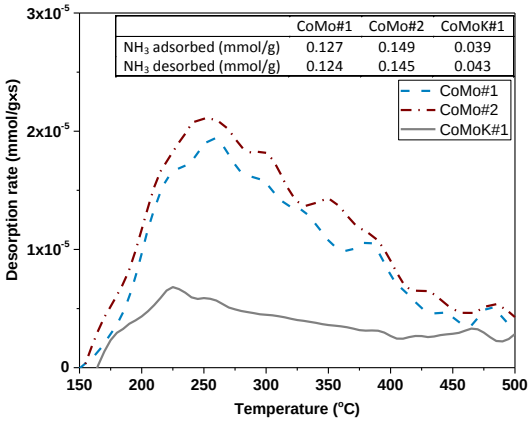

Figure 7.2 NH_3-TPD profiles for the fresh oxide precursors and the K-doped catalyst.

7.3.1.2 Raman spectroscopy

To gain insight into the phases of the prepared oxide precursors, they were analyzed by Raman spectroscopy applying the fluidized bed set-up as described by Beato et al. [36] (Figure 7.3). The samples were also analyzed by Raman microscopy at different spatial spots (see supplementary information Figure F.1), which evidenced some degree of phase heterogeneity for the individual samples. The bands observed at 407, 678, and 771 cm^{-1} are ascribed to the $MgAl_2O_4$ spinel carrier [37]. Since a monolayer of Mo on Al_2O_3 would correspond to 4.5 Mo/nm2 [38], the catalysts have between 80 and 87 % monolayer coverage, which should result in well dispersed $Co_xMo_yO_z$ phases. The spectra for CoMo#1 and CoMo#2 are fairly similar, indicating that these two catalysts contain largely the same phases. The main difference between CoMo#1 and CoMo#2 is the presence of a sharp doublet between 940-950 cm^{-1} for CoMo#1, which is characteristic for β-$CoMoO_4$ [39]. However, both samples show a small band at 870 cm^{-1} which together with the broad band at ~930 cm^{-1} is typical for the hydrated $CoMoO_4 \cdot xH_2O$ phase [39]. The metal coordination in β-$CoMoO_4$ and $CoMoO_4 \cdot xH_2O$ is very similar, both containing CoO_6 octahedra and MoO_4 tetrahedra [40]. The slight differences in the Raman spectra are therefore most probably related to a different degree of hydration which leads to a slight change in the relative rearrangement of the metal polyhedral [40]. Furthermore, no Co_3O_4 is observed, since the corresponding main Raman band at 692 cm^{-1} is not observed. Also the presence of crystalline α-MoO_3 can be excluded, since the characteristic sharp band at 992 cm^{-1} due to terminal Mo=O

stretching mode [38] was not observed. For the CoMoK#1 sample no distinguished bands between 200-230 cm^{-1} and 920-960 cm^{-1} are observed. Instead, two sharp bands at 887 and 914 cm^{-1} emerge, which are characteristic for isolated tetrahedral monomolybdate units [16]. This therefore indicates that doping the catalyst with potassium leads to the formation of more isolated MoO_x species. On the other hand, the additional bands at 821 and 851 cm^{-1} are typical for longer Mo-O bonds, which indicates the presence of some connectivity between the polyhedra. It is worth noting that for the CoMoK#1 sample a broad Raman band at around 593 cm^{-1} can be recognized, which has been assigned to supported CoOx species [41].

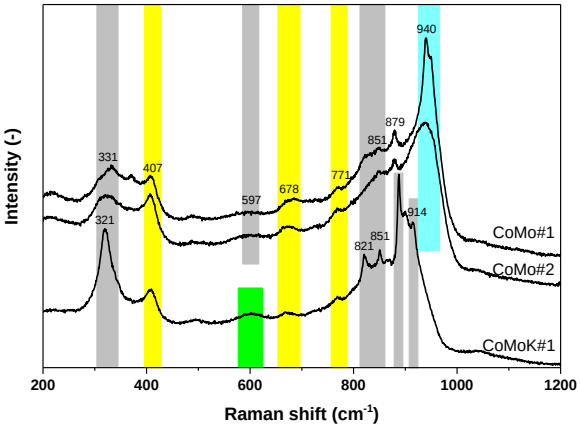

Figure 7.3 Baseline corrected Raman spectra of CoMo#1, CoMo#2, and CoMoK#1 in the oxide phase (calcined, not dehydrated). The Raman bands were assigned to hydrated MoO_x (gray), hydrated $CoMoO_4$ (blue), CoO_x (green), and $MgAl_2O_4$ (yellow).

7.3.2 Catalyst stability

The process and catalyst stability were evaluated by conducting a 16.2 h experiment over five days with CoMo#2 in the fluid bed reactor and a commercial $NiMo/Al_2O_3$ catalyst in the HDO reactor. Totally, 5182 g of beech wood was converted using the same catalyst loads. The temperature in the fluid bed reactor was between 452 and 455 °C, the temperature in the HDO reactor was between 366 and 373 °C and the biomass feeding rate varied between 240 and 276 g/h. The run time was approximately 3.5 h per day, except for on day 3, where the experiment was stopped after 2.2 h due problems with the biomass feeding system. An overview of the test conditions and mass balances is shown in Table 7.2. The mass balance closed between 100.3 and 103.1 wt.% daf based on the amount of biomass fed. The reason for the above 100 % mass balance is hydrogen incorporation. It was not possible to determine the char and coke yield each day, because that would require that the fluid bed reactor was unloaded. Instead the filter was unloaded each day and the solid yield in filter was determined. The catalyst carryover from the fluid bed to the filter was estimated to between 1 and 9 g per day, with a total carryover of 20 g after five days, corresponding to 40 wt.% of the total amount of catalyst loaded in the fluid bed. Experiment 2, shown in Table 7.2, has previously been published (see Chapter 5) and is here use as a reference.

Table 7.2 Test conditions and yields for each day of the 16.2 h experiment (1), a reference experiment (2) and the experiment with the potassium impregnated catalyst (3). (Catalyst in HDO reactor: 173 g $NiMo/Al_2O_3$)

Experiment	1 (day 1)	1 (day 2)	1 (day 3)	1 (day 4)	1 (day 5)	2	3
Conditions							
FB temperature (°C)	453	452	454	455	453	451	454
FB catalyst	CoMo#2	CoMo#2	CoMo#2	CoMo#2	CoMo#2	CoMo#1	CoMoK#1
FB catalyst amount (g)	49.99	-	-	-	-	50.03	49.98
FB catalyst lost (g)	5	9	3	2	1	ND	ND
HDO temperature (°C)	370	370	366	372	373	-	-
HDO catalyst	$NiMo/Al_2O_3$	$NiMo/Al_2O_3$	$NiMo/Al_2O_3$	$NiMo/Al_2O_3$	$NiMo/Al_2O_3$	-	-
HDO catalyst amount (g)	173	173	173	173	173	-	-
Pressure (bar)	26	26	26	26	26	26	26
Feed time (h)	3.5	3.5	2.2	3.5	3.5	3.5	3.5
Feeding rate (g/h)	274	276	240	274	273	275	268
H_2S conc.(ppm)	460	460	460	460	460	460	460
H_2 flow (NL/min)	82	82	82	82	82	82	82
N_2 flow (NL/min)	5	5	5	5	5	5	5
Yields (wt. daf %)							
Gas	29.4	30.0	29.6	30.7	31.2	26.1	24.9
Solid	10.9	13.8	14.6	13.2	13.6[a]	13.3[a]	14.6[a]
Aqueous phase	38.0	37.1	36.4	34.5	35.1	33.3	28.9
Organic phase	12.2	13.7	12.5	14.6	14.1	17.7	19.9
C_{4+} in the gas	9.9	9.2	8.7	8.3	9.1	7.5	4.1
Organics + C_{4+}	22.1	22.9	21.2	22.9	23.2	25.2	24.1
Mass balance	100.3	103.7	101.8	101.2	103.1	97.8	92.5
Carbon recovery (%)							
C_1-C_3	23	21	21	21	21	19	12
C_{4+}	17	15	15	14	15	13	7.1
$CO+CO_2$	11	12	12	13	13	11	13
Solid	15	18	20	19	19	ND	ND
Organic phase	20	22	23	24	23	26	28
Aqueous phase	0.039	0.052	0.044	0.085	0.17	3.2	3.2
Organic phase + C_{4+}	36	37	37	39	38	39	35
Organic phase composition							
Water (wt.%) [b]	ND	ND	ND	ND	ND	3.3	6.3
C [c] (wt.% db)	87.8	87.8	ND	87.9	88.1	81	81
H (wt.% db)	12.15	12.16	ND	12.06	11.85	9.39	9.12
O (wt ppm db)	40	162	228	988	2832	9.0×10^4	9.5×10^4
S (wt.% db)	0.055	0.015	0.018	0.0083	0.011	0.22	0.18
Organic phase physical properties							
Density at 40°C (g/ml)	0.8273	0.8307	0.8318	0.8347	0.8438	0.9428	0.9678
Viscosity at 40°C (cSt)	1.081	ND	ND	ND	1.254	ND	ND
Aqueous phase composition (wt.%)							
C	0.047	0.064	0.055	0.11	0.22	4.3	4.8
Gas composition (wt.% daf)							
CO	7.6	8.3	8.4	9.1	9.3	3.5	9.6
CO_2	8.2	8.1	8.4	8.7	9.2	9.2	8.6
C_1-C_3	14.4	13.6	13.1	13.3	13.2	10.3	6.3
C_{4+}	9.9	9.2	8.7	8.4	9.2	7.5	4.1
Solids in filter composition (wt.%)							
C	72.1	69.2	72.2	73.2	72.9	ND	ND
H	3.45	3.00	3.22	3.27	3.22	ND	ND
S	2.20	2.18	2.35	2.33	2.25	ND	ND
N	0.28	0.26	0.31	0.28	0.26	ND	ND
O	16.2	15.7	15.0	15.3	15.5	ND	ND
Ash	10.2	10.8	8.2	6.1	5.3	ND	ND

[a] Solid = Solid in filter + solid in fluid bed – catalyst loaded
[b] assumed below detection limit for all experiments with HDO reactor
[c] By difference

7.3.2.1 Product distribution

The condensable organic yield varied between 21.2 and 23.2 wt.% daf, shown in Figure 7.4(A). The lowest yield was obtained after 9.1 hours, but this was most likely due to the operational problems described above. Furthermore the condensable organics yield (21.2 wt.% daf), especially the condensed organics yield (12.2 wt.% daf), was low at TOS 3.5 h, however, this was probably due to an initial wetting of the setup. The total gas yield was fairly constant, see Figure 7.4(B), but the CO and CO_2 yield increased from 14.9 to 18.2 wt.% daf, while the C_1-C_3 yield decreased from 14.4 to 13.0 wt.% daf. The C_1-C_3 yield was significantly higher when the HDO reactor was used (experiment 1, C_1-C_3 yield: 14.4-13.1 wt.% daf) compared to the experiment without the HDO reactor (experiment 2, C_1-C_3 yield: 10.3 wt.% daf). The reason for the higher C_1-C_3 yield when the HDO reactor was used is probably a combination of cracking of larger molecules and HDO of the C_1-C_3 oxygenates detected in the aqueous phase when the HDO reactor was bypassed, see supplementary information Tables F.1-F.3. In the experiment without the HDO reactor the concentration of olefins in the gas (C_2-C_5) was 6.5 wt.% daf, while using the HDO reactor led to an initial total saturation of the C_2-C_5 hydrocarbon in the gas. However, the concentration of C_2-C_5 olefins increased to 0.06 wt.% daf after 9.1 hours and to 0.3 wt.% daf after 16.2 hours, indicating deactivation of the $NiMo/Al_2O_3$ catalyst in the HDO reactor. The total CO_2 and CO yield was initially the same with the HDO reactor as in the experiment without the HDO reactor, however, the CO to CO_2 molar ratio increased from 1.1 without the HDO reactor to 1.6 with the HDO reactor, indicating that reverse water gas shift takes place in the HDO reactor. This is opposite to what we previously observed with a commercial $CoMo/MgAl_2O_4$ catalyst in the fluid bed, where forward water gas shift was observed in the HDO reactor [21]. The reason for the difference was the CO/CO_2 ratio was 3.1 with the commercial $CoMo/MgAl_2O_4$ catalyst [21], and the CO/CO_2 ratio in the HDO reactor approaches equilibrium.

The solid yield was between 10.9 and 14.6 wt.% daf, see Figure 7.4(C). The low solid yield after day 1 (3.5 h) TOS was due to an initial char accumulation in the fluid bed, which therefore decreased the yield of collected solids. During the rest of the experiment the solid yield was fairly constant and varied from 13.1 to 14.6 wt.% daf, thus the solid yield was comparable to the char and coke yield obtained without the HDO reactor as expected.

As shown in Figure 7.4(D), the aqueous phase yield decreased from 38.0 to 35.1 wt.% daf. The decrease in the aqueous phase yield is almost equivalent to the increase in the yield of CO and CO_2, hence the decrease could be due to an increased decarbonylation and/or decarboxylation activity. However it could also be due to decreased hydrodeoxygenation activity in fluid bed reactor, which increased the life time of the very reactive oxygenates, which led to a higher decarbonylation and/or decarboxylation activity. The aqueous phase yield without the HDO reactor was only 33.3 wt.% daf, but this difference is because hydrodeoxygenation takes place in the HDO reactor, hence using the HDO reactor increases the amount of water formed.

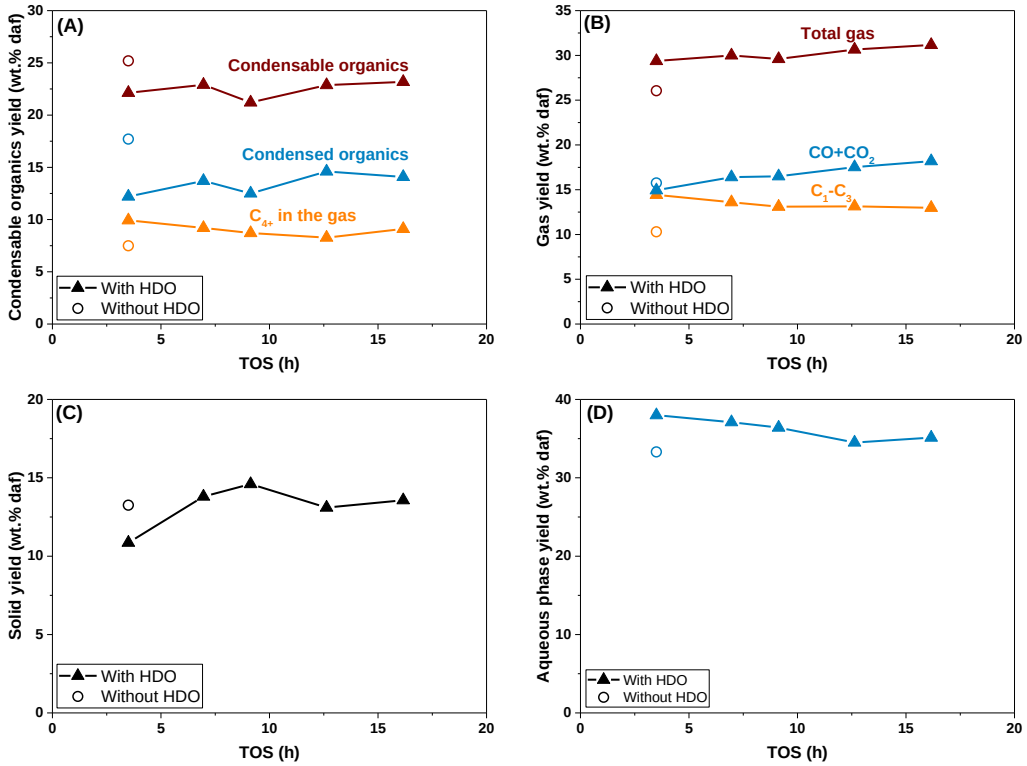

Figure 7.4 Effect of time on stream on the condensable organic yield (A), gas yield (B), solid yield (C), and aqueous phase yield (D). Conditions: Fluid bed temperature: 452-455°C, HDO temperature: 366-373 °C, pressure: 26 bar, biomass feeding rate: 240-277 g/h, biomass used: 5188 g, H_2 flow: 82 NL/min, N_2 flow: 5 NL/min, and H_2S conc: 460 ppm.

7.3.2.2 Chemical composition of the condensed liquids

The oxygen and hydrogen concentrations in the organic phase are shown in Figure 7.5(A). The oxygen concentration increased during the first 9.1 hours from 40 ppm to 228 ppm, after which the slope increased and the oxygen content in the organic phase increased to 2832 ppm, hence showing a decrease in the deoxygenation activity in either the fluid bed, HDO reactor or both reactors. The hydrogen concentration also decreased from 12.15 to 11.85 wt.% during the experiment, thus indicating that the concentration of olefins and/or aromatics in the organic phase increased, which indicates a decrease in the hydrogenation activity. This correlates with the observed decrease in the hydrogenation from the gas analysis.

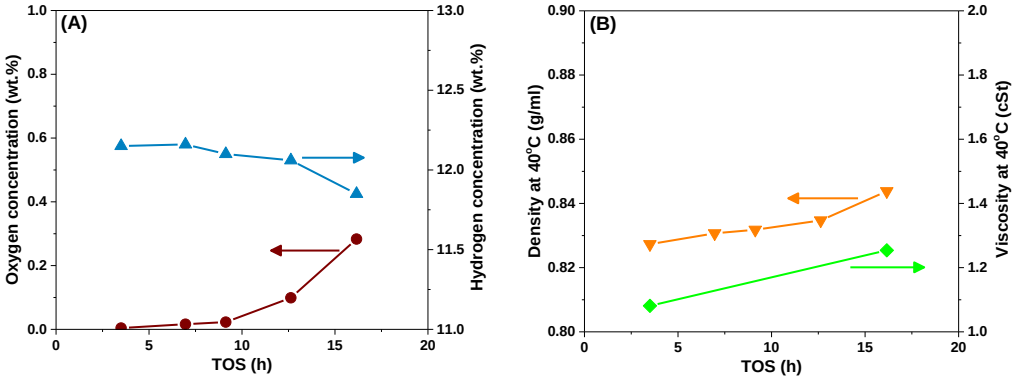

Figure 7.5 Effect of TOS on the oxygen and hydrogen concentration (A) and the density and viscosity (B) of the organic phase. Conditions: Fluid bed temperature: 452-455°C, HDO temperature: 366-373 °C, pressure: 26 bar, biomass feeding rate: 240-277 g/h, biomass used: 5188 g, H_2 flow: 82 NL/min, N_2 flow: 5 NL/min, and H_2S conc: 460 ppm.

The density of all the condensed organics was measured, while the viscosity was only measured on the condensed organics from the first and last day, see Figure 7.5(B). The density at 40°C increased during the experiment from 0.8273 to 0.8438 g/ml, which is due to the increased concentration of oxygen and decreased concentration of hydrogen in the organic phase. Furthermore, the boiling point of the organic phase also increased, see Figure 7.6, and the diesel fraction increased from 70 to 80 vol. %. This is probably also part of the reason for the increased density. The increase in the boiling point is most likely due to a decrease in the cracking activity, which agrees with the decrease in the C_1-C_3 yield in the gas. The deactivation also affected the viscosity, which increased from 1.081 to 1.254 cSt. It should be noted that the density of the produced organic phase was within the typical range of density for diesel, which is 0.82-0.85 g/ml, while the viscosity was below the viscosity of diesel, which is between 1.9 and 4.5 cSt [42]. The hydrogen content in diesel is typically 13 wt.% [42], thus further hydrogenation of the produced organics is needed before it can be used as such.

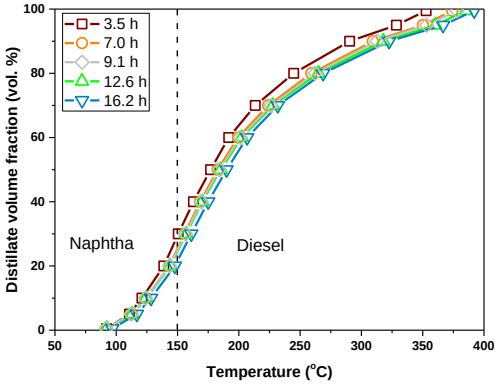

Figure 7.6 GC simulated distillation curves for the condensed organics. The curves are calculated using D86 according to ASTM D 7213 C.

The sulfur concentration in the condensed oil in the reference experiment without the HDO reactor was 0.22 wt.% and using the HDO reactor decreased it to between 0.055 and 0.008 wt.%. S specific GC-AED showed

that the sulfur in the organic phase from the experiment without the HDO reactor consisted of H_2S (382 ppm S), methylethylsulfide (150 ppm S), thiols (55 ppm S), thiophenes (80 ppm S) and benzothiophenes (29 ppm S). Furthermore, the condensed organics from 3.5 h TOS and 16.2 h TOS from the experiment with the HDO reactor were analyzed with S specific GC-AED (see supplementary information Table F.4). This indicated that most of sulfur in the organic phase was H_2S and only 21 ppm and 20 ppm S was ascribed to sulfur containing hydrocarbons after 3.5 and 16.2 h TOS, respectively. All the thiols were removed and the thiophene concentration was 2 ppm S at 3.5 h TOS and 0 at 16.2 h TOS, and the concentration of dibenzothiophenes was 4 ppm S at 3.5 h TOS, and was not detected at 16.2 h TOS. However, some larger unknown sulfur containing organics (13 ppm S) was detected in the condensed organics from 16.2 h TOS. The reason for the total removal of thiols is probably the low concentration of olefins, which can react with H_2S and form thiols [23]. Based on the results from the S specific GC-AED it can be assumed that catalytic hydropyrolysis followed by HDO can produce liquid fuels with a low S concentration and therefore requires none or little additional hydrotreating in order to obtain an acceptable level of sulfur.

In order to obtain a deeper understanding of the composition of the condensed organic phase they were analyzed with GC×GC-ToF/MS or –FID. The concentration of paraffins varied between 2.6 and 3.1 % area-FID and there was no apparent correlation between the TOS and the paraffin concentration. The concentration of naphthenes (Naph) was between 49.3 and 50.3 % area-FID during the first 12.6 hours, after which it decreased to 47.3 %, see Figure 7.7(A). The concentration of monoaromatics (mAro) decreased from 36.3 to 33.8 %-area FID during the first 7.0 hours, but was constant at 33.8-34.3 % during the rest of the experiment. The decrease was probably due to an increase in the di-and larger aromatics (diAro+), which increased from 10.6 to 12.1 % area-FID. The oxygenated aliphatics (O-ali) increased during the experiment from 0.01 to 0.2 % area-FID, shown in Figure 7.7(B). A small increase from 0.006 to 0.01 % area-FID in the oxygenated di- and larger aromatics (O-Aro) was also observed, but this is within the uncertainty of the measurement. The concentration of phenols (PhOH) was between 0.9 and 1.1 % area-FID during the first 9.1 hours, but then increased to 3.0 % after 16.2 hours. The increase in the concentration of phenols corresponds to the decrease in the naphthenes, which is most likely because the $NiMo/Al_2O_3$ mainly remove the phenols through the HYD pathway, hence a deactivation of this catalyst would lead to a decreased concentration of naphthenes. Furthermore, since only traces of oxygenated aliphatics were detected in the condensed organic phase the produced product is most likely stable and overall the HDO reactor remained fairly active and the observed deactivation is of minor importance.

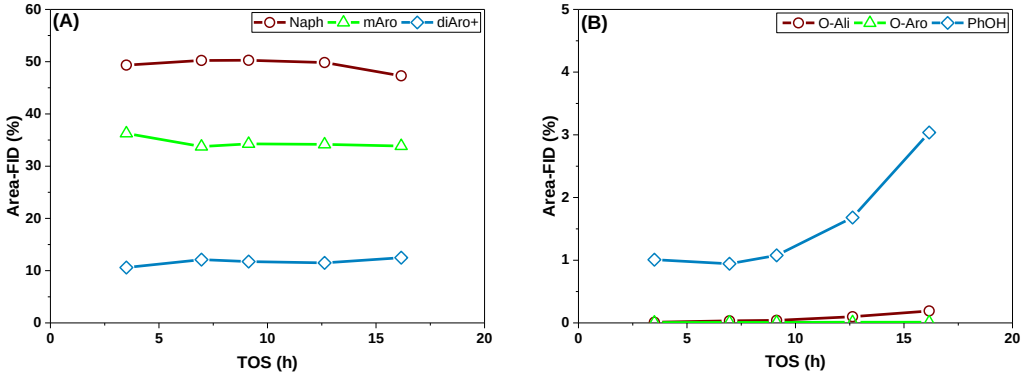

Figure 7.7 Effect of TOS on the organic phase composition. Conditions: Fluid bed temperature: 452-455°C, HDO temperature: 366-373 °C, pressure: 26 bar, biomass feeding rate: 240-277 g/h, biomass used: 5188 g, H_2 flow: 82 NL/min, N_2 flow: 5 NL/min, and H_2S conc: 460 ppm.

The carbon recovery in the aqueous phase was between 0.039 and 0.17 % and was constant during the first 9.6 hours after which it increased, as shown in Figure 7.8. However, the carbon recovery in the aqueous phase was significantly lower than in the experiment without the HDO reactor (3.2 %). GC-MS/FID on the aqueous phase after 16.2 hours, showed that it contained phenol (45 % area-FID), m-cresol (30 % area-FID), o-cresol (5.6 % area-FID), 2-ethyl-phenol (4.6 % area-FID), and 2,5 dimethyl phenol (5.3 % area-FID). Since neither furans, acids, or ketones were detected in the aqueous phase and only a very low concentration of oxygenated aliphatics (≤0.2 % area-FID) was detected in the organic phase, the observed deactivation of the catalyst in the HDO reactor resulted in mainly phenols not being deoxygenated.

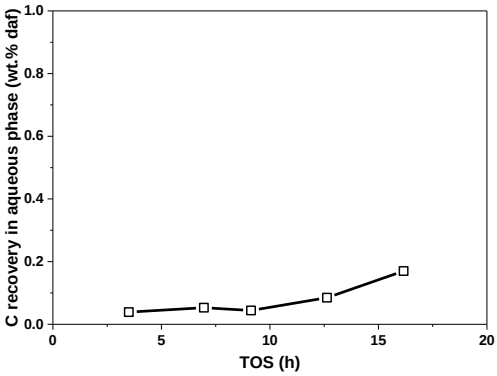

Figure 7.8 Carbon yield in the aqueous phase as a function of TOS. Conditions: Fluid bed temperature: 452-455°C, HDO temperature: 366-373 °C, pressure: 26 bar, biomass feeding rate: 240-277 g/h, biomass used: 5188 g, H_2 flow: 82 NL/min, N_2 flow: 5 NL/min, and H_2S conc: 460 ppm.

7.3.3 Effect of catalyst pre-deactivation with potassium

7.3.3.1 Product distribution

To investigate the effect of the transfer of potassium from the biomass to the catalyst a CoMo/$MgAl_2O_4$ catalyst was impregnated with K_2CO_3 corresponding to a potassium content of 1.94 wt.%, which corresponds to the amount of potassium in approximately 1 kg dry beech wood. The catalyst was tested without the HDO reactor and the mass balance closed at 92.5 wt.% daf, as shown in Table 7.2, which is lower than normally achieved. The produced organic phase was sticky and the reason for the low mass balance is probably that part the organic phase was accumulated in the setup.

The product distribution for the experiment with CoMoK#1 is compared to the reference experiment with CoMo#1 in Figure 7.9. The char and coke yield increased from 13.4 to 14.6 wt.% daf, when the CoMoK#1 was used, which indicates that potassium can act as a catalyst for polymerization reactions, the reason for this phenomenon is further investigated in Chapter 8. The C_1-C_3 yield decreased from 10.3 to 6.3 wt.% daf, which was mainly due to a decrease in the C_2-C_3 hydrocarbons from 6.8 to 3.1 wt.% daf. This shows that the cracking activity of the catalyst decreased after impregnation with K_2CO_3, which also decreased its acidity (see Figure 7.2). The C_2-C_3 paraffin to olefin ratio also decreased from 0.90 to 0.50 mol/mol, indicating a lower hydrogenation activity for CoMoK#1. The CO and CO_2 yield increased from 15.8 to 18.6 wt.% when replacing CoMo#1 with CoMoK#1, but the increase was due to an increase in the CO yield, while the CO_2 yield decreased from 9.2 to 8.6 wt.% daf, indicating a higher decarbonylation activity. However, the CO_2 concentration in the gas, which is normally constant, decreased during the experiment with CoMoK#1 from

0.6 to 0.3 mol % (see supplementary information Figure F.2), indicating that deactivation of the catalyst occurred during the experiment. Similarly Pan et al. [43] observed an increased CO and CO_2 yield when they conducted pyrolysis of potassium impregnated wood. In this work doping the catalyst with potassium also led to a significant decrease in the aqueous phase yield, from 33.3 to 28.9 wt.%, which was due to the increased decarboxylation activity and decreased hydrodeoxygenation activity. The total condensable organic yield was also lower with the CoMoK#1 than CoMo#1, but the reason is most likely that part of the organic phase had accumulated in the setup. The C_{4+} yield was also lower for the CoMoK#1, which was due to the decreased cracking activity.

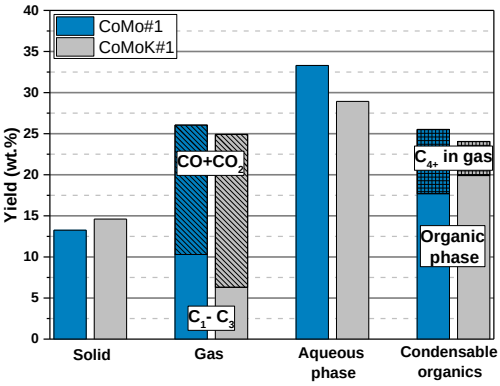

Figure 7.9 Product distribution for catalytic hydropyrolysis of beech wood with CoMoK#1 and CoMo#1. Conditions: Fluid bed temperature: 452-454°C, pressure: 26 bar, biomass feeding rate: 261-268 g/h, biomass used: 941-963 g, H_2 flow: 82 NL/min, N_2 flow: 5 NL/min, and H_2S conc: 460 ppm.

7.3.3.2 Chemical composition of the condensed liquids

The oxygen content in the condensed organic phase from the experiment with CoMoK#1 was 9.5 wt.% db while it was 9.0 wt.% db with CoMo#1, showing that the deoxygenation activity for CoMoK#1 is similar to the deoxygenation activity of CoMo#1. The hydrogen content decreased from 9.39 to 9.11 wt.% db when CoMoK#1 was used instead of CoMo#1, which indicates a decrease in the hydrogenation activity. Furthermore, the sulfur concentration in the condensed organic phase was 0.22 wt.% db when CoMo#1 was used and 0.18 wt.% db when CoMoK#1 was used. The condensed organic phase was also analyzed with sulfur specific GC-AED and the concentration of the different sulfur containing compounds are shown in Figure 7.10 and a detailed list of the detected molecules can be found in supplementary information Table F.5 and Table F.6. This showed that the thiol concentration was 41 ppm S, the thiophene concentration was 54 ppm S, and the benzothiophene concentration was 16 ppm when CoMoK#1 was used. The concentration of thiols was 55 ppm S, thiophenes 80 ppm S, and benzothiophenes 29 ppm S when CoMo#1 was used. The concentration of other types of sulfur containing molecules, such as methyl ethyl sulfide, and unidentified sulfur containing molecules was also significantly higher for CoMo#1 (659 wt-ppm S) than CoMoK#1 (267 wt-ppm S). This indicates that using CoMoK#1 instead of CoMo#1 in the fluid bed decreases the sulfur content in the organic phase. This is most likely not due to a higher hydrodesulfurization (HDS) activity for CoMoK#1 compared to CoMo#1, but rather lower sulfur incorporation into the organics. Sulfur incorporation reactions are typically acid catalyzed [44] and since the addition of potassium decreased the number of acidic sites on the catalyst, it is very likely that the lower sulfur content in organic phase from the experiment with CoMoK#1 compared to CoMo#1 is due to lower sulfur incorporation.

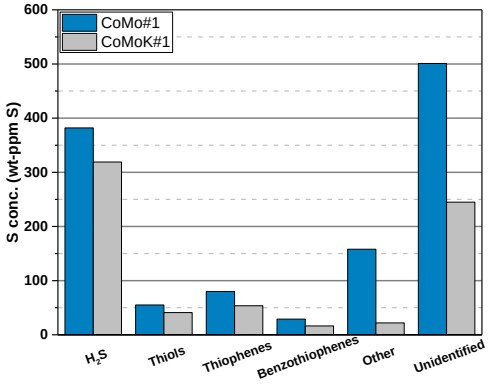

Figure 7.10 Concentration of sulfur species in the condensed organic phase from the experiment with CoMo#1 and CoMoK#1 determined with S specific GC-AED. Conditions: Fluid bed temperature: 452-454°C, pressure: 26 bar, biomass feeding rate: 261-268 g/h, biomass used: 941-963 g, H_2 flow: 82 NL/min, N_2 flow: 5 NL/min, and H_2S conc: 460 ppm.

Mortensen et al. [23] investigated the effect of potassium on sulfided NiMo by pre-impregnating the catalyst with KNO_3 and using phenol as a model compound. They found that potassium decreased the catalyst's de-oxygenation activity with 80 %, hence they observed a significantly larger effect of potassium in their study compared to ours. However, potassium has also been used as an additive to sulfided $CoMo/Al_2O_3$ catalysts used for HDS of gasoline, where the addition of potassium significantly decreases the hydrogenation activity, with only a minor decrease in the HDS activity [34,35,45]. The significant decrease in the deoxygenation activity that Mortensen et al. [23] observed could be because NiMoS removes the oxygen by first saturating the aromatic ring and then removes the oxygen (HYD pathway) [46,47], while CoMoS removes the oxygen without saturating the aromatic ring (DDO pathway) [17,46,48,49]. Potassium should therefore have a larger impact the deoxygenation activity for NiMoS than CoMoS. Another important difference is that Mortensen et al. [23] conducted their experiment at 280 °C, thus the temperature was 170°C lower compared to this study. It is therefore also likely that the effect of potassium decreases with increasing temperature.

GC×GC-FID/MS chromatograms of the condensed organics from the experiment with CoMo#1 and CoMoK#1 are shown in Figure 7.11. As indicated by the chromatograms, the organic phase from these two experiments were quite different and the chromatogram for CoMoK#1 contained more peaks than that for CoMo#1. An overlap between the aromatics and oxygenates in the chromatogram for CoMoK#1 was observed, thus making it difficult to analyze and compare with the chromatogram for CoMo#1. This is most likely also the reason for the significantly higher concentration of the oxygenates in the organic phase from experiment with CoMoK#1 (Figure 7.11(D)) compared to CoMo#1 (Figure 7.11(C)) determined with GC×GC-FID/MS. However, the condensed organic phase from both experiments consists of paraffins, naphthenes, mono, di, tri, and larger aromatics, oxygenated aliphatics, phenols, dihydroxybenzenes, and sterols. Interestingly, dimethyl dihydroxybenzene was the main dihydroxybenzene when CoMo#1 was used, while methyl dihydroxybenzene was the main dihydroxybenzene when CoMoK#1 was used. Likewise, methylpyrene was observed with CoMo#1 while pyrene was observed with CoMoK#1. Therefore the difference in peak intensity could indicate that doping the catalyst with potassium decreases the alkylation activity, which is most likely due the decreased acidity.

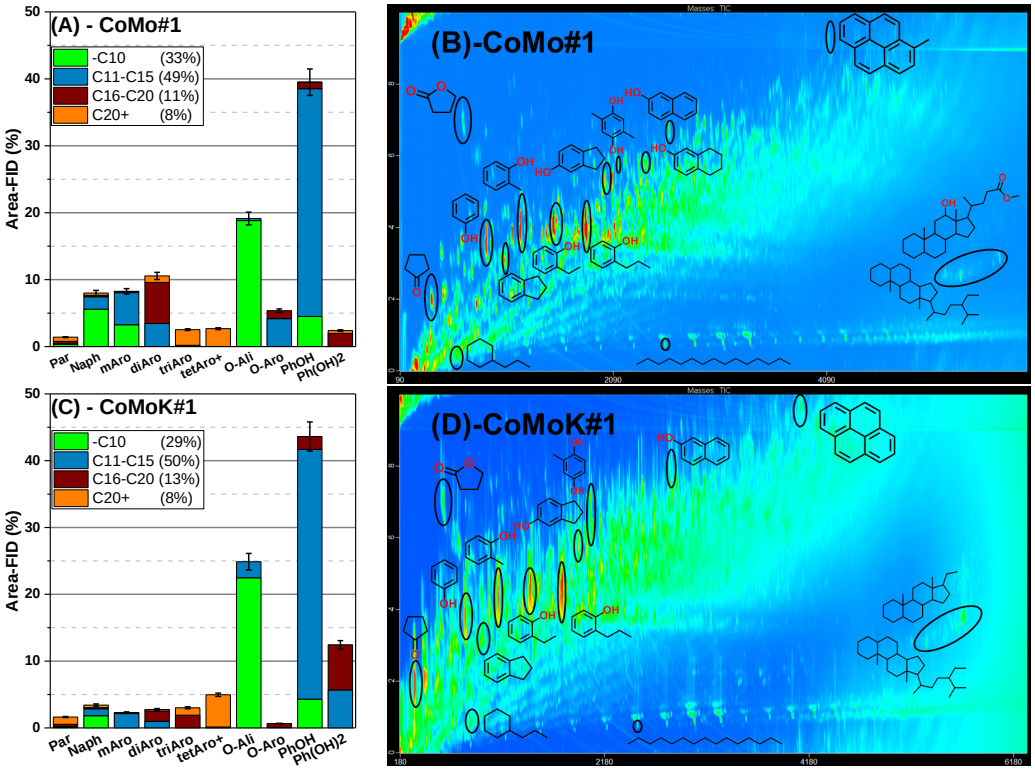

Figure 7.11 Composition (A) and chromatogram (B) of the condensed organic phase from the experiment with CoMo#1, and composition (C) and chromatogram (D) of the condensed organic phase from the experiment with CoMoK#1. The components in the condensed organics is divided into paraffins (Par), naphthenes (Naph), monoaromatics (mAro), diaromatics (diAro), triaromatics (triAro), tetraaromatics and larger aromatics (tetAro+), oxygenated aliphatics (O-ali), phenols (PhOH), dihydroxybenzenes (Ph(OH)2), and larger oxygenated aromatics (O-aro). Conditions: Fluid bed temperature: 452-454°C, pressure: 26 bar, biomass feeding rate: 261-268 g/h, biomass used: 941-963 g, H_2 flow: 82 NL/min, N_2 flow: 5 NL/min, and H_2S conc: 460 ppm.

The composition of the aqueous phases is shown in Figure 7.12. The carbon concentration in the aqueous phase was 4.3 and 4.8 wt.% when CoMo#1 and CoMoK#1 were used, respectively, however the carbon recovery was 2.6 % in the aqueous phase for both catalysts. This was due to the lower aqueous phase yield, but higher carbon concentration in the aqueous phase when the CoMoK#1 was used. A significant increase in the concentration of furans and ketones were observed, while the concentration of alcohols and phenols decreased when the catalyst was impregnated with K_2CO_3. Sugars was also observed in the aqueous phase when the CoMoK#1 was used, which is another indication of the lower degree of hydrogenation of the organics.

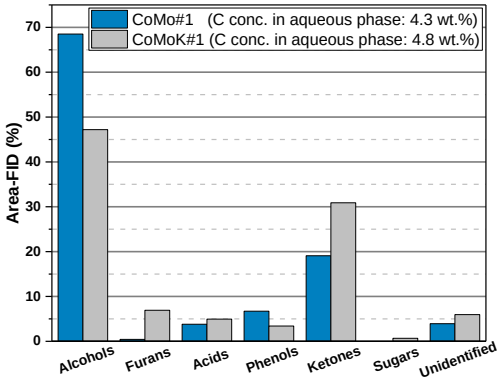

Figure 7.12 Composition of the aqueous phase when the CoMo#1 and CoMoK#1 is used in the fluid bed reactor. Conditions: Fluid bed temperature: 452-454°C, pressure: 26 bar, biomass feeding rate: 261-268 g/h, biomass used: 941-963 g, H_2 flow: 82 NL/min, N_2 flow: 5 NL/min, and H_2S conc: 460 ppm.

7.4 Conclusion

The catalyst stability was investigated by running the fluid bed hydropyrolysis setup for 16.2 hours over a period of 5 days (2.2-3.5 hours each day) with a sulfided CoMo catalyst followed by a deep HDO reactor with a sulfided NiMo catalyst. The condensed organics and C_{4+} yield varied between 21.2 and 23.2 wt.% daf, the aqueous phase yield decreased during the experiment from 38.0 to 35.1 wt.% daf, while the CO and CO_2 yield increased from 14.9 to 18.2 wt.%. The decrease in aqueous phase yield was ascribed to a decreasing hydrodeoxygenation activity, which led to an increasing decarbonylation/decarboxylation activity. The oxygen content in the produced organic phase increased during the experiment from 40 to 2832 wt. ppm, indicating that deactivation of catalyst in the fluid bed and HDO reactor occurred. Furthermore, 40 wt.% of the initial amount of catalyst loaded into the fluid bed reactor was lost due to entrainment, which most likely decreased the conversion of the oxygenates in the fluid bed.

Adding 1.9 wt.% potassium in the form of K_2CO_3 to the catalyst prior to sulfidation significantly decreased the catalyst's acidity, and thus decreased its cracking activity, which was most likely because potassium binds to the acid sites. It also increased the catalysts decarboxylation activity and the $CO+CO_2$ yield increased from 15.8 to 18.6 wt.% daf, which also indicates a decrease in the catalysts hydrodeoxygenation activity. However the catalyst decarboxylation activity decreased during the experiment, indicating that deactivation occurred. Nevertheless this indicates that the increased CO and CO_2 yield observed during the test of the catalyst stability could be due to potassium transferred from the biomass to the catalyst. Furthermore, the hydrogen content in condensed organic phase decreased from 9.39 to 9.12 wt.% and the C_2-C_3 paraffin to olefin ratio decreased from 0.90 to 0.50 mol/mol, indicating a decrease in the hydrogenation activity. However, the catalysts total deoxygenation activity was almost unchanged, thus the oxygen content in the organic phase only increased from 9.0 to 9.5 wt.% db. This therefore indicates that the transfer of potassium from the biomass to the catalyst does not necessarily lead to a decrease in the deoxygenation activity. GC×GC-Tof/MS-FID indicated that doping that catalyst with potassium decreased the degree of alkylation reactions, which is most likely also due to potassium binding to the acidic sites. Interestingly, doping the catalyst with potassium also decreased the sulfur content in the produced organic phase. Since the formation of thiols, thiophenes, and benzothiophenes are acid catalyzed reactions, the decrease in sulfur content was probably also due to potassium binding to the acidic sites. However, it should be noted that the solid yield (coke+char)

increased when the potassium doped catalyst was used, thus indicating that the potassium catalyzes polymerization reactions. This phenomenon is further investigated in Chapter 8.

Acknowledgments

This work is part of the H2CAP project (Hydrogen assisted catalytic pyrolysis for green fuels) conducted at The Department of Chemical and Biochemical Engineering at DTU, Denmark. The work was supported by The Danish Council for Strategic Research (now Innovation Fund Denmark, project 1377-00025A), The Programme Commission on Sustainable Energy and Environment. Funding from DTU is also gratefully acknowledged. The authors also acknowledge Aino Nielsen (Haldor Topsøe A/S) for technical assistance with the Raman spectroscopy, Søren Birk Rasmussen for assistance with NH_3-TPD, the Inorganic Analysis Department at Haldor Topsøe A/S for technical assistance with the elemental analysis, and the Organic Analysis Department at Haldor Topsøe A/S for analysis of the organic phase.

References

[1] T.L. Marker, L.G. Felix, M.B. Linck, M.J. Roberts, Integrated hydropyrolysis and hydroconversion (IH^2) for the direct production of gasoline and diesel fuels or blending components from biomass, Part 1: Proof of principle testing, Environ. Prog. Sustain. Energy. 31 (2012) 191–199. doi:10.1002/ep.10629.

[2] T.L. Marker, L.G. Felix, M.B. Linck, M.J. Roberts, P. Ortiz-Toral, J. Wangerow, Integrated hydropyrolysis and hydroconversion ($IH^{2®}$) for the direct production of gasoline and diesel fuels or blending components from biomass, Part 2: Continuous testing, Environ. Prog. Sustain. Energy. 33 (2014) 762–768. doi:10.1002/ep.11906.

[3] E. Maleche, R. Glaser, T. Marker, D. Shonnard, A preliminary life cycle assessment of biofuels produced by the $IH^{2\ TM}$ process, Environ. Prog. Sustain. Energy. 33 (2014) 322–329. doi:10.1002/ep.11773.

[4] J. Fan, J. Gephart, T. Marker, D. Stover, B. Updike, D.R. Shonnard, Carbon Footprint Analysis of Gasoline and Diesel from Forest Residues and Corn Stover using Integrated Hydropyrolysis and Hydroconversion, ACS Sustain. Chem. Eng. 4 (2016) 284–290. doi:10.1021/acssuschemeng.5b01173.

[5] D.C. Dayton, J. Carpenter, J. Farmer, B. Turk, R. Gupta, Biomass hydropyrolysis in a pressurized fluidized bed reactor, Energy & Fuels. 27 (2013) 3778–3785. doi:10.1021/ef400355t.

[6] D.C. Dayton, J. Hlebak, J.R. Carpenter, K. Wang, O.D. Mante, J.E. Peters, Biomass hydropyrolysis in a fluidized bed reactor, Energy & Fuels. 30 (2016) 4879–4887. doi:10.1021/acs.energyfuels.6b00373.

[7] K. Wang, D.C. Dayton, J.E. Peters, O.D. Mante, Reactive catalytic fast pyrolysis of biomass to produce high-quality bio-crude, Green Chem. 19 (2017) 3243–3251. doi:10.1039/C7GC01088E.

[8] D.P. Gamliel, L. Wilcox, J.A. Valla, The effects of catalyst properties on the conversion of biomass via catalytic fast hydropyrolysis, Energy & Fuels. 31 (2017) 679–687. doi:10.1021/acs.energyfuels.6b02781.

[9] D.P. Gamliel, G.M. Bollas, J.A. Valla, Bifunctional Ni-ZSM-5 catalysts for the pyrolysis and hydropyrolysis of biomass, Energy Technol. 5 (2017) 172–182. doi:10.1002/ente.201600136.

[10] D.P. Gamliel, G.M. Bollas, J.A. Valla, Two-stage catalytic fast hydropyrolysis of biomass for the production of drop-in biofuel, Fuel. 216 (2018) 160–170. doi:10.1016/j.fuel.2017.12.017.

[11] O.İ. Şenol, E.-M. Ryymin, T.-R. Viljava, A.O.I. Krause, Reactions of methyl heptanoate hydrodeoxygenation on sulphided catalysts, J. Mol. Catal. A Chem. 268 (2007) 1–8. doi:10.1016/j.molcata.2006.12.006.

[12] O.İ. Şenol, T.-R. Viljava, A.O.I. Krause, Hydrodeoxygenation of aliphatic esters on sulphided NiMo/γ-Al_2O_3 and CoMo/γ-Al2O3 catalyst: The effect of water, Catal. Today. 106 (2005) 186–189. doi:10.1016/j.cattod.2005.07.129.

[13] O.İ. Şenol, T.-R. Viljava, A.O.I. Krause, Effect of sulphiding agents on the hydrodeoxygenation of aliphatic esters on sulphided catalysts, Appl. Catal. A Gen. 326 (2007) 236–244.

doi:10.1016/j.apcata.2007.04.022.

[14] E.-M. Ryymin, M.L. Honkela, T.-R. Viljava, A.O.I. Krause, Competitive reactions and mechanisms in the simultaneous HDO of phenol and methyl heptanoate over sulphided NiMo/γ-Al_2O_3, Appl. Catal. A Gen. 389 (2010) 114–121. doi:10.1016/j.apcata.2010.09.010.

[15] A. Gutierrez, E.-M. Turpeinen, T.-R. Viljava, O. Krause, Hydrodeoxygenation of model compounds on sulfided CoMo/γ-Al2O3 and NiMo/γ-Al2O3 catalysts; Role of sulfur-containing groups in reaction networks, Catal. Today. 285 (2017) 125–134. doi:10.1016/j.cattod.2017.02.003.

[16] T.M.H. Dabros, A. Gaur, D.G. Pintos, P. Sprenger, M. Høj, T.W. Hansen, F. Studt, J. Gabrielsen, J.-D. Grunwaldt, A.D. Jensen, Influence of H2O and H2S on the composition, activity, and stability of sulfided Mo, CoMo, and NiMo supported on MgAl2O4 for hydrodeoxygenation of ethylene glycol, Appl. Catal. A Gen. 551 (2018) 106–121. doi:10.1016/j.apcata.2017.12.008.

[17] V.N. Bui, D. Laurenti, P. Afanasiev, C. Geantet, Hydrodeoxygenation of guaiacol with CoMo catalysts. Part I: Promoting effect of cobalt on HDO selectivity and activity, Appl. Catal. B Environ. 101 (2011) 239–245. doi:10.1016/j.apcatb.2010.10.025.

[18] A. Centeno, E. Laurent, B. Delmon, Influence of the support of CoMo sulfide catalysts and of the addition of potassium and platinum on the catalytic performances for the hydrodeoxygenation of carbonyl, carboxyl, and guaiacol-type molecules, J. Catal. 154 (1995) 288–298. doi:10.1006/jcat.1995.1170.

[19] M. Badawi, J.-F. Paul, S. Cristol, E. Payen, Guaiacol derivatives and inhibiting species adsorption over MoS_2 and CoMoS catalysts under HDO conditions: A DFT study, Catal. Commun. 12 (2011) 901–905. doi:10.1016/j.catcom.2011.02.010.

[20] T.N. Trinh, P.A. Jensen, K. Dam-Johansen, N.O. Knudsen, H.R. Sørensen, S. Hvilsted, Comparison of lignin, macroalgae, wood, and straw fast pyrolysis, Energy & Fuels. 27 (2013) 1399–1409. doi:10.1021/ef301927y.

[21] M.Z. Stummann, M. Høj, C.B. Schandel, A.B. Hansen, P. Wiwel, J. Gabrielsen, P.A. Jensen, A.D. Jensen, Hydrogen assisted catalytic biomass pyrolysis. Effect of temperature and pressure, Biomass and Bioenergy. 115 (2018) 97–107. doi:10.1016/j.biombioe.2018.04.012.

[22] P.M. Mortensen, D. Gardini, H.W.P. de Carvalho, C.D. Damsgaard, J.-D. Grunwaldt, P.A. Jensen, J.B. Wagner, A.D. Jensen, Stability and resistance of nickel catalysts for hydrodeoxygenation: Carbon deposition and effects of sulfur, potassium, and chlorine in the feed, Catal. Sci. Technol. 4 (2014) 3672–3686. doi:10.1039/c4cy00522h.

[23] P.M. Mortensen, D. Gardini, C.D. Damsgaard, J.-D. Grunwaldt, P.A. Jensen, J.B. Wagner, A.D. Jensen, Deactivation of Ni-MoS_2 by bio-oil impurities during hydrodeoxygenation of phenol and octanol, Appl. Catal. A Gen. 523 (2016) 159–170. doi:10.1016/j.apcata.2016.06.002.

[24] S. Houssenbay, E. Payen, S. Kasztelan, J. Grimblot, Oxidic precursors of molybdena supported on nickel and magnesium aluminate hydrotreating catalysts, Catal. Today. 10 (1991) 541–560. doi:10.1016/0920-5861(91)80038-B.

[25] H. Topsøe, The role of Co-Mo-S type structures in hydrotreating catalysts, Appl. Catal. A Gen. 322 (2007) 3–8. doi:10.1016/j.apcata.2007.01.002.

[26] C. Wivel, R. Candia, B.S. Clausen, S. Mørup, H. Topsøe, On the catalytic significance of a CoMoS phase in CoMo Al2O3hydrodesulfurization catalysts: Combined in situ Mössbauer emission spectroscopy and activity studies, J. Catal. 68 (1981) 453–463. doi:10.1016/0021-9517(81)90115-9.

[27] T.M.H. Dabros, A Step in Understanding and Optimizing Fuel Production from Solid Biomass PhD Thesis, Technical University of Denmark, Dept. of Chemical and Biochemical Engineering, 2017.

[28] B.K. Olsen, F. Kügler, F. Castellino, A.D. Jensen, Poisoning of vanadia based SCR catalysts by potassium: Influence of catalyst composition and potassium mobility, Catal. Sci. Technol. 6 (2016) 2249–2260. doi:10.1039/c5cy01409c.

[29] Y. Zheng, A.D. Jensen, J.E. Johnsson, Laboratory Investigation of Selective Catalytic Reduction Catalysts: Deactivation by Potassium Compounds and Catalyst Regeneration, Ind. Eng. Chem. Res. 43 (2004) 941–947. doi:10.1021/ie030404a.

[30] Y. Zheng, A.D. Jensen, J.E. Johnsson, J.R. Thøgersen, Deactivation of V2O5-WO3-TiO2SCR catalyst at biomass fired power plants: Elucidation of mechanisms by lab- and pilot-scale experiments, Appl. Catal. B Environ. 83 (2008) 186–194. doi:10.1016/j.apcatb.2008.02.019.

[31] J.P. Chen, R.T. Yang, Mechanism of poisoning of the V2O5 / TiO2 catalyst for the reduction of NO by NH3, J. Catal. 125 (1990) 411–420. doi:10.1016/0021-9517(90)90314-A.

[32] D. Nicosia, M. Elsener, O. Kröcher, P. Jansohn, Basic investigation of the chemical deactivation of V2O5/WO3-TiO2 SCR catalysts by potassium, calcium, and phosphate, Top. Catal. 42–43 (2007) 333–336. doi:10.1007/s11244-007-0200-4.

[33] M. Klimczak, P. Kern, T. Heinzelmann, M. Lucas, P. Claus, High-throughput study of the effects of inorganic additives and poisons on NH3-SCR catalysts-Part I: V2O5-WO3/TiO2 catalysts, Appl. Catal. B Environ. 95 (2010) 39–47. doi:10.1016/j.apcatb.2009.12.007.

[34] Y. Fan, J. Lu, G. Shi, H. Liu, X. Bao, Effect of synergism between potassium and phosphorus on selective hydrodesulfurization performance of Co-Mo/Al2O3FCC gasoline hydro-upgrading catalyst, Catal. Today. 125 (2007) 220–228. doi:10.1016/j.cattod.2007.02.022.

[35] D. Mey, S. Brunet, C. Canaff, F. Maugé, C. Bouchy, F. Diehl, HDS of a model FCC gasoline over a sulfided CoMo/Al23catalyst: Effect of the addition of potassium, J. Catal. 227 (2004) 436–447. doi:10.1016/j.jcat.2004.07.013.

[36] P. Beato, E. Schachtl, K. Barbera, F. Bonino, S. Bordiga, Operando Raman spectroscopy applying novel fluidized bed micro-reactor technology, Catal. Today. 205 (2013) 128–133. doi:10.1016/j.cattod.2012.09.030.

[37] V. D'Ippolito, G.B. Andreozzi, D. Bersani, P.P. Lottici, Raman fingerprint of chromate, aluminate and ferrite spinels, J. Raman Spectrosc. 46 (2015) 1255–1264. doi:10.1002/jrs.4764.

[38] H. Hu, I.E. Wachs, Surface structures of supported molybdenum oxide catalysts. Characterization by raman and Mo L3-edge XANES, J. Phys. Chem. 99 (1995) 10897–10910. doi:10.1021/j100027a034.

[39] E. Payen, M.C. Dhamelincourt, P. Dhamelincourt, J. Grimblot, J.P. Bonnelle, Study of Co(or Ni)-Mo Oxide Phase Transformation and Hydrodesulfurization Catalysts by Raman Microprobe Equipped with New Cells, Appl. Spectrosc. 36 (1982) 30–37. doi:10.1366/0003702824638953.

[40] K. Eda, Y. Uno, N. Nagai, N. Sotani, M.S. Whittingham, Crystal structure of cobalt molybdate hydrate CoMoO4· nH2O, J. Solid State Chem. 178 (2005) 2791–2797. doi:10.1016/j.jssc.2005.06.014.

[41] M.A. Vuurman, D.J. Stufkens, A. Oskam, G. Deo, I.E. Wachs, Combined Raman and IR study of MOx-V2O5/Al2O3(MOx= MoO3, WO3, NiO, CoO) catalysts under dehydrated conditions, J. Chem. Soc. - Faraday Trans. 92 (1996) 3259–3265. doi:10.1039/FT9969203259.

[42] T.M.H. Dabros, M.Z. Stummann, M. Høj, P.A. Jensen, J.-D. Grunwaldt, J. Gabrielsen, P.M. Mortensen, A.D. Jensen, Transportation fuels from biomass fast pyrolysis, catalytic hydrodeoxygenation, and catalytic fast hydropyrolysis, Prog. Energy Combust. Sci. 68 (2018) 268–309. doi:10.1016/j.pecs.2018.05.002.

[43] W.P. Pan, G.N. Richards, Influence of metal ions on volatile products of pyrolysis of wood, J. Anal. Appl. Pyrolysis. 16 (1989) 117–126. doi:10.1016/0165-2370(89)85011-9.

[44] P. Leflaive, J.L. Lemberton, G. Pérot, C. Mirgain, J.Y. Carriat, J.M. Colin, On the origin of sulfur impurities in fluid catalytic cracking gasoline - Reactivity of thiophene derivatives and of their possible precursors under FCC conditions, Appl. Catal. A Gen. 227 (2002) 201–215. doi:10.1016/S0926-860X(01)00936-X.

[45] D.I. Ishutenko, P.A. Nikul'shin, V. V. Konovalov, A.A. Pimerzin, Selective hydrotreating of cat-cracked gasoline over a K–CoMoS/Al2O3 catalyst, Kinet. Catal. 56 (2015) 747–757. doi:10.1134/S0023158415060038.

[46] C. Bouvier, Y. Romero, F. Richard, S. Brunet, Effect of H_2S and CO on the transformation of 2-ethylphenol as a model compound of bio-crude over sulfided Mo-based catalysts: propositions of promoted active sites for deoxygenation pathways based on an experimental study, Green Chem. 13 (2011) 2441–2451. doi:10.1039/c1gc15181a.

[47] E. Schachtl, J.S. Yoo, O.Y. Gutiérrez, F. Studt, J.A. Lercher, Impact of Ni promotion on the hydrogenation pathways of phenanthrene on MoS_2/γ-Al_2O_3, J. Catal. 352 (2017) 171–181. doi:10.1016/j.jcat.2017.05.003.

[48] V.N. Bui, D. Laurenti, P. Delichère, C. Geantet, Hydrodeoxygenation of guaiacol. Part II: Support effect for CoMoS catalysts on HDO activity and selectivity, Appl. Catal. B Environ. 101 (2011) 246–255. doi:10.1016/j.apcatb.2010.10.031.

[49] V.O.O. Gonçalves, S. Brunet, F. Richard, Hydrodeoxygenation of cresols over Mo/Al_2O_3 and $CoMo/Al_2O_3$ sulfided catalysts, Catal. Letters. 146 (2016) 1562–1573. doi:10.1007/s10562-016-1787-5.

Chapter 8 Deactivation of a CoMo catalyst during catalytic hydropyrolysis of biomass. Part II: Characterization of the spent catalysts and char

In this chapter the spent catalysts from Chapter 7 are characterized and the effect of using wheat straw as feedstock is investigated. The supplementary information can be found in Appendix G.

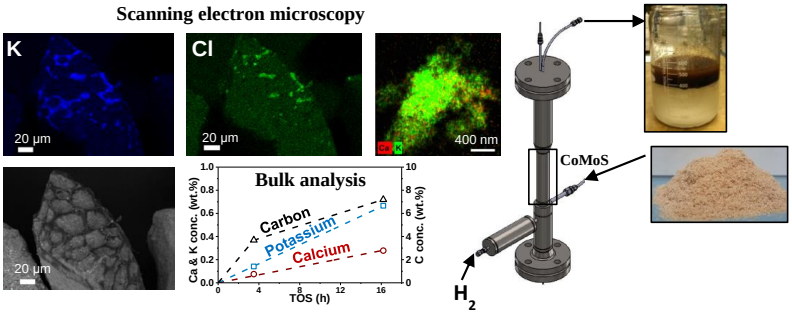

Abstract

In this work spent $CoMo(S)/MgAl_2O_4$ catalysts from a bench scale catalytic hydropyrolysis setup used for the conversion of biomass to liquid fuels were thoroughly characterized. The amount of potassium and calcium transferred to the catalyst increased proportionally with the time on stream (TOS) and was 0.67 and 0.28 wt.% after 16.2 h, respectively, when beech wood was used as feedstock with a feeding rate of approximately 270 g/h. The carbon content on the spent catalyst also increased with TOS and was 3.7 wt.% after 3.5 h and 7.2 wt.% after 16.2 h, indicating that the coking rate decreased over time. However, SEM-EDS indicated that that the carbon concentration increased more on the surface than in the bulk, thereby increasing the risk of pore blocking.

Doping the catalyst with K_2CO_3 corresponding to a potassium loading of 1.9 wt.%, prior to the sulfidation, led to a higher degree of stacking and increased the slab length of the MoS_2 particles. Furthermore, SEM images of the spent catalyst indicated that it became encapsulated with coke during the experiment, which was continuously removed by knock-off. This indicates that potassium acts as a catalyst for polymerization and coking reactions.

The effect of using wheat straw, which contains 10 times more potassium than beech wood, as feedstock was also investigated. This led to defluidization due to agglomeration within the first 0.29 h on stream. SEM images showed that agglomerates, with a diameter up to 5 mm, of char and catalyst particles were formed due to polymerization of the metaplast and tar. Additionally SEM-EDS images showed that potassium was well-distributed in the agglomerates, indicating that potassium catalyzed the formation of these agglomerates.

Abbreviations

BSE	Backscattered electron
daf	Dry, ash free basis
db	Dry basis
EDS	Energy dispersive X-ray spectroscopy
FB	Fluid bed
HAADF	High-angle annular dark-field
HDO	Hydrodeoxygenation
ICP-OES	Inductive coupled plasma optical emission spectroscopy
ND	Not determined
SEI	Secondary electron image
SEM	Scanning electron microscopy
STEM	Scanning transmission electron microscopy
Temp.	Temperature
TOS	Time on stream

8.1 Introduction

The world's energy consumption continues to increase [1], while the need for decreasing our greenhouse gas (GHG) emission becomes more urgent [2], making it necessary to replace fossil fuels with renewable fuels in the near future. During the last decades many researchers have investigated the possibility of producing carbon based fuels from biomass through fast pyrolysis [3,4]. However, the produced bio-oil has a high acidity and low heating value due to its high oxygen content [5]. In order to use it in the transportation sector it needs to be upgraded by hydrotreating, which is a catalyzed reaction at elevated temperatures (350-400°C) and pressures (80-300 bar), but catalyst deactivation and reactor plugging are common problems due to coking [6,7].

Recent research has indicated that catalytic hydropyrolysis could be a more optimal process for the production of carbon based fuels [8,9]. In this process the pyrolysis takes place in a hydrogen atmosphere in the presence of a hydrotreating catalyst. This enables the catalyst to remove the reactive oxygenates before they can participate in polymerization reactions. GTI has developed a process called IH^2® where the catalytic hydropyrolysis is followed by a fixed bed hydrodeoxygenation (HDO) reactor, which removes the remaining oxygen [8,9]. With this process they are able to obtain a condensed organic and C_{4+} yield between 26 and 28 wt.% dry ash free (daf) when using woody biomass, where the produced oil has an oxygen content below 2.2 wt.%. Lemna, microalgae, bagasse, macroalgae, and corn stover have also been tested in the IH^2 process, but not at comparable process conditions, thus making it difficult to compare the obtained results [8]. However, using different algae generally gave a high condensed organic and C_{4+} yield (up to 46 wt.% daf), while using corn stover gave a lower yield of 21 wt.% daf [8]. A 750 h pilot plant experiment with a biomass (wood) feeding rate of 50 kg per day showed no sign of deactivation and with a condensed organic and C_{4+} yield of 26 wt.% daf, but new catalyst was continuously added to the setup due to catalyst entrainment [9]. However, the composition of the fresh catalyst was not reported and the spent catalysts were not characterized. Other research groups have also tested a two-reactor system, where non-catalytic hydropyrolysis takes place in a fluid bed or a cyclone reactor followed by a fixed bed HDO reactor [10–12].

Dayton et al. [13–15] tested several different reduced catalysts in a fluid bed catalytic hydropyrolysis setup at temperatures between 375 and 500 °C, pressures between 1 and 21 bar, and obtained a carbon recovery in the condensed organic phase and C_{4+} in the gas between 25 and 43 %. They also conducted a 10 days experiment where 1 kg of biomass was used each day and the catalyst in the fluid bed was oxidized and reduced between each day in order to remove carbon [14]. The condensed organic yield and C_{4+} yield varied between 25 and 30 wt.% daf, with an oxygen content between 2 and 5 wt.% dry basis (db). However, due to catalyst loss new catalyst was added to the fluid bed during the experiment [14]. Meesuk et al. [16–18] studied catalytic hydropyrolysis of rice husk using a fluid bed reactor with a single shot biomass feeding system, and obtain bio-oil yields between 20 and 50 wt.%, but the oxygen content in the organic phase was generally above 20 wt.% and the spent catalysts were also not characterized. Other groups have studied catalytic hydropyrolysis using pyroprobes or similar micro-scale equipment [19–25], however none of the spent catalysts were analyzed. This clearly shows that there is a lack of knowledge on how the spent catalysts are affected by the type of biomass, time on stream, and process conditions.

In our previous research we have conducted catalytic hydropyrolysis of beech wood in a fluid bed reactor loaded with a sulfided CoMo catalyst followed by a fixed bed HDO reactor loaded with a sulfided NiMo catalyst and investigated the effect of varying the temperature and pressure [26]. The difference between using a sulfided CoMo, NiMo, and Mo catalyst in the fluid bed reactor has also been investigated, which showed that the CoMo catalyst has the highest HDO activity at similar metal loading at the applied tempera-

ture around 450 °C (see Chapter 5). Analysis of the spent catalysts showed that both potassium and calcium were transported from the biomass to the catalysts during the experiments (see Chapter 5), which over time may lead to catalyst deactivation [27]. In this study the effect of time on stream, doping the fresh catalyst with potassium, and the effect using wheat straw instead of beech wood were studied. In part I (see Chapter 7), we investigated the effect on the product distribution and composition while in this work we focus on characterization of the spent catalysts from the catalytic fluid bed hydropyrolysis reactor.

8.2 Material and methods

8.2.1 Biomass feedstock

Bark free beech wood and wheat straw were used as biomass feedstock. The beech wood has previously been used in catalytic hydropyrolysis experiments [26]. The moisture and ash contents in the beech wood was 6.72 wt.% and 0.59 wt.% db, respectively, and the particle size was between 200-700 µm [26]. The moisture content in the straw was 7.4 wt.% and the ash content was 4.2 wt.% db, the particle size was below 710 µm and 80 % of the particles were smaller than 315 µm. The composition of the beech wood and the straw is shown in Table 8.1.

Table 8.1. Composition of bark free beech wood and straw. The concentration of Mn was not determined (ND) in straw.

	Beech	**Straw**	
C	49.9	46.9	wt.% dry
H	6.0	6.0	wt.% dry
N	0.13	0.56	wt.% dry
O*	43.0	41.6	wt.% dry
K	0.12	1.4	wt.% dry
Ca	0.13	0.23	wt.% dry
S	48	1200	wt-ppm dry
Na	9.9	230	wt-ppm dry
Mg	350	960	wt-ppm dry
Si	140	3900	wt-ppm dry
P	75	910	wt-ppm dry
Cl	2.0	6500	wt-ppm dry
Mn	170	ND	wt-ppm dry
Fe	24	41	wt-ppm dry
Cu	2.1	ND	wt-ppm dry
Zn	4.9	ND	wt-ppm dry
Sr	4.6	ND	wt-ppm dry
Al	ND	44	wt-ppm dry
Ti	ND	540	wt-ppm dry
HHV	19.7**	18.9	MJ/kg

**Calculated by difference.*

***Calculated from Milne formula: 0.341×C+1.322×H-0.12*O-0.12×N+0.0686*S-0.0153×ash*[28]

8.2.2 Catalysts

Three CoMo catalysts (CoMo#1, CoMo#2, and CoMoK#1) were tested in the fluid bed reactor. The catalysts were prepared by sequential incipient wetness impregnation of $MgAl_2O_4$ with a surface area of 54-58 m^2/g

and a detailed description of the preparation and characterization of the catalysts can be found elsewhere (see section 7.2.2). CoMo#1 contained 3.41 wt.% Mo and 0.637 wt.% Co, CoMo#2 contained 3.29 wt.% Co and 0.615 wt.% Mo, and CoMoK#1 contained 3.43 wt.% Mo and 0.603 wt.% Co. CoMoK#1 was after the impregnation with Mo and Co also impregnated with K_2CO_3 and the K content was 1.94 wt.%

The catalysts were sulfided in-situ in the catalytic hydropyrolysis setup at 26 bar, 350°C with 1.8 mol % H_2S, 11 mol % N_2 in 87 mol % H_2 by feeding 2% H_2S in H_2 (flow: 4 NL/min) and N_2 (flow: 0.5 NL/min). The temperature ramp was 10 °C/min and the holding time was 2 hours. After the sulfidation the test conditions were established.

8.2.3 Catalyst and char characterization

Transmission electron microscopy was performed on a FEI Talos™ F200X transmission electron microscope equipped with high-brightness field emission gun (X-FEG) and Super-X G2 EDS detector. Images and elemental energy dispersive X-ray spectroscopy (EDS) maps were acquired in scanning transmission mode (STEM). Elemental EDS maps of 512 pixels x 512 pixels (2.1 µm x 2.1 µm) were acquired for 20 min in Brüker software (Esprit 1.9) using a probe current of 0.7 nA. The elemental EDS maps were processed in Esprit with a smoothing filter (3x3). The EDS analyses were complimented by high-resolution STEM imaging (probe size about 0.16nm) using the high-angle annular dark field detector (HAADF). For particle size measurements, HAADF-STEM images of 1024 pixels x 1024 pixels were recorded with a pixel size of 0.061 nm thus enabling the lattice spacing of 2H-MoS_2 (001) of 0.615 nm to be resolved. The sizes of the identified particles were measured manually from the images using ImageJ software. A more through description of the method can be found elsewhere (see section 5.2.4.3).

The scanning electron microscopy (SEM) was performed on a FEI QUANTA600 scanning electron microscope equipped with both a backscattered electron (BSE) and secondary electron detector making it possible to take both BSE and secondary electron images (SEI). The samples were sprinkled on carbon tabs on Al-stubs and conducted without any coating to prevent charging in the sample chamber. EDS element maps and quantifications were acquired on 0.11 mm x 0.11 mm areas at 3 kV, 5 kV, 10 kV and 15 kV to probe different interaction volumes between the incident electron beam and the sample. The maximum penetration depth of the incident electron beam in $MgAl_2O_4$ was estimated with the CASINO Monte Carlo Software v.3.3.04 to be approximately 0.170 µm for 3 kV and 1.60 µm for 15 kV, which gives a rough estimation the penetration depth. The composition of the sample was determined in EDAX software (version 5.2.42). The standard deviation for the carbon measurement was 1.5 wt.% at 3 kV, 0.8 wt.% at 5 kV, 1.0 wt.% at 10 kV and 1.5 wt.% at 15 kV, and the standard deviation for the potassium measurements was 0.6 wt.% at 5 kV, 0.3 wt.% at 10 kV, and 0.2 wt.% at 15 kV. A more detailed description of the analysis method can be found elsewhere (see section 5.2.4.3).

The bulk concentration of alkali metals (K and Ca) on the spent catalysts was also determined with inductive coupled plasma optical emission spectroscopy (IPC-OES). The carbon content was measured with a LECO CS-200, in which the sample was combusted in pure oxygen and the carbon content was calculated on the basis of the formed CO_2, which was measured with IR-absorption.

8.2.4 Experimental setup and procedure

8.2.4.1 Hydropyrolysis setup

The catalytic hydropyrolysis experiments were conducted in a bench scale setup. The setup is described in details elsewhere [29]. The setup consisted of a feeding system, which included a gas mixing system and a

screw feeder, a fluid bed hydropyrolysis reactor, a filter for char removal, a fixed bed hydrodeoxygenation (HDO) reactor, which could be bypassed, and a three stage condensation system (20°C, 2°C, and -40°C). The gas composition was measured with an online gas chromatograph (GC), which measured the gas composition (H_2, N_2, H_2S, CO, CO_2, C_1 to C_5 and C_{6+} hydrocarbons) every 10 min. After each finished experiment the catalyst and the remaining char was removed from the fluid bed, and replaced with the fresh catalyst for the subsequent experiment. During the 5 days experiment new catalyst was not added to the fluid bed reactor between each day. A detailed description of the experimental procedure can be found elsewhere (see section 7.2.4).

8.2.4.2 KCl transfer setup

Transfer of KCl to the catalyst was investigated by mixing KCl and CoMo#1 in a 10:1 ratio (w/w) in a crucible, placing it in a tube furnace (diameter: 6 cm), and heating it to 450 °C and varying the holding time, see Table 8.2. The KCl particles were larger than 355 µm and the CoMo#1 particles were smaller than 355 µm. After the experiment was finished the mixture was sieved and KCl and CoMo#1 was separated and the K and Cl concentration on the spent CoMo#1 particles was investigated by SEM-EDS.

Table 8.2 Test conditions for KCl transfer experiments. (Temperature: 450 °C, N_2 flow: 1.0 NL/min)

Hold time (h)	48	96	375
CoMo#1 (g)	1.49	1.48	1.47
KCl (g)	14.95	14.86	14.73

8.3 Results and Discussion

In order to evaluate the process stability a 5 days experiment was conducted with CoMo#2 in the fluid bed reactor and a commercial $NiMo/Al_2O_3$ catalyst in the HDO reactor. The total time on stream (TOS) was 16.2 hours and 5.18 kg of beech wood was consumed. The temperature in the fluid bed reactor was between 452 and 455 °C, the temperature in the HDO reactor was between 366 and 373 °C and the biomass feeding rate was between 240 and 276 g/h. The experimental time was 3.5 hours per day, except on day 3, where the experiment was stopped after 2.2 hours due problems with the biomass feeding system. An overview of the test conditions and mass balances is shown in Table 8.3. The mass balance closed between 100.3 and 103.1 wt.% daf based on the amount of biomass fed. Since hydrogen was incorporated into the organics by hydrogenation the mass balance closed above 100 %. It was not possible to determine the char and coke yield each day, because that would require unloading the fluid bed reactor. Instead the filter was unloaded each day and the solid yield in the filter was determined. The catalyst carryover from the fluid bed to the filter was estimated to between 1 and 9 g per day and the total amount of catalyst carryover was estimated to 20 g, corresponding to 40 wt.% of the total amount of catalyst loaded. A detailed analysis of the product distribution and composition can be found elsewhere (see Chapter 7).

Table 8.3 Test conditions and yields for stability test and reference experiment. (Catalyst in HDO reactor: 173 g NiMo/Al_2O_3 supplied by Haldor Topsøe A/S)

Test	1 (day 1)	1 (day 2)	1 (day 3)	1 (day 4)	1 (day 5)	2	3	4	5
Test conditions									
FB Temp. (°C)	453	452	454	455	453	451	454	453	453
FB catalyst	CoMo#2	CoMo#2	CoMo#2	CoMo#2	CoMo#2	CoMo#1	CoMoK#1	CoMo#2	CoMo#2
FB catalyst amount (g)	49.99	-	-	-	-	50.03	49.98	50.01	49.96
FB catalyst lost (g)	5	9	3	2	1	ND	ND	ND	ND
HDO Temp. (°C)	370	370	366	372	373	-	-	-	-
Biomass	beech	beech	beech	beech	beech	beech	beech	Straw	Straw
Pressure (bar)	26	26	26	26	26	26	26	26	26
Feed time (h)	3.5	3.5	2.2	3.5	3.5	3.5	3.5	0.26	0.29
Feeding rate (g/h)	274	276	240	274	273	275	268	400	<400
H_2S conc.(ppm)	460	460	460	460	460	460	460	460	447
H_2 flow (NL/min)	82	82	82	82	82	82	82	82	102
N_2 flow (NL/min)	5	5	5	5	5	5	5	5	5
Yields (wt. daf %)									
Gas	29.4	30.0	29.6	30.7	31.2	26.1	24.9	ND	ND
Solid	10.9	13.8	14.6	13.2	13.6**	13.3**	14.6**	ND	ND
Aqueous phase	38.0	37.1	36.4	34.5	35.115	33.3	28.9	ND	ND
Organic phase	12.2	13.7	12.5	14.6	14.1	17.7	19.9	ND	ND
C_{4+} in the gas	9.9	9.2	8.7	8.3	9.1	7.5	4.1	ND	ND
Organics + C_{4+}	22.1	22.9	21.2	22.9	23.2	25.2	24.1	ND	ND
Mass balance	100.3	103.7	101.8	101.2	103.1	97.8	92.5	ND	ND

*By difference

** Solid = Solid in filter + solid in fluid bed – catalyst loaded

The beech wood only contained 0.12 wt.% db potassium. Therefore, the effect of using Danish wheat straw was investigated with the test conditions shown in Table 8.2, experiments 4 and 5. The straw contained 1.4 wt.% potassium, thus it was assumed that deactivation by potassium would be more pronounced with straw. In the first experiment with straw the reactor defluidized after 0.26 h, which was observed as large temperature fluctuations of up to 130 °C (see supplementary information Figure G.1(B)), and lead to plugging of the biomass feeding tube. The straw was tested in a second experiment with an increased gas flow rate and each time a temperature fluctuation occurred the biomass feeding was paused and restarted when the temperature had stabilized, in an attempt to minimize the risk of plugging of the biomass feeding tube. The first larger temperature fluctuation was observed after 0.21 h, and 5 larger temperature fluctuations was observed before the biomass feeding tube plugged after 0.29 h (see supplementary information Figure G.1 (C)). Due to the short operational time not enough liquid was condensed to conduct any analysis and it was not possible to make a mass balance for the experiments with straw. However, the spent catalyst from the fluid bed was recovered, which showed that agglomeration had occurred in both experiments with straw and agglomerates with a diameter up to 5 mm was observed, as discussed in detail in section 8.3.1.2.3.

8.3.1 Characterization of spent catalysts and char

8.3.1.1 HAADF-STEM

The spent catalysts from experiments 1-3 were also studied with HAADF-STEM, see Figure 8.1, which showed a nanometer sized slab structure of bright contrast well distributed on the surface of the larger support particles, which has less image contrast. The CoMo#1 and CoMo#2 slabs were mainly found as single layer slabs (see Figure 8.1 (C) & (F)), but a few slabs with 2 or more layers (up to 4) were observed. As shown in Figure 8.1 (A), when two layer stacks were observed, the interlayer-distance between the slabs was 0.62 nm, consistent with a MoS_2 (001) spacing. On this basis the bright-contrasted slab structures are attributed to single, double- or multilayer MoS_2 nanocrystals viewed with the (001) basal plane along the electron beam direction, situated with the basal plane on the surface of the larger $MgAl_2O_4$ particles, which has

been reported previously [30]. Based on 10 images per catalyst and between 111 and 238 slabs per sample, the MoS_2 nanocrystals were mainly found as single layer slabs (>95%) for CoMo#1 and CoMo#2 with an average stacking of approximately 1.05. However, for the CoMoK#1 only 44% of the slabs were found as single layer structures and up to 13 layers stacked on each other was observed (see Figure 8.1 (I)), thus the average stacking for CoMoK#1 was 1.77. The measured slab length (Figure 8.1 (B) & (E)) for CoMo#1 and CoMo#2 was between 1 and 9.5 nm and the mean was 2.9 nm for CoMo#1 and 3.2 nm for CoMo#2. The slab size and distribution was thus comparable for CoMo#1 and CoMo#2 and it is therefore assumed that the MoS_2 edge dispersion of these catalysts was comparable. However, the slab length for CoMoK#1 was between 1.2 and 27 nm with an average of 4.3 nm, hence significantly higher than for CoMo#1 and CoMo#2. This indicates that potassium affects the sulfidation of the CoMo catalyst and promotes the formation of multilayer slabs and increases the slab length, which was also observed by Fan et al. [31]. The here observed formation of multilayer slabs could be due to weaker Mo-O-Al bonds [32] and indicates that the active type II CoMoS structure is formed instead of type I. Furthermore, stacking also decrease the amount of available Brim sites, which facilitates the hydrogenation reactions [32,33]. It was observed that doping the catalyst with potassium, decreased its cracking, hydrogenation, and hydrodeoxygenation activity, leading to more decarboxylation. The oxygen content in the condensed organic phase was 9.0 wt.% db for CoMo#1 and 9.5 wt.% for CoMoK#1 (see section 7.3.3), thus the deoxygenation activity for the two catalysts was the almost the same. The reason for this observation is most likely that CoMo#1 mainly consists of type I structures, while CoMoK#1 consists of both type I and type II structures and CoMoK#1 has therefore maintained a fairly high deoxygenation activity despite the addition of potassium.

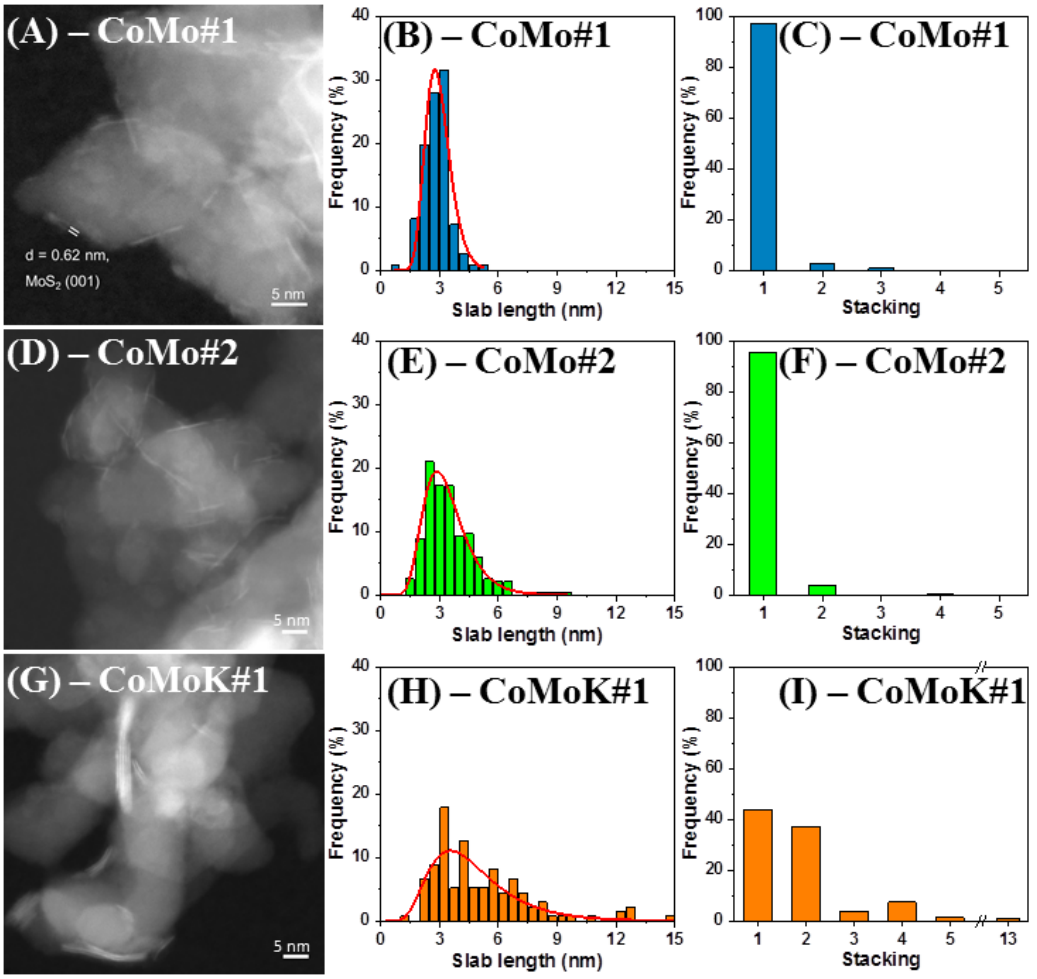

Figure 8.1 HAADF-STEM images of CoMo#1 (A), CoMo#2 (D), and CoMoK#1 (E), slab size distribution of CoMo#1 (B), CoMo#2 (E), and CoMoK#1 (H), stacking on CoMo#1 (C), CoMo#2 (F), and CoMoK#1 (I). The images in (A), (D), and (G) were contrast adjusted (gamma) to improve visibility. Fluid bed temperature: 451-455°C, pressure: 26 bar, biomass feeding rate: 240-277 g/h , H_2 flow: 82 NL/min, N_2 flow: 5 NL/min, and H_2S conc: 460 ppm.

The distribution of the cobalt, molybdenum, and sulfur on the spent catalysts is shown on the elemental maps in Figure 8.2 (For single EDS maps see supplementary information Figures G.3-G.5). For the CoMo#1 and CoMo#2 the molybdenum and sulfur were well distributed on the support, indicating a good dispersion of the MoS_2 phase in consistency with Figure 8.1. The molybdenum and sulfur were less distributed on the support for CoMoK#1, which is due to the longer slab and higher degree of stacking for CoMoK#1. A large CoMoS particle (~100 nm) was also observed for the CoMoK#1, which is most likely a highly stacked Co-MoS particle. The cobalt was also mainly located together with the molybdenum, which indicates an incorporation of cobalt into the MoS_2 structure, the so-called CoMoS phase [34]. However, larger Co particles (20-60 nm) were observed on CoMo#2 (Figure 8.2 (E)), indicating that not all the cobalt was incorporated into the MoS_2 structure and the Co particles are most likely the less active Co_9S_8 phase [34]. A single Co

particle (~50 nm), most likely Co_9S_8, was also observed on the CoMoK#2. The reason for the formation of CoS particles is unknown, but since it is observed for both CoMo#2 and CoMoK#1 it could be related to the potassium, which was observed on all the spent catalysts and was well distributed on the particles. Calcium was observed on both CoMo#1 (Figure 8.2 (C)) and CoMo#2 (Figure 8.2 (F)) as larger particles and was not well-distributed, which is most likely the reason why it was not observed on CoMoK#1. The calcium particles on CoMo#1 has diameters between 20 and 60 nm, while the particle diameters were below 20 nm on CoMo#2.

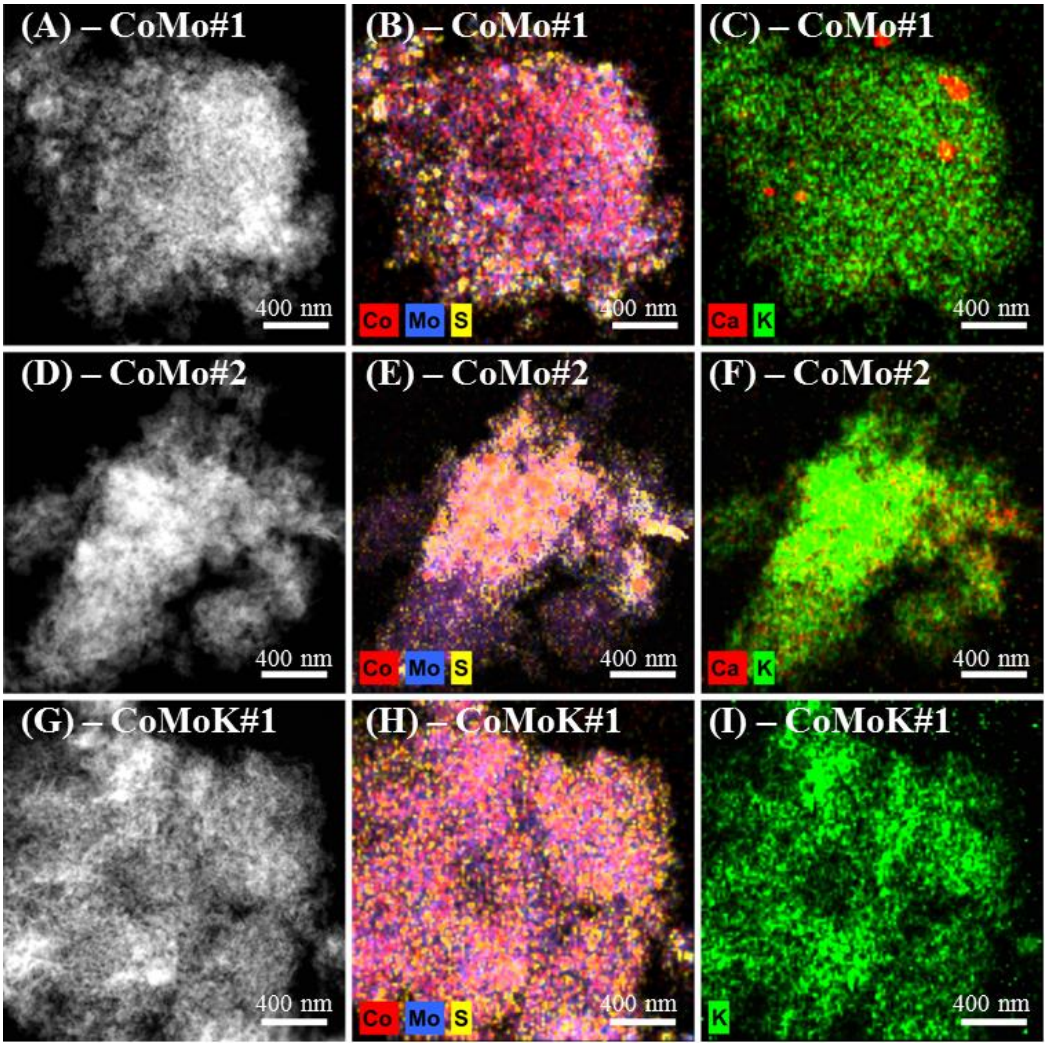

Figure 8.2 HAADF-STEM micrographs and molybdenum, cobalt, sulfur, potassium, and calcium EDS element maps on CoMo#1 (A-C), CoMo#2 (D-F), and CoMoK#1 (G-I). Fluid bed temperature: 451-455°C, pressure: 26 bar, biomass feeding rate: 240-277 g/h , H_2 flow: 82 NL/min, N_2 flow: 5 NL/min, and H_2S conc: 460 ppm.

8.3.1.2 SEM-EDS

8.3.1.2.1 Effect of time on stream

The degree of coking on the spent catalysts from experiment 1 and 2 was investigated by SEM-EDS and the carbon content is shown as a function of the acceleration voltage in Figure 8.3(A). At the low acceleration voltage (3 kV) the beam only penetrates into the surface of the sample, thus the carbon content corresponds to the surface concentration. As the acceleration voltage increases the beam penetrates deeper into the sample and at 15 kV a larger interaction volume towards the bulk was measured, integrating the signals from the surface and the bulk. However, it should be noted that the maximum penetration is 1.6 µm at 15 kV. The background carbon measurement from the carbon tape was accounted for by subtracting the measured carbon content on the fresh catalyst from the spent catalyst (see supplementary information Table G.1). The carbon content on the CoMo#1 catalyst, with 3.5 h on stream and only 0.96 kg biomass processed, had a carbon content between 1.5 and 3.3 wt.%. However, the catalyst (CoMo#2) with 16.2 h on stream using 5.18 kg biomass had a carbon content of 27 wt.% when measured at 3 kV and 15 wt.% when measured at 15 kV. This indicates that the carbon content increases with time on stream and increasing amount of biomass used. Furthermore, the increasing carbon content at the surface of the catalyst particles could over time lead to pore blocking.

Potassium was detected on the spent samples as shown in Figure 8.3 (B). Since potassium is a heavier element than carbon it cannot be excited at 3 kV, hence the surface concentration was not measured. The potassium content on the catalyst that had been in the fluid bed for 3.5 h was between 0.4 and 0.8 wt.% and it was between 1.5 and 2.4 wt.% for the sample that had been in the fluid bed for 16.2 h. No traces of potassium were detected on the fresh catalysts, indicating that the potassium is transferred from the biomass to the catalyst and that the potassium content increases with the amount of biomass used.

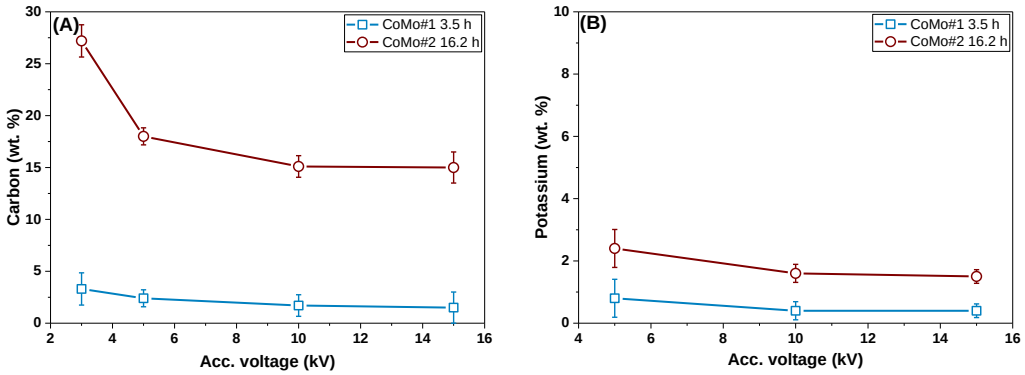

Figure 8.3 Carbon (A) and potassium (B) content measured with SEM combined with EDS on the spent catalyst from a one-day 3.5 h experiment (without the HDO reactor) and the 5 days, 16.2 h experiment (with the HDO reactor). Fluid bed temperature: 451-455°C, pressure: 26 bar, biomass feeding rate: 240-277 g/h , H_2 flow: 82 NL/min, N_2 flow: 5 NL/min, and H_2S conc: 460 ppm.

A small fraction of spent catalyst from the fluid bed reactor from experiment 1 and 2 were separated from the char particles and the bulk concentration of calcium and potassium were measured with ICP-OES and the bulk carbon content was measured by combustion (see Figure 8.4). This showed that the carbon concentration measured with SEM-EDS gives a fairly accurate estimation of the carbon content for CoMo#1, between 1.5 and 3.3 wt.% for EDS and 3.69 wt.% by combustion, but overestimates the carbon content on CoMo#2,

between 15 and 27 wt.% with EDS and 7.19 wt.% by combustion. The reason for the different results for the two methods for the spent CoMo#2 is that for the SEM-EDS analysis the carbon concentration at the surface also affects the measurement at 15 kV, thus leading to an overestimation of the carbon content at 15 kV. However, the reason for the difference could also be that the carbon concentration continues to decrease through the catalyst particle, hence giving a significantly higher concentration near the surface of the particle compared to the core. The potassium content was also overestimated by EDS, 0.4-0.8 wt.% for CoMo#1 and 1.5-2.4 wt.% for CoMo#2, when compared to the ICP-OES analysis: 0.141 wt.% for CoMo#1 and 0.666 wt.% for CoMo#2. The reason for the overestimation with EDS is that at low potassium concentrations the EDS signal becomes too low for an accurate measurement. Calcium is also detected with ICP-OES: 0.0750 wt.% for CoMo#1 and 0.278 wt.% for CoMo#2.

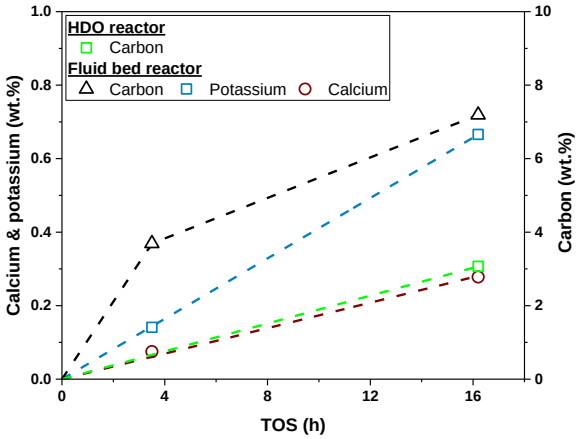

Figure 8.4 Carbon, calcium, and potassium content on the spent catalyst in the fluid bed from experiment 1 and 2 and the $NiMo/Al_2O_3$ HDO reactor catalyst from experiment 1. Fluid bed temperature: 451-455°C, pressure: 26 bar, biomass feeding rate: 240-277 g/h , H_2 flow: 82 NL/min, N_2 flow: 5 NL/min, and H_2S conc: 460 ppm. The calcium and potassium content was measured with ICP-OES and the carbon content was measured by combustion.

Interestingly, the potassium and calcium content increases proportionally with the time on stream (see Figure 8.4), hence proportionally with the amount of biomass used. It should be noted that the deposition of metal sulfides (mainly vanadium sulfide) on hydrotreating catalysts generally increases linearly with time on stream when hydrotreating atmospheric residue [35]. Interestingly the amount of potassium transferred to the catalyst after 3.5 h corresponds to 28 % saturation of the acidic sites (measured on fresh oxide precursor – see Figure 7.2), while the amount transferred after 16.2 h corresponds to 115 % saturation of acidic sites. Olsen et al. [36] studied the potassium mobility in vanadia based SCR catalysts and observed a saturation of Brønsted acidic sites, after which potassium no longer diffused into the catalyst. Analysis of catalyst from longer catalytic hydropyrolysis experiments are therefore needed to investigate if this is also the case in catalytic hydropyrolysis.

The carbon content on the spent catalyst from the fluid bed reactor indicates that the coke deposition rate decreases with TOS, which is well-known in hydrotreating of fossil oil [35,37]. The reason for the decreasing coke deposition rate could be that the coke build up at the surface of the catalyst (see Figure 8.3), which is well-known from hydrotreating of vacuum resid [38], thus makes coking inside the pores diffusion limited [35]. Another possible explanation could be that the coke initially builds up as a monolayer on the support

material [39,40], thus leading to a decreasing coking rate as the support becomes covered with coke, however the location of the coke is dependent of the used catalyst [41]. The carbon content on the spent NiMo/Al_2O_3 catalyst from the fixed bed HDO reactor in experiment 1 was 3.07 wt.% (see Figure 8.4), showing that some coking has taken place. However, the initial stabilization of the vapors, which occurs in the fluid bed, has most likely decreased the degree of coking in the HDO reactor.

8.3.1.2.2 Effect of doping the catalyst with potassium

The spent CoMoK#1 catalyst was studied with SEM using both a BSE and SEI detector. As shown in Figure 8.5(A), many of the spent catalyst particles were covered with a carbon layer (dark particles), which encapsulated the particles. An EDS measurement at spot "a" in Figure 8.5(D), shows that the layer consisted of 95.7 wt.% carbon (see Table 8.4), showing that this layer is coke. As showed by the EDS spot measurement "b" in Figure 8.5(D) and Table 8.4, the part of the spent catalyst, which was not encapsulated only gave a carbon signal of 15.9 wt.%, which might not be the actual carbon content since it is not corrected for the background signal from the carbon tape. The SEM images (Figure 8.5(A), (B), and (C)) indicate that the coke primarily grows from the already deposited coke on the catalyst, which also can explain the lower concentration at point "b" than "a" in Figure 8.5(D). Furthermore, this can also explain why some particles do not contain a coke layer. A coke flake is observed in Figure 8.5(C), which indicates that the coke was continuously removed during the experiment by attrition (or knock-off) in the fluid bed. This encapsulation of the catalyst particles was not observed for the CoMo#1 and CoMo#2 catalysts and has not been observed in our previous studies (Chapter 3-6), indicating that it is caused by the presence of potassium.

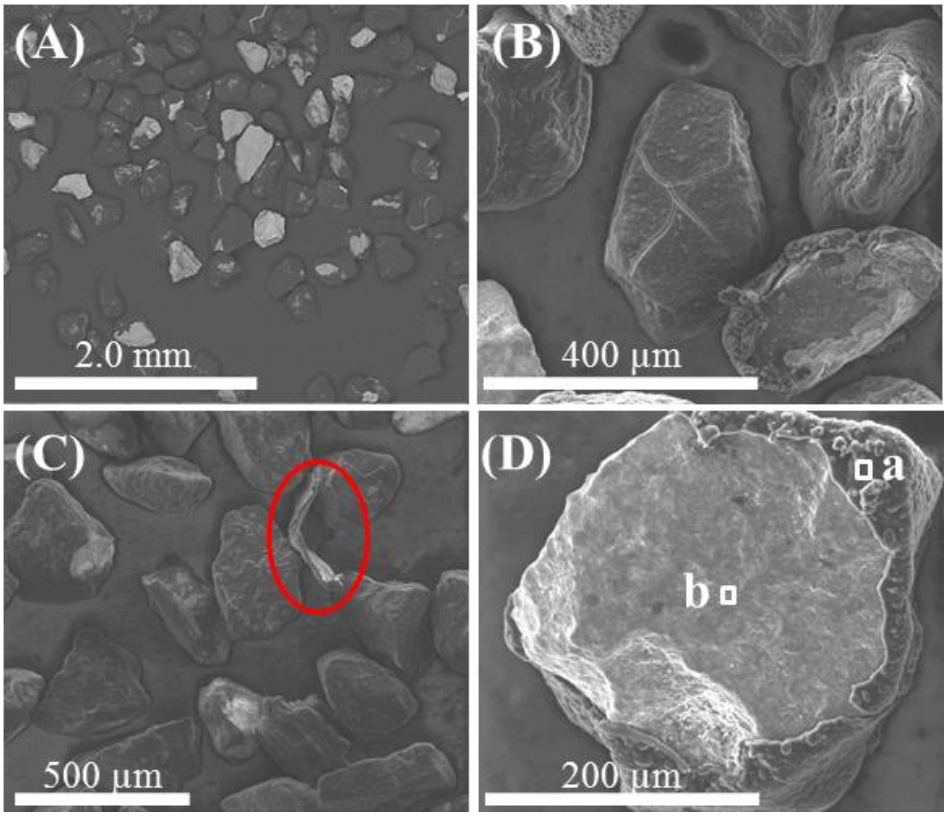

Figure 8.5 SEM images of the spent CoMoK#1 catalyst acquired with a BSE-detector (A) and (C) and with a SEI-detector (B) and (D). Fluid bed temperature: 454°C, pressure: 26 bar, biomass feeding rate: 268 g/h, H_2 flow: 82 NL/min, N_2 flow: 5 NL/min, and H_2S conc: 460 ppm.

Jensen et al. [42] investigated the effect of impregnating KCl on cellulose, hemicellulose and lignin in pyrolysis with a thermogravi metric analyzer using a heating rate of 10 °C/min and heating the samples up to 700 °C. They found that impregnating cellulose with KCl increased the char yield with a factor of 4, while KCl only had a minor influence on the char yield during the pyrolysis of hemicellulose and lignin. Their results indicate that potassium can act as a catalyst for char formation, which can explain the formation of coke on the surface of the CoMoK#1 catalyst, and this is probably also the reason for the higher solid yield with the CoMoK#1 compared to CoMo#1, as shown in Table 8.3.

Table 8.4 SEM-EDS measured concentrations of carbon, oxygen, sulfur, and potassium at spots a and b in Figure 8.5 (D)

Spot	a	b
C (wt.%)	95.7	15.9
O (wt.%)	3.0	23.2
S (wt.%)	1.4	10.1
K (wt.%)	0	1.4

8.3.1.2.3 Effect of using straw

Investigations of the spent catalyst from the fluid bed reactor when using wheat straw as biomass showed that agglomeration had taken place. Some of the particles retrieved from the fluid bed reactor had a diameter of approximately 5 mm, while the fresh catalyst had a diameter between 180-355 µm. The observed defluidization was therefore due to agglomeration. In order to obtain a deeper understanding of the agglomeration, the agglomerates were studied with SEM. As shown in Figure 8.6 the catalyst particles were trapped in a grid with no sign of carbon coating of the catalyst surface as observed with the CoMoK#1 catalyst in Figure 8.5. Instead, Figure 8.6 indicates that solidified tar have formed an agglomerate, which has captured several catalyst particles. Remarkably, no sign of the original cell structure of the straw is observed in this agglomerate indicating that the biomass has been molted during the pyrolysis.

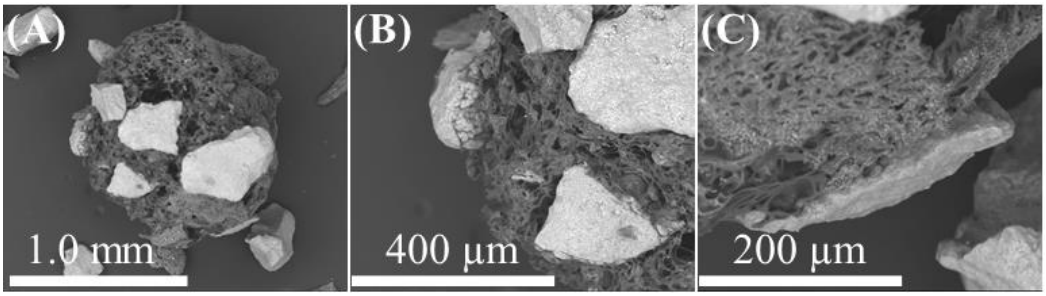

Figure 8.6 SEM-BSE images of the formed agglomerates from experiment 4. Fluid bed temperature: 453°C, pressure: 26 bar, biomass feeding rate: 400 g/h, H_2 flow: 82 NL/min, N_2 flow: 5 NL/min, and H_2S conc: 460 ppm, biomass type: straw.

On some of the spent catalyst particles a grid had been deposited on the surface of the particles, see Figure 8.7(A). EDS-element distribution indicated that this grid mainly consisted of carbon (Figure 8.7(D)), however the concentration of carbon was considerably lower on the part of the particle, which was not covered by the grid. It can therefore be assumed that this grid is not formed due to normal coke formation on the surface of the particle, but must come from solidification of tar or metaplast, a heavy intermediate formed during fast pyrolysis [43]. Furthermore potassium and chlorine was also detected in the grid, see Figure 8.7(B) and (C). It should be noted that the potassium and chlorine were observed at the same places, indicating that they are chemical bound as KCl. Both potassium and chlorine were also observed on the part of the particle, which was not covered by the carbon grid, indicating that these elements are transferred to catalyst independently of the tar and metaplast solidification. Since both potassium and chlorine are known for their abilities to deactivate HDO catalysts [27,44], these results indicate that even if agglomeration is avoided, it could be difficult to use straw as feedstock without removing these species by pretreating it, e.g. by washing.

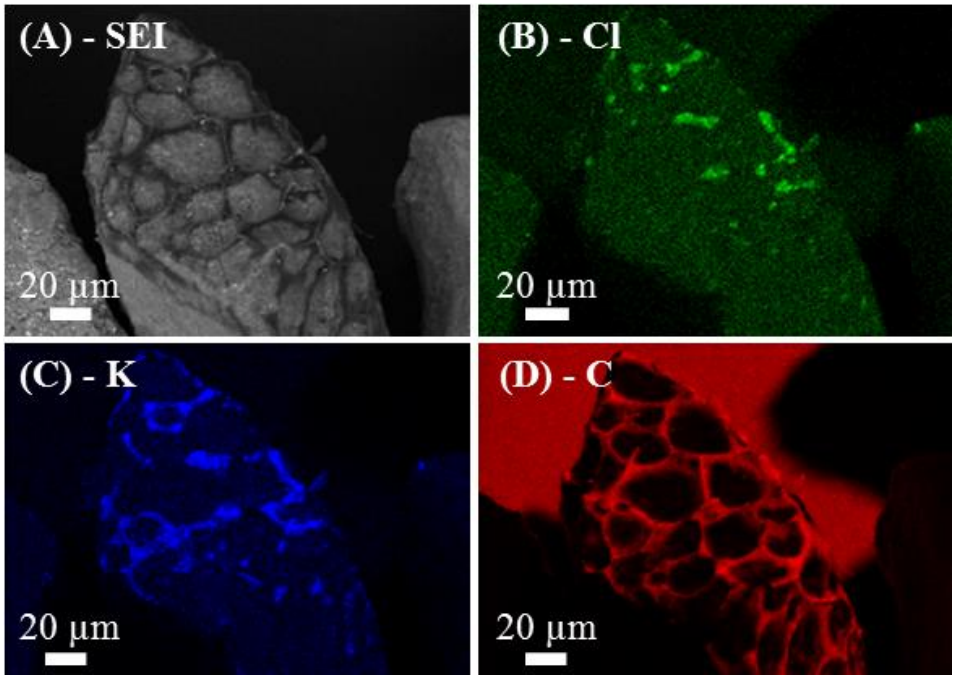

Figure 8.7 SEM-SEI micrograph (A) and EDS element distribution of chlorine (B), potassium (C), and carbon (D) on a spent catalyst particle from experiment 4. Fluid bed temperature: 453°C, pressure: 26 bar, biomass feeding rate: 400 g/h, H_2 flow: 82 NL/min, N_2 flow: 5 NL/min, and H_2S conc: 460 ppm, biomass type: straw.

8.3.1.2.4 Char morphology and structural transformation

The char from the experiments was also studied with SEM. Figure 8.8(A) shows a sample taken from the fluid bed reactor from experiment 2. The bright particles are the spent catalysts, while the dark particles are char. Two types of char particles are observed; one is elongated and has maintained the structure of the beech wood, while the other is shorter and more rounded (highlighted with red color). Two of the particles have several bright spots on the surface and EDS analysis of a similar particle indicates that these spots are due to calcium rich crystals (see supplementary information Figure G.5 and Table G.2). Figure 8.8(B) and (C) show two similar char particles from experiment 2. The cell structure is almost absent for the char particle in Figure 8.8(B), however, only a few bright spots are observed on this particle, while several crystals are observed in the char particle shown in Figure 8.8(C), which indicates that an up concentration of the calcium takes place. These results indicate that some of the beech wood particles partly melt during the catalytic hydropyrolysis. This has also been observed in other similar experiments conducted with the same beech wood (see supplementary information Figure G.5).

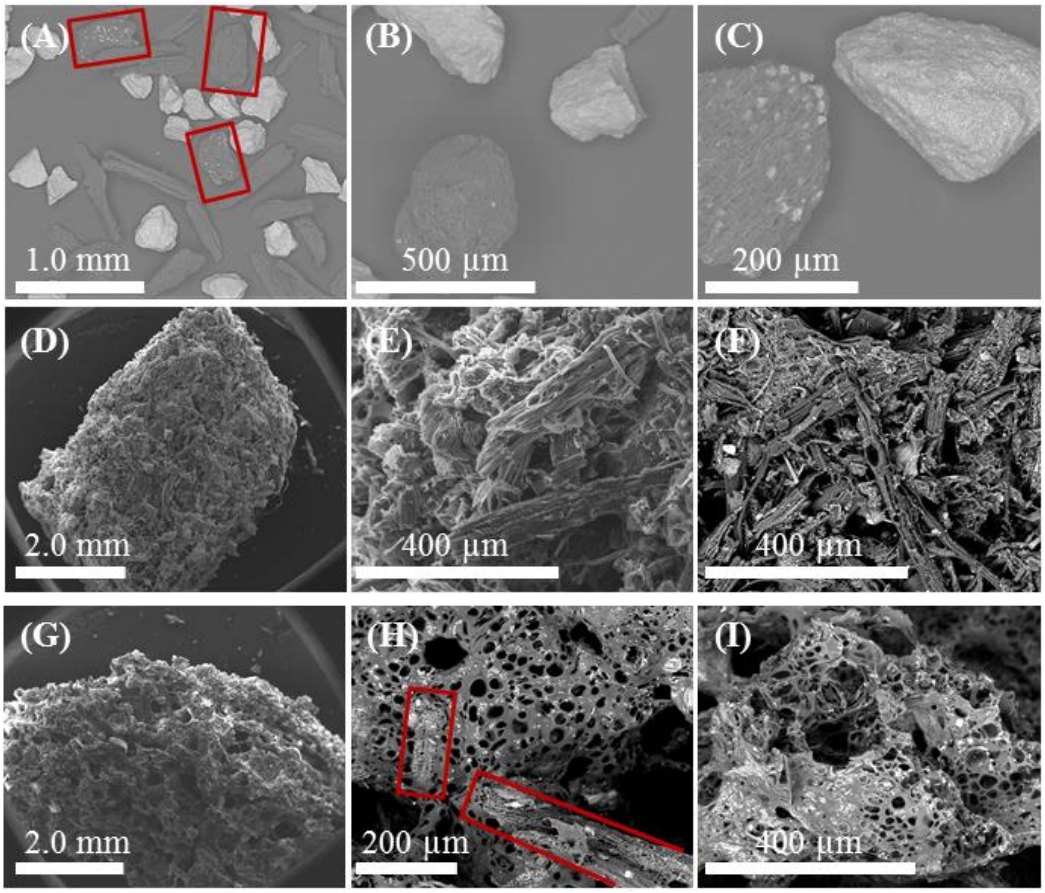

Figure 8.8 SEM images of solid particles from catalytic hydropyrolysis of beech wood in experiment 2 (A-C), and straw in experiment 4 (D-F) and experiment 5 (G-I). Fluid bed temperature: 451-454°C, pressure: 26 bar, biomass feeding rate: 275-400 g/h, H_2 flow: 82-102 NL/min, N_2 flow: 5 NL/min, and H_2S conc: 460 ppm.

The melting of the biomass was more pronounced when using straw instead of wood. Figure 8.8(D)-(F) show a large agglomerate from experiment 4, where most of the char particles (primary char) has maintained the structure from the straw, but has been stuck together by a solidified tar or metaplast (secondary char). EDS measurements showed that the agglomerate consisted of 68-71 wt.% carbon, 16-19 wt.% oxygen, 5-8 wt.% potassium, 1-3 wt.% chlorine, 1-3 wt. % silicon, 1-2 wt. % calcium and traces of magnesium, aluminum, sulfur, and phosphorus were also detected (see supplementary information Figure G.6 and Table G.3). The agglomerate from experiment 5 (Figure 8.8(G)-(I)) was very different from the one shown in Figure 8.8(D)-(F), as it does not consist of fiber like particles, but rather one big porous particle. Figure 8.8(H) shows two primary char particles (marked with red color) that has maintained the structure from the straw, but has been incorporated into the larger agglomerate. The agglomerate in Figure 8.8(G)-(I) was also studied with EDS (see supplementary information Figure G.7 and Table G.4), which showed that its composition is similar to the composition of the agglomerate in Figure 8.8(D)-(F), indicating that the biomass has formed a melt during the pyrolysis, which solidified into the larger agglomerate mainly consisting of secondary char.

This would also explain the formation of the agglomerate shown in Figure 8.6 and the carbon grid located on the catalyst particle in Figure 8.7. Furthermore, a catalyst particle with a partly melted char particle attached has been observed (see supplementary information Figure G.8). Partly hollow char particles, which have maintained the straw structure on the surface, have also been observed (see supplementary information Figure G.9), indicating that the core of the biomass particle has melted and leaving the outer original framework. These results clearly indicate that the biomass particles can form a melt at the applied conditions, which can lead to agglomeration if solidified around the primary char and catalyst particles. Furthermore, it should be noted, that the formed agglomerates are different from the agglomerates formed during combustion or gasification of alkaline rich fuel, where the agglomerates are formed due to alkaline melts [45–48] as opposed to the agglomerates in this study, which mainly are due to organic melts.

Agglomerates from experiment 4 using straw were also studied with SEM, see Figure 8.9. The structure of these agglomerates where similar to the agglomerate shown in Figure 8.8(I)-(G), indicating that agglomerates mainly consisting of secondary char were formed in both experiments with straw. In one of these agglomerates a primary char particle was observed (see Figure 8.9(B) and (C)) and several bright crystals were observed on the surface of the primary char particle. The composition of these crystals was investigated with EDS (see Figure 8.9(C) and detailed composition in supplementary information Table G.5), which showed that these crystals are silicates since they consisted of oxygen and silicon with an O/Si ratio between 2.4 and 3.4. In the secondary char small bright spot were observed (see Figure 8.9(D) and (E)) and EDS measurements indicated that these particles are KCl (detailed composition shown in supplementary information Table G.6). Additionally, an EDS element map of the secondary char showed that potassium was also well distributed in this phase (supplementary information Figure G.10). The observed potassium in the secondary char indicates that potassium acts a catalyst for the formation of secondary char, which is in agreement with observations from experiment 3 using the potassium promoted catalyst.

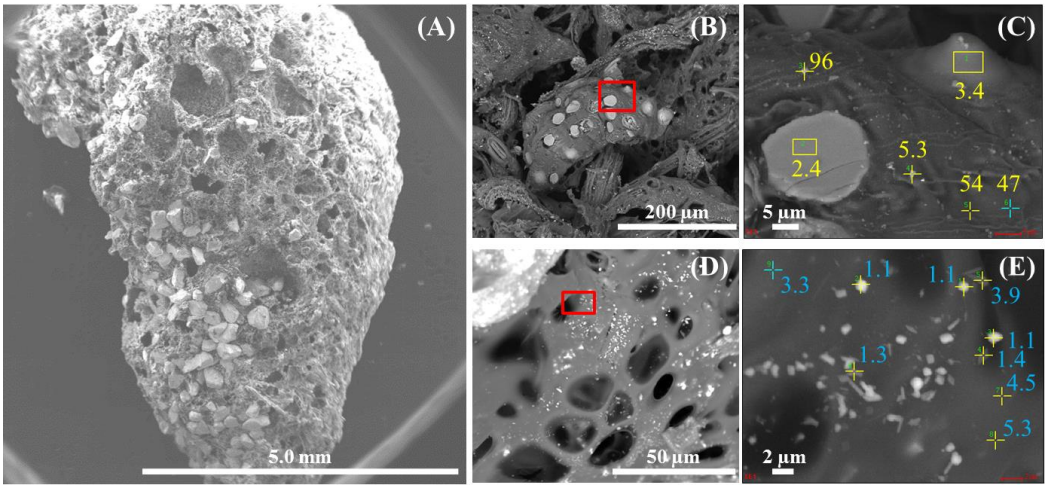

Figure 8.9 SEM image of a char agglomerate from experiment 4 using straw (A), SEM image of primary char found in the agglomerate (B,C), and SEM image of solidified metaplast (D-E). EDS measurements of the O/Si molar ratio at 6 different spots in (C) is highlighted with yellow and the K/Cl molar ratio at 9 different spots are highlighted with blue in figure (E). Fluid bed temperature: 453°C, pressure: 26 bar, straw feeding rate: 400 g/h, H_2 flow: 82 NL/min, N_2 flow: 5 NL/min, and H_2S conc: 460 ppm.

Dall'Ora et al.[49] studied pyrolysis of pine and beech wood at 1000 and 1300 °C and investigated the morphology of the produced char particles. They also observed a melting behavior of the biomass, the char produced from pine was porous spherical particles, while the morphology changes were less drastic for beech wood. Likewise Cetin et al. [50] studied the char morphology from pyrolysis of pine and eucalyptus sawdust, and bagasse both at high and low heating rates and at pressures between 1 and 20 bar. They also observed that at high heating rates the char showed signs of melting and at both high heating rate and high pressure the particles fused together to form hollow particles with a smooth surface. Furthermore, they observed smaller morphology changes for bagasse than for pine and eucalyptus, however, when both high heating rate and pressure was used it lost some of its structural integrity [50]. Trubetskaya et al.[51] also studied the morphology of char from pyrolysis of different types of biomass at temperatures between 350 and 1400 °C and heating rates between 10 and 3000 °C/s and found that the morphology changes appeared at 350 °C. Furthermore they found that at high heating rates bridge-breaking occurred before the cross-linking starts, and thus the biomass becomes a fluid (metaplast) [51]. However, with straw the char fluidity was reduced, which was ascribed to high levels of potassium and calcium, which acted as a catalyst for formation of char links [51]. This seems opposite of what was observed in this study. Nevertheless, the high heating rates obtained in the fluid bed reactor and the high pressure in this study is probably the reason for the observed deformation of the char particles.

8.3.2 Potassium and Chlorine transfer from KCl

Since it was observed that potassium was accumulated on the catalyst both when beech wood and straw was used as biomass, the transfer of potassium was further investigated. Fresh CoMo#1 catalyst was mixed with KCl and heated to 450 °C for between 48 and 375 h in a nitrogen atmosphere and the potassium and chlorine content on the catalyst was investigated with SEM-EDS. The potassium and chlorine concentration on the catalyst is shown as a function of time in Figure 8.10. The concentration of potassium is highest at 5 kV, indicating that the potassium transfer could be limited by internal diffusion limitations. Since the potassium uptake is known to be correlated with the number of acidic sites [36], the increase in the potassium between 96 and 375 h indicates that the acidic sites are not fully saturated at 96 h. Less chlorine compared to potassium is transferred to the catalyst, both on mass and molar basis, indicating that KCl reacts with the Brønsted acid site and produces HCl while potassium occupies the site, through the following reaction [36]:

$$-\mathrm{M}-\mathrm{OH}+\mathrm{KCl}\rightarrow-\mathrm{M}-\mathrm{OK}+\mathrm{HCl} \tag{8.1}$$

Furthermore, the chlorine concentration does not increase after 48 h, indicating that the catalyst is rapidly saturated with chlorine. It should be noted that the diffusion could also be dependent on the type potassium compound used, thus a different potassium concentration on the catalyst would possibly have been observed if K_2CO_3 or KOH had been used. Nevertheless, these results indicate that potassium and chlorine can be transferred from the biomass to the catalyst by diffusion.

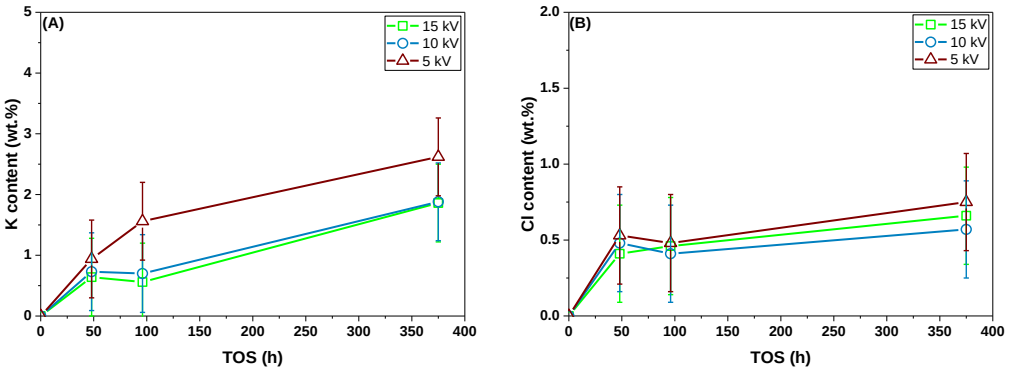

Figure 8.10 Potassium (A) and chlorine (B) concentration on CoMo#1 after KCl transfer experiments measured with SEM-EDS. Conditions: 450 °C, 1 atm, N_2 flow: 1 NL/min, catalyst to KCl ratio: 1:10 (g/g). (Concentration at 0 hours is the concentration on the fresh catalyst before mixing with KCl)

8.4 Conclusions

Spent CoMoS/$MgAl_2O_4$ catalysts from a bench scale catalytic hydropyrolysis setup, where beech wood was used as feedstock, have been characterized with HAADF-STEM, SEM-EDS, and ICP-OES. This showed that both calcium and potassium are transferred from the biomass to the catalyst and that the concentration of these alkali metals increases proportionally with time on stream. After 16.2 h and 5.18 kg biomass (beech wood) to 50 g of catalyst the concentration of calcium was 0.28 wt.% and the concentration of potassium was 0.67 wt.%, corresponding to 115 % saturation of the acidic sites on the oxide precursor. It should be noted that the number of acid sites on the sulfided catalyst is most likely higher than on the oxide precursor. Calcium was found as single particles on the spent catalysts, while potassium was well-distributed, which could potentially decrease the catalytic activity. Mixing KCl and a fresh CoMo catalyst and heating it in N_2 to 450 °C for 48-375 h and analyzing the resulting catalyst with SEM-EDS showed that potassium is transferred to catalyst by diffusion. The carbon content on the spent catalyst from the catalytic hydropyrolysis setup was 3.7 wt.% after 3.5 h which increased to 7.2 wt.% after 16.2 h, indicating that the coking rate decreases over time. Interestingly, SEM-EDS indicated that the coke content on the catalyst surfaces was 27 wt.% after 16.2 h, hence the coking is faster at the surface compared to the bulk of the particle. This can potentially lead to pore blocking.

In order to investigate the effect of potassium on the catalyst, a CoMo catalyst was prior to the sulfidation impregnated with K_2CO_3 corresponding to 1.9 wt.% potassium and compared to a similar CoMo catalyst without potassium. Interestingly, impregnation with potassium also altered the sulfidation by increasing the degree of stacking of the MoS_2 slabs and increasing the slab lengths. This has most likely decreased the number of Mo-O-Al bonds, thus increased the formation of the more active type II sites. SEM images of the spent potassium impregnated catalyst showed that some of the catalyst particles were covered with coke, but indicated that the coke also was removed as flakes in the fluid bed by attrition. Since this was not observed previously using fresh catalysts, which indicates that potassium can act as a catalyst for polymerization reactions.

The effect of using straw, which has a potassium content of 1.4 wt.%, instead of beech wood, which has a potassium content of 1.2 wt.%, was also studied. However, using straw led to defluidization within 0.29 h. Investigations of the catalyst and char from the fluid bed showed that severe agglomeration had taken place,

thus the particle size had increased from 180-355 µm to approximately 0.5 cm. SEM images showed that two types of agglomerates were found: primary char particles with intact cell structure that had formed an agglomerate due to an adhesive that bind them together and organic agglomerates where the cell structure was missing. It was also observed that the second type of agglomerate had captured the catalyst particles and primary char particles. The formation of these agglomerates was ascribed to repolymerization in the metaplast and tar. Potassium was well distributed in the agglomerates, again indicating that potassium catalyzes polymerization reactions.

Overall, the results indicate that alkali metal containing feedstocks may be challenging to use in catalytic hydropyrolysis, where catalysts and feed are mixed at elevated temperature. Further experiments at extended run-time is needed to clarify this.

Acknowledgments

This work is part of the H2CAP project (Hydrogen assisted catalytic pyrolysis for green fuels) conducted at The Department of Chemical and Biochemical Engineering at DTU, Denmark. The work was supported by The Danish Council for Strategic Research (now Innovation Fund Denmark, project 1305-00015B), The Programme Commission on Sustainable Energy and Environment. Funding from DTU is also gratefully acknowledged. The authors also acknowledge Aino Nielsen (Haldor Topsøe A/S) for technical assistant with the Raman spectroscopy and the Inorganic Analysis Department at Haldor Topsøe A/S for technical assistance with the elemental analysis of the spent catalysts by inductive coupled plasma optical emission spectroscopy (IPC-OES).

References

[1] Independent Statistics & Analysis - U.S. Energy Information Administration, International energy outlook 2016 - DOE/EIA-0484, 2016. https://www.eia.gov/outlooks/ieo/pdf/0484(2016).pdf (accessed July 7, 2017).

[2] IPCC - Intergovernmental Panel on Climate Change, Global Warming of 1.5°C an IPCC special report on the impacts of global warming of 1.5 °C above pre-industrial levels and related global greenhouse gas emission pathways, in the context of strengthening the global response to the threat of climate change, (2018). http://www.ipcc.ch/report/sr15/.

[3] A.V. Bridgwater, Review of fast pyrolysis of biomass and product upgrading, Biomass and Bioenergy. 38 (2012) 68–94. doi:10.1016/j.biombioe.2011.01.048.

[4] R.H. Venderbosch, W. Prins, Fast pyrolysis technology development, Biofuels, Bioprod. Biorefining. 4 (2010) 178–208. doi:10.1002/bbb.205.

[5] T.N. Trinh, P.A. Jensen, K. Dam-Johansen, N.O. Knudsen, H.R. Sørensen, S. Hvilsted, Comparison of lignin, macroalgae, wood, and straw fast pyrolysis, Energy & Fuels. 27 (2013) 1399–1409. doi:10.1021/ef301927y.

[6] P.M. Mortensen, J.-D. Grunwaldt, P.A. Jensen, K.G. Knudsen, A.D. Jensen, A review of catalytic upgrading of bio-oil to engine fuels, Appl. Catal. A Gen. 407 (2011) 1–19. doi:10.1016/j.apcata.2011.08.046.

[7] T.M.H. Dabros, M.Z. Stummann, M. Høj, P.A. Jensen, J.-D. Grunwaldt, J. Gabrielsen, P.M. Mortensen, A.D. Jensen, Transportation fuels from biomass fast pyrolysis, catalytic hydrodeoxygenation, and catalytic fast hydropyrolysis, Prog. Energy Combust. Sci. 68 (2018) 268–309. doi:10.1016/j.pecs.2018.05.002.

[8] T.L. Marker, L.G. Felix, M.B. Linck, M.J. Roberts, Integrated hydropyrolysis and hydroconversion (IH^2) for the direct production of gasoline and diesel fuels or blending components from biomass, Part 1: Proof of principle testing, Environ. Prog. Sustain. Energy. 31 (2012) 191–199. doi:10.1002/ep.10629.

[9] T.L. Marker, L.G. Felix, M.B. Linck, M.J. Roberts, P. Ortiz-Toral, J. Wangerow, Integrated

hydropyrolysis and hydroconversion ($IH^{2®}$) for the direct production of gasoline and diesel fuels or blending components from biomass, Part 2: Continuous testing, Environ. Prog. Sustain. Energy. 33 (2014) 762–768. doi:10.1002/ep.11906.

[10] L. Zhang, K. Gong, J. Lai, P. Alvey, Chemical composition and stability of renewable hydrocarbon products generated from a hydropyrolysis vapor upgrading process, Green Chem. 19 (2017) 3628–3641. doi:10.1039/c7gc01075c.

[11] V.K. Venkatakrishnan, J.C. Degenstein, A.D. Smeltz, W.N. Delgass, R. Agrawal, F.H. Ribeiro, High-pressure fast-pyrolysis, fast-hydropyrolysis and catalytic hydrodeoxygenation of cellulose: Production of liquid fuel from biomass, Green Chem. 16 (2014) 792–802. doi:10.1039/c3gc41558a.

[12] V.K. Venkatakrishnan, W.N. Delgass, F.H. Ribeiro, R. Agrawal, Oxygen removal from intact biomass to produce liquid fuel range hydrocarbons via fast-hydropyrolysis and vapor-phase catalytic hydrodeoxygenation, Green Chem. 17 (2015) 178–183. doi:10.1039/c4gc01746c.

[13] D.C. Dayton, J. Carpenter, J. Farmer, B. Turk, R. Gupta, Biomass hydropyrolysis in a pressurized fluidized bed reactor, Energy & Fuels. 27 (2013) 3778–3785. doi:10.1021/ef400355t.

[14] D.C. Dayton, J. Hlebak, J.R. Carpenter, K. Wang, O.D. Mante, J.E. Peters, Biomass hydropyrolysis in a fluidized bed reactor, Energy & Fuels. 30 (2016) 4879–4887. doi:10.1021/acs.energyfuels.6b00373.

[15] K. Wang, D.C. Dayton, J.E. Peters, O.D. Mante, Reactive catalytic fast pyrolysis of biomass to produce high-quality bio-crude, Green Chem. 19 (2017) 3243–3251. doi:10.1039/C7GC01088E.

[16] S. Meesuk, J.-P. Cao, K. Sato, Y. Ogawa, T. Takarada, The effects of temperature on product yields and composition of bio-oils in hydropyrolysis of rice husk using nickel-loaded brown coal char catalyst, J. Anal. Appl. Pyrolysis. 94 (2012) 238–245. doi:10.1016/j.jaap.2011.12.011.

[17] S. Meesuk, J.-P. Cao, K. Sato, Y. Ogawa, T. Takarada, Study of catalytic hydropyrolysis of rice husk under nickel-loaded brown coal char, Energy & Fuels. 25 (2011) 5438–5443. doi:10.1021/ef201266b.

[18] S. Meesuk, J.-P. Cao, K. Sato, Y. Ogawa, T. Takarada, Fast pyrolysis of rice husk in a fluidized bed: Effects of the gas atmosphere and catalyst on bio-oil with a relatively low content of oxygen, Energy & Fuels. 25 (2011) 4113–4121. doi:10.1021/ef200867q.

[19] S. Thangalazhy-Gopakumar, S. Adhikari, R.B. Gupta, M. Tu, S. Taylor, Production of hydrocarbon fuels from biomass using catalytic pyrolysis under helium and hydrogen environments., Bioresour. Technol. 102 (2011) 6742–9. doi:10.1016/j.biortech.2011.03.104.

[20] S. Thangalazhy-Gopakumar, S. Adhikari, R.B. Gupta, Catalytic pyrolysis of biomass over H^{+}ZSM-5 under hydrogen pressure, Energy & Fuels. 26 (2012) 5300–5306. doi:10.1021/ef3008213.

[21] O. Jan, R. Marchand, L.C.A. Anjos, G.V.S. Seufitelli, E. Nikolla, F.L.P. Resende, Hydropyrolysis of lignin using Pd/HZSM-5, Energy & Fuels. 29 (2015) 1793–1800. doi:10.1021/ef502779s.

[22] F. Melligan, M.H.B. Hayes, W. Kwapinski, J.J. Leahy, Hydro-pyrolysis of biomass and online catalytic vapor upgrading with Ni-ZSM-5 and Ni-MCM-41, Energy & Fuels. 26 (2012) 6080–6090. doi:10.1021/ef301244h.

[23] P. Choudhary, A. Malik, K.K. Pant, Mass-Scale Algal Biomass Production Using Algal Biofilm Reactor and Conversion to Energy and Chemical Precursors by Hydropyrolysis, ACS Sustain. Chem. Eng. 5 (2017) 4234–4242. doi:10.1021/acssuschemeng.7b00233.

[24] R.. Pindoria, A. Megaritis, A.. Herod, R. Kandiyoti, A two-stage fixed-bed reactor for direct hydrotreatment of volatiles from the hydropyrolysis of biomass: effect of catalyst temperature, pressure and catalyst ageing time on product characteristics, Fuel. 77 (1998) 1715–1726. doi:10.1016/S0016-2361(98)00079-9.

[25] J. Dilcio Rocha, C. a. Luengo, C.E. Snape, The scope for generating bio-oils with relatively low oxygen contents via hydropyrolysis, Org. Geochem. 30 (1999) 1527–1534. doi:10.1016/S0146-6380(99)00124-2.

[26] M.Z. Stummann, M. Høj, C.B. Schandel, A.B. Hansen, P. Wiwel, J. Gabrielsen, P.A. Jensen, A.D. Jensen, Hydrogen assisted catalytic biomass pyrolysis. Effect of temperature and pressure, Biomass and Bioenergy. 115 (2018) 97–107. doi:10.1016/j.biombioe.2018.04.012.

[27] P.M. Mortensen, D. Gardini, C.D. Damsgaard, J.-D. Grunwaldt, P.A. Jensen, J.B. Wagner, A.D. Jensen, Deactivation of Ni-MoS_2 by bio-oil impurities during hydrodeoxygenation of phenol and octanol, Appl. Catal. A Gen. 523 (2016) 159–170. doi:10.1016/j.apcata.2016.06.002.

[28] T.A. Milne, A.H. Brenan, B.H. Glenn, Sourcebook of Methods of Analysis for Biomass and Biomass

Conversion Processes, Elsevier Applied Science, New York, 1990.
[29] A.D. Stummann, M.Z.; Høj, M.; Schandel, C.B.; Hansen, A.B.; Wiwel, P.; Gabrielsen, J.; Jensen, P.A.; Jensen, Hydrogen assisted catalytic biomass pyrolysis. Effect of temperature and pressure, Biomass and Bioenergy. 115 (2018) 97–107. doi:10.1016/j.biombioe.2018.04.012.
[30] L.P. Hansen, E. Johnson, M. Brorson, S. Helveg, Growth mechanism for single- and multi-layer MoS2 nanocrystals, J. Phys. Chem. C. 118 (2014) 22768–22773. doi:10.1021/jp5069279.
[31] Y. Fan, J. Lu, G. Shi, H. Liu, X. Bao, Effect of synergism between potassium and phosphorus on selective hydrodesulfurization performance of Co-Mo/Al2O3FCC gasoline hydro-upgrading catalyst, Catal. Today. 125 (2007) 220–228. doi:10.1016/j.cattod.2007.02.022.
[32] H. Topsøe, The role of Co-Mo-S type structures in hydrotreating catalysts, Appl. Catal. A Gen. 322 (2007) 3–8. doi:10.1016/j.apcata.2007.01.002.
[33] A.K. Tuxen, H.G. Füchtbauer, B. Temel, B. Hinnemann, H. Topsøe, K.G. Knudsen, F. Besenbacher, J. V. Lauritsen, Atomic-scale insight into adsorption of sterically hindered dibenzothiophenes on MoS_2 and Co-Mo-S hydrotreating catalysts, J. Catal. 295 (2012) 146–154. doi:10.1016/j.jcat.2012.08.004.
[34] H. Topsøe, B.S. Clausen, F.E. Massoth, Catalysis - Science and Technology. Hydrotreating catalysis, Volume 11, Springer-Verlag, Berlin Heidelberg, Germany, 1996.
[35] A. Fonseca, P. Zeuthen, J.B. Nagy, ^{13}C n.m.r. quantitative analysis of catalyst carbon deposits, Fuel. 75 (1996) 1363–1376.
[36] B.K. Olsen, F. Kügler, F. Castellino, A.D. Jensen, Poisoning of vanadia based SCR catalysts by potassium: Influence of catalyst composition and potassium mobility, Catal. Sci. Technol. 6 (2016) 2249–2260. doi:10.1039/c5cy01409c.
[37] E. Furimsky, F.E. Massoth, Deactivation of hydroprocessing catalysts, Catal. Today. 52 (1999) 381–495. doi:10.1016/S0920-5861(99)00096-6.
[38] T.H. Fleisch, B.L. Meyers, J.B. Hall, G.L. Ott, Multitechnique analysis of a deactivated resid demetallation catalyst, J. Catal. 86 (1984) 147–157. doi:10.1016/0021-9517(84)90356-7.
[39] S.M. Richardson, H. Nagaishi, M.R. Gray, Initial Coke Deposition on a NiMo/γ-Al_2O_3 Bitumen Hydroprocessing Catalyst, Ind. Eng. Chem. Res. 35 (1996) 3940–3950. doi:10.1021/ie950761o.
[40] J. van Doorn, J.A. Moulijn, A model of coke on hydrotreating catalysts under reaction conditions, Fuel Process. Technol. 35 (1993) 275–287. doi:10.1016/0378-3820(93)90103-B.
[41] B. Guichard, M. Roy-Auberger, E. Devers, B. Rebours, A.A. Quoineaud, M. Digne, Characterization of aged hydrotreating catalysts. Part I: Coke depositions, study on the chemical nature and environment, Appl. Catal. A Gen. 367 (2009) 1–8. doi:10.1016/j.apcata.2009.07.024.
[42] A. Jensen, K. Dam-Johansen, M. a. Wójtowicz, M. a. Serio, TG-FTIR Study of the Influence of Potassium Chloride on Wheat Straw Pyrolysis, Energy & Fuels. 12 (1998) 929–938. doi:10.1021/ef980008i.
[43] R. Solomon P, G. Hamblen D, A. Serio m, z Yu, S. Charpenay, A characterization method and model for predicting coal conversion behaviour, Fuel. 72 (1993) 469–488. doi:DOI: 10.1016/0016-2361(93)90106-C.
[44] P.M. Mortensen, D. Gardini, H.W.P. de Carvalho, C.D. Damsgaard, J.-D. Grunwaldt, P.A. Jensen, J.B. Wagner, A.D. Jensen, Stability and resistance of nickel catalysts for hydrodeoxygenation: Carbon deposition and effects of sulfur, potassium, and chlorine in the feed, Catal. Sci. Technol. 4 (2014) 3672–3686. doi:10.1039/c4cy00522h.
[45] C.-L. Lin, M.-Y. Wey, C.-Y. Lu, Prediction of defluidization time of alkali composition at various operating conditions during incineration, Powder Technol. 161 (2006) 150–157. doi:10.1016/j.powtec.2005.10.010.
[46] V. Narayan, P.A. Jensen, U.B. Henriksen, P. Glarborg, W. Lin, R.G. Nielsen, Defluidization in fluidized bed gasifiers using high-alkali content fuels, Biomass and Bioenergy. 91 (2016) 160–174. doi:10.1016/j.biombioe.2016.05.009.
[47] J.D. Morris, S.S. Daood, S. Chilton, W. Nimmo, Mechanisms and mitigation of agglomeration during fluidized bed combustion of biomass: A review, Fuel. 230 (2018) 452–473. doi:10.1016/j.fuel.2018.04.098.
[48] P. Chaivatamaset, P. Sricharoon, S. Tia, B. Bilitewski, The characteristics of bed

agglomeration/defluidization in fluidized bed firing palm fruit bunch and rice straw, Appl. Therm. Eng. 70 (2014) 737–747. doi:10.1016/j.applthermaleng.2014.05.061.

[49] M. Dall'Ora, P.A. Jensen, A.D. Jensen, Suspension combustion of wood: Influence of pyrolysis conditions on char yield, morphology, and reactivity, Energy and Fuels. 22 (2008) 2955–2962. doi:10.1021/ef800136b.

[50] E. Cetin, B. Moghtaderi, R. Gupta, T.F. Wall, Influence of pyrolysis conditions on the structure and gasification reactivity of biomass chars, Fuel. 83 (2004) 2139–2150. doi:10.1016/j.fuel.2004.05.008.

[51] A. Trubetskaya, P.A. Jensen, A.D. Jensen, M. Steibel, H. Spliethoff, P. Glarborg, Influence of fast pyrolysis conditions on yield and structural transformation of biomass chars, Fuel Process. Technol. 140 (2015) 205–214. doi:10.1016/j.fuproc.2015.08.034.

Chapter 9 Trends in catalytic hydropyrolysis of biomass

In this chapter the results obtained in this project are discussed and a mechanistic model for catalytic hydropyrolysis is proposed. Furthermore, fast pyrolysis, catalytic fast pyrolysis and catalytic hydropyrolysis are compared.

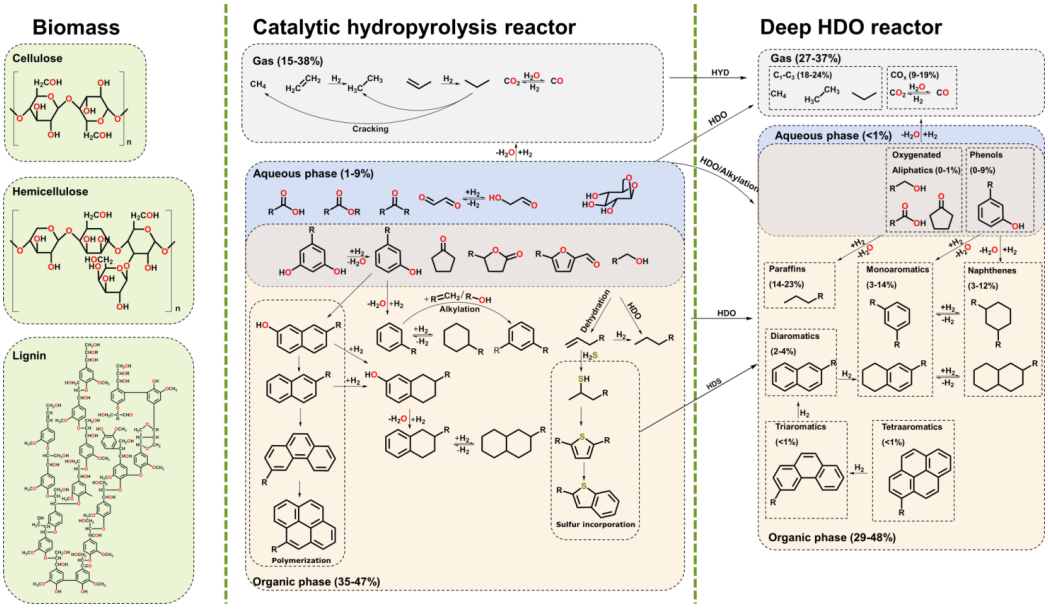

Abstract

Recent research has shown that catalytic hydropyrolysis of biomass is a promising method for production of liquid hydrocarbon fuels. However, only limited research has been conducted within this field and the process is still not well-understood. Based on the available literature and research in our laboratories we have been able to identify the most important reactions and propose a mechanistic model for catalytic hydropyrolysis. The correlation between the used catalyst and the product distribution, composition, and the deactivation of the catalyst is discussed and catalytic hydropyrolysis is compared with other pyrolysis technologies, such as non-catalytic and catalytic fast pyrolysis. Furthermore the challenges for catalytic hydropyrolysis is highlighted and different solutions are discussed and the necessary future steps for this process to be commercialized are addressed.

Abbreviations

BFB	Bubbling fluid bed
BI	Bog iron
BTX	Benzene, toluene, xylene
CFB	Circulating fluid bed
CFP	Catalytic fast pyrolysis
CHP	Catalytic hydropyrolysis
CR	Cyclone reactor
DDO	Direct deoxygenation
EFR	Entrained flow reactor
FB	Fluid bed
FCC	Fluid catalytic cracking
FP	Fast pyrolysis
GHG	Greenhouse gas
HDO	Hydrodeoxygenation
HDS	Hydrodesulfurization
HHV	Higher heating value
MgAl	$MgAl_2O_3$
OS	Olivine sand
PCR	Pyrolysis centrifuge reactor
RCFP	Reactive catalytic fast pyrolysis
Temp.	Temperature
ZA	H-ZSM-5 mixed with Al_2O_3

9.1 Introduction

Due to anthropogenic emissions of greenhouse gasses (GHG) global warming has become an increasing problem. Even the current target of a maximum temperature increase of 2°C can lead to a significant increase in the sea level [1,2], and thus we need to drastically decrease our GHG emission in the near future [3]. However, the global energy conversion continues to increase and will most likely continue to increase in the future due to modernization of non-OECD countries and increasing world population [4,5]. There is therefore an urgent needed to shift from fossil to renewable fuels. One of the advantages of converting biomass into liquid hydrocarbon fuels is that it contains carbon that was recently CO_2 in the atmosphere and can be used in our current transportation system. One technique for the production of biomass based fuels is fast pyrolysis, where the biomass is rapidly heated to approximately 500°C in an inert atmosphere, which produces char, light gasses, and so-called pyrolysis oil [6–8]. The pyrolysis oil typically has a water content of 15-30 wt.%, which cannot be removed through conventional distillation, since heating the pyrolysis oil lead to rapid polymerization forming coke [6,9,10]. Furthermore it has a high oxygen content, generally between 35-50 wt.% [6,9–11], resulting in a low higher heating value (HHV) between 16-21 MJ/kg, compared to 43 MJ/kg for diesel [8,10,12]. This also makes utilization of pyrolysis oil in internal combustion engines challenging [13–19]. Pyrolysis oil can be upgraded through hydrodeoxygenation, which takes place at elevated temperature (250-400°C) and pressure (100-300 bar) in the presence of a catalyst [8]. However, rapid catalyst deactivation and even reactor plugging due to coke formation is a common problem [8]. An alternative to fast pyrolysis is fast catalytic pyrolysis, where an acidic catalyst is present during the fast pyrolysis, which decreases the oxygen content in the produced organic phase. However, it also increases the formation of light gasses and solid carbon [20–22], resulting in a low yield of liquid fuel, which even typically still contains significant levels of oxygen.

Catalytic hydropyrolysis of biomass, where the pyrolysis takes place in a hydrogen atmosphere with a hydrotreating catalyst, have gained an increasing interest over the last decade. The concept for this process share some similarities with the Bergius process [23–25], but in the Bergius process coal and heavy oil are mixed into a slurry, while catalytic hydropyrolysis is carried out in the gas phase. Several studies from the 1970s and 1980s investigated catalytic and non-catalytic hydropyrolysis of coal with the objective to produce benzene, toluene, and xylene (BTX) and synthetics natural gas (SNG) [26–30]. The first hydropyrolysis study of biomass was also conducted in the 1980s by Steinberg et al. [31] at temperatures between 600 and 1000°C and mainly produced light gasses. First in the late 1990s began the research in catalytic hydropyrolysis of biomass for production of liquid fuels [32,33]. The interest for catalytic hydropyrolysis has significantly increased since Marker et al. [34,35] showed that it is possible to produce an oxygen free (<2.2 wt.%) oil with condensable organics (C_{4+} hydrocarbons) yields of 25-28 wt.% on dry ash free (daf) basis when using wood as feedstock with their process IH$^{2®}$. In this process the catalytic hydropyrolysis takes place at elevated pressures (up to 22.4 bar) and a hydrotreating reactor is placed after the catalytic hydropyrolysis reactor, thus ensuring that the produced organics are oxygen free hydrocarbons [34,35]. The positive results from this process have been partly confirmed by our group [36], where we with a similar experimental setup were able to obtain an oxygen free oil with condensable organic yields up to 25 wt.% daf (see Chapter 4). Furthermore, life cycle assessments of catalytic hydropyrolysis have shown that it is possible to reduce the GHG emission with 30-96 % compared to fossil fuels, where the lowest reduction is obtained with microalgae, while using corn stover and woody biomass generally gives a reduction between 70-90 % [37–39].

Nevertheless, despite that catalytic hydropyrolysis is a promising process for the production of renewable fuels, there is only a limited understanding of the reactions and mechanisms taking place in catalytic hydropyrolysis. This work provides a discussion of the chemical reactions and mechanisms in catalytic hydropy-

rolysis (Section 9.2), a discussion of the considerations when choosing a catalyst for the catalytic hydropyrolysis reactor (Section 9.3), and how it affects the deactivation of the downstream HDO reactor (Section 9.4). Furthermore fast pyrolysis, catalytic fast pyrolysis, and catalytic fast hydropyrolysis are compared in Section 9.5, and new possibilities for catalytic hydropyrolysis are discussed in Section 9.6. It should be noted that this work focuses on the results obtained in (semi) continuous bench scale and pilot plant reactors. Thus despite that several research groups have investigated catalytic hydropyrolysis in Pyroprobe reactors these results [32,40–45] are generally not taken into account in this work, due to their relatively poor comparability with results obtained from (semi) continuous reactors.

9.2 Reactions in catalytic hydropyrolysis

9.2.1 Chemical reactions in catalytic hydropyrolysis

Recent research has shown that catalytic hydropyrolysis of biomass consists of a complex network of catalytic reactions [46] (Chapter 3-8) and examples of the most important reactions are shown in Table 9.1. Both cracking and hydrocracking reactions occurs in catalytic hydropyrolysis, and these reactions are favorable to the extent where they decrease the molecular size to that of diesel or gasoline, but cracking and hydrocracking also leads to an increased yield of light gasses, which decreases the carbon recovery in the condensed organic phase. As shown in Figure 9.1(A) cracking reactions are equilibrium favorable at high temperatures (>500°C), while hydrocracking are equilibrium favorable (>90% conversion) in the temperature interval 200-600°C, where catalytic hydropyrolysis is performed. Decarbonylation and decarboxylation reactions decrease the oxygen content in the condensed organics, which stabilize the reactive oxygenates before they can participate in polymerization reactions and both reactions are equilibrium favorable (100% conversion at equilibrium see supplementary information Figure H.1). However, the concentration of CO and CO_2 is also affected by water gas shift (WGS), and catalysts used for catalytic hydropyrolysis might also catalyze this reaction, thus it can therefore be difficult experimentally to distinguish between decarbonylation and decarboxylation reactions. The concentration of CO and CO_2 is therefore also depending on the hydrogen pressure (Chapter 3), as indicated in Figure 9.1(A).

Hydrodeoxygenation (HDO) is one of the most important reactions in catalytic hydropyrolysis, where the oxygen in the organics reacts with hydrogen and form water. HDO can alternatively take place through first a dehydration step followed by hydrogenation (HYD) [47]. The important difference between HDO and decarbonylation/decarboxylation is that in HDO oxygen is removed without the loss of carbon, thus leading to a higher carbon yield in the liquid. HDO of phenols can take place either through the direct deoxygenation (DDO) pathway or the hydrogenation pathway (HYD), where the aromatic ring is saturated prior to the deoxygenation [48–52] (see Table 9.1 R.7 and R.8). The choice of path depends on the type of catalyst. As shown in Figure 9.1(B) not all HDO reactions are equilibrium favorable. HDO of methanol and HDO of phenol to benzene are favorable at temperatures between 200 and 600°C, while HDO of phenol to cyclohexane becomes thermodynamically less favorable as the temperature is increased and it is necessary to increase the hydrogen concentration in order for the reaction to take place at high temperatures.

Since hydrotreating catalysts are often used in catalytic hydropyrolysis, hydrogenation (HYD) of olefins and aromatics also takes place [36]. Hydrogenation of olefins are generally favored by equilibrium and 90 % conversion can theoretically be obtained at temperatures up to 600°C (see Figure 9.1 (C)) in a reaction with stoichiometric amounts of H_2 and butene. Decreasing the temperature increases the equilibrium conversion, thus having excess hydrogen and a HDO reactor at lower temperature after the catalytic hydropyrolysis reactor leads to full conversion of the olefins [36]. HYD of benzenes are favored at low temperatures, thus it is

necessary to have a high hydrogen pressure at elevated temperatures in order to convert them into naphthenes. This is also the reason for the high aromatic yield when conducting catalytic hydropyrolysis both with and without a HDO reactor [36]. It should be noted that complete saturation of particularly aromatics is difficult even in industrial refineries [53]. Alkylation reactions, which are acid catalyzed, can also take place in catalytic hydropyrolysis and can increase the carbon recovery in the condensed organic phase by incorporation of short hydrocarbons into aromatics [54]. Alkylation with alcohols can go through a dehydration step followed by alkylation with the olefin [54]. Alkylation is also favored by equilibrium at the temperatures used in catalytic hydropyrolysis (see supplementary information Figure H.1).

If H_2S is present during the catalytic hydropyrolysis, sulfur can be incorporated into the organic phase by recombination between H_2S and an olefin to a thiol, which can further react with a carbenium ion to form thiophene [55]. The sulfur incorporation reactions are also acid catalyzed [55], thus using a catalyst with a low acidity can decrease the sulfur content in the product. Recombination between 2-butene and H_2S becomes thermodynamically less favorable at high temperatures, as indicated in Figure 9.1(D), however the concentration of sulfur in diesel should be below 10 ppm S in many countries [56], and so HDS of the produced organic phase might be necessary.

Table 9.1 Catalytic reactions in catalytic hydropyrolysis

Cracking:	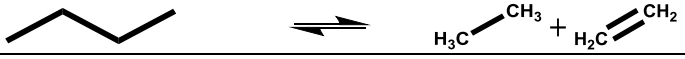	**R.1**
Hydrocracking:	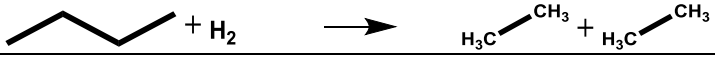	**R.2**
Decarbonylation:	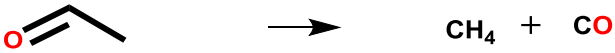	**R.3**
Decarboxylation:	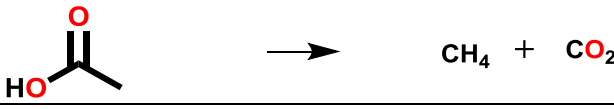	**R.4**
WGS:		**R.5**
HDO:	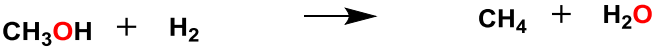	**R.6**
	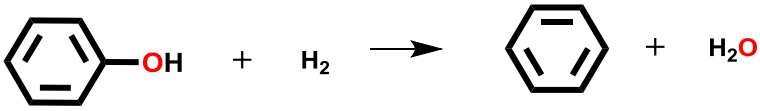	**R.7**
	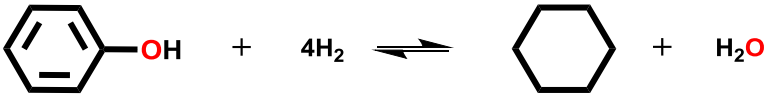	**R.8**
HYD:	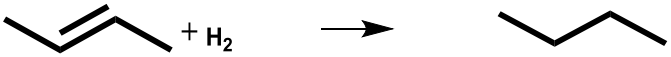	**R.9**
		**R.10**
Alkylation:	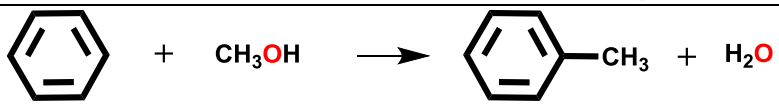	**R.11**
Recombination:	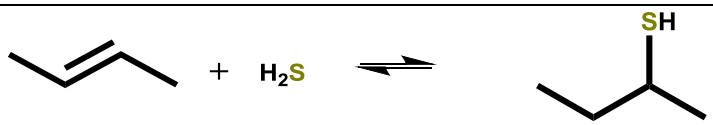	**R.12**
HDS:	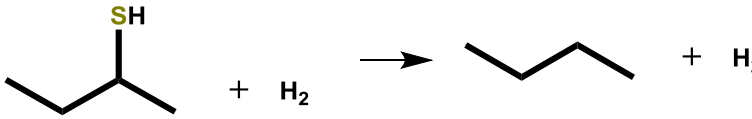	**R.13**
	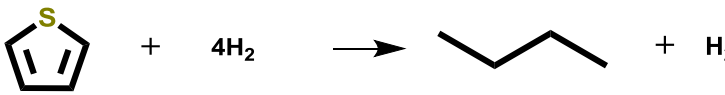	**R.14**

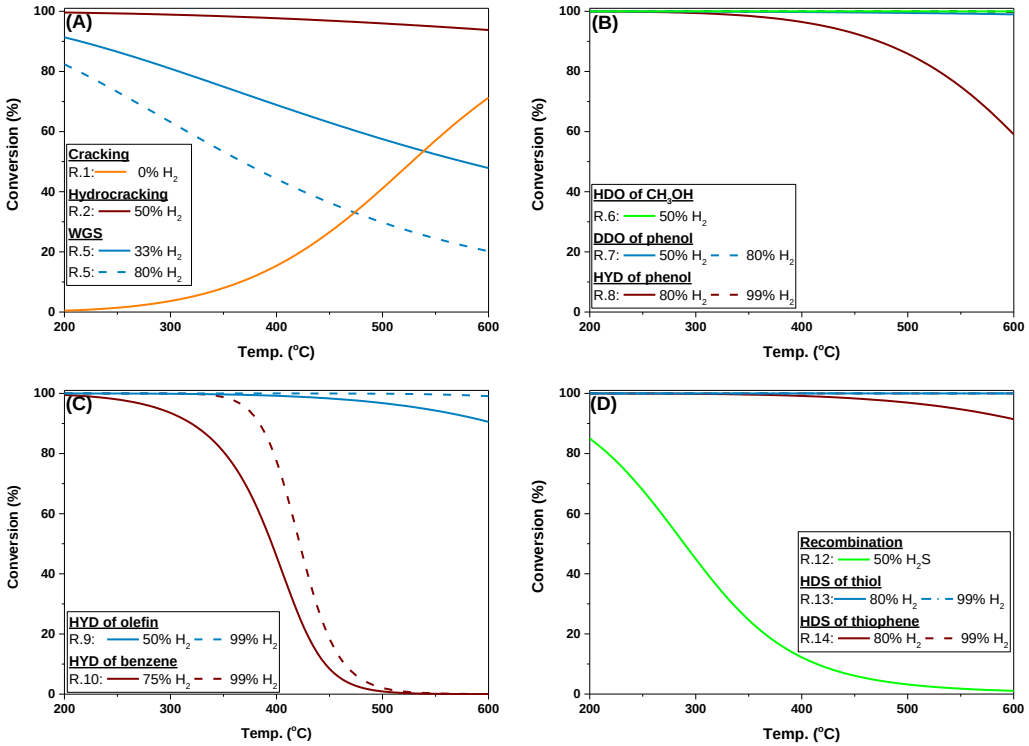

Figure 9.1 Conversions at equilibrium as a function of temperature at 26 bar for cracking, hydrocracking, and WGS (A), HDO (B), HYD (C), recombination and HDS (D). Calculated with the software package HSC Chemistry v.9.7.

9.2.2 A mechanistic model of catalytic hydropyrolysis

In conventional pyrolysis of biomass, the biomass is first decomposed into primary char, liquid metaplast, and light gasses [57], as shown in Figure 9.2(A). The metaplast can solidify and form secondary char on the primary char [58] or it can through cracking reactions form light gasses or evaporate as tar. The tar can also form secondary char by polymerization and light gasses through cracking [57]. The extent to which the different reactions occur depends on the biomass composition and particularly the ash content and its composition [59,60].

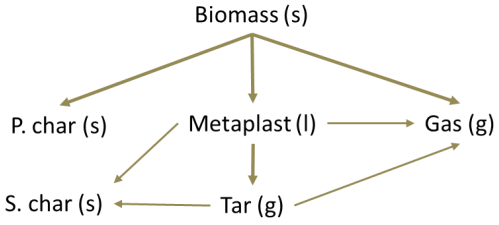

Figure 9.2 Reaction scheme for conventional pyrolysis of biomass. Char is divided into primary char (P. char) and secondary char (S. char). Solids are denoted "s", "liquid" is denoted "l", and gas is denoted "g".

In catalytic hydropyrolysis (Figure 9.3) the formed tar is deoxygenated by the catalyst to a more stable oil with a low oxygen content either through HDO, decarbonylation or decarboxylation reactions, but the catalyst can also increase the gas yield through cracking reactions [36,61] (Chapter 3-7). Deoxygenation of the tar leads to a decrease in the formation of secondary char [61], because less tar is available for polymerization reactions. Depending on the acidity of the catalyst alkylation reactions can also take place as previously discussed, which converts light hydrocarbons (olefins and alcohols) in the gas phase to tar with a low oxygen content. It should be noted that in the reaction scheme shown in Figure 9.3 it has been assumed that the catalyst only reacts with compounds in the gas phase. However, it is likely that some interaction between the metaplast and the catalyst takes place, which then generates tars with a low oxygen content and light gasses directly. Furthermore both the tar and metaplast can participate in polymerization reactions on the catalyst surface, forming coke.

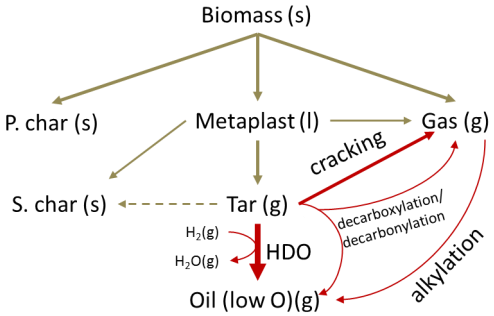

Figure 9.3 Reaction scheme for catalytic hydropyrolysis. The brown arrow shows, the conventional pyrolysis pathways, the red arrows shows the catalyzed pathways, the brown dash arrow indicates the pathway is minimized due to the catalyst. Char is divided into primary char (P. char) and secondary char (S. char). Solids are denoted "s", "liquid" is denoted "l", and gas is denoted "g".

Dayton et al. [61] and Meesuk et al. [62] observed a considerable decrease in the char yield during non-catalytic pyrolysis of biomass when they (partly) replaced the nitrogen atmosphere with hydrogen. This can not only be ascribed to stabilization of the vapors since Dayton et al. [61] only observed a decrease in the oxygen content of 1.2 wt.% when increasing the H_2 pressure from 0 to 0.48 bar (at 3.4 bar total pressure and 400 °C), while the char yield decreased from 40.5 to 17.5 wt.%. It is therefore plausible that conducting the pyrolysis in hydrogen increase the formation of metaplast, which for Dayton et al. [61] led to an increase in the liquid yield and for Meesuk et al. [62] lead to an increase in the gas yield. The differences in their observations are probably due to the very different temperatures (Dayton: 400°C, Meesuk: 650°C) and hydrogen partial pressure (Dayton: 0.48 bar, Meesuk: 1 bar). This hypothesis is supported by the coal pyrolysis and hydropyrolysis literature, where the hydropyrolysis takes place at approximately 100 bar hydrogen [29], from which it is known that hydropyrolysis leads to an increase the in devolatilization, eliminates oxygen, favors the production of lower molecular weight hydrocarbons [63,64], and stabilizes volatiles to form light hydrocarbons, which decreases secondary char-forming reactions [29,63]. The effect of the hydrogen is more evident with high oxygen concentrations in the coal [63] and thus a significant effect is expected also for biomass. Furthermore, the bridge breaking, which takes place during the formation of the metaplast is limited by the hydrogen availability, which in traditional coal pyrolysis is supplied by formation of new unbreakable bridges and the formed primary char consists of molecules bound by these unbreakable bridges [65]. In hydropyrolysis the hydrogen is available from the atmosphere, which increases the potential for met-

aplast formation and it thereby decreases the formation of primary char. Then depending on the applied temperatures the metaplast will either form gas, tar, or secondary char.

Overtime potassium and other alkali metals can be transported from the biomass to the catalyst (Chapter 5-6, and Chapter 8), which can decrease the catalytic activity [66,67] (Chapter 7), thus decreasing the formation of the catalyzed products, indicated by the red arrows in Figure 9.4. Interestingly, we found that doping a CoMoS catalyst with 1.9 wt.% potassium mainly decreased the hydrogenation and cracking activity, but only had a minor effect of the deoxygenation activity, partly due to an increased decarboxylation activity (Chapter 7). A decrease in the catalytic activity would most likely increase the formation of secondary char, because the catalyst will not be able to stabilize the reactive oxygenates or olefins before they can participate in polymerization reactions. Furthermore the potassium on the catalyst can act as a catalyst for char forming reactions [68] (Chapter 7 and 8) and react with the metaplast and tar, thus leading to an increased formation of secondary char on the catalyst instead of on the primary char (Chapter 8), as indicated by the black arrows in Figure 9.4.

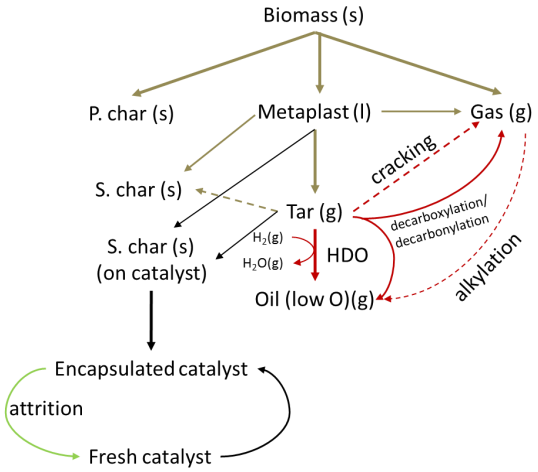

Figure 9.4 Reaction scheme for catalytic hydropyrolysis with a catalyst with high potassium content. The brown arrow shows the conventional pyrolysis pathways, the red arrows shows the catalyzed pathways, the brown dash arrow indicates the pathway minimized due to the catalyst, the red dashed arrow indicates the reactions, which are suppressed due to potassium poisoning, the black arrows shows the pathways catalyzed by the potassium, and the green arrow indicates the regeneration of the catalyst due to attrition. Char is divided into primary char (P. char) and secondary char (S. char). Solids are denoted "s", "liquid" is denoted "l", and gas is denoted "g".

We have observed that the formation of secondary char on the catalyst can lead to encapsulation of the catalyst (see Figure 9.5), which most likely decreases its activity (Chapter 8). However, the encapsulated catalyst particles were continuously regenerated in the fluid bed reactor by attrition (or knock-off), which removes the secondary char located at the surface of the particles (Chapter 8). It should be noted, that the relevance of this mechanism is dependent on catalyst loss by attrition. If the catalyst is crushed by attrition and transferred out of the fluid bed before the potassium content becomes high enough for this mechanism to take place, this mechanism is less relevant.

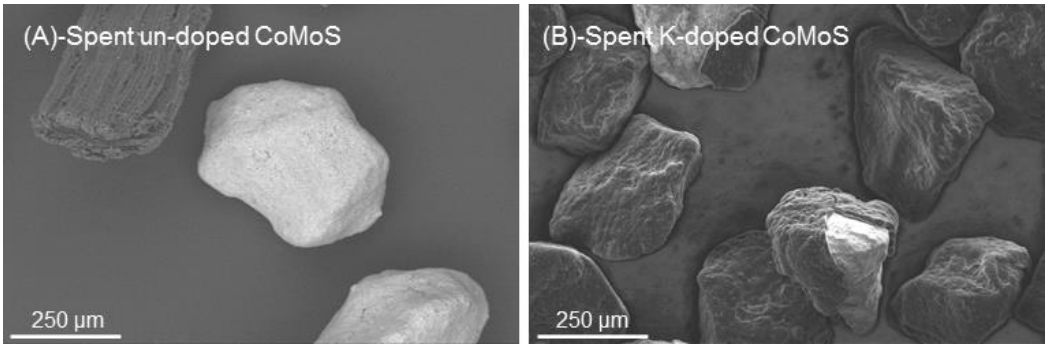

Figure 9.5 SEM image of an un-doped (A) and potassium (1.9 wt.%) doped (B) spent CoMoS catalyst. Test conditions: fluid bed temperature: 450-454°C, total pressure: 26 bar, biomass used: beech wood, biomass feeding rate: 268-280 g/h, feed time: 3.5 h, H_2 flow: 82 NL/min, N_2 flow: 5 NL/min, and H_2S conc: 460 ppm.

If the biomass, such as wheat straw, has a high concentration of potassium and/or other alkali metals, which can act as a secondary char formation catalyst (Chapter 7-8), the char formation is not limited to take place on solids, but can also take place in the metaplast itself (Chapter 8), as shown in the reaction scheme in Figure 9.6. This has been observed when straw was used as feed, which led to agglomeration, and SEM images of the agglomerates indicated that solidification in the metaplast had taken place, see Figure 9.7 (also discussed in Chapter 8). Interestingly, the larger agglomerates also contained primary char and catalyst particles, which had been incorporated (see Chapter 8). The agglomerates were fairly porous, thus diffusion of tars into and out of the catalyst might still be possible, but the catalyst activity will most likely decrease over time due to transfer of potassium from the biomass to the catalyst [69,70]. It is likely that some of the catalyst particles can be regenerated due to removal of char by attrition; however the agglomeration may over time lead to defluidization (Chapter 8). It is possible that secondary char formation in the metaplast is a larger problem in hydropyrolysis than in pyrolysis, since more metaplast is most likely formed in the former. This problem could possibly be overcome by washing the biomass [71] prior to feeding into the catalytic hydropyrolysis reactor, but this would increase the operating costs.

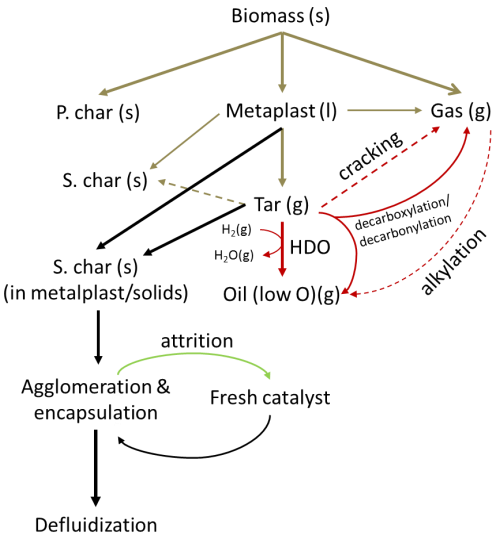

Figure 9.6 Reaction scheme for catalytic hydropyrolysis of biomass with a high potassium content. The brown arrow shows the conventional pyrolysis pathways, the red arrows shows the catalyzed pathways, the brown dash arrow indicates the pathway minimized due to the catalyst, the red dashed arrow indicates the reactions, which are suppressed due to potassium poisoning, the black arrows shows the pathways catalyzed by the potassium, and the green arrow indicates the regeneration of the catalyst due to attrition. Char is divided into primary char (P. char) and secondary char (S. char). Solids are denoted "s", "liquid" is denoted "l", and gas is denoted "g".

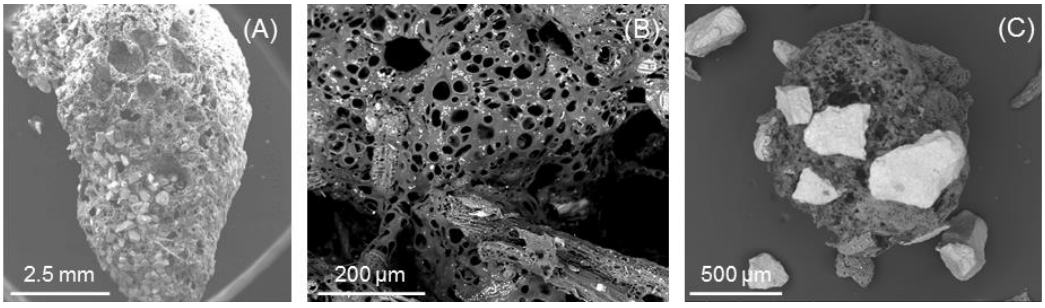

Figure 9.7 SEM image of a large agglomerate, which has captured several catalyst particles (A), a solidified metaplast, which has captured several primary char particles, and a smaller agglomerate consisting of solidified metaplast with several catalyst particles (C). Fluid bed temperature: 453°C, pressure: 26 bar, biomass feeding rate: 400 g/h, H_2 flow: 82-102 NL/min, N_2 flow: 5 NL/min, and H_2S conc: 447-460 ppm, biomass type: straw, catalyst: 50 g CoMoS.

9.2.3 Reaction scheme for catalytic hydropyrolysis and deep HDO catalytic hydropyrolysis vapors

Based on the discussed chemical reactions in section 9.2.1 and analysis of the organic phases from catalytic hydropyrolysis with and without a secondary HDO reactor (Chapter 2-7) a reaction scheme for the reactions taking place in catalytic hydropyrolysis and during deep HDO of catalytic hydropyrolysis vapors is proposed, see Figure 9.8. Lignocellulosic biomass mainly consists of cellulose, hemicellulose, and lignin, where the distribution varies depending on the type of biomass. Cellulose consist of linear polymers of β-(1→4)-D-glucopyranose and hemicellulose consists of different polymerized monosaccharides and the number of repeating units for hemicellulose is significantly smaller than for cellulose [72–77]. Lignin consists of branched phenolic polymers, see Figure 9.8 for a model of lignin from soft wood. Pyrolysis of cellulose, hemicellulose, and lignin leads to the formation of light gasses (H_2, CO_x, C_1-C_3), carbonyls and alcohols, while heterocyclic compounds such as furans and sugars are produced from cellulose and hemicellulose and phenols and aromatics mainly come from lignin [57].

In catalytic hydropyrolysis the short oxygenates can be deoxygenated either through hydrodeoxygenation, dehydration, or decarboxylation/decarbonylation (not indicated on Figure 9.8), and depending on the number of carbon atoms, the product will either end in the gas or organic phase. Dehydration of oxygenated aliphatics to olefins can lead to the formation of organosulfur compounds through recombination with H_2S (Chapter 5). Dihydroxybenzene and other phenols with two or more oxygen atoms are generally deoxygenated to phenols, which can be hydrodeoxygenated to benzene and further hydrogenated to naphthenes. Short oxygenated aliphatics can participate in C-C coupling reactions such as alkylation with aromatics, thus being moved from the aqueous phase to the organic phase and aromatics produced through catalytic hydropyrolysis are generally highly branched (see Figure 3.7 and Figure 7.11). The aromatics can also participate in polymerization and cyclization reactions and form di, tri, or larger aromatics, which can lead to coking of the catalyst. The carbon recovery in the different phases from catalytic hydropyrolysis is generally 15-38 % in the gas phase, 1-9 % in the aqueous phase, and 35-47 % in the organic phase, depending on the catalyst and operating conditions (Chapter 2-7). Upgrading the vapors from catalytic hydropyrolysis in a second HDO reactor generally decreases the carbon recovery in the aqueous phase to below 1 %, while the carbon recovery in gas is between 27-37 %, and the carbon recovery in the organic phase is 29-48 % [34](Chapter 2-4,7). In the HDO reactor the oxygenates are converted into paraffins, aromatics, and naphthenes, however, at low hydrogen partial pressures (3.0 bar) the carbon recovery for the phenols can be as high as 9 % (Chapter 3). The main component in the organic phase is paraffins (14-23 % carbon recovery – including C_{4+} in the gas), but significant amounts of monoaromatics (3-14 % carbon recovery) and naphthenes (3-12% carbon recovery) are also produced (Chapter 2-4,7), which indicates that the process also can be used for the production of chemicals such as BTX.

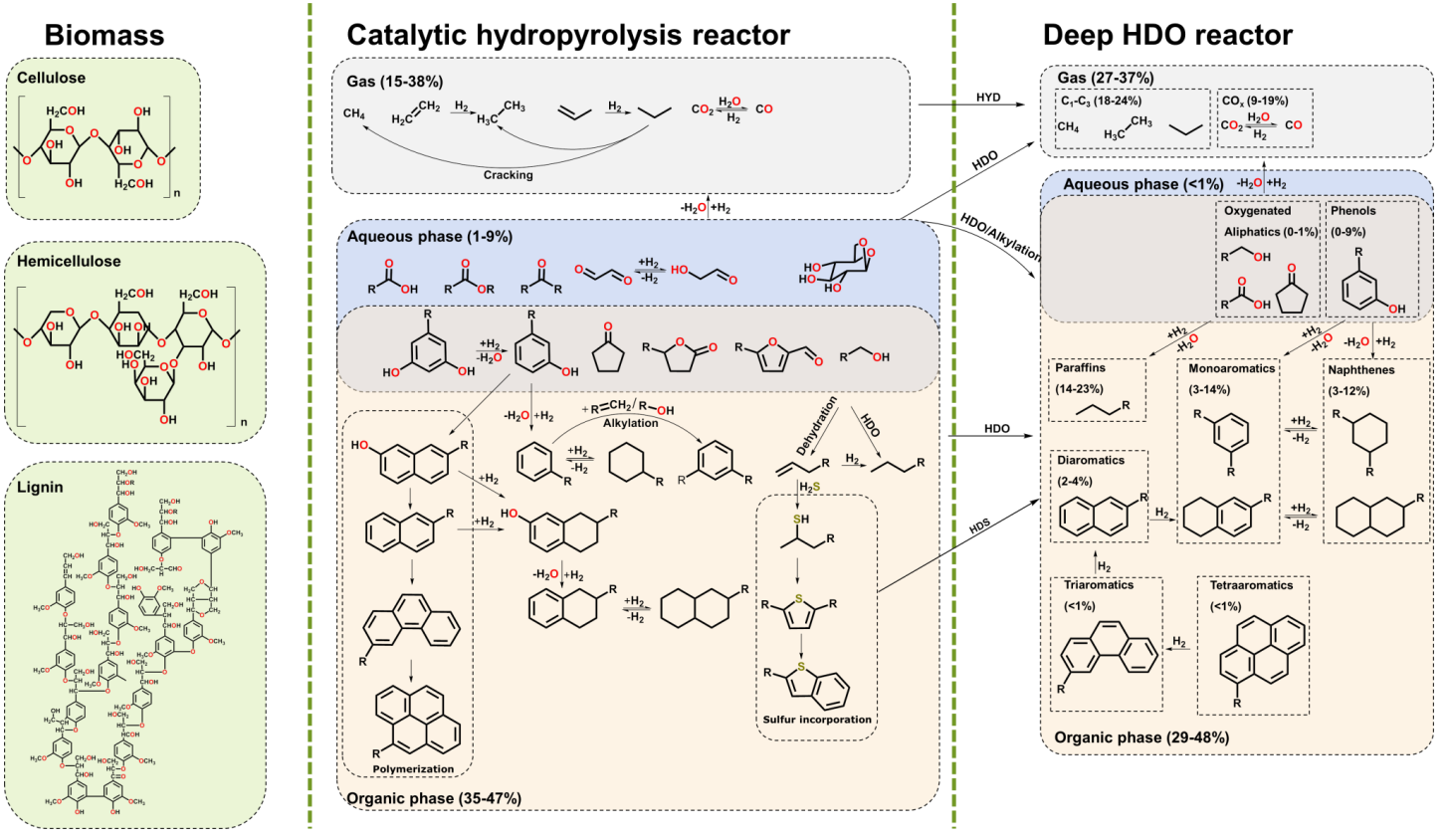

Figure 9.8 Reaction scheme for reactions taking place in a catalytic hydropyrolysis reactor and a deep HDO reactor for upgrading of the vapors from catalytic hydropyrolysis. An estimated carbon recovery is given in the brackets. The carbon recovery for the different component classes in the aqueous and organic phases is estimated on the basis of FID area and the total carbon recovery in that phase. Furthermore, it has been assumed that C_{4+} hydrocarbons in the gas phase are paraffins. It should be noted that the reactions in catalytic hydropyrolysis are gas phase reactions and the shown gas, aqueous, and organic phase on the figure only indicates where the different classes of molecules are found after condensation. The lignin structure was adapted with permission from Faravelli et al. [78].

It should be noted that a large fraction of the intermediates form in catalytic hydropyrolysis are known coke precursors, and it is well-known that di and larger aromatics can form coke through coupling reactions and through the formation of free-radicals [79,80]. Likewise olefins can polymerize into larger aromatics and form coke [81]. Oxygenates are also known coke precursors and multifunctional molecules such as guaiacol and acetic acid and can led to rapid coking of the catalyst [47,82]. However, oxygenates only containing one oxygen atom can also be problematic and furans are like other heterocyclic molecules known coke precursors while carbonyls can polymerize through aldol condensation [83,84]. It is therefore important that multifunctional oxygenates and other highly reactive oxygenates are rapidly converted into phenols and alcohols in the catalytic hydropyrolysis reactor. Furthermore larger aromatics should preferably be hydrogenated to naphthenes or monoaromatics.

9.3 Considerations when choosing a catalyst for catalytic hydropyrolysis

Using the catalyst as right bed material in the fluid bed reactor is key to obtain a high carbon recovery in the organic phase and a low oxygen content. For instance Dayton et al. [61] tested a commercial hydrotreating catalyst and a fluid catalytic cracking (FCC) catalyst at 450°C and obtained a bio-oil yield below 1 wt.%, indicating that a too active catalyst gives a low oil yield. The results from catalyst screening experiments in our laboratory are shown in Table 9.2. Using an inert bed material gives a high solid yield, and thus a low carbon recovery, which has also been observed by Dayton et al. [85] and Marker et al.[34]. Comparing the performance of a sulfided CoMo, NiMo, and Mo catalyst, shows that the NiMo catalyst has the highest cracking activity, a lower carbon recovery in the condensable organics, as shown in Figure 9.9 (Chapter 5). The Mo catalyst has a low cracking activity and therefore a high carbon recovery, but a low deoxygenation activity. The CoMo catalyst has the highest deoxygenation activity, but still a high carbon recovery. These results indicate that the CoMo catalyst is the most suitable of these catalysts to use in catalytic hydropyrolysis (Chapter 5).

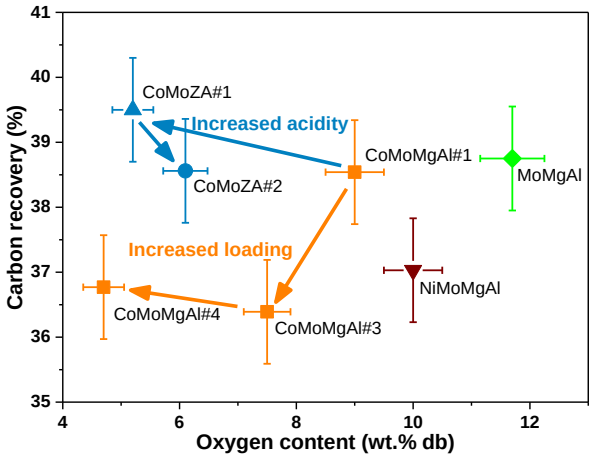

Figure 9.9 Carbon recovery in the C_{4+} organics versus the oxygen content in the organic phase (data taken from the Chapter 5 and 6. Fluid bed temperature: 450-455°C, total pressure: 26 bar, biomass feeding rate: 270-282 g/h, feed time: 2.5-3.5 h, H_2 flow: 82 NL/min, N_2 flow: 5 NL/min, and H_2S conc: 460 ppm.

Table 9.2 Overview of different catalysts for catalytic hydropyrolysis tested at DTU Chemical Engineering (Chapter 4-6). In the experiments with a HDO reactor approximately 173 g NiMo/Al_2O_3 catalyst supplied by Haldor Topsøe was used. $MgAl_2O_4$ is denoted as MgAl, zeolite mixed with alumina is denoted at ZA, bog iron sulfided and reduced is denoted at BI-S and BI-R, respectively. All catalysts with the expectation of BI-R were sulfided prior to the experiments. Catalysts supplied by Haldor Topsøe A/S are denoted as HT. Test conditions: fluid bed temperature: 443-455°C, total pressure: 26 bar, biomass used: beech wood, biomass feeding rate: 174-302 g/h, feed time: 2.5-4 h, H_2 flow: 54-89 NL/min, N_2 flow: 0.6-5 NL/min, and H_2S conc: 0-471 ppm.

Catalyst	MoMgAl	NiMoMgAl	CoMoMgAl#1	CoMoMgAl#2	CoMoMgAl#3	CoMoMgAl#4	CoMoZA#1	CoMoZA#2	CoMoMgAl(HT)	NiMoZA(HT)	BI-S	BI-R	MgAl	ZA
Catalyst composition														
Co (wt.%)	-	-	0.64	0.99	1.49	1.86	0.67	0.60	-	-	-	-	-	-
Ni (wt.%)	-	0.59	-	-	-	-	-	-	-	-	-	-	-	-
Mo (wt.%)	3.50	3.27	3.41	5.58	7.74	10.1	3.61	3.39	-	-	-	-	-	-
Support	MgAl	MgAl	MgAl	MgAl	MgAl	MgAl	ZA	ZA	MgAl	ZA	-	-	MgAl	ZA
Yields, carbon recovery and oxygen content without HDO reactor														
Gas (wt.% daf)	23.3	28.2	26.1	28.8	30.8	29.7	29.7	30.0	27.4	-	19.3	17.3	-	-
Solid (wt.% daf)	13.5	13.2	13.3	13.0	13.1	13.2	13.0	13.2	12.2	-	13.1	11.9	-	-
Aqueous phase (wt.% daf)	33.6	33.4	33.3	33.2	32.6	33.1	33.1	33.2	37.0	-	35.4	30.8	-	-
Organics + C_{4+} (wt.% daf)	26.4	24.3	25.2	23.5	22.7	22.7	24.4	24.1	20.4	-	27.0	34.4	-	-
Carbon recovery in C_{4+} (%)	39	37	39	-	36	37	40	39	35	-	33	47	-	-
Oxygen (wt.% db)	11.7	10.2	9.0	-	6.2	4.7	5.2	6.1	1.8	-	22.1	14.1	-	-
Yields, carbon recovery and oxygen content with HDO reactor														
Gas (wt.% daf)	-	-	29.4-31.2	-	-	-	-	-	31.5	29.7-30.2	25.2	24.6	27.9	28.6
Solid (wt.% daf)	-	-	10.9-14.6	-	-	-	-	-	11.4	13.0-13.1	13.5	11.9	18.7	21.1
Aqueous phase (wt.% daf)	-	-	34.5-38.0	-	-	-	-	-	35.2	32.8-34.0	36.3	44.6	37.0	21.2
Organics + C_{4+} (wt.% daf)	-	-	21.2-23.2	-	-	-	-	-	21.5	23.9-24.0	22.8	24.7	17.8	20.3
Carbon recovery in C_{4+} (%)	-	-	36-39	-	-	-	-	-	37	39-40	39	43	31	33
Oxygen (wt.% db)	-	-	0.004-0.28	-	-	-	-	-	0.003	0.037-0.11	0.02	0.005	0.008	0.037

Increasing the CoMo loading on a $MgAl_2O_4$ carrier from 4.0 to 12.0 wt.% decreased the oxygen content in the organic phase from 9.0 to 4.7 wt.% db, but also lead to a small decrease (~2 % point) in the carbon recovery (see Figure 9.9) due to increased cracking activity (Chapter 6). Using a more acidic support, zeolite mixed with alumina instead of $MgAl_2O_4$, decreased the oxygen content in the condensed organics from 9.0 to 5.2 wt.% db, but did not decrease the carbon recovery (Chapter 6). Analysis of the condensed organics showed that the decrease in the oxygen content with the zeolite supported catalysts mainly decreased the concentration of oxygenated aliphatics, while increasing the CoMo loading decreased the concentration of both oxygenated aliphatics and phenols (Chapter 6). The carbon recovery in the aqueous phase also decreased when using a zeolite based support due to a lower concentration of alcohols, which were most likely removed through alkylation reactions (Chapter 6). This also increased the concentration of aromatics from 24 to 51 % area-FID. Therefore, if the objective is to produce aromatics a catalyst with an acidic support is preferred. It is likely that the phenol yield can be increased by using Ni instead of Co as promoter, since the NiMo catalyst is less active in hydrodeoxygenation of phenols at the applied conditions (Chapter 5). However, it should be noted that the acidity will most likely decrease over time due to potassium being transferred from the biomass to the catalyst, which may deactivate the alkylation activity.

Gamliel et al. [86] also investigated the effect of the support material in catalytic hydropyrolysis with a pyroprobe reactor and concluded that it is important to have a support with a high Brønsted acidity in order to reduce the solid yield. However, continuous reactor experiments does not support that conclusion and shows that the total char and coke yield is not affected by the type of promoter, the total CoMo loading, nor the support acidity (see Table 9.2). This therefore indicates that it is not necessary to use a support with a high Brønsted acidity as long as a sufficiently active catalyst is used. Interestingly, when using a commercially CoMoS catalyst the solid yield, which was between 13.0 and 13.3 wt.% daf for all non-commercial Co(Ni)MoS catalysts, decreased to between 11.4 and 12.2 wt.% daf (see Table 9.2), indicating that using a very active catalyst can decrease the solid yield, probably by more effective suppression of polymerization reactions.

Dayton et al. [61,85,87] tested several different reduced (non-sulfided) catalysts in catalytic hydropyrolysis and obtained a C_{4+} carbon recovery between 25 and 43 % with an oxygen content in the condensed organic phase between 2.4 and 31 wt.% db [87,88]. This indicates that the reduced catalysts can give a high oil yield with a low oxygen content. However, it should be noted that most types of biomass contains sulfur [89], thus the catalysts will most likely be sulfided over time. Dayton et al.[88] conducted a 10 days experiment with a reduced NiMo catalyst in the fluid bed and oxidized and reduced the catalyst between each day, thereby removing the coke on the catalyst. This probably also to some extent removed the sulfur, thus ensuring that the catalyst remained reduced. In order for this concept to work on larger scale a second regeneration reactor is needed. In our work we have also used reduced bog iron, an iron rich natural mineral, as catalyst in the catalytic hydropyrolysis reactor followed by a fixed bed HDO reactor with an industrial sulfided $NiMo/Al_2O_3$ catalyst and obtained an oxygen free oil (<0.01 wt.%) with C_{4+} carbon recovery of 43 % (Chapter 4). Sulfiding the bog iron reduced the carbon recovery to 39 %, due to an increased cracking activity, however showing that bog iron is fairly sulfur tolerant.

There are three main problems for the catalyst used in catalytic hydropyrolysis: deactivation due to transfer of alkali metals from the biomass to the catalyst (Chapter 5,6,8), catalyst entrainment [35,85], and sulfur poisoning for non-sulfur tolerant reduced catalysts. In the $IH^{2®}$ continuous pilot plant the produced char was screened in order to recover the lost catalyst and 2 % catalyst was added to the reactor per day [35]. This could be challenging if the catalyst is crushed due to attraction and it is not possible to remove it from the char, because commercial hydrotrating catalysts are expensive and toxic and the produced char would proba-

bly have to be considered as toxic waste. Therefore using a cheap and non-toxic catalyst, such as bog iron, could be a solution to this problem. More research in needed to find cheap, non-toxic catalysts.

9.3.1 Incorporation of sulfur into the organics

As previously mentioned sulfur can be incorporated into the organics through recombination reactions, where H_2S and olefins react forming thiols [67,90,91]. The thiols can then undergo cyclization to form thiophenes, which subsequently can form benzothiophenes [55]. Comparing the sulfur content in the produced organic phase with the C_2-C_5 olefins gas yield, see Figure 9.10, shows that the sulfur content is correlated with the olefin yield, thus supporting the assumption that sulfur is incorporated into the organics through the olefins. Interestingly, it can be observed that the sulfur content is significantly higher when using sulfided Mo instead of the promoted sulfided Co(Ni)Mo, thus indicating that the sulfur content is also correlated with the catalyst activity. Since the sulfided Mo has lower HDS activity this leads to a higher sulfur content in the product.

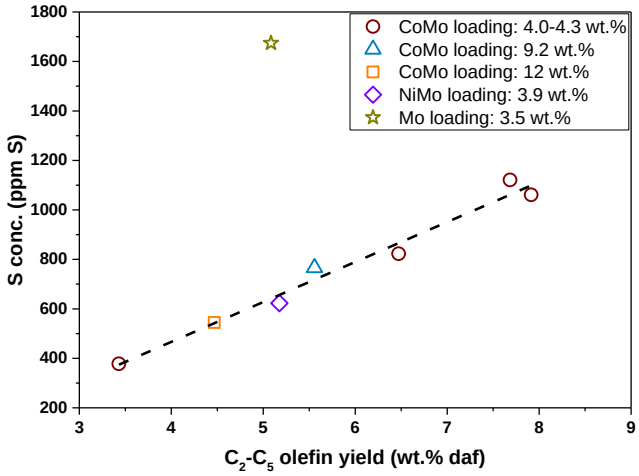

Figure 9.10 Effect of the C_2-C_5 olefin yield on the sulfur concentration in the condensed organic phase. Test conditions: fluid bed temperature: 450-455°C, total pressure: 26 bar, biomass used: beech wood, biomass feeding rate: 268-280 g/h, feed time: 2.5-3.5 h, H_2 flow: 82 NL/min, N_2 flow: 5 NL/min, and H_2S conc: 460 ppm. (Data taken from Chapter 5-7)

The concentration of sulfur in the organic phase, hence also the olefin concentration, are correlated with the catalysts acidity, the metal loading and the hydrogenation activity as indicated by Figure 9.11. Increasing the catalyst acidity increases the concentration of sulfur (red arrow in Figure 9.11), which is also in agreement with the observation that sulfur incorporation reactions are acid catalyzed [55]. Using $MgAl_2O_4$ and increasing the surface area, but maintaining the same surface metal concentration (atoms/nm^2), increased the number of acidic sites per mass of catalyst, but also increased the hydrogenation activity due to the higher total metal loading, which therefore decreased the olefin concentration available for recombination and less sulfur is incorporated (blue arrow in Figure 9.11). This also increased the HDS activity and more sulfur is removed as H_2S. Maintaining a constant support surface area and increasing the hydrogenation activity through promotion of Mo with Co and Ni decreased the olefin concentration available for recombination and less sulfur is incorporated (purple arrow in Figure 9.11)

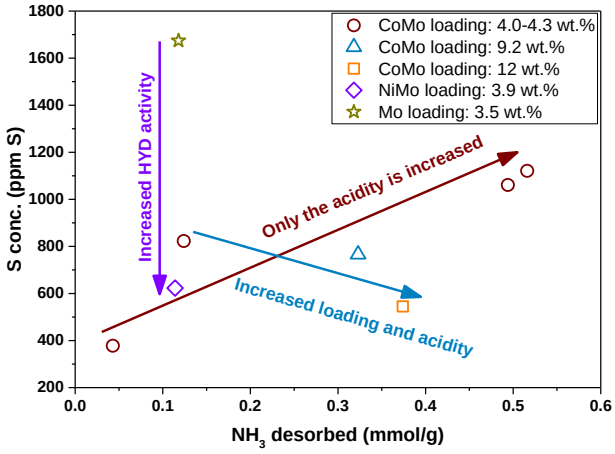

Figure 9.11 Effect of the acidity (red arrow), catalyst loading (blue arrow) and molybdenum sulfide promotion by Ni and Co (purple arrow) on the sulfur concentration in the condensed organic phase. Test conditions: fluid bed temperature: 450-455°C, total pressure: 26 bar, biomass used: beech wood, biomass feeding rate: 268-280 g/h, feed time: 2.5-3.5 h, H_2 flow: 82 NL/min, N_2 flow: 5 NL/min, and H_2S conc: 460 ppm. (Data taken from Chapter 5-7)

9.4 Effect of the catalyst in the fluid bed on the HDO reactor

One of the arguments for using catalytic hydropyrolysis is that it enables the removal of reactive oxygenates before they participate in polymerization reactions, thereby avoiding deactivation of the catalyst in the HDO reactor. It is therefore important to consider the amount of carbon on the spent catalyst from the HDO reactor, which is shown as a function of the amount of biomass used in Figure 9.12. The data points (dots) are divided into 3 areas: a) Experiments conducted with a commercial CoMo catalyst from Haldor Topsøe in the fluid bed at H_2 pressure between 3.0 and 8.2 bar. Here the catalyst with a carbon content of 2.9 wt.% was tested at 8.2 bar H_2, while the two others were tested at 3.0 bar H_2; b) Experiments conducted at H_2 partial pressures between 24.0 and 24.6 bar with catalysts in the fluid bed with varying activity, thus both pure supports ($MgAl_2O_4$, ZSM-5 mixed with Al_2O_3), olivine sand (OS), bog iron (BI), CoMo catalyst prepared at DTU, and NiMo and CoMo catalysts supplied by Haldor Topsøe have been tested; c) Experiments conducted with a CoMo catalyst supplied by Haldor Topsøe in the fluid bed at H_2 pressures between 15.9 and 35.8 bar. As indicated with the red arrow the carbon content on the spent NiMo catalyst in the HDO reactor increase with the amount of biomass used, which most likely have decreased the catalyst activity. However, it should be noted that the carbon deposition rate normally decreases over time, thus it can be assumed that when conducting longer experiments the carbon deposition will most likely mainly takes place in the beginning of the experiments. This is well-known from hydrotreating of fossil oil, where the coke content on the catalyst stabilizes after approximately one week [92,93].

Decreasing the H_2 partial pressure significantly increases the carbon content on the spent HDO reactor catalyst. This is probably because less deoxygenation takes place in the catalytic hydropyrolysis reactor and more reactive molecules therefore enters the HDO reactor, which leads to carbon deposition. It has previously been shown that the carbon content on hydrotreating catalysts increases with decreasing H_2 pressure [93,94]. This is because a lower H_2 pressure leads to a slower rate of conversion, which increases the life time of the species participating in polymerization reactions [80].

Having a more active catalyst in the fluid bed reactor also has an influence on the carbon content on the catalyst in the HDO reactor. Using a non-commercial CoMo catalyst in the catalytic hydropyrolysis reactor instead of a more active CoMo catalyst supplied by Haldor Topsøe more than doubled the carbon content on the spent catalyst in the HDO reactor. Similarly using pure $MgAl_2O_4$ in the fluid bed and using 0.96 kg biomass gave the same amount of carbon on the spent catalyst in the HDO reactor as when using Haldor Topsøe' s CoMo catalyst and 4.36 kg biomass. This is most likely because a catalyst with a low activity in the catalytic hydropyrolysis reactor does not remove all of the reactive oxygenates such as acids and furans are removed, which then can lead to coking in the HDO reactor. Interestingly, more carbon was located on the NiMo catalysts from the experiments at H_2 partial pressures between 3.0 and 8.0 bar with Haldor Topsøe' s CoMo in the fluid bed compared to when $MgAl_2O_4$ was used in the fluid bed reactor at 24.5 bar H_2, which shows the importance of using a high H_2 partial pressure.

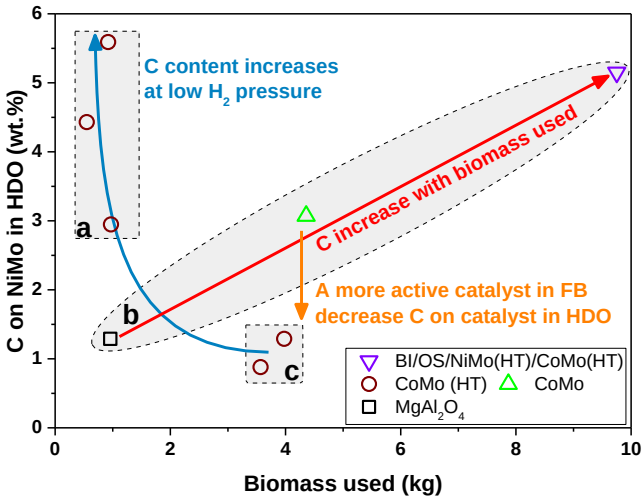

Figure 9.12 Carbon content on the spent $NiMo/Al_2O_3$ catalysts from HDO reactor. The experiments in region 'a' were conducted with a commercial $CoMo/MgAl_2O_4$ catalyst at low H_2 partial pressures between 8.2 and 3.0 bar. In region 'b' the various catalysts and bed materials with varying activity have been used and the H_2 partial pressure was between 24.0 and 24.6 bar. Furthermore it should be noted that in the experiment where 9.7 kg biomass was used, various catalysts was tested in the fluid bed reactor without changing the catalyst in the HDO reactor. The experiments in region 'c' were conducted with a commercial $CoMo/MgAl_2O_4$ catalyst at H_2 partial pressures between 15.9 and 35.8 bar. Test conditions: HDO temperature: 350-400 °C, biomass used: beech wood, biomass feeding rate: 160-390 g/h.

Three spent NiMo catalysts from the HDO reactor were analyzed with X-ray fluorescence (XRF) and the detected concentration of potassium, calcium, iron, silicon, phosphorous, sodium, and chlorine are shown in Table 9.3. Chlorine, which is a known poison for molybdenum sulfide based catalysts [67], was not detected in any of the three spent catalysts, thus indicating that chlorine is transformed into HCl during deposition of potassium on the catalyst. Likewise phosphorous and sodium were not detected indicating that these were not transferred to the catalyst. There was no correlation between the amount of potassium, calcium, iron, and silicon on the spent catalyst and the amount of biomass used, which is due to that the measured concentrations are within the uncertainty of the measurement.

Table 9.3 Potassium, calcium, iron, silicon, phosphorous, sodium, and chlorine on spent $NiMo/Al_2O_3$ catalyst from the HDO reactor. (The concentrations were measured with XRF, due to the low concentrations the uncertainty for this measurement was 66 % corresponding to two standard deviations). (HDO reactor temperature: 345-400 °C, pressure: 16-36 bar)

Biomass used (kg)	K (ppm)	Ca (ppm)	Fe (ppm)	Si (ppm)	Cl (ppm)	P (ppm)	Na (ppm)
3.6	300	98	460	180	0	0	0
4.6	56	60	0	86	0	0	0
9.7	260	140	150	85	0	0	0

The potassium, calcium, silicon, phosphorous, and sodium content were also measured in two of the condensed organic phases, see Table 9.4. The concentration of potassium, calcium, and sodium was below 0.02 ppm in both organic phases, while the concentration of silicon was between 89 and 138 ppm, and the concentration of phosphorous was between 1.4 and 1.5 ppm. This shows that some alkali metals are present in the produced organic phase, which potentially could deposit on the catalyst if the organic phase is further hydrotreated. However, the concentration of V and Ni in crude oil can be as high as several 1000 ppm [80], thus metal deposition is a well-known concept in hydrotreating and that it should be fairly easy to upgrade the produced organic phase to transportation fuels.

Table 9.4 Potassium, calcium, silicon, phosphorous, and sodium content in the condensed organic phases. Measured with inductively coupled plasma mass spectrometry. (Fluid bed temperature: 400-430°, HDO reactor temperature: 345-400 °C, pressure: 26 bar)

Test	K (ppm)	Ca (ppm)	Si (ppm)	P (ppm)	Na (ppm)
#1	<0.02	<0.02	89	1.4	<0.02
#2	<0.02	<0.02	138	1.5	<0.02

9.5 Comparison of pyrolysis technologies

As previously mentioned there are several different pyrolysis technologies. In fast pyrolysis (FB) the biomass is typically heated to approximately 500°C in an inert atmosphere, where sand is used as a heat carrier [6], while an acid catalysts is typically used as bed material in catalytic pyrolysis (CFP), thus enables the removal of oxygen during the pyrolysis. In reactive catalytic fast pyrolysis (RCFP), invented by Research triangle institute (RTI) ,hydrogen is co-fed into the reactor, as in catalytic hydropyrolysis (CHP), but takes place at atmospheric pressure [95]. Therefore in order to compare catalytic hydropyrolysis with other available pyrolysis based processes the oxygen content in the condensed organic phase versus the C_{4+} carbon recovery is shown in Figure 9.13 for FP, CFP, CHP, RCFP and catalytic hydropyrolysis followed by a hydrodeoxygenation reactor (CHP+HDO). Only data from experiments conducted in (semi) continuous setups are used and a list of references is given in Table 9.5. Additionally, only data from experiments where woody biomass was used are included in Figure 9.13. Fast pyrolysis generally gives a carbon recovery between 45 and 70 % for woody biomass with an oxygen content at approximately 35-45 wt.% db [11,60,96–98] and upgrading the pyrolysis oil to an oxygen free oil generally decreases the carbon recovery to between 35 and 45 % [20]. Catalytic fast pyrolysis can be used to decrease the oxygen content in the condensed organic phase, thus producing a more stable product; however as the oxygen content is decreased so is the carbon recovery. The carbon recovery in the C_{4+} organics and the oxygen content in the organic phase does therefore have a broad span, and the carbon recovery is typically between 10 and 45 %, while the oxygen concentration is between 9 and 34 wt.% db, with the correlation that high carbon recovery typically means high oxygen content [21,22,87,99–106]. The reason for the low carbon recovery in the C_{4+} organics is that a significant amount of the carbon is lost as char and coke (up to 50 %) [87].

Using catalytic hydropyrolysis decreases the oxygen content to between 2 and 18 wt.%, while maintaining a carbon recovery between 35 and 47 wt.%. The results show that this technology more selectively removes

the oxygen compared to catalytic fast pyrolysis. Combining catalytic hydropyrolysis with a second HDO reactor generally decreases the oxygen content to below 1 wt.%, while the carbon recovery is between 29 and 48 % depending on the catalyst and the operating conditions [34–36]. Non-catalytic hydropyrolysis followed by a HDO reactor have also been studied, which has the advantage that the temperature in the hydropyrolysis reactor can be optimized for pyrolysis and the catalyst is not poisoned by biomass ash. Venkatakrishnan et al. [107] used in their process, H_2Bioil, a cyclone reactor for the non-catalytic hydropyrolysis followed by a fixed bed HDO reactor and achieved an oxygen free product with a carbon recovery of 32 %, i.e. in the low end of the range achieved with catalytic hydropyrolysis followed by a HDO reactor. Zhang et al. [108] from Phillips 66 investigated a similar process where non-catalytic hydropyrolysis took place in a fluid bed reactor followed by HDO in a second fluid bed reactor and achieved a C_{5+} carbon recovery between 35 and 47 %, and oxygen content between 2 and 17 wt.% db. However the oxygen content increased with increasing carbon recovery. This indicates that the concept might be able to obtain similar yields as the IH$^{2®}$ process. However, more research within this process is needed and adding the necessary heat to the endothermic hydropyrolysis could be challenging in large scale, while catalytic hydropyrolysis is exothermic and does not require external heat addition.

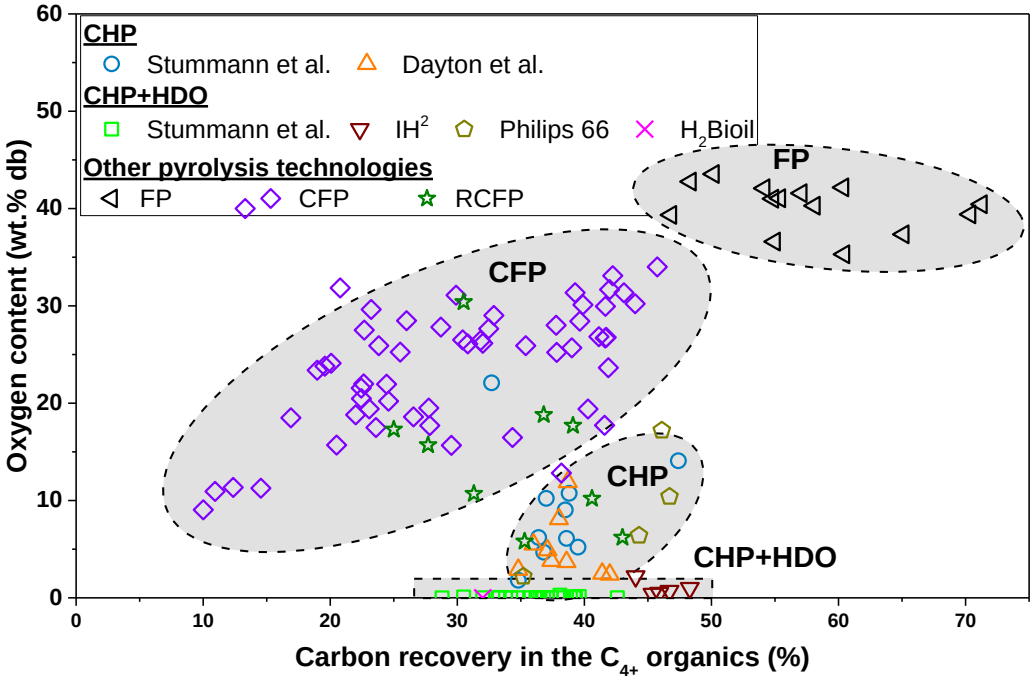

Figure 9.13 Oxygen content in the organic phase versus C_{4+} carbon recovery for fast pyrolysis (FP), catalytic fast pyrolysis (CFP), catalytic hydropyrolysis (HYP), and catalytic hydropyrolysis followed by a HDO reactor (CHP+HDO). (FP data were taken from ref [11,60,96–98]**, CFP data were taken from ref** [21,22,87,99–106]**, CHP data were taken from Chapter 2, 4-6 and ref** [36,85]**, RCFP data was taken from ref** [87]**, and CHP+HDO data were taken from Chapter 2,4,7 and ref** [34–36,107,108]**. Only data from studies with woody biomass was used).**

The composition of the condensed organic phase also depends on the used pyrolysis technology, as shown in the Van Krevelen diagram in Figure 9.14. The hydrogen to carbon atomic ratio in the organic phase produced from fast pyrolysis is generally between 1.2 and 1.6, thus very similar to the ratio in biomass. However, the oxygen to carbon atomic ratio decreases from between 0.6 to 0.8 for biomass to between 0.4-0.65 for

organics produced with fast pyrolysis. The organic phase from catalytic fast pyrolysis has a significantly lower oxygen to carbon ratio than that from fast pyrolysis, but the hydrogen to carbon ratio also decreases, which is most likely due to dehydration [20]. Interestingly, the organic phase from reactive catalytic fast pyrolysis is more similar to the organic phase from catalytic fast pyrolysis than the organic phase from catalytic hydropyrolysis, with an oxygen to carbon atomic ratio is between 0.05 and 0.38 and a hydrogen to carbon atomic ratio between 1.09 and 1.35 [62,87,109,110]. The organic phase from catalytic hydropyrolysis generally has a hydrogen to carbon atomic ratio between 1.2 and 1.4, and the oxygen to carbon ratio is between 0.02 and 0.14. The higher hydrogen to carbon ratio compared to organics from catalytic fast pyrolysis is due to the hydrogenation reactions in catalytic hydropyrolysis, which decreases the olefin and aromatic yield. Adding a HDO reaction after the catalytic hydropyrolysis reactor makes the oxygen to carbon ratio approach 0, while the hydrogen to carbon atomic ratio increases to between 1.46 and 1.97. However, the hydrogen to carbon ratio is generally below 1.8 when using woody biomass and higher ratios have only so far been achieved with different algae or bagasse [34]. Interestingly, the hydrogen to carbon molar ratio for heavy fuel and diesel is 1.6 and 1.8, respectively, indicating that the composition of the organic phase produced from catalytic hydropyrolysis combined with a second HDO reactor is similar to conventional fossil fuel. The reason that the organic phase from most experiments are more similar to heavy fuel than diesel is that it has a high concentration of aromatics, which decreases it hydrogen to carbon ratio.

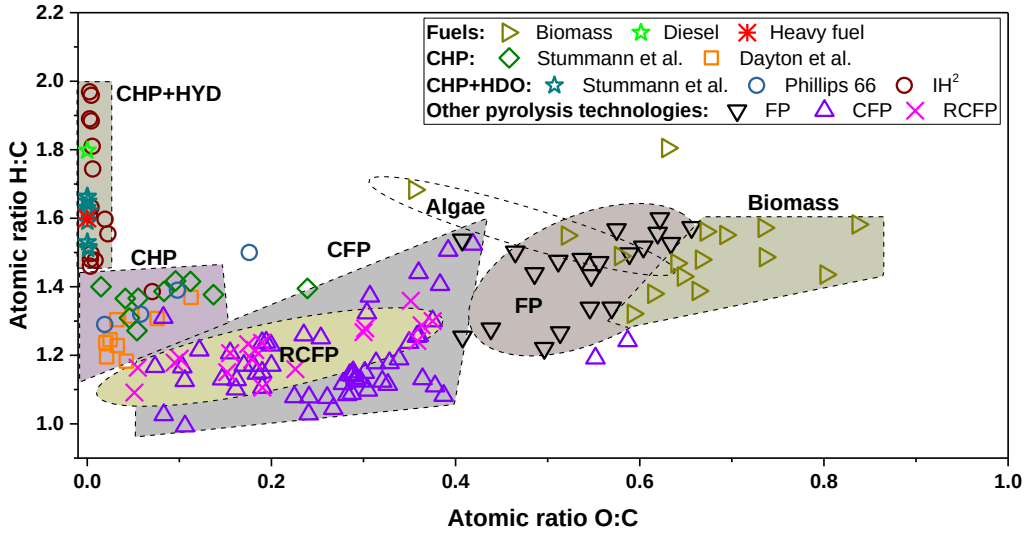

Figure 9.14 Van Krevelen diagram of bio-oil produced with different pyrolysis technologies. (FP data were taken from ref [11,60,96–98,111]**, CFP data were taken from ref** [21,22,87,99–106]**, CHP data were taken from Chapter 2, 4-6 and ref** [36,85]**, RCFP data was taken from ref** [87,109,110]**, CHP+HDO data were taken from Chapter 2,4,7, and ref** [34–36,107,108]**, and biomass data was taken from** [11,34,46,60]**.)**

Considering the low oxygen content in the condensed organic phase and the high carbon recovery, catalytic hydropyrolysis is a very promising technology for the production of liquid fuels. However, catalytic hydropyrolysis is a more complex technology than fast pyrolysis and catalytic fast pyrolysis. One of the advantages with both fast pyrolysis and catalytic fast pyrolysis are that the plants can be located where the biomass is produced, because the plants can be fairly small. These local plants can then send the pyrolysis oil to a centralized bio-refinery [112], where the pyrolysis oil is upgraded to gasoline and diesel. However, hydrotreating of pyrolysis oil generally leads to rapid catalyst deactivation and reactor plugging due to coking

[8,113]. Pyrolysis oil can also be upgraded by co-feeding it with fossil oil into a FCC unit [114–117], however, due to the high oxygen content in the pyrolysis oil it is immiscible with fossil oil and the alkali metals in the pyrolysis oil can potentially deactivate the FCC catalyst [116,118,119]. The pyrolysis oil can also be converted ex-situ at the pyrolysis plant by having a second catalytic reactor after the pyrolysis reactor, which decreases the potential catalyst deactivation by alkali metals, however, like catalytic pyrolysis it gives a fairly low oil yield, but high coke yield [120]. Alternatively, pyrolysis oil can be used to replace crude oil as fuel for boilers, but despite that the technology for fast pyrolysis is commercially available, the current market for pyrolysis oil in power plants is limited [8]. Furthermore, it should be noted that the organic phase from catalytic fast pyrolysis still contains furans and relatively high concentrations of acids [121].

Catalytic hydropyrolysis plants would most likely be larger centralized plants, which have the drawback that the biomass has to be transported over longer distances to the plant. However, it should be noted that wood pellets are already being transported globally to supply power plants [122], indicating that it can be economically feasible to transport biomass, even across continents. Another drawback with catalytic hydropyrolysis is that biomass needs to be fed into a system at high pressure, which could be challenging and has not been demonstrated at commercial scale yet [95]. Wang et al. [87] therefore suggested that reactive catalytic fast pyrolysis should be used instead and considering the C_{4+} carbon recovery and oxygen content in the produced organic phase (see Figure 9.13), the process seams very promising. However, it has been shown that coking of the catalyst in the hydropyrolysis reactor increases with decreasing hydrogen pressure (Chapter 3), thus rapid coking of the catalyst is expected in this process, but this can most likely be overcome by continuous catalyst regeneration by oxidation [95], at the cost of adding complexity to the plant. Furthermore, it will most likely also increase the carbon recovery in the aqueous phase (1.3-8.5 %) [87] (Chapter 3), thus increasing the operating cost due to water purification.

Table 9.5 References for pyrolysis technologies used in Figure 9.13 and Figure 9.14.

Catalyst	Hydrogen pressure	Feed	Temp.	Reactor system	Comment	Ref
		Catalytic hydropyrolysis with HDO reactor (CHP+HYD)				
$CoMo/MgAl_2O_4$,$NiMo/H\text{-}ZSM\text{-}5+Al_2O_4$, bog iron, olivine sand, H-ZSM-5, $MgAl_2O_4$	3.0-35.8 bar	Beech wood	365-511 °C	FB+PB	Both sulfided and reduced catalysts	[36]
CRI S-211, CRI S-4211		Mixed wood, maple, lemna derived, microalgae, bagasse macroalgae, corn stover		FB+PB		[34,35]
Sand, commercial hydrotreating catalyst	19 bar	Red oak	425°C	FB+FB	Sand was used in the hydropyrolysis reactor. Only C_{5+} carbon recovery stated.	[108]
PtMo/carbon	25 bar	Poplar, cellulose	480°C	CR+PB	Only catalyst in HDO reactor	[107]
		Catalytic hydropyrolysis (CHP) and reactive catalytic fast pyrolysis (RCFP)				
$CoMo/MgAl_2O_4$, $NiMo/MgAl_2O_4$, $Mo/MgAl_2O_4$, $CoMo/H\text{-}ZSM\text{-}5+Al_2O_4$, bog iron	24.5	Beech wood	450°C	FB		[36]
$NiMo/Al_2O_4$, Al_2O_3, tungsten oxide, SiC, iron oxide, molybdenum oxide, commercial hydrotreating catalyst	0.6-12.4 bar	Woody residue	375-500°C	FB	Reduced catalysts	[61,85,87]
Ni/char, Ni/Al_2O_3,$CoMo/Al_2O_3$, dolomite, sand	1 bar	Rice husk	500-650°C	FB	Single shot feeding of biomass	[62,109,110]
		Catalytic fast pyrolysis (CFP)				
SiC, Al_2O_3, molybdenum oxide, iron oxide	0 bar	Woody residue	500°C	FB		[87]
FCC, FeCrCu, CoMo	0-0.05 bar	Poplar wood	475°C	FB	The effect of using different recycling non-condensable gasses (H_2, CO, CO2)	[100]
Ca-Y zeolite, M/β-zeolite	0 bar	White oak	500°C	BFB		[21]
H-ZSM-5, Co/H-ZSM-5, M/H-ZSM-5	0 bar	Beech wood	500°C	PB, CFB	Experiments conducted both in a fixed bed and in a pilot plant.	[22,104]
ZSM-5	0 bar	wood	400-550°C	BFB		[101]
FCC, ZSM-5	0 bar	Poplar wood	470-520 °C	BFB		[99,106]
SiO_2, $NiSi_x$, VSi_x, NiVSi, NiV/H-ZSM-5	0 bar	Pine and spruce	450°C	FB		[102,103]
$Na_2CO_3/\gamma\text{-}Al_2O_3$	0 bar	Wood	400-550°C	EFR+PB	Catalytic upgrading takes place in separate PB reactor	[105]
		Fast pyrolysis (FP)				
None	0 bar	Lignin, Macroalgae, wood, straw	550°C	PCR		[11]
None	0 bar	Rice husk	550 °C	CFB	Commercial-scale fast pyrolysis plant (1-3 T/h)	[98]
None	0 bar	Beech, sprice, iroko, albizia, corn cob	465-470°C	FB		[60]
None	0 bar	White oak	400-550°C	FB		[96]
None	0 bar	Mallee	350-580°C	FB		[97]

FB = Fluid bed, PB = packed bed, BFB = bubbling fluid bed, CFB = circulating fluid bed, CR= cyclone reactor, EFR = entrained fall reactor, PCR = pyrolysis centrifuge reactor.

9.6 Outlook

Catalytic hydropyrolysis is a promising technology for the production of renewable liquid fuels from biomass and thermodynamic analysis of different catalytic hydropyrolysis systems have shown that it is possible to obtain an energy efficiency of up to 89 % based on a feed of biomass and hydrogen to the plant [123]. However, this requires that the hydrogen is produced from electrolysis and the char is gasified and converted into synthetic natural gas (SNG) along with the light gases. A simplified version of this process is shown in Figure 9.15 option 1. With this process the produced aqueous phase will be close to carbon free [36], thus only a minor treatment of the waste water is needed. However, the produced organic phase will most likely still need to be processed in a refinery for distillation and adjustment of the octane/cetane number. One important breakthrough for catalytic hydropyrolysis was the successful operation of the IH^{2}® demonstration plant in India with a capacity of 5 tons biomass per day, where the needed hydrogen is produced from the light gasses produced during the hydropyrolysis [124]. According to CRI the manufacturing cost of fuels from the IH$^{2®}$ process is approximately $2.25 per gallon, and the current (November 2018) gasoline and diesel price in the United States is $2.84 per gallon and $3.26 per gallon (including tax), respectively [125]. The gasoline and diesel price without taxes, distribution, and marketing is $1.9 per gallon and $2.4 per gallon [125], indicating that the IH^{2}® process might be able to compete against fossil fuels without governmental subsidies. Furthermore, Biozin plan to construct five IH$^{2®}$ plants in Norway, which will produce 120,000 m^{3} bio-oil per year. The bio-oil will be upgraded at a refinery before it can be used as transportation fuel [126].

Despite that this is a promising process from an energy perspective, it will most likely be beneficial to first construct more simple plants to prove the technology, where the required hydrogen still ideally comes from electrolysis or reforming of the produced gasses, but the produced vapors are condensed after the catalytic hydropyrolysis unit (Option 2 in Figure 9.15). The organic phase can then be co-fed with fossil oil into an industrial hydrotreating unit at a refinery for complete deoxygenation and desulfidation. Co-feeding of pyrolysis oil and catalytic pyrolysis oil with fossil fuel into a hydrotreating unit is a well-known concepts [114]. However, the organic phase produced by catalytic hydropyrolysis has the advantage, that it is mainly monofunctional (only contain single oxygen atom) and has a low concentration of acids and furans, while organics from fast pyrolysis and catalytic pyrolysis are multifunctional and more reactive [36,85]. It is therefore plausible that co-feeding of oil from catalytic hydropyrolysis will be easier than to co-feed pyrolysis oil and will not lead to the same degree of catalyst deactivation.

The aqueous phase produced in catalytic hydropyrolysis can contain up to 10 wt.% carbon (Chapter 4), which can be removed through waste water treatment. However, this is an expensive solution that decreases the carbon recovery. A better alternative would be to upgrade the aqueous phase in a separate reactor through C-C coupling of the oxygenates into valuable products such as BTX [127]. Several different catalytic systems can be used for C-C coupling reactions [128], were especially zeolites have promise [127]. However deactivation due to dealumination is a common problem in aqueous environments, and stabilization of the zeolite may be necessary e.g. by the addition of phosphorous [129]. The goal is naturally to become free of fossil fuels and the proposed process should therefore be considered as a stepping stone to a standalone catalytic hydropyrolysis process.

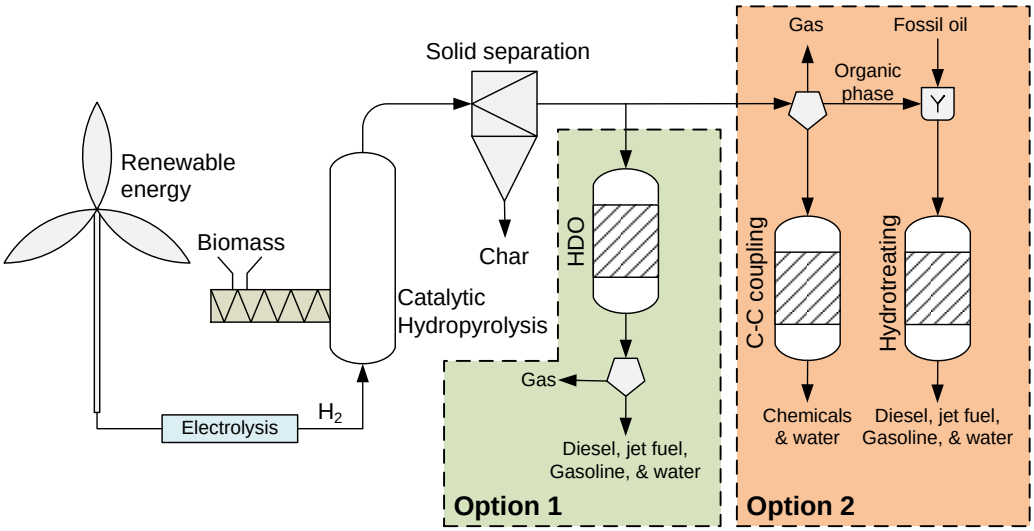

Figure 9.15 Proposed process diagram for catalytic hydropyrolysis with char separation and two downstream process options. Option 1: in-line upgrading of the produced vapors in a fixed bed HDO reactor to diesel, jet fuel, gasoline, water, and light gas (C_1-C_3, CO, and CO_2). Option 2: Bypassing the HDO reactor and the vapors are instead condensed and separated into an aqueous phase, organic phase and light gas. The organic phase can be co-feed into a hydrotreating unit together with fossil oil and the carbon in the aqueous phase is recovered through C-C coupling reactions producing water and chemicals.

As previously discussed one of the disadvantages with catalytic hydropyrolysis is the pressurized biomass feeding. One possibility for overcoming this problem is to distill the vapors before they enter the HDO reactor, see Figure 9.16. The light fraction and water could then be sent the HDO reactor, while the heavy fraction could be mixed with the biomass to produce a slurry, which can easily be pumped into the catalytic hydropyrolysis reactor. This would also make it easier to operate the process at a higher hydrogen partial pressure, which would increase the degree of hydrodeoxygenation and most likely also increase the catalyst life time. However, in order for this process to be beneficial the catalyst in the catalytic hydropyrolysis unit should have a low cracking activity and the alkylation reactions should therefore ideally take place in the HDO reactor. However, distilling the vapors could be too expensive for this concept to be economically feasible. Furthermore, the feasibility of this concept also depends on the needed amount of oil needed in order to make a slurry.

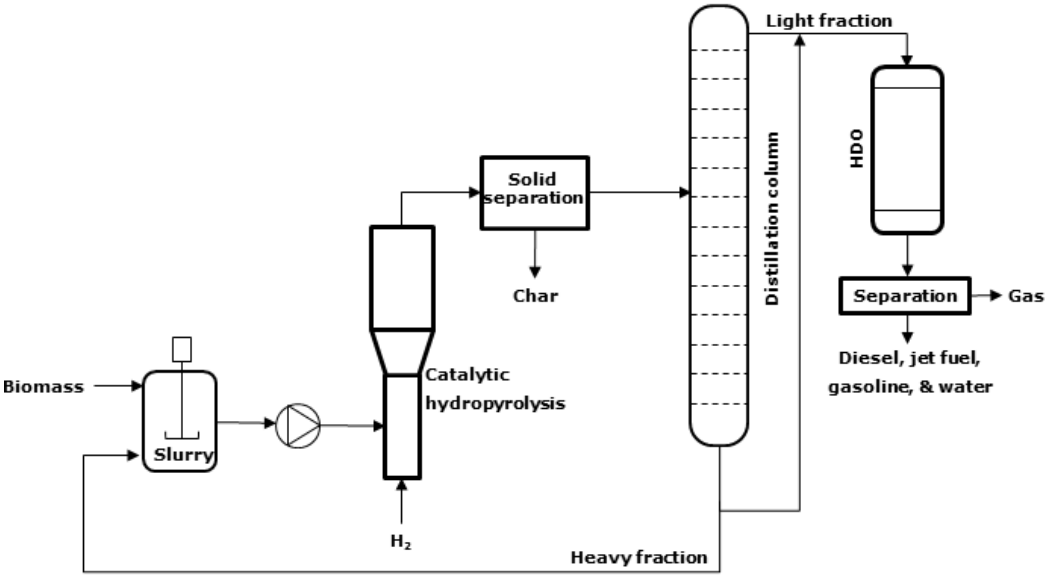

Figure 9.16 Proposed process diagram for catalytic hydropyrolysis of a slurry consisting of biomass and heavy oil.

9.7 Conclusions

Due to global warming and an increasing world population, the need for renewable fuels continues to increase. Recent research has shown that catalytic hydropyrolysis of biomass is a promising method for the production of liquid fuels, which can be used in the existing transportation sector. This study shows that catalytic hydropyrolysis consist of a complex set of chemical reactions and that an understanding of these reactions can be used to adjust the composition of the produced organic phase.

Selecting the right catalyst in the catalytic hydropyrolysis reactor is crucial in order to obtain a high oil yield. The acidity can be used to increase the degree of alkylation reactions, but using an acidic catalyst like a zeolite without any hydrogenating active phase gives a high solid yield. The oxygen content in the oil can be decreased by increasing the catalytic activity, e.g. by increasing the metal loading, but this also increases the gas yield, thus a catalyst with a moderate activity is preferred due to the fairly high temperature in the hydropyrolysis reactor. High oil yield has been obtained with both reduced and sulfided catalysts. Sulfided catalysts have the advantage that they are sulfur tolerant, but addition of sulfur (H_2S) is needed in order to maintain them in their sulfided state. This leads to incorporation of sulfur in the produced oil, which needs to be removed before it can be used as transportation fuel. However the sulfur content can be decreased by decreasing the catalysts acidity or increasing its hydrogenation activity.

Catalytic hydropyrolysis was compared with other pyrolysis technologies such as catalytic and non-catalytic pyrolysis. This showed that catalytic hydropyrolysis gives a C_{4+} carbon recovery between 35 and 47 % with an oxygen content between 2 and 18 wt.% db, while the C_{4+} carbon recovery for catalytic fast pyrolysis is between 10 and 45 %, but the oxygen content is typically between 9 and 34 wt.% db. This is still lower than the oxygen content in the product from fast pyrolysis, which is between 35-45 wt.% with a C_{4+} carbon recovery of 45-70 %. Furthermore using a HDO reactor after the catalytic hydropyrolysis reactor can decrease the oxygen content to almost 0 wt.%, with a C_{4+} carbon recovery as high as 48 %. However, there are some

drawbacks for catalytic hydropyrolysis. Pressurized biomass feeding can be challenging and current research indicates that catalytic hydropyrolysis should be conducted in larger centralized plants in order to obtain a high overall energy efficiency for the process, thus the biomass needs to be transported over longer distances. Furthermore, alkali metals from the biomass are transferred to the catalyst, which over time may lead to catalyst deactivation and catalyst loss due to attrition and entrainment can increase the operating costs. Reactive catalytic fast pyrolysis (i.e. low-pressure catalytic hydropyrolysis) is a promising method for obtaining a high oil yield with a low oxygen content. However, decreasing the hydrogen pressure leads to more rapid coking of the catalyst. The coke can be removed through oxidation in a regeneration reactor, but deactivation by alkali metals could still be a problem, which needs to be addressed. Alternatively, the hydropyrolysis can be conducted without a catalyst and the vapors be upgraded ex-situ, thus minimizing the catalyst deactivation by alkali metals, but most likely increasing the degree of coking in the HDO reactor due to more reactive oxygenates in the vapor.

In order to commercialize catalytic hydropyrolysis an interesting option is smaller plants which are located at existing refineries and where the produced vapors are condensed after the catalytic hydropyrolysis reactor and co-fed with fossil oil into an existing hydrotreating unit. This should be considered as a stepping stone for the commercialization of the process. Furthermore, mixing the heavy fraction from catalytic hydropyrolysis with biomass and pumping it into the hydropyrolysis reactor as a slurry would make it possible to run the process at a higher operating pressure and making the biomass feeding less challenging. So far wood has been used as biomass feedstock in most research and the effect of using other types of biomass or municipal solid waste should been investigated in more detail.

References

[1] J. Hansen, M. Sato, P. Hearty, R. Ruedy, M. Kelley, V. Masson-Delmotte, G. Russell, G. Tselioudis, J. Cao, E. Rignot, I. Velicogna, B. Tormey, B. Donovan, E. Kandiano, K. Von Schuckmann, P. Kharecha, A.N. Legrande, M. Bauer, Ice melt, sea level rise and superstorms: Evidence from paleoclimate data, climate modeling, and modern observations that 2 °C global warming could be dangerous, Atmos. Chem. Phys. 16 (2016) 3761–3812. doi:10.5194/acp-16-3761-2016.

[2] B.P. Horton, S. Rahmstorf, S.E. Engelhart, A.C. Kemp, Expert assessment of sea-level rise by AD 2100 and AD 2300, Quat. Sci. Rev. 84 (2014) 1–6. doi:10.1016/j.quascirev.2013.11.002.

[3] IPCC - Intergovernmental Panel on Climate Change, Global Warming of 1.5°C an IPCC special report on the impacts of global warming of 1.5 °C above pre-industrial levels and related global greenhouse gas emission pathways, in the context of strengthening the global response to the threat of climate change, (2018). http://www.ipcc.ch/report/sr15/.

[4] Independent Statistics & Analysis - U.S. Energy Information Administration, International energy outlook 2016 - DOE/EIA-0484, 2016. https://www.eia.gov/outlooks/ieo/pdf/0484(2016).pdf (accessed July 7, 2017).

[5] United Nations, World Population Prospects The 2017 Revision Key Findings and Advance Tables, World Popul. Prospect. 2017. (2017) 1–46. doi:10.1017/CBO9781107415324.004.

[6] A.V. Bridgwater, Review of fast pyrolysis of biomass and product upgrading, Biomass and Bioenergy. 38 (2012) 68–94. doi:10.1016/j.biombioe.2011.01.048.

[7] R.H. Venderbosch, W. Prins, Fast pyrolysis technology development, Biofuels, Bioprod. Biorefining. 4 (2010) 178–208. doi:10.1002/bbb.205.

[8] T.M.H. Dabros, M.Z. Stummann, M. Høj, P.A. Jensen, J.-D. Grunwaldt, J. Gabrielsen, P.M. Mortensen, A.D. Jensen, Transportation fuels from biomass fast pyrolysis, catalytic hydrodeoxygenation, and catalytic fast hydropyrolysis, Prog. Energy Combust. Sci. 68 (2018) 268–309. doi:10.1016/j.pecs.2018.05.002.

[9] S. Czernik, A.V. Bridgwater, Overview of applications of biomass fast pyrolysis oil, Energy & Fuels. 18 (2004) 590–598. doi:10.1021/Ef034067u.

[10] A. Oasmaa, S. Czernik, Fuel oil quality of biomass pyrolysis oils-State of the art for the end users, Energy & Fuels. 13 (1999) 914–921. doi:10.1021/ef980272b.
[11] T.N. Trinh, P.A. Jensen, K. Dam-Johansen, N.O. Knudsen, H.R. Sørensen, S. Hvilsted, Comparison of lignin, macroalgae, wood, and straw fast pyrolysis, Energy & Fuels. 27 (2013) 1399–1409. doi:10.1021/ef301927y.
[12] T.N. Trinh, P.A. Jensen, K. Dam-Johansen, N.O. Knudsen, H.R. Sørensen, Influence of the pyrolysis temperature on sewage sludge product distribution, bio-oil, and char properties, Energy & Fuels. 27 (2013) 1419–1427. doi:10.1021/ef301944r.
[13] D. Chiaramonti, A. Oasmaa, Y. Solantausta, Power generation using fast pyrolysis liquids from biomass, Renew. Sustain. Energy Rev. 11 (2007) 1056–1086. doi:10.1016/j.rser.2005.07.008.
[14] S. Lee, T. Kim, K. Kang, Performance and emission characteristics of a diesel engine operated with wood pyrolysis oil, Proc. Inst. Mech. Eng. Part D J. Automob. Eng. 228 (2014) 180–189. doi:10.1177/0954407013502951.
[15] Y. Solantausta, N.-O. Nylund, M. Westerholm, T. Koljonen, A. Oasmaa, Wood-pyrolysis oil as fuel in a diesel-power plant, Bioresour. Technol. 46 (1993) 177–188. doi:10.1016/0960-8524(93)90071-I.
[16] D. Chiaramonti, M. Bonini, E. Fratini, G. Tondi, K. Gartner, A.V. Bridgwater, H.P. Grimm, I. Soldaini, A. Webster, P. Baglioni, Development of emulsions from biomass pyrolysis liquid and diesel and their use in engines-Part 2: Tests in diesel engines, Biomass and Bioenergy. 25 (2003) 101–111. doi:10.1016/S0961-9534(02)00184-8.
[17] D. Chiaramonti, M. Bonini, E. Fratini, G. Tondi, K. Gartner, A.V. Bridgwater, H.P. Grimm, I. Soldaini, A. Webster, P. Baglioni, Development of emulsions from biomass pyrolysis liquid and diesel and their use in engines-Part 1: Emulsion production, Biomass and Bioenergy. 25 (2003) 85–99. doi:10.1016/S0961-9534(02)00183-6.
[18] A. Shihadeh, S. Hochgreb, Diesel engine combustion of biomass pyrolysis oils, Energy & Fuels. 14 (2000) 260–274. doi:10.1021/ef990044x.
[19] A. Shihadeh, S. Hochgreb, Impact of biomass pyrolysis oil process conditions on ignition delay in compression ignition engines, Energy & Fuels. 16 (2002) 552–561. doi:10.1021/ef010094d.
[20] R.H. Venderbosch, A Critical View on Catalytic Pyrolysis of Biomass, ChemSusChem. 8 (2015) 1306–1316. doi:10.1002/cssc.201500115.
[21] C.A. Mullen, A.A. Boateng, D.J. Mihalcik, N.M. Goldberg, Catalytic fast pyrolysis of white oak wood in a bubbling fluidized bed, Energy and Fuels. 25 (2011) 5444–5451. doi:10.1021/ef201286z.
[22] E.F. Iliopoulou, S. Stefanidis, K. Kalogiannis, A.C. Psarras, A. Delimitis, K.S. Triantafyllidis, A.A. Lappas, Pilot-scale validation of Co-ZSM-5 catalyst performance in the catalytic upgrading of biomass pyrolysis vapours, Green Chem. 16 (2014) 662–674. doi:10.1039/c3gc41575a.
[23] Friedrich Bergius, Chemical reactions under high pressure, Nobel Lect. (1932) 33.
[24] F. Bergius, J. Billwiller, Process for producing liquid or soluble organic combinations from hard coal and the like., US Patent 1,251,954, 1918.
[25] F. Bergius, Process for distilling and liquefying coal, US Patent 1,669,439, 1928.
[26] G. Löwenthal, W. Wanzl, K.H. van Heek, Kinetics of swelling and plasticity of coal during rapid pressurized pyrolysis and hydropyrolysis, Fuel. 65 (1986) 346–353. doi:10.1016/0016-2361(86)90294-2.
[27] M.I. Greene, C.J. Ladelfa, S.J. Bivacca, A process concept for the production of benzene-ethylene-SNG from coal using flash hydropyrolysis technology, Fuel Process. Technol. 3 (1980) 75–99. doi:10.1016/0378-3820(80)90013-2.
[28] H.D. Franklin, W.A. Peters, J.B. Howard, Mineral matter effects on the rapid pyrolysis and hydropyrolysis of a bituminous coal. 1. Effects on yields of char, tar and light gaseous volatiles, Fuel. 61 (1982) 155–160. doi:10.1016/0016-2361(82)90227-7.
[29] J.B. Howard, Fundamentals of Coal Pyrolysis and Hydropyrolysis, in: John Wiely & sons, New York, 1981.
[30] M. Steinberg, P. Fallon, COAL PROCESSING TECHNOLOGY:-FLASH HYDROPYROLYSIS OF COAL, Chem. Eng. Prog. 75 (1979) 63–68.
[31] M. Steinberg, P.T. Fallon, M.S. Sundaram, Flash pyrolysis of biomass with reactive and non-reactive gas, Biomass. 9 (1986) 293–315. doi:10.1016/0144-4565(86)90080-6.

[32] R.. Pindoria, A. Megaritis, A.. Herod, R. Kandiyoti, A two-stage fixed-bed reactor for direct hydrotreatment of volatiles from the hydropyrolysis of biomass: effect of catalyst temperature, pressure and catalyst ageing time on product characteristics, Fuel. 77 (1998) 1715–1726. doi:10.1016/S0016-2361(98)00079-9.

[33] J. Dilcio Rocha, C. a. Luengo, C.E. Snape, The scope for generating bio-oils with relatively low oxygen contents via hydropyrolysis, Org. Geochem. 30 (1999) 1527–1534. doi:10.1016/S0146-6380(99)00124-2.

[34] T.L. Marker, L.G. Felix, M.B. Linck, M.J. Roberts, Integrated hydropyrolysis and hydroconversion (IH^2) for the direct production of gasoline and diesel fuels or blending components from biomass, Part 1: Proof of principle testing, Environ. Prog. Sustain. Energy. 31 (2012) 191–199. doi:10.1002/ep.10629.

[35] T.L. Marker, L.G. Felix, M.B. Linck, M.J. Roberts, P. Ortiz-Toral, J. Wangerow, Integrated hydropyrolysis and hydroconversion ($IH^{2®}$) for the direct production of gasoline and diesel fuels or blending components from biomass, Part 2: Continuous testing, Environ. Prog. Sustain. Energy. 33 (2014) 762–768. doi:10.1002/ep.11906.

[36] M.Z. Stummann, M. Høj, C.B. Schandel, A.B. Hansen, P. Wiwel, J. Gabrielsen, P.A. Jensen, A.D. Jensen, Hydrogen assisted catalytic biomass pyrolysis. Effect of temperature and pressure, Biomass and Bioenergy. 115 (2018) 97–107. doi:10.1016/j.biombioe.2018.04.012.

[37] E. Maleche, R. Glaser, T. Marker, D. Shonnard, A preliminary life cycle assessment of biofuels produced by the $IH^{2\ TM}$ process, Environ. Prog. Sustain. Energy. 33 (2014) 322–329. doi:10.1002/ep.11773.

[38] J. Fan, J. Gephart, T. Marker, D. Stover, B. Updike, D.R. Shonnard, Carbon Footprint Analysis of Gasoline and Diesel from Forest Residues and Corn Stover using Integrated Hydropyrolysis and Hydroconversion, ACS Sustain. Chem. Eng. 4 (2016) 284–290. doi:10.1021/acssuschemeng.5b01173.

[39] O. Winjobi, H. Tavakoli, B. Klemetsrud, R. Handler, T. Marker, M. Roberts, D. Shonnard, Carbon Footprint Analysis of Gasoline and Diesel from Forest Residues and Algae using Integrated Hydropyrolysis and Hydroconversion Plus Fischer–Tropsch (IH 2 Plus cool GTL), ACS Sustain. Chem. Eng. 6 (2018) 10766–10777. doi:10.1021/acssuschemeng.8b02091.

[40] S. Thangalazhy-Gopakumar, S. Adhikari, R.B. Gupta, M. Tu, S. Taylor, Production of hydrocarbon fuels from biomass using catalytic pyrolysis under helium and hydrogen environments., Bioresour. Technol. 102 (2011) 6742–9. doi:10.1016/j.biortech.2011.03.104.

[41] S. Thangalazhy-Gopakumar, S. Adhikari, R.B. Gupta, Catalytic pyrolysis of biomass over H^+ZSM-5 under hydrogen pressure, Energy & Fuels. 26 (2012) 5300–5306. doi:10.1021/ef3008213.

[42] O. Jan, R. Marchand, L.C.A. Anjos, G.V.S. Seufitelli, E. Nikolla, F.L.P. Resende, Hydropyrolysis of lignin using Pd/HZSM-5, Energy & Fuels. 29 (2015) 1793–1800. doi:10.1021/ef502779s.

[43] F. Melligan, M.H.B. Hayes, W. Kwapinski, J.J. Leahy, Hydro-pyrolysis of biomass and online catalytic vapor upgrading with Ni-ZSM-5 and Ni-MCM-41, Energy & Fuels. 26 (2012) 6080–6090. doi:10.1021/ef301244h.

[44] P. Choudhary, A. Malik, K.K. Pant, Mass-Scale Algal Biomass Production Using Algal Biofilm Reactor and Conversion to Energy and Chemical Precursors by Hydropyrolysis, ACS Sustain. Chem. Eng. 5 (2017) 4234–4242. doi:10.1021/acssuschemeng.7b00233.

[45] F. Melligan, M.H.B. Hayes, W. Kwapinski, J.J. Leahy, A study of hydrogen pressure during hydropyrolysis of Miscanthus x giganteus and online catalytic vapour upgrading with Ni on ZSM-5, J. Anal. Appl. Pyrolysis. 103 (2013) 369–377. doi:10.1016/j.jaap.2013.01.005.

[46] A.D. Stummann, M.Z.; Høj, M.; Schandel, C.B.; Hansen, A.B.; Wiwel, P.; Gabrielsen, J.; Jensen, P.A.; Jensen, Hydrogen assisted catalytic biomass pyrolysis. Effect of temperature and pressure, Biomass and Bioenergy. 115 (2018) 97–107. doi:10.1016/j.biombioe.2018.04.012.

[47] T.M.H. Dabros, A Step in Understanding and Optimizing Fuel Production from Solid Biomass PhD Thesis, Technical University of Denmark, Dept. of Chemical and Biochemical Engineering, 2017.

[48] C. Bouvier, Y. Romero, F. Richard, S. Brunet, Effect of H_2S and CO on the transformation of 2-ethylphenol as a model compound of bio-crude over sulfided Mo-based catalysts: propositions of promoted active sites for deoxygenation pathways based on an experimental study, Green Chem. 13

(2011) 2441–2451. doi:10.1039/c1gc15181a.
[49] V.N. Bui, D. Laurenti, P. Afanasiev, C. Geantet, Hydrodeoxygenation of guaiacol with CoMo catalysts. Part I: Promoting effect of cobalt on HDO selectivity and activity, Appl. Catal. B Environ. 101 (2011) 239–245. doi:10.1016/j.apcatb.2010.10.025.
[50] V.N. Bui, D. Laurenti, P. Delichère, C. Geantet, Hydrodeoxygenation of guaiacol. Part II: Support effect for CoMoS catalysts on HDO activity and selectivity, Appl. Catal. B Environ. 101 (2011) 246–255. doi:10.1016/j.apcatb.2010.10.031.
[51] V.O.O. Gonçalves, S. Brunet, F. Richard, Hydrodeoxygenation of cresols over Mo/Al_2O_3 and $CoMo/Al_2O_3$ sulfided catalysts, Catal. Letters. 146 (2016) 1562–1573. doi:10.1007/s10562-016-1787-5.
[52] E. Schachtl, J.S. Yoo, O.Y. Gutiérrez, F. Studt, J.A. Lercher, Impact of Ni promotion on the hydrogenation pathways of phenanthrene on MoS_2/γ-Al_2O_3, J. Catal. 352 (2017) 171–181. doi:10.1016/j.jcat.2017.05.003.
[53] B.H. Cooper, B.B.L. Donnis, Aromatic saturation of distillates: An overview, Appl. Catal. A Gen. 137 (1996) 203–223. doi:10.1016/0926-860X(95)00258-8.
[54] D.E. Resasco, B. Wang, S. Crossley, Zeolite-catalysed C–C bond forming reactions for biomass conversion to fuels and chemicals, Catal. Sci. Technol. 6 (2016) 2543–2559. doi:10.1039/C5CY02271A.
[55] P. Leflaive, J.L. Lemberton, G. Pérot, C. Mirgain, J.Y. Carriat, J.M. Colin, On the origin of sulfur impurities in fluid catalytic cracking gasoline - Reactivity of thiophene derivatives and of their possible precursors under FCC conditions, Appl. Catal. A Gen. 227 (2002) 201–215. doi:10.1016/S0926-860X(01)00936-X.
[56] Mabanaft, Sulphur free diesel BS EN 590:2013, (2015). https://www.mabanaft.com/fileadmin/content/global_content/downloads/mabanaft/Mabanaft-Ltd_Prod-Spec_Diesel.pdf (accessed August 7, 2017).
[57] A. Anca-Couce, Reaction mechanisms and multi-scale modelling of lignocellulosic biomass pyrolysis, Prog. Energy Combust. Sci. 53 (2016) 41–79. doi:10.1016/j.pecs.2015.10.002.
[58] A. Trubetskaya, P.A. Jensen, A.D. Jensen, M. Steibel, H. Spliethoff, P. Glarborg, Influence of fast pyrolysis conditions on yield and structural transformation of biomass chars, Fuel Process. Technol. 140 (2015) 205–214. doi:10.1016/j.fuproc.2015.08.034.
[59] R. Fahmi, A.V. Bridgwater, I. Donnison, N. Yates, J.M. Jones, The effect of lignin and inorganic species in biomass on pyrolysis oil yields, quality and stability, Fuel. 87 (2008) 1230–1240. doi:10.1016/j.fuel.2007.07.026.
[60] A.M. Azeez, D. Meier, J. Odermatt, T. Willner, Fast pyrolysis of African and European lignocellulosic biomasses using Py-GC/MS and fluidized bed reactor, Energy & Fuels. 24 (2010) 2078–2085. doi:10.1021/ef9012856.
[61] D.C. Dayton, J. Carpenter, J. Farmer, B. Turk, R. Gupta, Biomass hydropyrolysis in a pressurized fluidized bed reactor, Energy & Fuels. 27 (2013) 3778–3785. doi:10.1021/ef400355t.
[62] S. Meesuk, J.-P. Cao, K. Sato, Y. Ogawa, T. Takarada, Fast pyrolysis of rice husk in a fluidized bed: Effects of the gas atmosphere and catalyst on bio-oil with a relatively low content of oxygen, Energy & Fuels. 25 (2011) 4113–4121. doi:10.1021/ef200867q.
[63] P. Laurent, C. Braekman-Danheux, J.N. Rouzaud, Microtextural study of cokes from hydropyrolysis of coals, Fuel. 74 (1995) 201–207. doi:10.1016/0016-2361(95)92655-P.
[64] P. Laurent, C. Braekman-Danheux, Chemical Characterization of Hydropyrolysis Chars, Butterworth-Heinemann Ltd, 1991. doi:10.1016/B978-0-7506-0387-4.50152-2.
[65] R. Solomon P, G. Hamblen D, A. Serio m, z Yu, S. Charpenay, A characterization method and model for predicting coal conversion behaviour, Fuel. 72 (1993) 469–488. doi:DOI: 10.1016/0016-2361(93)90106-C.
[66] P.M. Mortensen, D. Gardini, H.W.P. de Carvalho, C.D. Damsgaard, J.-D. Grunwaldt, P.A. Jensen, J.B. Wagner, A.D. Jensen, Stability and resistance of nickel catalysts for hydrodeoxygenation: Carbon deposition and effects of sulfur, potassium, and chlorine in the feed, Catal. Sci. Technol. 4 (2014) 3672–3686. doi:10.1039/c4cy00522h.
[67] P.M. Mortensen, D. Gardini, C.D. Damsgaard, J.-D. Grunwaldt, P.A. Jensen, J.B. Wagner, A.D.

Jensen, Deactivation of Ni-MoS_2 by bio-oil impurities during hydrodeoxygenation of phenol and octanol, Appl. Catal. A Gen. 523 (2016) 159–170. doi:10.1016/j.apcata.2016.06.002.

[68] A. Jensen, K. Dam-Johansen, M.A. Wójtowicz, M.A. Serio, TG-FTIR study of the influence of potassium chloride on wheat straw pyrolysis, Energy & Fuels. 12 (1998) 929–938. doi:10.1021/ef980008i.

[69] P.M. Mortensen, D. Gardini, C.D. Damsgaard, J.-D. Grunwaldt, P.A. Jensen, J.B. Wagner, A.D. Jensen, Deactivation of Ni-MoS2 by bio-oil impurities during hydrodeoxygenation of phenol and octanol, Appl. Catal. A Gen. 523 (2016) 159–170. doi:10.1016/j.apcata.2016.06.002.

[70] P.M. Mortensen, H.W.P. de Carvalho, J.-D. Grunwaldt, P.A. Jensen, A.D. Jensen, Activity and stability of Mo_2C/ZrO_2 as catalyst for hydrodeoxygenation of mixtures of phenol and 1-octanol, J. Catal. 328 (2015) 208–215. doi:10.1016/j.jcat.2015.02.002.

[71] A. Jensen, K. Dam-Johansen, M. a. Wójtowicz, M. a. Serio, TG-FTIR Study of the Influence of Potassium Chloride on Wheat Straw Pyrolysis, Energy & Fuels. 12 (1998) 929–938. doi:10.1021/ef980008i.

[72] D.J.M. Hayes, Biomass Composition and Its Relevance to Biorefining, in: Role Catal. Sustain. Prod. Bio-Fuels Bio-Chemicals, Elsevier, 2013: pp. 27–65. doi:10.1016/B978-0-444-56330-9.00002-4.

[73] D.J. Hayes, An examination of biorefining processes, catalysts and challenges, Catal. Today. 145 (2009) 138–151. doi:10.1016/j.cattod.2008.04.017.

[74] Y. Sun, J. Cheng, Hydrolysis of lignocellulosic materials for ethanol production: A review, Bioresour. Technol. 83 (2002) 1–11. doi:10.1016/S0960-8524(01)00212-7.

[75] D. Mohan, C.U. Pittman, P.H. Steele, Pyrolysis of Wood / Biomass for Bio-oil : A Critical Review, Energy & Fuesl. 20 (2006) 848–889. doi:10.1021/ef0502397.

[76] R.H. Venderbosch, a. R. Ardiyanti, J. Wildschut, a. Oasmaa, H.J. Heeres, Stabilization of biomass-derived pyrolysis oils, J. Chem. Technol. Biotechnol. 85 (2010) 674–686. doi:10.1002/jctb.2354.

[77] H. Yang, R. Yan, H. Chen, D.H. Lee, C. Zheng, Characteristics of hemicellulose, cellulose and lignin pyrolysis, Fuel. 86 (2007) 1781–1788. doi:10.1016/j.fuel.2006.12.013.

[78] T. Faravelli, A. Frassoldati, G. Migliavacca, E. Ranzi, Detailed kinetic modeling of the thermal degradation of lignins, Biomass and Bioenergy. 34 (2010) 290–301. doi:10.1016/j.biombioe.2009.10.018.

[79] E. Furimsky, Characterization of deposits formed on catalyst surfaces during hydrotreatment of coal-derived liquids, Fuel Process. Technol. 6 (1982) 1–8. doi:10.1016/0378-3820(82)90036-4.

[80] E. Furimsky, F.E. Massoth, Deactivation of hydroprocessing catalysts, Catal. Today. 52 (1999) 381–495. doi:10.1016/S0920-5861(99)00096-6.

[81] M. Absi-Halabi, A. Stanislaus, D.L. Trimm, Coke formation on catalysts during the hydroprocessing of heavy oils, Appl. Catal. 72 (1991) 193–215. doi:10.1016/0166-9834(91)85053-X.

[82] E. Laurent, A. Centeno, B. Delmon, Coke Formation during the Hydrotreating of Biomass Pyrolysis Oils: Influence of Guaiacol Type Compounds, Stud. Surf. Sci. Catal. 88 (1994) 573–578. doi:10.1016/S0167-2991(08)62790-1.

[83] A. Gangadharan, M. Shen, T. Sooknoi, D.E. Resasco, R.G. Mallinson, Condensation reactions of propanal over CexZr1-xO2mixed oxide catalysts, Appl. Catal. A Gen. 385 (2010) 80–91. doi:10.1016/j.apcata.2010.06.048.

[84] R.S. Weber, M.V. Olarte, H. Wang, Modeling the kinetics of deactivation of catalysts during the upgrading of bio-oil, Energy & Fuels. 29 (2015) 273−277. doi:10.1021/ef502483t.

[85] D.C. Dayton, J. Hlebak, J.R. Carpenter, K. Wang, O.D. Mante, J.E. Peters, Biomass hydropyrolysis in a fluidized bed reactor, Energy & Fuels. 30 (2016) 4879–4887. doi:10.1021/acs.energyfuels.6b00373.

[86] D.P. Gamliel, L. Wilcox, J.A. Valla, The effects of catalyst properties on the conversion of biomass via catalytic fast hydropyrolysis, Energy & Fuels. 31 (2017) 679–687. doi:10.1021/acs.energyfuels.6b02781.

[87] K. Wang, D.C. Dayton, J.E. Peters, O.D. Mante, Reactive catalytic fast pyrolysis of biomass to produce high-quality bio-crude, Green Chem. 19 (2017) 3243–3251. doi:10.1039/C7GC01088E.

[88] D.C. Dayton, J. Hlebak, J.R. Carpenter, K. Wang, O.D. Mante, J.E. Peters, Biomass Hydropyrolysis in a Fluidized Bed Reactor, Energy & Fuels. 30 (2016) 4879–4887. doi:10.1021/acs.energyfuels.6b00373.

[89] T.N. Trinh, P.A. Jensen, D.J. Kim, N.O. Knudsen, H.R. Sørensen, S. Hvilsted, Comparison of lignin, macroalgae, wood, and straw fast pyrolysis, Energy and Fuels. 27 (2013) 1399–1409. doi:10.1021/ef301927y.

[90] X. Si, D. Xia, Y. Xiang, Y. Zhou, Effect of H2S on the transformation of 1-hexene over NiMoS/γ-Al2O3 with hydrogen, J. Nat. Gas Chem. 19 (2010) 185–188. doi:10.1016/S1003-9953(09)60054-2.

[91] J.A. gregdffds. Anabtawi, S.A. Ali, M. Abdul Bari Siddiqui, S.M. Javaid Zaidi, Factors influencing the performance of naphtha hydro-desulfurization catalysts, in: Catal. Pet. Refin. Petrochemical Ind. 1995, 1996: pp. 225–234. doi:10.1016/S0167-2991(96)80023-1.

[92] A. Fonseca, P. Zeuthen, J.B. Nagy, ^{13}C n.m.r. quantitative analysis of catalyst carbon deposits, Fuel. 75 (1996) 1363–1376.

[93] J.M. Oelderik, S.T. Sie, D. Bode, Progress in the catalysis of the upgrading of petroleum residue. A review of 25 years of R&D on Shell's residue hydroconversion technology, Appl. Catal. 47 (1989) 1–24. doi:10.1016/S0166-9834(00)83258-3.

[94] S.M. Richardson, H. Nagaishi, M.R. Gray, Initial Coke Deposition on a NiMo/γ-Al_2O_3 Bitumen Hydroprocessing Catalyst, Ind. Eng. Chem. Res. 35 (1996) 3940–3950. doi:10.1021/ie950761o.

[95] M. Von Holle, J.R. Carpenter, D.C. Dayton, Reactive catalytic fast pyrolysis process and system, WO2015038754A1, 2013.

[96] H.J. Park, Y.-K. Park, J.-I. Dong, J.-S. Kim, J.-K. Jeon, S.-S. Kim, J. Kim, B. Song, J. Park, K.-J. Lee, Pyrolysis characteristics of Oriental white oak: Kinetic study and fast pyrolysis in a fluidized bed with an improved reaction system, Fuel Process. Technol. 90 (2009) 186–195. doi:10.1016/j.fuproc.2008.08.017.

[97] M. Garcia-Perez, X.S. Wang, J. Shen, M.J. Rhodes, F. Tian, W.-J. Lee, H. Wu, C.-Z. Li, Fast pyrolysis of oil mallee woody biomass: Effect of temperature on the yield and quality of pyrolysis products, Ind. Eng. Chem. Res. 47 (2008) 1846–1854. doi:10.1021/ie071497p.

[98] W. Cai, R. Liu, Performance of a commercial-scale biomass fast pyrolysis plant for bio-oil production, Fuel. 182 (2016) 677–686. doi:10.1016/j.fuel.2016.06.030.

[99] O.D. Mante, F.A. Agblevor, S.T. Oyama, R. McClung, Catalytic pyrolysis with ZSM-5 based additive as co-catalyst to Y-zeolite in two reactor configurations, Fuel. 117 (2014) 649–659. doi:10.1016/j.fuel.2013.09.034.

[100] O.D. Mante, F. a. Agblevor, S.T. Oyama, R. McClung, The influence of recycling non-condensable gases in the fractional catalytic pyrolysis of biomass, Bioresour. Technol. 111 (2012) 482–490. doi:10.1016/j.biortech.2012.02.015.

[101] V. Paasikallio, F. Agblevor, A. Oasmaa, J. Lehto, J. Lehtonen, Catalytic pyrolysis of forest thinnings with ZSM-5 catalysts: Effect of reaction temperature on bio-oil physical properties and chemical composition, Energy and Fuels. 27 (2013) 7587–7601. doi:10.1021/ef401947f.

[102] E. Kantarelis, W. Yang, W. Blasiak, Effects of silica-supported nickel and vanadium on liquid products of catalytic steam pyrolysis of biomass, Energy and Fuels. 28 (2014) 591–599. doi:10.1021/ef401939g.

[103] E. Kantarelis, W. Yang, W. Blasiak, Effect of zeolite to binder ratio on product yields and composition during catalytic steam pyrolysis of biomass over transition metal modified HZSM5, Fuel. 122 (2014) 119–125. doi:10.1016/j.fuel.2013.12.054.

[104] V. Paasikallio, K. Kalogiannis, A. Lappas, J. Lehto, J. Lehtonen, Catalytic Fast Pyrolysis: Influencing Bio-Oil Quality with the Catalyst-to-Biomass Ratio, Energy Technol. 5 (2017) 94–103. doi:10.1002/ente.201600094.

[105] A. Imran, E.A. Bramer, K. Seshan, G. Brem, High quality bio-oil from catalytic flash pyrolysis of lignocellulosic biomass over alumina-supported sodium carbonate, Fuel Process. Technol. 127 (2014) 72–79. doi:10.1016/j.fuproc.2014.06.011.

[106] O.D. Mante, F.A. Agblevor, S.T. Oyama, R. McClung, The effect of hydrothermal treatment of FCC catalysts and ZSM-5 additives in catalytic conversion of biomass, Appl. Catal. A Gen. 445–446 (2012) 312–320. doi:10.1016/j.apcata.2012.08.039.

[107] V.K. Venkatakrishnan, W.N. Delgass, F.H. Ribeiro, R. Agrawal, Oxygen removal from intact biomass to produce liquid fuel range hydrocarbons via fast-hydropyrolysis and vapor-phase catalytic hydrodeoxygenation, Green Chem. 17 (2015) 178–183. doi:10.1039/c4gc01746c.

[108] L. Zhang, K. Gong, J. Lai, P. Alvey, Chemical composition and stability of renewable hydrocarbon products generated from a hydropyrolysis vapor upgrading process, Green Chem. 19 (2017) 3628–3641. doi:10.1039/c7gc01075c.
[109] S. Meesuk, J.-P. Cao, K. Sato, Y. Ogawa, T. Takarada, The effects of temperature on product yields and composition of bio-oils in hydropyrolysis of rice husk using nickel-loaded brown coal char catalyst, J. Anal. Appl. Pyrolysis. 94 (2012) 238–245. doi:10.1016/j.jaap.2011.12.011.
[110] S. Meesuk, J.-P. Cao, K. Sato, Y. Ogawa, T. Takarada, Study of catalytic hydropyrolysis of rice husk under nickel-loaded brown coal char, Energy & Fuels. 25 (2011) 5438–5443. doi:10.1021/ef201266b.
[111] D.C. Elliott, T.R. Hart, G.G. Neuenschwander, L.J. Rotness, A.H. Zacher, Catalytic hydroprocessing of biomass fast pyrolysis bio-oil to produce hydrocarbon products, Environ. Prog. Sustain. Energy. 28 (2009) 441–449. doi:10.1002/ep.10384.
[112] P.M. Mortensen, J.-D. Grunwaldt, P.A. Jensen, K.G. Knudsen, A.D. Jensen, A review of catalytic upgrading of bio-oil to engine fuels, Appl. Catal. A Gen. 407 (2011) 1–19. doi:10.1016/j.apcata.2011.08.046.
[113] O.D. Mante, D.C. Dayton, J. Gabrielsen, N.L. Ammitzboll, D. Barbee, S. Verdier, K. Wang, Integration of catalytic fast pyrolysis and hydroprocessing: a pathway to refinery intermediates and "drop-in" fuels from biomass, Green Chem. 18 (2016) 6123–6135. doi:10.1039/c6gc01938b.
[114] A.A. Lappas, S. Bezergianni, I.A. Vasalos, Production of biofuels via co-processing in conventional refining processes, Catal. Today. 145 (2009) 55–62. doi:10.1016/j.cattod.2008.07.001.
[115] F.A. Agblevor, O. Mante, R. McClung, S.T. Oyama, Co-processing of standard gas oil and biocrude oil to hydrocarbon fuels, Biomass and Bioenergy. 45 (2012) 130–137. doi:10.1016/j.biombioe.2012.05.024.
[116] A. de R. Pinho, M.B.B. de Almeida, F.L. Mendes, L.C. Casavechia, M.S. Talmadge, C.M. Kinchin, H.L. Chum, Fast pyrolysis oil from pinewood chips co-processing with vacuum gas oil in an FCC unit for second generation fuel production, Fuel. 188 (2017) 462–473. doi:10.1016/j.fuel.2016.10.032.
[117] F. de M. Mercader, M.J. Groeneveld, S.R.A. Kersten, N.W.J. Way, C.J. Schaverien, J.A. Hogendoorn, Production of advanced biofuels: Co-processing of upgraded pyrolysis oil in standard refinery units, Appl. Catal. B Environ. 96 (2010) 57–66. doi:10.1016/j.apcatb.2010.01.033.
[118] A. d R. Pinho, M.B.B. de Almeida, F.L. Mendes, V.L. Ximenes, L.C. Casavechia, Co-processing raw bio-oil and gasoil in an FCC Unit, Fuel Process. Technol. 131 (2015) 159–166. doi:10.1016/j.fuproc.2014.11.008.
[119] M.S. Talmadge, R.M. Baldwin, M.J. Biddy, R.L. McCormick, G.T. Beckham, G.A. Ferguson, S. Czernik, K.A. Magrini-Bair, T.D. Foust, P.D. Metelski, C. Hetrick, M.R. Nimlos, A Perspective on Oxygenated Species in the Refinery Integration of Pyrolysis Oil, Green Chem. 16 (2014) 407–453. doi:10.1039/c3Gc41951g.
[120] K. Iisa, R.J. French, K.A. Orton, A. Dutta, J.A. Schaidle, Production of low-oxygen bio-oil via ex situ catalytic fast pyrolysis and hydrotreating, Fuel. 207 (2017) 413–422. doi:10.1016/j.fuel.2017.06.098.
[121] M. Kristensen, A.B. Hansen, O.D. Mante, D.C. Dayton, S. Verdier, P. Christensen, J.H. Christensen, Complementary Analysis of the Water-Soluble and Water-Insoluble Fraction of Catalytic Fast Pyrolysis Biocrudes by Two-Dimensional Gas Chromatography, Energy and Fuels. 32 (2018) 5960–5968. doi:10.1021/acs.energyfuels.8b00415.
[122] D. Thrän, D. Peetz, K. Schaubach, Global wood pellet industry and trade study 2017. IEA Bioenergy Task 40, 2017.
[123] T. Van Nguyen, L.R. Clausen, Thermodynamic analysis of polygeneration systems based on catalytic hydropyrolysis for the production of bio-oil and fuels, Energy Convers. Manag. 171 (2018) 1617–1638. doi:10.1016/j.enconman.2018.06.024.
[124] CRI, IH^2 DEMONSTRATION FACILITY, (2018). https://www.cricatalyst.com/cricatalyst/ih2/demonstration-facility.html (accessed November 3, 2018).
[125] Eia, Gasoline and Diesel Fuel Update, (2018). https://www.eia.gov/petroleum/gasdiesel/ (accessed November 3, 2018).
[126] BIOZIN, (2018). http://biozin.no/ (accessed November 28, 2018).
[127] A.K. Starace, B.A. Black, D.D. Lee, E.C. Palmiotti, K.A. Orton, W.E. Michener, J. ten Dam, M.J.

Watson, G.T. Beckham, K.A. Magrini, C. Mukarakate, Characterization and Catalytic Upgrading of Aqueous Stream Carbon from Catalytic Fast Pyrolysis of Biomass, ACS Sustain. Chem. Eng. 5 (2017) 11761–11769. doi:10.1021/acssuschemeng.7b03344.

[128] H. Li, A. Riisager, S. Saravanamurugan, A. Pandey, R.S. Sangwan, S. Yang, R. Luque, Carbon-Increasing Catalytic Strategies for Upgrading Biomass into Energy-Intensive Fuels and Chemicals, ACS Catal. 8 (2018) 148–187. doi:10.1021/acscatal.7b02577.

[129] G. Caeiro, P. Magnoux, J.M. Lopes, F.R. Ribeiro, S.M.C. Menezes, A.F. Costa, H.S. Cerqueira, Stabilization effect of phosphorus on steamed H-MFI zeolites, Appl. Catal. A Gen. 314 (2006) 160–171. doi:10.1016/j.apcata.2006.08.016.

Chapter 10 Conclusions

Recent research has shown that catalytic hydropyrolysis of biomass is a promising technology for the production of renewable hydrocarbon fuels, however there is limited information about this process available in the open literature. This thesis investigates and optimizes the process with the objective to obtain a high yield of high quality liquid fuel. This has been done through varying the operating conditions, temperature and pressure, and testing different catalysts.

The experiments were conducted in a beech scale setup, where up to 1 kg of biomass (mainly beech wood) was continuously fed into a fluid bed catalytic hydropyrolysis reactor, where char, light gasses, water, and oil was produced. The char was removed with a filter and the vapors were either condensed directly after the filter or sent to a fixed bed hydrodeoxygenation (HDO) reactor prior to the condensation. The uncondensed vapors were analyzed with an online GC-FID/TCD every 10 minutes. The experimental time varied between 45 minutes to 4 hours, but was in most experiments about 3.5 hours. The produced organic phase was thoroughly analyzed with sulfur and oxygen specific GC-AED, GC×GC-MS/FID, simulated distillation and the determination of density, viscosity, and the elemental composition S, H, O, C (C by difference) were measured. Both commercial catalysts supplied by Haldor Topsøe and catalysts prepared at DTU were tested in the setup, and the catalysts were characterized with N_2-physisorption, NH_3-TPD, XRD, Raman spectroscopy, SEM, HAADF-STEM, and elemental analysis to gain insights into the composition and morphology of the prepared catalysts.

In the first experimental campaigns (Chapter 2 and 3) a sulfided $CoMo/MgAl_2O_4$ catalyst was used in the fluid bed reactor and a $NiMo/Al_2O_3$ catalyst in the HDO reactor, both supplied by Haldor Topsøe A/S. The reactor temperatures (at hydrogen partial pressure: 24.5-25.8 bar) and hydrogen partial pressure (at a fluid bed temperature of 450°C) were varied. The condensable organic (condensed organics and C_{4+} in the gas) yield varied between 19.0 and 22.5 wt.% daf when the fluid bed temperature was varied between 400 and 511°C Decreasing the fluid bed temperature to 365°C decreased the yield to 16.6 wt.% daf. The char yield decreased from 18.5 to 9.6 wt.% daf and the gas (C_1-C_3, CO_x) increased from 23.9 to 32.2 wt.% daf when the fluid bed temperature was increased from 365 to 511 °C. Simulated distillation of the condensed organic phase showed that it consisted of 20 to 40 vol. % naphtha and 60 to 80 vol. % diesel. However, the uncondensed C4+ organics in the gas are most likely naphtha and between 50 to 70 wt.% of the condensed organics and C_{4+} in gas are therefore naphtha. GC×GC-MS/FID showed that the concentration of aromatics was between 42 and 75 % area-FID, and oxygen specific GC-AED showed that the oxygen concentration was below 0.01 wt.% at hydrogen partial pressures above 15.9 bar. Bypassing the HDO reactor (at 25.8 bar hydrogen) increased the oxygen concentration to 1.8 wt.%. Interestingly the concentration of the aromatics was not controlled by the temperature in the HDO reactor, but mainly by the temperature in the fluid bed reactor. Comparing the aromatics concentration with thermodynamic calculations indicated that the concentration was kinetically controlled at fluid bed temperatures below 430°C, but controlled by the chemical equilibrium at higher temperatures. Decreasing the hydrogen partial pressure to 8.0 bar increased the oxygen content in the condensed organic phase to 3.3 wt.% db, and further decreasing the hydrogen partial pressure to 3.0 bar increased the oxygen content to between 6.0 and 7.8 wt.% db, depending on the total pressure, where the remaining oxygen was present in different phenols. Interestingly, the concentration of monoaromatics (not including phenols) was highest at hydrogen partial 15.9 bar, indicating that it was controlled by the kinetics for deoxygenation of phenols at lower hydrogen partial pressure and controlled by the thermodynamics at

higher hydrogen partial pressures. The char and coke yield also increased from 11.0 to 15.7 wt.% daf when the hydrogen partial pressure was decreased from 15.9 to 3.0 bar, which was most likely due to polymerization reactions. To limit the char yield the catalytic activity and the hydrogen partial pressure must be high enough to immediately stabilize the reactive oxygenates formed by pyrolysis. Likewise, the carbon content on the spent catalyst from the fluid bed reactor was close to constant at hydrogen pressures between 15.9 and 35.8 bar, but increased at lower hydrogen partial pressures, most likely due to a longer life time for the reactive oxygenates.

An initial screening of the catalysts for the catalytic hydropyrolysis reactor (temperature: 450°C) was also conducted with a $NiMo/Al_2O_3$ catalyst in the HDO reactor (370-394 °C) at a total pressure of 26 bar (Chapter 4). Using support materials $MgAl_2O_4$ and zeolite mixed with alumina (H-ZSM-5-Al_2O_3) and olivine sand gave a high char and coke yield (18.7-21.1 wt.% daf), high CO and CO_2 yield (18.9-20.0 wt.% daf) and low condensable organic yield (17.8-20.4 wt.% daf). Using supported catalysts, $CoMoS/MgAl_2O_4$ and NiMoS/H-ZSM-5-Al_2O_3, decreased the char yield to between 11.4 and 13.1 wt.%, and increased the condensable organic yield to 21.5 and 24.0 wt.% daf, respectively. The carbon content on the spent supports and olivine sand was also significantly higher than the carbon content on the spent supported catalysts. Therefore, the high char and coke yield for the supports was ascribed to their low deoxygenation activity, which increased the reactivity of the produced vapors, thus leading to an increased degree of polymerization. As an alternative to the MoS_2 based catalysts, bog iron, a cheap, non-toxic natural mineral, was tested in the fluid bed reactor both in a sulfided and reduced state and gave a condensable organic yield of 22.8 and 24.7 wt.% daf, respectively. Furthermore, the coke content on the spent bog iron was in the same range as on the spent MoS_2 based catalysts, thus the high condensable organic yield for bog iron was ascribed to its low cracking activity, but fairly moderate deoxygenation activity. The energy recovery in the condensable organics was therefore 54 % for sulfided bog iron and 58 % for reduced bog iron, but only 51 % for $CoMoS/MgAl_2O_4$ and 53-54 % for NiMo/H-ZSM-5-Al_2O_3, thus bog iron is a very interesting catalyst for the catalytic hydropyrolysis reactor. XRD and HAADF-STEM of the spent bog iron catalysts indicated that the active phase for reduced bog iron and sulfided bog iron is magnetite and pyrrhotite, respectively.

In order to get a more in-depth understanding of the difference between using a sulfided CoMo, NiMo, or Mo catalyst in the catalytic hydropyrolysis reactor the catalysts were prepared at DTU, tested at 450°C and 26 bar, with the HDO reactor bypassed (Chapter 5). The total char and coke yield was not affected by the type of catalyst, but the condensable organic yield varied between 24.3 and 26.4 wt.% daf and was highest for the Mo and lowest for the NiMo catalyst. The NiMo catalyst also had the highest hydrogenation, cracking, and decarbonylation and/or decarboxylation activity. The oxygen content in the condensed organics was between 9.0 and 12.0 wt.% db, highest for the Mo catalyst, and lowest for the CoMo catalyst. The carbon recovery in the condensable organics was therefore 39 % for both the CoMo and Mo catalyst, but 37 % for the NiMo catalyst, indicating that the CoMo catalyst is the most suitable for the catalytic hydropyrolysis reactor. The carbon content on the spent CoMo and NiMo catalyst was between 0.9 and 3.3 wt.%, but was between 5.0 and 5.5 wt.% for the spent Mo catalyst, which was ascribed to its lower deoxygenation activity. Calcium particles (40-200 nm) and potassium were detected on all the spent catalysts with STEM-EDS, showing that alkali metals are transferred from the biomass to the catalyst, which can potentially lead to deactivation.

The effect of varying the CoMo(S) loading and the support acidity for the catalyst in the fluid bed reactor was also studied at 450°C and bypassing the HDO reactor (Chapter 5). Using $MgAl_2O_4$ as support material and increasing the CoMo loading from 4.1 to 12.0 wt.% decreased the oxygen content in the condensed organic phase from 9.0 to 4.7 wt.% db, but also decreased the carbon recovery from 39 to 37 %. Using H-

ZSM-5-Al_2O_3 as support martial instead of $MgAl_2O_4$, while maintaining a CoMo loading of 4.1 wt.%, decreased the oxygen content in organic phase to between 5.2 and 6.1 wt.% db depending on zeolite to alumina ratio. However, the carbon recovery for the condensable organics was between 39 and 40 % when using H-ZSM-5-Al_2O_3 as support material. The reason for the decreased oxygen content, but constant carbon recovery was ascribed to the zeolites higher alkylation activity, which binds light oxygenates and olefins to the aromatics through alkylation. Furthermore increasing the CoMo loading increased the C_1-C_3 yield, while increasing the support acidity only increased the C_2-C_3 yield due to hydrocracking, but decreased the CH_4 yield. However, potassium was detected on all the spent catalysts, which will most likely decrease the effect of the catalysts acidity with time on stream.

In order to test the process stability a semi-continuous 5 days experiment was conducted with a CoMoS/$MgAl_2O_4$ catalyst in the fluid bed reactor and a commercial NiMo/Al_2O_3 catalyst supplied by Haldor Topsøe A/S in the HDO reactor (Chapter 7 and 8). The setup was depressurized between each day and the screw feeder was refilled and the products were collected. Approximately 5 kg beech wood was fed in total and the total time on stream was 16.2 h. The condensable organic yield was fairly constant during the experiment and varied between 21.2 and 23.2 wt.% daf, but the CO and CO_2 yield increased during the experiment from 14.9 to 18.2 wt.% daf, hence indicating an increased decarbonylation and/or decarboxylation activity. However, it could also have been due to a decreased HDO activity, which increased the lifetime of the reactive oxygenates allowing for these competing reactions to occur. The oxygen content in the condensed organic phase also increased from 40 to 2832 wt-ppm, indicating that deactivation of the catalyst in the fluid bed and HDO reactor may have occurred. During the experiment 40 wt.% of the catalyst loaded in the fluid bed reactor was lost due to entrainment, which most likely decreased the conversion of the oxygenates and thereby accelerated the deactivation of the HDO reactor. Analysis of the spent CoMo catalyst from the fluid bed reactor showed that it contained 7.2 wt.% carbon and that the concentration of carbon at the surface could be as high as 27 wt.%, which potentially could lead to pore blocking. A bulk analysis by ICP-OES of the spent catalyst also showed that it contained 0.28 wt.% calcium and 0.67 wt.% potassium. For comparison, a bulk analysis of a similar CoMo catalyst, which had only been used for 3.5 h in the fluid bed reactor, showed a carbon content of 3.7 wt.%, 0.075 wt.% calcium and 0.14 wt.% potassium. This indicates that the potassium and calcium content on the spent catalyst is proportional with the time on stream, thus proportional to the amount of biomass used, while the rate of coking decreases with time on stream. However, the possible amount of potassium transferred to the catalyst is most likely controlled by the number acidic sites, thus the potassium content will most likely stop increasing when the acidic sites are saturated.

Furthermore, in order to test the effect of potassium on the catalytic activity, a CoMoS catalyst was doped with 1.9 wt.% potassium, tested without the HDO reactor, and compared to a similar un-doped CoMoS catalyst (Chapter 7 and 8). This showed that potassium decreases the cracking and hydrogenation activity, while increasing the decarboxylation activity. Interestingly doping the catalyst with potassium only increased the oxygen content in the condensable organics from 9.0 to 9.5 wt.% db. Furthermore, doping the catalyst with potassium altered the sulfidation of the catalyst, leading to more stacking and larger slabs, which most likely lead to formation of the more active type II site. SEM images of the spent potassium doped catalyst also showed that some of the catalyst particles were encapsulated by carbon, which could be removed by attrition. Additionally, the char and coke yield also increased from 13.3 to 14.6 wt.% daf when doping the catalyst with potassium, indicating that potassium acts as a catalyst for polymerization reactions. The effect of potassium was also investigated by using wheat straw, which has a potassium content of 1.4 wt.% db, instead of beech wood, which has a potassium content of 0.12 wt.% db. However, this led to defluidization within the first 0.29 h of the experiments and analysis of the bed material from the fluid bed reactor showed that severe

agglomeration had occurred. SEM-EDS images of the agglomerates indicated that polymerization in the metaplast had taken place, which was most likely catalyzed by potassium.

In the experiments where the HDO reactor was bypassed it was observed that a significant amount of the H_2S, added to maintain the catalyst in its sulfided phase, was incorporated into the organic phase (up to 0.2 wt.%) and the sulfur content generally increased with increasing olefin concentration in the uncondensed gasses. This indicates that sulfur is incorporated through recombination reactions of H_2S with the olefins forming thiols, which can be converted into thiophenes and benzothiophenes through cyclization. This mechanism for sulfur incorporation is similar to that known from fluid catalytic cracking (FCC). The sulfur content can be decreased by decreasing the catalysts acidity or/and increasing the hydrogenation activity. It should be noted that sulfur in fossil oil is removed through hydrodesulfidation (HDS) using MoS_2 based catalysts in modern refineries, and the sulfur content was decreased to 20 wt-ppm when the HDO reactor was used, showing that hydrodesulfidation of the produced organic phase is fairly easy.

Based on the obtained results and the information available in the open literature, the most important chemical reactions in catalytic hydropyrolysis have been identified and a mechanistic model for catalytic hydropyrolysis has been proposed (Chapter 9). Additionally, catalytic hydropyrolysis has been compared with other pyrolysis technologies, such as catalytic and non-catalytic hydropyrolysis, which indicates that catalytic hydropyrolysis is a viable process for the production of renewable hydrocarbon fuels. However, the following challenges should be addressed: i) Feeding biomass under high pressure ii) Catalyst loss due to attrition and entrainment iii) Catalyst poisoning due to the transfer of alkali metals from the biomass iv) Most studies have used wood as feedstock and the effect of using different types of biomass or municipal solid waste is still not well understood v) Development of mathematical models for catalytic hydropyrolysis.

Appendix A Supplementary information for Hydrogen assisted catalytic biomass pyrolysis. Effect of temperature and pressure

Masse balances on elemental basis

An overview of the carbon, hydrogen and oxygen recovery is shown in Table A.1.

Table A.1 Mass balances on elemental basis for carbon, hydrogen and oxygen

Test	1	2	3	4	5	6	7	8	9	10	11
Carbon recovery (%)											
C_1-C_3	21.5	19.7	23.1	22.9	21.6	19.4	22.5	24.3	18.9	20.7	19.0
C_{4+}	14.2	16.8	18.9	16.9	14.5	14.4	15.1	18.8	14.4	17.1	13.9
CO+CO_2	11.4	9.3	10.1	12.7	12.5	8.2	12.1	12.7	13.3	10.3	12.6
Char	20.9	21.0	22.0	17.3	18.2	26.4	17.2	15.5	15.5	18.9	18.4
Organics	19.9	15.1	17.2	20.3	22.6	13.6	21.4	19.6	19.4	18.6	20.9
Aqueous phase	0.0	0.0	0.0	0.0	0.0	0.0	0.0	0.0	0.0	0.0	0.6
Sum	87.9	82.0	91.3	90.1	89.5	82.0	88.4	90.9	81.4	85.5	85.4
Hydrogen recovery (%)											
C_1-C_3	48.3	44.1	51.7	52.0	49.0	43.3	50.7	55.3	42.8	46.8	43.0
C_{4+}	24.0	28.3	31.8	28.4	24.5	24.3	25.5	31.6	24.2	28.7	23.3
CO+CO_2	0.0	0.0	0.0	0.0	0.0	0.0	0.0	0.0	0.0	0.0	0.0
Char	9.2	9.7	9.9	6.8	7.6	13.3	7.3	5.8	6.7	7.9	7.3
Organics	23.7	17.8	19.1	21.6	25.0	15.1	24.3	20.2	20.5	20.5	20.4
Aqueous phase	66.5	70.2	66.8	67.1	67.2	58.0	65.7	66.5	62.0	70.4	69.1
Sum	171.8	170.3	179.3	175.8	173.3	153.9	173.5	179.4	156.2	174.3	163.1
Oxygen recovery (%)											
C_1-C_3	0.0	0.0	0.0	0.0	0.0	0.0	0.0	0.0	0.0	0.0	0.0
C_{4+}	0.0	0.0	0.0	0.0	0.0	0.0	0.0	0.0	0.0	0.0	0.0
CO+CO_2	24.2	19.7	20.2	25.1	25.7	16.5	25.3	23.7	26.6	18.4	24.0
Char	6.9	7.5	7.3	5.1	5.0	9.8	5.0	3.0	6.1	6.0	5.4
Organics	0.0	0.0	0.0	0.0	0.0	0.0	0.0	0.0	0.0	0.0	0.0
Aqueous phase	72.3	76.4	72.7	73.0	73.1	63.0	71.4	72.3	67.5	76.5	75.1
Sum	103.4	103.5	100.2	103.2	103.8	89.3	101.7	99.0	100.2	100.9	104.5

GC simulated distillation curves for the condensed organics

The effect of bypassing the HDO reactor is shown in Figure A.1, where the simulated distillation curve for experiment 7 and 11 are shown. Bypassing the HDO reactor clearly increases the final boiling point of the condensed organics; this is most likely due to the increase in the oxygen content. The effect of the temperature and pressure on the simulated distillation curve is shown in Figure A.1 B and Figure A.1 C. Increasing the fluid bed temperature decreases the final boiling point, this is because more cracking takes place at higher temperatures. No significant effect of varying the pressure on the distillation curve is observed.

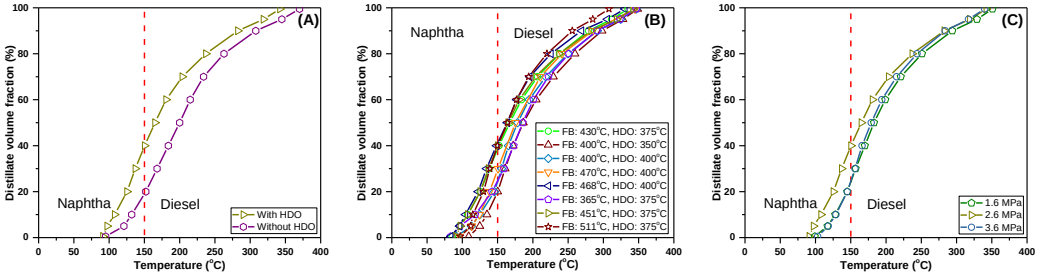

Figure A.1 GC simulated distillation curves for the condensed organics with and without HDO reactor (A), at different fluid bed and HDO reactor temperatures (B), and different total pressure (C). The curves are calculated using D86 according to ASTM D 7213 C.

Equilibrium calculations

Equilibrium concentrations were calculated using the HSC Chemistry 9 software package. GC×GC-MS shows that the produced oil is a very complex mixture and in our calculations we have therefore on the basis of the results from GC×GC-MS reduced the amount of hydrocarbons to 9 (shown in Figure A.2).

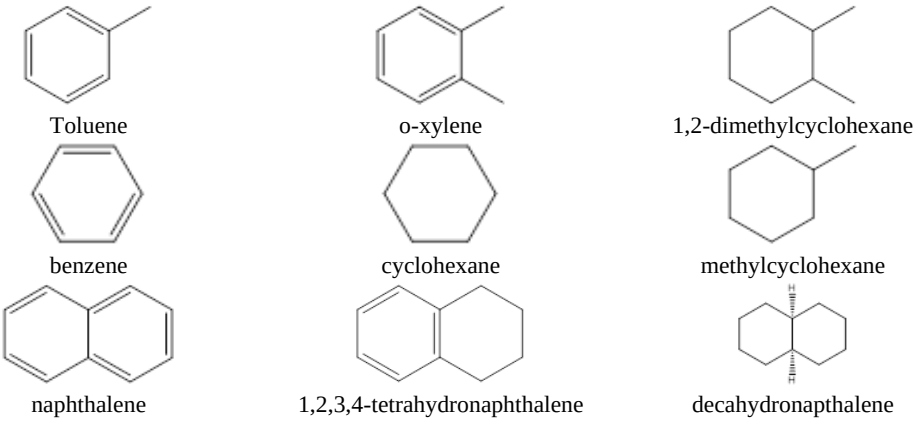

Figure A.2 Model compounds used to calculate equilibrium concentrations

The used initial molar distribution is shown in Table A.2.

Table A.2 Hydrogen free mole fraction of molecules used in equilibrium calculations

	Hydrogen free mole fraction
Benzene + cyclohexane	20 %
Toluene + methylcyclohexane	20 %
o-xylene +1,2-dimethylcyclohexane	20 %
Naphthalene+ 1,2,3,4-tetrahydronaphthalene +decahydronapthalene	40 %

The equilibrium concentration of the molecules as a function of temperature at different hydrogen partial pressures is shown in Figure A.3. The naphthenes are favored at lower temperature. At temperatures above approximately 405 ^{o}C at 99% H_2 the monoaromatics become the main components. When the hydrogen partial pressure is increased the naphthenes becomes more dominating. The fraction of diaromatics is close to zero at temperatures below 450 ^{o}C and when the gas consists of 99 % hydrogen.

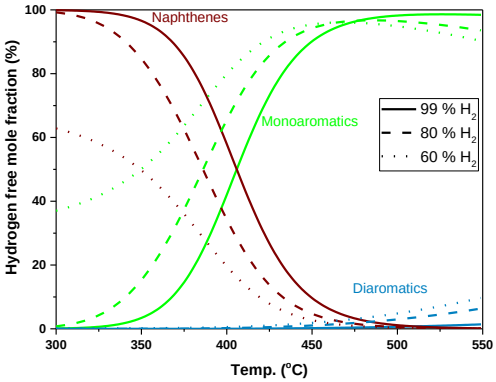

Figure A.3 The influence of temperature and hydrogen partial pressure on the equilibrium distribution between the molecules shown in Figure A.2. The calculations were conducted in HSC Chemistry 9 at 2.5 MPa.

The effect of varying the total pressure on naphthenes, monoaromatics, and diaromatics is shown in Figure A.4. The aromatics are more thermodynamically favored at a low total pressure. The monoaromatics have a maximum at 0.5 to 1 MPa. The concentration of diaromatics decreases with the total pressure and is close to zero when the pressure increases to above 1 MPa. The reason for the peak in monoaromatics is that at low pressure naphthalene is more equilibrium favorable than 1,2,3,4-tetrahydronaphthalene.

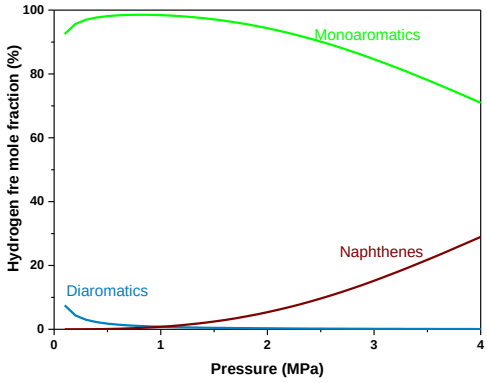

Figure A.4. The influence of the total pressure on the equilibrium distribution between the molecules shown in Figure A.2. The calculations were conducted in HSC Chemistry 9 at 450 °C with 99 % H_2 in the gas.

Chromatograms

The chromatograms for GC-AED on the condensed oil from experiment 7 and 11 are shown in **Figure A.5**. In the analysis of the condensed organics from experiment 7, 2-ethyl-phenol was used as internal standard (ISTD) and 4-fluoro-phenol was used as ISTD in the analysis of the condensed organics from experiment 11.

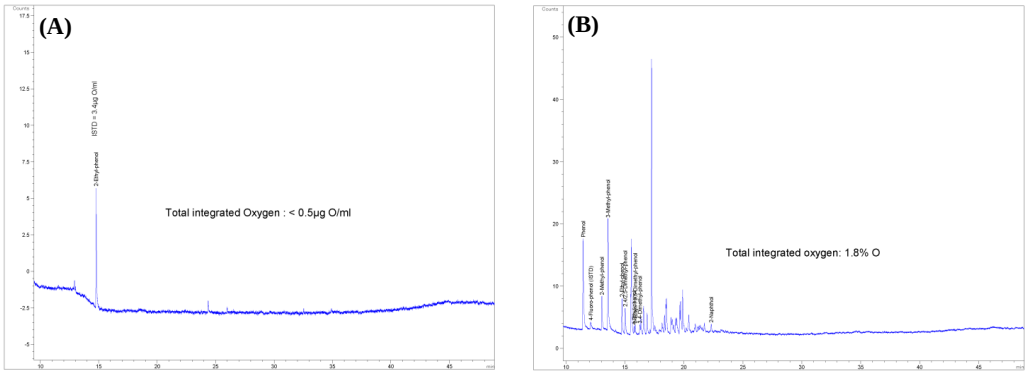

Figure A.5 Chromatograms for GC-AED of the condensed oil in experiment 7 (A) and experiment 11 (B). Conditions: Fluid bed temperature: 450 °C, HDO temperature in experiment 7: 371 °C, the HDO reactor was bypassed in experiment 11, pressure: 2.6 MPa, H_2 flow: 82-87.4, N_2 flow: 0.62-5 NL/min, biomass feeding rate: 174-250 g/h, H_2S concentration: 48-460 ppm.

Retention of organic Elements in the char

The retention of the elements is defined as:

$$Retention = \frac{element\ wt.\%\ daf\ in\ char}{element\ wt.\%\ daf\ in\ beech\ wood} \times char\ yield\ wt.\%\ daf \quad \text{(B.1)}$$

The retention of nitrogen, carbon, hydrogen and oxygen is shown in Figure A.6.

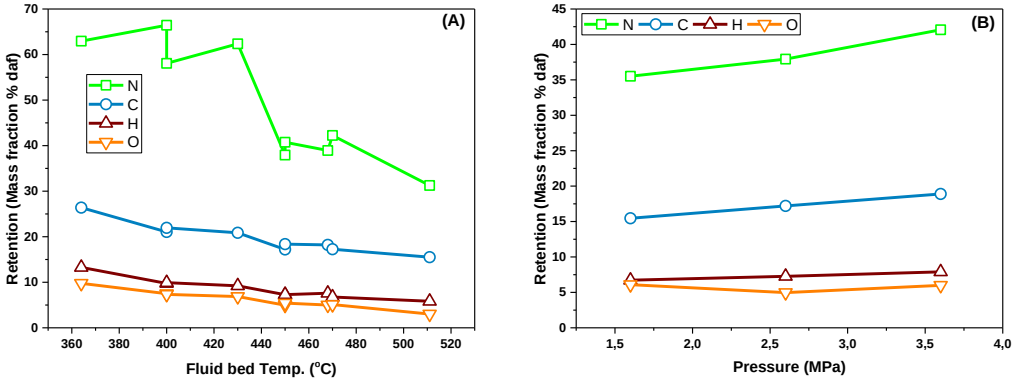

Figure A.6 Retention of nitrogen, carbon, hydrogen, and oxygen as a function fluid bed temperature (A) and pressure (B). Conditions: H_2 flow: 2.14-5.08 mole/min, N_2 flow: 0.02-0.2 mole/min, biomass feeding rate: 159-300 g/h, H_2S concentration: 0.47-4.6 $\times$ 10^{-3} mole fraction.

Gas residence time in setup

The vapor residence time in the different parts of the setup is shown in Table A.3. The first condenser was located directly after the HDO reactor, thus the residence time between these two is below 1 s.

Table A.3 Vapor residence time in setup

	Residence time
Flow screw feeder to fluid bed	~2 s
Fluid bed reaction zone	~1 s
Fluid bed disengagement zone	~2 s
Pipes between fluid bed, filter and HDO reactor	< 1 s
Filter	Up to 16 s
HDO reactor	~2 s

Appendix B Supplementary information for New insights into the effect of pressure on catalytic hydropyrolysis of biomass

Coke buildup on filter

Only a thin layer of dust (char) was located on the filter after the experiments when the hydrogen pressure was 15.9 bar or higher. However, decreasing the hydrogen pressure to below 15.9 bar increased the coke on the filter. Figure (A) shows an image of the filter after an experiment conducted at 8.2 bar, which shows a solid (coke) buildup on the filter, but not the char inlet pipe or the thermocouple. Conducting the experiment at 3.0 bar hydrogen produce a filter cake, which is approximately 5 mm thick and also a solids buildup on the char inlet pipe and thermocouple, see Figure B.1(B).

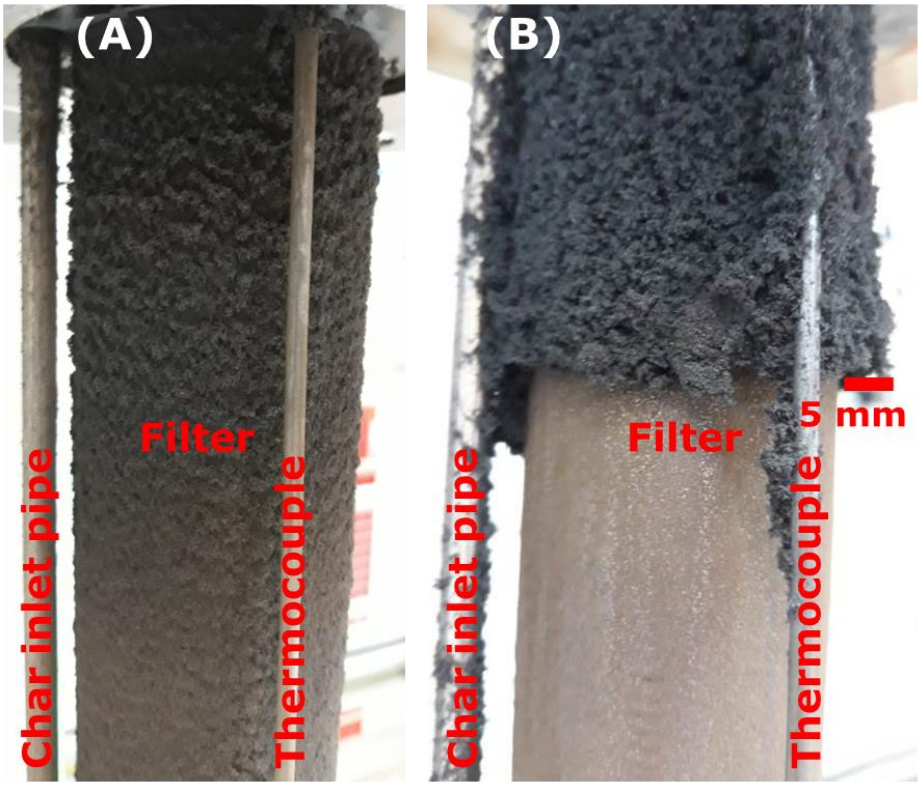

Figure B.1 Image of filter after an experiment conducted at 8.2 bar hydrogen (A) and 3.0 bar hydrogen (B). Conditions: fluid bed temperature 447-454 °C, HDO temperature: 364-386 °C, biomass feeding rate: 350-354 g/min, H_2S concentration: 464-475 ppm, H_2 flow: 11.4-30.9 NL/min, N_2 flow: 7.0-26.5 NL/min

GC×GC-FID/MS on the condensed organic phase

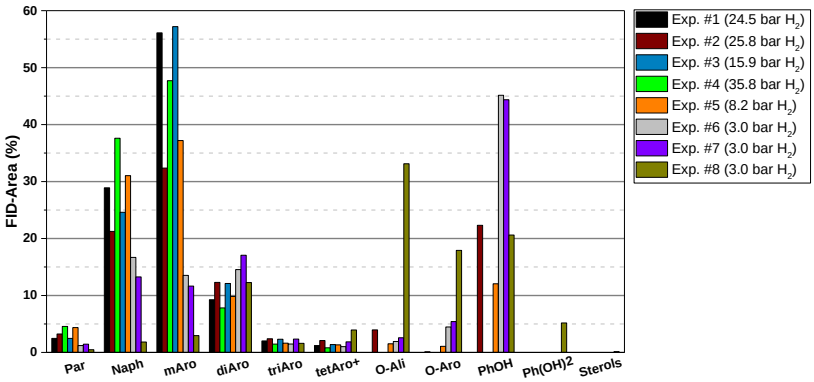

Figure B.2 Composition of the condensed organic phases. The components in the condensed organics are divided into paraffins (Par), naphthenes (Naph), monoaromatics (mAro), diaromatics (diAro), triaromatics (triAro), tetraaromatics and larger aromatics (tetAro+), oxygenated aliphatics (O-ali), phenols (PhOH), dihydroxybenzenes (Ph(OH)2), and larger oxygenated aromatics (O-aro).

Overview of sulfur containing molecules detected with sulfur specific GC-AED

Table B.1 List of detected molecules with sulfur specific GC-AED in the organic phase from experiment 1 (24.5 bar H_2)

Compound	Retention time (min)	Amount (wt-ppm S)
Unidentified	1.55	22.44
Hydrogensulfide	1.60	28.64
Methanethiol	1.98	3.32
Methylethylsulfide	6.36	10.65
Dimethyl disulfide	9.36	9.48
c-Trimethylthiophene	17.04	35.57
Benzothiophene	23.62	2.87
Unidentified	36.02	4.96
4-Methyl-DBT	36.12	48.08

Table B.2 List of detected molecules with sulfur specific GC-AED in the organic phase from experiment 5 (8.2 bar H_2)

Compound	Retention time (min)	Amount (wt-ppm S)	Compound	Retention time (min)	Amount (wt-ppm S)
Hydrogensulfide	1.45	63.70	2-Methylthiophene	10.15	6.06
Carbonylsulfide	1.50	11.30	Unidentified	11.76	2.79
2-Propanethiol	3.19	1.15	Unidentified	13.03	2.23
Unidentified	3.50	1.11	Benzothiophene	22.80	2.99
Unidentified	3.66	23.06	Dimethylbenzothiophene (a)	27.37	13.13
Unidentified	4.06	6.71	Unidentified	32.92	6.70
Thiophene	6.24	32.08			

Table B.3 List of detected molecules with sulfur specific GC-AED in the organic phase from experiment 6 (3.0 bar H_2)

Compound	Retention time (min)	Amount (wt-ppm S)	Compound	Retention time (min)	Amount (wt-ppm S)
Hydrogensulfide	1.45	16.80	Unidentified	13.77	9.00
Carbonylsulfide	1.51	3.53	a-Dimethylthiophene	13.81	8.25
Unidentified	3.67	4.13	b-Dimethylthiophene	14.15	4.92
Thiophene	6.23	250.40	a-Trimethylthiophene	16.29	2.61
Unidentified	9.46	7.44	b-Trimethylthiophene	16.45	4.58
Unidentified	9.64	2.47	d-Trimethylthiophene	16.63	1.27
2-Methylthiophene	10.10	121.83	c-Trimethylthiophene	16.80	3.01
3-Methylthiophene	10.35	26.95	e-Trimethylthiophene	17.10	2.11
Unidentified	11.76	1.61	Unidentified	19.03	2.04
Unidentified	13.01	2.45	Unidentified	19.46	2.34
2-Methyl-THT	13.40	17.41	Unidentified	32.81	2.43
3-Methyl-THT	13.57	19.75			

Table B.4 List of detected molecules with sulfur specific GC-AED in the organic phase from experiment 7 (3.0 bar H_2)

Compound	Retention time (min)	Amount (wt-ppm S)	Compound	Retention time (min)	Amount (wt-ppm S)
Hydrogensulfide	1.45	26.43	3-Methyl-THT	13.57	11.96
Carbonylsulfide	1.49	4.85	Unidentified	13.76	6.43
Unidentified	2.35	1.39	a-Dimethylthiophene	13.80	5.67
Unidentified	3.67	4.36	b-Dimethylthiophene	14.15	3.37
Methylethylsulfide	6.10	14.59	a-Trimethylthiophene	16.29	2.20
Thiophene	6.23	166.19	b-Trimethylthiophene	16.45	3.00
Unidentified	9.46	2.31	d-Trimethylthiophene	16.63	1.38
2-Methylthiophene	10.10	70.74	c-Trimethylthiophene	16.80	2.73
3-Methylthiophene	10.35	17.31	e-Trimethylthiophene	17.10	1.54
2-Methyl-THT	13.40	11.84			

Table B.5 List of detected molecules with sulfur specific GC-AED in the organic phase from experiment 8 (3.0 bar H_2, HDO reactor bypassed)

Compound	Retention time (min)	Amount (wt-ppm S)	Compound	Retention time (min)	Amount (wt-ppm S)
Hydrogensulfide	1.45	231.82	a-Dimethylthiophene	13.79	4.20
Unidentified	1.85	20.23	b-Dimethylthiophene	14.13	3.58
Unidentified	2.35	9.19	c-Dimethylthiophene	14.45	12.20
Thiophene	6.22	73.60	Dimethyl-THT	15.32	6.54
Unidentified	9.54	4.28	b-Trimethylthiophene	16.43	7.78
2-Methylthiophene	10.07	42.22	a-Trimethylthiophene	16.58	17.87
Unidentified	10.29	1.51	c-Trimethylthiophene	16.72	15.90
3-Methylthiophene	10.36	13.59	d-Trimethylthiophene	16.94	3.75
Unidentified	11.15	6.59	Unidentified	18.05	9.69
Unidentified	11.86	23.20	Unidentified	19.18	4.61
Unidentified	13.22	18.86	Unidentified	19.53	9.49
2-Methyl-THT	13.37	9.49	Unidentified	19.77	11.82
3-Methyl-THT	13.55	8.57	Methylbenzothiophene (a)	25.27	5.01
Unidentified	13.74	5.67			

Overview of hydrocarbons detected in the aqueous phase with GC-MS/FID

Table B.6 List of detected molecules with GC-MS/FID in the aqueous phase from experiment 2 (24.5 bar H_2, HDO reactor bypassed)

Compound	Retention time (min)	Area-FID (%)	Compound	Retention time (min)	Area-FID (%)
Methanol	2.47	9.70	1-butanol	3.28	1.69
Ethanol	2.55	32.82	Ethylene glycol	3.55	0.61
Acetone	2.62	13.94	Cyclopentanone	4.60	1.02
1-Propanol	2.78	5.20	Phenol	8.66	26.60
2-Butanone	2.94	3.51	3-methyl phenol	10.33	1.15
2-Me-1-PrOH	3.06	0.43	Unidentified	10.74	1.41

Table B.7 List of detected molecules with GC-MS/FID in the aqueous phase from experiment 5 (8.2 bar H_2)

Compound	Retention time (min)	Area-FID (%)	Compound	Retention time (min)	Area-FID (%)
Acetone	2.62	0.46	Unidentified	15.95	2.88
Unidentified	4.15	0.25	Unidentified	16.04	1.77
Phenol	8.62	11.99	Unidentified	16.23	6.83
Unidentified	9.38	1.17	Unidentified	16.53	2.88
Unidentified	9.64	1.83	Unidentified	16.70	2.99
Cresol	10.23	2.05	Unidentified	16.86	2.21
Cresol	10.61	2.55	Unidentified	17.04	1.91
2 ethyl phenol	10.88	0.08	Unidentified	17.24	0.67
Unidentified	11.38	0.38	Unidentified	17.31	0.70
Unidentified	11.51	0.76	Unidentified	17.42	0.58
Unidentified	11.74	0.32	Unidentified	17.49	0.41
Unidentified	12.05	1.58	Unidentified	17.72	3.82
Unidentified	12.23	2.47	Unidentified	17.94	1.68
Unidentified	12.34	0.58	Unidentified	18.13	4.20
Unidentified	12.43	0.30	Unidentified	18.27	4.44
Unidentified	12.54	0.37	Unidentified	18.56	2.18
Unidentified	12.66	0.37	Unidentified	18.72	1.62
Unidentified	12.90	0.64	Unidentified	18.91	3.55
Unidentified	13.05	0.54	Unidentified	19.13	1.34
Unidentified	13.15	0.35	Unidentified	19.24	0.94
Unidentified	13.32	0.09	Unidentified	19.44	1.18
Unidentified	13.38	0.09	Unidentified	19.59	2.64
Unidentified	13.58	0.28	Unidentified	19.95	1.23
Unidentified	13.66	0.18	Unidentified	20.09	1.31
Unidentified	13.80	0.18	Unidentified	20.25	1.51
Unidentified	13.91	0.12	Unidentified	20.48	0.58
Unidentified	14.40	0.12	Unidentified	20.58	0.61
Unidentified	14.58	0.48	Unidentified	20.70	0.25
Unidentified	14.78	0.82	Unidentified	20.82	1.06
Unidentified	15.33	0.13	Unidentified	20.93	1.68
Unidentified	15.53	0.43	Unidentified	21.08	2.92
Unidentified	15.63	0.81	Unidentified	21.34	2.62
Unidentified	15.69	0.62	Unidentified	21.55	0.61
Unidentified	15.83	0.51	Unidentified	21.80	0.28

Table B.8 List of detected molecules with GC-MS/FID in the aqueous phase from experiment 6 (3.0 bar H_2)

Compound	Retention time (min)	Area-FID (%)	Compound	Retention time (min)	Area-FID (%)
Ethanol	2.54	1.41	Unidentified	15.24	2.64
Acetone	2.61	9.71	Unidentified	15.64	1.98
Aceic acid	2.82	1.13	Unidentified	15.94	3.27
2-Butanone	2.92	1.79	Unidentified	16.27	4.06
Cyclopentaone	4.72	0.15	Unidentified	16.45	0.58
Phenol	8.61	12.01	Unidentified	16.54	1.74
Cresol	10.22	1.85	Unidentified	16.81	3.45
Cresol	10.61	3.61	Unidentified	17.13	3.00
2-ethyl phenol	11.75	0.88	Unidentified	17.42	4.26
Unidentified	11.95	0.58	Unidentified	17.62	1.03
3-ethyl phenol	12.25	0.45	Unidentified	17.71	2.63
3.4-dimethyl phenol	12.66	0.25	Unidentified	18.06	2.59
Unidentified	13.25	2.13	Unidentified	18.41	2.45
Unidentified	13.67	1.88	Unidentified	18.79	2.03
Unidentified	13.90	0.56	Unidentified	19.19	1.73
Unidentified	14.01	0.53	Unidentified	19.66	1.67
Unidentified	14.17	1.24	Unidentified	20.16	1.91
Unidentified	14.35	1.45	Unidentified	20.57	2.45
Unidentified	14.55	4.04	Unidentified	21.12	3.09
Unidentified	14.76	0.78	Unidentified	21.34	0.35
Unidentified	14.89	1.52	Unidentified	21.61	1.83
Unidentified	14.97	1.72	Unidentified	21.77	0.95
Unidentified	15.11	0.67			

Table B.9 List of detected molecules with GC-MS/FID in the aqueous phase from experiment 7 (3.0 bar H_2)

Compound	Retention time (min)	Area-FID (%)	Compound	Retention time (min)	Area-FID (%)
Ethanol	2.54	7.40	Unidentified	13.33	0.29
Acetone	2.61	9.43	Unidentified	15.20	0.37
1-propanol	2.77	0.44	Unidentified	15.36	0.42
acetic acid	2.83	11.53	Unidentified	15.47	0.49
Unidentified	2.92	3.10	Unidentified	15.58	0.44
Propanoic acid	3.34	0.75	Unidentified	15.77	0.69
Unidentified	4.16	0.32	Unidentified	16.49	0.73
Butanoic acid	4.27	0.34	Unidentified	16.66	2.58
Cyclopentanon	4.72	0.69	Unidentified	17.06	1.49
2-methyl cyclopentanon	5.61	0.11	Unidentified	17.43	1.63
phenol	8.62	27.25	Unidentified	17.84	0.70
Cresol	10.22	4.99	Unidentified	18.23	1.21
Cresol	10.61	8.32	Unidentified	19.17	2.94
2-ethyl phenol	11.75	0.88	Unidentified	19.59	3.29
2.5-dimethyl phenol	11.95	1.28	Unidentified	20.08	1.00
3-ethyl phenol	12.24	1.63	Unidentified	20.90	0.32
2.3-dimethyl phenol	12.44	0.51	Unidentified	21.11	0.36
3.4-dimethylphenol	12.66	0.36	Unidentified	21.72	1.74

Table B.10 List of detected molecules with GC-MS/FID in the aqueous phase from experiment 8 (3.0 bar H_2, HDO reactor bypassed)

Compound	Retention time (min)	Area-FID (%)	Compound	Retention time (min)	Area-FID (%)
Methanol	2.45	6.00	Unidentified	12.10	0.12
Ehanol	2.53	1.46	3-ethyl phenol	12.23	0.22
Acetone	2.61	2.11	Unidentified	12.34	0.04
Methyl acetate	2.69	0.59	Unidentified	12.43	0.15
Acetic acid	2.91	27.03	1,2-Benznediol	12.68	1.55
2-Propanon	3.29	7.24	Unidentified	12.97	0.44
Propanoic acid	3.38	1.56	Unidentified	13.26	1.48
Ethylene glycol	3.48	0.97	1,3-Cyclopentanedione	13.38	0.41
2-Butanone	3.65	0.79	Unidentified	13.46	0.30
2-methyl propanoic acid	3.90	0.22	Unidentified	13.56	0.17
3-Penten-2-one	3.96	0.17	Unidentified	13.68	0.80
Propanal	4.15	0.19	Unidentified	13.75	1.37
Glycolic acid	4.26	0.45	Unidentified	13.98	0.77
1-Hydroxy2-butanone	4.31	2.27	Unidentified	14.14	0.17
Unidentified	4.46	1.07	Unidentified	14.20	0.28
Unidentified	4.56	0.24	Unidentified	14.38	0.26
Cyclopentanone	4.71	2.90	Unidentified	14.48	0.32
Unidentified	4.91	0.22	Unidentified	14.63	0.37
Unidentified	5.01	0.08	Phenol, 2,6-dimethoxy	14.81	1.01
4-hydroxy-2-petanone	5.15	0.26	Unidentified	15.00	0.43
2-cyclopentene-1-one	5.44	5.60	Unidentified	15.16	0.46
2-methyl cyclopentanone	5.60	0.36	Unidentified	15.28	0.20
3-methylcyclopentanone	5.72	0.13	Unidentified	15.37	0.10
3-methyl 2 heptanone	5.81	0.62	Unidentified	15.46	0.27
2-propanone, 1-(acetyloxy)	5.93	0.27	Unidentified	15.53	0.29
Pentanoic acid	6.04	0.28	Unidentified	15.67	0.23
2-cyclopenene-1-one, 3-methyl	6.19	0.21	Unidentified	15.88	0.56
Unidentified	6.35	0.11	Unidentified	16.01	0.27
2H-Pyran-3(4H)-one, dihydro	6.48	0.13	Unidentified	16.17	0.15
2-Furanol, tetrahydro-2-methyl	6.57	0.13	Beta-D-glucopyranose	16.40	2.78
Furan, tetrahydro-2.5-dimethyloxy	6.73	0.09	Unidentified	16.58	0.33
Cyclohexanone	6.83	0.06	Unidentified	16.70	0.26
Unidentified	6.92	0.75	Unidentified	16.77	0.11
2-cyclopeten-1-one, 2-methyl	7.06	0.84	Unidentified	16.83	0.20
Unidentified	7.17	1.58	Unidentified	16.92	0.52
1.2-cyclopentanedione	7.42	1.45	Unidentified	17.09	0.10
2(5H)-Furanone, 5-methyl	7.77	0.45	Unidentified	17.17	0.12
Unidentified	7.97	0.08	Unidentified	17.29	0.19
Unidentified	8.04	0.06	Unidentified	17.38	0.25
2(3H)-Furanone, dihydro-5-methyl	8.12	0.19	Unidentified	17.46	0.10

Unidentified	8.23	0.18	Unidentified	17.54	0.10
2-Cyclopenten-1-one, 3-methyl	8.44	0.92	Unidentified	17.64	0.13
Phenol	8.62	0.62	Unidentified	17.74	0.13
Unidentified	8.71	0.34	Unidentified	17.85	0.23
Unidentified	8.92	0.14	Unidentified	18.02	0.21
2-Cyclopentn-1-one, 3,4-dimethyl	9.06	0.08	Unidentified	18.12	0.21
Unidentified	9.18	0.41	Unidentified	18.23	0.08
Unidentified	9.48	0.06	Unidentified	18.30	0.11
Unidentified	9.54	0.09	Unidentified	18.47	0.24
1,2-Cyclopentanedione, 3-methyl	9.75	1.71	Unidentified	18.61	0.10
Unidentified	10.04	0.53	Unidentified	18.73	0.11
Unidentified	10.11	0.21	Unidentified	18.86	0.20
cresol	10.22	0.29	Unidentified	18.96	0.07
Unidentified	10.32	0.22	Unidentified	19.04	0.12
Furan, tetrahydro-2-methyl	10.40	0.17	Unidentified	19.21	0.19
Unidentified	10.51	0.11	Unidentified	19.34	0.09
cresol	10.61	0.58	Unidentified	19.44	0.12
Unidentified	10.81	0.45	Unidentified	19.63	0.09
Unidentified	10.92	0.11	Unidentified	19.76	0.07
Phenol, 4 methoxy	11.02	0.26	Unidentified	19.83	0.08
Unidentified	11.08	0.33	Unidentified	20.06	0.22
Unidentified	11.19	0.18	Unidentified	20.45	0.06
Unidentified	11.29	0.19	Unidentified	20.62	0.14
Unidentified	11.42	0.19	Unidentified	20.80	0.04
2-Cyclopenten-1-one, 3-ethyl-2-hydroxy	11.51	0.35	Unidentified	20.86	0.04
Unidentified	11.69	0.30	Unidentified	21.09	0.04
Unidentified	11.91	0.33	Unidentified	21.43	0.11

Scanning Electron Microscopy

Table B.11 Carbon content measured with EDS at different acceleration voltages on fresh catalyst and spent catalysts

	3 kV	5 kV	10 kV	15 kV
Fresh Catalyst	3.3	3.9	4.6	5.0
Spent catalysts				
Exp. #1 (24.5 bar H_2)	10.5	9.7	11.2	10.5
Exp. #2 (25.8 bar H_2)	11.2	10.4	10.1	11.2
Exp. #3 (15.9 bar H_2)	7.8	8.1	9.0	9.8
Exp. #4 (35.8 bar H_2)	7.6	8.1	9.4	11.0
Exp. #5 (8.2 bar H_2)	14.4	15.2	14.5	13.8
Exp. #6 (3.0 bar H_2)	17.1	17.9	17.4	17.2
Exp. #7 (3.0 bar H_2)	24.1	22.6	21.6	21.0
Exp. #8 (3.0 bar H_2)	28.9	26.4	25.8	25.7

In order to account for the carbon measured from the background the carbon content on the spent catalyst are calculated from equation S.1 and the carbon content is shown as function of the acceleration voltage in

$$\text{Carbon content} = C_{\text{on spent catalyst}} - C_{\text{on fresh catalyst}} \tag{B.1}$$

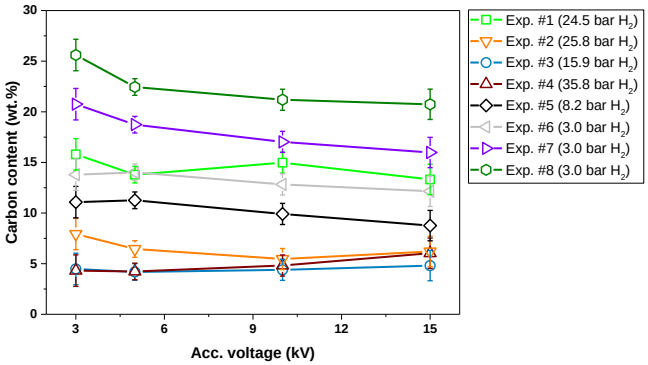

Figure B.3 Carbon content on the spent catalysts measured as a function of the acceleration voltage.

Appendix C Supplementary information for: Effect of the catalyst in fluid bed catalytic hydropyrolysis

Catalyst composition and particle size

The concentration of Al, Ca, Cr, Fe, Mg, Mn, Ni, Si of olivine was measured with inductively coupled plasma optical emission spectroscopy (ICP-OES) and the result is shown in Table C.1.

Table C.1 Composition of olivine sand

Al	0.156	wt.%
Ca	160	ppm
Cr	0.137	wt.%
Fe	5.01	wt.%
Mg	27.6	wt.%
Mn	760	ppm
Ni	0.283	wt.%
Si	19.0	wt.%

The chemical and physical properties reported by LKAB minerals is shown in Table C.2 and shows that olivine sand mainly consists of MgO and SiO_2.

Table C.2 Chemical and physical properties of olivine sand F grade supplied by LKAB minerals

Chemical properties		
MgO	50.03	wt.%
SiO_2	41.58	wt.%
Fe_2O_3	7.21	wt.%
Al_2O_3	0.41	wt.%
Cr_2O_3	0.19	wt.%
Mn_3O_4	0.10	wt.%
CaO	0.06	wt.%
Physical properties		
Total moisture	≤0.5	%
Bulk Density	1700-1900	kg/m^3
pH	8.9-9.5	
Hardness	6.5-7.0	Mohs

The concentration of As, Fe, Ni, P, Si, Al, Ca, and K in bog iron is shown in Table C.3.

Table C.3 Elemental composition of bog iron

As	140 ppm
Fe	46.4 wt.%
Ni	<10 ppm
P	0.708 wt.%
Si	1.57 wt.%
Al	0.246 wt.%
Ca	0.653 wt.%
K	110 ppm

The particle size and surface area of the used catalysts are shown in Table C.4.

Table C.4 Particle size and surface area

	CoMo	MgAl	OS	BI	ZA	NiMoZA
Particle size (µm)	180-355	180-355	106-212	150-300	180-355	180-355
Surface area (m^2/g)	ND	83	0.6	121	ND	ND

Scanning Electron Microscopy

The reproducibility of the EDS measurement was tested on the spent NiMoZA catalysts from experiment 10 and 11 by measuring the carbon content at different acceleration voltages on 3 different spent catalyst particles from each experiment, see Figure C.1.

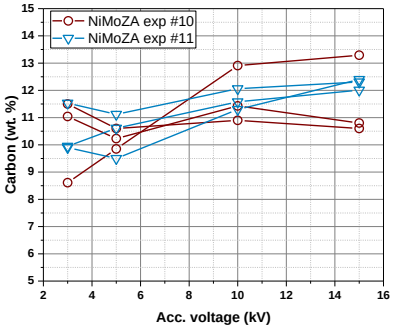

Figure C.1 Carbon content as a function of acceleration voltage on the spent NiMoZA catalysts. (Fluid bed temperature: 453 °C, HDO temperature: 370 °C, pressure: 26 bar, biomass feeding rate: 277 g/h, H_2S concentration: 462 ppm, H_2 flow: 60 NL/min, N_2 flow: 5 NL/min)

The mean and standard deviation of the carbon content on the two spent NiMoZA catalysts are shown in Table C.5. The highest standard deviation observed is 1.55 wt.% at 3 kV for the NiMoZA from experiment 10, which shows that the results are fairly reproducible. Furthermore, the similar carbon content on the two different catalysts also shows the catalytic hydropyrolysis experiments are reproducible.

Table C.5 Mean and standard deviation on the carbon content at different accelerations voltages on the spent NiMoZA catalysts from experiment 10 and 11. (Fluid bed temperature: 453 °C, HDO temperature: 370 °C, pressure: 26 bar, biomass feeding rate: 277 g/h, H_2S concentration: 462 ppm, H_2 flow: 60 NL/min, N_2 flow: 5 NL/min)

	Mean (wt.%)		Standard deviation (wt.%-points)	
Acc. Voltage (kV)	**NiMoZA exp #10**	**NiMoZA exp #11**	**NiMoZA exp #10**	**NiMoZA exp #11**
15	11.6	12.2	1.50	0.20
10	11.7	11.6	1.04	0.38
5	11.1	10.4	0.37	0.82
3	11.5	10.5	1.55	0.93

The measured carbon content on the fresh and spent catalysts are shown in Table C.6.

Table C.6 Carbon content measured with EDS at different acceleration voltages on fresh and spent catalysts

		3 kV	5 kV	10 kV	15 kV
Fresh catalysts					
CoMo		3.3	3.9	4.6	5.0
MgAl		2.6	2.5	2.6	3.6
OS		7.1	5.3	4.9	5.6
BI		7.6	7.5	8.9	10.0
ZA		6.4	6.6	6.6	6.1
NiMoZA		7.5	6.7	6.0	6.1
Spent catalysts					
CoMo	exp #1	10.5	9.7	11.2	10.5
CoMo	exp #2	11.2	10.4	10.1	11.2
MgAl	exp #3	70.5	60.3	52.6	53.0
OS	exp #4	79.4	49.2	31.9	29.0
BI-S	exp #5	12.7	12.7	11.6	11.9
BI-S	exp #6	11.6	10.7	10.4	10.6
BI-R	exp #7	15.1	15.7	11.9	13.4
BI-R	exp #8	18.5	16.5	16.4	19.2
ZA	exp #9	51.1	44.7	42.5	42.0
NiMoZA	exp #10.1	11.5	10.6	10.9	10.6
NiMoZA	exp #10.2	8.6	9.9	12.9	13.3
NiMoZA	exp #10.3	11.0	10.2	11.4	10.8
NiMoZA	exp #11.1	9.9	9.5	11.3	12.4
NiMoZA	exp #11.2	10.0	10.6	11.6	12.0
NiMoZA	exp #11.3	11.5	11.1	12.1	12.3
ZA	exp #12	25.9	25.2	26.8	27.4

Element mapping (STEM-EDS) of sulfided and reduced bog iron

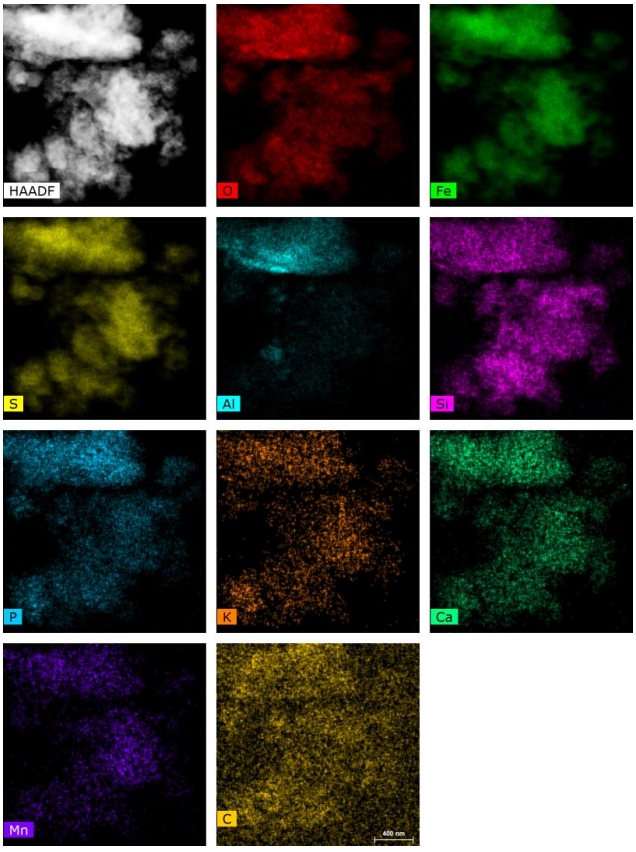

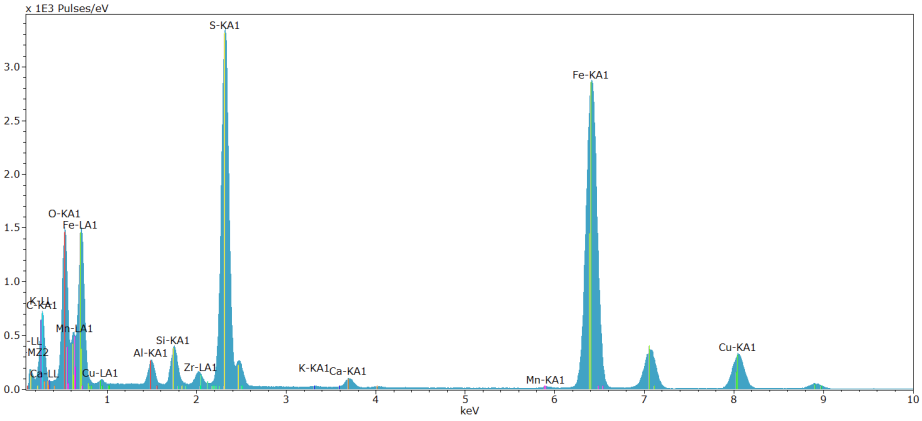

Figure C.2 STEM-HAADF micrograph and EDS element distribution on BI-S (experiment 6) using the Kα-lines, respectively, from the EDS spectrum. The Cu and C signal are expected from the carbon coated Cu-TEM grid and the Zr-peak is attributed to a system peak.

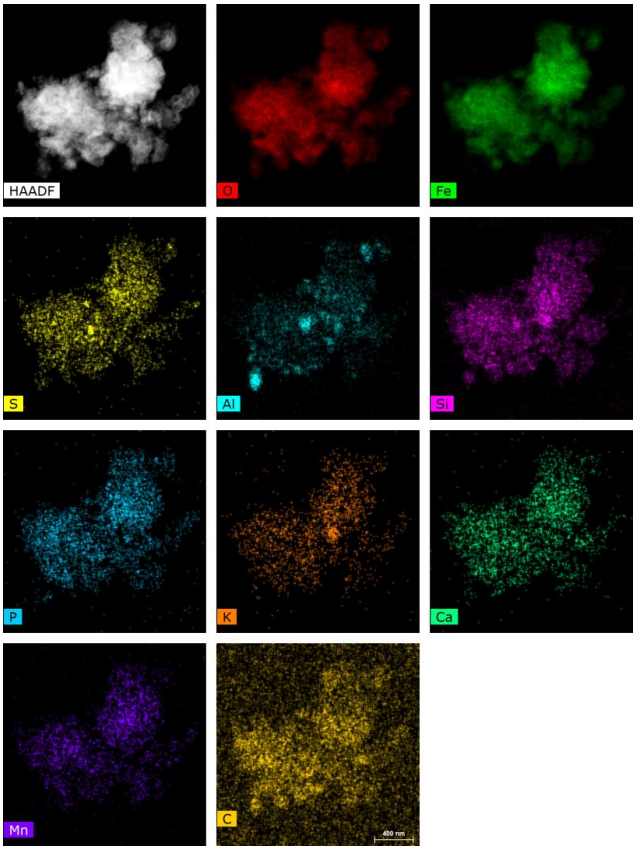

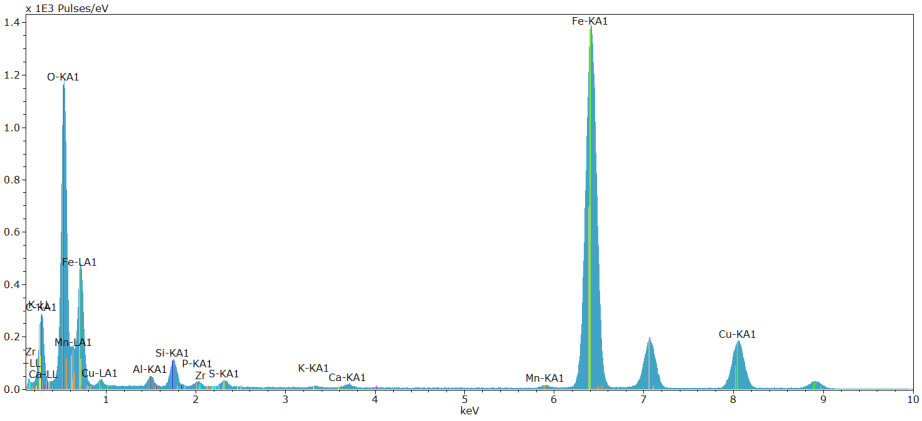

Figure C.3 STEM-HAADF micrograph and EDX element distribution on BI-R (experiment 8) using the Kα-lines, respectively, from the EDS spectrum. The Cu and C signal are expected from the carbon coated Cu-TEM grid and the Zr-peak is attributed to a system peak.

Effect of start of biomass feeding on the fluid bed temperature

The effect of starting the biomass feeding on the fluid bed temperature is shown for the different experiments in Figure C.4. The fluid bed temperature decreased in experiment 3 and 4 where MgAl and OS were used as bed material, respectively, while it increased in the remaining experiments indicating exothermic HDO reactions.

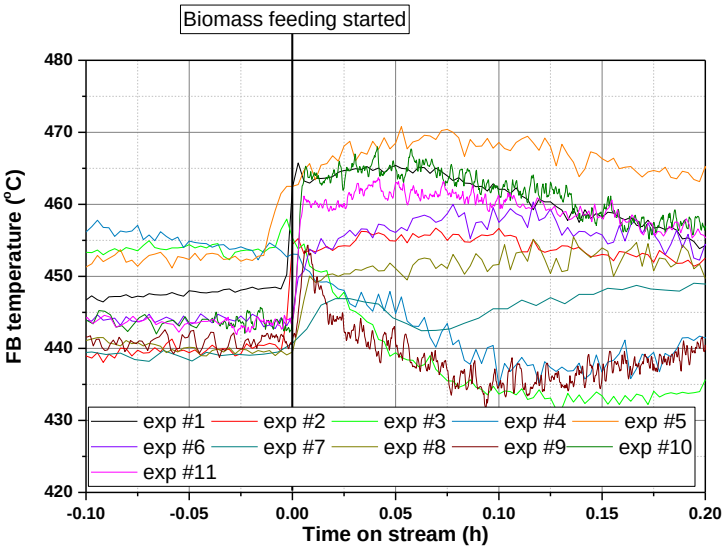

Figure C.4 Effect of start of biomass feeding on the fluid bed temperature. (Fluid bed temperature: 443-454 °C, HDO temperature: 370-394 °C, pressure: 26 bar, biomass feeding rate: 174-302 g/h, H_2S concentration: 0-471 ppm, H_2 flow: 54.4-89.2NL/min, N_2 flow: 0.62-5 NL/min)

Carbon Balance

The carbon balances for the conducted experiments are shown in Table C.7.

Table C.7 Carbon balance

Test:	1	2	3	4	5	6	7	8	9	10	11
Yields (%)											
C_1-C_3	22.5	19.0	14.1	14.1	17.6	7.8	18.2	5.8	13.5	20.9	20.9
CO+CO_2	12.1	12.6	13.2	12.9	9.8	9.7	9.1	9.0	13.8	11.3	11.7
Char and coke	17.2	18.4	ND	ND	ND	ND	ND	ND	ND	ND	ND
Aqueous phase	0.012	0.96	0.0032	0.0028	0.0043	6.8	0.0099	4.8	0.12	0.033	0.044
Organics phase	21.4	20.9	19.9	15.3	26.0	27.5	26.1	42.84	23.5	25.7	24.6
C_{4+} in the gas	15.2	13.9	10.6	11.4	13.2	5.2	16.5	5.3	9.8	13.7	15.0
Organics + C_{4+}	36.5	34.8	30.5	28.8	39.2	32.7	42.6	47.4	33.3	39.3	39.6

Gas Composition

The detailed gas compositions are shown in Table C.8. Only paraffins were observed in the gas when the HDO reactor was.

Table C.8 Detailed gas compositions

Experiment:	1	2	3	4	5	6	7	8	9	10	11
Yields (wt.% daf)											
C_1	4.6	4.0	3.0	3.1	3.7	2.5	3.5	1.9	2.9	3.1	3.2
C_2	5.7	4.8	3.3	3.1	4.1	1.1	4.0	0.7	3.3	5.3	5.2
C_3	4.1	3.3	2.7	2.7	3.5	0.7	4.1	0.6	2.4	4.9	4.9
C_4	3.0	2.4	2.2	2.3	2.7	0.7	3.0	0.5	2.2	3.6	3.7
C_5	1.9	1.7	1.4	1.5	1.4	0.6	1.6	0.6	0.9	1.4	1.5
C_{6+}	4.3	4.3	2.8	4.4	3.4	1.8	5.4	2.0	2.8	3.2	3.8
CO	9.0	5.7	9.4	8.8	7.5	5.1	6.4	4.3	9.3	7.5	7.8
CO_2	8.1	3.1	9.5	9.9	6.5	9.9	6.7	9.9	10.8	8.9	9.1

GC×GC-FID on Condensed Organic Phase

The composition of the condensed organics from the experiments with the HDO reactor is shown in Figure C.5.

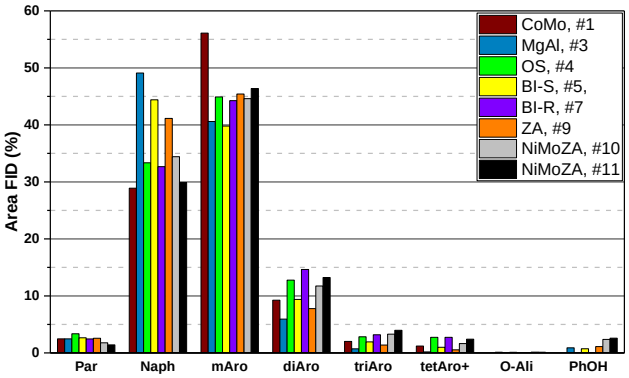

Figure C.5 The composition of the condensed organic phase from the experiments with the HDO reactor. The components in the condensed organics is divided into paraffins (Par), naphthenes (Naph), monoaromatics (mAro), diaromatics (diAro), triaromatics (triAro), tetraaromatics and larger aromatics (tetAro+), oxygenated aliphatics (O-Ali), phenols (PhOH), and oxygenated aromatics (ArOH). (Fluid bed temperature: 443-454 °C, HDO temperature: 370-394 °C, pressure: 26 bar, biomass feeding rate: 174-302 g/h, H_2S concentration: 0-471 ppm, H_2 flow: 54.4-89.2NL/min, N_2 flow: 0.62-5 NL/min)

The molecular size distribution based on number of carbon atoms is shown in Figure C.6 for the condensed organics from the experiments with the HDO reactor.

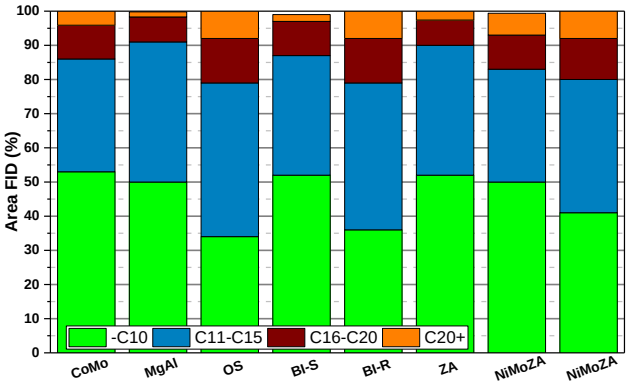

Figure C.6 Relative number of carbon atoms in the molecules in the condensed organics from the experiments with the HDO reactor. The number of carbon atoms in the condensed organics is divided into less than 10 carbon atoms (-C10), between 11 and 15 carbon atoms (C10-C15), between 16 and 20 carbon atoms (C15-C20), and more than 20 carbon atoms (C20+). (Fluid bed temperature: 443-454 °C, HDO temperature: 370-394 °C, pressure: 26 bar, biomass feeding rate: 174-302 g/h, H_2S concentration: 0-471 ppm, H_2 flow: 54.4-89.2NL/min, N_2 flow: 0.62-5 NL/min)

The effect of bypassing the HDO reactor on the composition of the condensed organics is shown in Figure C.7.

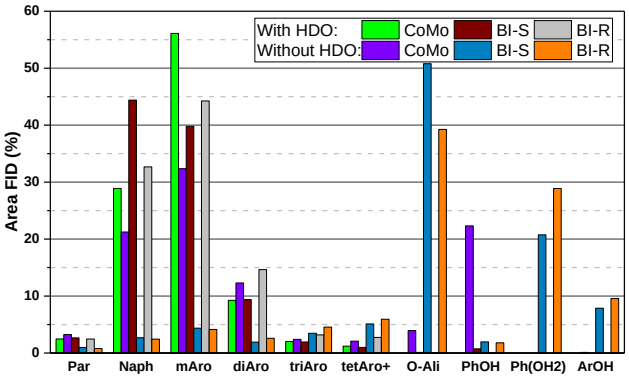

Figure C.7 The effect of bypassing the HDO reactor on the composition of the condensed organics. The components in the condensed organics is divided into paraffins (Par), naphthenes (Naph), monoaromatics (mAro), diaromatics (diAro), triaromatics (triAro), tetraaromatics and larger aromatics (tetAro+), oxygenated aliphatics (O-Ali),dihydroxybenzenes (Ph(OH2)), phenols (PhOH), and oxygenated aromatics (ArOH). (Fluid bed temperature: 450-454 °C, HDO temperature: 371-394 °C, pressure: 26 bar, biomass feeding rate: 174-302 g/h, H2S concentration: 0-470 ppm, H_2 flow: 87.4-89.2NL/min, N_2 flow: 0.62-5 NL/min)

The effect of bypassing the HDO reactor the molecular size is shown in Figure C.8.

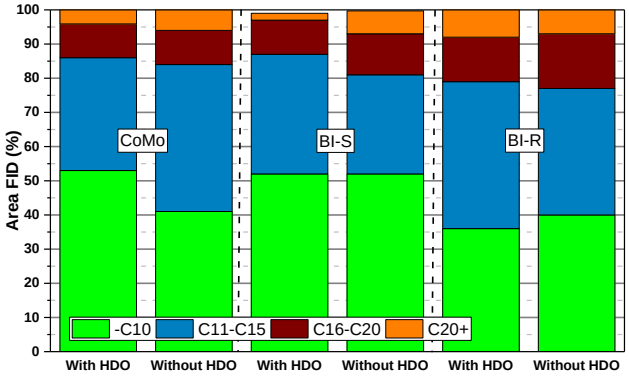

Figure C.8 Effect of bypassing the HDO reactor on the relative number of carbon atoms in the molecules in the condensed organics . The number of carbon atoms in the condensed organics is divided into less than 10 carbon atoms (-C10), between 11 and 15 carbon atoms (C11-C15), between 16 and 20 carbon atoms (C15-C20), and more than 20 carbon atoms (C20+). (Fluid bed temperature: 450-454 °C, HDO temperature: 371-394 °C, pressure: 26 bar, biomass feeding rate: 174-302 g/h, H2S concentration: 0-470 ppm, H_2 flow: 87.4-89.2NL/min, N_2 flow: 0.62-5 NL/min)

Appendix D Supplementary information for Catalytic hydropyrolysis of biomass using molybdenum sulfide based catalyst. Effect of promoters

NH_3-TPD of the oxide catalyst precursors

NH_3-TPD for the oxide precursors is shown in Figure D.1and the concentration of acid sites is shown in Table D.1. No significant difference in the acidity of the oxide precursors was observed.

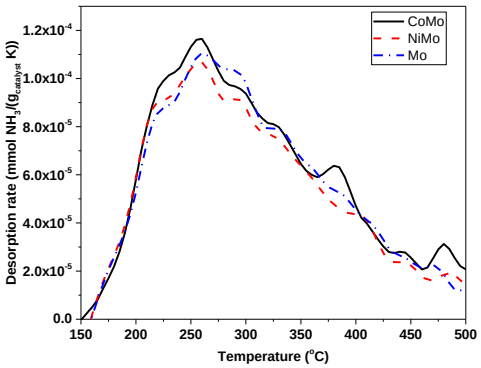

Figure D.1 NH_3-TPD profiles for the oxide precursors of tested CoMo, NiMo, and Mo catalysts.

Table D.1 Concentration of acid sites (NH_3-TPD) for the oxide precursors.

Catalyst	CoMo	NiMo	Mo
NH_3 adsorbed (mmol/g)	0.127	0.116	0.119
NH_3 desorbed (mmol/g)	0.124	0.114	0.118

Penetration depth for electron beam in $MgAl_2O_4$

It was assumed that the analyzed sample consisted of magnesium spinel ($MgAl_2O_4$) with a density of 3.579 g/cm^3, a Mg:Al:O ratio of 17.08: 37.93: 44.98 and the particle diameter was 200 µm. The following simulation parameters were used: beam diameter: 1 µm, beam raster grid: 1x1 µm with 100 nm spacing, beam energy: 15, 10, 5, and 3 kV, and the displayed trajectories was set to 2000.

The maximum penetration is shown as a function of the accelerating voltage in Table D.2.

Table D.2 Maximum interaction depth in $MgAl_2O_4$ as a function of accelerating voltage (Simulation preformed in CASINO Monte Carlo Software v.3.3.0.4)

Acc. Voltage (kv)	Depth (nm)
15	1600
10	800
5	340
3	170

The results were double-checked by performing the same simulation in an older version of the software (v.2.5.1.0), however in this version it was not possible to assume that the particle was as sphere and instead a series of planar layers was used. The results using the old version of Casino is shown in Figure D.2 and shows that there is a good agreement between the old and new version of the software.

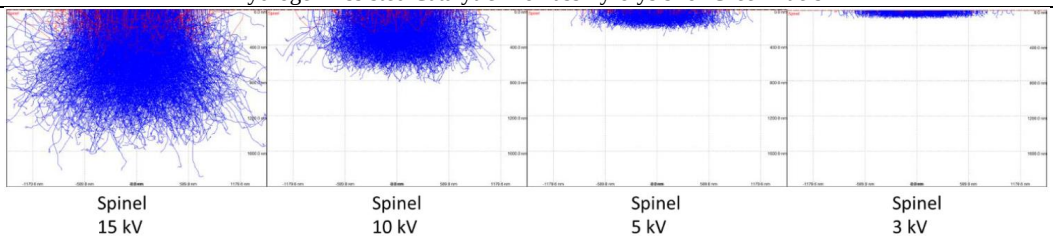

Figure D.2 Effect of acceleration voltage on the penetration in $MgAl_2O_4$, the red trajectories shows the back scatter electrons (Simulation preformed in CASINO Monte Carlo Software v.2.5.1.0).

The effect of adding a carbon layer on $MgAl_2O_4$ is shown in Figure D.3, and shows that carbon does not influence the maximum depth of interaction, but shrinks the interaction volume and cause more backscattered electrons. The effect of Mo and (Co/Ni) is neglected due to the relatively low amount of these elements.

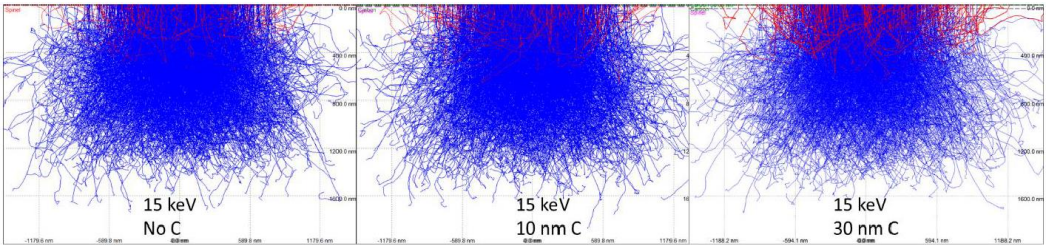

Figure D.3 Effect of C thickness carbon layer on the penetration in $MgAl_2O_4$, the red trajectories shows the back scatter electrons. (Simulation preformed in CASINO Monte Carlo Software v.2.5.1.0)

Detailed gas composition

A detailed composition of the hydropyrolysis gas product is shown in Table D.3.

Table D.3 Detailed gas composition. Conditions: Fluid bed temperature: 451-452°C, pressure: 26 bar, biomass feeding rate: 261-275 g/h, biomass used: 946-964 g, H_2 flow: 82 NL/min, N_2 flow: 5 NL/min, and H_2S conc: 460 ppm.

Test:	CoMo	NiMo	Mo
Paraffin yields (wt.% daf)			
C_1	3.53	3.94	3.05
C_2	2.44	3.38	2.15
C_3	0.70	1.24	0.62
C_4	0.37	0.75	0.35
C_5	0.25	0.46	0.28
Olefin yields (wt.% daf)			
C_2	1.87	1.18	1.78
C_3	1.75	1.45	1.33
C_4	1.55	1.39	1.03
C_5	1.30	1.15	0.95
C_{6+}, CO and CO_2 yields (wt.% daf)			
C_{6+}	4.02	4.07	3.75
CO	6.54	7.61	4.82
CO_2	9.20	9.40	9.54

The C_2 and C_3 paraffins and olefins yields for the tested catalysts are shown in Figure D.4.

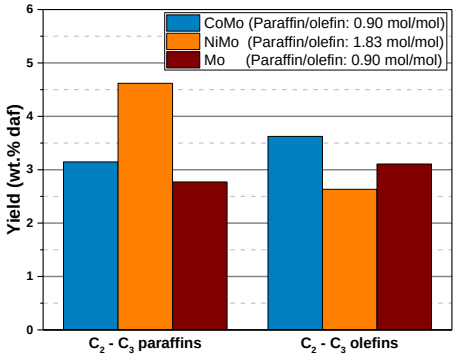

Figure D.4 Comparison of the C_2-C_3 paraffins and olefins yields for the tested catalysts.

Equilibrium calculations

The equilibrium ratio between CO and CO_2 was calculated using the HSC Chemistry 9 software package and is shown in Figure D.5. The following initial concentrations were used in the calculations: 0.26 % CO, 0.23 % CO_2, 2.84 % H_2O, and 96.7 % H_2. The ratio between the components corresponds to the measured ratio on the GC and the collected amount of water from experiment 1 (CoMo).

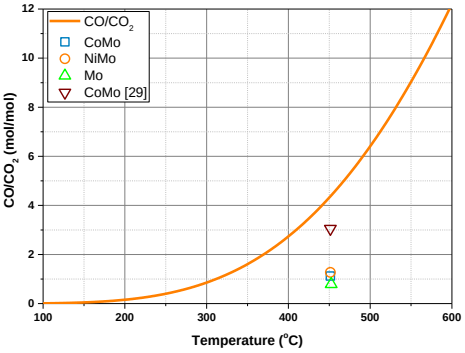

Figure D.5 Equilibrium ratio between CO and CO_2 as a function of temperature. The calculations were conducted in HSC Chemistry 9 at 26 bar, and assumed the following initial composition of the gas phase: 0.26 % CO, 0.23 % CO_2, 2.84 % H_2O, and 96.7 % H_2.

Overview of sulfur containing molecules detected with sulfur specific GC-AED

Table D.4 List of detected molecules with sulfur specific GC-AED when the CoMo catalyst is used in the fluid bed reactor. (DMDS = dimethyl disulfide, THT = tetrahydrothiophene)

Compound	Retention time (min)	Amount (ppms)	Compound	Retention time (min)	Amount (ppms)
Hydrogensulfide	1.47	382.18	c-Trimethylthiophen	17.14	4.42
Methanethiol	1.88	23.86	d-Trimethylthiophen	17.19	1.61
Unidentified	2.01	2.46	e-Trimethylthiophen	17.95	4.72
Unidentified	2.39	60.72	Unidentified	19.11	3.83
Ethanethiol	2.51	26.64	Unidentified	19.32	3.75
Unidentified	2.69	4.53	Unidentified	19.42	2.33
Unidentified	3.26	1.75	Unidentified	19.81	3.32
Unidentified	4.16	7.39	Unidentified	20.78	9.72
Unidentified	4.38	6.85	Unidentified	21.17	8.33
Unidentified	4.55	6.48	Unidentified	21.32	9.66
1-Propanethiol	4.64	2.35	Unidentified	21.58	3.35
Unidentified	6.07	4.16	Unidentified	22.37	11.58
Unidentified	6.24	28.26	Unidentified	22.53	1.31
Methylethylsulfide	6.33	150.13	Benzothiophen	22.69	1.32
Unidentified	7.48	1.68	Unidentified	22.73	2.38
Unidentified	7.85	2.49	Unidentified	23.46	8.92
Unidentified	8.02	6.33	Unidentified	23.67	8.67
Unidentified	8.27	2.58	Unidentified	23.81	5.59
Tetra Hydrothiophen	8.48	2.56	Unidentified	23.94	2.85
DMDS	9.40	1.98	Unidentified	24.09	3.53
Unidentified	9.56	4.74	Unidentified	24.14	2.11
Unidentified	9.65	5.97	Unidentified	24.52	1.94
Unidentified	10.18	109.25	Unidentified	24.69	1.92
2-Methylthiophen	10.47	18.63	Unidentified	25.01	13.80
2-Methyl-THT	11.26	20.74	Methylbenzothiophen (b)	25.19	5.03
Unidentified	11.56	1.92	Methylbenzothiophen (a)	25.38	1.78
3-Methyl-THT	11.83	2.69	Methylbenzothiophen (c)	25.68	7.64
Unidentified	11.88	9.16	Methylbenzothiophen (d)	25.83	2.07
Unidentified	12.42	7.02	Unidentified	25.93	4.15
Unidentified	12.60	5.27	Unidentified	26.10	5.28
Unidentified	12.84	9.59	Unidentified	26.28	2.04
Unidentified	13.48	20.25	Unidentified	26.49	1.93
Unidentified	13.66	22.21	Unidentified	27.10	2.59
Unidentified	13.85	11.59	Unidentified	27.17	1.90
Unidentified	13.89	8.53	Unidentified	27.30	6.22
a-Dimethylthiophen	13.97	5.87	Unidentified	27.42	4.01
b-Dimethylthiophen	14.24	6.32	Dimethylbenzothiophen (a)	27.73	5.75
c-Dimethylthiophen	14.31	3.91	Dimethylbenzothiophen (b)	28.08	2.37
d-Dimethylthiophen	14.66	2.62	Dimethylbenzothiophen (c)	28.21	3.04
Dimethyl-THT	14.98	4.45	Unidentified	29.22	4.23
Unidentified	16.38	3.24	Unidentified	29.42	1.75
Unidentified	16.54	3.26	Unidentified	29.90	2.37
a-Trimethylthiophen	16.72	1.27	Unidentified	32.92	3.59
b-Trimethylthiophen	16.89	3.04			

Table D.5 List of detected molecules with sulfur specific GC-AED when the NiMo catalyst is used in the fluid bed reactor. (THT = tetrahydrothiophene, DBT = dibenzothiophene)

Compound	Retention time (min)	Amount (ppm S)	Compound	Retention time (min)	Amount (ppm S)
Unidentified	1.45	437.39	Unidentified	23.59	13.12
Methanethiol	1.85	12.67	Unidentified	23.73	15.33
Unidentified	2.00	2.93	Unidentified	24.08	1.03
Unidentified	2.24	0.82	Unidentified	24.28	1.23
Unidentified	2.33	43.04	Unidentified	24.38	1.23
Unidentified	2.47	13.19	Unidentified	24.45	3.78
Unidentified	2.95	0.94	Unidentified	24.59	1.72
Carbondisulfide	3.21	2.71	Unidentified	24.94	9.89
Unidentified	4.10	3.11	Unidentified	25.11	5.99
Unidentified	4.31	3.59	Methylbenzothiophen	25.30	3.91
Unidentified	4.49	6.65	Unidentified	25.43	2.98
1-Propanethiol	4.57	3.62	Methylbenzothiophen	25.61	7.31
Unidentified	6.00	5.18	Methylbenzothiophen	25.74	2.03
Unidentified	6.16	14.95	Methylbenzothiophen	25.88	12.35
Methylethylsulfide	6.25	42.00	Unidentified	26.02	14.58
Unidentified	7.77	4.18	Unidentified	26.21	1.19
Unidentified	7.94	3.63	Unidentified	26.41	2.84
Unidentified	8.20	3.41	Unidentified	27.01	13.70
Unidentified	8.40	2.27	Unidentified	27.22	4.43
DMDS	9.48	6.84	Unidentified	27.33	15.72
Unidentified	9.56	2.03	Dimethylbenzothiophen	27.60	5.46
Unidentified	10.11	33.94	Unidentified	27.77	1.50
2-Methylthiophen	10.40	6.17	Dimethylbenzothiophen	27.99	1.97
2-Methyl-THT	11.19	2.99	Unidentified	28.13	8.86
Unidentified	11.49	2.96	Dimethylbenzothiophen	28.29	5.32
3-Methyl-THT	11.81	9.70	Dimethylbenzothiophen	28.51	1.89
Unidentified	12.34	5.28	Unidentified	29.18	8.14
Unidentified	12.53	3.89	Unidentified	29.32	8.05
Unidentified	12.76	2.12	Unidentified	29.50	2.12
Unidentified	13.03	1.74	Unidentified	29.78	3.21
Unidentified	13.41	7.12	Unidentified	29.91	1.80
Unidentified	13.58	6.75	Unidentified	30.08	2.16
Unidentified	13.78	1.90	Unidentified	30.47	2.53
a-Dimethylthiophen	13.81	2.25	Unidentified	30.96	2.83
b-Dimethylthiophen	14.16	1.94	Unidentified	31.08	5.04
d-Dimethylthiophen	14.61	4.65	Unidentified	31.20	8.00
Dimethyl-THT	14.90	5.10	Unidentified	32.81	23.25
Unidentified	16.39	2.27	Unidentified	32.97	2.81
a-Trimethylthiophen	16.55	1.26	Unidentified	33.07	2.14
b-Trimethylthiophen	16.80	2.84	Unidentified	33.14	2.63
c-Trimethylthiophen	17.09	1.82	Unidentified	33.74	2.52
e-Trimethylthiophen	17.80	2.16	DBT	34.40	2.31

Unidentified	17.88	2.07	Unidentified	34.56	9.49
Unidentified	18.43	2.44	Unidentified	34.97	2.08
Unidentified	18.67	1.62	Unidentified	36.12	3.01
Unidentified	19.35	1.67	4-Methyl-DBT	36.17	4.54
Unidentified	20.57	1.79	4.6-Dimethyl-DBT	37.62	1.71
Unidentified	20.70	13.84	Diphenyldisulfid	37.72	1.87
Unidentified	21.08	34.54	Unidentified	37.83	2.71
Unidentified	21.23	40.37	Methyldiphenyldisulfid	37.90	3.57
Unidentified	21.51	5.26	Methyldiphenyldisulfid	38.30	2.33
Unidentified	22.46	3.44	4.6.c-Trimethyl-DBT	39.06	2.68
Benzothiophen	22.61	1.63	4.6.b-Trimethyl-DBT	39.19	3.52
Unidentified	22.65	2.37	4.6.a-Trimethyl-DBT	39.37	2.80
Unidentified	23.43	5.10			

Table D.6 List of detected molecules with sulfur specific GC-AED when the Mo catalyst is used in the fluid bed reactor. (THT = tetra-hydrothiophene, DBT = dibenzothiophene)

Compound	Retention time (min)	Amount (ppm S)	Compound	Retention time (min)	Amount (ppm S)
Hydrogensulfide	1.47	572.22	Unidentified	19.05	1.77
Methanethiol	1.88	43.92	Unidentified	19.11	2.44
Unidentified	2.01	1.17	Unidentified	19.31	6.63
Unidentified	2.29	0.20	Unidentified	19.42	2.48
Unidentified	2.39	117.75	Unidentified	19.67	3.70
Ethanethiol	2.51	31.51	Unidentified	19.80	7.47
Unidentified	2.69	7.22	Unidentified	20.46	2.89
Unidentified	3.26	1.06	Unidentified	20.64	3.43
Unidentified	4.16	16.68	Unidentified	20.78	26.10
Unidentified	4.38	8.47	Unidentified	21.17	13.89
Unidentified	4.55	16.39	Unidentified	21.32	17.81
1-Propanethiol	4.64	7.74	Unidentified	21.58	12.47
Unidentified	6.07	3.33	Unidentified	22.13	1.01
Unidentified	6.24	23.50	Unidentified	22.35	56.88
Methylethylsulfide	6.33	127.27	Unidentified	22.53	5.77
Unidentified	7.49	3.89	Benzothiophen	22.69	3.66
Unidentified	7.56	1.44	Unidentified	22.73	4.71
Unidentified	7.85	5.24	Unidentified	22.95	1.24
Unidentified	8.01	7.72	Unidentified	23.35	2.05
Unidentified	8.27	4.48	Unidentified	23.45	12.97
Tetra Hydrothiophen	8.48	4.38	Unidentified	23.67	14.10
DMDS	9.41	2.61	Unidentified	23.81	10.88
Unidentified	9.56	2.76	Unidentified	23.92	10.45
Unidentified	9.65	16.45	Unidentified	24.08	5.82
Unidentified	10.18	123.06	Unidentified	24.15	1.01
2-Methylthiophen	10.48	19.21	Unidentified	24.21	1.31
2-Methyl-THT	11.27	260.89	Unidentified	24.28	3.35
Unidentified	11.57	5.24	Unidentified	24.36	1.29
3-Methyl-THT	11.83	4.04	Unidentified	24.46	1.28
Unidentified	11.90	21.40	Unidentified	24.52	4.44

Unidentified	12.44	27.37	Unidentified	24.69	3.61
Unidentified	12.61	6.47	Unidentified	24.82	2.89
Unidentified	12.85	80.06	Unidentified	25.01	27.18
Unidentified	13.12	1.45	Unidentified	25.18	3.15
Unidentified	13.37	1.58	Methylbenzothiophen (a)	25.38	1.78
Unidentified	13.49	33.28	Methylbenzothiophen (b)	25.51	4.49
Unidentified	13.66	19.51	Methylbenzothiophen (c)	25.68	8.32
Unidentified	13.86	10.88	Methylbenzothiophen (d)	25.83	3.39
Unidentified	13.89	8.31	Unidentified	25.93	5.99
a-Dimethylthiophen	13.97	30.94	Unidentified	26.10	9.89
b-Dimethylthiophen	14.06	1.25	Unidentified	26.29	4.03
Unidentified	14.18	1.70	Unidentified	26.49	4.05
Unidentified	14.24	6.93	Unidentified	27.10	1.86
c-Dimethylthiophen	14.32	10.06	Unidentified	27.18	3.62
d-Dimethylthiophen	14.55	3.28	Unidentified	27.30	11.13
Unidentified	14.63	13.73	Unidentified	27.42	4.10
Unidentified	14.71	1.70	Dimethylbenzothiophen (a)	27.68	3.01
Unidentified	14.85	1.56	Unidentified	27.74	3.57
Dimethyl-THT	14.98	16.24	Unidentified	27.86	1.62
Dimethyl-THT	15.45	8.54	Dimethylbenzothiophen (b)	28.09	2.66
Dimethyl-THT	15.71	3.42	Unidentified	28.17	1.04
Unidentified	15.91	2.44	Dimethylbenzothiophen (c)	28.22	2.83
Unidentified	15.97	2.74	Dimethylbenzothiophen (d)	28.37	2.71
Unidentified	16.16	6.66	Unidentified	29.24	6.42
Unidentified	16.38	4.52	Unidentified	29.42	2.17
Unidentified	16.53	4.09	Unidentified	29.68	1.77
a-Trimethylthiophen	16.71	1.66	Unidentified	29.94	5.94
b-Trimethylthiophen	16.89	1.58	Unidentified	30.16	1.57
d-Trimethylthiophen	16.99	12.19	Unidentified	30.29	6.26
c-Trimethylthiophen	17.14	7.11	Unidentified	30.78	4.50
e-Trimethylthiophen	17.76	1.78	Unidentified	31.07	2.37
Unidentified	17.83	2.68	Unidentified	31.25	3.26
Unidentified	17.93	17.27	Unidentified	31.57	3.05
Unidentified	18.21	3.29	Unidentified	32.93	3.72
Unidentified	18.42	18.33	DBT	33.85	3.92
Unidentified	18.74	4.95			

Overview of hydrocarbons detected in the aqueous phase with GC-MS/FID

Table D.7 List of detected compounds in the aqueous phase with GC-MS/FID when the CoMo catalyst is used in the fluid bed reactor.

Compound	Retention time (min)	Area-FID (%)	Compound	Retention time (min)	Area-FID (%)
Methanol	2.47	19.04	Unidentified	5.95	0.26
Ethanol	2.55	40.28	Unidentified	6.11	0.07
Acetone	2.62	12.36	Unidentified	6.57	0.06
1-Propanol	2.78	5.70	Unidentified	7.18	0.05
Acetic acid	2.84	3.81	Unidentified	8.10	0.06
2-Heptanone, 3-methyl-	2.93	3.76	Unidentified	8.29	0.17
1-Propanol, 2-methyl-	3.06	0.39	Phenol	11.71	4.24
Furan, tetrahydro-	3.13	0.43	Unidentified	16.83	0.32
1-butanol	3.28	2.08	Unidentified	18.35	0.87
2-Pentanone	3.48	0.57	Unidentified	24.59	0.16
2-Hydroxy-3-pentanone	3.56	0.47	Unidentified	28.93	0.05
Unidentified	3.69	0.35	Unidentified	31.69	0.07
Unidentified	3.87	0.08	Unidentified	33.57	0.08
Unidentified	3.96	0.25	Unidentified	33.71	0.11
Unidentified	4.19	0.14	Unidentified	34.86	0.05
1-Butanol, 3-methyl-	4.33	0.61	Unidentified	45.62	0.09
Unidentified	4.50	0.20	Unidentified	47.78	0.06
Cyclopentanol	4.69	0.40	Unidentified	47.99	0.14
Cyclopentanone	4.85	1.91	Unidentified	51.38	0.05
Unidentified	5.76	0.20			

Table D.8 List of detected compounds in the aqueous phase with GC-MS/FID when the NiMo catalyst is used in the fluid bed reactor.

Compound	Retention time (min)	Area-FID (%)	Compound	Retention time (min)	Area-FID (%)
Methanol	2.47	16.51	Cyclopentanol	4.69	0.44
Ethanol	2.55	41.89	Cyclopentanone	4.85	2.11
Acetone	2.62	12.55	Unidentified	5.77	0.11
1-Propanol	2.78	6.63	Unidentified	5.95	0.26
Acetic acid	2.85	3.34	Unidentified	6.11	0.08
2-Heptanone, 3-methyl-	2.93	3.79	Unidentified	6.58	0.05
1-Propanol, 2-methyl-	3.06	0.42	Unidentified	7.18	0.08
Furan, tetrahydro-	3.13	0.43	Unidentified	7.68	0.04
1-Butanol	3.28	2.25	Unidentified	7.95	0.06
2-Pentanone	3.48	0.59	Unidentified	8.10	0.04
2-Hydroxy-3-pentanone	3.57	0.47	Phenol	11.71	4.94
2-Hydroxy-3-pentanone	3.70	0.37	Unidentified	16.84	0.25
Unidentified	3.87	0.06	Unidentified	18.36	0.79
Unidentified	3.96	0.28	Unidentified	24.60	0.10
Unidentified	4.19	0.12	Unidentified	48.28	0.06
1-Butanol, 3-methyl-	4.34	0.66	Unidentified	48.58	0.05
Unidentified	4.51	0.18			

Table D.9 List of detected compounds in the aqueous phase with GC-MS/FID when the Mo catalyst is used in the fluid bed reactor.

Compound	Retention time (min)	Area-FID (%)	Compound	Retention time (min)	Area-FID (%)
Methanol	2.47	17.33	Cyclopentanone, 2-methyl-	6.11	0.15
Ethanol	2.55	40.87	Unidentified	6.23	0.08
Acetone	2.62	11.70	Unidentified	6.57	0.10
1-Propanol	2.78	6.20	Unidentified	6.74	0.06
Acetic acid	2.83	4.55	Unidentified	6.98	0.03
2-Butanone	2.93	3.84	Unidentified	7.17	0.10
1-Propanol, 2-methyl-	3.06	0.38	Unidentified	7.29	0.04
Furan, tetrahydro-	3.13	0.43	Unidentified	7.68	0.04
Formic acid, butyl ester	3.28	2.39	Unidentified	7.93	0.04
2-Pentanone	3.48	0.63	Unidentified	8.08	0.14
2-Hydroxy-3-pentanone	3.56	0.49	Unidentified	8.27	0.31
Unidentified	3.69	0.36	Unidentified	11.04	0.04
Unidentified	3.87	0.12	Phenol	11.71	2.09
Unidentified	3.96	0.18	Unidentified	16.84	0.15
Unidentified	4.03	0.12	Unidentified	18.36	0.35
Unidentified	4.22	0.22	Unidentified	24.61	0.06
Unidentified	4.33	0.70	Unidentified	31.70	0.09
1-Butanol, 3-methyl-	4.49	0.24	Unidentified	33.58	0.05
Cyclopentanol	4.68	0.53	Unidentified	33.70	0.06
Unidentified	4.85	3.44	Unidentified	34.89	0.03
Cyclopentanone	5.75	0.51	Unidentified	51.49	0.33
2-Cyclopenten-1-one	5.94	0.44			

Scanning Electron Microscopy

Table D.10 Carbon and potassium content measured with EDS at different acceleration voltages on fresh and spent catalysts

	C content (wt.%)				K content (wt.%)			
	3 kV	5 kV	10 kV	15 kV	3 kV	5 kV	10 kV	15 kV
Fresh catalysts								
CoMo	2.5	2.9	3.0	3.0	-	0.0	0.0	0.0
NiMo	2.5	2.6	2.9	3.3	-	0.0	0.0	0.0
Mo	2.0	2.1	2.6	3.5	-	0.0	0.0	0.0
Spent catalysts								
CoMo	5.8	5.3	4.7	4.5	-	0.8	0.4	0.4
NiMo	5.6	5.1	4.4	4.2	-	0.5	0.4	0.3
Mo	8.6	7.5	6.7	6.3	-	1.5	0.5	0.3

Elemental maps (STEM-EDS)

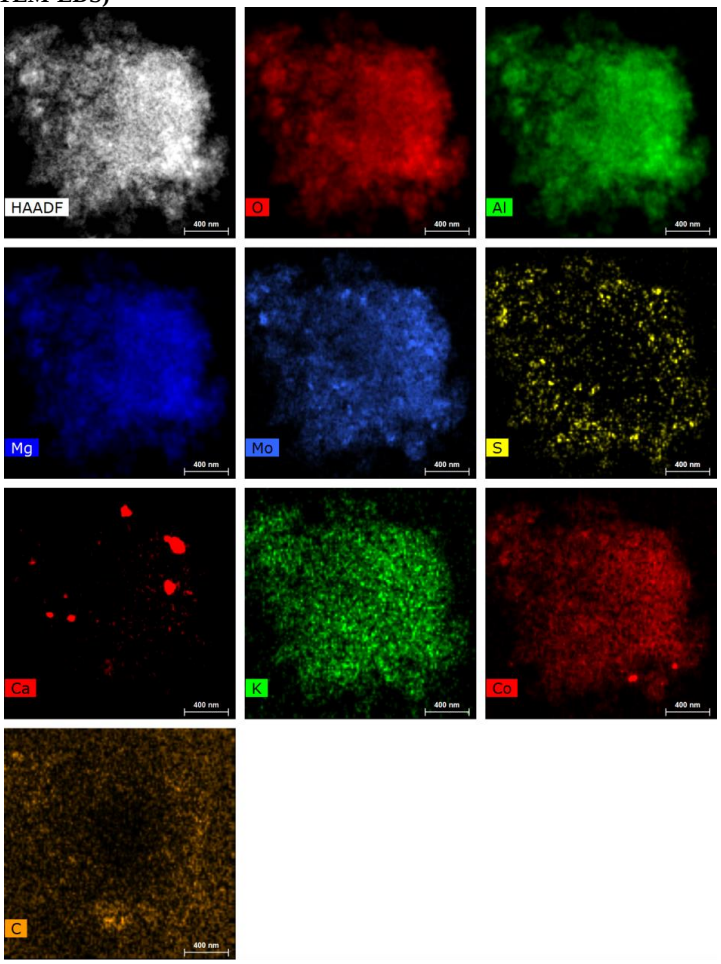

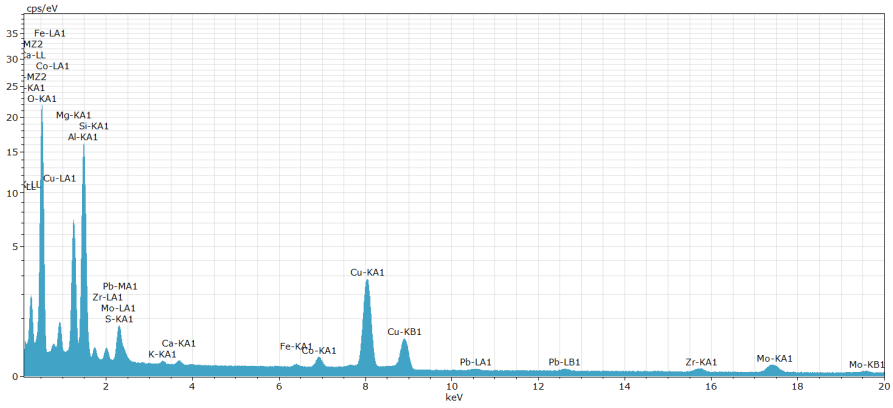

Figure D.6 STEM-EDS element map of the CoMo catalyst displaying net counts after background subtraction and deconvolution of the EDX spectrum. The Si, Fe, Cu, Zr, Pb signals were attributed to system peaks from the microscope, TEM grid, specimen holder and x-ray detectors.

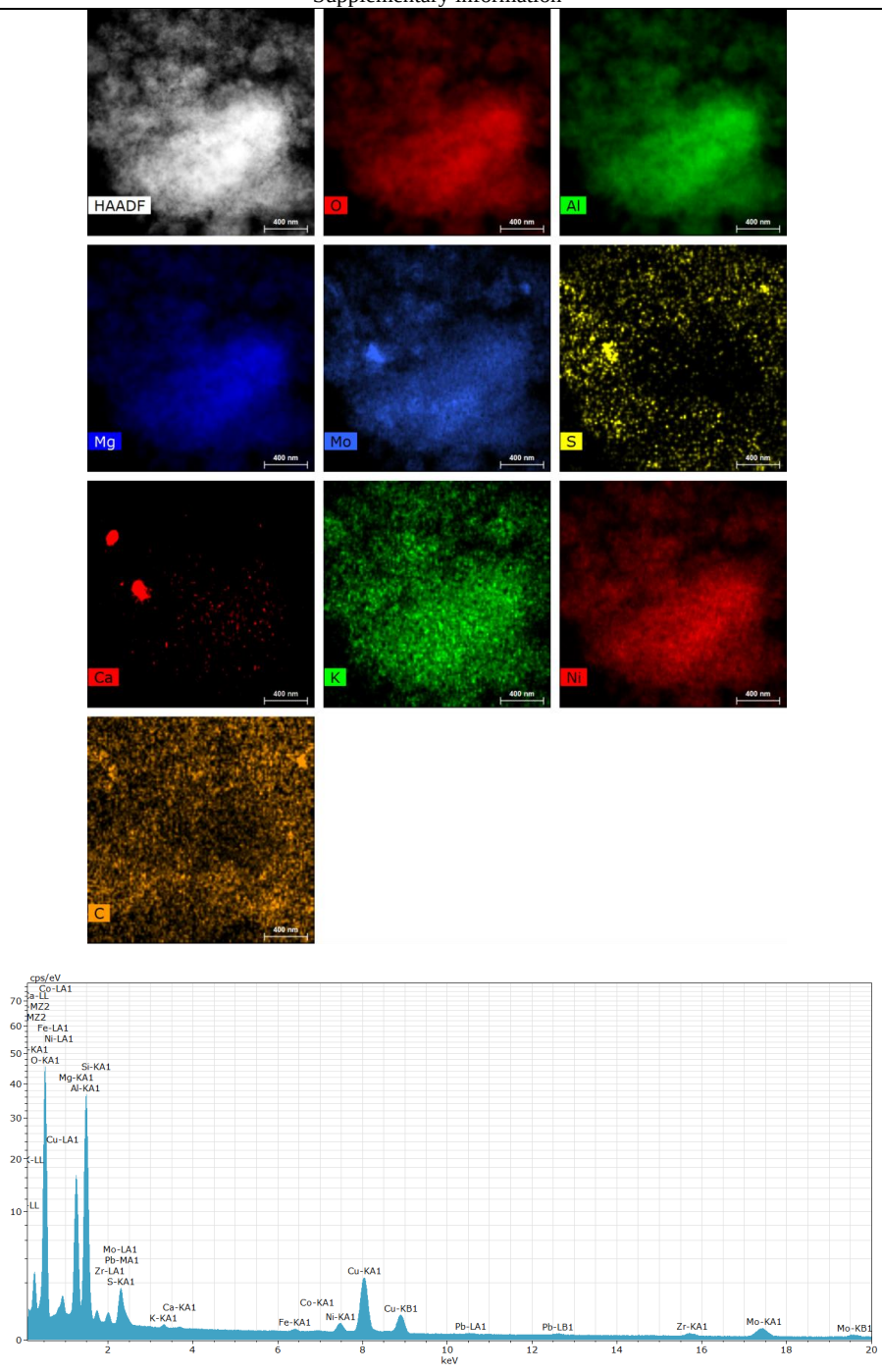

Figure D.7 STEM-EDS element map of the NiMo catalyst displaying net counts after a background subtraction and deconvolution of the EDX spectrum. The Si, Fe, Cu, Zr, Pb signals were attributed to system peaks from the microscope, TEM grid, specimen holder and x-ray detectors.

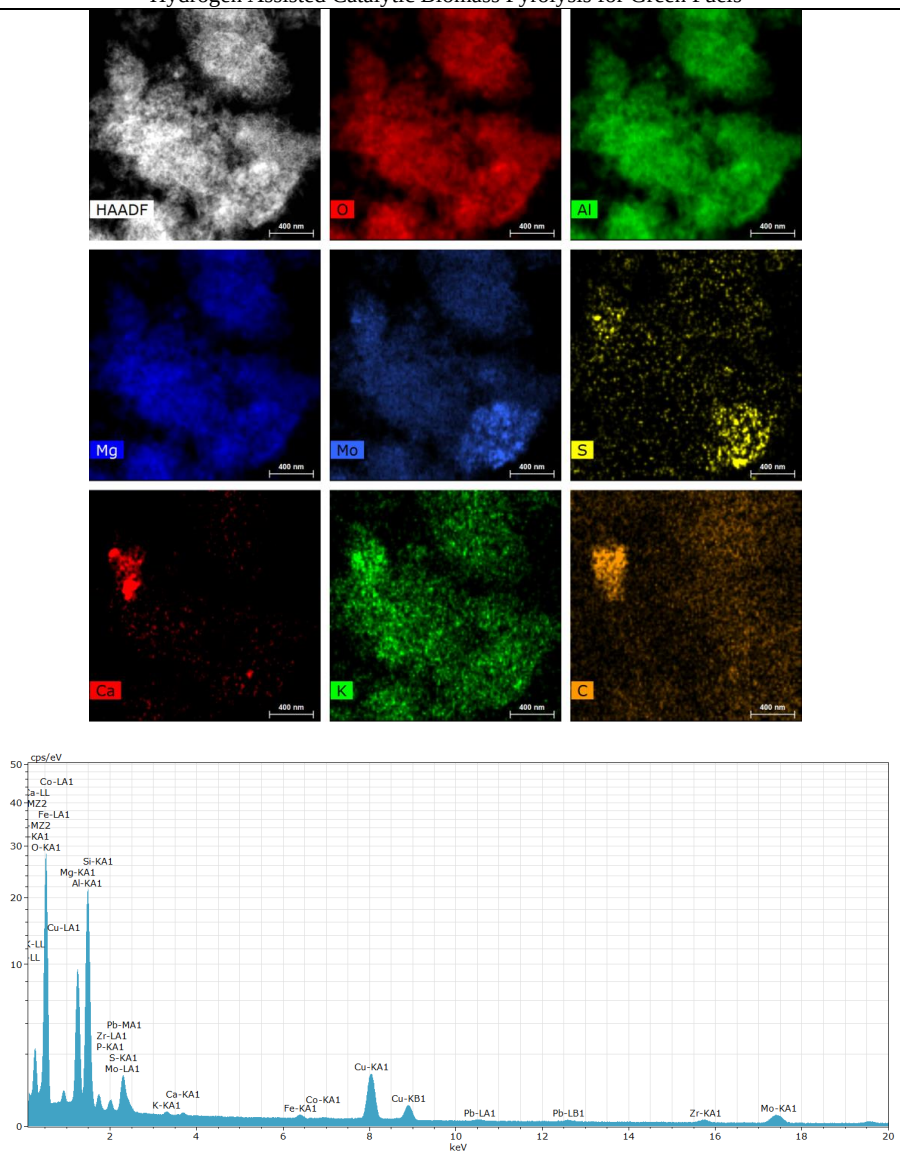

Figure D.8 STEM-EDS element map of a Mo catalyst displaying net counts after a background subtraction and deconvolution of the EDX spectrum. The Si, Fe, Cu, Zr, Pb signals were attributed to system peaks from the microscope, TEM grid, specimen holder and x-ray detectors.

Appendix E Supplementary information for Catalytic hydropyrolysis – Effect of CoMo loading and support acidity

Detailed gas composition

A detailed composition of the hydropyrolysis gas product is shown in Table E.1.

Table E.1 Detailed gas composition. Conditions: Fluid bed temperature: 450-455°C, total pressure: 26 bar, biomass feeding rate: 270-282 g/h, feed time: 2.5-3.5 h, H_2 flow: 82 NL/min, N_2 flow: 5 NL/min, and H_2S conc: 460 ppm.

Test:	CoMoMgAl#1	CoMoMgAl#2	CoMoMgAl#3	CoMoMgAl#4	CoMoZA#1	CoMoZA#2
Paraffin yield (wt.% daf)						
C_1	3.53	3.98	4.40	4.25	2.88	3.33
C_2	2.44	3.93	4.76	5.08	4.06	4.05
C_3	0.70	1.54	2.16	2.53	1.75	1.96
C_4	0.37	0.82	1.21	1.51	0.79	1.06
C_5	0.25	0.50	0.76	0.97	0.33	0.43
Olefin yield (wt.% daf)						
C_2	1.87	1.38	1.05	0.78	1.76	1.90
C_3	1.75	1.85	1.68	1.33	2.50	2.64
C_4	1.55	1.69	1.62	1.36	1.96	2.02
C_5	1.30	1.25	1.20	1.00	1.46	1.35
C_{6+}, CO and CO_2 yield (wt.% daf)						
C_{6+}	4.02	5.79	5.78	5.98	5.55	5.01
CO	6.54	8.35	8.88	8.85	6.66	7.72
CO_2	9.20	7.72	7.81	6.91	8.31	8.42

Equilibrium calculations

The equilibrium ratio between CO and CO_2 was calculated using the HSC Chemistry 9 software package and is shown in Figure E.1. The following initial concentrations were used in the calculations: 0.26 % CO, 0.23 % CO_2, 2.84 % H_2O, and 96.7 % H_2. The ratio between the components corresponds to the measured ratio on the GC and the collected amount of water from experiment 1 (CoMo). The results show that that the mixture does not reach thermodynamic equilibrium.

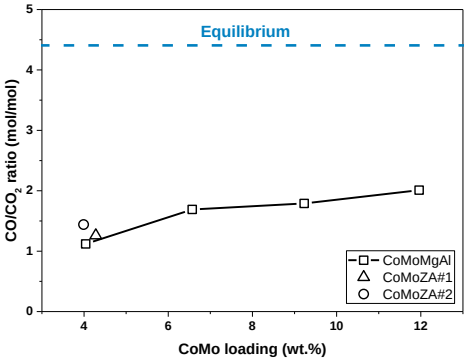

Figure E.1 Equilibrium ratio between CO and CO_2 as a function of temperature. The calculations were conducted in HSC Chemistry 9 at 26 bar, assumed the following initial composition of the gas phase: 0.26 % CO, 0.23 % CO_2, 2.84 % H_2O, and 96.7 % H_2.

GC×GC-FID on the produced organic phases

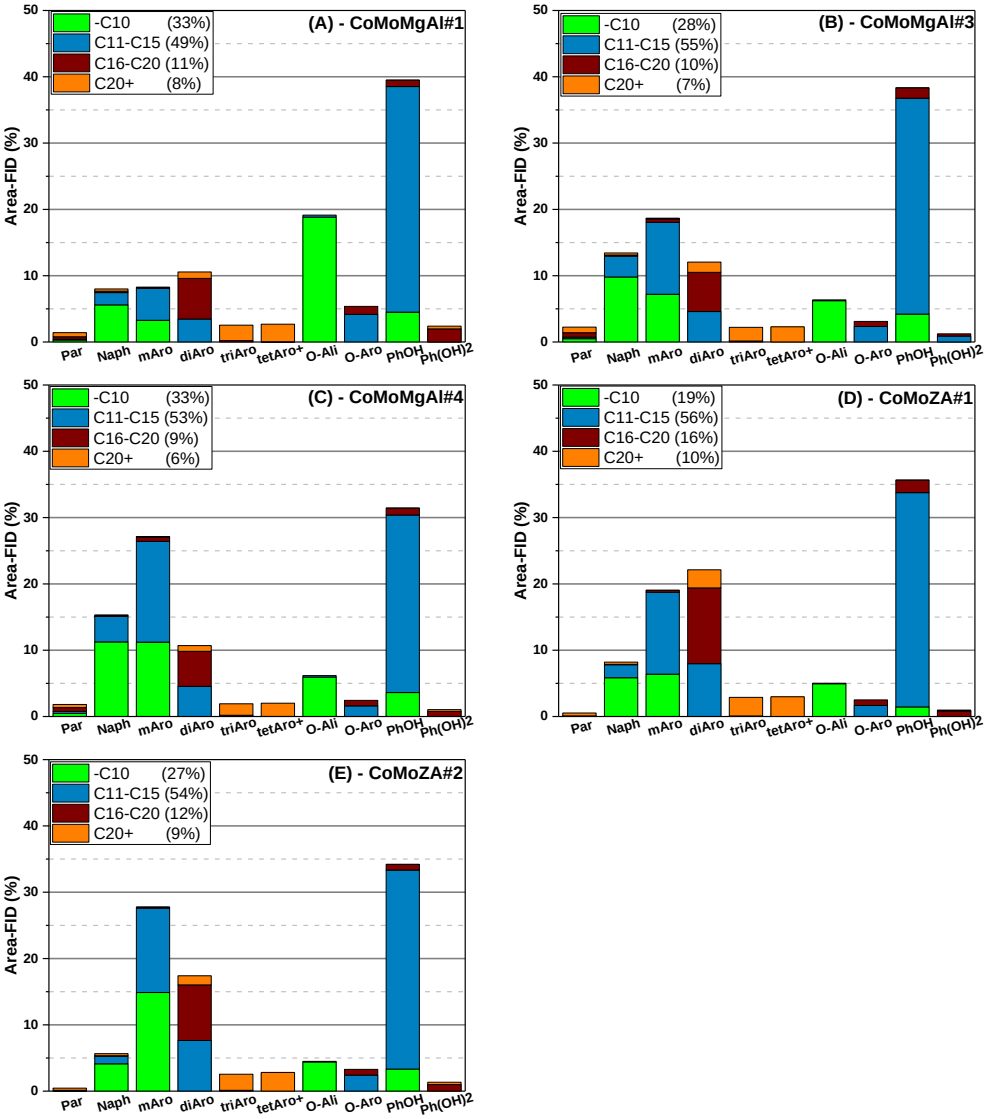

Figure E.2 The composition of the condensed organic phase from experiment 1 with the CoMoMgAl#1 catalyst (A), experiment 3 with the CoMoMgAl#2 catalyst (B), experiment 4 with the CoMoMgAl#4 catalyst (C), experiment 5 with the CoMoZA#1 catalyst (D), and experiment 6 with the CoMoZA#2 catalyst. The components in the condensed organic are divided into paraffins (Par), naphthenes (Naph), monoaromatics (mAro), diaromatics (diAro), triaromatics (triAro), tetraaromatics and larger aromatics (tetAro+), oxygenated aliphatics (o-Ali), phenols (PhOH), larger oxygenated aromatics (O-Aro), and dihydroxybenzenes (Ph(OH)2). The components are also divided into the following groups based on the number of carbon atoms in the components: up to 10 carbons atoms (-C10) between 11 and 15 carbons atoms (C11-C15), between 16 and 20 carbon atoms (C16-C20), more than 20 carbon atoms (C20+)

Overview of sulfur containing molecules detected with sulfur specific GC-AED

Table E.2 List of detected molecules with sulfur specific GC-AED when the CoMoMgAl#1 catalyst is used in the fluid bed reactor. (DMDS = dimethyl disulfide, THT = tetrahydrothiophene)

Compound	Retention time (min)	Amount (wt-ppm S)	Compound	Retention time (min)	Amount (wt-ppm S)
Hydrogensulfide	1.47	382.18	c-Trimethylthiophen	17.14	4.42
Methanethiol	1.88	23.86	d-Trimethylthiophen	17.19	1.61
Unidentified	2.01	2.46	e-Trimethylthiophen	17.95	4.72
Unidentified	2.39	60.72	Unidentified	19.11	3.83
Ethanethiol	2.51	26.64	Unidentified	19.32	3.75
Unidentified	2.69	4.53	Unidentified	19.42	2.33
Unidentified	3.26	1.75	Unidentified	19.81	3.32
Unidentified	4.16	7.39	Unidentified	20.78	9.72
Unidentified	4.38	6.85	Unidentified	21.17	8.33
Unidentified	4.55	6.48	Unidentified	21.32	9.66
1-Propanethiol	4.64	2.35	Unidentified	21.58	3.35
Unidentified	6.07	4.16	Unidentified	22.37	11.58
Unidentified	6.24	28.26	Unidentified	22.53	1.31
Methylethylsulfide	6.33	150.13	Benzothiophen	22.69	1.32
Unidentified	7.48	1.68	Unidentified	22.73	2.38
Unidentified	7.85	2.49	Unidentified	23.46	8.92
Unidentified	8.02	6.33	Unidentified	23.67	8.67
Unidentified	8.27	2.58	Unidentified	23.81	5.59
Butanethiol/Tetra Hydrothiophen	8.48	2.56	Unidentified	23.94	2.85
DMDS	9.40	1.98	Unidentified	24.09	3.53
Unidentified	9.56	4.74	Unidentified	24.14	2.11
Unidentified	9.65	5.97	Unidentified	24.52	1.94
Unidentified	10.18	109.25	Unidentified	24.69	1.92
2-Methylthiophen	10.47	18.63	Unidentified	25.01	13.80
2-Methyl-THT	11.26	20.74	Methylbenzothiophen (b)	25.19	5.03
Unidentified	11.56	1.92	Methylbenzothiophen (a)	25.38	1.78
3-Methyl-THT	11.83	2.69	Methylbenzothiophen (c)	25.68	7.64
Unidentified	11.88	9.16	Methylbenzothiophen (d)	25.83	2.07
Unidentified	12.42	7.02	Unidentified	25.93	4.15
Unidentified	12.60	5.27	Unidentified	26.10	5.28
Unidentified	12.84	9.59	Unidentified	26.28	2.04
Unidentified	13.48	20.25	Unidentified	26.49	1.93
Unidentified	13.66	22.21	Unidentified	27.10	2.59
Unidentified	13.85	11.59	Unidentified	27.17	1.90
Unidentified	13.89	8.53	Unidentified	27.30	6.22
a-Dimethylthiophen	13.97	5.87	Unidentified	27.42	4.01
b-Dimethylthiophen	14.24	6.32	Dimethylbenzothiophen (a)	27.73	5.75
c-Dimethylthiophen	14.31	3.91	Dimethylbenzothiophen (b)	28.08	2.37
d-Dimethylthiophen	14.66	2.62	Dimethylbenzothiophen (c)	28.21	3.04
Dimethyl-THT	14.98	4.45	Unidentified	29.22	4.23
Unidentified	16.38	3.24	Unidentified	29.42	1.75
Unidentified	16.54	3.26	Unidentified	29.90	2.37
a-Trimethylthiophen	16.72	1.27	Unidentified	32.92	3.59
b-Trimethylthiophen	16.89	3.04			

Table E.3 List of detected molecules with sulfur specific GC-AED when the CoMoMgAl#3 catalyst is used in the fluid bed reactor. (THT = tetrahydrothiophene, DBT = dibenzothiophene)

Compound name	Retention time (min)	Amount (wt-ppm S)	Compound name	Retention time (min)	Amount (wt-ppm S)
Hydrogensulfide	1.45	744.40	Unidentified	21.07	22.79
Carbonylsulfide	1.50	95.29	Unidentified	21.22	34.80
Unidentified	1.85	15.04	Unidentified	21.92	5.56
Unidentified	2.32	24.95	Benzothiophen	22.14	8.08
Ethanethiol	2.47	5.84	Unidentified	23.58	11.12
Unidentified	2.94	5.07	Unidentified	23.72	18.34
1-Propanethiol	4.47	5.24	Unidentified	23.86	5.80
Unidentified	4.55	3.82	Unidentified	24.03	3.92
Unidentified	5.97	10.19	Methylbenzothiophen (d)	25.87	6.47
Methylethylsulfide	6.10	22.96	Methylbenzothiophen (c)	26.01	8.35
Thiophen	6.23	100.38	Unidentified	27.05	36.24
Unidentified	9.45	16.63	Dimethylbenzothiophen (a)	27.31	11.45
2-Methylthiophen	10.10	85.26	Dimethylbenzothiophen (b)	28.14	12.50
3-Methylthiophen	10.35	16.20	Dimethylbenzothiophen (c)	28.27	4.82
Unidentified	12.30	6.44	Unidentified	29.17	3.57
Unidentified	13.00	6.54	Unidentified	29.30	5.51
2-Methyl-THT	13.40	14.02	Unidentified	31.06	6.16
3-Methyl-THT	13.57	16.44	Unidentified	31.18	4.98
Unidentified	13.76	7.39	Dihexyldisulfid	32.78	48.87
a-Dimethylthiophen	13.80	7.17	DBT	34.49	8.12
b-Dimethylthiophen	14.14	4.30	Unidentified	34.53	8.30
a-Trimethylthiophen	16.40	2.20	Diphenyldisulfid	36.10	5.46
c-Trimethylthiophen	16.81	3.53	4-Methyl-DBT	36.15	5.53
Unidentified	19.03	4.53			

Table E.4 List of detected molecules with sulfur specific GC-AED when the CoMoMgAl#4 catalyst is used in the fluid bed reactor. (THT = tetrahydrothiophene, DBT = dibenzothiophene)

Compound name	Retention time (min)	Amount (wt-ppm S)	Compound name	Retention time (min)	Amount (wt-ppm S)
Hydrogensulfide	1.45	969.51	c-Trimethylthiophen	16.71	4.42
Unidentified	1.85	14.74	d-Trimethylthiophen	16.82	3.78
Unidentified	2.32	29.49	Unidentified	18.71	5.46
Ethanethiol	2.46	5.51	Unidentified	19.03	5.15
Unidentified	2.94	5.24	Unidentified	21.08	19.55
1-Propanethiol	4.47	6.02	Unidentified	21.22	22.50
Unidentified	4.55	4.21	Unidentified	21.75	7.91
Unidentified	5.96	11.68	Unidentified	21.89	14.19
Methylethylsulfide	6.10	19.10	Benzothiophen	22.24	7.58
Thiophen/ 2-Butanethiol	6.23	65.09	Unidentified	23.58	15.62
Unidentified	9.45	13.32	Unidentified	23.72	13.76
2-Methylthiophen	10.10	64.92	Unidentified	23.96	5.79
3-Methylthiophen	10.35	12.35	Methylbenzothiophen (a)	25.09	6.10
Unidentified	12.31	7.83	Methylbenzothiophen (c)	25.61	4.39
Unidentified	12.50	5.75	Methylbenzothiophen (d)	25.86	7.40
Unidentified	13.01	5.13	Methylbenzothiophen (b)	26.01	10.15
2-Methyl-THT	13.43	11.19	Dimethylbenzothiophen (a)	27.04	22.59
3-Methyl-THT	13.57	13.89	Dimethylbenzothiophen (b)	28.13	10.80
Unidentified	13.77	6.68	Dimethylbenzothiophen (c)	28.24	7.15
a-Dimethylthiophen	13.81	5.96	Unidentified	30.92	5.43
b-Dimethylthiophen	14.14	3.53	Dihexyldisulfid	32.78	16.11
a-Trimethylthiophen	16.41	8.26	DBT	34.49	9.71

Table E.5 List of detected molecules with sulfur specific GC-AED when the CoMoMgAl#4 catalyst is used in the fluid bed reactor. (THT = tetrahydrothiophene, DBT = dibenzothiophene)

Compound name	Retention time (min)	Amount (wt-ppm S)	Compound name	Retention time (min)	Amount (wt-ppm S)
Hydrogensulfide	1.45	246.09	Unidentified	23.57	10.82
Carbonylsulfide	1.49	69.46	Unidentified	23.72	13.65
Unidentified	1.84	7.91	Unidentified	24.00	6.43
Unidentified	1.98	5.80	Unidentified	24.45	4.39
Unidentified	2.23	1.93	Unidentified	24.59	2.56
Unidentified	2.31	38.15	Unidentified	24.69	3.64
Ethanethiol	2.46	10.75	Unidentified	24.93	5.59
Unidentified	2.93	3.72	Unidentified	25.09	3.22
Unidentified	4.06	2.21	Unidentified	25.16	3.00
Unidentified	4.28	2.82	Methylbenzothiophen (a)	25.29	3.21
1-Propanethiol	4.45	3.91	Methylbenzothiophen (c)	25.44	2.80
Unidentified	4.53	3.44	Methylbenzothiophen (b)	25.60	6.76
Unidentified	5.93	2.56	Methylbenzothiophen (d)	25.87	6.29
Methylethylsulfide	6.06	125.66	Unidentified	26.00	5.74
Thiophen/ 2-Butanethiol	6.20	133.25	Unidentified	26.60	5.29
Unidentified	7.89	2.13	Unidentified	26.72	2.14
Unidentified	9.27	10.41	Unidentified	26.83	10.26
Unidentified	9.43	16.90	Unidentified	27.00	10.81
2-Methylthiophen	10.06	96.97	Unidentified	27.05	8.25
3-Methylthiophen	10.32	26.09	Unidentified	27.21	6.97
Unidentified	11.72	3.47	Unidentified	27.32	16.06
Unidentified	12.48	3.62	Dimethylbenzothiophen (a)	27.60	5.88
Unidentified	12.98	6.37	Dimethylbenzothiophen (b)	28.16	8.78
2-Methyl-THT	13.37	20.50	Dimethylbenzothiophen (c)	28.29	3.08
3-Methyl-THT	13.55	14.35	Dimethylbenzothiophen (d)	28.52	8.07
Unidentified	13.74	14.93	Unidentified	28.71	3.32
a-Dimethylthiophen	13.78	14.90	Unidentified	28.82	5.83
b-Dimethylthiophen	14.12	7.15	Unidentified	28.97	3.91
c-Dimethylthiophen	14.59	2.63	Unidentified	29.09	4.71
Dimethyl-THT	15.20	2.61	Unidentified	29.17	3.88
Dimethyl-THT	15.31	1.88	Unidentified	29.30	8.13
a-Trimethylthiophen	16.25	4.61	Unidentified	29.38	2.75
b-Trimethylthiophen	16.41	3.91	Unidentified	29.47	2.57
Unidentified	16.61	3.05	Unidentified	29.67	3.25
d-Trimethylthiophen	16.66	2.59	Unidentified	30.05	5.92
c-Trimethylthiophen	16.77	7.06	Unidentified	30.47	5.73
e-Trimethylthiophen	17.07	2.49	Unidentified	30.67	4.67
Unidentified	18.99	2.55	Unidentified	30.82	2.79
Unidentified	19.20	4.09	Unidentified	30.96	6.55
Unidentified	19.31	4.49	Unidentified	31.07	2.87
Unidentified	19.42	4.24	Unidentified	31.12	1.84
Unidentified	19.48	1.78	Unidentified	31.20	4.94
Unidentified	21.05	26.04	Unidentified	31.49	3.63
Unidentified	21.20	29.85	Unidentified	31.59	2.94

Unidentified	21.58	3.80	Unidentified	31.99	3.86
Unidentified	21.74	11.95	Unidentified	32.08	2.40
Unidentified	21.87	3.73	Unidentified	32.17	3.09
Unidentified	22.02	2.82	Unidentified	32.30	6.39
Unidentified	22.08	2.96	Unidentified	32.46	4.86
Unidentified	22.14	3.15	Unidentified	32.68	5.86
Unidentified	22.25	2.52	Unidentified	32.80	21.03
Unidentified	22.46	3.66	Unidentified	32.91	4.63
Benzothiophen	22.59	5.18	Dihexyldisulfid	33.13	2.88
Unidentified	22.89	4.41	Unidentified	33.90	3.16
Unidentified	23.20	6.77	DBT	34.39	4.73
Unidentified	23.38	4.40	Unidentified	34.50	3.39
Unidentified	23.46	2.71	Unidentified	34.54	5.53

Table E.6 List of detected molecules with sulfur specific GC-AED when the CoMoZAl#2 catalyst is used in the fluid bed reactor (THT = tetrahydrothiophene)

Compound name	Retention time (min)	Amount (wt-ppm S)	Compound name	Retention time (min)	Amount (wt-ppm S)
Hydrogensulfide	1.45	185.47	c-Dimethylthiophen	14.62	10.21
Carbonylsulfide	1.50	70.45	a-Trimethylthiophen	16.28	7.19
Unidentified	1.85	3.64	b-Trimethylthiophen	16.44	9.02
Unidentified	2.32	22.68	d-Trimethylthiophen	16.69	14.89
Unidentified	2.35	26.12	c-Trimethylthiophen	16.81	12.62
Ethanethiol	2.47	7.23	e-Trimethylthiophen	17.10	12.73
Unidentified	4.06	9.06	Unidentified	17.95	4.10
1-Propanethiol	4.47	4.01	Unidentified	19.23	5.14
Unidentified	4.55	4.07	Unidentified	19.33	4.35
Methylethylsulfide	6.09	176.93	Unidentified	19.53	7.59
Thiophen/ 2-Butanethiol	6.23	162.11	Unidentified	19.57	2.19
Unidentified	9.30	13.45	Unidentified	21.08	9.08
Unidentified	9.46	17.45	Unidentified	21.24	14.44
2-Methylthiophen	10.12	153.57	Unidentified	21.76	7.80
3-Methylthiophen	10.35	92.08	Unidentified	23.74	4.46
Unidentified	11.74	5.39	Unidentified	27.01	6.15
2-Methyl-THT	13.41	33.39	Dimethylbenzothiophen	27.33	7.69
3-Methyl-THT	13.60	18.91	Unidentified	32.80	12.47
a-Dimethylthiophen	13.83	61.10	Dihexyldisulfid	32.93	9.17
b-Dimethylthiophen	14.15	17.64			

Overview of hydrocarbons detected in the aqueous phase with GC-MS/FID

Table E.7 List of detected compounds in the aqueous phase with GC-MS/FID when the CoMoMgAl#1 catalyst is used in the fluid bed reactor.

Compound name	Retention time (min)	Area-FID (%)	Compound name	Retention time (min)	Area-FID (%)
Methanol	2.47	19.04	Unidentified	5.95	0.26
Ethanol	2.55	40.28	Unidentified	6.11	0.07
Acetone	2.62	12.36	Unidentified	6.57	0.06
1-Propanol	2.78	5.70	Unidentified	7.18	0.05
Acetic acid	2.84	3.81	Unidentified	8.10	0.06
2-Heptanone, 3-methyl-	2.93	3.76	Unidentified	8.29	0.17
1-Propanol, 2-methyl-	3.06	0.39	Phenol	11.71	4.24
Furan, tetrahydro-	3.13	0.43	Unidentified	16.83	0.32
1-butanol	3.28	2.08	Unidentified	18.35	0.87
2-Pentanone	3.48	0.57	Unidentified	24.59	0.16
2-Hydroxy-3-pentanone	3.56	0.47	Unidentified	28.93	0.05
Unidentified	3.69	0.35	Unidentified	31.69	0.07
Unidentified	3.87	0.08	Unidentified	33.57	0.08
Unidentified	3.96	0.25	Unidentified	33.71	0.11
Unidentified	4.19	0.14	Unidentified	34.86	0.05
1-Butanol, 3-methyl-	4.33	0.61	Unidentified	45.62	0.09
Unidentified	4.50	0.20	Unidentified	47.78	0.06
Cyclopentanol	4.69	0.40	Unidentified	47.99	0.14
Cyclopentanone	4.85	1.91	Unidentified	51.38	0.05
Unidentified	5.76	0.20			

Table E.8 List of detected compounds in the aqueous phase with GC-MS/FID when the CoMoMgAl#3 catalyst is used in the fluid bed reactor.

Compound Name	Retention time (min)	Area-FID (%)	Compound Name	Retention time (min)	Area-FID (%)
Methyl Alcohol	2.47	13.68	Unidentified	4.70	0.33
Ethanol	2.56	23.33	Cyclopentanone	4.87	0.83
Acetone	2.63	5.62	Unidentified	6.60	0.33
1-Propanol	2.79	3.06	Phenol	11.73	30.32
Acetic Acid	2.86	2.88	Phenol, 3/2-methyl-	16.82	2.89
Unidentified	2.95	1.41	Phenol, 3/2-methyl	18.35	7.46
Unidentified	3.07	0.21	2-ethyl phenol	22.79	0.52
Unidentified	3.14	0.18	Unidentified	23.42	0.27
1-Butanol	3.29	0.71	2.5-dimethyl phenol	23.50	0.26
Unidentified	3.37	0.76	4-ethyl phenol	24.46	0.36
Unidentified	3.49	0.16	3-ethyl phenol	24.57	1.51
Unidentified	3.57	0.17	Unidentified	25.09	0.27
Unidentified	3.72	0.21	Unidentified	25.89	0.22
Unidentified	4.24	0.15	3-propyl phenol	28.90	0.92
Unidentified	4.36	0.79			

Table E.9 List of detected compounds in the aqueous phase with GC-MS/FID when the CoMoMgAl#4 catalyst is used in the fluid bed reactor.

Compound Name	Retention time (min)	Area-FID (%)	Compound Name	Retention time (min)	Area-FID (%)
Methanol	2.46	11.25	cyclopentanol	4.68	0.36
Ethanol	2.55	18.20	Cyclopentanone	4.85	1.17
Acetone	2.62	6.42	Unidentified	5.94	0.17
1-Propanol	2.78	2.43	Pentanoic acid	6.56	0.66
Acetic acid	2.81	3.73	Phenol	11.70	31.58
1,3-butanediol	2.94	1.82	Phenol, 3/2-methyl-	16.78	3.97
Unidentified	3.06	0.19	Phenol, 3/2-methyl-	18.32	8.04
Unidentified	3.13	0.19	ethyl phenol	22.75	0.80
1-butanol	3.28	0.77	Unidentified	23.39	0.46
Unidentified	3.32	1.26	Unidentified	23.46	0.50
Unidentified	3.48	0.22	Unidentified	24.42	0.55
Unidentified	3.56	0.27	2.5-dimethyl phenol	24.54	1.53
Unidentified	3.69	0.32	Unidentified	25.06	0.29
Unidentified	3.93	0.23	2.3-dimeethyl phenol	25.85	0.26
Unidentified	4.21	0.31	3-propyl phenol	28.87	0.95
Heptanoic acid	4.32	1.09			

Table E.10 List of detected compounds in the aqueous phase with GC-MS/FID when the CoMoZA#1 catalyst is used in the fluid bed reactor.

Compound Name	Retention time (min)	Area-FID (%)	Compound Name	Retention time (min)	Area-FID (%)
Methanol	2.47	6.34	dimethyl phenol	20.77	0.86
Ethanol	2.55	13.67	ethyl phenol	22.77	1.25
Acetone	2.63	13.42	dimethyl phenol	23.47	3.10
1-Propanol	2.79	1.08	2.5-dimethyl phenol	24.56	2.11
Acetic acid	2.83	5.70	Unidentified	25.06	1.03
2-Butanone	2.94	4.26	2.3-dimeethyl phenol	25.86	0.54
Unidentified	3.35	0.83	Unidentified	26.44	0.37
Unidentified	4.23	0.40	trimethyl phenol	27.78	0.71
Unidentified	4.34	0.58	3-propyl phenol	28.92	0.64
Cyclopentanone	4.85	2.32	trimethyl phenol	29.28	0.54
Phenol	11.71	24.05	Unidentified	29.47	0.64
Phenol, 3/2-methyl-	16.79	8.09	tetramethylphenol	32.93	0.52
Phenol, 3/2-methyl-	18.34	6.95			

Table E.11 List of detected compounds in the aqueous phase with GC-MS/FID when the CoMoZA#2 catalyst is used in the fluid bed reactor.

Compound Name	Retention time (min)	Area-FID (%)	Compound Name	Retention time (min)	Area-FID (%)
Methyl Alcohol	2.47	6.98	dimethyl phenol	20.78	0.41
Ethanol	2.55	8.63	ethyl phenol	22.77	0.73
Acetone	2.62	12.50	dimethyl phenol	23.40	0.68
1-Propanol	2.74	0.48	dimethyl phenol	23.47	1.38
Acetic acid	2.83	4.57	2.5-dimethyl phenol	24.56	1.61
2-Butanone	2.94	3.68	Unidentified	25.07	0.76
Propanoic acid	3.35	0.68	2.3-dimeethyl phenol	25.87	0.43
2-pentanone	3.48	0.22	trimethyl phenol	27.78	0.30
Pentanoic acid	4.34	0.36	3-propyl phenol	28.92	0.45
Cyclopentanone	4.85	1.41	trimethyl phenol	29.29	0.22
Phenol	11.71	36.50	Unidentified	29.48	0.22
Phenol, 3/2-methyl-	16.79	7.54	tetramethylphenol	32.93	0.23
Phenol, 3/2-methyl-	18.33	8.60	Unidentified	51.92	0.43

NH_3-TPD

The NH_3 desorption rate for the oxide precursors are shown in Figure E.3. Here the desorption rate is calculated on the basis of the surface area, which shows that the increased acidity when the CoMo loading is increased from 4.0 to 12.0 wt.% is due to a higher surface area.

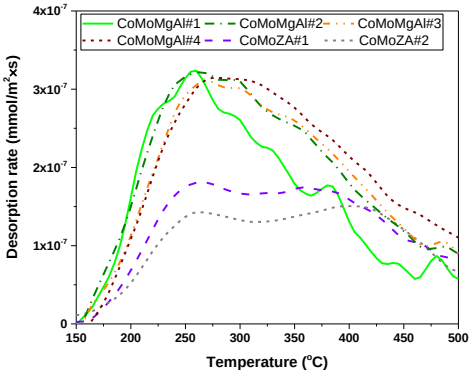

Figure E.3 NH_3-TPD profiles for the oxide precursors.

Raman spectroscopy

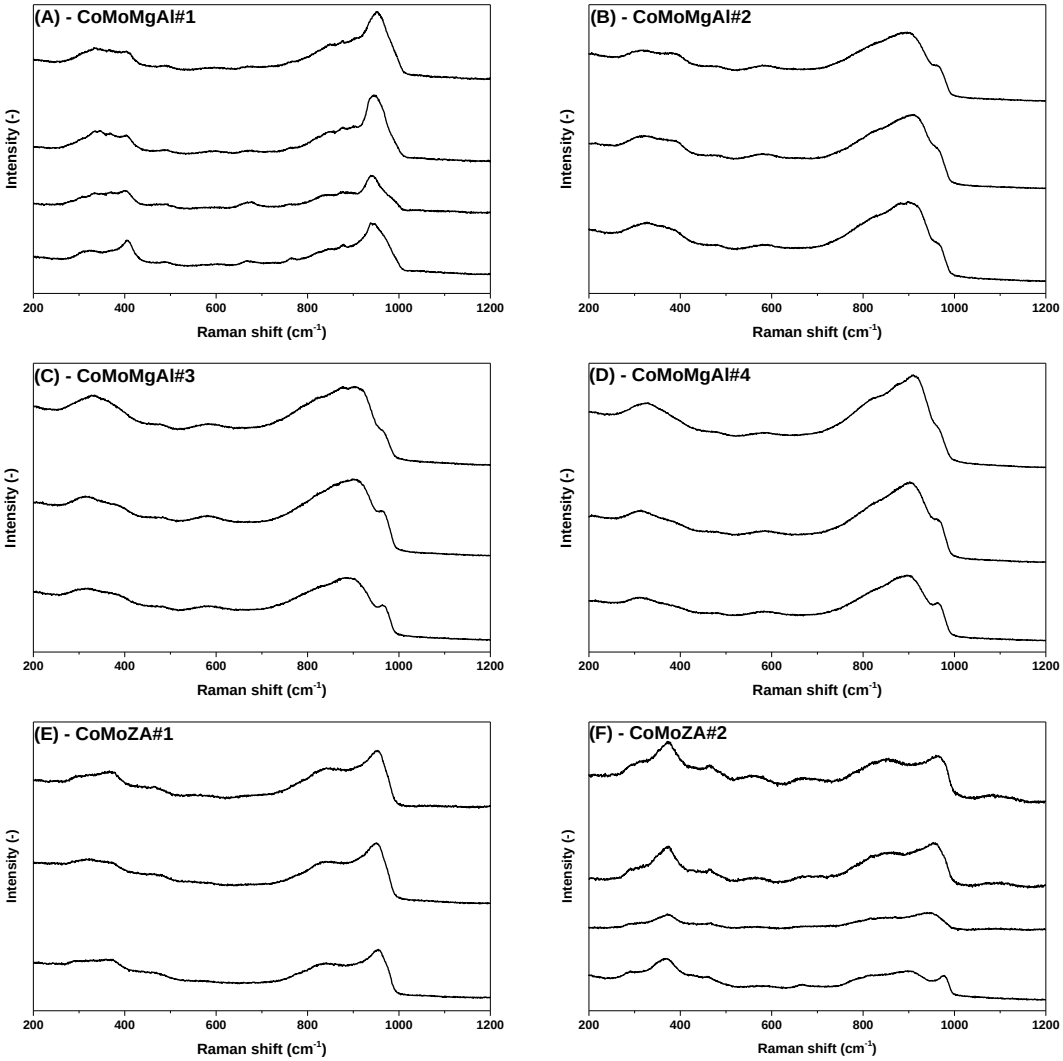

Figure E.4 Raman spectra of different spots on CoMoMgAl#1 (A), CoMoMgAl#2 (B), CoMoMgAl#3 (C), CoMoMgAl#4 (D), CoMoZA#1 (E), and CoMoZA#2 (F) in the oxide phase.

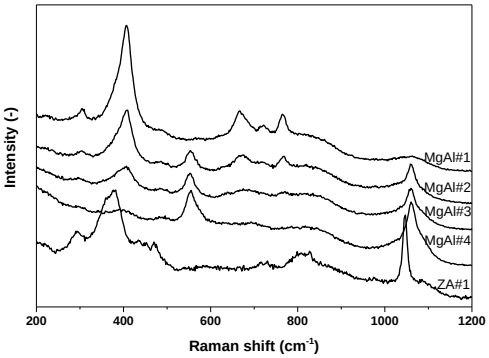

Figure E.5 Raman spectrum on the used supports MgAl#1, MgAl#2, MgAl#3, MgAl#4, and ZA#1 before impregnation.

Scanning Electron Microscopy

Table E.12 Carbon and potassium content measured with SEM-EDS at different acceleration voltages on fresh and spent catalysts

	C content (wt.%)				K content (wt.%)			
	3 kV	5 kV	10 kV	15 kV	3 kV	5 kV	10 kV	15 kV
Fresh catalysts								
CoMoMgAl#1	2.5	2.9	3.0	3.0	0.0	0.0	0.0	0.0
CoMoMgAl#2	2.3	2.1	2.4	3.0	0.0	0.0	0.0	0.0
CoMoMgAl#3	3.0	3.2	3.2	3.3	0.0	0.0	0.0	0.0
CoMoMgAl#4	3.4	3.0	2.3	2.4	0.0	0.0	0.0	0.0
CoMoZA#1	4.5	3.7	3.7	3.4	0.0	0.0	0.0	0.0
CoMoZA#2	3.2	2.7	3.2	3.1	0.0	0.0	0.0	0.0
Spent catalysts								
CoMoMgAl#1	5.8	5.3	4.7	4.5	0.0	0.8	0.4	0.4
CoMoMgAl#2	8.3	7.7	7.2	7.3	0.0	0.0	0.7	0.6
CoMoMgAl#3	12.6	10.5	9.8	11.0	0.0	0.0	0.5	0.5
CoMoMgAl#4	9.1	10.1	11.4	14.3	0.0	0.0	0.4	0.5
CoMoZA#1	9.2	9.9	10.8	13.1	0.0	0.0	0.7	0.5
CoMoZA#2	10.8	11.4	9.9	9.7	0.0	0.0	0.5	0.4

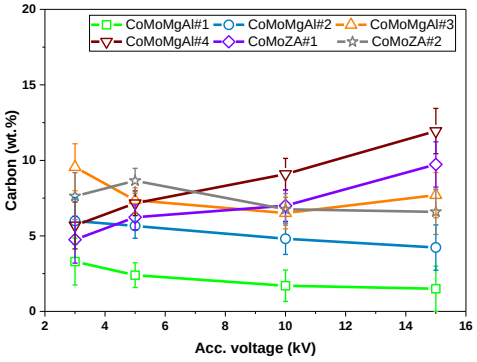

Figure E.6 Carbon content on spent catalysts (carbon spent catalyst – carbon on fresh catalyst) as a function of acceleration voltage.

Elemental maps (STEM-EDS)

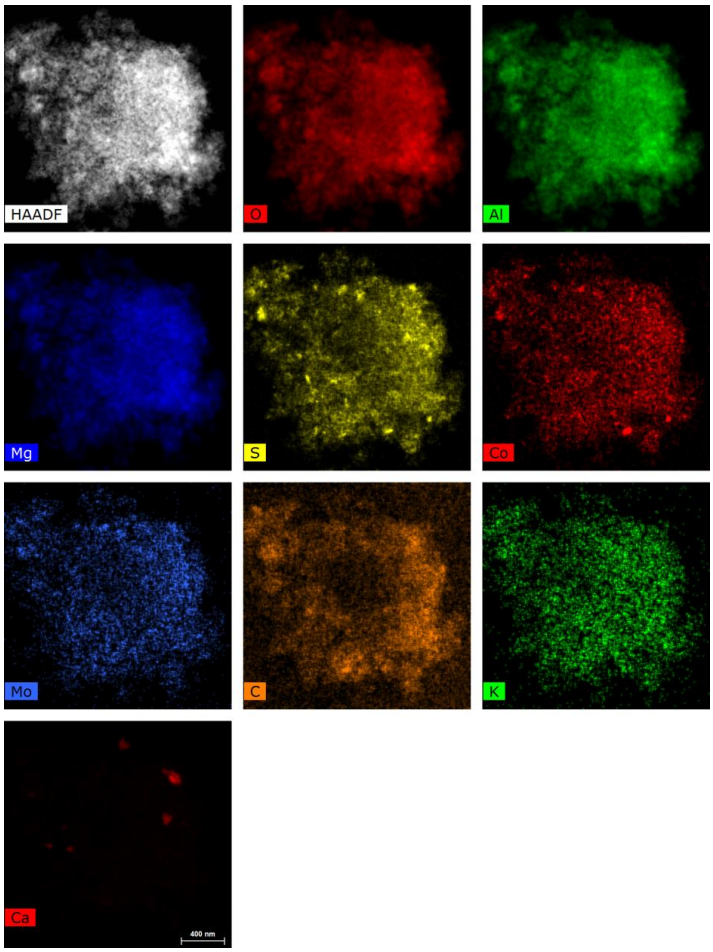

Figure E.7 STEM-EDS element map of the CoMoMgAl#1 catalyst displaying unprocessed counts in the EDX spectrum.

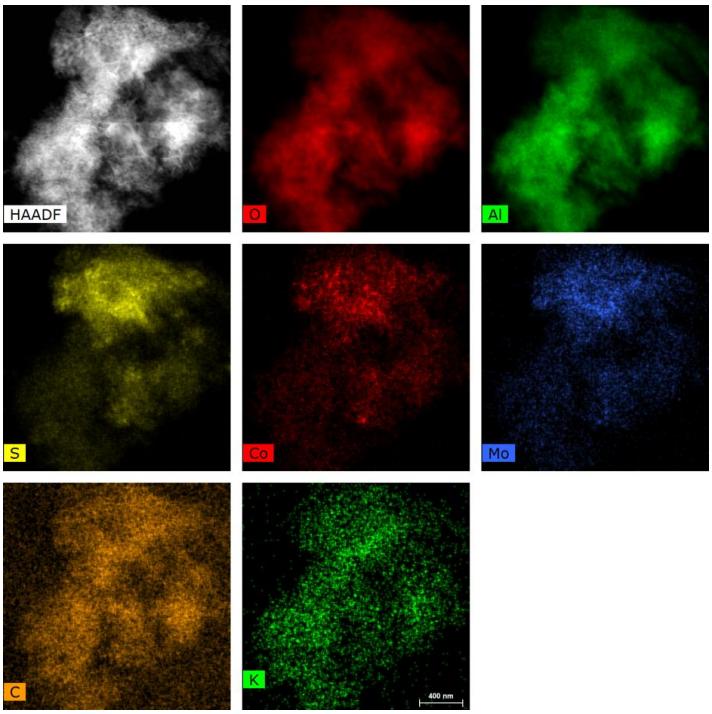

Figure E.8 STEM-EDS element map of the CoMoMgAl#2 catalyst displaying unprocessed counts in the EDX spectrum.

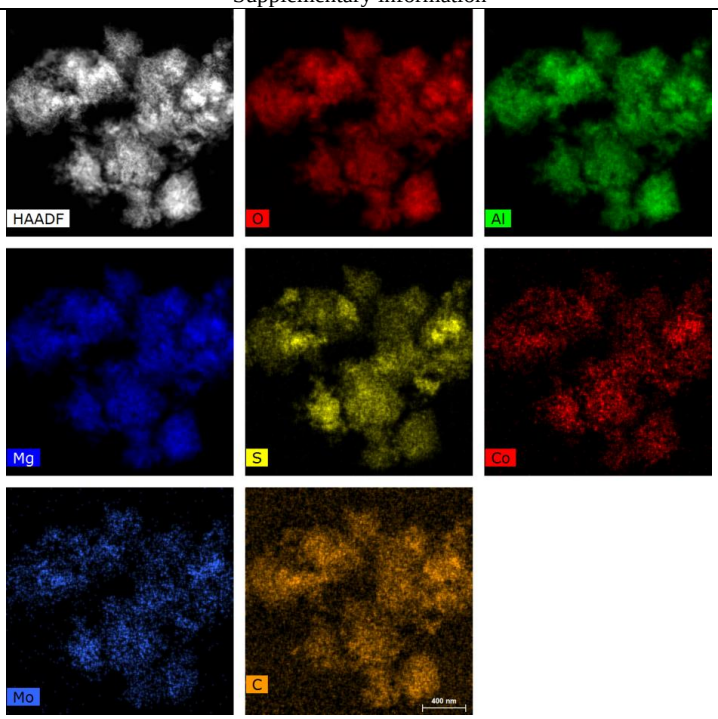

Figure E.9 STEM-EDS element map of the CoMoMgAl#3 catalyst displaying unprocessed counts in the EDX spectrum.

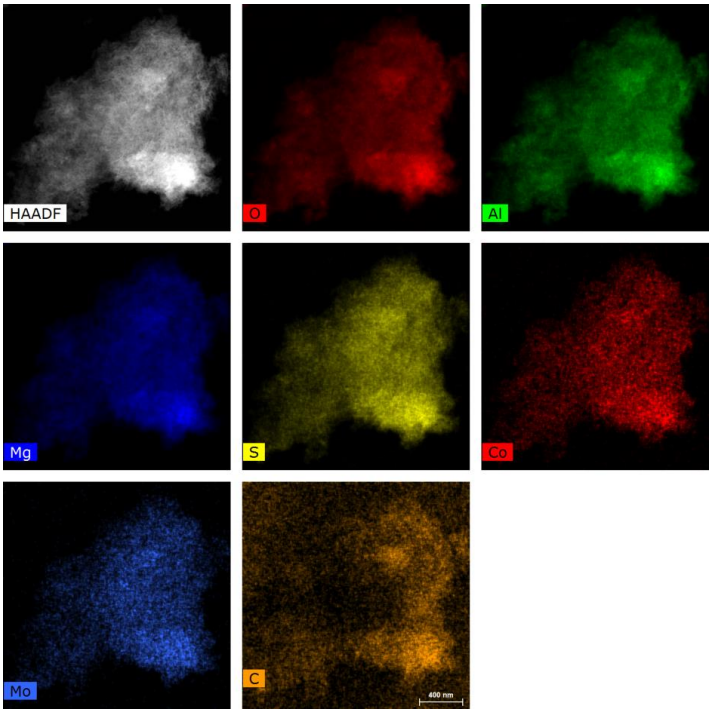

Figure E.10 STEM-EDS element map of the CoMoMgAl#4 catalyst displaying unprocessed counts in the EDX spectrum.

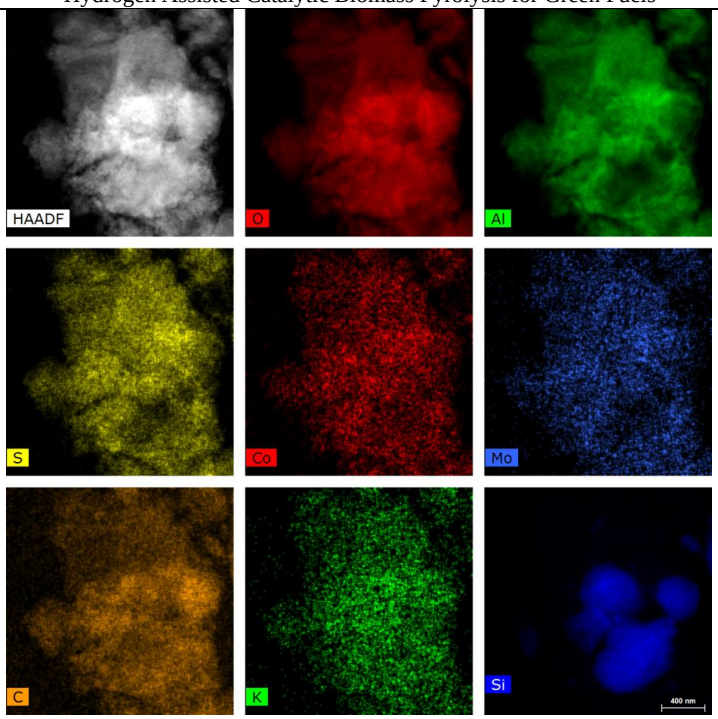

Figure E.11 STEM-EDS element map of the CoMoZA#1 catalyst displaying unprocessed counts in the EDX spectrum.

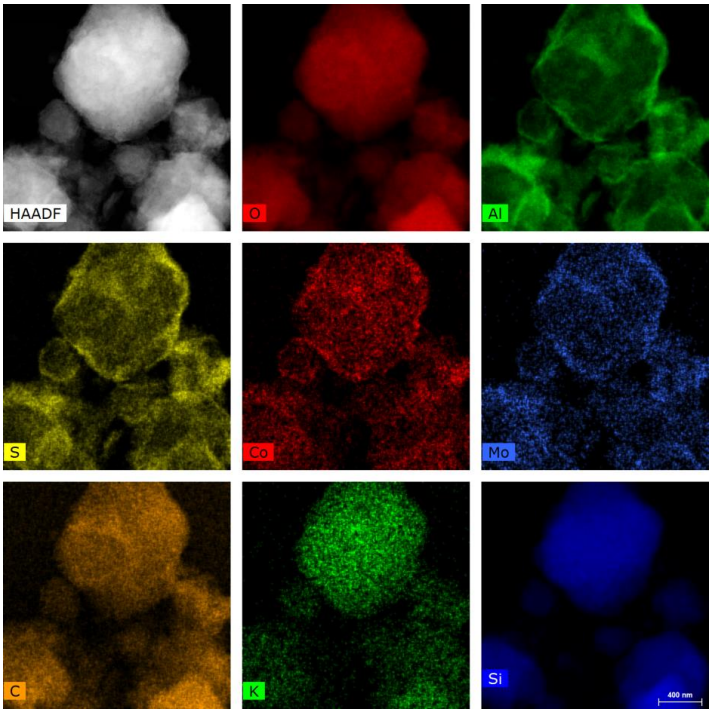

Figure E.12 STEM-EDS element map of the CoMoZA#2 catalyst displaying unprocessed counts in the EDX spectrum.

Appendix F Supplementary Information for Deactivation of a CoMo catalyst during catalytic hydropyrolysis of biomass. Part I: Product distribution and composition

Raman spectroscopy of oxide precursors

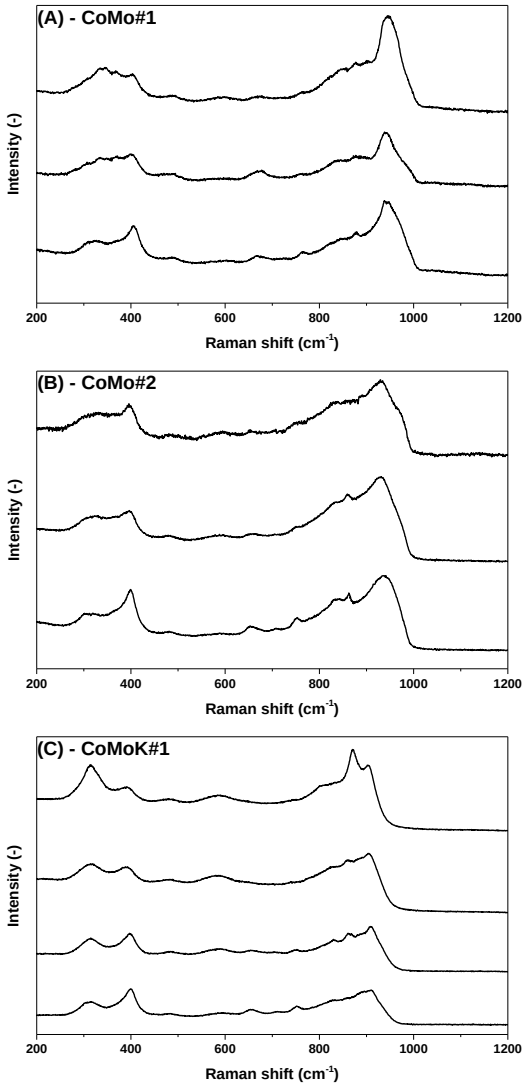

Figure F.1 Raman spectra at different spots on the oxide precursor for CoMo#1, CoMo#2, and CoMoK#1.

Overview of hydrocarbons detected in the aqueous phase with GC-MS/FID

Table F.1 List of detected compounds in the aqueous phases with GC-MS/FID from experiment 1 (CoMo#2)

Day		**1**	**2**	**3**	**4**	**5**
Compound	**Retention time (min)**	**Area-FID (%)**	**Area-FID (%)**	**Area-FID (%)**	**Area-FID (%)**	**Area-FID (%)**
Unidentified	2.39	2.44	6.65	8.10	1.12	0.29
Unidentified	2.46	2.10	4.31	4.05	0.73	0.18
Unidentified	2.55	-	-	-	-	0.11
acetone	2.62	86.48	33.12	5.88	0.61	0.11
Unidentified	4.24	3.83	28.38	23.77	3.44	1.03
Unidentified	5.89	5.15	-	-	-	-
Phenol	11.72	-	-	-	36.20	45.42
m-cresol	16.80		27.54	58.21	46.31	30.37
o-cresol	18.39	-	-	-	-	5.61
Unidentified	20.80	-	-	-	-	1.03
2-ethyl-phenol	22.78	-	-	-	5.45	4.56
2,5 dimethyl phenol	23.49	-	-	-	6.15	5.26
Unidentified	24.61	-	-	-	-	1.80
Unidentified	25.08	-	-	-	-	0.86
Unidentified	25.45	-	-	-	-	0.25
Unidentified	27.30	-	-	-	-	0.21
Unidentified	27.57	-	-	-	-	0.31
Unidentified	27.78	-	-	-	-	0.55
Unidentified	28.05	-	-	-	-	0.42
Unidentified	28.24	-	-	-	-	0.57
Unidentified	29.01	-	-	-	-	0.48
Unidentified	29.32	-	-	-	-	0.23
Unidentified	29.50	-	-	-	-	0.33

Table F.2 List of detected compounds in the aqueous phase with GC-MS/FID from experiment 2 (CoMo#1).

Compound	Retention time (min)	Area-FID (%)	Compound	Retention time (min)	Area-FID (%)
Methanol	2.47	19.04	Unidentified	5.95	0.26
Ethanol	2.55	40.28	Unidentified	6.11	0.07
Acetone	2.62	12.36	Unidentified	6.57	0.06
1-Propanol	2.78	5.70	Unidentified	7.18	0.05
Acetic acid	2.84	3.81	Unidentified	8.10	0.06
2-Butanone	2.93	3.76	Unidentified	8.29	0.17
1-Propanol, 2-methyl-	3.06	0.39	Phenol	11.71	4.24
Furan, tetrahydro-	3.13	0.43	Unidentified	16.83	0.32
1-butanol	3.28	2.08	Unidentified	18.35	0.87
2-Pentanone	3.48	0.57	Unidentified	24.59	0.16
2-Hydroxy-3-pentanone	3.56	0.47	Unidentified	28.93	0.05
Unidentified	3.69	0.35	Unidentified	31.69	0.07
Unidentified	3.87	0.08	Unidentified	33.57	0.08
Unidentified	3.96	0.25	Unidentified	33.71	0.11
Unidentified	4.19	0.14	Unidentified	34.86	0.05
1-Butanol, 3-methyl-	4.33	0.61	Unidentified	45.62	0.09
Unidentified	4.50	0.20	Unidentified	47.78	0.06
Cyclopentanol	4.69	0.40	Unidentified	47.99	0.14
Cyclopentanone	4.85	1.91	Unidentified	51.38	0.05
Unidentified	5.76	0.20			

Table F.3 List of detected compounds in the aqueous phase with GC-MS/FID from experiment 3.

Compound	Ret.Time (min)	Area-FID (%)	Compound	Ret.Time (min)	Area-FID (%)
Methyl Alcohol	2.47	19.27	Furanone,dihydro-5-methyl	10.20	0.35
Ethanol	2.55	22.97	Unidentified	10.55	0.10
Acetone	2.62	10.16	Unidentified	10.99	0.11
Acetic acid	2.78	4.95	Phenol	11.71	1.65
1-Propanol	2.85	5.32	Unidentified	12.38	0.08
2-Butanone	2.93	4.17	Unidentified	14.84	0.11
1.3-Butanediol	3.06	0.06	Unidentified	15.81	0.05
Unidentified	3.14	0.07	m-cresol	16.80	0.22
1-Butanol	3.28	1.27	Unidentified	17.97	0.05
2-Propanone, 1-hydroxy-	3.31	3.32	o-cresol	18.33	0.84
2-Propanone, 1,3-dihydroxy-	3.49	2.10	Unidentified	18.91	0.04
1-Propanol, 3-ethoxy	3.56	0.64	2-methoxy phenol	19.54	0.10
Unidentified	3.69	0.71	4-hydroxy cyclohexanone	21.82	0.13
1,2 propanediol	3.92	1.21	Unidentified	23.39	0.08
1-hydroxy-butanone	4.18	0.09	4-ethyl phenol	24.43	0.13
Unidentified	4.22	0.12	3-ethyl phenol	24.55	0.28
Unidentified	4.37	1.60	Unidentified	25.90	0.08
Unidentified	4.50	0.18	1,4:3,6-Dianhydro alpha d-glucopyranose	26.55	0.20
Cyclopentanol	4.68	1.77	2-propyl phenol	28.87	0.20
Cyclopentanone	4.85	7.35	Unidentified	30.00	0.05
Unidentified	5.09	0.07	Unidentified	31.36	0.08
Unidentified	5.37	0.06	Unidentified	31.66	0.04
2-Cyclopenten-1-one	5.74	0.74	Unidentified	32.18	0.10
Cyclopentanone, 2-methyl-	5.94	1.28	Unidentified	32.42	0.07
3-Methylcyclopentanone	6.10	0.49	Unidentified	32.51	0.11
Unidentified	6.24	0.13	Unidentified	33.18	0.20
Unidentified	6.56	0.17	Unidentified	33.54	0.06
Unidentified	6.78	0.13	Unidentified	34.74	0.03
Unidentified	7.26	0.33	Unidentified	34.82	0.08
Unidentified	7.50	0.08	Unidentified	35.70	0.05
Cyclohexanone	7.67	0.34	Unidentified	36.19	0.13
Pentanedial	7.82	0.74	Unidentified	36.42	0.06
Unidentified	8.07	0.28	Beta D-Glucopyranose, 1,6-anhydro	36.54	0.47
Butyrolactone	8.23	1.19	Unidentified	37.70	0.05
Unidentified	8.78	0.06	Unidentified	38.08	0.03
Unidentified	9.59	0.10	Unidentified	38.81	0.12

Overview of sulfur containing molecules detected with sulfur specific GC-AED

Table F.4 List of detected molecules with sulfur specific GC-AED in the organic phase from experiment 1 (CoMo#2).

Day		**1**	**5**
Compound	**Retention time (min)**	**Amount (ppm S)**	**Amount (ppm S)**
Hydrogensulfide	1.48	86.71	-
Unidentified	3.00	1.85	-
Unidentified	3.73	5.35	5.32
Methylethylsulfide	6.33	-	2.04
Dimethyl-thiophane	15.53	2.03	-
Unidentified	33.03	5.49	-
Dibenzothiophene	34.58	1.56	-
4.6-Dimethyldibenzothiophene	37.60	2.47	-
Unidentified	57.52	-	3.65
Unidentified	57.65	-	4.72
Unidentified	57.77	-	4.25

Table F.5 List of detected molecules with sulfur specific GC-AED in the organic phase from experiment 2 (CoMo#1). (DMDS = dimethyl disulfide, THT = tetrahydrothiophene)

Compound	Retention time (min)	Amount (ppm S)	Compound	Retention time (min)	Amount (ppm S)
Hydrogensulfide	1.47	382.18	c-Trimethylthiophen	17.14	4.42
Methanethiol	1.88	23.86	d-Trimethylthiophen	17.19	1.61
Unidentified	2.01	2.46	e-Trimethylthiophen	17.95	4.72
Unidentified	2.39	60.72	Unidentified	19.11	3.83
Ethanethiol	2.51	26.64	Unidentified	19.32	3.75
Unidentified	2.69	4.53	Unidentified	19.42	2.33
Unidentified	3.26	1.75	Unidentified	19.81	3.32
Unidentified	4.16	7.39	Unidentified	20.78	9.72
Unidentified	4.38	6.85	Unidentified	21.17	8.33
Unidentified	4.55	6.48	Unidentified	21.32	9.66
1-Propanethiol	4.64	2.35	Unidentified	21.58	3.35
Unidentified	6.07	4.16	Unidentified	22.37	11.58
Unidentified	6.24	28.26	Unidentified	22.53	1.31
Methylethylsulfide	6.33	150.13	Benzothiophen	22.69	1.32
Unidentified	7.48	1.68	Unidentified	22.73	2.38
Unidentified	7.85	2.49	Unidentified	23.46	8.92
Unidentified	8.02	6.33	Unidentified	23.67	8.67
Unidentified	8.27	2.58	Unidentified	23.81	5.59
Butanethiol/Tetra Hydrothiophen	8.48	2.56	Unidentified	23.94	2.85
DMDS	9.40	1.98	Unidentified	24.09	3.53
Unidentified	9.56	4.74	Unidentified	24.14	2.11
Unidentified	9.65	5.97	Unidentified	24.52	1.94
Unidentified	10.18	109.25	Unidentified	24.69	1.92
2-Methylthiophen	10.47	18.63	Unidentified	25.01	13.80
2-Methyl-THT	11.26	20.74	Methylbenzothiophen (b)	25.19	5.03
Unidentified	11.56	1.92	Methylbenzothiophen (a)	25.38	1.78
3-Methyl-THT	11.83	2.69	Methylbenzothiophen (c)	25.68	7.64
Unidentified	11.88	9.16	Methylbenzothiophen (d)	25.83	2.07
Unidentified	12.42	7.02	Unidentified	25.93	4.15
Unidentified	12.60	5.27	Unidentified	26.10	5.28
Unidentified	12.84	9.59	Unidentified	26.28	2.04
Unidentified	13.48	20.25	Unidentified	26.49	1.93
Unidentified	13.66	22.21	Unidentified	27.10	2.59
Unidentified	13.85	11.59	Unidentified	27.17	1.90
Unidentified	13.89	8.53	Unidentified	27.30	6.22
a-Dimethylthiophen	13.97	5.87	Unidentified	27.42	4.01
b-Dimethylthiophen	14.24	6.32	Dimethylbenzothiophen (a)	27.73	5.75
c-Dimethylthiophen	14.31	3.91	Dimethylbenzothiophen (b)	28.08	2.37
d-Dimethylthiophen	14.66	2.62	Dimethylbenzothiophen (c)	28.21	3.04
Dimethyl-THT	14.98	4.45	Unidentified	29.22	4.23

Unidentified	16.38	3.24	Unidentified	29.42	1.75
Unidentified	16.54	3.26	Unidentified	29.90	2.37
a-Trimethylthiophen	16.72	1.27	Unidentified	32.92	3.59
b-Trimethylthiophen	16.89	3.04			

Table F.6 List of detected molecules with sulfur specific GC-AED in the organic phase from experiment 3 (CoMoK#1). (DMDS = domethyl disulfide, THT = tetrahydrothiophene)

Compound	Retention time (min)	Amount (ppm S)	Compound	Retention time (min)	Amount (ppm S)
Hydrogensulfide	1.45	319.24	a-Trimethylthiophen	16.73	2.66
Methanethiol	1.86	30.46	b-Trimethylthiophen	16.83	13.06
Unidentified	2.34	38.58	d-Trimethylthiophen	17.06	1.17
Unidentified	2.48	11.55	c-Trimethylthiophen	17.11	1.21
Unidentified	4.10	6.56	e-Trimethylthiophen	17.75	2.99
Unidentified	4.32	4.86	Unidentified	18.07	1.02
Unidentified	4.49	5.90	Unidentified	18.18	4.10
1-Propanethiol	4.57	4.45	Unidentified	18.40	1.17
Unidentified	5.99	2.89	Unidentified	18.66	1.21
Unidentified	6.18	28.42	Unidentified	19.23	2.27
Methylethylsulfide	6.24	18.26	Unidentified	19.33	2.09
Unidentified	7.76	3.73	Unidentified	19.62	1.90
Unidentified	7.93	5.12	Unidentified	19.73	1.47
Unidentified	8.20	3.53	Unidentified	20.55	1.42
DMDS	9.37	3.86	Unidentified	20.69	4.51
Unidentified	9.57	3.56	Unidentified	21.07	3.74
Unidentified	10.10	14.23	Unidentified	21.22	3.92
2-Methylthiophen	10.42	6.71	Unidentified	21.35	1.43
2-Methyl-THT	11.21	4.87	Unidentified	21.49	1.23
Unidentified	11.50	2.31	Unidentified	22.22	3.18
Unidentified	11.76	2.05	Unidentified	22.45	4.39
3-Methyl-THT	11.82	0.89	Benzothiophen	22.64	2.60
Unidentified	11.89	4.16	Unidentified	23.33	2.25
Unidentified	12.40	11.87	Unidentified	23.56	3.15
Unidentified	12.56	13.06	Unidentified	23.70	3.02
Unidentified	12.78	1.93	Unidentified	23.79	1.51
Unidentified	12.93	2.53	Unidentified	23.84	1.44
Unidentified	13.24	2.08	Unidentified	24.07	2.42
Unidentified	13.41	4.43	Unidentified	24.15	1.65
Unidentified	13.59	3.26	Unidentified	24.28	2.38
a-Dimethylthiophen	13.83	6.41	Unidentified	24.35	1.03
b-Dimethylthiophen	14.18	2.22	Unidentified	24.41	2.20
c-Dimethylthiophen	14.25	2.08	Methylbenzothiophen (a)	24.91	2.89
d-Dimethylthiophen	14.49	4.67	Methylbenzothiophen (d)	25.85	2.02
Dimethyl-THT	14.91	3.53	Methylbenzothiophen (c)	25.98	3.95
Dimethyl-THT	15.25	2.29	Methylbenzothiophen (b)	26.16	1.44
Dimethyl-THT	15.36	2.94	Dimethylbenzothiophen (a)	27.19	2.06
Dimethyl-THT	15.64	1.71	Dimethylbenzothiophen (b)	27.97	1.38
Unidentified	15.83	4.73	Unidentified	30.19	2.34
Unidentified	16.46	1.03			

CO and CO_2 concentration in the exit gas

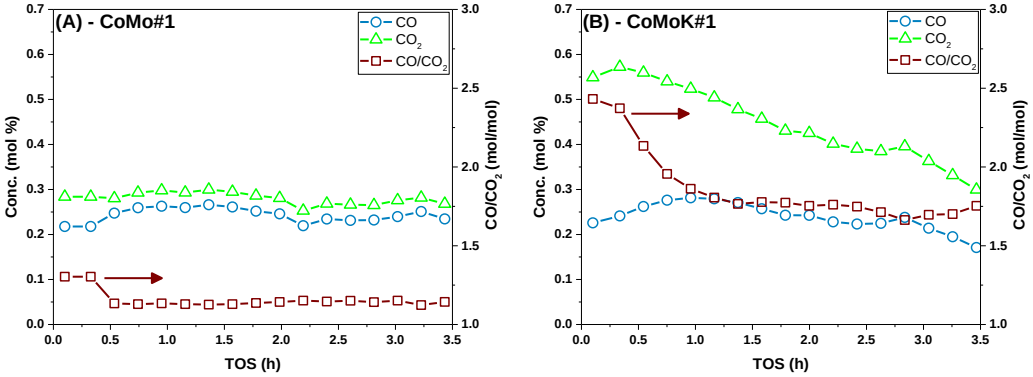

Figure F.2 CO and CO_2 concentration and the CO/CO_2 molar ratio during the experiments with CoMo#1 (A) and CoMoK#1 (B)

Appendix G Supplementary information for Deactivation of a CoMo catalyst during catalytic hydropyrolysis of biomass. Part II: Characterization of spent catalysts

Temperature profile in fluid bed reactor during catalytic hydropyrolysis of straw

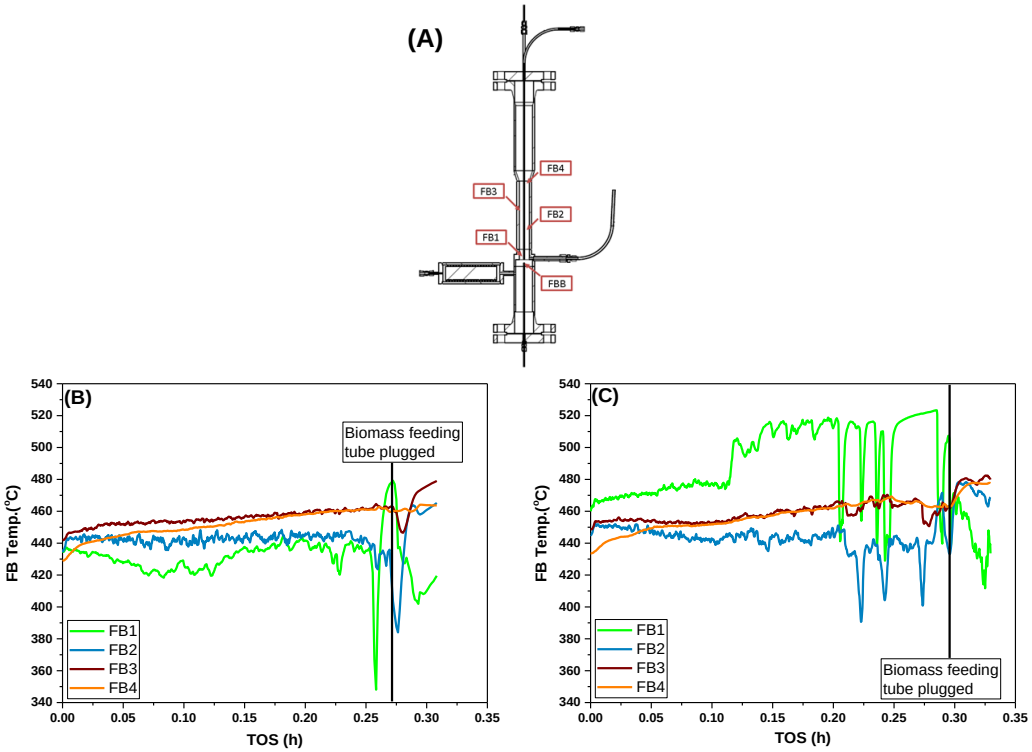

Figure G.1 Location of the thermocouples in fluid bed reactor and the temperature in the fluid bed in experiment 4 (A) and 5 (B). Pressure: 26 bar, straw feeding rate: ≤400 g/h, H_2 flow: 82-102 NL/min, N_2 flow: 5 NL/min, and H_2S conc: 460 ppm.

Scanning Electron Microscopy

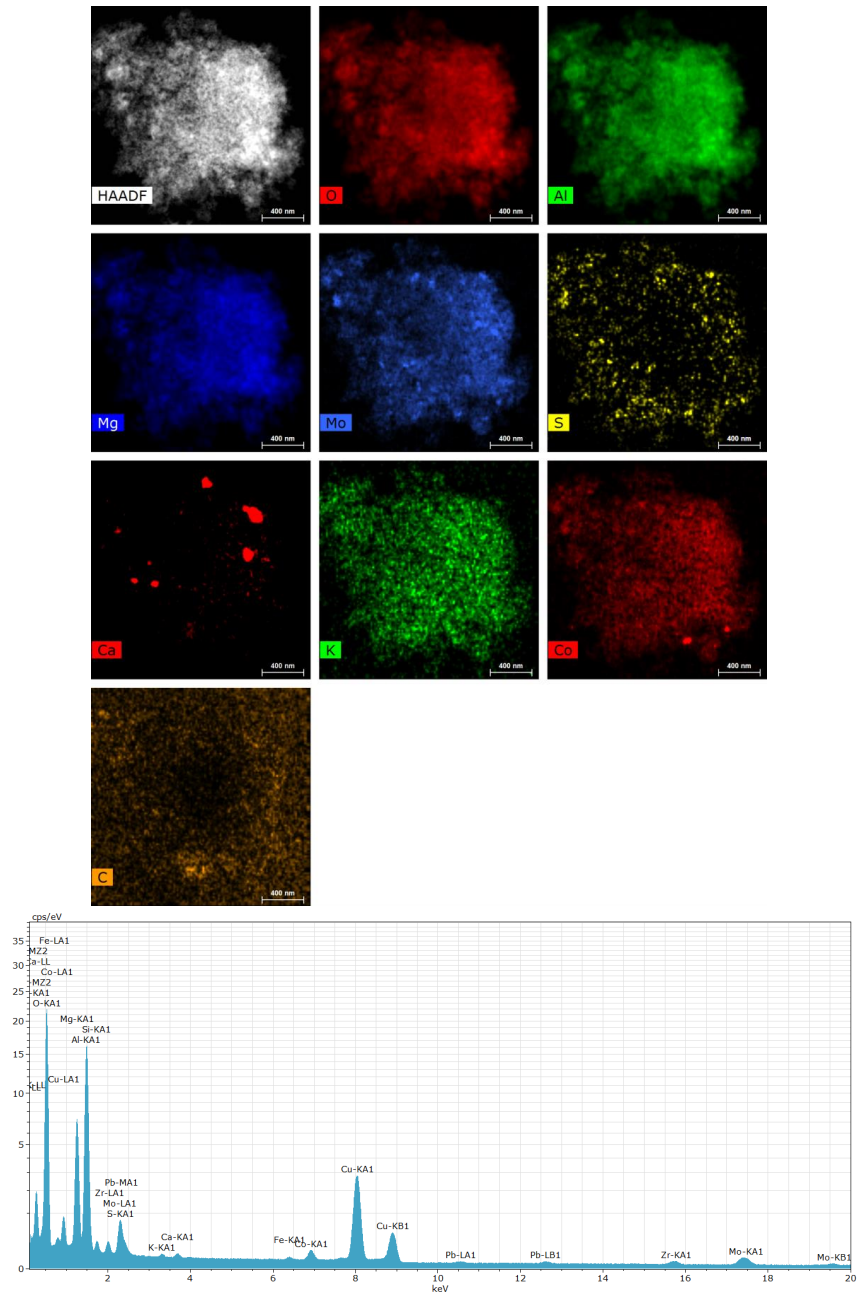

Figure G.2 STEM-EDS element map of the CoMo#1 catalyst displaying net counts after a background subtraction and de-convolution of the EDX spectrum. The Si, Fe, Cu, Zr, Pb signals were attributed to system peaks from the microscope, TEM grid, specimen holder and X-ray detectors.

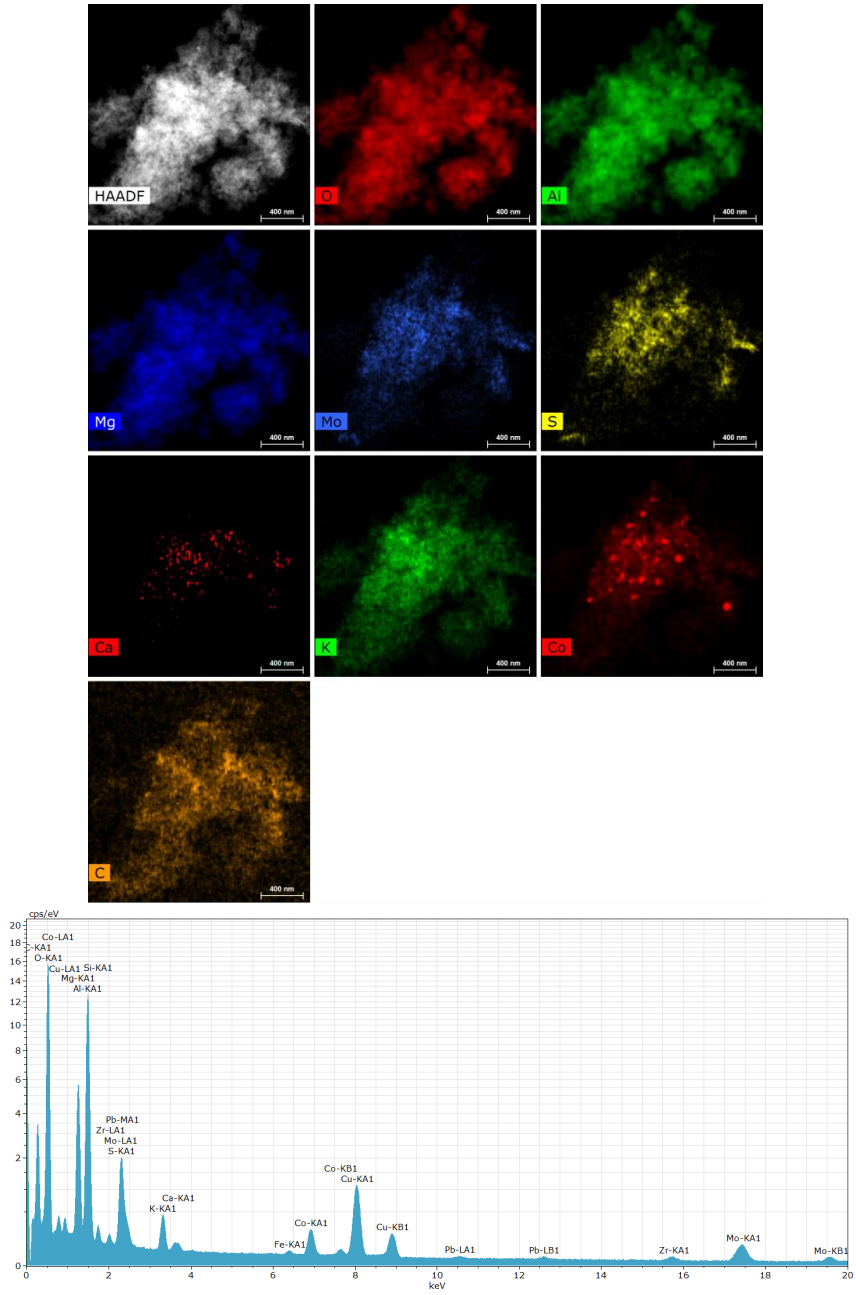

Figure G.3 STEM-EDS element map of the CoMo#2 catalyst displaying net counts after a background subtraction and deconvolution of the EDX spectrum. The Si, Fe, Cu, Zr, Pb signals were attributed to system peaks from the microscope, TEM grid, specimen holder and X-ray detectors.

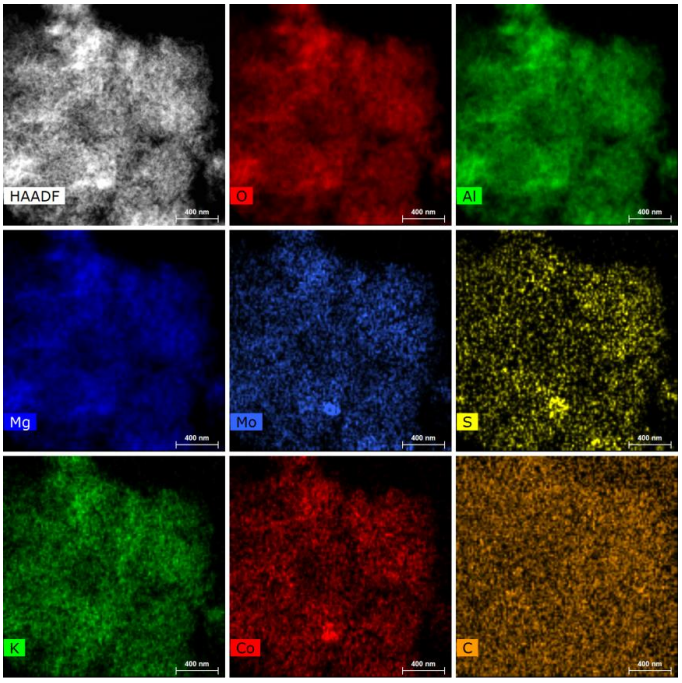

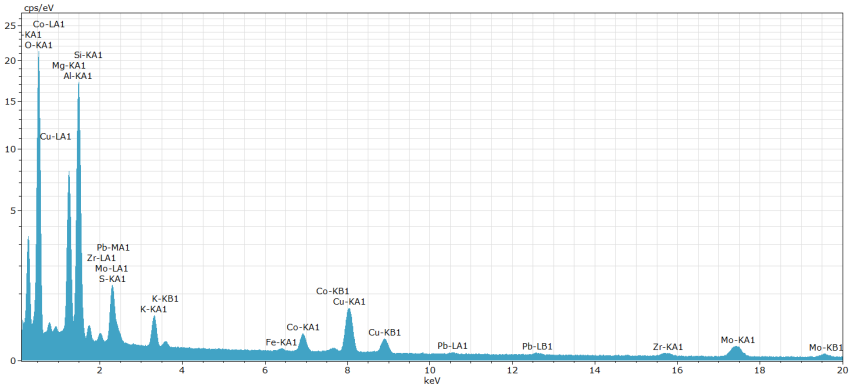

Figure G.4 STEM-EDS element map of the CoMoK#1 catalyst displaying net counts after a background subtraction and deconvolution of the EDX spectrum. The Si, Fe, Cu, Zr, Pb signals were attributed to system peaks from the microscope, TEM grid, specimen holder and X-ray detectors.

Table G.1 Carbon and potassium content measured with EDS at different acceleration voltages on fresh and spent CoMo#1 and CoMo#2 catalyst

	C content (wt.%)				K content (wt.%)			
	3 kV	5 kV	10 kV	15 kV	3 kV	5 kV	10 kV	15 kV
Fresh catalysts								
CoMo#1	2.5	2.9	3.0	3.0	-	0.0	0.0	0.0
CoMo#2	2.5	2.9	3.0	3.0	-	0.0	0.0	0.0
Spent catalysts								
CoMo#1	5.8	5.3	4.7	4.5	-	0.8	0.4	0.4
CoMo#2	27.2	18.0	15.1	15.0	-	2.4	1.6	1.5

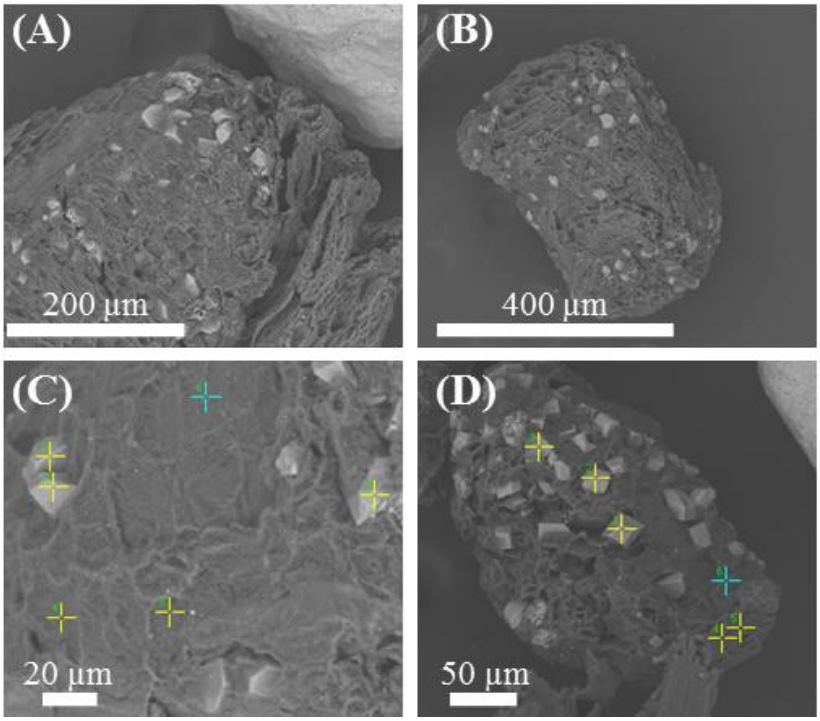

Figure G.5 SEM images of char particles from catalytic hydropyrolysis experiments of beech wood. EDX measurements on the points shown in figure C and D is shown in Table G.2 Fluid bed temperature: 450°C, pressure: 26 bar, biomass feeding rate: 270 g/h, H_2 flow: 82 NL/min, N_2 flow: 5 NL/min, and H_2S conc: 460 ppm.

Table G.2 EDS measurement on points shown in Figure G.5 (C) and (D).

Point	C (wt.%)	O (wt.%)	S (wt.%)	K (wt.%)	Ca (wt.%)
C.1	6.8	0	1.3	0	91.9
C.2	0	0	1.6	0	98.5
C.3	21.9	14.9	5.1	0.94	57.1
C.4	64.4	35.6	0	0	0
C.5	ND	ND	ND	ND	ND
C.6	58.8	33.9	0	0	7.3
D.1	19.3	48.5	3.7	0.22	28.3
D.2	24.8	40.7	5.0	0.3	29.1
D.3	44.1	19.7	4.7	0	31.5
D.4	69.7	26.1	1	0.27	3
D.5	79.6	19.1	0.3	0	0.9
D.6	88.27	10.68	0.19	0	0.85

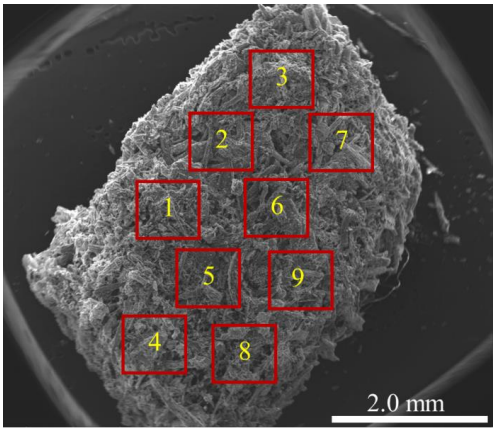

Figure G.6 SEM image of a char agglomerate from experiment 4 using straw. Fluid bed temperature: 453°C, pressure: 26 bar, straw feeding rate: 400 g/h, H_2 flow: 82 NL/min, N_2 flow: 5 NL/min, and H_2S conc: 460 ppm.

Table G.3 EDS measurement on the points shown in Figure G.6.

Point	C (wt.%)	O (wt.%)	Mg (wt.%)	Al (wt.%)	Si (wt.%)	P (wt.%)	S (wt.%)	Cl (wt.%)	K (wt.%)	Ca (wt.%)
1	68.9	16.8	0.5	0.2	1.5	0.4	0.6	2	7.3	1.6
2	68	19.3	0.7	0.1	3.1	0.4	0.6	1	5.2	1.6
3	68	17.6	0.5	0.2	1.9	0.5	0.5	1.9	7	1.6
4	69	16.9	0.4	0.1	2.7	0.3	0.6	2.4	6.5	1
5	70.1	17	0.4	0	1.5	0.5	0.8	1.5	6.3	1.8
6	70.8	18.2	0.3	0.1	1.8	0.3	0.5	1.4	5.4	1.1
7	70	17	0.4	0.2	1.5	0.3	0.7	2.4	6.6	1
8	68.5	16.1	0.6	0.1	1.9	0.4	0.6	2.7	7.5	1.6
9	71.2	16.6	0.5	0.1	1	0.4	0.6	2.1	6.3	1.3

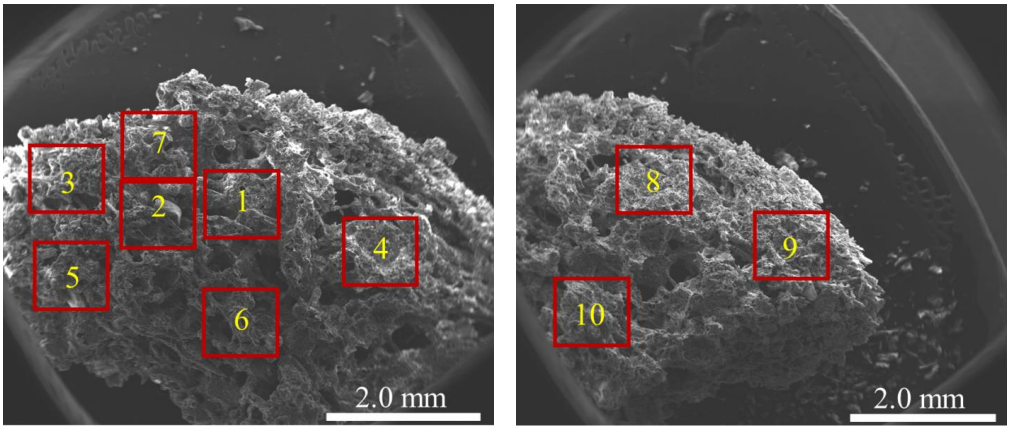

Figure G.7 SEM images of a char agglomerate from experiment 5 using straw. Fluid bed temperature: 453°C, pressure: 26 bar, straw feeding rate: <400 g/h, H_2 flow: 102 NL/min, N_2 flow: 5 NL/min, and H_2S conc: 460 ppm.

Table G.4 EDS measurement on the points shown in Figure G.7

Point	C (wt.%)	O (wt.%)	Mg (wt.%)	Si (wt.%)	P (wt.%)	S (wt.%)	Cl (wt.%)	K (wt.%)	Ca (wt.%)
1	74.2	15.2	0.3	1.0	0.2	0.6	1.8	5.6	1.1
2	62.4	23.3	0.2	5.2	0.2	0.4	1.7	5.7	1.0
3	72.8	15.2	0.3	1.1	0.3	0.5	2.0	7.0	1.0
4	74.9	13.6	0.2	1.0	0.6	0.5	1.9	6.0	1.2
5	73.1	16.8	0.3	1.3	0.3	0.4	1.6	5.4	1.0
6	73.5	12.6	0.3	1.3	0.4	0.9	2.3	7.7	1.0
7	74.2	15.2	0.3	1.4	0.3	0.4	1.6	5.6	1.0
8	72.4	16.0	0.4	1.3	0.3	0.5	1.8	6.0	1.4
9	73.6	16.3	0.4	1.2	0.4	0.4	1.5	5.4	1.0
10	70.3	15.0	0.3	1.8	0.5	0.5	2.5	8.2	1.0

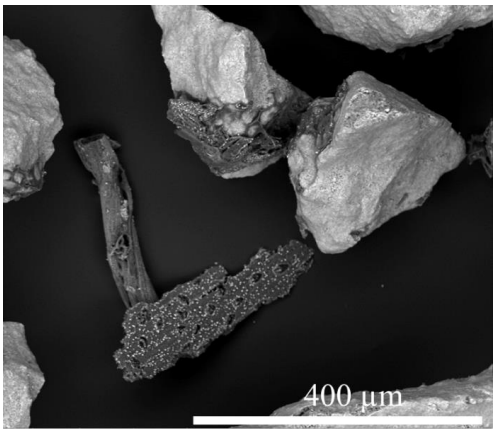

Figure G.8 SEM image of partly melted char particle attached to a catalyst particle from experiment 5 using straw. Fluid bed temperature: 453°C, pressure: 26 bar, straw feeding rate: <400 g/h, H_2 flow: 102 NL/min, N_2 flow: 5 NL/min, and H_2S conc: 460 ppm.

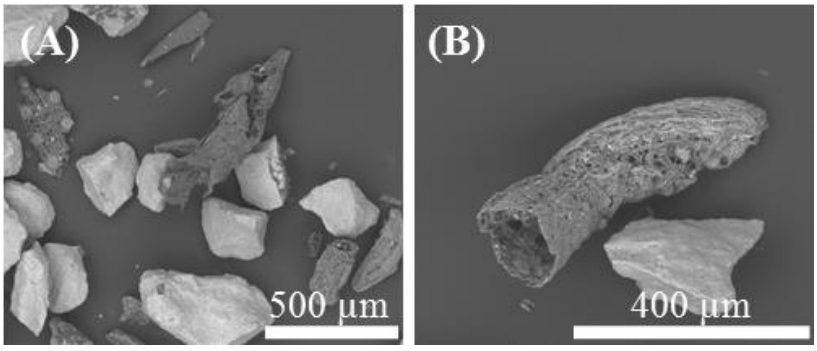

Figure G.9 SEM images of hollow char particles from experiment 5 using straw. Fluid bed temperature: 453°C, pressure: 26 bar, straw feeding rate: <400 g/h, H_2 flow: 102 NL/min, N_2 flow: 5 NL/min, and H_2S conc: 460 ppm.

Table G.5 EDS measurement on the points shown in Figure 8.9(C)

Point		C	O	Mg	Al	Si	S	Cl	K	Ca	O/Si	K/Cl
		(wt.%)	(wt.%)	(wt.%)	(wt.%)	(wt.%)	(wt.%)	(wt.%)	(wt.%)	(wt.%)	(mol/mol)	(mol/mol)
1	9.96	11.7	55.87	0.28	0.29	28.59	0.4	0.41	2.15	0.31	3.4	4.7
2	10.66	6.58	52.91	0.06	0.15	38.81	0.32	0.18	0.79	0.19	2.4	4.2
3	12.5	67.97	25.08	1.03	0.14	0.46	0.42	0.59	3.58	0.73	95.9	5.6
4	12.68	53.7	31.35	0.65	0.16	10.48	0.21	0.51	2.48	0.45	5.3	4.4
5	12.94	69.25	23.32	0.93	0.08	0.75	0.6	0.62	3.86	0.61	54.4	5.8
6	12.62	68.41	24.68	0.92	0.11	0.92	0.34	0.61	3.54	0.47	47.1	5.3

Table G.6 EDS measurement on the points shown in Figure 8.9(E)

Point	C	O	Mg	Al	Si	S	Cl	K	Ca	O/Si	K/Cl
	(wt.%)	(wt.%)	(wt.%)	(wt.%)	(wt.%)	(wt.%)	(wt.%)	(wt.%)	(wt.%)	(mol/mol)	(mol/mol)
1	68.54	7.27	0.22	0.4	0.12	0.23	10.41	12.48	0.32	111.0	1.1
2	69.38	7.52	0.3	0.27	0.14	0.28	9.91	11.82	0.39	97.6	1.1
3	70.29	8.34	0.33	0.48	0.18	0.52	8.69	10.82	0.35	83.2	1.1
4	76.81	11.07	0.29	0.29	0.24	0.56	4.11	6.29	0.33	84.7	1.4
5	78.85	16.36	0.37	0.35	0.24	0.66	0.58	2.46	0.14	120.3	3.9
6	78.86	12.15	0.28	0.26	0.2	0.33	3.05	4.32	0.55	111.4	1.3
7	79.23	16.52	0.41	0.4	0.32	0.5	0.36	1.78	0.47	88.8	4.5
8	81.46	13.16	0.42	0.59	0.55	0.53	0.42	2.41	0.46	42.4	5.3
9	77.25	17.39	0.57	0.2	0.11	0.78	0.61	2.16	0.95	283.2	3.3

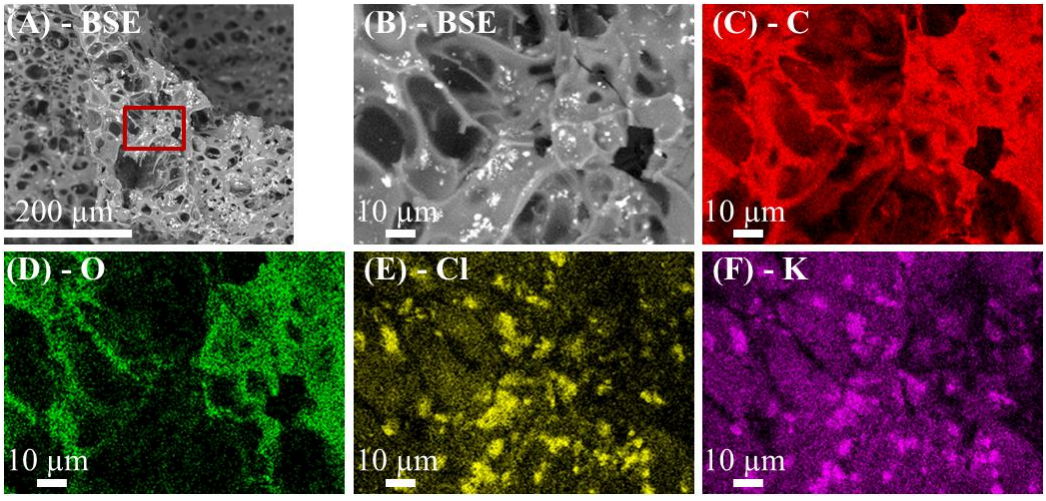

Figure G.10 SEM-BSE micrograph (A), SEM-SEI micrograph (B) and EDX element distribution of C (C), O (D), Cl (E), and K (F) on a char particle located above a spent catalyst particle from experiment 5. Fluid bed temperature: 453°C, pressure: 26 bar, straw feeding rate: <400 g/h, H_2 flow: 102 NL/min, N_2 flow: 5 NL/min, and H_2S conc: 460 ppm.

Appendix H Supplementary information for Trends in catalytic hydropyrolysis of biomass

Equilibrium conversion

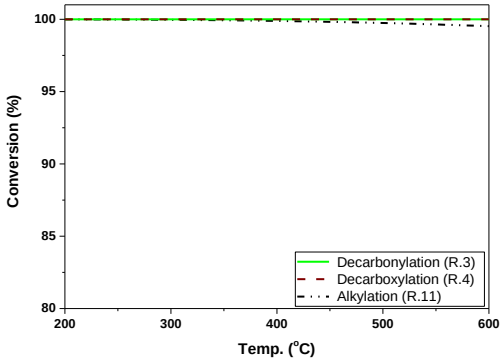

Figure H.1 Conversions at equilibrium as a function of temperature at 26 bar for decarbonylation of ethanone, decarboxylation of acetic acid, and alkylation between benzene and metahol. Calculated with the software package HSC Chemistry v.9.7.

Appendix I Supplementary information for the hydrogen assisted catalytic hydropyrolysis setup

The setup is a continuous flow testing facility and a picture of it is shown in Figure I.1 and the PI diagram is shown in Figure I.2. It was not possible to have a totally leak free setup, due to small leaks at the flanges, and if the setup was left at 26 bar the pressure would normally decrease with 1 bar overnight. Therefore ventilation boxes were placed on all sections containing flanges, see Figure I.1, thereby ensuring the pilot hall would not smell of H_2S.

The gas is fed into the setup through a serious of mass flow controllers, 4 of them leads gas into the fluid bed reactor through the gas preheater, 2 goes through the biomass feeding pipe, thus carries the biomass from the screw feeder into the fluid bed. The maximum operating pressure for the setup was 39 bar. It is possible to use a reduced catalyst in the fluid bed reactor and a sulfided catalyst in the HDO reactor.

Figure I.1 Picture of the catalytic hydropyrolysis setup

Feeding section

The used screw feeder can contain 2.5 L, which corresponds to between 800-1050 g biomass depending on the density and a drawing of the screw feeder is shown in Figure I.3. The biomass in the screw feeder was stirred with a propeller during the experiment to avoid bridging of the biomass inside the screw feeder. During the first year of operating the screw conveyor was modified in order to minimize the risk for plugging of biomass in the screw feeder and the modified screw conveyor is shown in Figure I.4. However, problems with biomass plugging still occurred from time to time in the funnel, but adding a vibrator to the funnel removed this problem. The screw feeder and setup was flushed after loading to remove any oxygen.

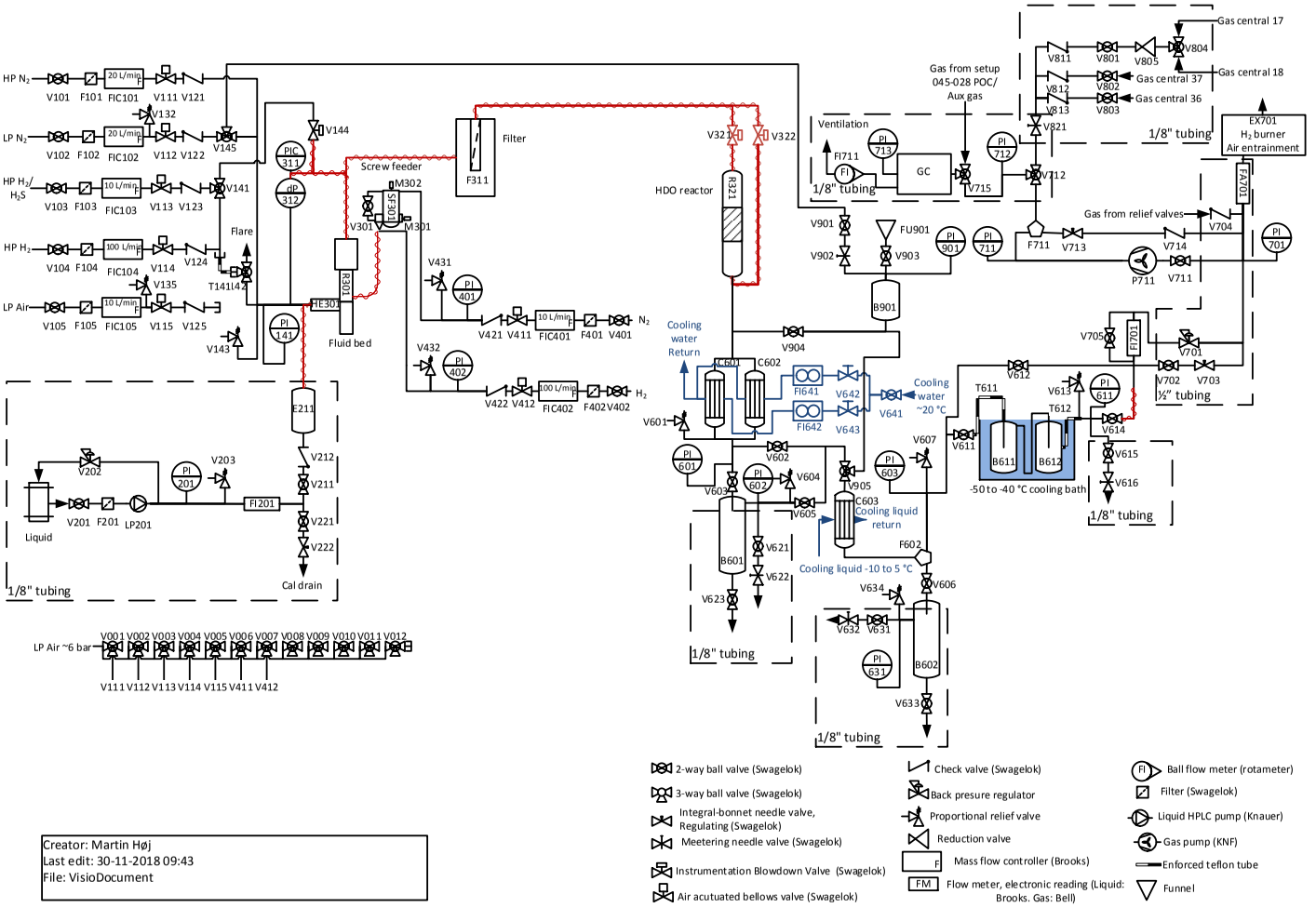

Figure I.2 PI diagram

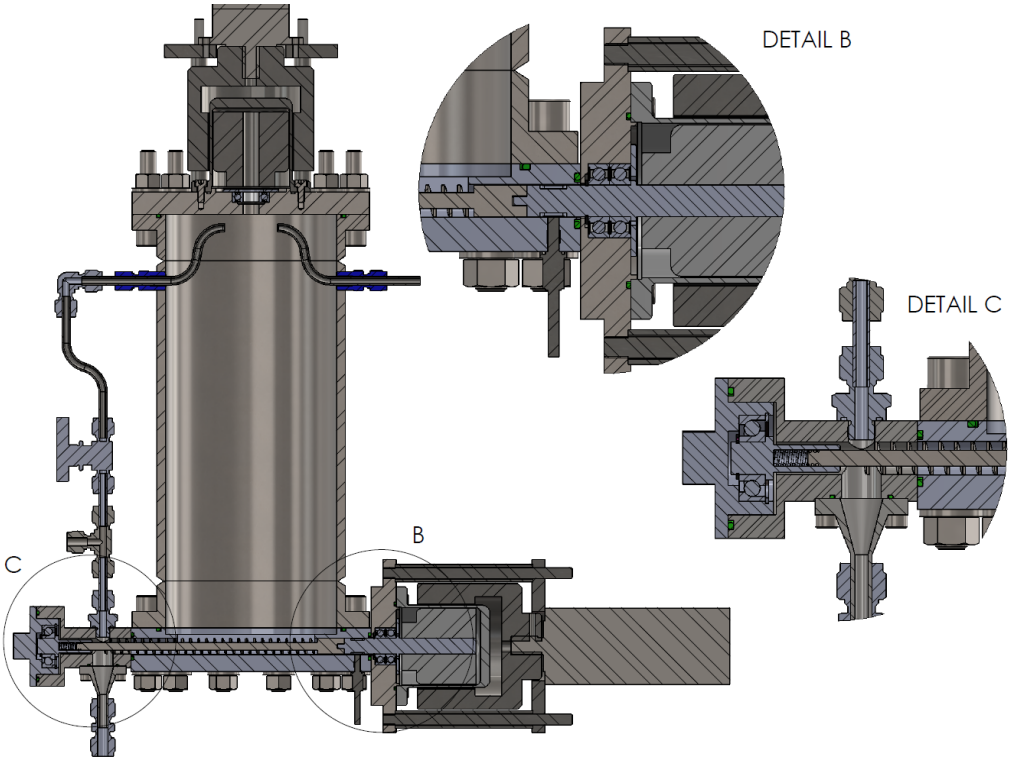

Figure I.3 Drawing of screw feeder

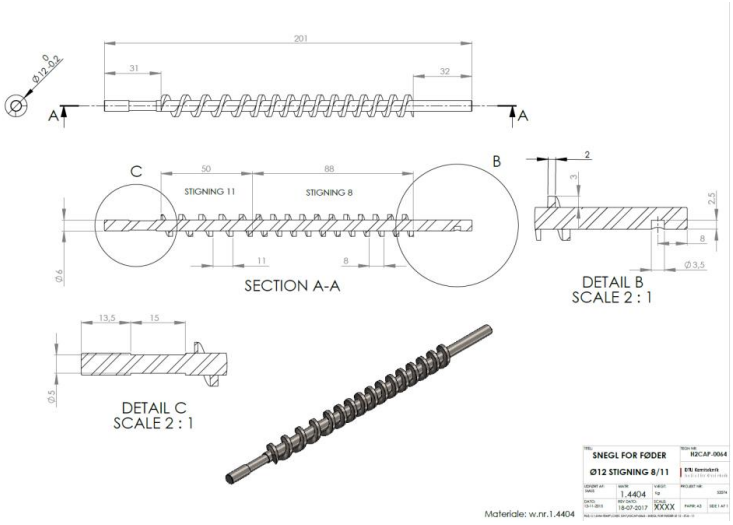

Figure I.4 Optimized screw feeder

The screw feeder's feeding rate was carefully studied and calibrated prior the experiments in the HDO reactor. This was done by feeding biomass into a beaker located on a weight below the screw feeder. The biomass feeding rate is shown as a function of time in Figure I.5, which indicates that the biomass feeding rate was fairly constant as long as there are more than 50 g of biomass left in the screw feeder. Other experiments also showed that the biomass feeding rate was not affected by the on degree of compression of biomass in the screw feeder and changing the particle size only had a limited effect of the biomass feeding rate. However, the biomass feeding rate was very depend on the total pressure and increased with increasing pressure.

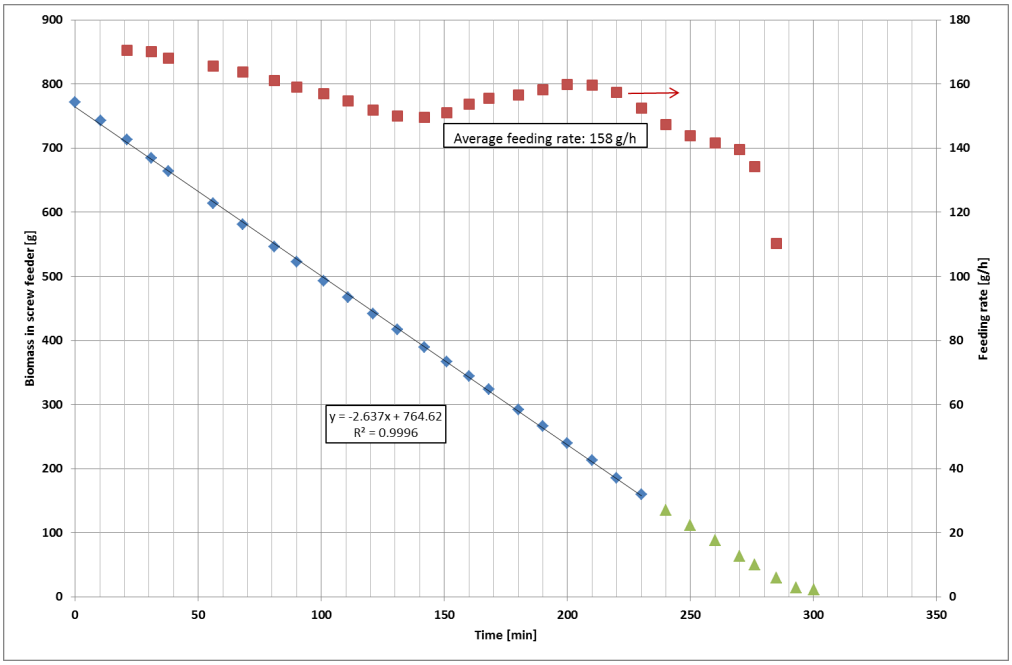

Figure I.5 Biomass feeding stability (biomass used: beech wood)

Fluid bed reactor

The fluid bed reactor consisted of 5 heating zones, see Figure I.6. The heating mantle for the gas preheater (HE301), the reactor bottom (R301H1), and reactor zone (R301H2) could withstand up to 700 °C, however due to the fairly cold (<200°C) gas coming from the screw feeder, the gas preheater was often operating at 660-690°C in order to maintain the desired temperature in the fluid bed reactor. The heating mantle for the disengage zone and top flange could withstand up to 450°C.

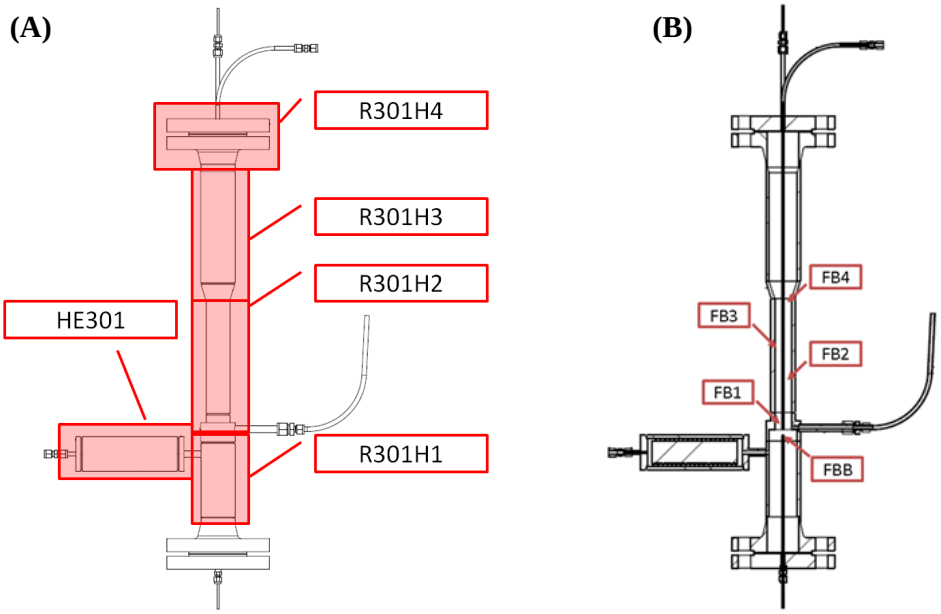

Figure I.6 Heating zone on the fluid bed reactor (A) and thermocouples in the fluid bed reactor (B)

The temperature in the fluid bed reactor was measured at 4 different points as shown in Figure I.6. FBB measure the temperature below the sinter plate, thus just below the reactor zone. FB1 measures the temperature just above the sinter plate, and this temperature could vary from experiment to experiment and large fluctuations were also often observed for during the experiments. FB1 and FB3 are located in the center of the reactor zone the fluid bed temperature was calculated on the basis of these two thermocouples. FB4 was placed just below a disengage zone.

An example of the temperatures in the fluid bed reactor is shown Figure I.7. When the biomass feeding starts at time 0 h, the temperature increases with approximately 10 °C, furthermore the slope for the temperature is lower for FB4 compared to the other thermocouples in the fluid bed. This is because it is located above the catalyst before the experiment starts, but as the amount of biomass used increases the amount of char accumulated in the bed also increases, which increases the bed height.

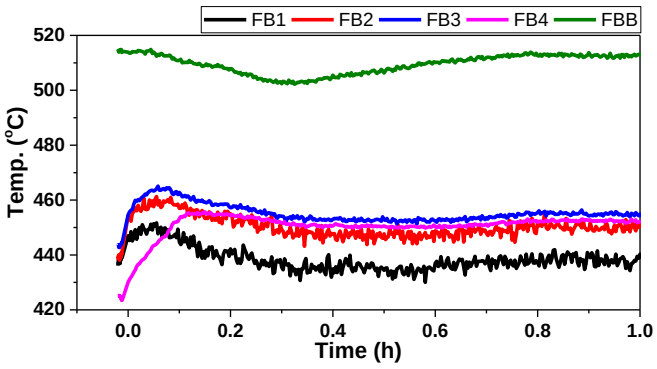

Figure I.7 Example of temperature in the fluid bed during the start of an experiment

In first the experiments DMDS was used to sulfidate the catalysts, however, this lead to a large pressure drop over the fluid bed reactor as shown in Figure I.8(A). This was due to coking of the sinter plate and the gasprehater (see Figure I.8(B)), which had to be replaced. Using bottled H_2S (2% in H_2) removed the problem with coking of the gas preaheater, however the sinter plate still had to be changed after approximately 3 experiments. Changing the sinter plate generally takes 2 to 3 hours.

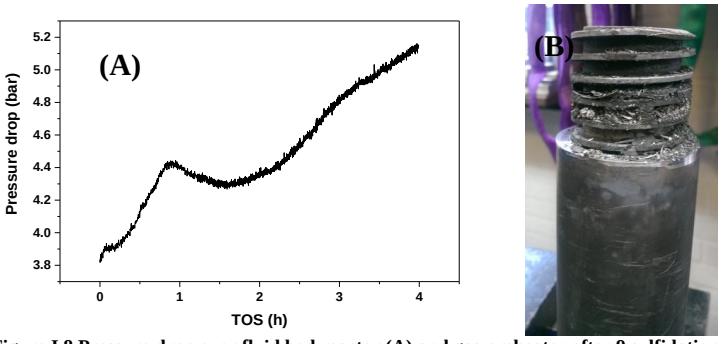

Figure I.8 Pressure drop over fluid bed reactor (A) and gas preheater after 9 sulfidations

HDO reactor

The temperature in the HDO reactor was controlled by 3 heating zones, as shown in Figure I.9. The top part (20 cm) of the HDO reactor was filled with glass beads, and the objective of this part of the reactor was to adjust the temperature to the desired inlet temperature. The catalyst bed was approximately 36 cm long and the temperature was measured at 4 different points in the bed.

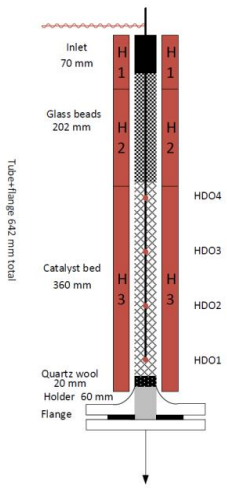

Figure I.9 Drawing of the HDO reactor

The temperature in the HDO reactor during the first experiment on the setup is shown in Figure I.10. The temperature in the top and bottom of the HDO reactor was typically a bit lower than in the center of the bed. This could possibly be optimized by having different heating zone for the reactor zone. It should also be noted the temperature in this reactor also increases when the biomass feeding starts.

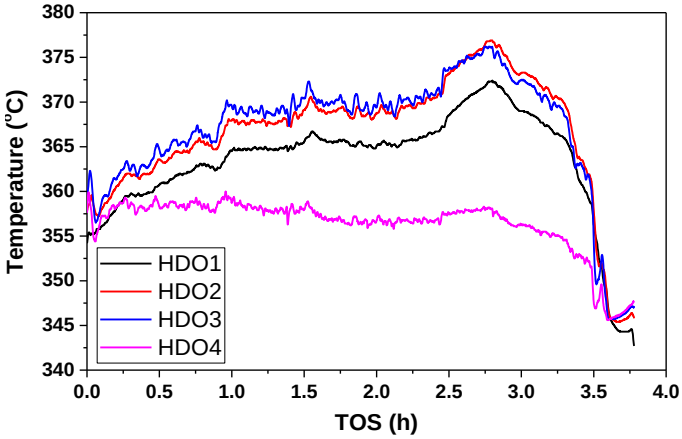

Figure I.10 Temperature in the HDO reactor during an experiment

Condensation system

A 3 step condensation system was used to condense the vapors. In the first heat exchanger the vapors was cooled to approximately 25°C, where cooling water (15-20°C) from the build supply was used. This heat exchanger consists of two identical parallel heat exchangers (see Figure I.11). The hot vapors flow on the inside of the pipe, while the cooling water flows on the outside. The surface area was increased by placing a spiral inside the pipe.

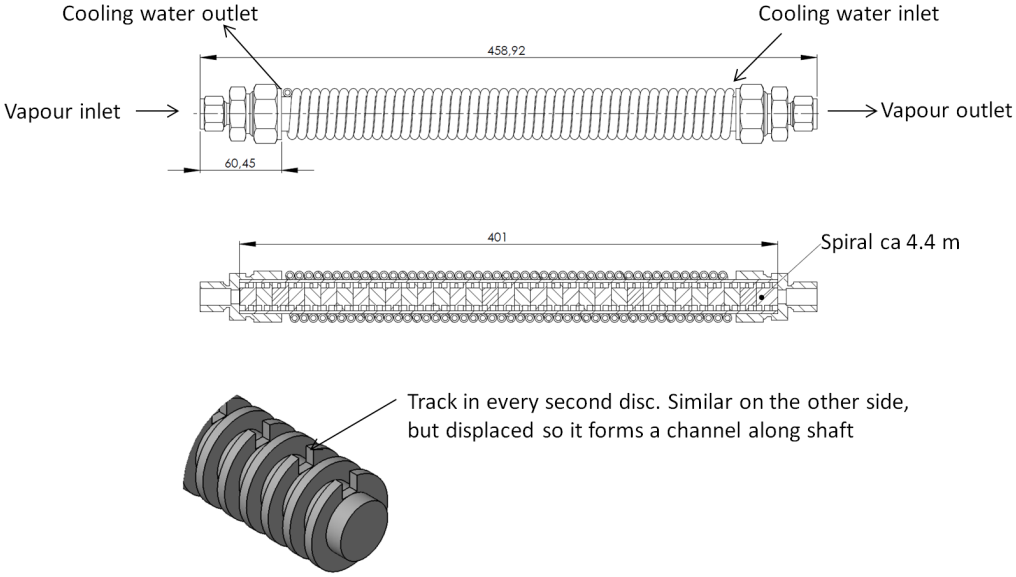

Figure I.11 Drawing of heat exchanger (C601)

The condensed liquid was collected in vessel and the vapors continued to a second heat exchanger, shown in Figure I.12. The original plan was to cool the vapors to between 0 and – 10°C, however not all of the water was condensed in the first heat exchanger, therefore running the second heat exchanger at -10°C led to formation of ice inside the tubes. The cooling used in this heat exchanger was therefore increased to 2°C. In order to condensate the aerosols the vapors passed through a coalescing filter placed after the heat exchanger and the liquid was collected in a vessel below the filter. To minimize the contaminations between each experiment the coalescing filter should ideally be change between each experiment, where the HDO reactor is not used.

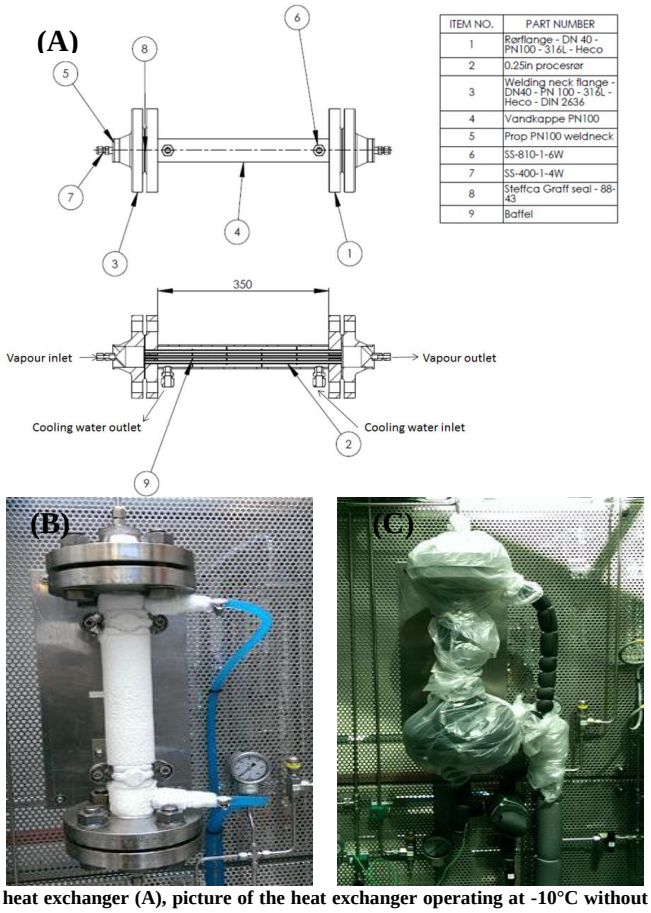

Figure I.12 Drawing of heat exchanger (A), picture of the heat exchanger operating at -10°C without (B) and with insolation (C).

In the last heat exchanger two collection vessels were located in a cooling bath operating at -40°C, shown in Figure I.13. After a successful experiment the collection vessels were bypassed and the unit was depressurized and flushed with N_2.

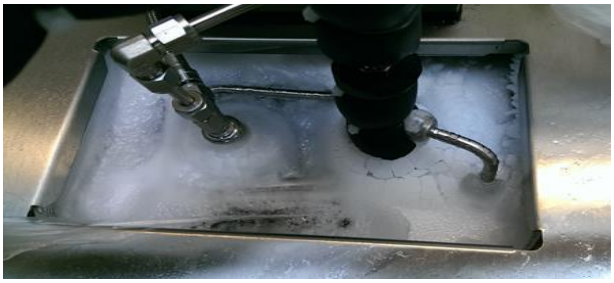

Figure I.13 Picture of the 3 condenser. A lid was place on top of the cooling bath during the experiments to minimize the amount of water condensed in the cooling bath.

Back pressure regulator

The pressure inside the unit was controlled with a back pressure regulator. This regulator was carefully tuned using the continuous cycling method [1]. It was very important that the pressure did not fluctuate during the experiments, the reason for this is that if the pressure suddenly increased rapidly the back pressure regulator needed to rapidly decrease the pressure, which increased the gas velocity in the fluid bed reactor, which could led to catalyst entrainment. Furthermore if the pressure became too low the back regulator needed to close in order build up the pressure, however, this decreased the gas velocity, which led to defluidization, which can led to blocking of the biomass feeding tube. This was a common problem for the setup and an example of the measured pressure during an experiment is shown in Figure I.14. The reason for this was that the formation of wax could occur in the pipes between the two vessels in the last cooling bath operating at -40°C, this generally led to a 5 to 10 bar pressure drop over this cooling bath. Therefore in order to minimize the risk of plugging of the biomass feeding tube, the software was programmed to stop the screw feeder if the difference between measured pressure and the set point was more than 0.5 bar, this significantly decreased the amount of failed experiments. Bypassing the cooling bath and depressurizing it generally removed the plug, but it was sometimes necessary to heat to 15°C in order to remove the plug. This did not have an impact on the mass balance.

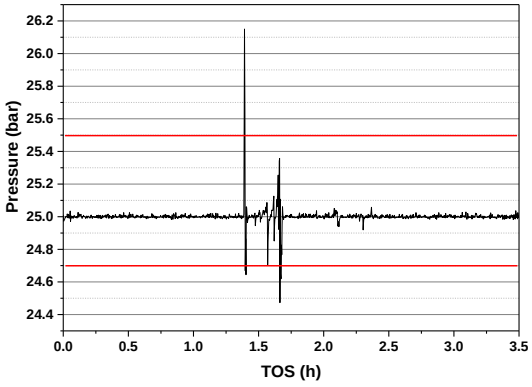

Figure I.14 Example of the measure pressure during an experiment.

References

[1] D.E. Seborg, T.F. Edgar, D.A. Mellichamp, F.J. Dayle II, Process Dynamics and Control, Third Edit, Wiley, 2011.

Appendix J Effect of H_2O partial pressure

Introduction

The experiments conducted in this work the used biomass has relative low moisture content of 6.72 wt.%, however, the moisture content in fresh biomass will normally be significantly higher. Therefore the effect of increasing the water vapor pressure was investigated.

Material and methods

Bark free beech wood, which has a moisture content of 6.72 wt.%, was used as biomass feedstock.
The used catalyst had a Mo content of 7.74 wt.% and Co of 1.49 wt.% and the preparation and characterization of it is described in detailed in Chapter 6. The catalyst was sulfided prior to the experiments, which was conducted on the catalytic hydropyrolysis setup described in detailed in Chapter 2.
The catalyst was tested without the fixed bed reactor at two different H_2O vapor pressures: 0.8 bar H_2O, which was the H_2O pressure when no additional water was fed to the setup, and 1.6 bar H_2O, which was achieved by pumping H_2O (2 ml/min) into the setup through the gas preheater.

Results and discussion

The effect of the H_2O partial pressure on the overall product composition is shown in Figure J.1. The char and coke yield was 13.1 wt.% daf both at 0.8 and 1.6 bar H_2O partial pressure. The C_1-C_3 yield between 13.9 and 14.1 wt.% daf, however, the total gas yield increased from 30.8 to 31.8 wt.% daf when the H_2O partial pressure was increased. A small increase (1 % point) was also observed in the aqueous phase yield when H_2O partial pressure was increased and the C_{4+} hydrocarbon yield was 22.7 and 22.8 wt.% daf at both H_2O partial pressures. This indicates that the H_2O partial pressure has a neglectable effect on the char and coke yield and on the condensable organic yield

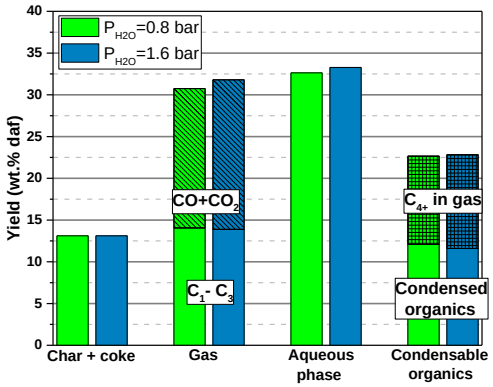

Figure J.1 Effect of H_2O partial pressure on the product distribution. Operating condition: fluid bed temperature: 450°C, Biomass feeding rate: 275 g/h, H_2 flow: 82 NL/min, N_2 flow: 5 NL/min, total pressure: 26 bar.

The effect of the H_2O partial pressure on the gas composition is shown in Figure J.2. In both experiments the methane yield was between 4.3 and 4.4 wt.% daf, however, the concentration C_2-C_3 paraffins increased from 6.9 to 7.2 wt.% daf, while the concentration of C_2-C_3 olefins decreased from 2.7 to 2.4 wt.% daf when H_2O partial pressure was increased from 0.8 to 1.6 bar. Likewise the concentration of C_4-C_5 paraffins increased from 2.0 to 2.2 wt.% daf and the concentration of C_4-C_5 olefins decreased from 0.8 to 2.6 wt.% daf. The con-

centration of CO_2 also increased from 7.8 to 8.9 wt.%, but only a minor increase was observed in the CO yield, which increased from 8.9 to 9.0 wt.% daf.

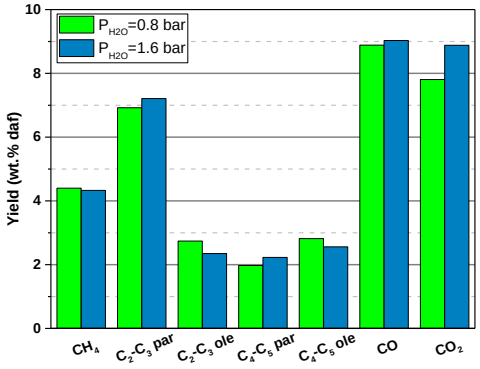

Figure J.2 Effect of H_2O partial pressure on the gas composition. Operating condition: fluid bed temperature: 450°C, Biomass feeding rate: 275 g/h, H_2 flow: 82 NL/min, N_2 flow: 5 NL/min, total pressure: 26 bar. (par is an abbreviation for paraffins and ole is an abbreviation for olefins)

These results therefore indicate that the addition of water mainly affects the water-gas shift reaction (see Reaction J.1) by converting water and CO into CO_2 and H_2. This increases the concentration of H_2, which therefore increases the degree of hydrogenation of the olefins. Unfortunately the produced liquid phases was contaminated with oxygenates from the previous experiments and the results from the analysis of the organic and aqueous phase are therefore excluded and the effect of the H_2O partial pressure on the degree of deoxygenation is therefore unknown.

$$CO + H_2O \rightleftharpoons CO_2 + H_2 \tag{J.1}$$

Conclusion

Increasing the H_2O partial pressure from 0.8 to 1.6 bar did not affect the yield of C_{4+} hydrocarbons, but increased the CO_2 yield from 7.8 to 8.9 wt.% daf due to water gas shift reactions. This led to a small increase in the hydrogenation of the olefins in the gas. This therefore indicates that using biomass with a high water content will not decrease the oil yield. However, using biomass with a high moisture content still has some drawbacks for instance: more energy is needed to evaporate the water in the wood, it increases the amount of water, which needs to purify, thereby increases the transportation cost. Furthermore if alumina is used as support material it increases the risk that it is converted into boehmite.

Appendix K Cold fluidized bed experiments
Investigation of Optimal Particle Size for Char Removal

Theoretically Considerations

Calculation of u_{mf} and reactor flow

The minimal gas fluidization velocity (u_{mf}) is depended on the gas viscosity, gas density, particle density, and particle size. The viscosity at a given temperature can be calculated from Sutherland's formula:

$$\mu = \mu_0 \frac{T_0 + C}{T + C}\left(\frac{T}{T_0}\right)^{3/2} \tag{K.1}$$

The gas density can be calculated from the ideal gas law:

$$\rho_g = \frac{P}{RT} M_g \tag{K.2}$$

U_{mf} is calculated from Archimedes and Reynolds number:

$$Ar = \frac{d_p^3 \rho_g \rho_s - \rho_g g}{\mu^2} \tag{K.3}$$

$$\mathrm{Re}_{mf} = \left(33.7^2 + 0.0408 Ar\right)^{1/2} - 33.7 \tag{K.4}$$

$$u_{mf} = \frac{\mathrm{Re}_{mf}\, \mu}{d_p \rho_g} \tag{K.5}$$

In order to ensure that the bed is fluidized, 3 times u_{mf} is used. 3 u_{mf} for catalyst and sand particles is shown in table Table K.1.

Table K.1 $3u_{mf}$ for catalyst (ρ_s=1500 kg/m^3) and sand (ρ_s=2600 kg/m^3) in air and hydrogen. The particle diameter is assumed to be 212 mm and the reactor diameter is assumed to be 3 cm.

	Catalyst	Sand
$3u_{mf}$ (H_2, 450 °C, 25 bar)	7.68 cm/s	13.3 cm/s
$3u_{mf}$ (air, 22 °C, 1 atm)	7.09 cm/s	11.2 cm/s

Terminal velocity for char particles

The method for calculating the terminal velocity depends on the drag coefficient (C_D), which depends on the flow region. Reynolds number for particles in a fluid can be calculated as:

$$\mathrm{Re}_p = \frac{d_p u \rho_p}{\mu_g} \tag{K.6}$$

The correlation for C_D depends on the flow region as shown in Table K.2.

Table K.2 Reynolds number ranges for single particle drag coefficient correlations[1]

Region	Stokes	Intermediate	Newton's law
Re_p	<0.3	$0.3<Re_p<500$	$500<Rep<2x10^5$
C_D	$24/Re_p$	$\frac{24}{Re_p}\left(1+0.15Re_p^{0.687}\right)$	~0.44

Haider and Levenspiel have proposed a correlation for C_D, which covers the entire range[1]:

$$C_D = \frac{24}{Re_p}\left(1+0.1806Re_p^{0.6459}\right)+\left(\frac{0.4251}{1+\frac{6880.95}{Re_p}}\right) \tag{K.7}$$

In Stokes' law region the terminal velocity for sphere can be calculates as[1]:

$$u_T = \frac{d_p\left(\rho_p-\rho_g\right)}{18\mu} \tag{K.8}$$

In Newton's law region, where C_D is 0.44, the terminal velocity for a sphere is given by[1]:

$$u_T = 1.74\left(\frac{d_p\left(\rho_p-\rho_g\right)g}{\rho_g}\right)^{1/2} \tag{K.9}$$

In the intermediate region the terminal velocity can be calculated from the empiric formula:

$$u_T = 0.153\left(\frac{\left(\rho_p-\rho_g\right)d_p^{1.6}g}{\mu^{0.6}\rho_g^{0.4}}\right)^{0.714} \tag{K.10}$$

By taking the drag coefficient into account the terminal velocity for the entire flow region can be calculated as:

$$u_T = \sqrt{\frac{4gd_p\left(\rho_p-\rho_g\right)}{3\rho_g C_D}} \tag{K.11}$$

Figure K.1 shows the terminal velocity as a function of the biomass particle diameter. For these calculations it has been assumed that the biomass density is 300 kg/m^3. With the used biomass particles the Re is between 0.5 and 52, thus it is difficult to determine if the fluid is within Stokes's region or in the intermediate region. Therefore the terminal velocity is calculated for the two different assumptions; the flow in Stokes's region and the fluid is in the intermediate region. $3u_{mf}$ has been calculated for sand in the reactor zone (d = 3 cm) and is denoted as u(d = 3 cm) in Figure K.1. The velocity in the disengage zone (d = 5 cm) at $3u_{mf}$ in the reactor zone is denoted as u(d = 5 cm).

The figure indicates that with the test conditions applied in the hydrogen assisted catalytic pyrolysis (H2CAP) setup the char should be below 95-110 µm in order to remove it from the reactor zone and should be below 55 µm in order to be removed from the disengage zone. In the cold fluid bed reactor the char should have a diameter below 80-115 µm before it is removed from the reactor zone and below 70 µm to be removed from the disengage zone. Thus the theoretical calculations indicate that it is more difficult to remove the char from the H2CAP unit, than the cold fluid bed. The difference between the H2CAP setup and the cold fluidized bed reactor, besides the temperature and pressure, is that hydrogen is used in the H2CAP unit and air is used in the cold fluidization, hence the pressure and temperature dependency of the carrier gas is different.

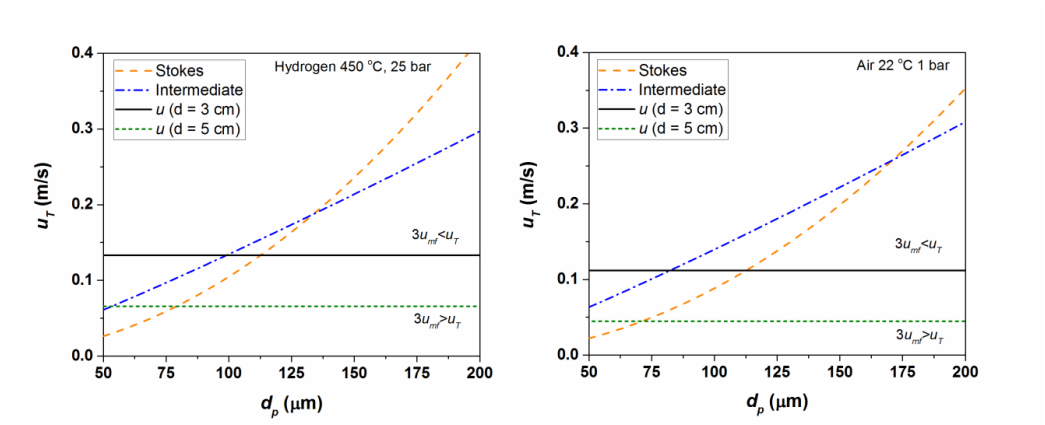

Figure K.1 Effect of biomass particle diameter on the terminal velocity. u (d = 3 cm) and u(d = 5 cm) is the velocity in the reactor and disengage zone, respectively, at u = $3u_{mf}$ in the reactor zone for sand.

The density of the biomass can vary and pyrolysis of biomass has shown that the density of the char can be as high as 370 kg/m^3, thus indicating that the uncertainty of the terminal velocity for Stokes and intermediate region is at least 24 % and 16 %, respectively. The impact of the uncertainty is shown in Figure K.2. It is therefore obvious that the density of the char must be known, before a useful estimate of the terminal velocity for the particles can be calculated.

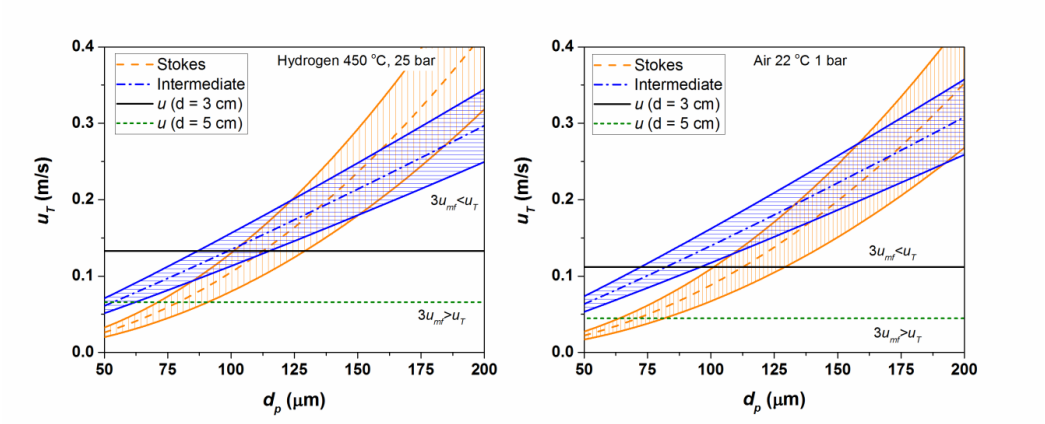

Figure K.2 Effect of the uncertainty of the density for char particle diameter on the terminal velocity. u (d = 3 cm) and u(d = 5 cm) is the velocity in the reactor and disengage zone, respectively, at u = $3u_{mf}$ in the reactor zone for sand.

Experimental Set-up

The char used in these experiments was produced by pyrolysis in the setup blue oven (045-05). The temperature was set to 450 °C and the biomass was first added to the oven after this temperature was reached. The hold time was 1 hour, but the char was first collected when the temperature had decreased to below 50 °C. The pyrolysis was conducted in a nitrogen atmosphere. The char yield was between 30 and 33 wt. %.

The effect of char particle size and test conditions on the char removal was tested in a glass tube. The glass tube consisted of a reactor zone, with a diameter of 3 cm and a disengage zone with a diameter of 5 cm. The diameter's for these zones are identical to the diameters for the fluid bed reactor in the H2CAP setup, however the length of the reactor and disengage zone is larger in this cold fluidization setup than in the H2CAP setup. Air was used as fluidization gas and the flow was controlled by a ball flow meter. The char was collected in a separator. A picture of the unit is shown on Figure K.3.

In all the experiments approximately 60 g sand (150-212 µm) with a density of 2600 kg/m^3 was used instead of catalyst. At the start of each experiments the char and sand was mixed by either shaking the gas tube or by short fluidization of the particles. Afterwards the weight of the separator and the bed height was measured. The funnel/pipe was then positioned and the experiment was started. For each measurement the air flow was stopped and most of the char was removed from the pipe by knocking on the pipes before measuring the separator weight and bed height.

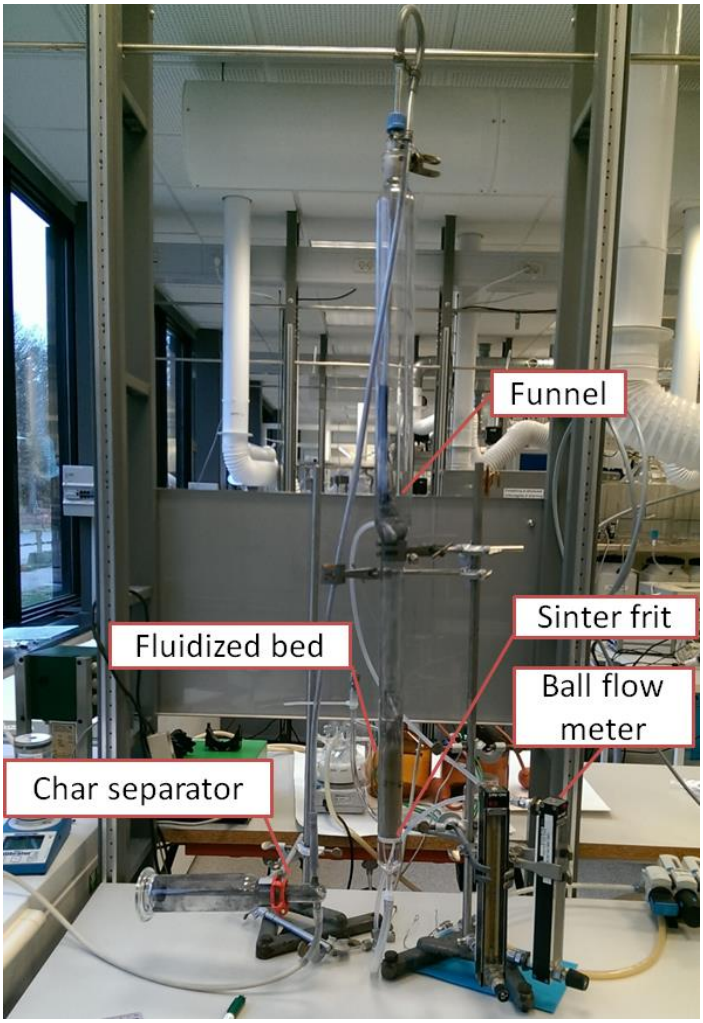

Figure K.3 Picture of experimental setup

The conducted experiments can be divided into 3 groups;

1) Test of the effect of char particle size; Char derived from biomass with particle size between 0-200 µm, 200-400 µm, 400-630 µm, and 630-1000 µm have been tested. In these experiments 1 g of char was used.
2) Effect of char particle size; Sieve char particle fractions between 63-106 µm and 106-150 µm have been tested. In this experiment two different funnel positions have been used 45 cm and 37 cm above sinter frit in the bed, which corresponds to position B and C in Figure K.4. 2 g of char was used in each of these experiments
3) Effect of using 10 g char with a particle size between 0-200 µm. In these experiments the position of a funnel or pipe was also carefully studied and all the funnel/pipe positions shown in K.4 were used.

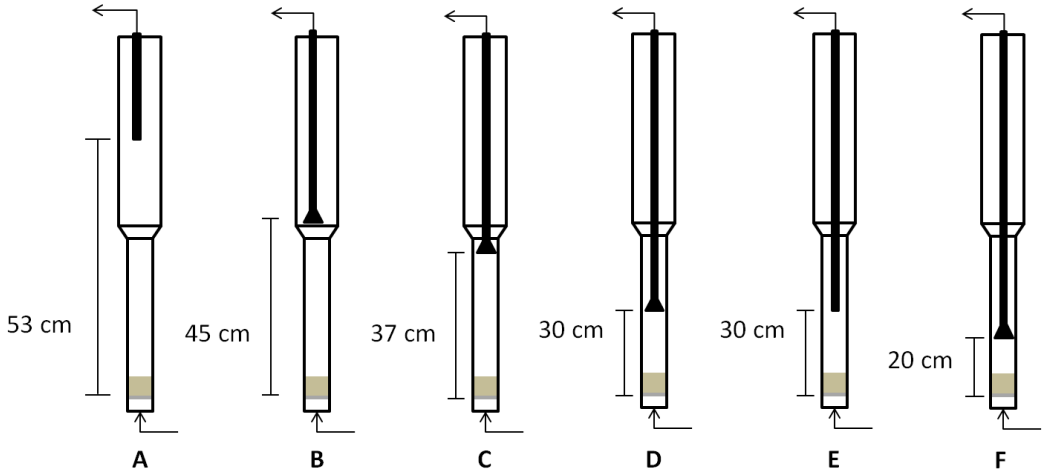

Figure K.4 Cold fluidization setup

Ideally the reactor would be emptied after each test and new sand would be used. However, due to lack of sand, the sand was often reused, but in many of the experiments the char was almost completely removed by the end of the experiment.

Results and Discussion

Effect of particle size, when using particle size between 0-1000 µm

In the first experiments approximately 60 g sand was mixed with 1 g char derived from biomass with a diameter between 200-400 µm, 400-630 µm, and 630-1000 µm individually. In the experiment with char derived from 200-400 µm and 400-630 µm biomass particles, the pipe was located 55 cm above the sinter frit, while a funnel was located 45 cm above the sinter frit the experiment with char derived from 630-1000 µm biomass particles. Thus the pipe/funnel was located in the disengage zone in all the experiments. Only negligible amounts of char were removed in these experiments.

In order to obtain measureable char removal an experiment with 3.6 g char with a particle size between 200-1000 µm was tested. The initial bed height was 9 cm and the funnel was located 23 cm above the sinter frit. After 23.5 hours the separator weight had increased with 0.29 g corresponding to a char removal rate of 3.8 mg/($g_{char\ in\ bed}$h).

The removal of char derived from biomass with a particle size 0-200 µm have been tested by mixing 1.89 g char with sand in the fluidized bed reactor. The funnel was located 25 cm from the sinter frit, thus being located in the reactor zone. After 8 hours on stream the static bed height had decreased with 1.6 cm. Figure K.5shows the initial size distribution of char and the distribution of char in the separator at the end of the experiment. It would have been expected that the fraction of small particles in the separator is significantly larger compared with the initial fraction, but the opposite is observed. The most likely explanation for this observation is that the smallest particles are more likely to pass through the filter in the separator.

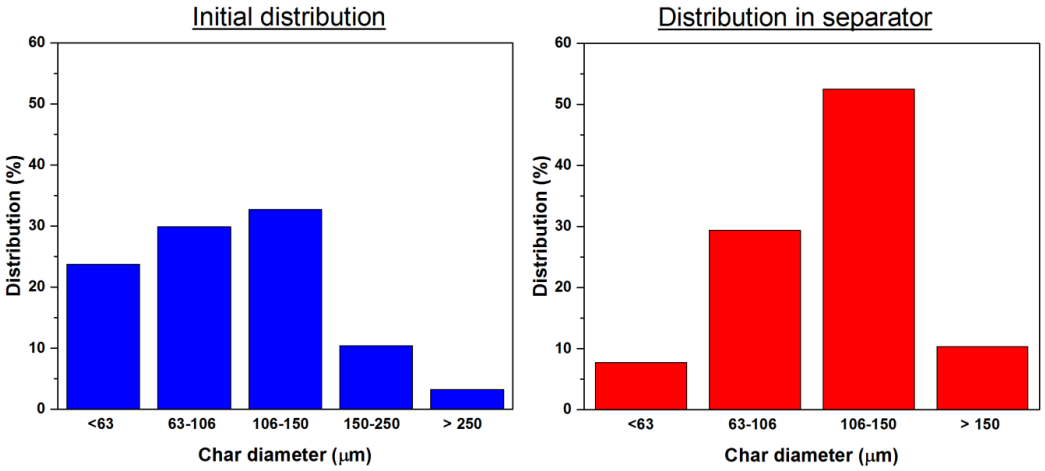

Figure K.5 Initial distribution of char and distribution of char at the end of the experiment in the separator (Char produced through pyrolysis of biomass with a particle size between 0-200 μm).

The char particles left in the reactor was studied by light microscopy (see Figure K.6). The char particles were generally fairly long with a cylinder formed shape, thus the assumption that the particles are spherical is very rough. This shape makes it more difficult to remove the char particles from the fluid bed, because in the Stokes region the particles have their longest surface area parallel to the direction of the fluid, while the opposite is the case in the Newton region [1]. The particles will therefore most like turn their smallest surface area towards to gas in the flow region used for H2CAP.

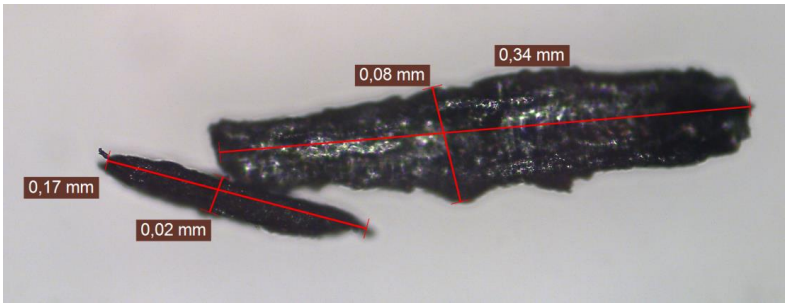

Figure K.6 Picture taken with light microscopy of the char left in the fluidized bed reactor

Effect of particle size, when using particle size between 63-150 μm

In this section the effect of using two different char fractions 63-106 μm and 106-150 μm will be discussed. These two fractions have been obtained by pyrolysis of biomass particles with a diameter below 200 μm and the formed char has been sieve in order to obtain the two fractions.

The char removal rate for particles when the funnel is located in the disengage zone (corresponding to Figure K.4 B) is shown in Figure K.7. The removal rate decreases rapidly when the amount of char decreases. When there is less than 1.9 g char left in the bed, the removal rate for the two sieved fractions of particles is between 0 and 0.1 $g/g_{char\ in\ bed}h$.

Placing the funnel in the reactor zone instead of the disengage zone increases the removal rate, as shown in Figure K.8. Particles with a diameter between 106-150 µm have been tested with the funnel placed 37 cm and 20 cm from the bottom, which corresponds to position C and F shown on Figure K.4, respectively. Comparing the char removal for these two different funnel positions in the reactor indicates that the char removal rate is highest when the funnel is located at position C. However, the char removal as a function of time shows that the char is initially removed with the same rate when the funnel is located at position C and F. The main differences between the two positions is that the char removal rate decreases more rapidly with decreasing amount of char when the funnel is located at position C than F. Interestingly the char removal rate of the small particles (63-106 µm) is smaller than the char removal rate of the larger particles (106-150 µm), this could be due to static electricity, which makes the char stick to the sand, pipe, and glass.

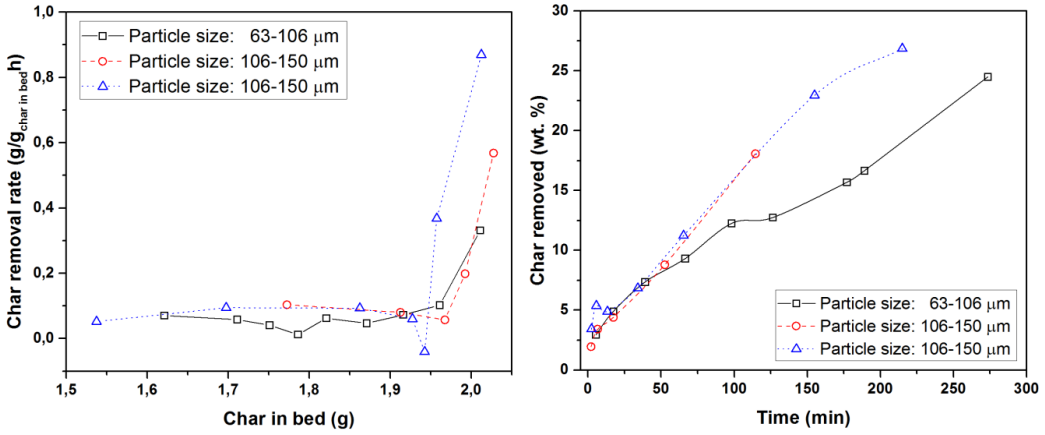

Figure K.7 Char removal rate for particles with a diameter between 63-106 µm and 106-150 µm when the funnel is located in disengage zone corresponding to Figure K. B. (Initial static bed height: 7.7-8.0 cm, initial amount of char: 2 g)

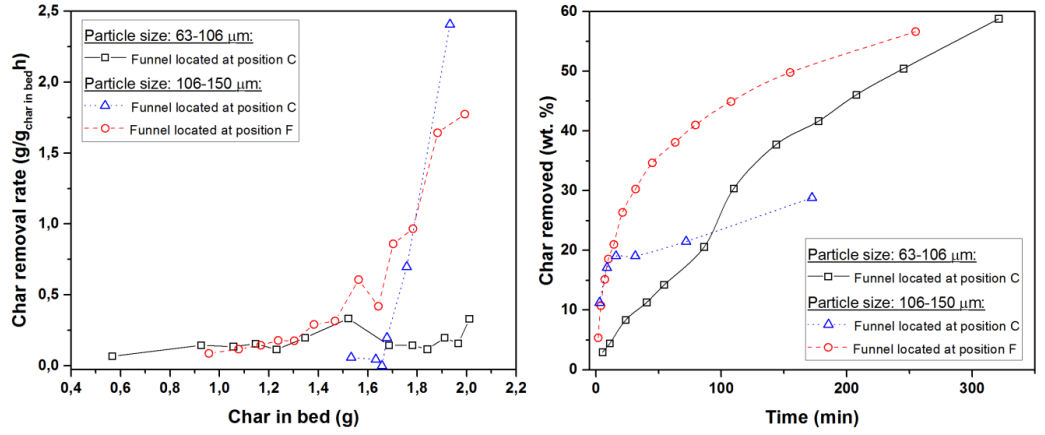

Figure K.8 Char removal with a particles diameter between 63-106 µm and 106-150 µm when the funnel is located in the reactor zone. The different funnel positions correspond to the positions shown in Figure K.4. (Initial static bed height: 7.3-7.8 cm, initial amount of char: 2 g)

Effect of using 10 g char with a particle size between 0-200 µm

For the experiments with 10 g char (particle size: 0-200 µm) the funnel/pipe position A-F on Figure K.4 was tested. In the first few seconds of each experiment slugging occurred, which made it difficult to investigate the effect of position F (the funnel located 20 cm from the bottom). Because of the slugging the top 5-10 cm of the bed was lifted into the funnel and significant sand removal was observed.

The char removal as a function of time for funnel/pipe position A-E is shown in Figure K.9. Comparing case E (pipe located 30 cm from the bottom) with case D (funnel located 30 cm from the bottom) indicates that a pipe is just as efficient for char removal as a funnel. The reason is most likely that since the pipe/funnel is the only outlet in the system the velocity vectors will be orientated towards this outlet, thus carrying the char particles towards this position. From this figure it is also obvious, that it is not only important to determine if the pipe should be in the reactor or disengage zone, but that char removal is also very dependent on the distance from the bed to the pipe position.

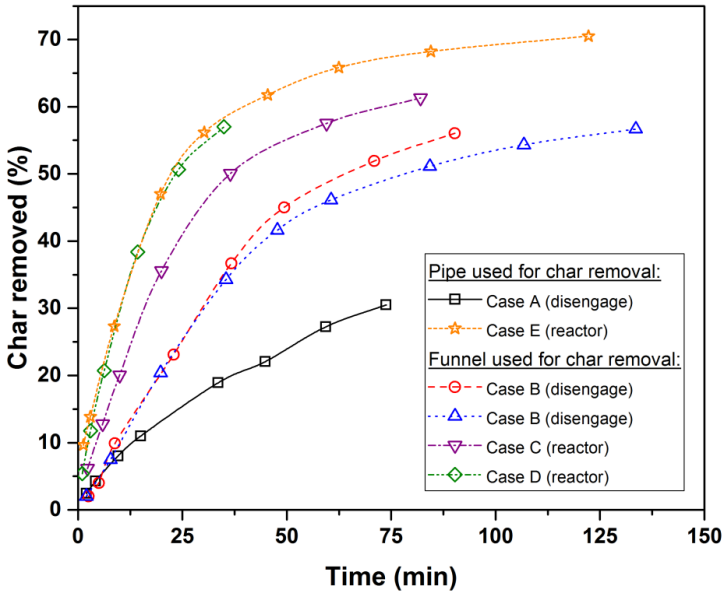

Figure K.9 Char removal (diameter 0- 200 µm) as a function of time at different funnel and pipe positions. Different cases correspond to the different funnel and pipe positions shown in Figure K.4. (Initial static bed height: 17.5-14 cm, initial char amount: 10 – 9.4 g)

The char removal rate when the pipe is located in the disengage zone and reactor zone is shown in Figure K.10. In both tests with the funnel located at position B, it was observed that the char removal rate first increased with decreasing char content until it peak at approximately 6.2 g char in the bed, after which it decreased. Generally it was observed that the char removal rate was below 1 g/($g_{char\ in\ bed}$h), assuming that 30 g char will be produced per hour the char content in the bed will increase to above 10 g with a funnel position in the disengage zone.

For all the experiments with the funnel/pipe in the reactor zone a significantly higher char removal rate was observed in the start of the experiment (corresponding to the data point at the highest char content in bed) than for the rest of the experiments. A possible expiation could be that the smallest and easiest char particles

are removed within the first minutes of the experiment, thus the average char particle size increases. Another important factor is that when the char content decreases the bed height decreases, thus the distance that the particles has to travel before entering the tube/funnel increases.

Char removal rates above 3 g/($g_{char\ in\ bed}$ h) have been observed when the funnel/pipe is in the reactor zone, which indicates that it is possible to maintain a char content below 10 g. However, these rates were only observed in the beginning of the experiments, it is therefore uncertain if this high removal rate will be observed at steady state. When the char content in the bed was between 5 and 7 g char removal rate was approximately 2 g/($g_{char\ in\ bed}$ h), indicating that the char content in the bed could increase to above 10 g. However, extrapolating the results in Figure 10 to higher char contents in the bed is with high degree of uncertainty and it is therefore not possible to make any accurate prediction of the char content in the reactor at steady state.

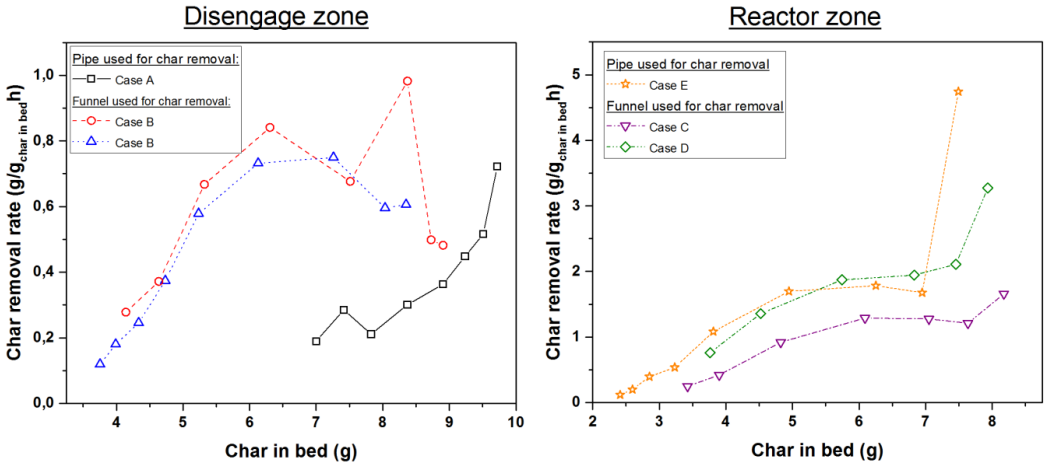

Figure K.10 Char removal rate (diameter 0-200 µm) as a char content with different funnel and pipe positions. Different cases correspond to the different funnel and pipe positions shown in Figure K.4. (Initial static bed height: 17.5-14 cm, initial char amount: 10 – 9.4 g)

During the experiments it was observed that the fluid bed can be divided into 4 zones; the bottom zone is mainly sand with a low concentration of char. The second zone contains close to equal amounts of char and sand. The third zone contains only very low amounts of sand, and the last zone (splash zone) only contains char, which is also shown in Figure K.11. As the char content in the bed decreases the volume of the 3 zones in the top decreases, while the volume of the bottom zone, which main consists of sand, remains constant.

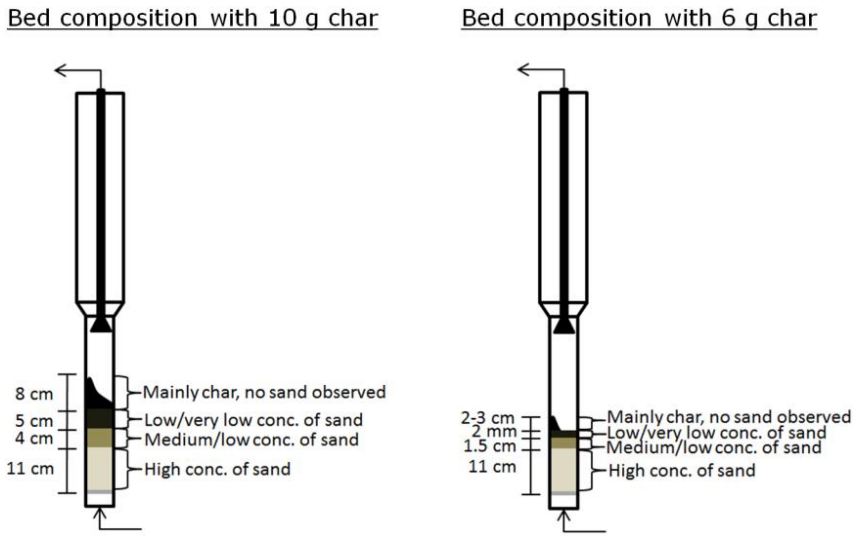

Figure K.11 Fluid bed composition with 10 g and 6 g char

Concluding Remarks

In these experiments beech has been used, however, in the H2CAP unit we are planning to use scots pine. Beech has a density of ~800 kg/m^3, while pine has density of 500 kg/m^3 [2], this would most likely have an impact on the char density, thus making it easier to remove pine than beech. Furthermore the char was produced in the blue oven at same temperature as in the H2CAP unit, but at different pressure and residence time, which also could have an impact on the density of the char.
During the experiments between 2 and 12 vol. % of the char was lost mainly because it could pass through the filter in the separator, thus the calculated char removal rates are lower than the actual char removal rate.
The most important difference between the experiments in the cold fluidization reactor and the H2CAP reactor is that the height of reactor zone in the cold fluidization reactor is 30 cm and 20 cm in the H2CAP unit. Considering that the total bed height with the splash zone when using 10 g char was 27 cm (see Figure K.11) indicates that char content in the bed will be below 10 g because the top layer of the char will be located in disengage zone, where the outlet pipe is.

Biomass particles with a diameter between 0 and 400 µm is most likely going to be used in the H2CAP unit, which makes the experiments with char particle size above 200 µm interesting. Unfortunately these experiments showed that these large particles are extremely difficult to remove from the reactor. However, these experiments were conducted with very low amounts of char (< 4 g), which has a significant impact on the char removal rate. Furthermore it is important to consider that the reactor zone is shorter in the H2CAP reactor, thus the char removal is most likely not going to be an insuperable problem.

References

[1] M. Rhodes, “Single Particles in a Fluid,” in *Introduction to Particle Technology*, 2nd ed., Wiley, 2008, pp. 29–49.
[2] “Wood Densities,” *The Engineering Toolbox*. [Online]. Available: http://www.engineeringtoolbox.com/wood-density-d_40.html.

Department of Chemical and Biochemical Engineering - CHEC
Technical University of Denmark

Søltofts Plads, Building 229
2800 Kgs. Lyngby
Denmark
Phone: +45 45 25 28 00

www.kt.dtu.dk